Transactions of the ASME®

Transactions of the ASME, Journal of Heat Transfer (ISSN 0022-1481) is published bi-monthly (Feb., Apr., June, Aug., Oct., Dec.) by The American Society of Mechanical Engineers, Three Park Avenue, New York, NY 10016. Periodicals postage paid at New York, NY and additional mailing offices. POSTMASTER: Send address changes to Transactions of the ASME, Journal of Heat Transfer, c/o THE AMERICAN SOCIETY OF MECHANICAL ENGINEERS, 22 Law Drive, Box 2300, Fairfield, NJ 07007-2300. **CHANGES OF ADDRESS** must be received at Society headquarters seven weeks before they are to be effective. Please send old label and new address.

Journal of Heat Transfer

Published Bimonthly by The American Society of Mechanical Engineers

VOLUME 125 • NUMBER 1 • FEBRUARY 2003

TECHNICAL PAPERS

(Contents continued on inside back cover)

This journal is printed on acid-free paper, which exceeds the ANSI Z39.48-1992 specification for permanence of paper and library materials. ♾™
♻ 85% recycled content, including 10% post-consumer fibers.

(Contents continued)

TECHNICAL NOTES

(Contents continued on facing page)

(**Contents continued**)

ERRATUM

ANNOUNCEMENTS

The ASME Journal of Heat Transfer is abstracted and indexed in the following:

Applied Science and Technology Index, AMR Journal Article Abstracts Database, Chemical Abstracts, Chemical Engineering and Biotechnology Abstracts (Electronic equivalent of Process and Chemical Engineering), Civil Engineering Abstracts, Compendex (The electronic equivalent of Engineering Index), Corrosion Abstracts, Current Contents, E & P Health, Safety, and Environment, Ei EncompassLit, Engineered Materials Abstracts, Engineering Index, Enviroline (The electronic equivalent of Environment Abstracts), Environment Abstracts, Environmental Engineering Abstracts, Environmental Science and Pollution Management, Fluidex, Fuel and Energy Abstracts, Index to Scientific Reviews, INSPEC, International Building Services Abstracts, Mechanical & Transportation Engineering Abstracts, Mechanical Engineering Abstracts, METADEX (The electronic equivalent of Metals Abstracts and Alloys Index), Petroleum Abstracts, Process and Chemical Engineering, Referativnyi Zhurnal, Science Citation Index, SciSearch (The electronic equivalent of Science Citation Index), Theoretical Chemical Engineering

Some Analytical and Numerical Solutions to Inverse Problems Applied to Optimizing Phase-Transformation Tracking in Gas Quenching

Michael Vynnycky

Jérôme Ferrari

FaxénLaboratoriet,
KTH, 100 44 Stockholm, Sweden

Noam Lior

Department of Mechanical Engineering and
Applied Mechanics,
University of Pennsylvania,
Philadelphia, PA 19104-6315

A transient inverse heat conduction problem focused on gas quenching of steel plates and rings is posed and solved, both analytically and numerically. The quenching objective is to calculate the transient convective heat transfer coefficient which would produce an optimized phase transformation cooling curve. The governing nonlinear heat equation is nondimensionalised, and a small parameter, the reciprocal of the Fourier number, is identified. This allows the construction of an analytic solution in the form of an asymptotic series. For higher values of the reciprocal Fourier number, a numerical scheme incorporating the function specification and Keller Box methods is used to generate solutions. Comparison of the results proves favorable, and suggests that for this inverse problem asymptotic methods provide an attractive alternative to solely numerical ones. [DOI: 10.1115/1.1517271]

Keywords: Inverse Heat Transfer Solutions, Gas Quenching, Heat Treatment, Metal Phase Transformation, Transient Heat Conduction

Introduction

Quenching is one of the most critical operations in the heat treatment of many metallic parts, affecting internal structure, both mechanical properties and the shape of the product. In the case of steel alloys, one desirable aim is to be able to convert austenite to martensite, while limiting the formation of pearlite and bainite, through appropriately rapid cooling of the quenched part. The cooling rate is determined by ensuring that the temperature during the cooling process never exceeds anywhere in the part the temperature which would cause transformation to undesirable phases at that location. The transformation temperatures can be found in applicable cooling-transformation phase change diagrams for the alloy in question. Practically, this leads to the prescription of a time-dependent temperature profile in the interior of the considered geometry, an objective being to find the magnitude and time dependence of the surface cooling convective heat transfer coefficient which would bring this curve about; this amounts to the formulation of an inverse heat conduction problem (IHCP). In the last decade or so, gas quenching has been gradually and increasingly developed, for environmental, quality and economical reasons to replace the traditional quenching in liquids. This process imposes new computational and fluid dynamics challenges with which FaxénLaboratoriet at the Royal Institute of Technology (KTH) has been involved for the past several years (cf. [1]). This paper presents an approach to the solution of some basic inverse heat conduction problems related to the process. Reference citations to past work related to this subject are given below in the body of the paper.

Quenched part geometries of a plate and of a ring, as in Figs. 1(*a*) and 1(*b*) respectively, with temperature-dependent thermal conductivity, are considered. Analytical and numerical approaches are adopted for the plate. Nondimensionalisation of the governing equations gives the Fourier number (Fo) as a controlling parameter which, if large enough (as is the case for thin enough rings or plates), permits the construction of an asymptotic series solution. An interesting feature here is that the inverse problem is reduced to an infinite sequence of direct initial value problems, analogous to the analytical solution of Burggraf [2], although obtained by a different approach. For smaller values of the Fourier number, a numerical approach is necessary and this is done through a novel application of the function specification method using future time steps, coupled with the Keller Box method for a nonlinear heat equation, a related linear sensitivity equation and a further variational equation. Good agreement with the heat transfer coefficient that would be required to achieve a desired cooling curve is obtained in the thin plate case, and the numerical scheme developed allows an estimate of the validity of the asymptotic method as the plate thickness is increased.

The equivalent problem for the ring is found, however, to have considerably more possibilities; amongst these is the fact that unequal cooling at its inner and outer surface can lead to a change in position of the maximum temperature point, and thence to a more intricate mathematical formulation for the inverse problem. Consequently, this problem is deferred to later work. For the case of a thin ring, however, asymptotic analytic progress is again possible and, under symmetrical heating conditions, the heat transfer coefficient required is found to differ from that for a thin plate only at $O(\mathrm{Fo}^{-3})$.

Formulation

Consider the cooling of a steel plate of thickness $2L$, initially at a uniform temperature T_i. At time $t>0$, the outer surfaces of the plate at $x=\pm L$ are subjected to cooling by means of a time-dependent heat transfer coefficient $h(t)$. Throughout the process, the ambient temperature T_∞ is assumed to be constant. One-dimensional heat conduction in the plate is then given by

$$\rho c_p(T)\frac{\partial T}{\partial t}=\frac{\partial}{\partial x}\left(k(T)\frac{\partial T}{\partial x}\right), \tag{1}$$

where, most generally, the specific heat capacity c_p and the

Contributed by the Heat Transfer Division for publication in the JOURNAL OF HEAT TRANSFER. Manuscript received by the Heat Transfer Division May 30, 2001; revision received August 5, 2002. Associate Editor: G. S. Dulikravich.

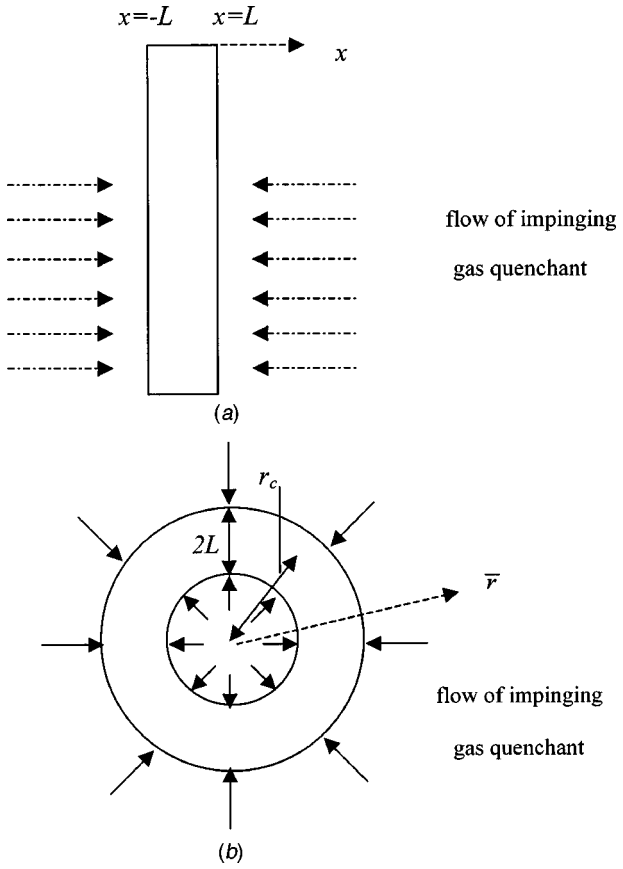

Fig. 1 Schematic of the problem for: (*a*) a plate; (*b*) a ring.

thermal conductivity k are assumed to be functions of temperature. Assuming symmetry about $x=0$, we have the boundary conditions

$$\frac{\partial T}{\partial x}=0 \quad \text{at } x=0, \tag{2}$$

$$k\frac{\partial T}{\partial x}=-h(T-T_\infty) \quad \text{at } x=L, \tag{3}$$

and the initial condition

$$T=T_i \quad \text{at } t=0. \tag{4}$$

In direct problems, $h(t)$ and T_∞, are prescribed, enabling the straightforward determination of the temperature at any location within the plate. However, of greater interest here is the inverse problem, where a certain temperature profile (meaning a temperature-time curve) is desired at a location within the plate, and an appropriate $h(t)$ must be found to satisfy this constraint. Typically, inverse heat conduction problems of this type have been motivated by the need to determine surface heat transfer coefficients from experimental measurements taken in the interior of a given body; consequently, the associated literature contains numerous contributions which deal with treating the effects of experimental uncertainty (see [3] for a comprehensive recent review). Here, on the other hand, the focus is on being able to cool the plate in such a way as to convert austenite to martensite, whilst limiting the formation of bainite and pearlite, all that at cooling rates which vary with the progress of the phase transformation in a way that tends to minimize distortion of the part and gas fan power consumption. At the simplest level, this involves coupling information derived from a metal phase transformation TTT-diagram (time-temperature-transformation) with the solution to the heat equation. For example, it is clear that martensite concentration can be maximized simply by ensuring that the hottest point of the plate follows a cooling curve lying below the pearlite and bainite 'noses,' which can be seen in Fig. 2. In quenching practice, conventionally using liquid quenchants, the cooling rate is constant and determined by the highest temperature profile slope dictated by the transformation diagram. Since it is more difficult to attain high cooling rates when using gas as quenchant, the cooling rate can be reduced during the process to achieve just the needed one. Furthermore, it is evident that this strategy would offer a better way of controlling the final composition than, for instance, cooling at a constant rate, as is given in continuous cooling transformation (CCT) diagrams such as Fig. 2. We proceed therefore by requesting

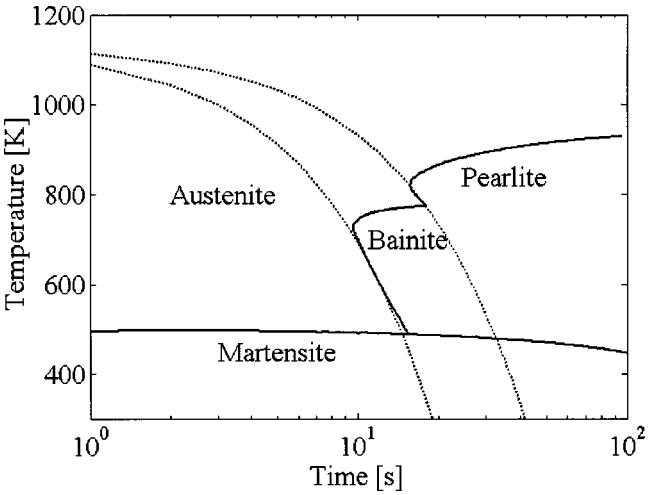

Fig. 2 CCT diagram for SAE 52100 steel

$$T=T_w(t) \quad \text{at } x=0, \tag{5}$$

where, for $0\leqslant t\leqslant t_f$, where t_f denotes the finishing time for quenching, the profile $T_w(t)$ lies below the curves for phase transformation to bainite and pearlite; for the case of a plate, it is at once clear that, in the absence of heat evolved during phase transformation, the maximum temperature will always be found at $x=0$.

Nondimensionalising with

$$X=\frac{x}{L}, \quad \tau=\frac{t}{t_f}, \quad \theta=\frac{T}{T_i},$$

we have, for $0\leqslant X\leqslant 1$ and $0\leqslant \tau\leqslant 1$,

$$\tilde{c}_p(\theta)\frac{\partial\theta}{\partial\tau}=\mathrm{Fo}\frac{\partial}{\partial X}\left(\tilde{k}(\theta)\frac{\partial\theta}{\partial X}\right), \tag{6}$$

where $\tilde{k}$ and $\tilde{c}_p$ denote, respectively, the dimensionless thermal conductivity and specific heat capacity, given by

$$\tilde{k}=\frac{k}{[k]}, \quad \tilde{c}_p=\frac{c_p}{[c_p]}.$$

Here, $[k]$ and $[c_p]$ denote characteristic values for these quantities, and are also used in the definition of the Fourier number, Fo, through

$$\mathrm{Fo}=\frac{[k]t_f}{\rho[c_p]L^2}.$$

Equation (6) is then subject to the boundary conditions

$$\frac{\partial\theta}{\partial X}=0, \quad \theta=\theta_w(\tau) \quad \text{at } X=0, \tag{7}$$

where $\theta_w=T_w/T_i$, and the initial condition

$$+gv=1 \quad \text{at } \tau=0. \tag{8}$$

As usual in the inverse formulation, Eq. (3) is used *a posteriori* to determine the required heat transfer coefficient, which in terms of the dimensionless variables is given by

$$h=-\frac{[k]}{L}\left[\tilde{k}(\theta)\frac{\partial\theta}{\partial X}\Big/(\theta-\theta_\infty)\right]_{X=1}, \tag{9}$$

where $\theta_\infty=T_\infty/T_i$.

Asymptotic Analysis for Fo $\gg$ 1: Plates

For sufficiently large values of the Fourier number, corresponding to thin plates, an asymptotic series solution is possible. Writing

$$\theta(X,\tau)=\theta_0(X,\tau)+\mathrm{Fo}^{-1}\theta_1(X,\tau)+\mathrm{Fo}^{-2}\theta_2(X,\tau)+O(\mathrm{Fo}^{-3})$$

Eq. (6), at $O(\mathrm{Fo}^0)$, is reduced to

$$\frac{\partial}{\partial X}\left(\tilde{k}(\theta_0)\frac{\partial\theta_0}{\partial X}\right)=0 \tag{10}$$

subject to

$$\frac{\partial\theta_0}{\partial X}=0, \quad \theta_0=\theta_w(\tau) \quad \text{at } X=0 \tag{11}$$

At $O(\mathrm{Fo}^{-1})$, we have

$$\tilde{c}_p(\theta_0)\frac{\partial\theta_0}{\partial\tau}=\frac{\partial}{\partial X}\left(\tilde{k}(\theta_0)\frac{\partial\theta_1}{\partial X}+\theta_1\tilde{k}'(\theta_0)\frac{\partial\theta_0}{\partial X}\right) \tag{12}$$

subject to

$$\frac{\partial\theta_1}{\partial X}=0, \quad \theta_1=0 \quad \text{at } X=0 \tag{13}$$

whilst at $O(\mathrm{Fo}^{-2})$,

$$\tilde{c}_p(\theta_0)\frac{\partial\theta_1}{\partial\tau}+\theta_1\tilde{c}_p'(\theta_0)\frac{\partial\theta_0}{\partial\tau}=\frac{\partial}{\partial X}\left(\tilde{k}(\theta_0)\frac{\partial\theta_2}{\partial X}+\theta_1\tilde{k}'(\theta_0)\frac{\partial\theta_1}{\partial X}+\left\{\theta_2\tilde{k}'(\theta_0)+\frac{1}{2}\theta_1^2\tilde{k}''(\theta_0)\right\}\frac{\partial\theta_0}{\partial X}\right) \tag{14}$$

subject to

$$\frac{\partial\theta_2}{\partial X}=0, \quad \theta_2=0 \quad \text{at } X=0 \tag{15}$$

At $O(\mathrm{Fo}^{-3})$,

$$\tilde{c}_p(\theta_0)\frac{\partial\theta_2}{\partial\tau}+\theta_1\tilde{c}_p'(\theta_0)\frac{\partial\theta_1}{\partial\tau}+\left\{\theta_2\tilde{c}_p'(\theta_0)+\frac{1}{2}\theta_1^2\tilde{c}_p''(\theta_0)\right\}\frac{\partial\theta_0}{\partial\tau}=\frac{\partial}{\partial X}\left(\tilde{k}(\theta_0)\frac{\partial\theta_3}{\partial X}+\tilde{k}'(\theta_0)\frac{\partial(\theta_1\theta_2)}{\partial X}+\frac{1}{6}\tilde{k}''(\theta_0)\frac{\partial(\theta_1^3)}{\partial X}\right)+\frac{\partial}{\partial X}\left(\left[\tilde{k}'(\theta_0)\theta_3+\tilde{k}''(\theta_0)\theta_1\theta_2+\frac{1}{6}\tilde{k}'''(\theta_0)\theta_1^3\right]\frac{\partial\theta_0}{\partial X}\right) \tag{16}$$

subject to

$$\frac{\partial\theta_3}{\partial X}=0, \quad \theta_3=0 \quad \text{at } X=0 \tag{17}$$

Here, primes denote differentiation with respect to θ.

From these, it becomes clear that we have obtained from the original inverse formulation a sequence of direct problems for the terms in the asymptotic expansion. In particular, we arrive at

$$\theta_0(X,\tau)=\theta_w(\tau) \tag{18}$$

$$\theta_1(X,\tau)=\frac{1}{2}\left(\frac{\tilde{c}_p(\theta_w)}{\tilde{k}(\theta_w)}\right)\dot{\theta}_w(\tau)X^2 \tag{19}$$

$$\theta_2(X,\tau)=\frac{\tilde{c}_p^2(\theta_w)}{24\tilde{k}^2(\theta_w)}\left(\ddot{\theta}_w+2\left\{\frac{\tilde{c}_p'(\theta_w)}{\tilde{c}_p(\theta_w)}-2\frac{\tilde{k}'(\theta_w)}{\tilde{k}(\theta_w)}\right\}\dot{\theta}_w^2\right)X^4 \tag{20}$$

where dots denote differentiation with respect to τ. These are essentially the solutions obtained by Burggraf [2], although for this paper we also evaluated θ_3 using the Maple symbolic manipulation package [4]. The subsequent expression is extremely lengthy, and we do not present it here. Using these, we can arrive at the appropriate asymptotic expansion for the heat transfer coefficient, which turns out to be of the form

$$h=\frac{[k]\mathrm{Fo}^{-1}}{L}\{h_0+\mathrm{Fo}^{-1}h_1+\mathrm{Fo}^{-2}h_2+O(\mathrm{Fo}^{-3})\}$$

where

$$h_0=-\frac{\tilde{c}_p(\theta_w)\dot{\theta}_w}{\theta_w-\theta_\infty} \tag{21}$$

$$h_1=\frac{-\tilde{c}_p^2(\theta_w)}{6\tilde{k}(\theta_w)(\theta_w-\theta_\infty)}\left[\ddot{\theta}_w+\left(2\frac{\tilde{c}_p'(\theta_w)}{\tilde{c}_p(\theta_w)}-\frac{\tilde{k}'(\theta_w)}{\tilde{k}(\theta_w)}-\frac{3}{(\theta_w-\theta_\infty)}\right)\dot{\theta}_w^2\right] \tag{22}$$

The expression for h_2 is also lengthy and not presented here.

Issues that are of some interest here are whether the solution generated in this way is stable and whether the asymptotic series is convergent. As for stability, it is well-known (e.g., [8]) that the method is unstable, since arbitrarily small changes in θ_w can lead to large errors in h. From a practical point of view, as our comparison of analytical and numerical results will show, the impact of this on the quality of the method or solution decreases as Fo increases. As for convergence, some guidelines can be obtained for the linear IHCP using the Stefan solution for θ, which can be written as

$$\theta(X,\tau)=\sum_{i=0}^{\infty}\mathrm{Fo}^{-i}\frac{d^i\theta_w}{d\tau^i}(\tau)\frac{X^{2i}}{(2i)!}. \tag{23}$$

This suggests that the solution should be convergent for all values of Fo, provided that θ_w is infinitely differentiable. For the nonlinear IHCP, however, there cannot be any corresponding statement, and the issue can only be resolved, in general numerically, on a case-by-case basis for different θ_w.

Asymptotic Analysis for Fo $\gg$ 1: Rings

We consider an analogous formulation for a quenched ring, assumed to be one-dimensional (no axial variation). Consider the cooling of a steel ring of thickness $2L$, initially at a uniform temperature T_i. At time $t>0$, the outer and the inner surfaces of the ring, taken to be at $\bar{r}=r_c\pm L$ respectively, are subjected to cooling characterized by a time-dependent heat transfer coefficient $h(t)$. One-dimensional heat conduction in the ring is then given by

$$\rho c_p(T)\frac{\partial T}{\partial t}=\frac{1}{\bar{r}}\frac{\partial}{\partial\bar{r}}\left(\bar{r}k(T)\frac{\partial T}{\partial\bar{r}}\right) \tag{24}$$

Again, we require that the maximum temperature should not exceed $T_w(t)$; however, unlike the plate, it is not possible to specify *a priori* where in the ring this will be, since there is no available symmetry condition; furthermore, it is possible that the location of

this point with maximum temperature is a function of time. Taking the heat transfer coefficients on the inner and outer surfaces to be $h_-(t)$ and $h_+(t)$ respectively, we have

$$k\frac{\partial T}{\partial \bar{r}} = \mp h_\pm(t)(T-T_\infty) \quad \text{at } \bar{r}=r_c\pm L \tag{25}$$

Nondimensionalising for t and T as before, but now with $R=\bar{r}/L$, Eqs. (24) and (25) become, respectively,

$$\tilde{c}_p(\theta)\frac{\partial\theta}{\partial\tau} = \mathrm{Fo}\frac{1}{R}\frac{\partial}{\partial R}\left(R\tilde{k}(\theta)\frac{\partial\theta}{\partial R}\right) \tag{26}$$

and

$$\left(\frac{[k]}{L}\right)\tilde{k}(\theta)\frac{\partial\theta}{\partial R} = \mp h_\pm(\tau)(\theta-\theta_\infty) \quad \text{at } R=R_c\pm 1 \tag{27}$$

where $R_c=r_c/L$.

The thin ring limit does, however, permit some analytical progress. Writing $R_c=\varepsilon^{-1}(\ll 1)$, and introducing

$$\tilde{R}=R-\frac{1}{\varepsilon}$$

we have for $-1\leqslant\tilde{R}\leqslant 1$,

$$\tilde{c}_p(\theta)\frac{\partial\theta}{\partial\tau} = \frac{\mathrm{Fo}}{1+\varepsilon\tilde{R}}\frac{\partial}{\partial\tilde{R}}\left([1+\varepsilon\tilde{R}]\tilde{k}(\theta)\frac{\partial\theta}{\partial\tilde{R}}\right) \tag{28}$$

and

$$\left(\frac{[k]}{L}\right)\tilde{k}(\theta)\frac{\partial\theta}{\partial\tilde{R}} = \mp h_\pm(\tau)(\theta-\theta_\infty) \quad \text{at } \tilde{R}=\pm 1 \tag{29}$$

This time, we have two small parameters, Fo^{-1} and ε, and the form of the asymptotic series will depend on their relative magnitudes. Typically (see physical parameters below), $\mathrm{Fo}^{-1}\sim\varepsilon$, although this feature only turns out to affect the solution at $O(\mathrm{Fo}^{-2})$, as shown below.

At $O(\mathrm{Fo}^0)$, we have

$$\frac{\partial}{\partial\tilde{R}}\left(\tilde{k}(\theta_0)\frac{\partial\theta_0}{\partial\tilde{R}}\right)=0 \tag{30}$$

subject to

$$\left(\frac{[k]}{L}\right)\tilde{k}(\theta_0)\frac{\partial\theta_0}{\partial\tilde{R}}=0 \quad \text{at } \tilde{R}=\pm 1 \tag{31}$$

Equation (30) now requires that $\tilde{k}(\theta_0)\partial\theta_0/\partial\tilde{R}$ is a function of τ, but Eq. (31) implies that the only possibility is $\partial\theta_0/\partial\tilde{R}=0$. This, combined with the requirement that the temperature should not exceed $\theta_w(\tau)$, gives as before

$$\theta_0(\tilde{R},\tau)=\theta_w(\tau) \tag{32}$$

Next, at $O(\mathrm{Fo}^{-1})$, we have

$$\tilde{c}_p(\theta_0)\frac{\partial\theta_0}{\partial\tau} = \frac{\partial}{\partial\tilde{R}}\left(\tilde{k}(\theta_0)\frac{\partial\theta_1}{\partial\tilde{R}}+\theta_1\tilde{k}'(\theta_0)\frac{\partial\theta_0}{\partial\tilde{R}}\right) \tag{33}$$

subject to

$$\tilde{k}(\theta_0)\frac{\partial\theta_1}{\partial\tilde{R}} = \mp h_{0\pm}(\tau)(\theta_0-\theta_\infty) \quad \text{at } \tilde{R}=\pm 1 \tag{34}$$

where $h_{0\pm}$ is the first term in the asymptotic series for $h_\pm$, through

$$h_\pm=\frac{[k]\mathrm{Fo}^{-1}}{L}\{h_{0\pm}+\mathrm{Fo}^{-1}h_{1\pm}+O(\mathrm{Fo}^{-2})\}$$

The general form for the solution for θ_1 will be

$$\theta_1(\tilde{R},\tau)=\frac{1}{2}\left(\frac{\tilde{c}_p(\theta_w)}{\tilde{k}(\theta_w)}\right)\dot{\theta}_w(\tau)\tilde{R}^2+A_1(\tau)\tilde{R}+B_1(\tau) \tag{35}$$

Equation (34) can be used to obtain

$$A_1(\tau)=\frac{(h_{0-}(\tau)-h_{0+}(\tau))(\theta_w-\theta_\infty)}{2\tilde{k}(\theta_w)}$$

which implies that, regardless of the form of $B_1(\tau)$, the location of the maximum temperature is to be found at

$$\tilde{R}=-\frac{(h_{0-}(\tau)-h_{0+}(\tau))(\theta_w-\theta_\infty)}{2\tilde{c}_p(\theta_w)\dot{\theta}_w}$$

Furthermore, this point will move outwards if $h_{0-}(\tau)>h_{0+}(\tau)$, inwards otherwise. Conversely, and analogous to Eq. (21), we have the result that the ring cools with the profile $\theta_w(\tau)$ at leading order provided that

$$h_{0+}(\tau)+h_{0-}(\tau)=\frac{-2\tilde{c}_p(\theta_w)\dot{\theta}_w}{(\theta_w-\theta_\infty)} \tag{36}$$

Also, to ensure that the temperature at the hottest point of the ring should not exceed $\theta_w(\tau)$, we require

$$B_1(\tau)=\frac{(h_{0-}(\tau)-h_{0+}(\tau))^2(\theta_w-\theta_\infty)^2}{8\tilde{k}(\theta_w)\tilde{c}_p(\theta_w)\dot{\theta}_w}$$

Note that in the case when $h_{0-}(\tau)=h_{0+}(\tau)$, the thin plate solution for θ_1 is recovered, as is the expression for h_0 in Eq. (21).

At $O(\mathrm{Fo}^{-2})$, setting $\varepsilon=\chi\mathrm{Fo}^{-1}$, where χ is an $O(1)$ constant, we have

$$\left(\tilde{c}_p(\theta_w)\left(\frac{\partial\theta_1}{\partial\tau}+\chi\tilde{R}\frac{\partial\theta_w}{\partial\tau}\right)+\theta_1\tilde{c}_p'(\theta_w)\frac{\partial\theta_w}{\partial\tau}\right) = \frac{\partial}{\partial\tilde{R}}\left(\tilde{k}(\theta_w)\left[\frac{\partial\theta_2}{\partial\tilde{R}}+\chi\tilde{R}\frac{\partial\theta_1}{\partial\tilde{R}}\right]+\theta_1\tilde{k}'(\theta_w)\frac{\partial\theta_1}{\partial\tilde{R}}\right) \tag{37}$$

subject to

$$\tilde{k}(\theta_w)\left(\frac{\partial\theta_2}{\partial\tilde{R}}-\frac{\theta_1}{\theta_w-\theta_\infty}\frac{\partial\theta_1}{\partial\tilde{R}}\right)+\tilde{k}'(\theta_w)\theta_1\frac{\partial\theta_1}{\partial\tilde{R}} = \mp h_{1\pm}(\theta_w-\theta_\infty) \quad \text{at } \tilde{R}=\pm 1 \tag{38}$$

We omit the remaining details here, except to comment that an equation for $h_{1-}(\tau)$ and $h_{1+}(\tau)$ analogous to Eq. (36) can be expected. Instead, we derive a solution based on the assumption that $h_-(\tau)=h_+(\tau)$. At $O(\mathrm{Fo}^0)$ and $O(\mathrm{Fo}^{-1})$, the solutions for θ_0 and θ_1, respectively, are the same as for the plate, but from Eq. (37) we see that θ_2 will have an antisymmetric component due to ring curvature. Proceeding as before, we have

$$\theta_2(\tilde{R},\tau)=\frac{\tilde{c}_p^2(\theta_w)}{24\tilde{k}^2(\theta_w)}\left(\ddot{\theta}_w+2\left\{\frac{\tilde{c}_p'(\theta_w)}{\tilde{c}_p(\theta_w)}-2\frac{\tilde{k}'(\theta_w)}{\tilde{k}(\theta_w)}\right\}\dot{\theta}_w^2\right)\tilde{R}^4 - \frac{\chi\tilde{c}_p(\theta_w)\dot{\theta}_w}{6\tilde{k}(\theta_w)}\tilde{R}^3+A_2(\tau)\tilde{R}+B_2(\tau) \tag{39}$$

From Eq. (38), we have

$$A_2(\tau)=\frac{\chi\tilde{c}_p(\theta_w)\dot{\theta}_w}{2\tilde{k}(\theta_w)} \tag{40}$$

with $B_2(\tau)$ being chosen to ensure that $\theta_2(\tilde{R},\tau)$ is everywhere negative. Finally, we arrive at

$$h_1=\frac{-\tilde{c}_p^2(\theta_w)}{6\tilde{k}(\theta_w)(\theta_w-\theta_\infty)}\left[\ddot{\theta}_w+\left(2\frac{\tilde{c}_p'(\theta_w)}{\tilde{c}_p(\theta_w)}-\frac{\tilde{k}'(\theta_w)}{\tilde{k}(\theta_w)}-\frac{3}{(\theta_w-\theta_\infty)}\right)\dot{\theta}_w^2\right] \tag{41}$$

indicating that although the temperature is affected by the curvature at this order, the heat transfer coefficient is not.

Numerical Solution

In what follows, the analytical solutions presented above are used to test our numerical scheme for the solution of the inverse problem. Furthermore, the availability of both analytical and numerical methods provides an estimate of the range of validity of the asymptotic series.

Numerous algorithms can be found in the literature for the nonlinear IHCP. Amongst these are the function specification method [9], space-marching techniques [6] and those based on the infinite dimensional adjoint method [7]. Here, we develop a variant on existing methods, in that we implement the function specification method [9] by means of the Keller Box scheme [10] and Newton iteration, a combination which, in spite of its versatility for the solution of nonlinear parabolic direct problems, appears not to have been used at all for inverse problems of this type. In fact, the method proves to be particularly suitable for handling the resulting sensitivity equations, as well as for updating the latest surface heat flux iterate, as shown below. In addition, it is not necessary to employ quasi-linearization of the temperature-dependent properties, as has been done in some numerical schemes [5,11,12]; this feature is desirable, since it ensures that the scheme remains second-order accurate in both time and space variables, which becomes of increasing importance if the thermal properties vary strongly with temperature. Thus, our treatment of the direct problem is accurate as it can be without going to higher-order schemes, and accuracy is only limited by the nature of the inverse algorithm, which is known to be unstable if too small time steps are used [9]; for details regarding numerical uncertainty, therefore, we refer to [9]. In what follows, we consider plate solutions, where the location of the maximum temperature is known; solutions for rings are postponed for future work.

Writing Eq. (6) as the two first-order equations

$$Q=\frac{\partial\theta}{\partial X} \tag{42}$$

$$\tilde{c}_p(\theta)\frac{\partial\theta}{\partial\tau}=\mathrm{Fo}\frac{\partial}{\partial X}(\tilde{k}(\theta)Q) \tag{43}$$

and introducing a rectangular mesh with grid points at $(\tau_j)_{j=0,\ldots,M}$ and $(X_i)_{i=0,\ldots,N}$, where M and N are the number of points in τ and X respectively, the function specification method proceeds as follows. Assuming that θ and Q have been determined for $0\leqslant\tau\leqslant\tau_{m-1}$, where $1\leqslant m\leqslant M$, we temporarily assume that $Q_{N,k}=\beta$ for r future time steps $(\tau_{m-1}\leqslant\tau\leqslant\tau_{m-1+r})$, and solve the direct problem for $\tau=\tau_m,..,\tau_{m-1+r}$, with the boundary conditions $Q_{N,k}=\beta$ and $Q_{0,k}=\beta$ $(k=m,..,m-1+r)$. Next it is required to minimize the functional

$$S:=\sum_{l=1}^{r}(\theta_{0,m-1+l}-\theta_w(\tau_{m-1+l}))^2 \tag{44}$$

with respect to β; this requires $\partial S/\partial\beta=0$, i.e.,

$$\sum_{l=1}^{r}(\theta_{0,m-1+l}-\theta_w(\tau_{m-1+l}))\frac{\partial\theta_{0,m-1+l}}{\partial\beta}=0$$

which in turn requires knowledge about the sensitivity coefficients, i.e., the function $\partial\theta/\partial\beta$.

Defining $\tilde{\theta}:=\partial\theta/\partial\beta$ and $\tilde{Q}:=\partial Q/\partial\beta$, we obtain the governing equation for $\tilde{\theta}$ by differentiating Eqs. (42) and (43) with respect to β to obtain

$$\tilde{Q}=\frac{\partial\tilde{\theta}}{\partial X} \tag{45}$$

$$\left(\tilde{c}_p(\theta)\frac{\partial\tilde{\theta}}{\partial\tau}+\tilde{c}_p'(\theta)\tilde{\theta}\frac{\partial\theta}{\partial\tau}\right)=\mathrm{Fo}\frac{\partial}{\partial X}(\tilde{k}(\theta)\tilde{Q}+\tilde{k}'(\theta)\tilde{\theta}Q) \tag{46}$$

This is subject to the boundary conditions

$$\left.\begin{aligned}\tilde{Q}&=0 \quad \text{at } X=0\\ \tilde{Q}&=1 \quad \text{at } X=1\end{aligned}\right\} \quad \text{for} \quad \tau_m\leqslant\tau\leqslant\tau_{m-1+r} \tag{47}$$

and the initial condition

$$\tilde{\theta}=0 \quad \text{at} \quad \tau=\tau_{m-1} \tag{48}$$

This constitutes a linear direct problem for $\tilde{\theta}$ and $\tilde{Q}$ which needs to be solved at every time step; this is in contrast to the linear IHCP for which the sensitivity coefficients can be determined once and for all with just one *a priori* computation.

Now writing

$$\varphi:=\sum_{l=1}^{r}(\theta_{0,m-1+l}-\theta_w(\tau_{m-1+l}))\tilde{\theta}_{0,m-1+l} \tag{49}$$

we require $\varphi=0$, for which an iterative loop for β is required. Denoting by v the iteration index for β, we update β using Newton iteration according to

$$\beta^{(v+1)}=\beta^{(v)}-\varphi\Big/\frac{\partial\sigma}{\partial\beta}$$

where

$$\frac{\partial\varphi}{\partial\beta}=\sum_{l=1}^{r}(\theta_{0,m-1+l}-\theta_w(\tau_{m-1+l}))\frac{\partial\tilde{\theta}_{0,m-1+l}}{\partial\beta}+\sum_{l=1}^{r}\tilde{\theta}_{0,m-1+l}^2$$

For the linear IHCP, the sensitivity coefficients are independent of β, so that $\partial\varphi/\partial\beta$ would already be available, since $\tilde{\theta}$ has already been solved for. For the nonlinear IHCP, this is not the case, and additional variational equations for

$$\hat{\theta}:=\frac{\partial\tilde{\theta}}{\partial\beta},\quad \hat{Q}:=\frac{\partial\tilde{Q}}{\partial\beta}$$

have to be solved. Differentiating Eqs. (45)–(48) with respect to β gives

$$\hat{Q}=\frac{\partial\hat{\theta}}{\partial X} \tag{50}$$

$$\left(\tilde{c}_p(\theta)\frac{\partial\hat{\theta}}{\partial\tau}+\tilde{c}_p'(\theta)\hat{\theta}\frac{\partial\theta}{\partial\tau}\right)=\mathrm{Fo}\frac{\partial}{\partial X}(\tilde{k}(\theta)\hat{Q}+\tilde{k}'(\theta)\hat{\theta}Q)+q \tag{51}$$

where

$$q=\mathrm{Fo}\frac{\partial}{\partial X}(2\tilde{k}'(\theta)\tilde{\theta}\tilde{Q}+\tilde{k}''(\theta)\tilde{\theta}^2Q)-2\tilde{c}_p'(\theta)\tilde{\theta}\frac{\partial\tilde{\theta}}{\partial\tau}-\tilde{c}_p''(\theta)\tilde{\theta}^2\frac{\partial\theta}{\partial\tau}$$

subject to the boundary conditions

$$\left.\begin{aligned}\hat{Q}&=0 \quad \text{at } X=0\\ \hat{Q}&=0 \quad \text{at } X=1\end{aligned}\right\} \quad \text{for} \quad \tau_m\leqslant\tau\leqslant\tau_{m-1+r} \tag{52}$$

and the initial condition

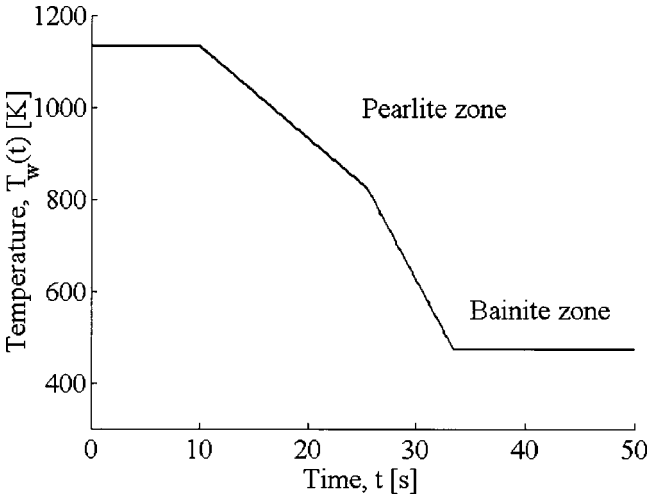

Fig. 3 Cooling curve used in this study

$$\hat{\theta}=0 \quad \text{at} \quad \tau=\tau_{m-1} \tag{53}$$

This also constitutes a linear direct problem for $\hat{\theta}$ and $\hat{Q}$ which needs to be solved at every time step.

Finally in this section, we note the computational budget for this method in order to advance one time step, relative to the budget for a one-step advance for the nonlinear direct problem. With the convergence criterion at the jth time step for Eqs. (42) and (43) taken to be

$$\max_{i=0,\ldots,N} \quad (|\theta_{i,j}^{(n+1)}-\theta_{i,j}^{(n)}|,|Q_{i,j}^{(n+1)}-Q_{i,j}^{(n)}|)<10^{-9}$$

the number of Newton iterations N_{newt} was typically found to be 3–4. However, a one time-step advance for the nonlinear inverse problem requires

1) Eqs. (42) and (43) to be solved over r time steps (rN_{newt} operations);

2) Eqs. (45) and (46) to be solved over r time steps (r operations);

3) Eqs. (50) and (51) to be solved over r time steps (r operations);

4) steps 1–3 to be repeated until convergence for β is obtained ($rN_{\text{var}}(N_{\text{newt}}+2)$ operations.

Here, one "operation" is denoted to mean the solution of $(M+1)$ linear equations, either those arising from the linearisation in step 1, or those in steps 2 and 3. In summary, the total budget ratio is found to be

$$\frac{rN_{\text{var}}(N_{\text{newt}}+2)}{N_{\text{newt}}}$$

so that, with N_{var} also typically 3–4, approximately $6r$ as many operations are required to solve the inverse problem as are required to solve the direct problem. For the majority of computations carried out here, we took $M=201$, $N=100$, and $r=4$; with these specifications, a solution was obtained within several seconds on a 500 MHz Compaq Alphaserver with 3GB RAM. Additional computations for $N=200$ were also carried out to test for grid independence in respect of the space variable, X; no difference was observed between results for $N=100$ and $N=200$, and subsequently only the coarser mesh was used. Of considerably greater significance is the total future time $r\Delta\tau$, where $\Delta\tau$ is the mesh spacing in time; here, a uniform mesh was used throughout, so that $\Delta\tau=1/(M-1)$. The results of investigations of this combined effect are given in the next section. Additionally, since the numerical scheme is second-order accurate, we have that the numerical uncertainty for all the runs is $O(10^{-4})$.

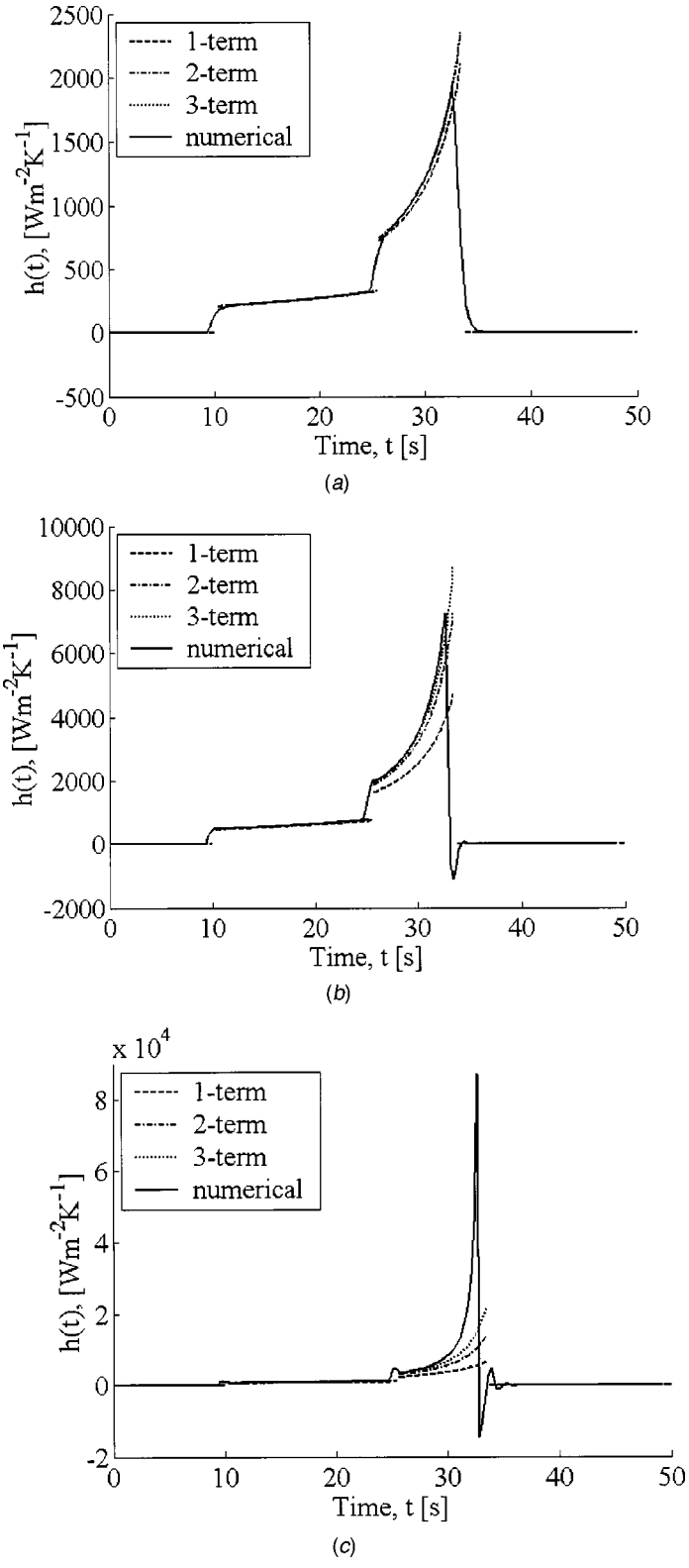

Fig. 4 The required convective heat transfer coefficient, $h(t)$, as calculated by the analytical method using 1, 2, and 3 series expansion terms, and by a numerical method: (*a*) $\text{Fo}^{-1}=0.02$; (*b*) $\text{Fo}^{-1}=0.1$; and (*c*) $\text{Fo}^{-1}=0.2$.

As for numerical validation of the scheme, this is provided in the next section through comparison with truncations of the asymptotic series. In addition, the code was checked against the

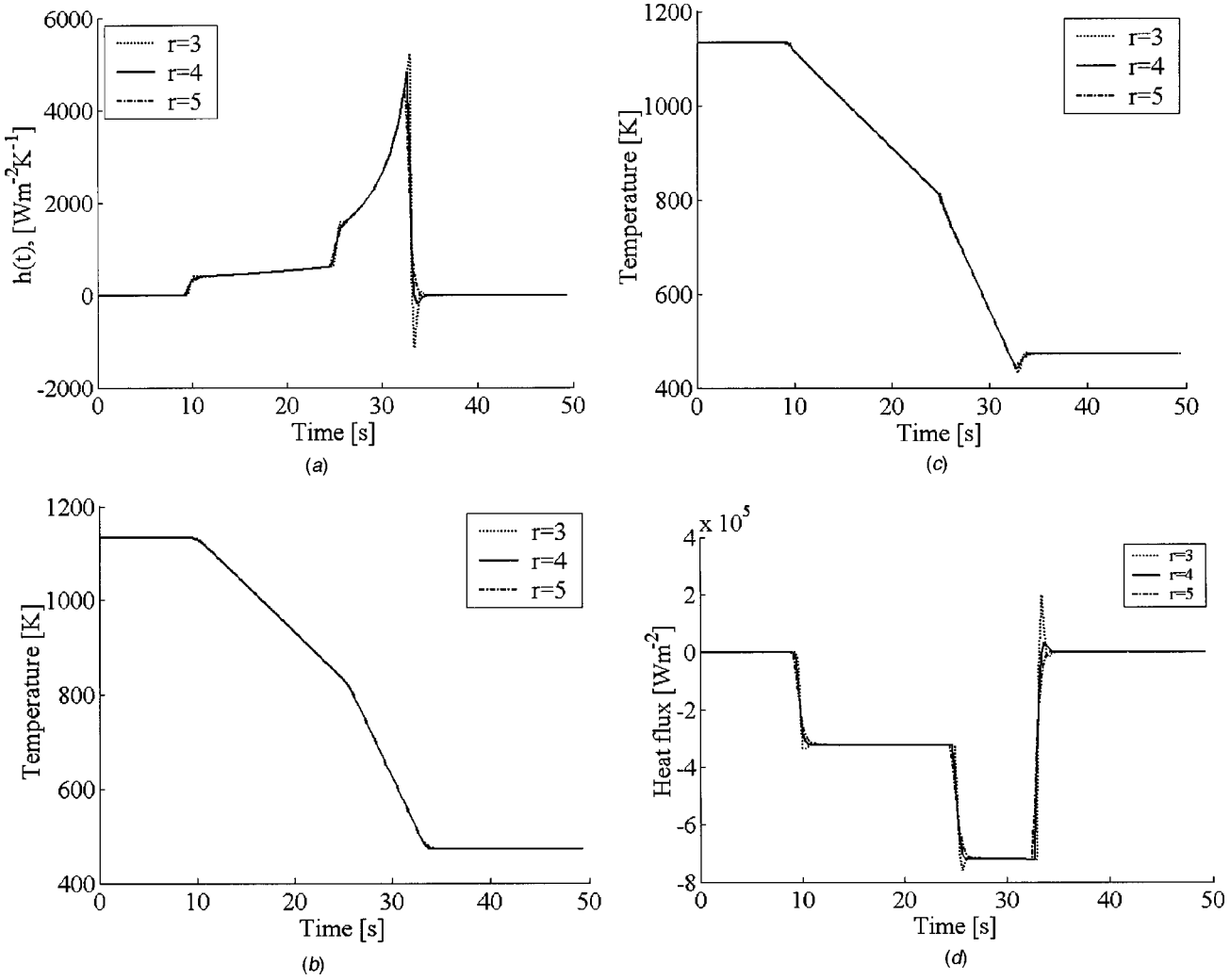

Fig. 5 Selected quantities as numerically computed for 3, 4, and 5 future time steps in the model ($Fo^{-1}=0.07$): (*a*) the convective heat transfer coefficient, $h(t)$, at $x=L$; (*b*) the temperature, $T_w(t)$, at $x=0$; (*c*) the surface temperature at $x=L$; and (*d*) the surface heat flux at $x=L$.

test case of a triangular heat flux given in [9] (e.g., see p. 169), and excellent agreement was found, although for the sake of brevity we do not present the results here.

Results

The analytical and numerical considerations given above are implemented for the quenching of SAE 52100 steel. The physical properties used are:

$$k(T)=k_0+k_1T,\quad c_p(T)=c_0 \tag{54}$$

so that $[k]=k_0$, $[c_p]=c_{0,}$ and then

$$\tilde{k}(\theta)=1+\mu\theta,\quad \tilde{c}_p(\theta)=1$$

where $\mu=k_1T_i/k_0$. We take $T_i=860$ C, $T_i=20$ C, $t_f=50$ s, $c_0=635$ Jkg^{-1} C^{-1}, $k_0=15.0$ Wm^{-1} C^{-1}, $k_1=0.0142$ Wm^{-1} C^{-2}, $\rho=7810$ kgm^{-3}. As for geometrical parameters, the computations are based around the quenching of a ring with inner radius 0.028 m and outer radius 0.034 m. Consequently, we have $L=0.003$ m and $r_c=0.031$ m, and so $Fo^{-1}\approx 0.07$, $\varepsilon\approx 0.1$. Thus, although we present only solutions for a plate, they should constitute good first approximations to a ring of the same thickness.

Results are presented for the cooling curve shown in Fig. 3, which has been constructed in such a way that it approaches the 1 percent pearlite ''nose'' more closely than would a conventional constant cooling curve and thus allow slowest cooling rates (which is industrially desirable both to minimize cooling cost and product distortion); after that, more rapid cooling is used to avoid the 1 percent bainite ''nose.'' Using Eqs. (21) and (22), we have

$$h_0=\frac{-\dot{\theta}}{\theta_w-\theta_\infty}$$

$$h_1=\frac{-1}{6(1+\mu\theta_w)(\theta_w-\theta_\infty)}\left[\ddot{\theta}_w-\frac{\mu\dot{\theta}_w^2}{(1+\mu\theta_w)}-\frac{3\dot{\theta}_w^2}{(\theta_w-\theta_\infty)}\right]$$

It is instructive to discuss the behavior of the solution in terms of the value of Fo^{-1}. This is done in Figs. 4(*a–c*), which compare the heat transfer coefficients for the asymptotic analytical solution and the numerical solution for $Fo^{-1}=0.02$, 0.1, and 0.2, respectively.

In Fig. 4(*a*), good agreement is obtained between the results of the numerical method and the one and two-term expansions of the analytical method. At gradient discontinuities of $T_w(t)$, the analytical method gives discontinuities in $h(t)$, whereas the numerical scheme smoothes these out. Note here the interpretations of the solution behavior at each of these three discontinuities. For the first two, the behavior is similar, with a moderately rapid increase in the heat transfer coefficient profile being necessary to attain the desired temperature profile; at the third, however, an initially

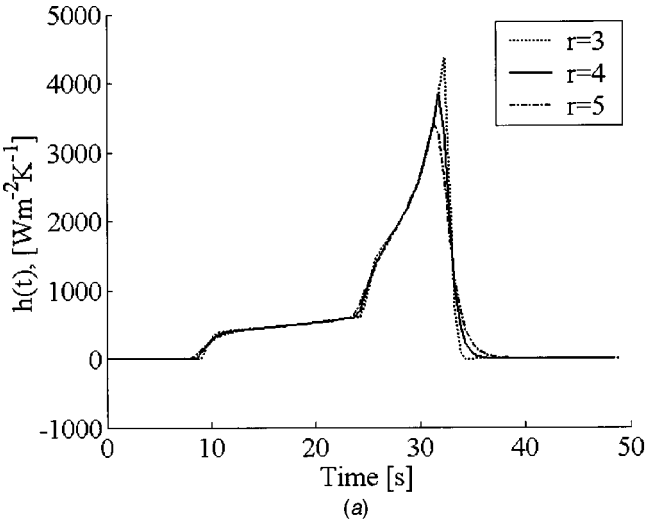

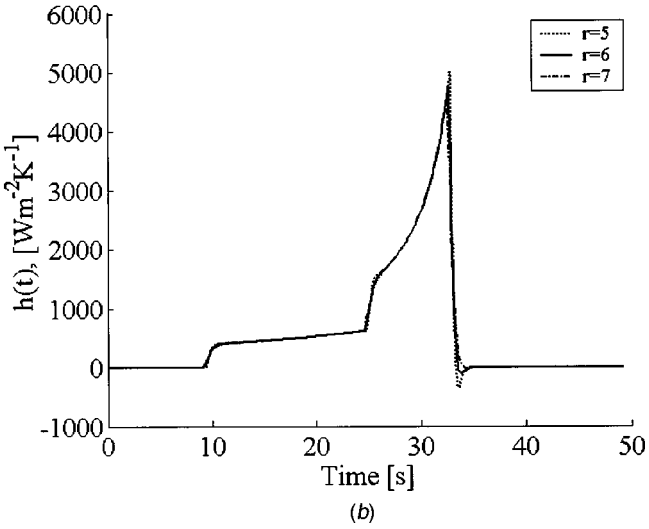

Fig. 6 The convective heat transfer coefficient, $h(t)$, at $x=L$ for $Fo^{-1}=0.07$ with: (*a*) $\Delta\tau=1/100$, $r=3, 4, 5$; and (*b*) $\Delta\tau=1/300$, $r=5, 6, 7$.

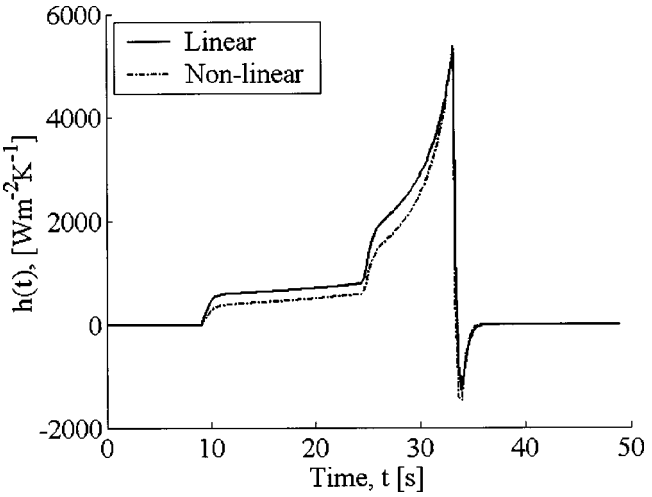

Fig. 7 Comparison of the numerically computed convective heat transfer coefficient with constant ("linear") and temperature-dependent ("nonlinear") thermal conductivity ($Fo^{-1}=0.07, r=4$)

negative value, corresponding to heating, is required. Note also that the peak prior to this discontinuity is not due to the discontinuity itself, but simply as a consequence of the fact that θ_w is decreasing whilst $\dot{\theta}_w$ is constant (cf. Eq. (21)).

Increasing Fo^{-1} further to $Fo^{-1}=0.1$, Fig. 4(*b*) shows that, for the final part of the quenching curve, an oscillation in $h(t)$ appears in order to maintain the desired temperature of 200°C; this we interpret as an instability in our numerical scheme which arises as Fo^{-1} is increased, in combination with the sudden jump in the gradient of $T_w(t)$. Prior to this, we see that the three truncated asymptotic series agree well with the numerical solution until 25 s, but then the one-term series severely underpredicts the required heat transfer coefficient; the two-term series performs significantly better, and the three-term series better still, but it appears that more terms in the asymptotic expansion would be necessary to provide even better agreement.

In Fig. 4(*c*) for $Fo^{-1}=0.2$, it becomes even clearer that further terms in the asymptotic expansion must be added, although as in Fig. 4(*b*) the trend appears to be in the right direction. An important mathematical point here is that since the asymptotic solution is composed of analytical solutions to ordinary differential equations, it is free of the oscillations that a numerical solution to a partial differential equations may possess due, for example, to unsmooth boundary conditions; as a consequence, the asymptotic series may provide a useful, and often very accurate, approximation to the full numerical solution, provided enough terms are calculated. For this case, the numerical instability mentioned in Fig. 4(*b*) appears to be even more severe for $r=4$, with oscillations occurring at all three gradient discontinuities of $T_w(t)$. However, as shown below, the way to alleviate these appears to be to increase the value of r.

We give also some results for a plate for which $Fo^{-1}=0.07$. Fig. 5(*a*) demonstrates the effect of the number of future time steps used, r, on the heat transfer coefficient; the effect appears to be noticeable only at the gradient discontinuities of $T_w(t)$, but we notice here that increasing r from 3 to 5 removes the unphysical oscillation at $t=33$ s. Figure 5(*b*) gives a comparison of the specified temperature $T_w(t)$, with that actually computed numerically for $r=3,4,5$. Note here that whilst the numerical scheme copes well with the first two gradient discontinuities, it copes less well with the third, with the functional S in Eq. (44) being minimized in such a way that the computed temperature undershoots the desired profile (cf. Fig. 3), although the extent of the undershoot decreases with increased r. Fig. 5*c* gives the temperature profile at the quenched surface, and a comparison of Figs. 5(*b*) and 5(*c*) indicates the extent to which plate is a lumped body. Fig. 5(*d*) shows the heat flux at the quenched surface; here, as in Fig. 5(*a*), the higher values of r appear to confer increased stability on the solution at the gradient discontinuities of $T_w(t)$.

Figures 6(*a*) and 6(*b*), in tandem with Fig. 5(*a*), explore the combined effect of $r\Delta\tau$ on the solution for $Fo^{-1}=0.07$. As is evident, all perform in qualitatively similar fashion, but perhaps the most interesting quantitative conclusion concerns the stability of the scheme near $t=33$ s. In particular, the common feature we find is that the non-physical oscillations in $h(t)$ there can be removed provided that $r\Delta\tau$ exceeds a certain critical value: in Fig. 5(*a*), this value is in the range [0.02,0.025]; for Fig. 6(*a*), [0.033,0.04]; for Fig. 6(*b*) [0.02,0.0233].

Finally, Fig. 7 compares the results of a nonlinear computation, using Eq. (54), with those of a linear one where the thermal conductivity is taken to be

$$k(T)\equiv k_0+k_1T_{av}$$

where $T_{av}=530°C$, the average of the start and end temperatures. As is apparent, for this particular case, the linear formulation leads to an underestimate in the heat transfer coefficient required to obtain the desired quenching conditions.

Conclusions

This paper has considered a one-dimensional nonlinear inverse heat conduction problem in the industrial process of quenching, using both analytical and numerical methods. The governing equations were nondimensionalised and the Fourier number (Fo) was identified as a key controlling dimensionless parameter. Asymptotic series could be constructed using this parameter, and these were found on the whole to compare well with results from a numerical scheme that was also implemented. The nature of the cooling temperature profile used, a piecewise linear function of time, indicates some of the features of inverse problems with unsmooth boundary conditions: whilst both methods agree well on smooth portions of the cooling profile, difficulties were encountered with the numerical scheme at gradient discontinuities, although not necessarily so. Associated with this is the number of future time steps, r, that were required. Where the cooling curve is smooth, $r=3$ was sufficient; otherwise, as many as 5 or 6 were necessary to stabilize the solution after a gradient discontinuity, and our experiences show that higher values of Fo^{-1}, corresponding to thicker geometries, lead to greater difficulties in this respect. As for the asymptotic series, it proved advisable to use a symbolic manipulator to compute its terms, since the algebra becomes exceedingly lengthy after just a couple of terms. However, a two-term series appeared to be sufficient for predicting the heat transfer coefficient to within a couple of percent for Fo as high as 10 for the cooling curves used here.

This work is our first attempt to couple heat transfer to the control of phase transformations in quenching in an inverse way, i.e., by predicting the convective heat transfer coefficient that would be necessary to produce a quenched product with a desired composition, and which follows the progress of the phase transformation in a way which tends to optimize the process (see, for instance, [13] for another example, although not related to quenching). The plate/ring quenching analogy provided here was useful for sufficiently large values of the Fourier number, although solutions were presented mainly for the plate. Finally, we should note the advantages of the twin analytical/numerical approach presented here. In particular, nondimensionalisation identifies the magnitudes of key controlling parameters, and thence possibly simple closed-form series solutions that would not have been evident from the original formulation. These solutions can then serve as a quantitative check against numerical algorithms for the IHCP; in fact, to the authors' knowledge, this may well be the first time that this has been done. In particular, we note how the approaches complement each other as Fo^{-1} is increased (cf. Figs. 4(a–c): the numerical approach gives the desired solution, although this can prove unreliable as a singularity in the boundary conditions is reached; at this point, the analytical solution can provide a guide as to how the desired solution should behave. In addition, the fact that we have implemented the versatile and efficient Keller Box scheme within an inverse problem setting indicates that it should be possible to incorporate, in an expedient way, more of the physical features associated with gas quenching, such as phase transformations and distortion.

Naturally, a full treatment of a coupled inverse/optimization problem of this sort in gas quenching would involve the inverse prediction of the optimal time-dependent heat transfer coefficients in three dimensions for arbitrary complex geometries, with all physical phenomena modeled in the numerical simulation. Nevertheless, the validation of computer codes for such calculations would require benchmark comparisons in simple geometries, such as those presented here. Finally, the algorithm presented would be useful in practice in reducing computational time for inverse problems involving simpler geometries, where there is no need to use the full multidimensional functionality typically provided in vendor software.

Acknowledgment

This work was partially supported by AGA AB, SKF Engineering and Research Center, B.V., Volvo Personvagnar Komponenter AB and Ipsen International GmbH.

Nomenclature

$c_p(T)$ = temperature-dependent specific heat capacity, $\mathrm{Jkg}^{-1}\mathrm{K}^{-1}$
$\tilde{c}_p(\theta)$ = dimensionless temperature-dependent dimensionless specific heat capacity
$[c_p]$ = specific heat capacity scale, $\mathrm{Jkg}^{-1}\mathrm{K}^{-1}$
Fo = Fourier number
$h(t)$ = time-dependent heat transfer coefficient, $\mathrm{Wm}^{-2}\mathrm{K}^{-1}$
$(h_i)_{i=0,1,..}$ = terms in the asymptotic expansion for $h(t)$
$h_{\pm}(t)$ = time-dependent heat transfer coefficient on inner and outer ring surfaces, $\mathrm{Wm}^{-2}\mathrm{K}^{-1}$
$(h_{i\pm})_{i=0,1,.}$ = terms in the asymptotic expansion for $h_{\pm}(t)$
$k(T)$ = temperature-dependent thermal conductivity, $\mathrm{Wm}^{-1}\mathrm{K}^{-1}$
$\tilde{k}(\theta)$ = dimensionless temperature-dependent dimensionless thermal conductivity
$[k]$ = thermal conductivity scale, $\mathrm{Wm}^{-1}\mathrm{K}^{-1}$
L = plate/ring half thickness, m
M = number of points for discretisation in τ
N = number of points for discretisation in X
N_{newt} = number of Newton iterations for Eqs. (42) and (43)
N_{var} = number of times that the variational equations (50) and (51) are solved
q = source term in Eq. (51)
Q = $\partial\theta/\partial X$
$\tilde{Q}$ = $\partial Q/\partial\beta$
$\hat{Q}$ = $\partial\tilde{Q}/\partial\beta$
r = radial coordinate (ring), m
R = dimensionless radial coordinate (ring)
$\tilde{R}$ = scaled dimensionless radial coordinate (ring)
r_c = average ring radius, m
R_c = dimensionless average ring radius
r = number of future time steps used for the function specification method
S = functional defined in Eq. (44)
t = time, s
T = temperature, K
t_f = quenching end time, seconds
T_i = initial uniform temperature, K
$T_w(t)$ = time-dependent desired quenching temperature, K
T_∞ = ambient temperature, K
x = normal coordinate (plate), m
X = dimensionless normal coordinate (plate)
β = guess for $\partial\theta/\partial X$ at quenched surface
ε = reciprocal of the dimensionless average ring radius (R_c^{-1})
θ = dimensionless temperature
$\tilde{\theta}$ = $\partial\theta/\partial\beta$
$\hat{\theta}$ = $\partial\tilde{\theta}/\partial\beta$
$\theta_w(\tau)$ = dimensionless desired quenching temperature
$(\theta_i)_{i=0,1,.}$ = terms in the asymptotic expansion for θ
θ_∞ = dimensionless ambient temperature
ρ = density, kgm^{-3}
τ = dimensionless time
φ = functional defined in Eq. (49)
χ = $O(1)$ constant ($\varepsilon\mathrm{Fo}$)

References

[1] Thuvander, A., Melander, A., Lind, M., Lior, N., and Bark, F., 1999, "Prediction of Convective Heat Transfer Coefficients and Their Effects on Distortion

and Mechanical Properties of Cylindrical Steel Bodies Quenched by Gas Cooling,'' Paper AJTE99-6289, presented at ASME/JSME Joint Thermal Engng. Conf., San Diego, CA, March 15–19, 1999.
[2] Burggraf, O. R., 1964, ''An Exact Solution of the Inverse Problem in Heat Conduction Theory and Applications,'' ASME J. Heat Transfer, **86C**, pp. 373–382.
[3] Özişik, M. N., and Orlande, H. R. B., 2000, *Inverse Heat Transfer*, Taylor & Francis, New York.
[4] http://www.maplesoft.com
[5] Beck, J. V., Litkouhi, B., and St. Clair, C. R., Jr., 1982, ''Efficient Sequential Solution of the Nonlinear Inverse Heat Conduction Problem,'' Numer. Heat Transfer, **5**, pp. 275–286.
[6] Raynaud, M., and Bransier, J., 1986, ''A New Finite-Difference Method for the Nonlinear Inverse Heat Conduction Problem,'' Numer. Heat Transfer, **9**, pp. 27–42.
[7] Jarny, Y., Özişik, M. N., and Bardon, J. P., 1991, ''A General Optimization Method Using Adjoint Equation for Solving Multidimensional Inverse Heat Conduction,'' Int. J. Heat Mass Transf., **34**, pp. 2911–2919.
[8] Alifanov, O. M., 1994, *Inverse Heat Transfer Problems*, Springer-Verlag.
[9] Beck, J. V., Blackwell, B., and St. Clair, C. R., Jr., 1985, *Inverse Heat Conduction-III Posed Problems*, Wiley, New York.
[10] Cebeci, T., and Bradshaw, P., 1984, *Physical and Computational Aspects of Convective Heat Transfer*, Springer, Berlin.
[11] Archambault, P., and Azim, A., 1995, ''Inverse Resolution of the Heat-Transfer Equation: Application to Steel and Aluminum Alloy Quenching,'' J. Mater. Eng. Perform., **4**, pp. 730–736.
[12] Archambault, P., Denis, S., and Azim, A., 1997, ''Inverse Resolution of the Heat-Transfer Equation With Internal Heat Source: Application to the Quenching of Steels With Phase Transformations,'' J. Mater. Eng. Perform., **6**, pp. 240–246.
[13] Matsevityi, Y. M., Multanovskii, A. V., and Nemirovskii, I. A., 1991, ''Optimization of the Heat-Engineering Processes Involving Utilization of Control and Identification Methods,'' J. Eng. Phys., **59**, pp. 1055–1063.

Nusselt Number Behavior on Deep Dimpled Surfaces Within a Channel

N. K. Burgess

M. M. Oliveira

P. M. Ligrani

Convective Heat Transfer Laboratory,
Department of Mechanical Engineering,
MEB 2202, 50 S. Central Campus Drive,
University of Utah,
Salt Lake City, UT 84112-9208

Experimental results, measured on a dimpled test surface placed on one wall of a channel, are given for a ratio of air inlet stagnation temperature to surface temperature of approximately 0.94, and Reynolds numbers R_{eH} *from 12,000 to 70,000. These data include friction factors, local Nusselt numbers, spatially-resolved local Nusselt numbers, and globally-averaged Nusselt numbers. The ratio of dimple depth to dimple print diameter* δ/D *is 0.3, and the ratio of channel height to dimple print diameter is 1.00. These results are compared to measurements from other investigations with different ratios of dimple depth to dimple print diameter* δ/D *to provide information on the influences of dimple depth. At all Reynolds numbers considered, local and spatially-resolved Nusselt number augmentations increase as dimple depth increases (and all other experimental and geometric parameters are held approximately constant). These are attributed to: (i) increases in the strengths and intensity of vortices and associated secondary flows ejected from the dimples, as well as (ii) increases in the magnitudes of three-dimensional turbulence production and turbulence transport. The effects of these phenomena are especially apparent in local Nusselt number ratio distributions measured just inside of the dimples, and just downstream of the downstream edges of the dimples.* [DOI: 10.1115/1.1527904]

Keywords: Fluids, Heat Transfer, Internal, Turbines, Vortex

Introduction

Dimples are used on the surfaces of internal flow passages because they produce substantial heat transfer augmentations, with pressure drop penalties which are smaller than other types of heat augmentation devices, such as rib turbulators. Arrays of dimples accomplish this: (i) by ejecting multiple pairs of vortices, which increase local, three-dimensional turbulence transport, as they advect downstream, and (ii) by not protruding into the flow, and therefore, by not increasing losses due to form drag [1]. Also important are the unsteadiness associated with vortex pair shedding, and the reattachment of the shear layer which forms across the top of each dimple. Dimples are also attractive heat transfer augmentation devices because they generally require uncomplicated manufacturing procedures, particularly if the dimple shape is a spherical indentation. Because of this characteristic, dimples do not add extra weight onto a component, especially if surface material is removed to form the dimples. On thinner materials, an indentation producing device can be used to form the dimples, which then gives protrusions on the opposite side. This then leads to another advantage because substantial heat transfer augmentations are also provided by the array of protrusions.

A number of heat transfer studies from Russia utilize dimples. These studies employ flows over flat walls with regular arrays of spherical pits [2], flows in annular passages with a staggered array of concave dimples on the interior cylindrical surface [3], flows in single hemispherical cavities [4,5], flows in diffuser and convergent channels each with a single hemispherical cavity [6], and flows in a narrow channel with spherically shaped dimples placed in relative positions on two opposite surfaces [7]. Heat transfer augmentations as high as 150 percent, compared to smooth surfaces, are reported, sometimes with appreciable pressure losses [3].

More recently, Chyu et al. [8] present data on the influences of Reynolds number on local heat transfer coefficient distributions on surfaces imprinted with staggered arrays of two different shapes of concavities. In some cases, enhancement of the overall heat transfer rate is about 2.5 times smooth surface values over a range of Reynolds numbers, and pressure losses are about half the values produced by conventional rib turbulators. Lin et al. [9] present computational simulation results of the flow structures, flow streamlines, temperature distributions, and resulting surface heat transfer distributions for the same geometries and flow conditions. Moon et al. [10] give data that illustrate the effects of channel height on heat transfer and pressure losses on a surface with a staggered pattern of dimples. According to the investigators, improvements in heat transfer intensification and pressure losses remain at approximately constant levels over the ranges of Reynolds number and channel height investigated. Mahmood et al. [1] describe the mechanisms responsible for local and spatially-averaged heat transfer augmentations on flat channel surfaces with an array of dimples on one wall. Only one channel height, equal to 50 percent of the dimple print diameter, is used in the investigation.

In the present study, spatially-resolved surface Nusselt numbers, spatially-averaged surface Nusselt numbers, and friction factors are presented for a stationary channel with an aspect ratio of 8, and an array of dimples located on one of the widest surfaces. Of particular interest are the effects of dimple depth, as the dimple print diameter, spacing between the dimples, and experimental conditions are all held constant. Because deep dimples (with depth equal to 30 percent of the print diameter) are used, and because comparisons are made regarding the effects of dimple depth, the present investigation is different from other existing studies. The present experiment is designed to model internal cooling passages of the airfoils employed in gas turbines used for utility power generation. However, the improvements in surface heat transfer augmentation produced by arrays of dimples are also useful in a variety of other practical applications, including electronics cooling, heat exchangers, micro-scale passages, bio-medical devices, and combustion chamber liners.

Contributed by the Heat Transfer Division for publication in the JOURNAL OF HEAT TRANSFER. Manuscript received by the Heat Transfer Division April 29, 2002; revision received September 13, 2002. Associate Editor: C. Amon.

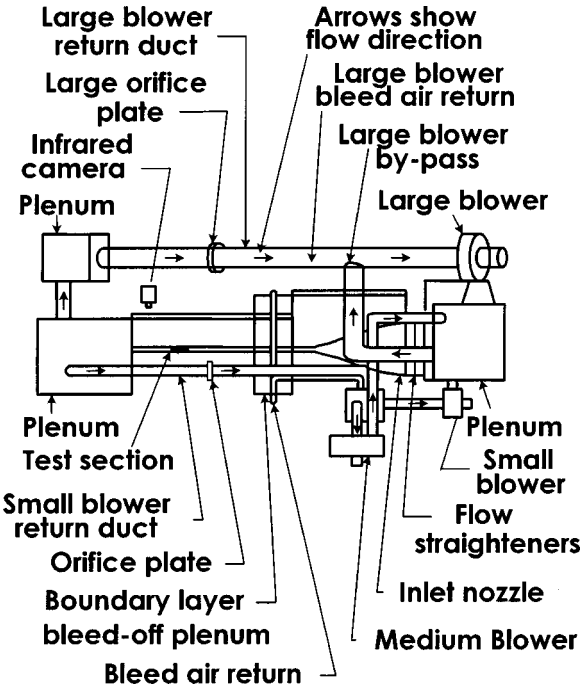

Fig. 1 Schematic diagram of the experimental apparatus used for heat transfer measurements

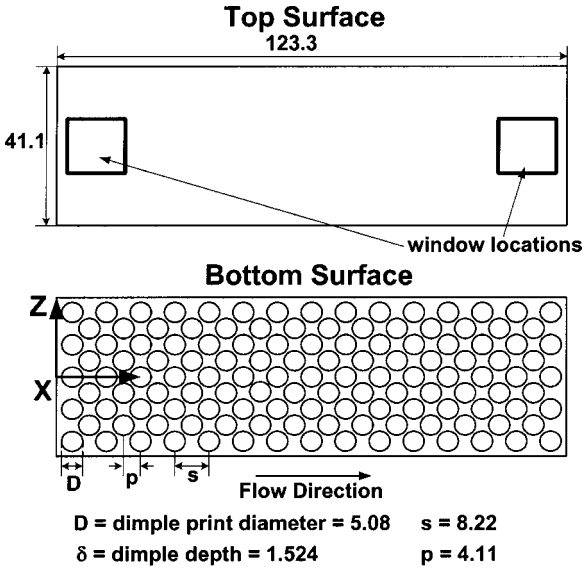

Fig. 2 Schematic diagrams of the top and bottom dimpled test surfaces. All dimensions are given in cm.

Experimental Apparatus and Procedures

Channel and Test Surface for Heat Transfer Measurements. A schematic of the facility used for heat transfer measurements is shown in Fig. 1. The air used within the facility is circulated in a closed-loop. One of three circuits is employed, depending upon the Reynolds number requirements in the test section. For Reynolds numbers Re_H less than 10,000, a 102 mm inner diameter pipe is used, which is connected to the intake of an ILG Industries 10P type centrifugal blower. For Reynolds numbers between 10,000 and 25,000, the 102 mm pipe is connected to the intake of a Dayton 7C554 radial drive blower. For higher Reynolds numbers, a 203 mm inner diameter pipe is employed with a New York Blower Co. 7.5 HP, size 1808 pressure blower. In each case, the air mass flow rate from the test section is measured (upstream of which ever blower is employed) using an ASME standard orifice plate and Validyne M10 digital pressure manometer. The blower then exits into a series of two plenums (0.9 m square and 0.75 m square). A Bonneville cross-flow heat exchanger is located between two of these plenums. As the air exits the heat exchanger, it enters the second plenum, from which the air passes into a rectangular bell mouth inlet, followed by a honeycomb, two screens, and a two-dimensional nozzle with a contraction ratio of 10. This nozzles leads to a rectangular cross-section, 411 mm by 50.8 mm inlet duct which is 1219 mm in length. This is equivalent to 13.5 hydraulic diameters (where hydraulic diameter is 90.4 mm). Boundary layer trips are employed on the top and bottom surfaces of the inlet duct, just upstream of the test section, which follows with the same cross-section dimensions. It exits to a 0.60 m square plenum, which is followed by two pipes, each containing an orifice plate, mentioned earlier.

Figure 2 presents geometric details of the test section, including the bottom dimpled test surface, and the top smooth surface. Dimple geometry details are given in Fig. 3 for the present study as well as for dimples from Mahmood et al. [1], which are used for comparison. In the present study, a total of 29 rows of dimples are employed in the streamwise direction, with 4 or 5 dimples in each row. The dimples are positioned on the surface in a staggered array. Also identified in Fig. 2 is the test section coordinate system employed for the study. Note that the Y coordinate is normal from the test surface.

All exterior surfaces of the facility (between the heat exchanger and test section) are insulated with Styrofoam ($k = 0.024$ W/mK), or 2 to 3 layers of 2.54 cm thick, Elastomer Products black neoprene foam insulation ($k = 0.038$ W/mK) to minimize heat losses. Calibrated copper-constantan thermocouples are located between the three layers of insulation located around the entire test section to determine conduction losses. Between the first layer and the 3.2 mm thick acrylic, dimpled test surface is a custom-made Electrofilm etched-foil heater (encapsulated between two thin layers of Kapton) to provide a constant heat flux boundary condition on the bottom dimpled test surface. This custom-made heater is designed and constructed so that it follows the convex contour of the test surface behind each dimple. The bottom dimpled acrylic surface contains 24 copper-constantan thermocouples. Each of these thermocouples is located 0.051 cm just below this surface to provide measurements of local surface temperatures, after correction for thermal contact resistance and temperature drop through the 0.051 cm thickness of acrylic. A cross-sectional view of a similar test section is presented by Mahmood and Ligrani [11]. Acrylic is chosen because of its low thermal conductivity ($k = 0.16$ W/mK at 20°C) to minimize streamwise and spanwise conduction along the test surface, and thus minimize ''smearing'' of spatially varying temperature gradients along the test surface. The power to the foil heater is controlled

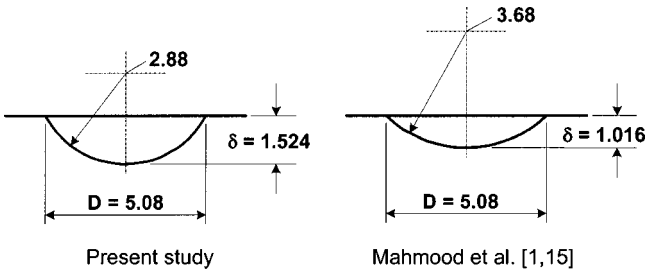

Fig. 3 Schematic diagrams of individual dimple geometry details for the present study and for Mahmood et al. [1]. All dimensions are given in cm.

and regulated using a variac power supply. Energy balances, performed on the heated test surface, then allow determination of local magnitudes of the convective heat flux.

Local Nusselt Number Measurement. The mixed-mean stagnation temperature of the air entering the test section is measured using five calibrated copper-constantan thermocouples spread across the inlet cross-section. To determine this temperature, measured temperatures are corrected for thermocouple wire conduction losses, channel velocity variations, as well as for the differences between stagnation and recovery temperature. Magnitudes of the local mixed mean temperatures at different locations though the test section, T_{mx}, are then determined using energy balances, and the mixed mean temperature at the inlet of the test section. Because of the way in which it is measured, this inlet temperature is also a stagnation value. The thermal conductivity k used to determine local Nusselt numbers is based on this inlet stagnation temperature. Because mixed mean temperature variations through the test section are always less than 3.0°C, thermal conductivity magnitudes based on inlet stagnation temperature are only slightly different from values based on local mixed mean temperature.

Five calibrated copper-constantan thermocouples are also spread over the exit of the test section duct. Mixed-mean temperatures, estimated from measured temperatures, match values determined from energy balances within a few percent for all experimental conditions investigated. All measurements are obtained when the test facility is at steady-state, achieved when each of the temperatures from the 24 thermocouples (on the bottom dimpled test surface) vary by less than 0.1°C over a 10 minute period.

To determine the surface heat flux (used to calculate heat transfer coefficients and local Nusselt numbers), the total convective power level, provided by the etched foil heater, is divided by the flat, projected test surface area corresponding to that foil heater. Spatially-resolved temperature distributions along the bottom test surface are also determined using infrared imaging in conjunction with thermocouples, energy balances, digital image processing, and *in situ* calibration procedures. To accomplish this, the infrared radiation emitted by the heated interior surface of the channel is captured using a VideoTherm 340 Infrared Imaging Camera, which operates at infrared wavelengths from 8 μm to 14 μm. Temperatures, measured using the calibrated, copper-constantan thermocouples distributed along the test surface adjacent to the flow, are used to perform the *in situ* calibrations simultaneously as the radiation contours from surface temperature variations are recorded.

This is accomplished as the camera views the test surface through a custom-made, zinc-selenide window (which transmits infrared wave lengths between 6 and 17 μm) located on the top wall of the test section. As shown in Fig. 2, this window can be positioned either at an upstream location or a downstream location. Note that all results given in the present paper are obtained at the downstream location, when the window is located just above the 26^{th} to 29^{th} rows of dimples downstream from the leading edge of the test surface. Twelve thermocouple junction locations are present in the infrared field viewed by the camera. The exact spatial locations and pixel locations of these thermocouple junctions and the coordinates of a 12.7 cm by 12.7 cm field of view are known from calibration maps obtained prior to measurements. During this procedure, the camera is focused, and rigidly mounted and oriented relative to the test surface in the same way as when radiation contours are recorded. Voltages from the thermocouples are acquired using a Hewlett-Packard 44422T data acquisition card installed in a Hewlett-Packard 3497A data acquisition control unit, which is controlled by a Hewlett-Packard A4190A Series computer.

With these data, gray scale values at pixel locations within video taped images from the infrared imaging camera are readily converted to local Nusselt number values. Because such calibration data depend strongly on camera adjustment, the same brightness, contrast, and aperture camera settings are used to obtain the experimental data. The *in situ* calibration approach rigorously and accurately accounts for these variations.

Images from the infrared camera are recorded as 8-bit gray scale directly into the memory of a Dell Dimension XPS T800r PC computer using a Scion Image Corporation Frame grabber video card, and Scion image v.1.9.2 software. Three sets of 60 frames are recorded at a rate of one frame per second. All of 180 resulting images are then ensemble averaged to obtain the final gray scale data image. This final data set is then imported into Matlab version 6.0.0.88 (Release 12) software to convert each of 256 possible gray scale values to local Nusselt number at each pixel location using calibration data. Each individual image covers approximately a 250 pixel by 250 pixel area. Additional details of the infrared imaging and measurement procedures are provided by Oliveira [12] and Mahmood [15].

Friction Factor Measurement. Wall static pressures are measured along the test section simultaneously as the heat transfer measurements are conducted, using 12 static pressure taps, located 25.4 mm to 80 mm apart along one of the test section side walls. These measurements are made in the test section with the dimples, as well as in a baseline test section with smooth surfaces on all four walls. Friction factors are then determined from streamwise pressure gradient magnitudes. Pressures from the wall pressure taps are measured using Celesco LCVR pressure transducers. Signals from these transducers are processed using Celesco CD10D Carrier-Demodulators. Voltages from the Carrier-Demodulators are acquired using a Hewlett-Packard 44422A data acquisition card installed in a Hewlett-Packard 3497A data acquisition control unit, which is controlled by a Hewlett-Packard A4190A Series computer. With this apparatus, 100 sequential measurements are acquired and measured from each pressure transducer, over a time period of about 20 seconds.

Uncertainty Estimates. Uncertainty estimates are based on 95 percent confidence levels, and determined using procedures described by Kline and McClintock [13] and Moffat [14]. Uncertainty of temperatures measured with thermocouples is ± 0.15°C. Spatial and temperature resolutions achieved with the infrared imaging are about 0.5 mm and 0.8°C, respectively. This magnitude of temperature resolution is due to uncertainty in determining the exact locations of thermocouples with respect to pixel values used for the *in situ* calibrations. Local Nusselt number uncertainty is then about ± 6.8 percent. Corresponding Nusselt number ratio uncertainty is about ± 0.19 (for a ratio of 2.00), or ± 9.6 percent. Note that all uncertainties of local Nusselt numbers consider variations of surface heat flux which may be present due to small changes of the thickness of the acrylic which comprises the dimpled test surface. Reynolds number uncertainty is about ± 1.7 percent for Re_H of 12,000.

Experimental Results and Discussion

Baseline Nusselt Numbers. Two different sets of baseline Nusselt numbers are measured for two different purposes. In both cases, constant-property baseline Nusselt numbers are measured in a smooth rectangular test section with smooth walls on all surfaces and no dimples, for a ratio of inlet stagnation temperature to surface temperature of 0.93–0.94. The baseline measurements are also time-averaged, and made in the downstream portion of the test section, where the channel flow is hydraulically and thermally fully developed. The *first set* is measured in a channel with an aspect ratio of 4 with heating on all four channel surfaces (with constant heat flux boundary condition around the entire test section) to verify the experimental apparatus and procedures employed. The *second set* is measured in a channel with an aspect ratio of 8 (which is the same aspect ratio employed for the present

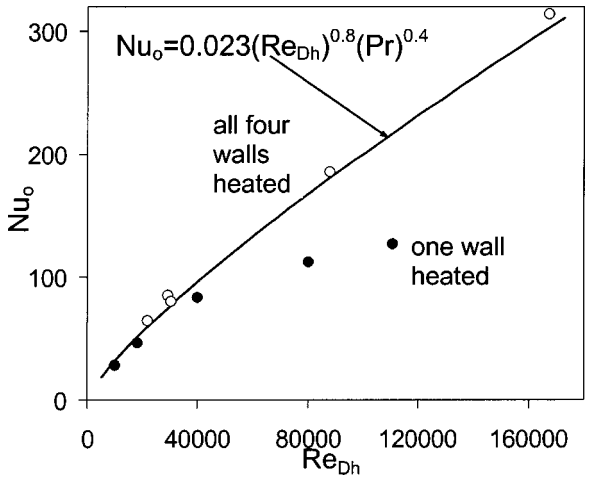

Fig. 4 Baseline, constant property Nusselt numbers, measured with smooth channel surfaces and constant heat flux boundary condition, for a ratio of inlet stagnation temperature to surface temperature of 0.93–0.94, as dependent upon Reynolds number based on hydraulic diameter. Data are given for all four walls heated, and for one wall heated.

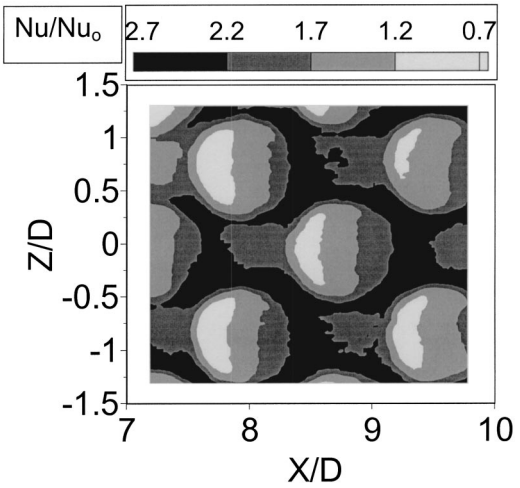

Fig. 5 Local Nusselt number ratio data from a channel with dimples and heating on one channel surface, for $\delta/D=0.2$, $H/D=1$, and $Re_H=20{,}000$ from Mahmood [15]

dimple surface measurements) to provide baseline Nusselt numbers Nu_o to normalize values measured on the dimpled surface. In this case, only the bottom channel surface is heated to provide the same type of thermal boundary condition as when the dimples are installed. Except for the absence of the dimples, all geometric characteristics of the channel are then the same as when the dimpled test surface is installed.

Baseline Nusselt numbers for both sets of conditions are shown in Fig. 4. Also included in this figure is the Dittus-Boelter smooth circular tube correlation [16], which is given by

$$Nu_o = 0.023\,Re_{Dh}^{0.8}Pr^{0.4} \tag{1}$$

The agreement between Eq. (1) and the first set of baseline data (obtained with all four walls heated), shown in Fig. 4 for the entire range of Reynolds numbers Re_{Dh} examined, provides a check on the experimental apparatus and procedures. This first set of spatially-averaged Nusselt numbers are determined from measurements made on the top and bottom walls.

Because of the different thermal boundary conditions employed, Fig. 4 shows that baseline Nusselt numbers with heating only on one wall are generally lower than the values given by Eqn. (1), when compared at the same Reynolds number based on hydraulic diameter. As mentioned, these values are employed to normalize dimpled surface Nusselt numbers. In some cases, this is accomplished by interpolating between the darkened data points in Fig. 4 using a polynomial equation.

Local Nusselt Number Variations. Local Nusselt number ratios, measured on a dimpled surface by Mahmood [15], are shown in Fig. 5. These data are obtained using the same dimple print diameter, same dimple spacing, same channel aspect ratio, and same H/D ratio as for the present study. As indicated in Fig. 3, the depth of these dimples is 1.016 cm, giving $\delta/D=0.2$, whereas $\delta/D=0.3$ is used in the present study. Like the present study, the Mahmood [15] data are obtained with dimples placed only on the bottom surface. Both investigations also employ heating with a constant flux only on the bottom wall (with unheated side and top walls). Thus, the baseline Nusselt numbers, measured in each study, are obtained using the same thermal boundary conditions and heating arrangement as when dimples are used on the measurement surfaces. In addition, heat transfer coefficients and heat flux values (used to determine Nusselt numbers) are based on flat projected areas in both cases.

The bulk flow direction in Fig. 5 is from left to right in the direction of increasing X/D. Each $\delta/D=0.2$ dimple is located in the vicinity of each circular Nusselt number distribution. Notice that local Nu/Nu_o values are lowest in the upstream halves of the dimples. Each of these is positioned beneath a region of recirculating flow, where advection velocities in the flow located adjacent to the surface are very low. Nusselt number ratios then increase progressively with X/D along the dimpled surface. Values then become highest near the diagonal and downstream edges of the dimples, and on the flat surfaces just downstream of these locations. Here, local Nu/Nu_o augmentations are greater than 2.2, and are as high as 3.3 because of reattachment of the shear layer which forms across the top of each dimple, and because of the multiple vortex pairs which are periodically shed from each dimple. When $\delta/D=0.2$, $Re_H=20{,}000$, and $H/D=1.0$ (as for the data in Fig. 5), one relatively large vortex pair is shed from the central part of each dimple, and two smaller vortex pairs are shed from the spanwise edges of each dimple [1,17]. These edge formed vortex pairs then strengthen as they advect downstream next to the edges of other dimples. This occurs because of the staggered arrangement of the dimples on the test surface, which causes each ''edge'' vortex pair to be located first on the right edge of a dimple, then on the left edge of another dimple, and so on. The result is interconnected regions of high local Nusselt number ratios, located diagonally between adjacent dimples, as shown in Fig. 5.

Another result is a highly elliptic flow field in which flow events in one dimple communicate with flow events in other dimples. Similar communications between different flow events are observed in other types of flows with vortex structures and high levels of unsteadiness that enhance mixing. For example, channels interrupted by quadrangular elements [18,19], and channels with rectangular grooves [20] produce periodic, unsteady vortex ejections and interactions, as well as self-sustained flow oscillations, which also result in enhanced surface heat transfer levels.

Similar events occur in the present dimpled channel. Here, local Nusselt numbers are augmented beneath the vortex pairs because of the action of their secondary flows in advecting heat over different length scales, and in spreading shear gradients over larger flow volumes. This latter effect increases turbulence production, and three-dimensional turbulence transport.

Comparing results from Mahmood [15] to ones from the present study provides information on the effects of dimple depth. This is accomplished by comparing distributions of Nusselt number ratios Nu/Nu_o (instead of dimensional Nusselt numbers) from

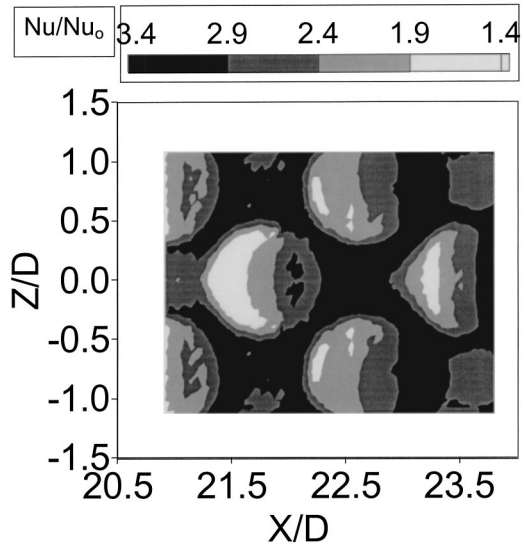

Fig. 6 Local Nusselt number ratio data from a channel with dimples on one channel surface, and heating on one channel surface, for $\delta/D=0.3$, $H/D=1$, and $Re_H=17{,}200$

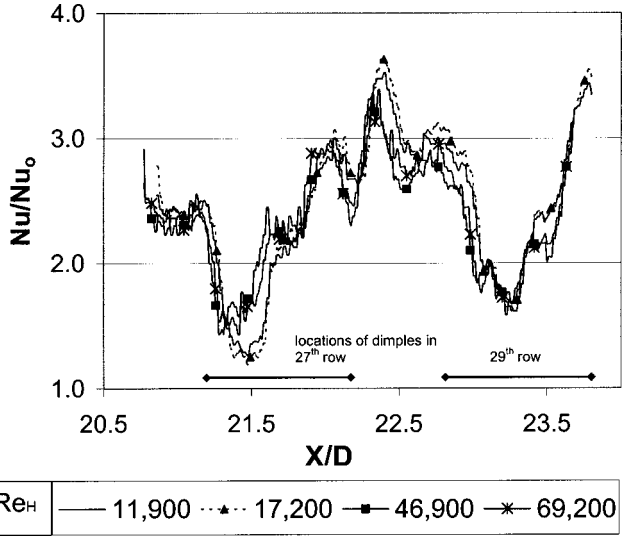

Fig. 8 Local dimpled channel Nusselt number ratios as dependent upon X/D along the spanwise centerline at $Z/D=0$ for $\delta/D=0.3$, $H/D=1$, and different Re_H from the present study

the two studies. Compared to the results in Fig. 5 (for $\delta/D=0.2$), the Nu/Nu$_o$ distribution in Fig. 6 (for $\delta/D=0.3$) show a number of important differences which are due to different dimple depths. First, ratios are generally higher at each test surface location for the deeper dimples. These differences are especially apparent in the downstream portions of the dimples, where heat transfer augmentations are the highest. Here, increased Nu/Nu$_o$ values are also spread over a larger portion of the dimpled surface area for the deeper dimples ($\delta/D=0.3$). In addition, Nusselt number ratios first increase, then decrease, and then increase again with X/D in the downstream parts of many of the deeper dimples shown in Fig. 6. This local decrease of local Nu/Nu$_o$ values is not present in the downstream parts of the $\delta/D=0.2$ dimples shown in Fig. 5.

Such differences in behavior for different δ/D values are further illustrated by the results shown in Fig. 7. Here, local data from Figs. 5 and 6 are shown as they vary with X/D along the spanwise centerline of the test section at $Z/D=0.0$. Note that the X/D values of the Mahmood [15] data are shifted so that they are positioned at the same relative location with respect to the dimples. The X/D ranges of values for dimples located in the 27th and 29th rows are also shown in Fig. 7. The $\delta/D=0.3$ Nusselt number ratio data are generally higher than the $\delta/D=0.2$ data for almost every X/D location shown in Fig. 7. As X/D increases and one moves along the dimple surface, the $\delta/D=0.2$ Nusselt number ratio data from Mahmood [15] first decrease in the first 25 percent of the dimple, and then increase continuously over the last 75 percent of the dimple. The highest local Nu/Nu$_o$ value is then present just inside of the downstream edge of the dimple.

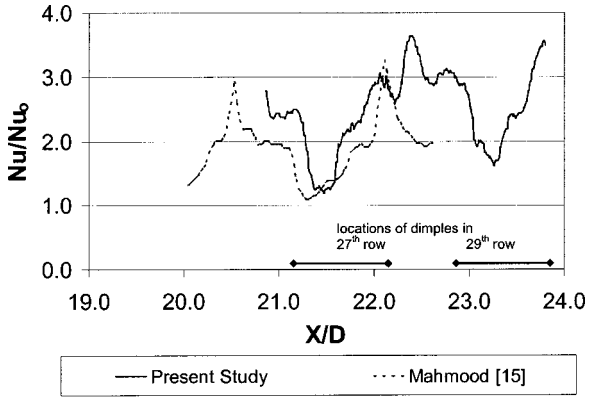

Fig. 7 Local dimpled channel Nusselt number ratios as dependent upon X/D along the spanwise centerline at $Z/D=0$. Data are given for $\delta/D=0.3$, $H/D=1$, and $Re_H=17{,}200$ from the present study, and for $\delta/D=0.2$, $H/D=1$, and $Re_H=20{,}000$ from Mahmood [15].

Local Nusselt number ratios for $\delta/D=0.3$ in Fig. 7 also show a decrease with X/D in the first 25 percent of the dimple. In the last 75 percent, Nu/Nu$_o$ values increase until a double local peak is present at a location which is positioned about 85 percent through the dimple. Values then decrease to give a local minima near the downstream edge of the dimple. This is just downstream of the location where the Nu/Nu$_o$ maximum is present for $\delta/D=0.2$. The data in Fig. 7 then increase as X/D increases further to give a maximum Nu/Nu$_o$ value of about 3.7 near $X/D=22.3$, which is on the flat surface just downstream of the dimple. These differences for different δ/D are due to shedding of vortex pairs with different strengths, and to different shear layer formation, development, and reattachment. The shear layer which forms near the tops of the dimples is stronger, with more pronounced shear layer reattachment for the deeper dimples. Because $\delta/D=0.3$, the reattachment location of this shear layer is slightly farther upstream then for the shallow dimples with $\delta/D=0.2$. However, in both cases, the location of this reattachment zone changes with time in a periodic fashion, in phase with the sequence of vortex pair shedding and flow inrush to the dimples (which occur periodically and continuously). These alternating phenomena result partially from continuity considerations, which probably cause larger volumes of fluid to periodically move into and out of the deeper dimples (compared to the shallow dimples). Because of this, the ejection and local jetting of flow from the deeper dimples is stronger, which results in vortex pairs with stronger and more pronounced secondary flows. The net result is higher Nu/Nu$_o$ values on the flat surfaces just downstream of the deeper dimples with $\delta/D=0.3$ in Fig. 7.

Although quantitative changes are present, the overall qualitative characteristics of these flow phenomena do not change much within and around the $\delta/D=0.3$ dimples as the Reynolds number changes. This is evident from the results presented in Figs. 8 and 9. Figure 8 shows local Nu/Nu$_o$ variations as they vary with X/D for $Z/D=0$. Figure 9 shows local Nu/Nu$_o$ variations as they vary with Z/D for $X/D=23.2$. In the first of these figures, the local

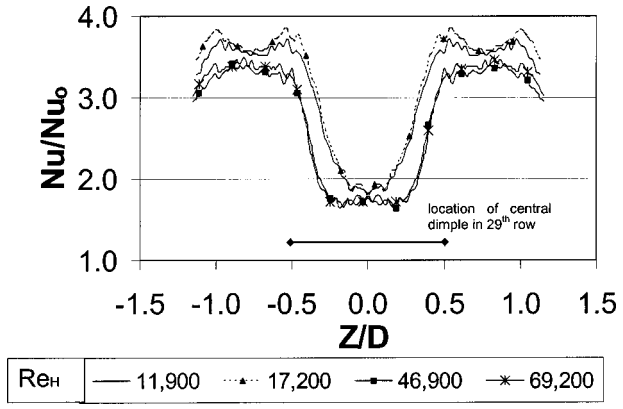

Fig. 9 Local dimpled channel Nusselt number ratios as dependent upon Z/D along a line at $X/D=23.2$ for $\delta/D=0.3$, $H/D=1$, and different Re_H from the present study

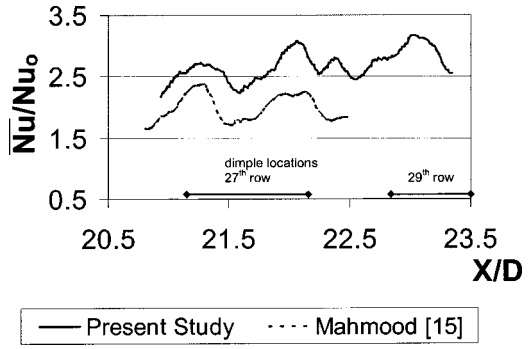

Fig. 10 Spanwise-averaged dimpled channel Nusselt number ratios as dependent upon X/D for $\delta/D=0.3$, $H/D=1$, and $Re_H=17{,}200$ from the present study, and for $\delta/D=0.2$, $H/D=1$, and $Re_H=20{,}000$ from Mahmood [15]

Nu/Nu_o variations for each Re_H show the same qualitative Nu/Nu_o variations, as shown by the data in Fig. 7 for $\delta/D=0.3$, except that the data in Fig. 8 are shown for approximately two complete periods of dimple surface geometry. For example, regardless of the value of the Reynolds number, local Nu/Nu_o increase, decrease, and then increase again with X/D in the downstream parts of the dimples and on the flat surfaces just downstream of the dimples. In some cases, local Nusselt number ratios at some X/D values then increase somewhat as Re_H decreases.

These qualitative variations with Re_H are also apparent in Fig. 9, which shows Nu/Nu_o variations (for $X/D=23.2$) across the span of the measurement plane. Here, values are highest on the flat surfaces between and downstream of the dimples (at $Z/D=-0.3$ to $Z/D=-1.3$, and at $Z/D=+0.3$ to $Z/D=+1.3$), and lowest with the upstream parts of the dimples (at Z/D from -0.3 to $+0.3$). The $X/D=23.2$ location, where the Fig. 9 data are measured, lies just downstream of dimples in the 28th row and in the upstream portion of a dimple in the 29th row. These positions are at or near the locations of highest and lowest Nu/Nu_o, respectively. According to Fig. 9, local Nu/Nu_o values generally increase as Re_H decreases, with the largest changes occurring as this Reynolds number changes from 17,200 to 46,900. Similar variations with Re_H are also evident in Fig. 8 at $X/D=22.2$ to 22.7, which is positioned on the flat part of the test surface just downstream of the dimples, where local Nu/Nu_o values are highest. This trend is due to higher mainstream cross-flow speeds, produced at the higher Reynolds numbers, which tend to suppress the development and turbulent transport capabilities of the secondary flows and vortices which are shed from the dimples. The variations shown in Fig. 9 at Z/D from -0.5 to $+0.5$ are a result of recirculating flows within the dimples, which may become stronger as the Reynolds number increases. This is believed to trap flow within the recirculating zone, which then has characteristics which are somewhat like a partially insulating pocket of fluid.

Spatially-Averaged Nusselt Number Variations. Spatially-averaged Nusselt number ratios are given in Figs. 10, 11, and 12. The spanwise-averaged data in Figs. 10 and 11 are obtained by averaging local data in the spanwise direction over one complete period of dimple surface geometry. The streamwise-averaged data in Fig. 12 are averaged in the streamwise direction over one complete period of dimple surface geometry.

The streamwise location of the dimples in the twenty-seventh row are shown in Fig. 10. Here, spanwise-averaged values from Mahmood [15] for $\delta/D=0.2$ are significantly lower than values from the present study for $\delta/D=0.3$. In each case, the lowest $\overline{Nu}/Nu_o$ values are positioned at the same locations as the upstream portions of dimples in the twenty-seventh row. The highest $\overline{Nu}/Nu_o$ values are then located at positions which correspond to the downstream parts of dimples in the twenty-seventh row, as well as on flat regions located just downstream. Of particular interest is the double peak in the $\overline{Nu}/Nu_o$ distribution for $\delta/D=0.3$, which is located at $X/D=21.8$ to $X/D=22.5$. The $\delta/D=0.2$ distribution shows only a single peak in the $\overline{Nu}/Nu_o$ variation at about the same X/D locations. Such variations are a result of local Nu/Nu_o variations like the ones shown in Figs. 5, 6, and 7.

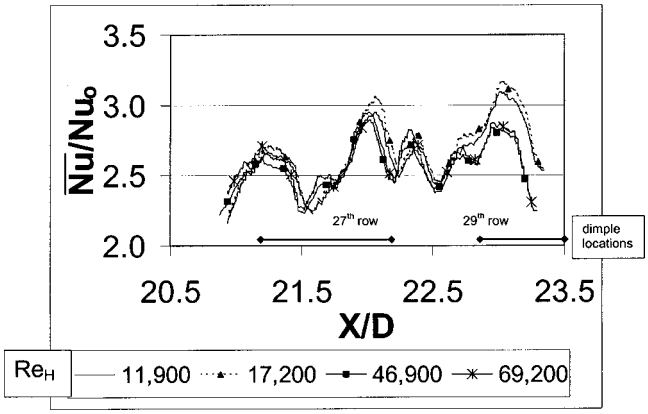

Fig. 11 Spanwise-averaged dimpled channel Nusselt number ratios as dependent upon X/D for $\delta/D=0.3$, $H/D=1$, and different Re_H from the present study

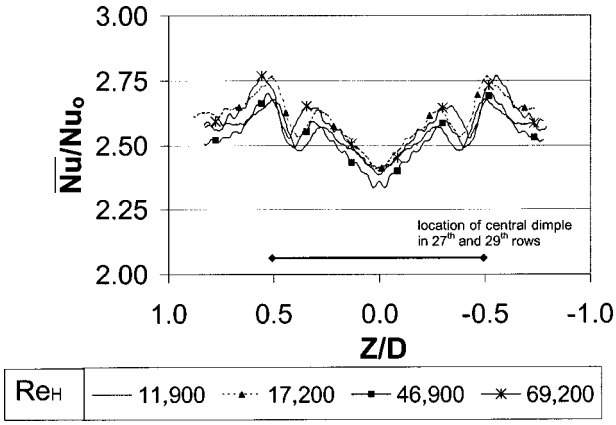

Fig. 12 Streamwise-averaged dimpled channel Nusselt number ratios as dependent upon Z/D for $\delta/D=0.3$, $H/D=1$, and different Re_H from the present study

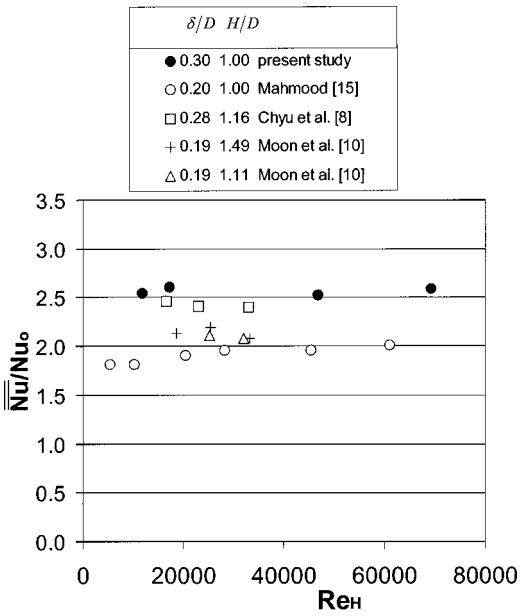

Fig. 13 Globally-averaged dimpled channel Nusselt number ratios as dependent upon Reynolds number Re_H for $\delta/D=0.3$ and $H/D=1$. Results from the present study are compared to results from Mahmood [15], Chyu et al. [8], and Moon et al. [10] for different values of δ/D, the ratio of dimple depth to dimple print diameter.

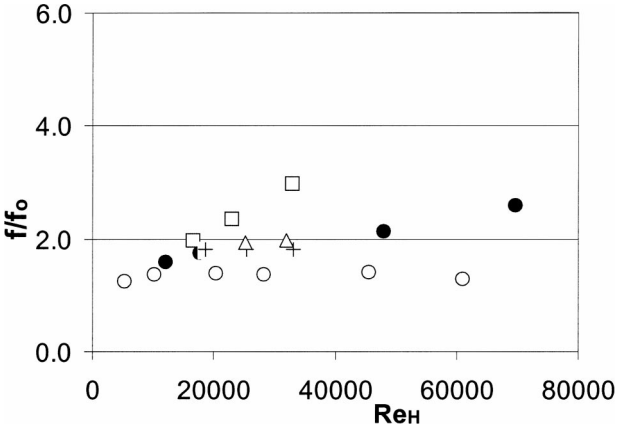

Fig. 14 Dimpled channel friction ratio as dependent upon Reynolds number Re_H for $\delta/D=0.3$ and $H/D=1$. Results from the present study are compared to results from Mahmood [15], Chyu et al. [8], and Moon et al. [10] for different values of δ/D, the ratio of dimple depth to dimple print diameter. Symbols are defined in Fig. 13.

Spanwise-averaged Nusselt number ratio data, obtained at different Re_H values (from the present study) are given in Fig. 11. As for the data in earlier figures, these results are obtained for $\delta/D=0.3$, and $H/D=1.0$ along a downstream portion of the test surface where dimples in rows 26, 27, 28, and 29 are located. Nusselt number ratios here follow the same general qualitative trend as the $\delta/D=0.3$ data in the previous figure. For example, relatively low $\overline{Nu}/Nu_o$ values are present at locations which correspond to the upstream portions of dimples in the 27th row, and relatively high $\overline{Nu}/Nu_o$ values are present at locations which correspond to the downstream portions of dimples in the 27th row (and to positions of dimples on flat surfaces just downstream). In all cases, $\overline{Nu}/Nu_o$ data in Fig. 11 are generally about the same as Re_H changes at some X/D locations, with increasing $\overline{Nu}/Nu_o$ as Re_H decreases at other X/D locations.

The same $\overline{Nu}/Nu_o$ trend with as Re_H is evident in Fig. 12, where streamwise-averaged data are presented. For each Re_H, $\overline{Nu}/Nu_o$ values are generally lower near $Z/D=0$, which corresponds to the deepest parts of dimples located along the spanwise centerline of the test surface. $\overline{Nu}/Nu_o$ values are then highest at locations which correspond to, or are near to, the spanwise edges of dimples located along the central part of the test surface.

Globally Averaged Nusselt Number Ratio Behavior. Globally-averaged Nusselt numbers are determined by averaging local data over one complete period of dimple geometry. These averages are thus conducted in both the spanwise and streamwise directions over a rectangular area from the center to center of adjacent dimples in the 27th and 29th rows. The baseline Nusselt numbers Nu_o (used for normalization) are obtained at the same Reynolds numbers as the Nusselt numbers measured on the dimpled surface.

Note that the present globally-averaged Nusselt number ratios for $\delta/D=0.3$ are about constant as Re_H increases in Fig. 13. This is consistent with Nusselt number ratios from Mahmood [15] for $\delta/D=0.2$, which increase slightly or are about constant as Re_H changes. The present data in Fig. 13 are also compared to results from Chyu et al. [8] for $\delta/D=0.28$ and $H/D=1.155$, and to results from Moon et al. [10] for $\delta/D=0.19$ and two values of H/D of 1.11 and 1.49. In all cases, heat transfer coefficients and heat flux magnitudes are based on flat projected areas. Note that Chyu et al. [8] utilize dimples on two opposite channel surfaces, whereas the present study, Mahmood [15], and Moon et al. [10] use dimples only on one channel surface.

For all Re_H examined, the data in Fig. 13 generally show increasing globally-averaged Nusselt number ratios as δ/D increases from 0.19 to 0.30. This further illustrates the effects of this parameter in augmenting local and spatially-averaged Nusselt numbers at different values of the Reynolds number, Re_H.

Friction Factors. Figure 14 shows that friction factor ratios from the present study, for $\delta/D=0.3$ and $H/D=1$, increase continuously as Re_H increases. Values range from 1.6 to 2.6 for Reynolds numbers from 12,000 to 70,000. The present dimpled surface friction factor ratios are thus less than magnitudes measured in several types of turbulated passages, where f/f_o range from 2.5 to 75 [21].

Ratios from Mahmood [15] ($\delta/D=0.2$), Chyu et al. [8] ($\delta/D=0.28$) and Moon et al. [10] (for $\delta/D=0.19$), are also included in Fig. 14 for comparison. Values from Chyu et al. [8] are higher than ratios from the present investigation, whereas values from Mahmood [15] are lower than ratios from the present investigation. This is because values generally increase as either the number of dimpled surfaces increases (i.e., from 1 to 2), or as δ/D increases.

Summary and Conclusions

Experimental results, measured on a dimpled test surface placed on one of the widest walls of a channel (with an aspect ratio of 8), are given for Reynolds numbers from 12,000 to 70,000, and a ratio of air inlet stagnation temperature to surface temperature of approximately 0.94. These include friction factors, local Nusselt numbers, spatially-resolved local Nusselt numbers, and globally averaged Nusselt numbers. The ratio of channel height to dimple print diameter is 1.00, and the ratio of dimple depth to dimple print diameter δ/D is 0.3. These results are compared to measurements from Mahmood [15] and other investigations to provide information on the influences of dimple depth. The Mahmood [15] results offer an excellent basis for comparison, because the ratio of dimple depth to dimple print diameter δ/D is 0.2, and because dimples are placed only on one channel

surface. In addition, the same dimple print diameter, same dimple spacing, same channel aspect ratio, same H/D ratio, and same type of thermal boundary condition are utilized.

At all Reynolds numbers considered, local and spatially-resolved Nusselt number augmentations increase as the ratio of dimple depth to dimple print diameter δ/D increases from 0.2 to 0.3 (and all other experimental and geometric parameters are held constant). This is because the deeper dimples produce: (i) increases in the strengths and intensity of vortices and associated secondary flows ejected from the dimples, as well as (ii) increases in the magnitudes of three-dimensional turbulence production and turbulence transport. The effects of these phenomena are especially apparent in local Nusselt number ratio distributions measured just inside of the dimples, and just downstream of the downstream edges of the dimples. Here, two local maxima are evident in local Nusselt number ratios when $\delta/D=0.3$, compared to a single maximum value when $\delta/D=0.2$.

Decreasing *local* Nusselt number ratios with increasing Reynolds number within the upstream portions of the dimples are attributed to larger regions of stronger re-circulating flow. These are believed to trap fluid which then acts as a partially insulating pocket to decrease local Nusselt numbers compared to values measured at lower Reynolds numbers.

Acknowledgments

The work presented in this paper was sponsored by a AGTSR Advanced Gas Turbine Research Program research subcontract sponsored by the U.S. Department of Energy-National Energy Technology Laboratory through a cooperative agreement with the South Carolina Institute for Energy Studies at Clemson University. Mr. Eli Comeau helped in acquiring and processing some of the data presented.

Nomenclature

D = dimple print diameter
Dh = channel hydraulic diameter
f = channel friction factor
f_o = baseline friction factor measured in a channel with smooth surfaces and no dimples
H = channel height
h = heat transfer coefficient based on flat projected surface area, $\dot{q}_o''/(T_w-T_{mx})$
k = thermal conductivity
Nu = local Nusselt number, hDh/k
Nu_o = baseline Nusselt number in a channel with smooth surfaces and no dimples
p = streamwise spacing of adjacent dimple rows
$\dot{q}_o''$ = surface heat flux based on flat projected surface area
R_{eH} = Reynolds number based on channel height, $H\overline{U}/\upsilon$
R_{eDh} = Reynolds number based on channel hydraulic diameter, $Dh\overline{U}/\upsilon$
s = streamwise spacing of every other dimple row
T = temperature
$\overline{U}$ = streamwise bulk velocity averaged over the channel cross-section
X = streamwise coordinate measured from test section inlet
Y = normal coordinate measured from test surface dimple horizon
Z = spanwise coordinate measured from test section center-line

Greek Symbols

ν = kinematic viscosity
δ = dimple depth

Subscripts

mx = time-averaged, local mixed-mean value
w = local wall value

Superscripts

$\overline{\ }$ = spatially-averaged value
$=$ = globally-averaged value

References

[1] Mahmood, G. I., Hill, M. L., Nelson, D. L., Ligrani, P. M., Moon, H.-K., and Glezer, B., 2001, "Local Heat Transfer and Flow Structure On and Above a Dimpled Surface in a Channel," ASME J. Turbomach., **123**(1), pp. 115–123.
[2] Afanasyev, V. N., Chudnovsky, Y. P., Leontiev, A. I., and Roganov, P. S., 1993, "Turbulent Flow Friction and Heat Transfer Characteristics for Spherical Cavities on a Flat Plate," Exp. Therm. Fluid Sci., **7**, pp. 1–8.
[3] Belen'kiy, M. Y., Gotovskiy, M. A., Lekakh, B. M., Fokin, B. S., and Dolgushin, K. S., 1994, "Heat Transfer Augmentation Using Surfaces Formed by a System of Spherical Cavities," Heat Transfer Research, **25**(2), pp. 196–203.
[4] Kesarev, V. S., and Kozlov, A. P., 1994, "Convective Heat Transfer in Turbulized Flow Past a Hemispherical Cavity," Heat Transfer Research, **25**(2), pp. 156–160.
[5] Terekhov, V. I., Kalinina, S. V., and Mshvidobadze, Y. M., 1995, "Flow Structure and Heat Transfer on a Surface With a Unit Hole Depression," Russ. J. Eng. Thermophys., **5**, pp. 11–33.
[6] Schukin, A. V., Koslov, A. P., and Agachev, R. S., 1995, "Study and Application of Hemispherical Cavities For Surface Heat Transfer Augmentation," ASME Paper No. 95-GT-59.
[7] Gortyshov, Y. F., Popov, I. A., Amirkhanov, R. D., and Gulitsky, K. E., 1998, "Studies of Hydrodynamics and Heat Exchange in Channels With Various Types of Intensifiers," *Proceedings of 11th International Heat Transfer Congress*, **6**, pp. 83–88.
[8] Chyu, M. K., Yu, Y., Ding, H., Downs, J. P., and Soechting F. O., 1997, "Concavity Enhanced Heat Transfer in an Internal Cooling Passage," ASME Paper No. 97-GT-437.
[9] Lin, Y.-L., Shih, T. I.-P., and Chyu, M. K., 1999, "Computations of Flow and Heat Transfer in a Channel With Rows of Hemispherical Cavities," ASME Paper No. 99-GT-263.
[10] Moon, H.-K., O'Connell, T., and Glezer, B., 1999, "Channel Height Effect on Heat Transfer and Friction in a Dimpled Passage," ASME Paper No. 99-GT-163.
[11] Mahmood, G. I., and Ligrani, P. M., 2002, "Heat Transfer in a Dimpled Channel: Combined Influences of Aspect Ratio, Temperature Ratio, Reynolds Number, and Flow Structure," Int. J. Heat Mass Transf., **45**(10), pp. 2011–2020.
[12] Oliveira, M. M., 2002, "Heat Transfer and Skin Friction Coefficients in a Channel With Deep Dimples," M. S. thesis, Department of Mechanical Engineering, University of Utah, Salt Lake City, UT.
[13] Kline, S. J., and McClintock, F. A., 1953, "Describing Uncertainties in Single Sample Experiments," Mech. Eng. (Am. Soc. Mech. Eng.), **75**, pp. 3–8.
[14] Moffat, R. J., 1988, "Describing the Uncertainties in Experimental Results," Exp. Therm. Fluid Sci., **1**(1), pp. 3–17.
[15] Mahmood, G. I., 2001, "Heat Transfer and Flow Structure From Dimples in an Internal Cooling Passage," Ph.D. thesis, Department of Mechanical Engineering, University of Utah, Salt Lake City, UT.
[16] Lienhard, J. H., 1987, *A Heat Transfer Textbook*, Second Edition, Prentice-Hall Inc., Englewood Cliffs, New Jersey, pp. 338–343.
[17] Ligrani, P. M., Harrison, J. L., Mahmood, G. I., and Hill, M. L., 2001, "Flow Structure Due to Dimple Depressions on a Channel Surface," Phys. Fluids, **13**(11), pp. 3442–3451.
[18] Amon, C. H., Majumdar, D., Herman, C. V., Mayinger, F., Mikic, B. B., and Sekulic, D. P., 1992, "Numerical and Experimental Studies of Self-Sustained Oscillatory Flows in Communicating Channels," Int. J. Heat Mass Transf., **35**(11), pp. 3115–3129.
[19] Majumdar, D., and Amon, C. H., 1997, "Oscillatory Momentum Transport Mechanisms in Transitional Complex Geometry Flows," ASME J. Fluids Eng., **119**(1), pp. 29–35.
[20] Nigen, J. S., and Amon, C. H., 1994, "Time-Dependent Conjugate Heat Transfer Characteristics of Self-Sustained Oscillatory Flows in a Grooved Channel," ASME J. Fluids Eng., **116**(3), pp. 499–507.
[21] Ligrani, P. M., Oliveira, M. M., and Blaskovich, T., 2003, "Comparison of Heat Transfer Augmentation Techniques," *AIAA Journal*, to appear.

A Numerical Study of Flow and Heat Transfer in Rotating Rectangular Channels ($AR=4$) With 45 deg Rib Turbulators by Reynolds Stress Turbulence Model

Mohammad Al-Qahtani[1]
Turbine Heat Transfer Laboratory,
Department of Mechanical Engineering,
Texas A&M University,
College Station, TX 77843

Hamn-Ching Chen
Ocean Engineering Program,
Department of Civil Engineering,
Texas A&M University,
College Station, TX 77843

Je-Chin Han
Turbine Heat Transfer Laboratory,
Department of Mechanical Engineering,
Texas A&M University,
College Station, TX 77843

Computations were performed to study three-dimensional turbulent flow and heat transfer in stationary and rotating 45 deg ribbed rectangular channels for which experimental heat transfer data were available. The channel aspect ratio (AR) is 4:1, the rib height-to-hydraulic diameter ratio (e/D_h) is 0.078 and the rib-pitch-to-height ratio (P/e) is 10. The rotation number and inlet coolant-to-wall density ratios, $\Delta\rho/\rho$, were varied from 0.0 to 0.28 and from 0.122 to 0.40, respectively, while the Reynolds number was fixed at 10,000. Also, two channel orientations ($\beta=90$ deg and 135 deg from the rotation direction) were investigated with focus on the high rotation and high density ratios effects on the heat transfer characteristics of the 135 deg orientation. These results show that, for high rotation and high density ratio, the rotation induced secondary flow overpowered the rib induced secondary flow and thus change significantly the heat transfer characteristics compared to the low rotation low density ratio case. A multi-block Reynolds-Averaged Navier-Stokes (RANS) method was employed in conjunction with a near-wall second-moment turbulence closure. In the present method, the convective transport equations for momentum, energy, and turbulence quantities are solved in curvilinear, body-fitted coordinates using the finite-analytic method. [DOI: 10.1115/1.1527907]

Keywords: Augmentation, Computational, Heat Transfer, Rotating, Turbines

1 Introduction

1.1 Motivation. To improve thermal efficiency, gas-turbine stages are being designed to operate at increasingly higher inlet temperatures. A widely used method for cooling turbine blades is to bleed lower-temperature gas from the compressor and circulate it within and around each blade. The coolant typically flows through a series of straight ducts connected by 180 deg bends and roughened with ribs or pin fins to enhance heat transfer. These cooling ducts may not only be square in cross section or normal to the rotational direction of the blade. In fact, the aerodynamic shape of the turbine blade dictates the use of cooling channels that are rectangular in cross section (with different aspect ratios) and are at an angle, β, from the direction of rotation. Rotation of the turbine blade cooling passages adds another complexity to the problem. It gives rise to Coriolis and buoyancy forces that can significantly alter the local heat transfer in the internal coolant passages from the non-rotating channels. The presence of rib turbulators adds a further complexity since these ribs produce complex flow fields such as flow separation, reattachment and secondary flow between the ribs, which produce a high turbulence level that leads to high heat transfer coefficients.

1.2 Literature Review: Experimental Studies. The complex coupling of the Coriolis and buoyancy forces with flow separation/reattachment by ribs has prompted many investigators to study the flow and temperature fields generated in heated, rotating ribbed wall passages. Most experimental studies on internal cooling passages have focused on non-rotating ducts. See, for example, Han and Park [1], Han et al. [2] Ekkard and Han [3] and Liou et al. [4] and the references cited there. Experimental studies on rotating ducts have been less numerous. Wagner et al. [5], Dutta and Han [6], Soong et al. [7] and Azad et al. [8] investigated rotating ducts with smooth and ribbed walls. Wagner et al. [9], Johnson et al. [10] and [11], Parsons et al. [12] and Zhang et al. [13] reported studies on rotating square channels with normal and angled ribs. Azad et al. [8] also investigated the effect of channel orientation on rotating ribbed two pass rectangular channel. Griffith et al. [14] studied the effect of channel orientation on rotating smooth and ribbed rectangular channels with channel aspect ratio of 4:1. They investigated a broad range of flow parameters including Reynolds number (Re=5000–40000), rotation number (Ro=0.04–0.3) and coolant to wall density ratio ($\Delta\rho/\rho$ =0.122). Their experimental results provided a database for the present work.

1.3 Literature Review: Numerical Studies. In addition to the experimental studies mentioned above, several studies have been made to predict numerically the flow and heat transfer in radially rotating smooth and ribbed ducts. Stephens et al. [15,16] studied inclined ribs in a straight non-rotating square duct. Lin et al. [17] investigated the effect of angled ribs on the heat transfer coefficients in a rotating two-passage duct using a shear-stress transport (SST) turbulence model. They studied the effects of Reynolds numbers, rotation numbers, and buoyancy parameters. Prakash and Zerkle [18], employing a high Reynolds number k-ε turbulence model with wall function, performed a numerical prediction of flow and heat transfer in a ribbed rectangular duct (90

[1]Current address: Assistant Professor, King Fahd University, Saudi Arabia.

Contributed by the Heat Transfer Division for publication in the JOURNAL OF HEAT TRANSFER. Manuscript received by the Heat Transfer Division April 10, 2002; revision received September 10, 2002. Associate Editor: M. Faghri.

deg rib) with and without rotation. However, their calculations used periodicity and neglected buoyancy effects. They suggested that a low Reynolds number turbulence model is necessary to simulate real gas turbine engine conditions and a Reynolds stress model is required to capture anisotropic effects. Bonhoff et al. [19] calculated the heat transfer coefficients and flow fields for rotating U-shaped coolant channels with angled ribs (45 deg). They used a Reynolds stress turbulence model with wall functions in the FLUENT CFD code. Using the periodicity of the flow, lacovides [20] computed flow and temperature fields in a rotating straight duct with 90 deg ribs. Two zonal models of turbulence were tested: a k-ε with a one-equation model of k transport across the near-wall region and a low-Re differential stress model. He concluded that the differential stress model thermal computations were clearly superior to those of the k-ε/one-equation model.

Using the same model and method of Chen et al. [21,22], Jang et al. [23,24] studied flow and heat transfer behavior in a nonrotating two-pass square channels with 60 deg and 90 deg ribs, respectively. Their results were in good agreement with Ekkad and Han's [3] detailed heat transfer data which validated their code and demonstrated the second-moment closure model superiority in predicting flow and heat transfer characteristics in the ribbed duct. In a later study, Jang et al. [25] predicted flow and heat transfer in a rotating square channel with 45 deg angled ribs by the same second-moment closure model. Heat transfer coefficient prediction was well matched with Johnson et al. [11] data for both stationary and rotating cases. Al-Qahtani et al. [26] predicted flow and heat transfer in a rotating two-pass rectangular channel with 45 deg angled ribs by the same second-moment closure model of Chen et al. [21,22]. Heat transfer coefficient prediction was compared with the data of Azad et al. [8] for both stationary and rotating cases. It predicted fairly well the complex three-dimensional flow and heat transfer characteristics resulting from the angled ribs, sharp 180 deg turn, rotation, centrifugal buoyancy forces and channel orientation.

In practice, the aerodynamic shape of the turbine blade dictates the use of cooling channels that are rectangular in cross section and are at an angle β from the direction of rotation. The effect of rotation, channel orientation and large channel aspect ratio on the secondary flow and heat transfer in rectangular channels may vary from the square channels. None of the previous studies predicted the characteristics of fluid flow and heat transfer in rotating rectangular channels that have an aspect ratio, *AR*, of 4:1 whether perpendicular or at an angle from the direction of rotation.

The objective of this study is to use the second moment RANS method of Chen et al. [21,22] to (1) predict the three-dimensional flow and heat transfer for rotating smooth and ribbed one-pass rectangular ducts ($AR=4:1$) and compare with the experimental data of Griffith et al. [14] and (2) to investigate the effect of high rotation and high density ratios on the secondary flow field and the heat transfer characteristics in a ribbed duct at 135 deg orientation.

2 Description of Problem

A schematic diagram of the geometry is shown in Fig. 1. It has a rectangular cross section with channel aspect ratio, *AR*, of 4:1. Two of the four side walls, in the rotational direction, are denoted as the leading and trailing surfaces, respectively, while the other two side walls are denoted as the top and bottom surfaces. The channel hydraulic diameter, D_h, is 0.8 in (2.03 cm). The distance from the inlet of the channel to the axis of rotation (Y-axis) is given by $R_r/D_h=20.0$ and the length of the channel is given as $L/D_h=22.5$. The channel consists of unheated starting smooth length ($L_1/D_h=9.92$), heated ribbed section ($L_2/D_h=7.58$) and unheated exit smooth section ($L_3/D_h=5.00$). The arc length S is measured from the beginning of the heated section to the end of it. In the ribbed section, the leading and trailing surfaces are roughened with nine equally spaced ribs of square cross section. The rib height-to-hydraulic diameter ratio (e/D_h) is 0.078 and the rib-

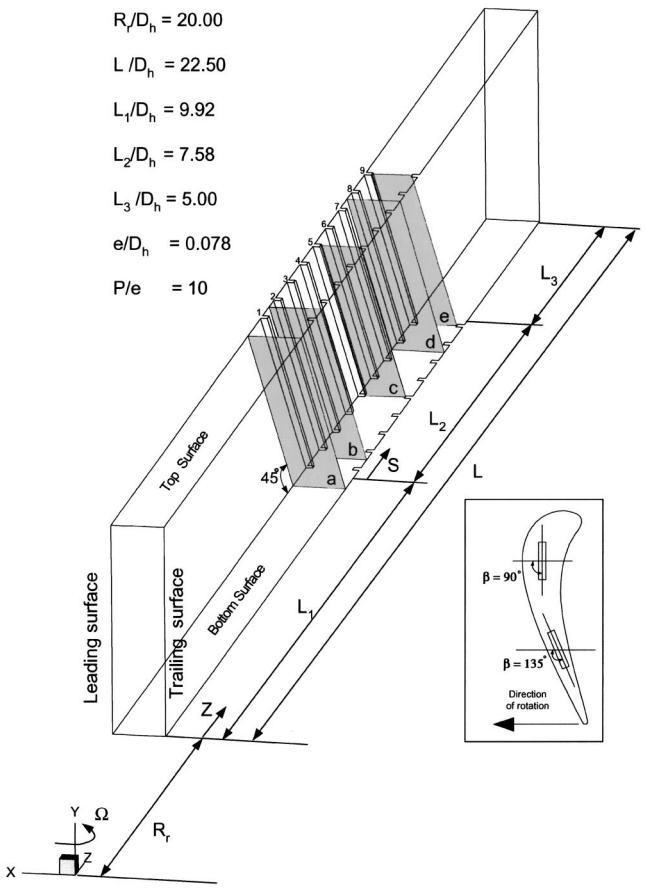

Fig. 1 Geometry

pitch-to-height ratio (P/e) is 10. All ribs are inclined at an angle $\alpha=45$ deg with respect to the flow under an in-line arrangement. Two channel orientations are studied: $\beta=90$ deg corresponding to the mid-portion of a turbine blade and $\beta=135$ deg corresponding to the trailing edge region of a blade. A summary of the cases studied is given in Table 1.

3 Computational Procedure

3.1 Overview. The Reynolds-Averaged Navier-Stokes equations in conjunction with a near wall Reynolds stress turbulence model are solved using the chimera RANS method of Chen et al. [21,22]. The governing equations with the second-moment closure turbulence model were described in detail by Chen et al. [21,22] and will not be repeated here. The flow is considered to be incompressible since the Mach number is quite low. However, the density in the centrifugal force terms is approximated by $\rho=\rho_o T_o/T$ to account for the density variations caused by the temperature differences. ρ_o and T_o are the density and temperature at the inlet of the cooling channel. In general, the density is also a function of the rotating speed because the centrifugal force creates a pressure gradient along the duct. In the experiments of Griffith

Table 1 Summary of cases studied, Re=10,000

Case #	Surface	Ro	$\Delta\rho/\rho$	β	Expt.
1	Ribbed	0.00	0.122	-	yes
2	Ribbed	0.14	0.122	90°	yes
3	Ribbed	0.14	0.122	135°	NA
4	Ribbed	0.28	0.122	135°	NA
5	Ribbed	0.28	0.200	135°	NA
6	Ribbed	0.28	0.400	135°	NA

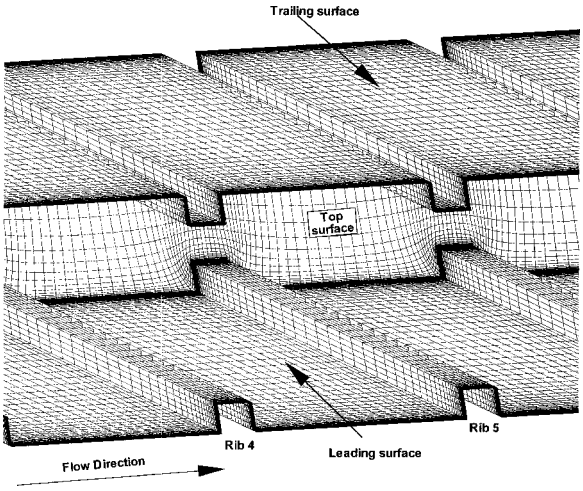

Fig. 2 Numerical grid

et al. [14], the maximum pressure variation between the channel inlet and the exit is approximately 0.0113 atm for the highest rotation number of 0.28 (i.e., $\Omega = 550$ rpm) considered in the present study. This gives a maximum density variation of only about 1.1 percent from the inlet to the exit of the duct at the highest rotation number. It is therefore reasonable to omit the density variation caused by the pressure gradients induced by the channel rotation in this paper.

3.2 Boundary Conditions. A uniform velocity profile was used at the inlet of the duct ($Z=0$). The unheated length (L_1) was long enough for the velocity profile to be fully developed turbulent profile before the heating start-point ($Z=L_1$). At the exit of the duct, zero-gradient boundary conditions were specified for the mean velocity and all turbulent quantities, while linear extrapolation was used for the pressure field. The coolant fluid at the inlet of the duct is air at uniform temperature $T=T_o$ (i.e., $\theta=(T-T_o)/(T_w-T_o)=0$). The wall temperature of the unheated sections is kept constant at $T=T_o$ ($\theta=0$) while the wall temperature of the heated section is kept constant at $T=T_w$ ($\theta=1$).

3.3 Computational Grid Details. Figure 2 shows the computational grid around the ribs for the ribbed duct. The grid was generated using an interactive grid generation code GRIDGEN [27]. It was then divided into five overlapped chimera grid blocks to facilitate the implementation of the near-wall turbulence model and the specification of the boundary conditions. To provide adequate resolutions of the viscous sublayer and buffer layer adjacent to a solid surface, the minimum grid spacing in the near-wall region is maintained at 10^{-3} of the hydraulic diameter which corresponds to a wall coordinate y^+ of the order of 0.5. The number of grid points in the streamwise direction from inlet to outlet is 394 for the ribbed duct. The number of grid points in the cross-stream plane is 33×75. The number of grid points and their distributions in the present ribbed duct were obtained based on extensive grid-refinement studies that were performed in Chen et al. [21,22], Jang et al. [23–25] and Al-Qahtani [26] for similar channels of a square and rectangular cross sections. The interested reader is referred to these references for the details of the grid refinement studies performed on the similar smooth and ribbed channels. In all calculations, the root-mean-square (rms) and maximum absolute errors for both the mean flow and turbulence quantities were monitored for each computational block to ensure complete convergence of the numerical solutions and a convergence criterion of 10^{-5} was used for the maximum rms error.

4 Results and Discussion

As summarized in Table 1, computations were performed for one Reynolds number (10,000), rotation numbers ranging from 0 to 0.28 and inlet coolant-to-wall density ratios $\Delta\rho/\rho$ ranging from 0.122 to 0.40 with two channel orientations of $\beta=90$ deg and 135 deg. The Nusselt numbers presented here were normalized with a smooth tube correlation by Dittus-Boelter/McAdams (Rohsenow and Choi [28]) for fully developed turbulent non-rotating tube flow:

$$\mathrm{Nu}_o = 0.023\,\mathrm{Re}^{0.8}\mathrm{Pr}^{0.4}$$

4.1 Velocity and Temperature Fields. Before discussing the detailed computed velocity field, a general conceptual view about the secondary flow patterns induced by angled ribs and rotation is summarized and sketched in Fig. 3. The parallel angled ribs in the non-rotating duct (Fig. 3(*a*)) produce symmetric counter rotating vortices that impinge on the top surface. The Coriolis force in the $\beta=90$ deg rotating duct (Fig. 3(*b*)) produces two additional counter-rotating vortices that push the cooler fluid from the core to the trailing surface. For the $\beta=135$ deg rotating duct (Fig. 3(*c*)), the Coriolis force produces two long vortices parallel to the ribbed surfaces and a third small vortex near the corner of the top-trailing surfaces. The effect of this rotation secondary flow is to combine destructively (opposite directions) with the rib induced secondary flow along the whole leading and trailing surfaces. This is an important concept that will help explain some of the coming flow and heat transfer characteristics.

At several axial stations as defined in Fig. 1, Figs. 4 through 7 show the calculated secondary flow vectors and constant temperature contours for the ribbed cases as mentioned in Table 1. Figure 4 shows the calculated secondary flow vectors and constant temperature contours for the non-rotating case (case 1). Since the ribs are oriented at a negative 45 deg angle, the fluid adjacent to the top and ribbed surfaces will reach the ribs first and change direction along the ribbed surfaces toward the bottom surface (Fig. 4(*a*)). It then returns back to the top surface along the centerline of the inclined cross-stream plane. In the same figure, one can also notice the early stages of two symmetric counter-rotating vortices, which become two full symmetric counter-rotating vortices in the midsection of any two ribs (Fig. 4(*b*)). Along the streamwise direction, the size of these two vortices oscillates from the largest in the middle of each inter-rib distance to the smallest on the rib tops (Fig. 4(*c*)). This pattern keeps repeating until the last rib (Fig. 4(*d*) and 4(*e*)). The effect of the secondary flow on the temperature

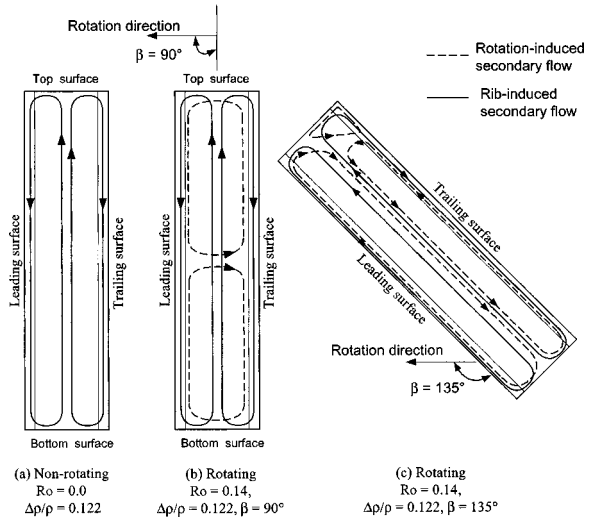

Fig. 3 Conceptual view of the secondary flow induced by angled ribs and rotation

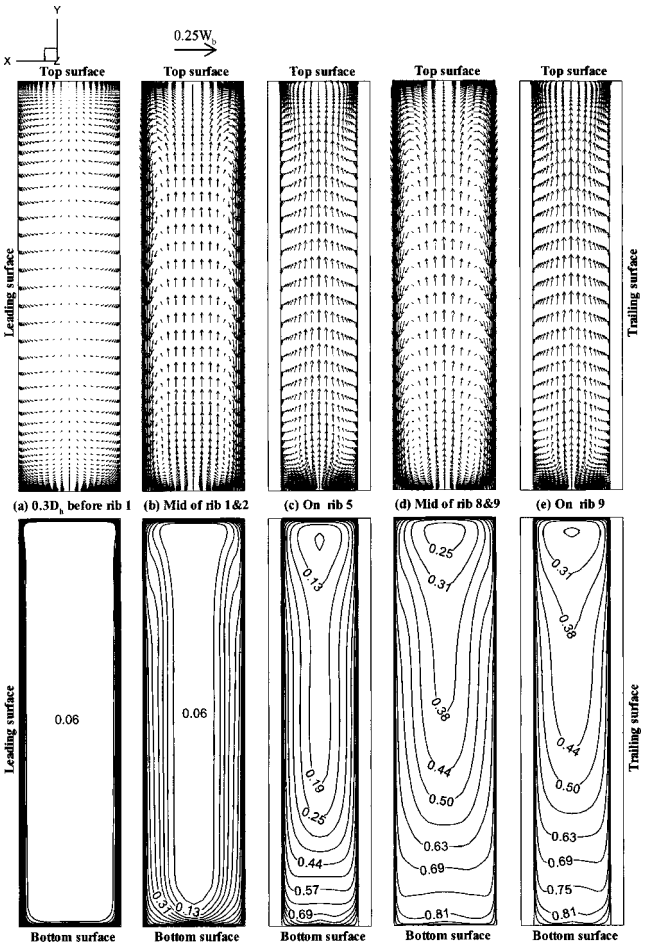

Fig. 4 Secondary flow and temperature $[\theta=(T-T_o)/(T_w-T_o)]$ for non-rotating ribbed duct, Ro=0.00

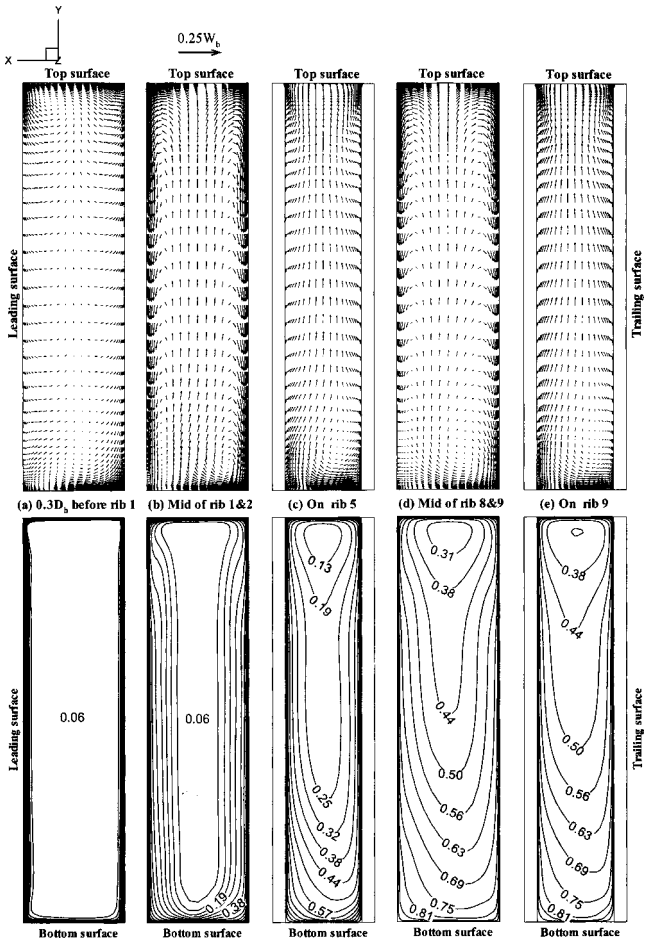

Fig. 5 Secondary flow and temperature $[\theta=(T-T_o)/(T_w-T_o)]$ for rotating ribbed duct, Ro=0.14 and β=90 deg

field is convecting the cooler fluid from the top surface and along the ribbed surfaces towards the bottom surface. It then moves back to the top surface which results in steep temperature gradients and high heat transfer coefficients on both the top and ribbed surfaces as seen in the corresponding temperature contours.

Figure 5 shows the cross-stream velocity vectors and temperature contours for case 2 (Ro=0.14 and β=90 deg) at the same planes as in the non-rotating ribbed duct (case 1). As the flow approaches the first rib, this Coriolis force induced secondary flow starts to distort the secondary flow started by the inclined ribs. This effect can be clearly seen by comparing Figs. 5(*a*) through 5(*e*) with Figs. 4(*a*) through 4(*e*). From this comparison, the following conclusions can be drawn. (1) The magnitude of the Coriolis force induced secondary flow is weaker than the rib induced secondary flow. (2) In the midsections of each of two ribs, the rib induced vortex near the bottom surface is distorted slightly in the midsection of rib 1 and 2 (Fig. 5(*b*)) but this distortion increases as the fluid proceeds downstream the duct (Fig. 5(*d*)). (3) On the ribs (Fig. 5(*c*)), both vortices shrink in size and get distorted only near the bottom. This pattern repeats itself until the last rib (Fig. 5(*e*)). The general effect of the Coriolis force induced secondary flow is to distort the rib-induced vortices. Consequently, the temperature contours are shifted toward the trailing surface, which affects the heat transfer coefficients from both the leading and trailing surfaces as seen from the corresponding temperature contour plot.

Figure 6 shows the cross-stream velocity vectors and temperature contours for the low rotation low density ratio β=135 deg (case 3) at the same planes as in cases 1 and 2. Comparing Fig. 6 with Fig. 5, the following can be noticed. Just before the ribbed section, the rotation induced secondary flow is still dominant as can be seen from comparing Figs. 6(*a*) and 5(*a*). However, from rib 1 on, this low rotation induced secondary flow is dominated by the rib induced secondary flow. A careful comparison between the secondary flow fields of case 3 and case 2 (e.g., Fig. 6(*d*) with Fig.

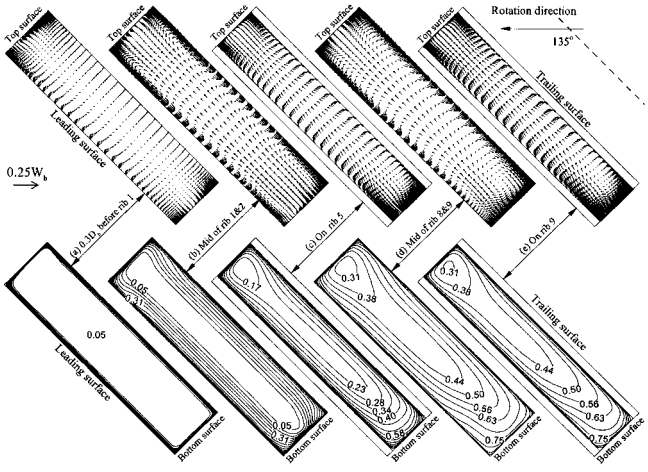

Fig. 6 Secondary flow and temperature $[\theta=(T-T_o)/(T_w-T_o)]$ for rotating ribbed duct, Ro=0.14, $\Delta\rho/\rho$=0.122 and β=135 deg

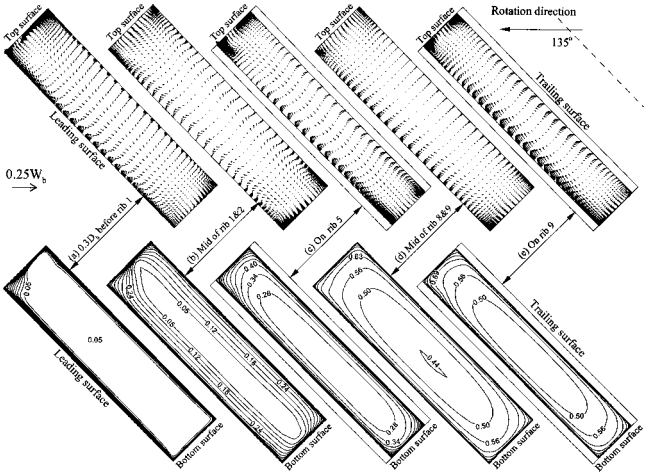

Fig. 7 Secondary flow and temperature $[\theta=(T-T_o)/(T_w-T_o)]$ for rotating ribbed duct, Ro=0.28, $\Delta\rho/\rho$=0.40 and β=135 deg

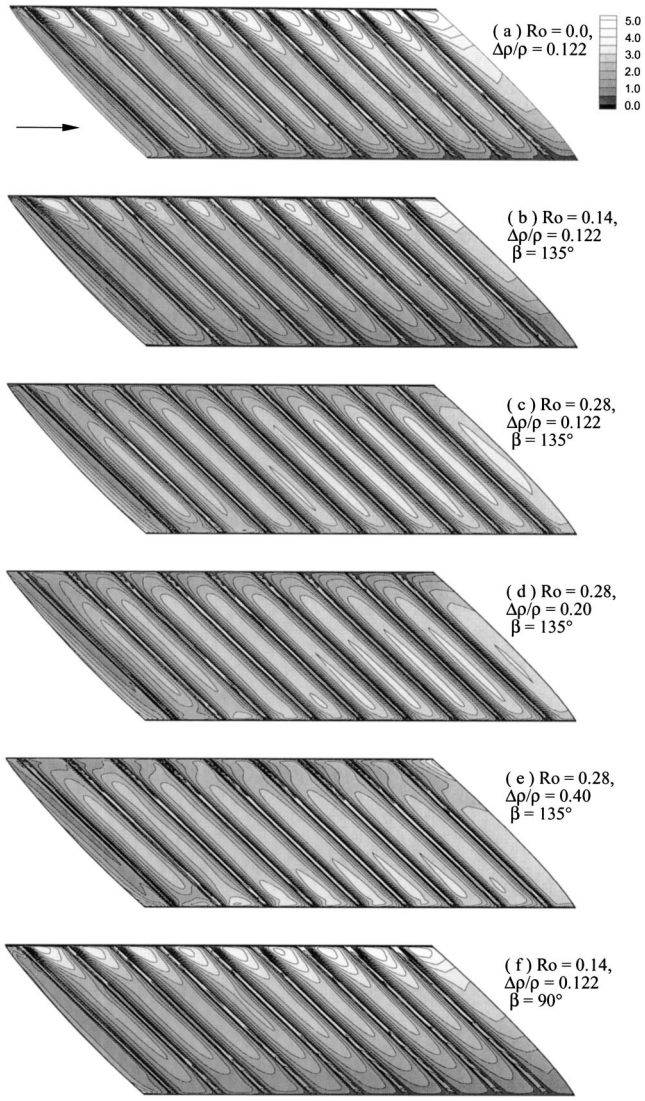

Fig. 8 Leading surface detailed Nusselt number ratio distribution in ribbed duct

5(d)) shows that there is only minor change in the net effect of the secondary flow fields. This minor change appears more clearly in the temperature field. By comparing the temperature contours in Fig. 6 with Fig. 5, we notice that the cooler fluid is pushed back toward the leading surface, reducing the steep temperature gradients on the trailing surface.

As we increase the rotation number and density ratio, the strength of the rotation-induced secondary flow increases and gradually overcomes the rib induced secondary flow (recall Fig. 3(c)). By reaching a rotation number of 0.28 and a density ratio of 0.40 as shown in Fig. 7 (case 6), the rotation-induced secondary flow is found to be dominant over the rib induced secondary flow especially downstream of the channel. This is very clear by comparing the corresponding axial stations in Figs. 7 and 6. This important result has its own consequence on the temperature field and thus the Nusselt number ratio distribution. The rib induced secondary flow is not any more able to drive the secondary flow from the ribs leading side (near the top surface) to the ribs trailing side (near the bottom surface). On the contrary, the rotation induced secondary flow moves the cold fluid from the bottom surface along the ribbed surfaces with the secondary flow along the leading surface is much stronger than the one on the trailing surface. The temperature contours in Fig. 7 indicate that the cold fluid is moved toward the bottom surface compared to Fig. 6.

4.2 Detailed Local Heat Transfer Coefficient Distribution. For various rotation numbers and density ratios, Figs. 8 and 9 show the local Nusselt number ratio contours of the ribbed leading and trailing surfaces, respectively. The non-rotating case in Fig. 8(a) (9(a) for the trailing surface) will be used as a baseline for comparison and discussion. Figures 8(b) through 8(e) (9(b) through 9(e) for the trailing surface) are for β=135 deg while Fig. 8(f) (9(f) for the trailing surface) is for β=90 deg. The entrance and exit regions were cut to focus on the ribbed heated section. First, the effect of the channel orientation on the Nusselt number ratios is discussed via comparing Figs. 8(b) and 8(f) (9(b) and 9(f) for the trailing surface). Second, the effect of increasing the rotation number on the β=135 deg Nusselt number ratios is discussed via Figs. 8(a) through 8(c) (9(a) through 9(c) for the trailing surface). Third, the effect of increasing the density ratio on the β=135 deg Nusselt number ratios is discussed via Figs. 8(c) through 8(e) (9(c) through 9(e) for trailing surface).

In Fig. 8(a), the highest Nusselt number ratios were obtained on the top of the ribs, and the lower Nusselt number ratios were obtained right before and after the ribs. Between any two ribs, the Nusselt number ratios are highest near the top surface and decrease as we move towards the bottom surface. This is due to the rib induced secondary flow that moves from the top surface (and parallel to the ribbed walls) to the bottom surface.

Effect of Channel Orientation on the Leading and Trailing Surfaces. For fixed rotation number and density ratio (Ro=0.14 and $\Delta\rho/\rho$=0.122), Figs. 8(b) and 8(f) show the Nusselt number ratios contours on the leading side for β=135 deg and 90 deg, respectively. Comparing these figures with the non-rotating leading side (Fig. 8(a)), it is noticed that the Nusselt number ratios decreased in both cases with the decrease in the β=135 deg case being the most (a 19 percent decrease compared to a 10 percent decrease in the 90 deg case). Figures 9(b) and 9(f) show the Nusselt number ratios contours on the trailing side for β=135 deg and 90 deg, respectively. Comparing these figures with the nonrotating trailing side (Fig. 9(a)) it is noticed that the Nusselt number increased in both cases with the increase in β=135 deg being the least (a 1 percent increase compared to a 5 percent increase in the β=90 deg case). The reason why the Nusselt number ratios in the β=135 deg case decreased more on the leading side and increased less on the trailing side compared to β=90 deg case can be understood in light of the conceptual secondary flow diagram in Fig. 3. The rotation induced vortex in the β=135 deg configuration move along the full face of the leading or trailing surfaces. How-

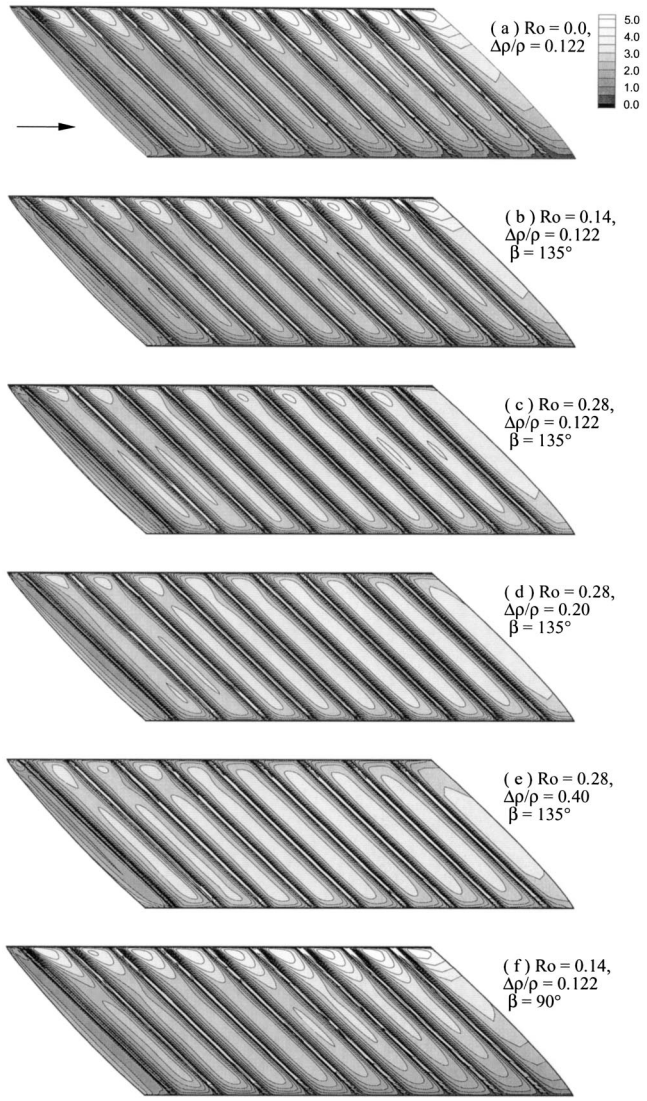

Fig. 9 Trailing surface detailed Nusselt number ratio distribution in ribbed duct

ever, the rotation induced vortex in the $\beta=90$ deg configuration moves along only one half the face of the leading or trailing surfaces. With this in mind, we notice in Fig. 3 that the two secondary flows produced by rotation and angled ribs for the rotating $\beta=135$ deg duct combine destructively (opposite direction) and thus reduce heat transfer on both the leading surface and the trailing surface. On the other hand, the two secondary flows produced by rotation and angled ribs for the rotating $\beta=90$ deg duct combine to (*i*) constructively (same direction) enhance heat transfer for only one half of each of the leading and trailing surfaces and (*ii*) destructively (opposite direction) reduce heat transfer for the other half of each of the leading and trailing surfaces.

Effect of Increasing the Rotation Number on the Leading Surface. In Fig. 8(*b*), the rotation number is increased to 0.14 while the density ratio is kept fixed at 0.122. As discussed before, this causes the Nusselt number ratios to decrease by 19 percent compared to the non-rotating case (Fig. 8(*a*)). But when the rotation number was increased to 0.28 (Fig. 8(*c*)), the Nusselt number ratios decreased only by 10 percent compared to the non-rotating case. Moreover, it is noted that the high Nusselt number ratios regions are shifted to the middle of the ribbed surface. This is because of the rotation induced secondary flow getting stronger and gradually overcomes the rib induced secondary flow.

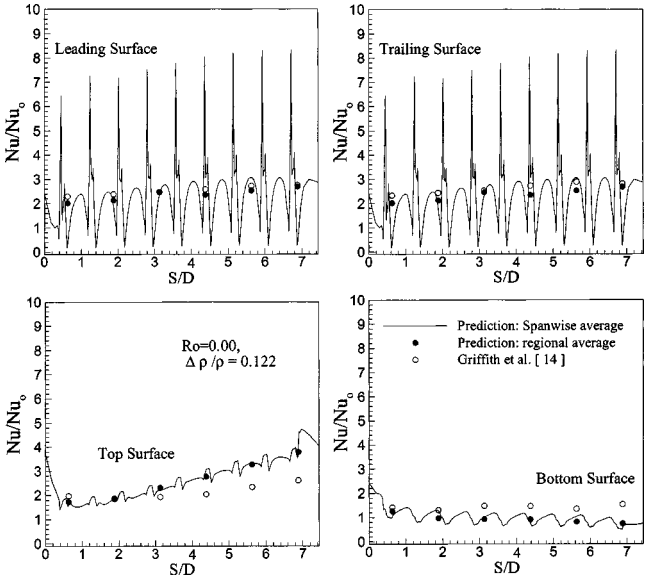

Fig. 10 Calculated and measured Nusselt number ratio distribution for non-rotating ribbed duct, Re=10,000

Effect of Increasing the Density Ratio on the Leading Surface In Fig. 8(*d*), the rotation number is kept fixed at 0.28 while the density ratio is increased to 0.20. It is seen from this figure that the high Nusselt number ratios regions are moved further toward the bottom surface. Increasing the density ratio further to 0.40 (Fig. 8(*e*)), we notice that the high Nusselt number ratios regions are now existing next to the bottom surface with a total decrease of only 4 percent compared to the non-rotating case.

Effect of Increasing the Rotation Number on the Trailing Surface. Figure 9 shows the same information as in Fig. 8 but for the trailing surface. Figure 9(*a*) (Ro=0.00) will be used as the baseline for comparison and discussion. As discussed before, increasing the rotation number to 0.14 (Fig. 9(*b*)) causes the Nusselt number ratios to increase only by 1 percent compared to the non-rotating case. In Fig. 9(*c*), the rotation number is increased further to 0.28 while the density ration is kept fixed at 0.122. This causes the Nusselt number ratios to increase by 6 percent compared to the non-rotating case. Also, it is seen from this figure that the high Nusselt number ratios regions are spreading toward the bottom surface.

Effect of Increasing the Density Ratio on the Trailing Surface In Fig. 9(*d*), the rotation number is kept fixed at 0.28 while the density ratio is increased to 0.20. It is seen in this figure that the high Nusselt number ratios regions are pushed slightly more toward the bottom surface. Increasing the density ratio further to 0.40 (Fig. 9(*e*)) causes the Nusselt number ratios to increase by 12 percent compared to the non-rotating case. It is also seen from this figure that, upstream of the channel, the high Nusselt number ratios are moved toward the bottom surface while downstream they dominate most of the inter-rib regions.

4.3 Spanwise-Averaged Heat Transfer Coefficients and Comparison With Experimental Data. Figures 10 and 11 show the spanwise-averaged and regional-averaged Nusselt number ratios (Nu/Nu_o) for the ribbed cases 1 (non-rotating) and 2 ($\beta=90$ deg rotating). The rotation number and the inlet coolant-to-wall density ratio were held constant at values of 0.14, and 0.122, respectively. Note that the experimental regional-averaged Nusselt number in Griffith et al. [14] is based on the projected area of each copper plate rather than the true heat transfer surface area which includes the 45 deg rib-increased area. However, our predicted regional-averaged Nusselt Number is based on the true heat transfer area for the test surfaces with 45 deg ribs which is 1.25 times

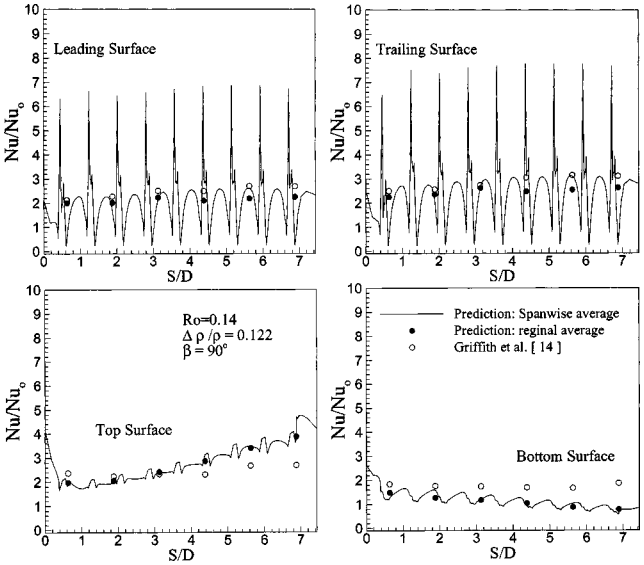

Fig. 11 Calculated and measured Nusselt number ratio distribution for rotating ribbed duct (Ro=0.14), Re=10,000

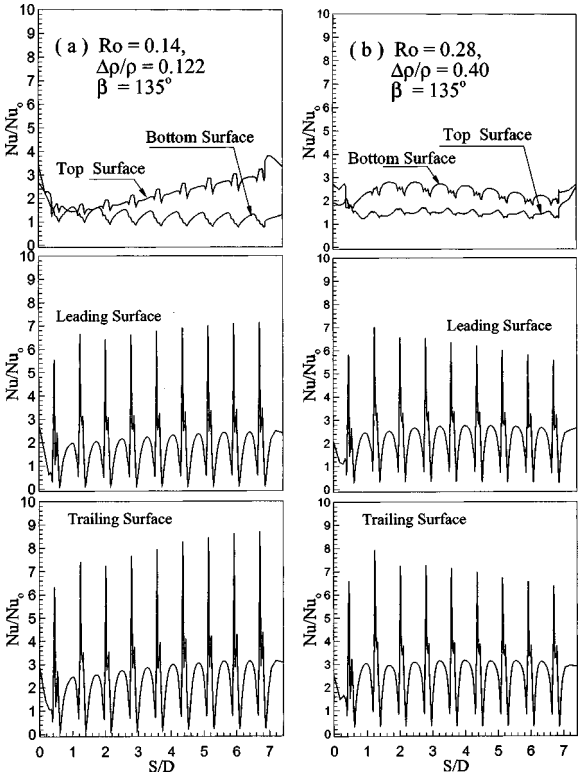

Fig. 12 Effect of rotation and density ratio on 135 deg Nusselt number ratio distribution for Re=10,000

the projected area. Therefore, the experimental data were divided by 1.25 to reasonably compare with our regional-averaged Nusselt number, except for the inner and outer surfaces where there were no ribs. The predicted Nusselt number ratios on the leading and trailing surfaces are in good agreement with Griffith et al. [14] data for the non-rotating case (Fig. 10) while relatively close to the experimental data in the rotating case (Fig. 11). Downstream of the channel, the predicted Nusselt numbers on the top and bottom surfaces are mildly over-predicted and under-predicted, respectively. This may be partly attributed to the fact that the predicted Nusselt number ratios are based on a uniform wall temperature boundary condition while the experimental ones are based on a uniform wall heat flux boundary condition.

The spanwise-averaged Nusselt number distributions on the leading and trailing surfaces of Figs. 10 and 11 show periodic spikes. The higher spikes which occur on the ribs tops are caused by the flow impingement on the ribs, and the lower spikes (which occur right before and after the ribs) are caused by the flow reattachment between the ribs. The Nusselt number ratios are high in the regions between the ribs. The Nusselt number ratios increase until the last rib, which is similar to the results obtained in Jang's et al. [25] 45 deg-ribbed square channel and Al-Qahtani's et al. [26] 45 deg-ribbed rectangular channel ($AR=2$). This phenomenon is caused by the rib-induced secondary flow becoming stronger along the duct as discussed in Figure 4. The Nusselt number distribution on the top surface of Figs. 10 and 11 shows that it increases all the way to rib 9 as a result of the secondary flow that pushes the cold fluid towards the top surface. For the same reason, the Nusselt number distribution on the bottom surface is decreasing (although mildly) since it receives the heated fluid from the ribbed surfaces.

Figure 12 shows the spanwise-averaged Nusselt number ratios (Nu/Nu_o) for the $\beta=135$ deg ribbed cases 3 and 6 which presents a comparison between the low-rotation low-density ratio case and the high-rotation high-density ratio cases which is close to the real rotor cooling conditions. The following observations are obtained by comparing Fig. 12(*a*) with 12(*b*). (1) It is seen that the Nusselt number ratios on the top surface of case 3 were higher than the ones on the bottom surface due to the rib induced secondary flow which convects the cooler fluid along the ribbed surfaces and then back to the top surface resulting in higher Nusselt number ratios on the top surface. However, in case 6 which represents the high rotation high density ratio range, the situation is reversed where the Nusselt number ratios on the bottom surface are higher than the ones on the top surface. This is a direct result of the rotation induced secondary flow which pushes the cold fluid toward the bottom surface. For the leading and trailing surfaces, the Nusselt number ratios spikes are higher in case 3 compared to case 6, however, the Nusselt number ratios in the inter-rib regions are higher in case 6 compared to case 3. It is found that the overall Nusselt number ratios of case 6 on the leading and trailing surface are higher than those in case 3 by 18 percent and 11 percent, respectively.

5 Conclusions

A multi-block RANS method was employed to predict three-dimensional flow and heat transfer in stationary and rotating ribbed rectangular channels with aspect ratio of 4:1 and for various rotation numbers and inlet coolant-to-wall density ratios. Two channel orientations are studied: $\beta=90$ deg and 135 deg. The present near-wall second-moment closure model results were compared with the experimental data of Griffith et al. [14]. It predicted fairly well the complex three-dimensional flow and heat transfer characteristics resulting from the large channel aspect ratio, rotation, centrifugal buoyancy forces and channel orientation. The main findings of the study may be summarized as follows.

1 The inclined ribs start two counter-rotating vortices that oscillate in size along the streamwise direction. For case 1 (non-rotating), the secondary flow results in steep temperature gradients and high heat transfer coefficients on both the top and ribbed surfaces.

2 For case 2 ($\beta=90$ deg), the rotation-induced cross-stream secondary flow distorts the rib-induced vortices and consequently, rotation shifts the temperature contours and affects the heat transfer coefficients from both the leading and trailing surfaces.

For case 3, 4, 5, and 6 ($\beta=135$ deg):

3 The rib-induced vortices are slightly distorted by low rotation-induced secondary flow (case 3) but significantly changed by the high rotation high density ratio induced secondary flow. This results into reversing the flow on the leading surface and reduces significantly the magnitude of rib-induced secondary flow on the trailing surface

4 The effect of increasing the rotation number (with fixed density ratio) is to monotonically increase the Nusselt number ratio on the trailing surface. On the leading surface, the Nusselt number ratio decreases first (case 3) and then increases (case 4)

5 The effect of increasing the density ratio (with fixed rotation number) is to have higher and uniform Nusselt number ratio on the leading and trailing surfaces

6 From design point of view, it is clear that the rib angle and the direction of rotation should be chosen such that the secondary flows that are induced by the rib angle and rotation direction should combine constructively to give maximum heat transfer.

Acknowledgments

The leading author, Mohammad Al-Qahtani, received a fellowship from King Fahd University; Saudi Arabia, for his Ph.D. study at Texas A&M University. The project was also supported by the DOE Advanced Gas Turbine Systems Research (AGTSR) Program through project number SR-082. The computations were performed on the Cray J90 at the Texas A&M Supercomputer Center under a supercomputer research grant, and Cray C90 of Cray Research Inc. under the sponsorship of Frank Kampe. The GRIDGEN software was supported by Pointwise Inc. The support of all of the above institutions is greatly appreciated.

Nomenclature

AR = channel aspect ratio
D_h, D = hydraulic diameter
e = rib height
h = heat transfer coefficient
k = thermal conductivity of coolant
Nu = local Nusselt number, hD/k
Nu_o = Nusselt number in fully-developed turbulent non-rotating tube flow, hD/k
Pr = Prandtl number
Re = Reynolds number, $\rho W_b D_h/\mu$
Ro = rotation number, $\Omega D_h/W_b$
R_r = radius from axis of rotation
S = streamwise distance
T = local coolant temperature
T_o = coolant temperature at inlet
T_w = local wall temperature
W_b = bulk velocity in streamwise direction
α = rib angle
β = channel orientation measured from direction of rotation
ρ = density of coolant
$\Delta\rho/\rho$ = inlet coolant-to-wall density ratio, $(T_w-T_o)/T_w$
Ω = rotational speed
θ = dimensionless temperature, $(T-T_o)/(T_w-T_o)$
μ = dynamic viscosity of coolant

References

[1] Han, J. C., and Park, J. S., 1988, ''Developing Heat Transfer in Rectangular Channel with Rib Turbulators,'' Int. J. Heat Mass Transf., **31**(1), pp. 183–195.
[2] Han, J. C., Zhang, Y. M., and Lee, C. P., 1991, ''Augmented Heat Transfer in Square Channels with Parallel, Crossed, and V-Shaped Angled Ribs,'' ASME J. Heat Transfer, **113**, pp. 590–596.
[3] Ekkad, S. V., and Han, J. C., 1997, ''Detailed Heat Transfer Distributions in Two-Pass Square Channels With Rib Turbulators,'' Int. J. Heat Mass Transf., **40**(11), pp. 2525–2537.
[4] Liou T.-M., Tzeng, Y.-Y., and Chen, C.-C., 1998, ''Fluid Flow in a 180 Deg Sharp Turning Duct with Different Divider Thicknesses,'' ASME Paper 98-GT-189.
[5] Wagner, J. H., Johnson, B. V., and Kopper, F. C., 1991, ''Heat Transfer in Rotating Serpentine Passage With Smooth Walls,'' ASME J. Turbomach., **113**(3), pp. 321–330.
[6] Dutta, S., and Han, J. C., 1996, ''Local Heat Transfer in Rotating Smooth and Ribbed Two-Pass Square Channels With Three Channel Orientations,'' ASME J. Heat Transfer, **118**(3), pp. 578–584.
[7] Soong, C. Y., Lin, S. T., and Hwang, G. J., 1991, ''An Experimental Study of Convective Heat Transfer in Radially Rotating Rectangular Ducts,'' ASME J. Heat Transfer, **113**, pp. 604–611.
[8] Azad, G. M. S., Uddin, M. J., Han, J. C., Moon, H. K., and Glezer, B., 2002, ''Heat Transfer in a Two-Pass Rectangular Rotating Channel with 45 deg Angled Rib Turbulators,'' ASME J. Turbomach., **124**(2), pp. 251–259.
[9] Wagner, J. H., Johnson, B. V., Graziani, R. A., and Yeh, F. C., 1992, ''Heat Transfer in Rotating Serpentine Passages with Trips Normal to the Flow,'' ASME J. Turbomach., **114**(4), pp. 847–857.
[10] Johnson, B. V., Wagner, J. H., Steuber, G. D., and Yeh, F. C., 1994, ''Heat Transfer in Rotating Serpentine Passage With Trips Skewed to the Flow,'' ASME J. Turbomach., **116**, pp. 113–123.
[11] Johnson, B. V., Wagner, J. H., Steuber, G. D., and Yeh, F. C., 1994, ''Heat Transfer in Rotating serpentine Passage With Selected Model Orientations for Smooth or Skewed Trip Walls,'' ASME J. Turbomach., **116**, pp. 738–744.
[12] Parsons, J. A., Han, J. C., and Zhang, Y. M., 1995, ''Effects of Model Orientation and Wall Heating Condition on Local Heat Transfer in a Rotating Two-Pass Square Channel with Rib Turbulators,'' Int. J. Heat Mass Transf., **38**(7), pp. 1151–1159.
[13] Zhang, Y. M., Han, J. C., Parsons, J. A., and Lee, C. P., 1995, ''Surface Heating Effect on Local Heat Transfer in a Rotating Two-pass Square Channel with 60 deg Angled Rib Turbulators,'' ASME J. Turbomach., **117**, pp. 272–280.
[14] Griffith, T. S., Al-Hadhrami, L., and Han, J. C., 2002, ''Heat Transfer in Rotating Rectangular Cooling Channels ($AR=4$) with Angled Ribs,'' ASME J. of Heat Transfer, **124**(3), pp. 617–625.
[15] Stephens, M. A., Shih, T. I-P., and Civinskas, K. C., 1995, ''Computation of Flow and Heat Transfer in a Rectangular Channel with Ribs,'' AIAA Paper 95-0180.
[16] Stephens, M. A., Chyu, M. K., and Shih, T. I-P., 1996, ''Computation of Convective Heat Transfer in a Square Duct with Inclined Ribs of Rounded Cross Section,'' ASME Paper 96-WA/HT-12.
[17] Lin, Y.-L., Shih, T. I-P., Stephens, M. A., and Chyu, M. K., 2001, ''A Numerical Study of Flow and Heat Transfer in a Smooth and a Ribbed U-Duct with and without Rotation,'' ASME J. Heat Transfer, **123**, pp. 219–232.
[18] Prakash, C., and Zerkle, R., 1995, ''Prediction of Turbulent Flow and Heat Transfer in a Ribbed Rectangular Duct with and without Rotation,'' ASME J. Turbomach., **177**, pp. 255–264.
[19] Bonhoff, B., Tomm, U., Johnson, B. V., and Jennions, I., 1997, ''Heat Transfer Predictions For Rotating U-Shaped Coolant Channels with Skewed Ribs and with Smooth Walls,'' ASME Paper 97-GT-162.
[20] Iacovides, H., 1998, ''Computation of Flow and Heat Transfer Through Rotating Ribbed Passage,'' Int. J. Heat Fluid Flow, **19**, pp. 393–400.
[21] Chen, H. C., Jang, Y. J., and Han, J. C., 2000, ''Computation of Heat Transfer in Rotating Two-Pass Square Channels by a Second-Moment Closure Model,'' Int. J. Heat Mass Transf., **43**(9), pp. 1603–1616.
[22] Chen, H. C., Jang, Y. J., and Han, J. C., 2000, ''Near-Wall Second-Moment Closure for Rotating Multi-pass Cooling Channels,'' J. Thermophys. Heat Transfer, **14**(2), pp. 201–209.
[23] Jang, Y. J., Chen, H. C., and Han, J. C., 2001, ''Computation of Flow and Heat Transfer in Two-Pass Channels with 60 deg Ribs,'' ASME J. Heat Transfer, **123**(3), pp. 563–575.
[24] Jang, Y. J., Chen, H. C., and Han, J. C., 2001b, ''Numerical Prediction of the Flow and Heat Transfer in a Two-Pass Square Duct with 90 deg Ribs,'' Int. J. Rotating Mach., **7**(3), pp. 195–208.
[25] Jang, Y. J., Chen, H. C., and Han, J. C., 2001, ''Flow and Heat Transfer in a Rotating Square Channel with 45 deg Angled Ribs by Reynolds Stress Turbulence Model,'' ASME J. Turbomach., **123**(1), pp. 124–132.
[26] Al-Qahtani, M. S., Jang, Y. J., Chen, H. C., and Han, J. C., 2002, ''Prediction of Flow and Heat Transfer in Rotating Two-Pass Rectangular Channels with 45 deg Rib Turbulators,'' ASME J. Turbomach., **124**(2), pp. 242–250.
[27] *GRIDGEN User Manual*, 1999, Version 13.3, Pointwise Inc.
[28] Rohsenow, W. M., and Choi, H., 1961, *Heat, Mass and Momentum Transfer*, Prentice-Hall, Englewood Cliffs, NJ.

Large Eddy Simulation of Constant Heat Flux Turbulent Channel Flow With Property Variations: Quasi-Developed Model and Mean Flow Results

Lyle D. Dailey[1]
Ning Meng
Richard H. Pletcher

Department of Mechanical Engineering,
Iowa State University,
Ames, IA 50011

Turbulent planar channel flow has been computed for uniform wall heating and cooling fluxes strong enough to cause significant property variations using large eddy simulation. Channels with both walls either heated or cooled were considered, with wall-to-bulk temperature ratios as high as 1.5 for the heated case, and as low as 0.56 for the cooled case. An implicit, second order accurate finite volume scheme was used to solve the time dependent filtered set of equations to determine the large eddy motion, while a dynamic subgrid-scale model was used to account for the subgrid scale effects. Step-periodicity was used based on a quasi-developed assumption. The effects of strong heating and cooling on the flow were investigated and compared with the results obtained under low heating conditions. [DOI: 10.1115/1.1518499]

Keywords: Channel Flow, Computational, Heat Transfer, Turbulence

1 Introduction

Large eddy simulation (LES) and direct numerical simulation (DNS) provide means for determining detailed information about turbulent flows that may be difficult to obtain experimentally. One such class of flows was considered for this work: turbulent planar channel flow with constant and uniform heat transfer fluxes at the walls of magnitudes large enough to cause significant property variations. Experiments on this type of flow have been largely limited to determining wall parameters only, e.g., (friction factors and Nusselt numbers) and in a few instances (Perkins [1], Shehata [2], Shehata and McEligot [3,4]) mean velocity and temperature profiles. This is because small tube diameters or channel heights were required to measure dominant forced convection; the test sections were frequently too small to obtain detailed measurements of temperature and velocity mean and fluctuating profiles.

A significant amount of research was conducted for this class of flows in the late 1960s and early 1970s (McEligot et al. [5], Schade and McEligot [6], Bankston and McEligot [7]). The efforts primarily employed boundary layer codes and simple mixing length turbulence models for the Reynolds averaged equations. The thermal entry region was studied extensively. Interest in gas-cooled nuclear reactors and nuclear propulsion systems necessitated the understanding of forced convection heat transfer with strongly varying properties. More recently, computational studies of this class of flow have employed a more complete mathematical description of conservation equations, usually the Reynolds averaged Navier-Stokes (RANS) equations, with a range of turbulence models. See, for example, Ezato et al. [8], where the emphasis was on strong heating in a vertical pipe. A trend toward laminarization is often observed in flows with strong heating.

This particular class of flows with heat transfer is of current interest in the computational fluid dynamics (CFD) community for a couple of reasons. For one, large eddy simulation has been used for a very limited set of turbulent flows including heat transfer, especially using the compressible form of the governing equations. An increasing number of such problems need to be investigated to develop and discern the limits of subgrid-scale modeling for such flows. More importantly, recent concerns have been raised about the validity of the commonly used law-of-the-wall for both the velocity and especially the temperature (see Bradshaw and Huang [9]). The simulation of flows with strong heating and variable properties will help to determine the validity and/or limits of these basic relationships that are used extensively in many CFD design and analysis codes.

The present paper deals with the large eddy simulation of turbulent planar channel flows with uniform heating and cooling fluxes of magnitudes large enough to cause significant property variations. A compressible formulation of the dynamic subgrid-scale model of Germano et al. [10] was used to simulate the flows. The effects of heating versus cooling on turbulent fluctuations were investigated. Comparisons were made to the limited experimental data for such flows, which mainly consisted of wall parameters such as friction factors and Nusselt numbers. Comparisons were also made to simulations of flows under low heating conditions, which produced results very similar to passive scalar analyses and for which there exists detailed experimental and DNS data of mean and fluctuating quantities.

2 Review of Related Numerical Studies

Numerical simulations of this class of flows are also practically nonexistent, mainly because of the nonhomogeneity in the streamwise direction. The exception appears to be the DNS study of Satake et al. [11], which provided results on laminarization of forced gas flows in circular tubes with strong heating. The present research is the first known LES study of a constant heat flux channel flow with variable properties.

The velocity parameters for the low heating cases can be compared to the incompressible DNS results of Kim et al. [12] and experimental results of Niederschulte et al. [13]. In addition, the temperature profiles for the low heating cases can be compared to the DNS of constant heat flux turbulent channel flow where the temperature field was treated as a passive scalar [14]. In this pa-

[1]Current address: General Electric Aircraft Engines, Cincinnati, OH 45215

Contributed by the Heat Transfer Division for publication in the JOURNAL OF HEAT TRANSFER. Manuscript received by the Heat Transfer Division November 14, 2000; revision received July 23, 2002. Associate Editor: D. A. Kaminski.

per, the variable property, high heat flux results are compared to the results from the low heating cases to determine the effects of high heating and high cooling.

A similar but distinctly different variable property channel flow was simulated by Wang and Pletcher [15]. They performed the LES of low Mach number channel flows with one hot isothermal wall and one cold isothermal wall, with temperature ratios as high as $T_{\text{hot}}/T_{\text{cold}}=3$. The hot wall corresponded to heating, and the cold wall corresponded to cooling. However, the heat transferred to the hot wall was removed from the channel through the cold wall, so that unlike the present simulations, there was no change in the bulk temperature. The compressible formulation of the dynamic SGS model was utilized in a staggered grid finite volume method that was fully implicit. Nicoud and Poinsot [16] reported a variable property DNS study for a similar channel flow with one hot wall and one cold wall.

Another simulation of interest was the DNS of supersonic isothermal-wall channel flow by Coleman et al. [17]. The Mach numbers, based on the bulk velocity and sound speed at the walls, were 1.5 and 3.0, resulting in significant density and temperature variations in the channel. The compressible effects were found to be mostly due to these large mean property variations. The heat generated near the walls due to dissipation was transferred out of the channel, so that no bulk temperature rise occurred for this flow as well.

3 Governing Equations

The governing equations for large eddy simulation are obtained by filtering the compressible form of the equations for the conservation of mass, momentum, and energy. The filtering operation, which separates the effects of the large-scale and small-scale motions, can be written in terms of a convolution integral as

$$\overline{f}(\vec{x},t)=\int_D G(\vec{x},\vec{\xi})f(\vec{\xi},t)d\vec{\xi}, \tag{1}$$

where G is some spatial filter with a width on the order of the grid spacing, and D is the flow domain.

The equations are recast in terms of Favre averages (mass-weighted), where $\tilde{f}=\overline{\rho f}/\overline{\rho}$, and nondimensionalized with respect to a reference length (channel half-height) L_r, velocity V_r, temperature T_r, density ρ_r, and viscosity μ_r. The resulting set of equations governing the large eddy motion is

$$\frac{\partial\overline{\rho}}{\partial t}+\frac{\partial(\overline{\rho}\tilde{u}_i)}{\partial x_i}=0, \tag{2}$$

$$\frac{\partial(\overline{\rho}\tilde{u}_i)}{\partial t}+\frac{\partial(\overline{\rho}\tilde{u}_i\tilde{u}_j)}{\partial x_j}=-\frac{\partial\overline{p}}{\partial x_i}+\frac{\partial\hat{\sigma}_{ij}}{\partial x_j}-\frac{\partial\tau_{ij}}{\partial x_j}, \tag{3}$$

$$\frac{\partial(\overline{\rho}\hat{E})}{\partial t}+\frac{\partial[(\overline{\rho}\hat{E}+\tilde{p})\tilde{u}_j]}{\partial x_j}=\frac{\partial(\tilde{u}_i\hat{\sigma}_{ij})}{\partial x_j}-\frac{\partial\hat{q}_j}{\partial x_j}-\frac{\partial Q_j}{\partial x_j}. \tag{4}$$

where the resolved total energy is $\hat{E}=c_v\tilde{T}+1/2\tilde{u}_i\tilde{u}_i$, the viscous stress tensor is

$$\hat{\sigma}_{ij}=\frac{2\mu}{\text{Re}_L}\left(\tilde{S}_{ij}-\frac{1}{3}\tilde{S}_{kk}\delta_{ij}\right), \tag{5}$$

and the strain rate tensor and heat flux vector are

$$\tilde{S}_{ij}=\frac{1}{2}\left(\frac{\partial\tilde{u}_i}{\partial x_j}+\frac{\partial\tilde{u}_j}{\partial x_i}\right) \tag{6}$$

$$\hat{q}_j=\frac{c_p\mu}{\text{Re}_L\,\text{Pr}}\frac{\partial\tilde{T}}{\partial x_j}. \tag{7}$$

The Favre filtered equation of state is $\overline{p}=\overline{\rho}R\tilde{T}$.

The effects of the small scales are present in the above equations through the SGS stress tensor in the filtered momentum equation,

$$\tau_{ij}=\overline{\rho}(\widetilde{u_iu_j}-\tilde{u}_i\tilde{u}_j) \tag{8}$$

and the SGS heat flux in the filtered energy equation,

$$Q_j=\overline{\rho}c_v(\widetilde{Tu_j}-\tilde{T}\tilde{u}_j). \tag{9}$$

Several other subgrid-scale terms have been omitted from the total energy equation; the terms were neglected since only low Mach number flows were considered [18]. Vreman et al. [19] demonstrated that this assumption was appropriate for Mach numbers below 0.2.

The compressible formulation for the dynamic model first proposed by Moin et al. [20] was utilized in this research.

Using the Boussinesq assumption relating the SGS stress to the rate of mean strain, the model parametrization for the SGS stress tensor is

$$\tau_{ij}-\frac{2}{3}q^2\delta_{ij}=-2C_d\overline{\rho}\overline{\Delta}^2|\tilde{S}|\left(\tilde{S}_{ij}-\frac{1}{3}\tilde{S}_{kk}\delta_{ij}\right), \tag{10}$$

$$q^2=\frac{1}{2}\tau_{kk}=C_I\overline{\rho}\overline{\Delta}^2|\tilde{S}|^2 \tag{11}$$

where

$$|\tilde{S}|=(2\tilde{S}_{ij}\tilde{S}_{ij})^{1/2} \tag{12}$$

and the grid filter length is $\Delta=(\Delta_x\Delta_y\Delta_z)^{1/3}$. τ_{kk} was neglected by setting $C_I=0.0$ because several researchers have shown this term to be negligible compared to the thermodynamic pressure (Spyropoulos and Blaisdell [21], Squires [22]). The dynamic subgrid stress model uses the information at two different grid levels (original filter and test filter) to determine dynamically the coefficient C_d. Let

$$t_{ij}=\overline{\rho u_iu_j}-\overline{\rho}\tilde{u}_i\tilde{u}_j \tag{13}$$

which is the stress term after applying the grid filter. In a similar manner, we compute

$$T_{ij}=\widehat{\rho u_iu_j}-\frac{\widehat{\rho u}_i\widehat{\rho u}_j}{\hat{\rho}} \tag{14}$$

which is the stress term after applying the test filter that is usually twice larger than the grid filter. The algebraic identity of Germano et al. [10] in the compressible case gives

$$D_{ij}=T_{ij}-\hat{t}_{ij}=\left(\frac{\widehat{\rho u_i\rho u_j}}{\overline{\rho}}\right)-\frac{\widehat{\rho u}_i\widehat{\rho u}_j}{\hat{\rho}} \tag{15}$$

If it is assumed that t_{ij} and T_{ij} can be modeled by the same functional form that utilizes the same coefficient, C_d, then

$$t_{ij}-\frac{\delta_{ij}}{3}\cdot t_{kk}=-2C_d\overline{\rho}\overline{\Delta}^2|\tilde{S}|\left(\tilde{S}_{ij}-\frac{\delta_{ij}}{3}\tilde{S}_{kk}\right) \tag{16}$$

and

$$T_{ij}-\frac{\delta_{ij}}{3}\cdot T_{kk}=-2C_d\hat{\rho}\hat{\Delta}^2|\hat{\tilde{S}}|\left(\hat{\tilde{S}}_{ij}-\frac{\delta_{ij}}{3}\hat{\tilde{S}}_{kk}\right) \tag{17}$$

where $\hat{\tilde{S}}_{ij}=\frac{1}{2}((\partial\hat{\tilde{u}}_i/\partial x_j)+(\partial\hat{\tilde{u}}_j/\partial x_i))$ and $|\hat{\tilde{S}}|=\sqrt{2\hat{\tilde{S}}_{ij}\hat{\tilde{S}}_{ij}}$ in which C_d is a coefficient to be computed. Substituting Eq. (16) and Eq. (17) into Eq. (15) gives

$$D_{ij}-\frac{\delta_{ij}}{3}\cdot D_{kk}$$

$$=2C_d\left(\overline{\rho\Delta^2}|\widetilde{S}|\left(\widetilde{S}_{ij}-\frac{\delta_{ij}}{3}\widetilde{S}_{kk}\right)-\hat{\bar{\rho}}\hat{\bar{\Delta}}^2|\hat{\widetilde{S}}|\left(\hat{\widetilde{S}}_{ij}-\frac{\delta_{ij}}{3}\hat{\widetilde{S}}_{kk}\right)\right)$$

$$=2C_dP_{ij} \tag{18}$$

A least-squares approach suggested by Lilly [23] is used to calculate C_d using Eq. (18)

$$C_d=\frac{1}{2}\frac{\langle D_{ij}P_{ij}\rangle}{\langle P_{ij}P_{ij}\rangle} \tag{19}$$

4 Dynamic Prandtl Number

A gradient transport formulation is usually a convenient and efficient way to approximate the turbulent heat flux. For example, the SGS heat flux $q_{tj}=\overline{\rho u_i T}-\overline{\rho}\widetilde{u}_i\widetilde{T}$ can be expressed as

$$q_{ti}=-\frac{\mu_t c_p}{\mathrm{Pr}_t}\frac{\partial\widetilde{T}}{\partial x_i}$$

where Pr_t is the SGS turbulent Prandtl number, and ν_t is the SGS eddy viscosity.

The SGS turbulent Prandtl number can be determined by the information from two different grid resolutions: test filtered and grid filtered. For the test filtered scalar flux

$$Q_{ti}=\widehat{\rho u_i T}-\hat{\bar{\rho}}\hat{\widetilde{u}}_i\hat{\widetilde{T}} \tag{20}$$

and grid filtered scalar flux,

$$q_{ti}=\overline{\rho u_i T}-\overline{\rho}\widetilde{u}_i\widetilde{T} \tag{21}$$

an algebraic identity exists

$$E_i=Q_{ti}-\hat{q}_{tj}=\{\widehat{\rho u_i T}-\hat{\bar{\rho}}\hat{\widetilde{u}}_i\hat{\widetilde{T}}\}-\{\widehat{\rho u_i T}-\widehat{\overline{\rho}\widetilde{u}_i\widetilde{T}}\}=\widehat{\overline{\rho}\widetilde{u}_i\widetilde{T}}-\hat{\bar{\rho}}\hat{\widetilde{u}}_i\hat{\widetilde{T}} \tag{22}$$

Using a gradient transport form for the turbulent heat flux and the SGS eddy viscosity determined from the dynamic SGS model for the momentum equations, one can write

$$E_i=-\frac{C_d}{\mathrm{Pr}_t}\left(\hat{\bar{\rho}}\hat{\bar{\Delta}}\hat{\bar{\rho}}^2|\hat{\widetilde{S}}|\frac{\partial\hat{\widetilde{T}}}{\partial x_j}-\overline{\Delta^2\overline{\rho}|\widetilde{S}|\frac{\partial\widetilde{T}}{\partial x_j}}\right) \tag{23}$$

Writing the above vector equation in symbolic form yields

$$E_i=-\frac{c_pC_d\overline{\Delta^2}}{\mathrm{Pr}_t}F_i \tag{24}$$

where

$$E_i=\widehat{\overline{\rho}\widetilde{u}_i\widetilde{T}}-\hat{\bar{\rho}}\hat{\widetilde{u}}_i\hat{\widetilde{T}} \tag{25}$$

and

$$F_i=\hat{\bar{\rho}}\alpha|\hat{\widetilde{S}}|\frac{\partial\hat{\widetilde{T}}}{\partial x_i}-\overline{\overline{\rho}|\widetilde{S}|\frac{\partial\widetilde{T}}{\partial x_i}} \tag{26}$$

where α is the square of the ratio of these two different grid resolutions. That is,

$$\alpha=\frac{\hat{\bar{\Delta}}^2}{\overline{\Delta^2}}$$

Equation (24) is a system of three equations for a single unknown Pr_t. We can employ the least squares approach to calculate the turbulent Prandtl number as

$$\mathrm{Pr}_t=-c_pC_d\overline{\Delta^2}\frac{\langle F_kF_k\rangle}{\langle E_kF_k\rangle} \tag{27}$$

The dynamic model coefficients, C_d and Pr_t, were averaged along the only homogeneous direction (spanwise) in this research to help suppress numerical instability. C_d tended to be approaching zero near the solid wall, but Pr_t sometimes gave unreasonably large values at the first grid point from the wall, and was reset as 0.9 for the sake of stability when this occurred.

5 Finite Volume Method

The structured grid finite volume method used to numerically solve the governing equations is a three-dimensional extension of the code described in Dailey and Pletcher [24]. The code used Cartesian hexahedral control volumes, and solved for the primitive variables (p,u,v,w,T) which were stored at the cell centers. Time integration was performed using an implicit LU-SGS scheme in a dual time stepping approach. Time-derivative preconditioning was used to enable the computation of low Mach number flows with property variations. The solver was second-order accurate in space and time. The multiblock code was parallelized using the message passing interface (MPI). Artificial dissipation was not used for the simulations in this study.

6 Problem Description

The problem of interest was turbulent, nonreacting flow of air in a two-dimensional horizontal planar channel. At the upper and lower walls of the channel, a constant heat flux was applied of sufficient magnitude to cause significant variation in the temperature-dependent fluid properties, as shown in Fig. 1. For gases, the density, thermal conductivity, and molecular viscosity all vary at about the same rate as the absolute temperature. The variation can be represented with a power-law dependence with exponents of 0.7–0.8 for both the thermal conductivity and viscosity. The specific heats vary only slightly with temperature, and the Prandtl number does not vary significantly. Therefore, for the present simulations, the molecular viscosity was specified with the power-law, $\mu=T^{0.7}$, the Prandtl number was assumed to have a constant value of $\mathrm{Pr}=0.71$, and the specific heats were assumed to be constant. The ratio of specific heats was $\gamma=1.4$.

The flows were computed at low Mach numbers ($M_r=0.001$) so that the effects of viscous dissipation were negligible. Assuming a horizontal orientation for the channel axis, the Froude number, $\mathrm{Fr}=\mathrm{Gr}/\mathrm{Re}^2$, where Gr is the Grashof number, was small so that buoyancy effects were assumed to be negligible. The Peclet number was small such that axial conduction was negligible. Although the simulation parameters were set up so that viscous dissipation, axial conduction, and buoyancy were negligible, the vis-

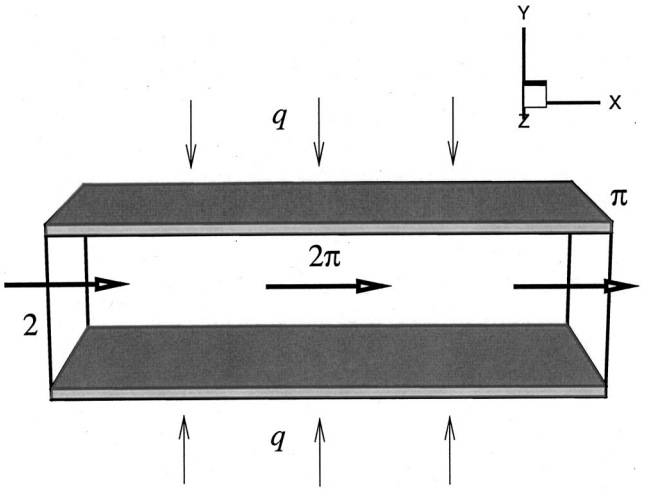

Fig. 1 Diagram of two-dimensional plane channel with constant wall heating rate, q_w

cous dissipation and axial conduction terms remained in the governing equations being solved; the buoyancy terms were not included in the governing equations.

For uniform wall heating (or cooling) with constant fluid properties under the assumptions given above, turbulent channel flows approach a fully developed state in which the time averaged streamwise velocity, u, and the nondimensional temperature, $\theta = (T_w - T)/(T_w - T_b)$, profiles no longer change in the streamwise direction, and the wall-normal velocity, v, is zero. Consequently, the local, wall, and bulk temperatures increase (or decrease) linearly along the channel at the same rate, which is directly related to the amount of heat being added (or removed) from the flow.

For strong heating or cooling, the assumption of constant fluid properties is no longer valid. For air flows, the large variations in temperature result in significant variations in density, molecular viscosity, and thermal conductivity. In general, a fully developed state is never achieved. The temperature increases (or decreases) in the streamwise direction leading to decreasing (or increasing) density. The velocity must correspondingly increase (or decrease) to maintain a constant mass flow rate in the channel. Also, the temperature variations lead to changes in the fluid thermal conductivity at the wall, so the temperature gradient at the wall, and hence the nondimensional temperature profile, changes to maintain the constant wall heat flux.

Performing the LES of a developing channel flow with strong heating or cooling conditions is beyond the capability of current supercomputers. Fortunately, far downstream of the entry region, typically 20 to 40 tube diameters, experiments show that the flow evolves into a ''quasi-developed'' state [5] where thermal entry effects are no longer important. This is the region of interest for the simulations discussed in this paper.

7 Quasi-Developed Assumption

In this section, two calculations of laminar, two-dimensional, constant heat flux channel flow are compared for variable property flow. The first calculation was of the hydrodynamically and thermodynamically developing channel flow, where the flow develops from uniform conditions at the inlet to the downstream, quasi-developed region. The second calculation used ''stepwise'' periodic boundary conditions, described later in this section, to compute a short segment of the channel in the downstream, or quasi-developed region. Agreement between the two calculations validated the assumed stepwise periodic boundary conditions, which were subsequently used for turbulent simulations.

7.1 Developing Laminar Channel Flow. The first calculation, referred to as the ''developing channel'' calculation throughout the remainder of this paper, was initially performed to better understand the downstream region, as well as to validate the stepwise periodic boundary conditions. The bulk Reynolds number based on hydraulic diameter was $\mathrm{Re}_D = 80$, and the nondimensional length of the channel was $L_x = 10$ (with respect to the channel half-height). This low Reynolds number was chosen to minimize the length of the channel. The nondimensional wall heat flux was $Q^+ = q_w D_h/(k_b T_b) = 20$, where q_w is the wall heat flux, D_h is the hydraulic diameter, T_b is the bulk temperature, and k_b is the thermal conductivity based on T_b. The inlet flow was uniform with the temperature and velocities specified, while the static pressure was extrapolated from the interior flow domain. The desired Reynolds number was obtained by specifying the appropriate static pressure at the outlet, while all other variables were extrapolated at the outlet.

Although not shown here, the resulting contours of density, streamwise velocity, streamwise momentum, and temperature indicated that after the initial developing region ($x < 4$) of the channel, the flow asymptotically achieved a quasi-developed state. The normalized profile shapes were essentially unchanged, even though the absolute value was continually increasing (for u and T) or decreasing (for ρ). The normalized streamwise momentum profile was nearly invariant in the streamwise direction.

Interrogation of the solution revealed that the following conditions held *approximately* in the downstream region ($x > 5$):

$$\frac{\partial(\rho u)}{\partial x} = 0 \tag{28}$$

$$\frac{\partial v}{\partial x} = 0; \quad v \neq 0 \tag{29}$$

$$\frac{\partial p}{\partial x} = \text{constant} \tag{30}$$

$$\frac{\partial T}{\partial x} = \text{constant}. \tag{31}$$

Thus, it appeared that a short section of the downstream region could be computed in a ''stepwise periodic'' manner with the following streamwise boundary conditions:

$$\rho u(0,y) = \rho u(L_x,y) \tag{32}$$

$$v(0,y) = v(L_x,y) \tag{33}$$

$$w(0,y) = w(L_x,y) \tag{34}$$

$$p_p(0,y) = p_p(L_x,y) \tag{35}$$

$$T(0,y) = T(L_x,y) - \Delta T_x, \tag{36}$$

where L_x is the length of the channel in the streamwise direction, and p_p is the periodic component of the pressure, $p(x,y) = \beta x + p_p(x,y)$.

The temperature difference, ΔT_x, in Eq. 36 is related to the net heat transferred to the flow in the solution domain, and was found by integrating the energy equation around the boundaries. For constant properties ΔT_x is given by

$$\Delta T_x = \frac{q_w}{c_p \dot{m}/A_c} L_x. \tag{37}$$

However, for variable properties ΔT_x is a function of y because the streamwise temperature gradient varies in the y direction.

The developing channel calculation indicated that this variation could be approximated by a linear function of y as

$$\Delta T_x(y) = c_1|y| + c_2. \tag{38}$$

By specifying the wall streamwise temperature gradient and the bulk temperature rise for the channel, the constants c_1 and c_2 were derived as discussed in [22], giving

$$c_1 = \frac{\Delta T_b - \Delta T_w}{I_{\rho u y} - 1} \tag{39}$$

$$c_2 = \frac{I_{\rho u y}\Delta T_w - \Delta T_b}{I_{\rho u y} - 1}, \tag{40}$$

where

$$I_{\rho u y} = \frac{1}{2\rho_b u_b}\int_{-1}^{1} \rho u|y|\,dy. \tag{41}$$

7.2 Quasi-Developed Laminar Channel Flow. The purpose of the second laminar calculation was to attempt to validate the stepwise periodic boundary conditions for the quasi-developed region given by Eqs. (32)–(36). The flow was computed in a short section of the channel of nondimensional length $L_x = 0.5$ in the downstream region. This computation is referred to as the ''quasi-developed'' channel flow in the remainder of this section.

The values of ΔT_b and ΔT_w in Eqs. (39) and (40) were specified. However, several trials were required to obtain values of these parameters that provided the desired wall heat flux and net

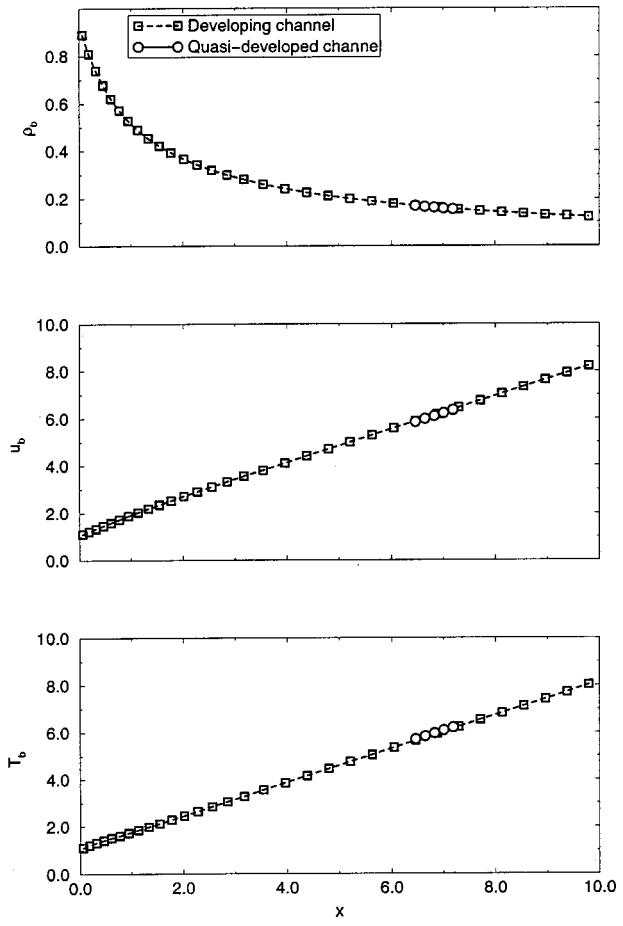

Fig. 2 Streamwise variation of bulk properties for two-dimensional, laminar, constant heat flux channel flow

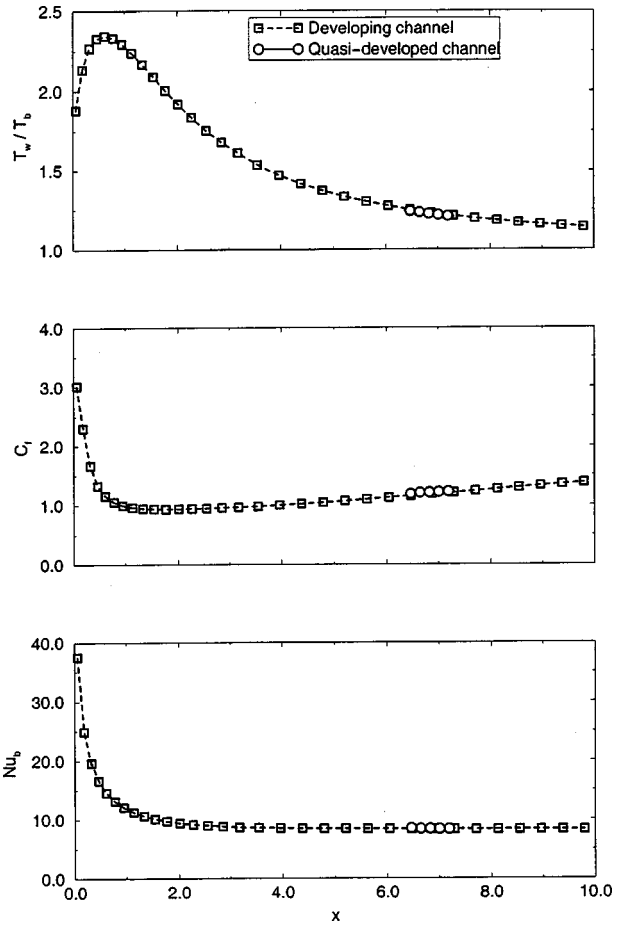

Fig. 3 Streamwise variation of flow parameters for two-dimensional, laminar, constant heat flux channel flow

heat transfer to the channel. The pressure gradient parameter, β, was adjusted iteratively to provide the desired mass flow rate.

The results for the quasi-developed channel and the developing channel flows are compared in Figs. 2 and 3. The streamwise variation of the bulk density, velocity, and temperature are shown in Fig. 2, and the streamwise variation of the wall-to-bulk temperature ratio, friction coefficient, and Nusselt number, all based on bulk properties, are shown in Fig. 3. The results demonstrated excellent agreement between the two computations for these parameters.

Profiles of the streamwise velocity, wall-normal velocity, and temperature, normalized by the local bulk properties were compared at a streamwise location where the Reynolds number based on local bulk properties was the same for both calculations. Excellent agreement was obtained for the streamwise velocity. However, the wall-normal velocity was nearly zero for the quasi-developed computation, whereas a significantly larger, yet negligibly small variation in v across the channel was observed for the developing channel computation. For higher Reynolds numbers, such as those for the turbulent simulations presented later in this paper, the variation in v is expected to be even less significant based on the results of Swearingen and McEligot [25], so the current assumptions should be satisfactory.

Overall, the use of the stepwise periodic boundary conditions, given by Eqs. (32)–(36), allowed duplicate results to be obtained in the quasi-developed region compared to the developing flow calculation for constant wall heat fluxes. The apparent existence of quasi-developed conditions in the downstream region of a tube flow with constant wall heat fluxes has also been observed for turbulent flows [26]. Consequently, it was assumed that the stepwise periodic boundary conditions would also be useful for turbulent simulations.

One slight modification to the stepwise periodic boundary conditions was made for the turbulent simulations presented later in this paper. The turbulent simulations were performed at much higher Reynolds numbers ($\mathrm{Re}_D = 10{,}800 - 11{,}400$), resulting in less than 1.2 percent variation of the temperature in the streamwise direction. Therefore, it was satisfactory to assume ΔT_x was independent of y, so that Eq. (37) could be used instead of Eq. (38).

8 Turbulent Simulations

Details of running the turbulent constant heat flux channel flow simulations are discussed in this section. The cases of interest are described, followed by a discussion of the difficulties encountered in setting up the desired flow conditions. Details of computing the turbulence statistics for this problem are also given.

8.1 Case Descriptions. Four turbulent simulations of quasi-developed turbulent plane channel flow with constant wall heat transfer rates are presented in this paper. Two cases with ''low heating'' are referred to as cases LHQW and LHTW, where LHQW was simulated with a specified constant wall heat flux boundary condition, and case LHTW was simulated with a fixed, but linearly varying, wall temperature boundary condition that resulted in a nearly constant wall heat flux. The rate of heat addition, $Q^+ = 0.8$, was low enough that the properties were essentially constant. In many of the figures, the ''low heating'' cases are referred to collectively as case LH, because many of the mean

Table 1 Control volume dimensions in wall units

Case	Δx^+	Δy^+_{nw}	Δy^+_{max}	Δz^+
LHTW	22.7	2.3	8.0	11.4
LHQW	22.6	2.3	8.0	11.3
HH	14.1	1.4	5.0	7.1
HC	44.5	4.5	15.6	22.2

flow and turbulence statistics, especially for the velocity field, were nearly identical. Case HH, referred to as ''high heating'' in the figures, was run with constant heat addition ($Q^+=15.0$) that resulted in a wall-to-bulk temperature ratio, T_w/T_b, of 1.5. Finally, case HC, referred to as ''high cooling'' in the figures, was run with constant cooling ($Q^+=-15.0$) that resulted in $T_w/T_b=0.56$. The constant heat flux condition for cases HH and HC were also achieved by specifying a fixed, but linearly varying wall temperature.

All simulations reported here were run with a domain size of $2\pi\times2\times\pi$ with the same grid that had $48\times64\times48$ control volumes in the x, y, z directions, respectively. A grid study for the low heating simulations indicated that this grid size provided accurate results compared to constant property DNS [12] and experimental data [13]. Comparisons with results obtained on a $32\times32\times24$ grid and experimental data can be found in [27], Meng et al. [28], and Meng [29]. The grid spacing was uniform in the x and z directions, but was stretched towards the wall using hyperbolic tangent stretching in the y direction to give $y^+\approx1$ for the near-wall control volume. Turbulence statistics were collected using about 10,000 time steps after the flow was deemed to be statistically stationary. The time steps were $\Delta t^+=0.00193$, 0.00240, 0.00153 for cases LH, HH, and HC, respectively. The control volume dimensions are given in Table 1. The superscript, $^+$, represents a quantity in wall units, where in terms of nondimensional variables, $x^+=\mathrm{Re}_\tau u_\tau x/\nu_w$ and $t^+=tu_\tau$.

The simulations were run with the dual time stepping, preconditioned LU-SGS scheme with relaxation factors $w=1.0$ and $r_A=r_B=r_C=1.0$. Cases HH and HC were run with subiteration tolerance levels of $\mathrm{TOL}=1.0\times10^{-6}$, which required about 6–7 iterations per physical time step, and resulted in 1–1.5 orders of magnitude drop in the residuals. The LH cases were run with $TOL=1.0\times10^{-7}$, which required about 11–12 iterations per physical time step, and resulted in 1.5–2.5 orders of magnitude drop in the residuals. The lower tolerance was used for the LH cases because of problems resolving the mid-channel temperature fluctuations, as discussed in Dailey and Pletcher [27]. The simulations were typically run with 17 processors on an IBM SP-2 for a fine-grid ($48\times64\times48$) simulation. Roughly, it took one–two hours of wall clock time per 1000 time steps.

Kasagi et al. [30] reported that the specification of a constant wall heat flux boundary condition for LES and DNS leads to unphysically high values of near wall temperature fluctuations. More realistic temperature fluctuations are predicted for turbulent air flows with a fixed wall temperature, as opposed to a fixed wall heat flux, boundary condition. Consequently, the present turbulent simulations were first run 3–4000 time steps with a constant heat flux boundary condition to determine an estimate of the average wall temperature distribution. The constant heat flux boundary condition was then replaced with a fixed, but linearly varying wall temperature boundary condition, $T_w(x)$, based on the earlier simulations. The resulting wall heat flux, averaged in the z direction and in time, was nearly constant with less than one percent variation in the streamwise direction. The temperature difference, ΔT_x, in Eq. (36) was set to the desired heating or cooling level using Eq. (37).

8.2 Setting the Quasi-Developed State. For the fully developed region of a channel flow with constant properties, downstream of any entrance effects, the bulk density, velocity, and hence, Reynolds numbers are invariant in the streamwise direction. Consequently, the ''state'' at each streamwise location is the same, where here the ''state'' refers to the local values of the bulk density, velocity, and Reynolds number. Conversely, for the quasi-developed region of a channel with variable properties, there is an infinite number of ''states'' because the properties vary in the streamwise direction. Setting the flow parameters to obtain a desired state can be quite difficult.

It was somewhat difficult to construct the flow parameters for a given simulation to provide the desired effect. The parameters included the wall temperature distribution, $T_w(x)=T_w(0)+(dT_w/dx)x$, initial bulk velocity and temperature distributions (and hence, wall-to-bulk temperature ratio), and the streamwise temperature difference, which is directly related to the wall heat flux. The goal was to adjust these parameters to achieve a desired wall-to-bulk temperature ratio and heating or cooling level.

Recall that the quasi-developed region is far downstream from the entrance region for a developing channel flow. The local bulk Reynolds number provides an indication of how close one is to the entrance region. For instance, in the case of heating, Re_b decreases in the streamwise direction because T_b, and hence ν_b, increases in the streamwise direction.

For the present turbulent high heating simulations, it was found that if Re_b was too large, velocity profiles with dual peaks or maximums were obtained. The dual peak velocity profiles are characteristic of the entry region [25]. In order to study the effects of variable properties, a large value of T_w/T_b was desired. However, as shown in Fig. 3(*a*), the largest values of T_w/T_b occur in the entry region, and T_w/T_b approaches unity far downstream in the channel. Thus, the difficulty of simulating this class of flows lies in setting the appropriate levels of T_w/T_b, ρ_b, u_b, T_b, and Re_b to provide the desired wall-normal temperature variation while remaining in the downstream, or quasi-developed region.

For heating, another possible limit exists for the Reynolds number. As one goes farther downstream, or correspondingly decreases Re_b, there is the potential for laminarization of the flow [31]. In addition, as higher heating rates are applied, the streamwise variation in the properties will become more important, and the present assumption that the property variations in the streamwise direction are negligible compared to the wall-normal variations would no longer be appropriate. Thus, corrections such as those given by Eq. (38) would be necessary.

8.3 Turbulence Statistics. The conventional Reynolds (or ensemble) average of a quantity is denoted as $\langle\ \rangle$, and the Favre ensemble average as $\{\ \}$, where

$$\{f\}=\langle\rho f\rangle/\langle\rho\rangle. \tag{42}$$

A single prime,$'$, and a double prime,$''$, denote the turbulent fluctuations with respect to the Reynolds or Favre ensemble average, respectively. For the simulations with low heating, the density variations were assumed to be small enough that the Reynolds and Favre averages were equivalent. For the results in this paper, fluctuations with respect to Reynolds averages were used for rms values so that the effect of heat transfer and variable properties on these fluctuations could be studied.

The velocity fluctuations were obtained at each time step as

$$\tilde{u}_i'(x,y)=\tilde{u}_i(x,y)-\langle\tilde{u}_i\rangle_z(x,y) \tag{43}$$

where $\langle\ \rangle_z$ denotes an average in the z direction only. The ensemble averaged root-mean-square (rms) values were subsequently obtained as

$$\tilde{u}'_{\mathrm{rms}}(x,y)=\sqrt{\frac{\langle\tilde{u}'(x,y)^2\rangle}{N_{\mathrm{stat}}}} \tag{44}$$

where $\langle\ \rangle$ denotes an average in z and in time, and N_{stat} is the number of time steps used to compute the statistics.

Shear stress and heat flux distributions were also computed as part of the turbulence statistics. The computed shear stress contributions were

$$\tau_{\text{res}} = -\langle \rho \tilde{u}'' \tilde{v}'' \rangle \tag{45}$$

$$\tau_{\text{vis}} = -\left\langle \frac{\mu}{\text{Re}} \frac{\partial \tilde{u}}{\partial y} \right\rangle \tag{46}$$

$$\tau_{\text{sgs}} = -\left\langle \mu_t \frac{\partial \tilde{u}}{\partial y} \right\rangle \tag{47}$$

where τ_{res} is the resolvable Reynolds shear stress, τ_{vis} is the viscous shear stress, and τ_{sgs} is the modeled SGS stress. Similarly, the computed heat flux contributions were

$$q_{\text{res}} = -\langle \rho \tilde{v}'' \tilde{T}'' \rangle \tag{48}$$

$$q_{\text{con}} = -\left\langle \frac{\mu c_p}{\text{Re Pr}} \frac{\partial \tilde{T}}{\partial y} \right\rangle \tag{49}$$

$$q_{\text{sgs}} = -\left\langle \frac{\mu_t c_p}{\text{Pr}_t} \frac{\partial \tilde{T}}{\partial y} \right\rangle \tag{50}$$

where q_{res} is the resolvable turbulent heat flux, q_{con} is the heat conduction, and q_{sgs} is the modeled SGS heat flux.

9 Results

9.1 Average Flow Parameters. Table 2 lists some globally averaged parameters for the entire solution domain. The pressure gradient parameter, β, was observed to be 56 percent higher for case HH compared to the low heating results, whereas for case HC, β was 51 percent lower. Correspondingly, the friction velocity was 24 percent higher for case HH, and 21 percent lower for case HC compared to the low heating results. The average turbulent kinetic energy, k and k^+, are averages of k at every control volume in the solution domain. The average turbulent kinetic energy, normalized by the square of the reference velocity, was 5.4 percent lower for case HH, and 21 percent higher for case HC.

Because the high heat flux channel flows are nonhomogeneous in the x direction, profiles are only shown at a single x or streamwise location, which was a plane near mid-channel. The bulk flow parameters at this local position in the channel, averaged in z and time, are given in Tables 3 and 4.

9.2 Mean Profiles. The profiles of mean quantities shown throughout the remainder of this paper are for a streamwise location near mid-channel. The profiles have been ensemble averaged in the z direction and in time.

The mean temperature profile is shown in Fig. 4 normalized by the bulk temperature, and the mean density profile is shown in Fig. 5 normalized by the bulk density. The figures show the significant variation in temperature leading to significant variations in density, viscosity, and thermal conductivity. The distribution of the mean velocity and mass flux, $\langle \rho u \rangle$, are shown in Figs. 6 and 7, respectively. Figure 7 reveals the redistribution of the mass flow (compared to low heating) towards the center of the channel for high heating, and towards the wall for high cooling. This is because the density is higher in the center of the channel for high heating, while the density is higher near the wall for high cooling.

The mean streamwise velocity profile is plotted in wall coordinates in Fig. 8, where

$$u^+ = \frac{u}{u_\tau}; \quad u_\tau = \sqrt{\frac{\tau_w}{\rho_w}}; \quad y^+ = \text{Re}_\tau \frac{\delta_y u_\tau}{\nu_w} \tag{51}$$

and δ_y is the distance to the wall. The incompressible DNS results of Kim et al. [12] and experimental results of Niederschulte et al.

Table 2 Simulation parameters (average for complete solution domain)

Case	β	$u_{\tau,avg}$	k/V_r^2	k^+
LHTW	-0.00395	0.0620	0.00749	1.95
LHQW	-0.00397	0.0619	0.00741	1.93
HH	-0.00618	0.0770	0.00705	1.19
HC	-0.00194	0.0490	0.00904	3.77

Table 3 Local bulk friction properties

Case	Re_D	u_τ	C_f
LH	11,390	0.0590	0.00755
HH	10,810	0.0799	0.00776
HC	10,900	0.0465	0.00747

Table 4 Local bulk heat transfer parameters

Case	q_w	T_w/T_b	Nu_D
LH	2.11×10^{-3}	1.05	33.9
HH	2.08×10^{-2}	1.48	31.2
HC	-2.01×10^{-2}	0.56	33.1

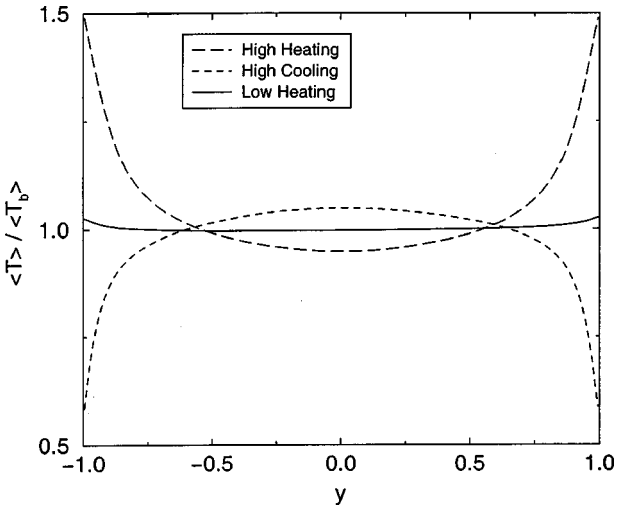

Fig. 4 Mean temperature normalized by bulk temperature

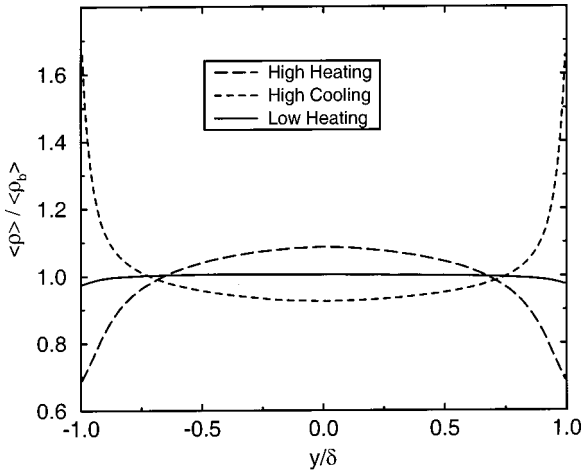

Fig. 5 Mean density normalized by bulk density

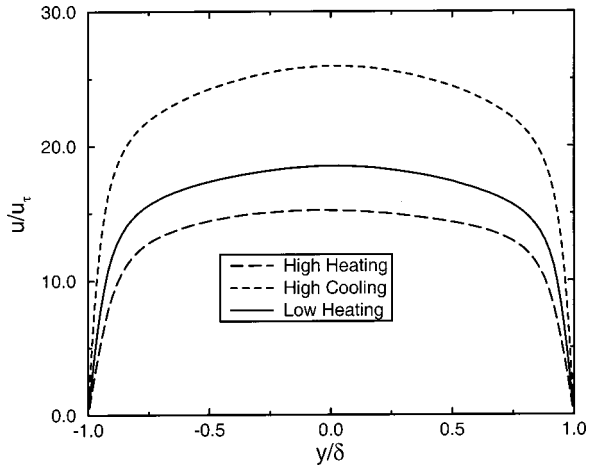

Fig. 6 Mean velocity profiles

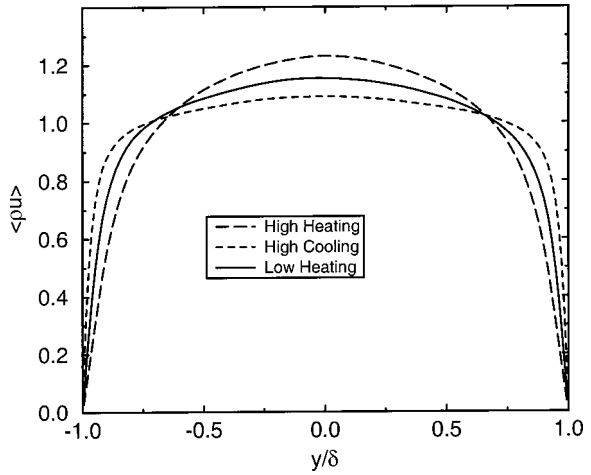

Fig. 7 Mean *x*-momentum

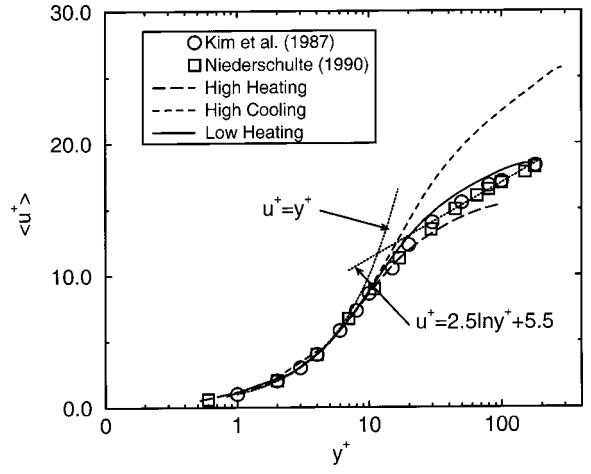

Fig. 8 Mean streamwise velocity in wall coordinates

[13] are shown for comparison purposes. Also shown is the linear law, $u^+ = y^+$, and the log-law recommended by Kim et al. at these low Reynolds numbers, $u^+ = 2.5 \ln y^+ + 5.5$. As shown, the high heating and high cooling velocity profiles depart markedly from the incompressible results.

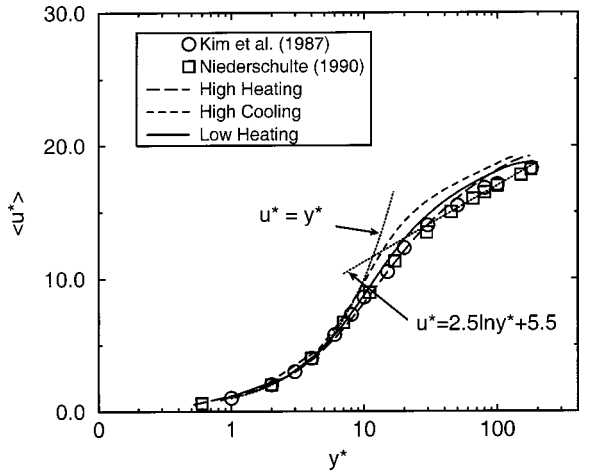

Fig. 9 Mean streamwise velocity in semi-local coordinates

For flows with significant variations in the density, Huang et al. [32] recommended the use of semi-local coordinates, u^* versus y^*, where local values of density and molecular viscosity are used instead of wall values, giving

$$u^* = \frac{u}{u_\tau^*}; \quad u_\tau^* = \sqrt{\frac{\tau_w}{\rho(y)}} \tag{52}$$

and

$$y^* = \mathrm{Re}_\tau \frac{\delta_y u_\tau^*}{\nu(y)}. \tag{53}$$

Figure 9 shows the mean streamwise velocity plotted in semi-local coordinates. The velocity profiles have nearly collapsed to a single curve matching the incompressible results. However, the slopes in the logarithmic region do not match perfectly.

The mean temperature difference is given in wall coordinates as

$$\theta^+ = \frac{\langle T_w \rangle - \langle T \rangle}{T_\tau}; \quad T_\tau = \frac{q_w}{\rho_w c_p u_\tau} \tag{54}$$

and in semi-local coordinates as

$$\theta^* = \frac{\langle T_w \rangle - \langle T \rangle}{T_\tau^*}; \quad T_\tau^* = \frac{q_w}{\rho(y) c_p u_\tau^*}. \tag{55}$$

The mean temperature profiles are plotted in wall coordinates and semi-local coordinates in Figs. 10 and 11, respectively. The in-

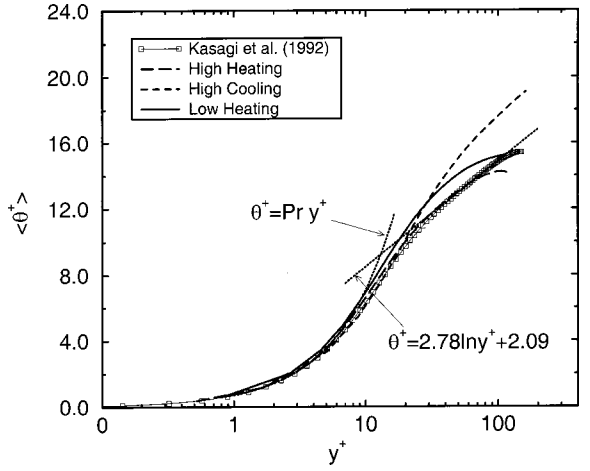

Fig. 10 Mean temperature in wall coordinates

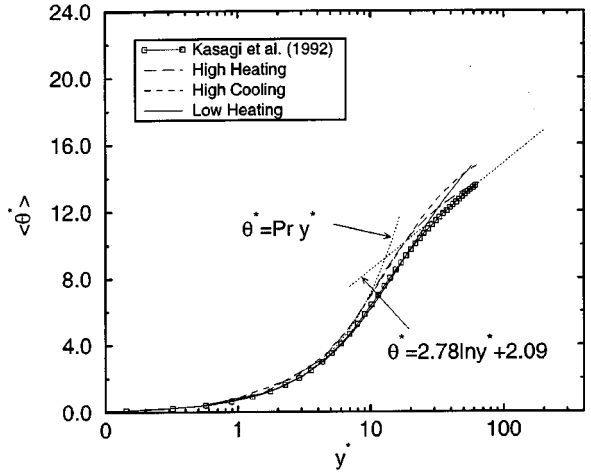

Fig. 11 Mean temperature in semi-local coordinates

compressible passive scalar DNS results of Kasagi et al. [14] and the thermal law-of-the-wall are shown for comparison purposes. The thermal linear law is $\theta^+ = \mathrm{Pr}\, y^+$, and the thermal log-law is $\theta^+ = 2.78 \ln y^+ + 2.09$. As for the velocity profiles, the high heating and high cooling profiles in wall coordinates departed from the incompressible results. However, the curves did not agree as well with the incompressible results with semi-local coordinates as they did for the velocity profiles.

9.3 Shear Stress and Heat Flux Profiles. Figure 12 shows the resolved, viscous, and modeled SGS shear stress distributions

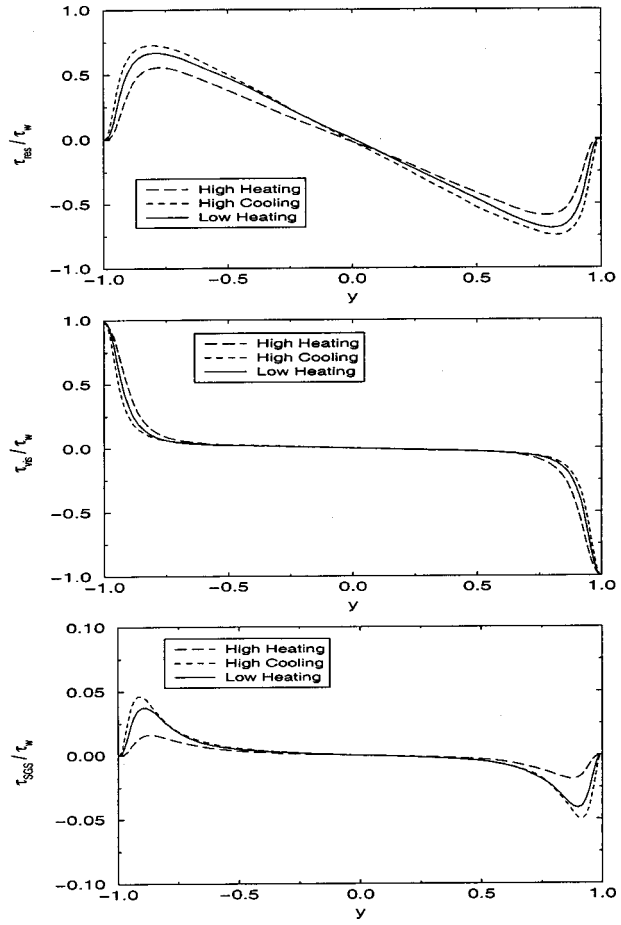

Fig. 12 Shear stress distributions scaled by wall shear stress

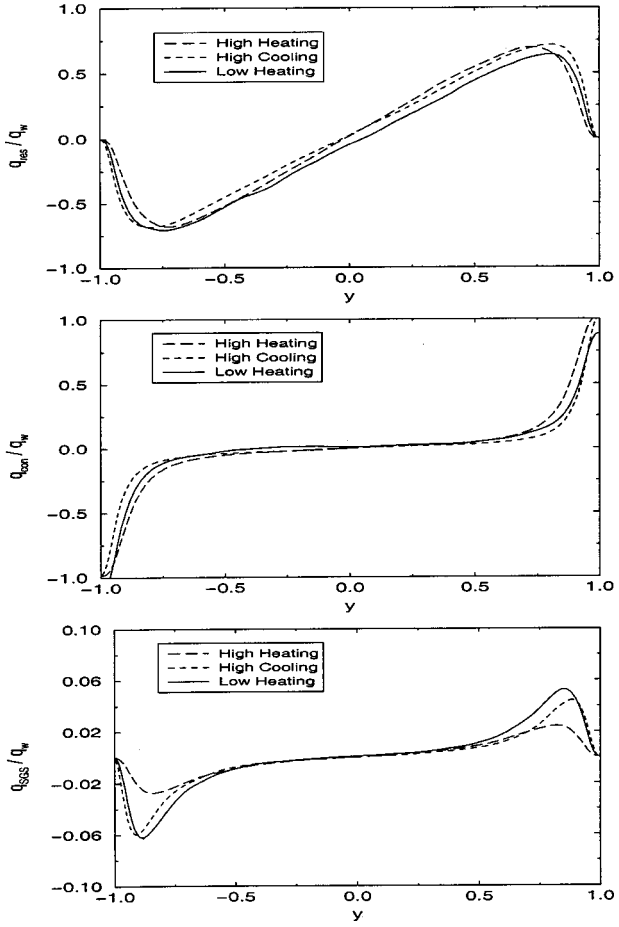

Fig. 13 Heat flux distributions scaled by wall heat flux

normalized by the wall shear stress. The results indicate that high cooling increased the turbulent resolved shear stress, while the viscous shear stress decreased slightly. The opposite trends were observed for high heating. The effect on the turbulent shear stress for heating versus cooling was more pronounced than the trend observed by Wang and Pletcher [15] for constant wall temperature. For instance, in the present simulations, the peak value of $\tau_{\mathrm{res}} = \langle \rho u'' v'' \rangle$ was 0.693 for low heating, decreased to 0.590 for high heating, and increased to 0.734 for high cooling. Wang and Pletcher obtained peak values of 0.658 for a low temperature ratio case. For a large temperature ratio case after adjusting values to account for differences in normalization, the hot (or heated) wall peak value increased to 0.686 and the cold (or cooled) wall peak value decreased to 0.681. The reason for the different trends observed in the present results and Wang and Pletcher's results is not well understood, but could be due to the difference in the thermal conditions imposed.

For low heating, the peak modeled SGS stress was only 2.5 percent of the wall shear stress. For high heating, the peak value decreased to 1.03 percent, and for high cooling the peak value increased to 7.28 percent of the wall shear stress.

Figure 13 shows the resolved heat flux, heat conduction, and modeled SGS heat flux distributions normalized by the wall heat flux. The same trends were observed as for the shear stress distributions, with the exception that the increase of the resolved heat flux with high cooling was not as pronounced. However, the heat conduction was decreased and the modeled SGS heat flux was increased with high cooling.

Finally, Fig. 14 shows the wall-normal distribution of the SGS turbulent Prandtl number obtained from the dynamic model. These values were averaged in both time and the homogeneous

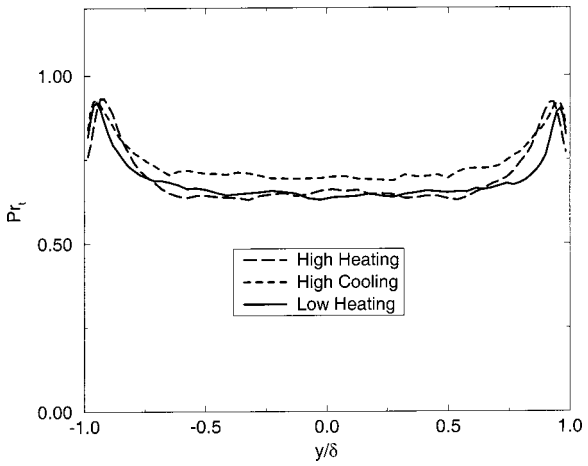

Fig. 14 Dynamic turbulent Prandtl number distributions

spatial direction. The Prandtl number reaches a maximum of about 0.9 near the walls and settles to a value near 0.7 in the central region of the channel. The values for the high cooling case are slightly higher than those for the heating cases.

9.4 Empirical Correlations. Fairly comprehensive experimental data exist for heat transfer to circular ducts. Far less is known about planar channel flow, the subject of the present study, particularly concerning the effects of property variations. Bhatti and Shah [33] discuss the flat (planar) channel and point out that the Nusselt number given by the constant property analysis of Kays and Leung [34] for a flat channel may be greater than given by the Gnielinski correlation [35] by up to 23 percent for Reynolds numbers between 10,000 and 30,000. The Kays and Leung analysis predicts a Nusselt number of approximately 35.6 for the conditions of the low heat transfer case (approximately constant properties) of the present study compared to our result of 33.9, a difference of about five percent. The experimental data of Novotny et al. [36] for a channel of aspect ratio 0.1 indicates a value of about 34 for these conditions. More direct comparisons for the present higher heat flux cases are more difficult to obtain. Instead, comparisons are cited below with correlations for circular pipe data recognizing that the present planar channel Nusselt number results are expected to be somewhat higher than given by the circular duct correlations.

The two most common methods for correcting the constant property circular pipe correlations for variable property effects are the reference temperature method and property ratio method. The reference temperature method involves choosing a characteristic temperature at which to evaluate properties in the constant property correlations, such that variable property behavior is obtained. The more commonly used property ratio method involves determining the properties with the bulk temperature, but the variable property effects are lumped into ratios of one property at the surface temperature to that at the bulk temperature.

For gases, the property ratio method is in terms of the wall-to-bulk temperature ratio as

$$\frac{\mathrm{Nu}}{\mathrm{Nu}_{cp}}=\left(\frac{T_w}{T_b}\right)^n \quad \frac{f}{f_{cp}}=\left(\frac{T_w}{T_b}\right)^m, \tag{56}$$

where the subscript cp refers to the corresponding constant property correlation. The correlations compared to here are discussed in detail in Dailey [22].

The results for the present simulations are compared to various variable property correlations in Tables 5, 6, and 7, for cases LH, HH, and HC, respectively. In the tables, the correlations are abbreviated as Petukhov and Popov (PP) [37], Humble, Lowdermilk, and Desmon (HLD) [38], Barnes and Jackson (BJ) [39], McEligot (ME) [31], and Kays and Crawford (KC) [40]. The agreement for the low heating case, Table 6, is good, with differences of less than eight percent for both the friction coefficient and Nusselt number for all correlations. The best agreement is obtained with the HLD and BJ correlations, with less than two percent difference for the Nusselt numbers. These two correlations are valid for lower Reynolds number ranges than the other correlations.

Table 5 Comparison to variable property correlations for low heating (case LH)

Correlation	f	% difference	Nu_D	% difference
Case LH	0.00755	—	33.9	—
PP	0.00754	0.1	32.3	5.0
HLD	—	—	34.4	-1.5
BJ	—	—	34.5	-1.7
ME	—	—	31.4	8.0
KC	0.00711	6.2	31.8	6.6

Table 6 Comparison to variable property correlations for high heating (case HH)

Correlation	f	% difference	Nu_D	% difference
Case HH	0.00776	—	31.2	—
PP	0.00658	17.9	26.9	16.0
HLD	—	—	27.2	14.7
BJ	—	—	28.8	8.3
ME	—	—	25.3	23.3
KC	0.00690	12.5	25.7	21.4

Table 7 Comparison to variable property correlations for high cooling (case HC)

Correlation	f	% difference	Nu_D	% difference
Case HC	0.00747	—	33.1	—
PP	0.00935	-20.1	39.2	-15.6
HLD	—	—	34.0	-2.6
KC	0.00759	1.6	31.5	5.1

Good agreement was also obtained with the correlations for the high cooling case, shown in Table 7. Best agreement is again obtained with the HLD correlation.

The high heating cases did not compare as favorably with the correlations, with the correlations suggesting more of a decrease in the Nusselt number due to heating than was obtained with the present results. The differences ranged from 8.3 to 14.7 percent for the two low Reynolds number correlations (HLD and BJ). However, differences as high as 23.3 percent were observed with other correlations.

10 Concluding Remarks

Two-dimensional, laminar, hydrodynamically and thermodynamically developing channel flow with constant wall heating rates was computed to study the quasi-developed region far downstream from the entrance region. A suitable set of approximate streamwise boundary conditions was found, such that the flow in the quasi-developed region could be computed in a step-wise periodic manner. The same boundary conditions were applied to the turbulent simulations.

Turbulent channel flows with constant wall heating or cooling rates of magnitudes large enough to cause significant variation in the temperature-dependent fluid properties were simulated. The simulations were performed for high heating (and cooling), with a resulting bulk temperature increase (and decrease). The results were compared to nearly incompressible simulations with low

heating. Comparisons were also made to LES and DNS results of other similar, but distinctly different, compressible or variable property channel flows.

Heating and cooling clearly influenced the mean velocity and temperature profiles, especially when plotted in wall coordinates. However, use of semi-local coordinates tended to collapse the mean velocity data toward the incompressible log-law. A similar trend toward collapse, although not as good, was observed for the near wall temperature profile when the semi-local coordinates were used.

The average turbulent kinetic energy was seen to decrease for the high heating case and increase for the high cooling case compared to the level for the low heating flow. On the other hand, the friction velocity was 26 percent higher for the high heating case and 27 percent lower for the high cooling case compared to the low heating results largely because of the great differences in the fluid density at the wall. The pressure gradient parameter, β, was more than three times larger with high heating than with high cooling.

The peaks in the resolved turbulent stress were somewhat smaller for the high heating case and slightly larger for the high cooling case compared to the low heating results. A similar trend was observed for the resolved turbulent heat flux.

Finally, extensive comparisons were made to empirical correlations for the friction coefficient and Nusselt number. The high cooling results compared favorably to most of the correlations, while the high heating results did not show as large a decrease in the Nusselt number as suggested by the correlations.

Observations for fluctuating and instantaneous quantities will be reported in a paper to follow.

Acknowledgments

This research was supported in part by the Air Force Office of Scientific Research under grants F49620-94-1-0168 and F49620-00-1-0229 and by the National Science Foundation under grants CTS-9414052 and CTS-9806989. The first author was supported by a Department of Defense National Defense Science and Engineering Graduate Fellowship. The use of computer resources provided by the Cornell Theory Center, the Maui High Performance Computing Center, and the Minnesota Supercomputing Institute, are gratefully acknowledged.

Nomenclature

Symbols

C_d, C_I = dynamic subgrid-scale model coefficients
L, V, T, ρ, μ = length, velocity, temperature, density, viscosity
$\hat{E}$ = resolved total energy ($=c_v\tilde{T}+\frac{1}{2}\tilde{u}_i\tilde{u}_i$)
$\tilde{S}_{ij}$ = strain rate tensor
$\hat{q}_j$ = heat flux vector
Q_j = SGS heat flux
$\hat{\sigma}_{ij}$ = viscous stress tensor
$\dot{m}$ = mass flow rate
Pr = Prandtl number ($=\mu c_p/k$)
Pr_t = turbulent Prandtl number
p = thermodynamic pressure
R = gas constant or cross-correlation coefficient
Re = generic Reynolds number
u_τ = friction velocity ($=\sqrt{\tau_w/\rho_w}$)
u_τ^* = semi-local friction velocity ($=\sqrt{\tau_w/\rho(y)}$)
γ = ratio of specific heats
Δ = grid filter width
$\hat{\Delta}_t$ = test filter width
δ = channel half-height or Dirac delta
θ = temperature difference ($=T_w-T$)
θ^+ = temperature in wall coordinates ($=\theta/T_\tau$)
κ = von Karman constant
τ_{ij} = subgrid-scale stress tensor
t_{ij} = solution-grid turbulent stress
T_{ij} = test-grid turbulent stress
β = pressure gradient

Subscripts

r = reference variables
b = bulk property
w = wall value
con = conduction contribution
res = resolved contribution
rms = root-mean-square
sgs = subgrid-scale contribution
vis = viscous contribution

Superscripts and Other Symbols

$*$ = dimensional variable or semi-local coordinates
$+$ = wall coordinates
$'$ = fluctuation with respect to ensemble average, or
$\cdot$ = unresolved or subgrid-scale component of filtered quantity
$''$ = fluctuation with respect to Favre ensemble average, or unresolved or subgrid-scale component of Favre filtered quantity
$\vec{\ }$ = vector quantity
$\bar{\ }$ = resolved or large scale component of filtered quantity
$\tilde{\ }$ = resolved or large scale component of Favre filtered quantity
$\hat{\ }$ = quantity that is nonlinear function of Favre filtered quantities
$\hat{\hat{\ }}$ = test filtered quantity

Abbreviations

CFD = computational fluid dynamics
DNS = direct numerical simulation
LES = large eddy simulation
LU-SGS = lower-upper symmetric-Gauss-Seidel
MPI = message passing interface
PVM = parallel virtual machine
RANS = Reynolds-averaged Navier-Stokes
SGS = subgrid-scale

References

[1] Perkins, K. R., 1975, "Turbulence Structure in Gas Flows Laminarizing by Heating," Ph.D. thesis, University of Arizona, Tucson, AZ.
[2] Shehata, A. M., 1984, "Mean Turbulence Structure in Strongly Heated Air Flows," Ph.D. thesis, University of Arizona, Tucson, AZ.
[3] Shehata, A. M., and McEligot, D. M., 1995, "Turbulence Structure in the Viscous Layer of Strongly Heated Gas Flows," Tech. Report INEL-95/0223, Idaho National Engineering Laboratory, Idaho Falls, ID.
[4] Shehata, A. M., and McEligot, D. M., 1998, "Mean Turbulence Structure in the Viscous Layer of Strongly Heated Internal Gas Flows. Measurements," Int. J. Heat Mass Transf., **41**, pp. 4297–4313.
[5] McEligot, D. M., Magee, P. M., and Leppert, G., 1965, "Effect of Large Temperature Gradients on Convective Heat Transfer: The Downstream Region," ASME J. Heat Transfer, **87**, p. 67.
[6] Schade, K. W., and McEligot, D. M., 1971, "Turbulent Flow Between Parallel Plates With Gas Property Variation," ASME Paper 71-FE-38.
[7] Bankston, C. A., and McEligot, D. M., 1970, "Numerical Solutions for Turbulent and Laminar Thermal Entries With Gas Property Variations," Int. J. Heat Mass Transf., **13**, p. 319.
[8] Ezato, K., Shehata, A. M., Kunugi, T., and McEligot, D. M., 1999, "Numerical Prediction of Transitional Features of Turbulent Forced Gas Flows in Circular Tubes With Strong Heating," ASME J. Heat Transfer, **121**, pp. 546–555.
[9] Bradshaw, P., and Huang, G. P., 1995, "The Law of the Wall in Turbulent Flow," Proc. R. Soc. London, Ser. A, **451**, pp. 165–188.
[10] Germano, M., Piomelli, U., Moin, P., and Cabot, W., 1991, "A Dynamic Subgrid-Scale Eddy Viscosity Model," Phys. Fluids A, **3**, pp. 1766–1771.
[11] Satake, S.-I, Kunugi, T., Shehata, A. M., and McEligot, D. M., 1999, "Direct Numerical Simulation on Laminarization of Turbulet Forced Gas Flows in Circular Tubes With Strong Heating," Proceedings of the First Symposium of Turbulence and Shear Flow Phenomena, Banerjee, S. and Eaton, J. K., eds., Begell House, Santa Barbara, CA.
[12] Kim, J., Moin, P., and Moser, R., 1987, "Turbulence Statistic in Fully Devel-

oped Channel Flow at Low Reynolds Number,'' J. Fluid Mech., **177**, pp. 133–166.
[13] Niederschulte, M. A., Adrian, R. J., and Hanratty, T. J., 1990, ''Measurements of Turbulent Flow in a Channel at Low Reynolds Numbers,'' Exp. Fluids, **9**, pp. 222–230.
[14] Kasagi, N., Tomita, Y., and Kuroda, A., 1992, ''Direct Numerical Simulation of Passive Scalar Field in a Turbulent Channel Flow,'' ASME J. Heat Transfer, **114**, pp. 598–606.
[15] Wang, W.-P., and Pletcher, R. H., 1996, ''On the Large Eddy Simulation of a Turbulent Channel Flow With Significant Heat Transfer,'' Phys. Fluids, **8**, pp. 3354–3366.
[16] Nicoud, F., and Poinsot, T., 1999, ''DNS of a Channel Flow With Variable Properties,'' *Proceedings of the First Symposium of Turbulence and Shear Flow Phenomena*, Santa Barbara, CA.
[17] Coleman, G. N., Kim, J., and Moser, R. D., 1995, ''A Numerical Study of Turbulent Supersonic Isothermal-Wall Channel Flow,'' J. Fluid Mech., **305**, pp. 159–183.
[18] Dailey, L. D., 1997, ''Large Eddy Simulation of Turbulent Flows With Variable Property Heat Transfer Using a Compressible Finite Volume Formulation,'' Ph.D. thesis, Iowa State University.
[19] Vreman, B., Geurts, B., and Kuerten, H., 1995, ''Subgrid-Modelling in LES of Compressible Flow,'' Appl. Sci. Res., **54**, pp. 191–203.
[20] Moin, P., Squires, K., Cabot, W., and Lee, S., 1991, ''A Dynamic Subgrid-Scale Model for Compressible Turbulence and Scalar Transport,'' Phys. Fluids A, **3**, pp. 2746–2757.
[21] Spyropoulos, E. T., and Blaisdell, G. A., 1997, ''Large-Eddy Simulation of a Spatially Evolving Compressible Boundary Layer Flow,'' AIAA Paper 97-0429.
[22] Squires, K. D., 1991, ''Dynamic Subgrid-Scale Modeling of Compressible Turbulence,'' Annual Research Briefs, *Center for Turbulence Research*, Stanford University, Stanford, CA, pp. 207–233.
[23] Lilly, D. K., 1992, ''A Proposed Modification of the Germano Subgrid-Scale Closure Method,'' Phys. Fluids A, **4**, pp. 633–635.
[24] Dailey, L. D., and Pletcher, R. H., 1996, ''Evaluation of Multigrid Acceleration for Preconditioned Time-Accurate Navier-Stokes Algorithms,'' Comput. Fluids, **25**, pp. 791–811.
[25] Swearingen, T. B., and McEligot, D. M., 1971, ''Internal Laminar Heat Transfer With Gas-Property Variation,'' ASME J. Heat Transfer, **93**, pp. 432–440.
[26] McEligot, D. M., Smith, S. B., and Bankston, C. A., 1970, ''Quasi-Developed Turbulent Pipe Flow With Heat Transfer,'' ASME J. Heat Transfer, **92**, pp. 641–650.
[27] Dailey, L. D., and Pletcher, R. H., 1997, ''Evaluation of a Second-Order Accurate Compressible Finite Volume Formulation for the Large Eddy Simulation of Turbulent Flow,'' *Advances in DNS/LES*, C. Liu, and Z. Liu, eds., Greyden Press, Columbus, OH, pp. 571–578.
[28] Meng, N., Dailey, L. D., and Pletcher, R. H., 1999, ''Large Eddy Simulation of Constant Heat Flux Turbulent Channel Flow With Property Variations Using a Dynamic Subbrid-Scale Model,'' AIAA Paper 99–3356.
[29] Meng, N., 2000, ''Large Eddy Simulation of Turbulent Flows With Property Variations, Rotation, and Complex Geometry,'' Ph.D. thesis, Iowa State University, Ames, IA.
[30] Kasagi, N., Kuroda, A., and Hirata, M., 1989, ''Numerical Investigation of Near-Wall Turbulent Heat Transfer Taking Into Account the Unsteady Heat Conduction in the Solid Wall,'' ASME J. Heat Transfer, **111**, pp. 385–392.
[31] McEligot, D. M., 1985, ''Convective Heat Transfer in Internal Gas Flows With Temperature-Dependent Properties,'' Advances in Transport Processes, **4**, J. Wiley, NY, pp. 113–200.
[32] Huang, P. G., Coleman, G. N., and Bradshaw, P., 1995, ''Compressible Turbulent Channel Flow—A Close Look Using DNS Data,'' AIAA Paper 95-0584.
[33] Bhatti, M. S., and Shah, R. K., 1987, ''Turbulent and Transition Flow Convective Heat Transfer in Ducts,'' *Handbook of Single-Phase Convective Heat Transfer*, John Wiley and Sons, NY, pp. 4.1–4.166.
[34] Kays, W. M., and Leung, E. Y., 1963, ''Heat Transfer in Annular Passages: Hydrodynamically Developed Turbulent Flow With Arbitrarily Prescribed Heat Transfer,'' Int. J. Heat Mass Transf., **6**, pp. 537–557.
[35] Gnielinski, V., 1976, ''New Equations for Heat and Mass Transfer in Turbulent Pipe and Channel Flow,'' Int. Chem. Eng., **16**, pp. 359–368.
[36] Novotny, J. L., McComas, S. T., Sparrow, E. M., and Eckert, E. R. G., 1964, ''Heat Transfer for Turbulent Flow in Rectangular Ducts With Two Heated and Two Unheated Walls,'' AIChE J., **10**, pp. 466–470.
[37] Petukhov, B. S., and Popov, V. N., 1963, ''Theoretical Calculation of Heat Exchange and Frictional Resistance in Turbulent Flow in Tubes of an Incompressible Fluid With Variable Physical Properties,'' High Temp., **1**, pp. 69–83.
[38] Humble, L. V., Lowdermilk, W. H., and Desmon, L. G., 1951, ''Measurement of Average Heat Transfer and Friction Coefficients for Subsonic Flow of Air in Smooth Tubes at High Surface and Fluid Temperatures,'' NACA Report 1020.
[39] Barnes, J. F., and Jackson, J. D., 1961, ''Heat Transfer to Air, Carbon Dioxide and Helium Flowing Through Smooth Circular Tubes Under Conditions of Large Surface/Gas Temperature Ratio,'' J. Mech. Eng. Sci., **3**, pp. 303–314.
[40] Kays, W. M., and Crawford, M. E., 1993, *Convective Heat and Mass Transfer*, 3rd ed., McGraw-Hill, Inc., New York.

Heat and Mass Transfer Characteristics of a Temperature and Concentration Combined Convection Due to a Vertical Ice Plate Melting

M. Sugawara
Department of Mechanical Engineering,
Faculty of Engineering and Resource Science,
Akita University,
Akita 010-8502, Japan

Thomas F. Irvine
Department of Mechanical Engineering,
State University of New York at Stony Brook,
Stony Brook, NY 11794, USA

M. Tago
Department of Mechanical Engineering,
Faculty of Engineering and Resource Science,
Akita University,
Akita 010-8502, Japan

The melting of a vertical ice plate into a calcium chloride aqueous solution ($CaCl_2$-H_2O *mixture) in a rectangular cavity is considered numerically and experimentally. The ice plate melts spontaneously with decreasing temperature at the melting front even when there exists no initial temperature difference between ice and liquid. Visual observations in the liquid reveal a complicated natural convection affected by the concentration/temperature gradients which appear near the melting front. Melt water gradually contaminates an upper region in the initially homogeneous liquid, that causes the melting rate to decrease. Aspect ratio H/W of the liquid region does not affect the melting rate within an early melting stage, however large aspect ratio causes the melting rate to decrease during the melting process. A two-dimensional numerical model reflecting actual ice melting conditions predicts, approximately, the transient melting mass, and the transient temperature/concentration decrease in the melting system. It is seen that the Sherwood number at the melting front is larger when compared with previous results concerning double diffusive convection. The Nusselt number at the melting front is quantitatively considered experimentally and analytically.* [DOI: 10.1115/1.1513577]

Keywords: Double Diffusion, Experimental, Heat Transfer, Melting, Natural Convection, Numerical Methods

Introduction

Melting process of ice in mixture induces concentration and thermal gradients near the melting front in the initially homogeneous liquid. These gradients cause transient double diffusive convection which significantly influences the melting behavior of ice. Some studies on the melting have been previously reported by Griffin [1], Marschall [2], Huppert and Turner [3], Josberger and Martin [4], Carey and Gebhart [5,6], Sammakia and Gebhart [7], Johnson and Mollendorf [8], Sugawara et al. [9], Beckermann and Viskanta [10], Schütz and Beer [11], Fukusako et al. [12], Sugawara and Sasaki [13]. However, the quantitative predictions for the melting rate, abrupt temperature depression at the melting front, and the melting Nusselt and Sherwood numbers at the melting front have not been fully considered experimentally and numerically in the above studies.

Recently, Sugawara and Fujita [14] and Sugawara and Irvine [15] studied the melting of a vertical ice plate and a horizontal ice plate from above with the double effect of temperature and concentration, respectively, and presented a quantitative prediction of the melting rate and the abrupt temperature depression at the melting front under the restricted condition of the same temperature of ice and liquid initially. More recently Mergui and Gobin [16] reported the numerical investigations of transient double diffusive convection for a similar model to our previous study [14], however the boundary conditions of temperature and concentration at the cold wall in their model do not account for ice melting.

This paper is concerned with the heat and mass transfer characteristics due to the melting of a vertical ice plate into an initially homogeneous calcium chloride aqueous solution inside a square cavity, which is considered as an extension of the previous work [14]. The effect of the initial liquid volume (i.e., aspect ratio H/W) on the melting rate is considered experimentally and analytically. A two-dimensional ideal numerical calculation is presented to predict the melting rate, an abrupt temperature decrease at the melting front and the mean melting Nusselt and Sherwood numbers.

Analytical Procedure

Figure 1 shows a two-dimensional physical model and coordinate system considered in the present study. H is the height of the liquid and ice plate, and W is the width of the liquid. The ice plate thickness δ is a half of the thickness 2δ used in the experiment because of a symmetry of the melting system which is appropriate to measure precise ice plate temperature T_1 and transient mean melting mass M. Heat conduction in the walls of styrofoam and lucite plates are also calculated consistent with the experimental melting system. It is assumed in the analysis that the flow in the liquid is two-dimensional, laminar, and the Boussinesq approximation is applicable to avoid complex calculations. Also, the volumetric change of the solid and liquid due to the phase change is not considered because of a comparatively short melting time.

Governing Equations in the Liquid, Ice, Lucite and Styrofoam Plates

Liquid

Continuity

$$\frac{\partial}{\partial x_j}(\rho_L u_j) = 0 \tag{1}$$

Contributed by the Heat Transfer Division for publication in the JOURNAL OF HEAT TRANSFER. Manuscript received by the Heat Transfer Division May 24, 2001; revision received June 26, 2002. Associate Editor: P. S. Ayyaswamy.

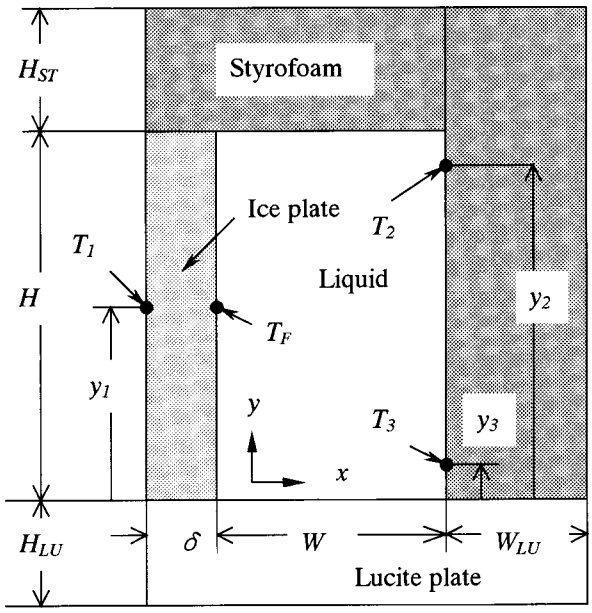

Fig. 1 Schematic of the physical model and coordinate system

Momentum, Energy, and Species

$$\frac{\partial}{\partial t}(\rho_L \phi)+\frac{\partial}{\partial x_j}(\rho_L u_j \phi)$$

$$=\frac{\partial}{\partial x_j}\left(\Gamma_\phi \frac{\partial \phi}{\partial x_j}\right)+S_\phi$$

$$S_T=0, \quad S_C=0$$

$$S_u=-\frac{\partial p}{\partial x} \tag{2}$$

$$S_v=-\frac{\partial p}{\partial y}+\rho_L g \beta_T (T_L-T_r)+\rho_L g \beta_C (C-C_r)$$

$$\Gamma_{u,v}=\mu_L, \quad \Gamma_T=\lambda_L/c_L, \quad \Gamma_C=\rho_L D$$

where the independent variable of x_j and dependent variables of u_j and ϕ will become more clear below.

$$x_1=x, \quad x_2=y, \quad u_1=u, \quad u_2=v$$

$$\phi=u, \ v, \ T_L, \ C$$

Ice, Lucite, and Styrofoam Plates

Energy Equation

$$\frac{\partial}{\partial t}(\rho_\Phi T_\Phi)=\frac{\partial}{\partial x_j}\left(\frac{\lambda_\Phi}{c_\Phi}\frac{\partial T_\Phi}{\partial x_j}\right) \tag{3}$$

where subscript Φ indicates *S* (ice), *LU* (lucite), and *ST* (styrofoam).

Boundary and Initial Conditions. All the velocities at the interfaces between the liquid and the walls (ice, lucite and styrofoam) are assumed to be zero. The continuity of heat flux is applied on the interfaces between the liquid and the lucite or styrofoam plate. The outsides of the ice, lucite and styrofoam are assumed to be adiabatic, consistent with the experimental condition of using styrofoam plates as insulators.

The most important boundary conditions are at the melting front since these will play a key role in the determination of the melting rate. The heat balance generally used in the classical Stefan problem [17] is necessary as follows.

Heat Balance

$$h_f \dot{m}_{\text{ice}}=\lambda_L\left(\frac{\partial T_L}{\partial x}\right)_F-\lambda_S\left(\frac{\partial T_S}{\partial x}\right)_F \tag{4}$$

It is better to express Eq. (4) by the following average expression for discussing the mean melting Nusselt number as seen later.

$$q_{\text{ice}}=q_L+q_S \tag{4'}$$

However, it is impossible to determine the melting rate by using only Eq. (4) and another important condition is needed.

Mass Balance

$$C_F \dot{m}_{\text{mix}}=\rho_L D\left(\frac{\partial C}{\partial x}\right)_F \tag{5}$$

where C_F is the concentration at the melting front, and can be assumed to be in thermodynamic equilibrium and related to the thermodynamic equilibrium temperature at the melting front T_F (local equilibrium assumption). However, C_F and T_F will change with time and accordingly it is impossible to pre-set C_F and T_F as the boundary conditions to solve the energy and species equations. Since the melting front is a semi-permeable plane for the solute ($CaCl_2$), the relation of $\dot{m}_{\text{ice}}=\dot{m}_{\text{mix}}$ holds (Eckert and Drake [18]). Since the liquid is assumed to be quiescent before the melting begins, u and v are zero initially. The initial temperatures of the liquid, ice, lucite and styrofoam are all the same, -5°C, and therefore there exists no temperature difference between ice and liquid at the beginning of melting.

Determination of T_F and C_F and Solution Procedure. Since it is impossible to pre-set T_F and C_F to solve the energy and species equations, an iterative method was employed in the present numerical calculations to determine the transient T_F, C_F and also to obtain the converged solutions of u, v, T, and C utilizing the SIMPLER algorithm [19] as shown in the previous studies [14,15].

An iteration convergence criterion and convergence test such as time step, mesh size and relaxation factor were considered according to the previous procedures [14,15]. Since the numerical solution will be largely dependent on the x-direction mesh size Δx due to the very complicated flow in the melt liquid and the very thin diffusion boundary layer adjacent to the melting front as seen later in Figs. 4 and 5, it is necessary to set very small mesh sizes to obtain precise numerical solutions. In this calculation, variable mesh sizes were adopted in the x-direction as shown in the previous studies [14,15]. Especially the effect of the melting front mesh size Δx_F on the melting rate was carefully considered, and eventually $\Delta x_F=0.1$ mm was adopted after some consideration for mesh size dependency. In a calculation reported in the present study, grids of 111×201 nodal points were selected in only the liquid domain for $W=50$ mm and $H=100$ mm. Therefore, many more grids are needed for calculations in the melting system including an ice plate, lucite and styrofoam plates.

Definition of Mean Melting Mass, Nusselt and Sherwood Numbers, and Physical Properties. Since the present study was mainly to focus on the mechanism of an ice plate melting during a relatively short melting time (i.e., $t=10$ min), the mean melting thickness of the ice plate was very small, less than about 0.8 mm as confirmed by experiments. Therefore neglecting the movement of the melting front in the present numerical predictions does not prevent resolution of the melting mechanism. In other words, it is possible to predict the mean melting rate $\dot{m}_m$

Table 1 Physical properties of $CaCl_2$-H_2O mixtures for $T=-5°C$, $C=0.2$ (20 wt%)

c_L [kJ/kg K]	3.044
h_f [kJ/kg]	334.1
β_C [1/(kg/kg)]	−0.916
β_T [1/K]	0.00033
λ_L [kJ/m s K]	5.35×10^{-4}
μ_L [kg/m s]	0.00386
ρ_L [kg/m^3]	1193.9
Pr	22

($=q_{\text{ice}}/h_f$) and the transient mean melting mass M from the $\dot{m}_{\text{ice}}$ predicted under the condition of a fixed melting front.

$$\dot{m}_m=\int_0^H \dot{m}_{\text{ice}}dy/H \tag{6}$$

$$M=\int_0^t \dot{m}_m dt \tag{7}$$

Mean melting Nusselt and Sherwood numbers, thermal Grashof and concentration Grashof numbers and buoyancy ratio are defined as follows.

$$\text{Nu}_{Ll}=\frac{\alpha_L l}{\lambda_L},\quad \text{Nu}_{\text{ice}l}=\frac{\alpha_{\text{ice}} l}{\lambda_L},\quad \text{Sh}_l=\frac{h_D l}{D}$$

$$\text{Gr}_{Tl}=\frac{g\beta_T\Delta T l^3}{\upsilon^2},\quad \text{Gr}_{Cl}=\frac{g|\beta_C|\Delta C l^3}{\upsilon^2} \tag{8}$$

$$N=\frac{\text{Gr}_{Cl}}{\text{Gr}_{Tl}}$$

where α_{ice} and α_L in Eq. (8) are both the heat transfer coefficient at the melting front, and supplemental relations are defined as follows.

$$q_L=\alpha_L\Delta T,\quad q_{\text{ice}}=\alpha_{\text{ice}}\Delta T,\quad \Delta T=|T_{Fm}-T_{Rm}|$$

$$\dot{m}_m=h_D\rho_L\Delta C,\quad \Delta C=|C_{Fm}-C_{Rm}|$$

$$l=W:\quad \text{Nu}_{LW},\ \text{Nu}_{\text{ice}W},\ \text{Sh}_W$$

$$l=H:\quad \text{Nu}_{LH},\ \text{Nu}_{\text{ice}H},\ \text{Sh}_H$$

Table 1 shows the physical properties used in the present numerical predictions [20]. The thermal expansion coefficient β_T and the concentration expansion coefficient β_C were calculated from their definition by a least square approximation of the relation of density and temperature. Since it is difficult to find the mass diffusion coefficient D of a $CaCl_2$ aqueous solution for high concentrations and low temperatures which appears in the present study, $D=0.3\times10^{-9}$ m^2/s was adopted as a plausible value of mixtures. This approach was adopted because D for high concentration and low temperature is in the range $D=0.1\times10^{-9}$–0.5×10^{-9} m^2/s as described in [14,15]. As seen later, the effect of the mass diffusion coefficient on the mean melting mass is considered in detail (see Fig. 8).

Experiment

All ice melting experiments were carried out in a temperature controlled room. The initial temperatures of the ice plate and liquid were arranged by adjusting the room temperature. The room temperature was maintained slightly below the initial temperature during the melting process. Figure 2 shows a schematic view of the ice plate and test cell used in this experiment. The test cell was made of lucite and styrofoam plates. The height of the ice plate H is fixed as 100 mm, which also corresponded to the depth of the liquid, and the liquid width is W. The length of the test cell, normal to the flow plane (x-y), is 100 mm for each width W. The length dimension is large enough to justify the two-dimensional treatment used and laminar flow, which is validated by the visualization results. A square cross sectional gap having a dimension of 2δ was manufactured on the center position in the test cell so as to slide down a vertical ice plate at the beginning of the experiment. The width W of the liquid was adjusted by setting the desired thick styrofoam plate in the cell as shown in Fig. 2. The vertical side styrofoam plate had two thermocouple sensors with copper foil for temperature measurement of T_2 and T_3. The ice plate was formed inside a lucite made frame to prevent crush and corner melting of it. The greatest difficulty in this experiment was to measure the temperature at the melting front T_F. It is difficult to measure T_F directly because of a steep temperature gradient near the melting front. The temperature in the ice plate T_1 was measured to overcome this difficulty. Except in the early stage of melting, T_1 can be taken equal to T_F due to the larger thermal conductivity of ice compared to that of the liquid. The transient temperature depression in the ice plate, T_1, was measured with a thermocouple placed in a thin stainless tube located in the middle of the ice plate (y_1). These thermocouples were connected to a digital multi-meter (Yokogawa, Model-7561), a programmable scanner (Yokogawa, Model-7501), and a personal computer (NEC, PC9801) through which each temperature could be measured. A bias limit of temperature measurement was about 0.1°C. Measurement of the initial concentration C_i of the mixture was conducted by measuring the mass of $CaCl_2$ and distilled water with a bias limit of 0.2 wt%. Relative uncertainty for the mean melting mass M is estimated as about 6% in 99% confidence level.

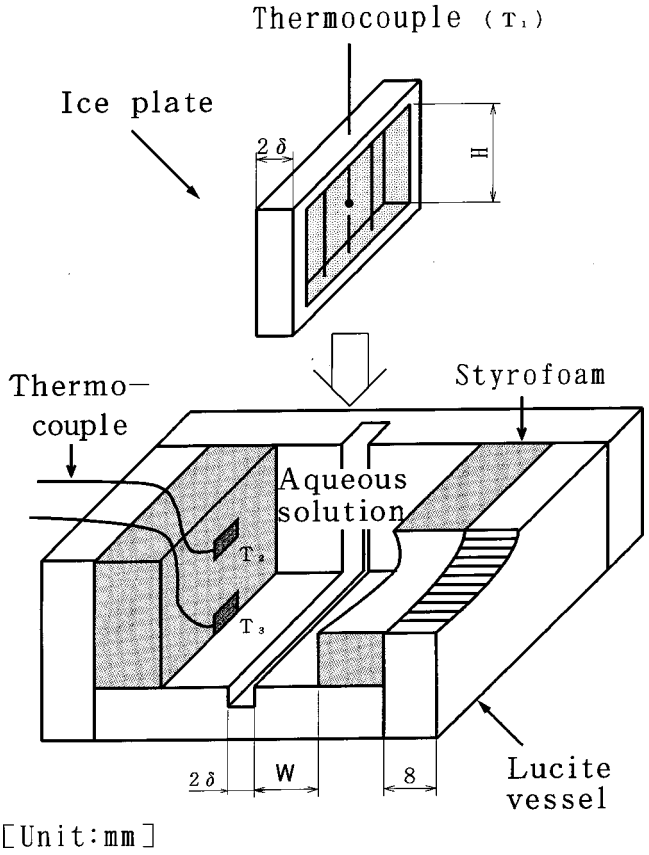

Fig. 2 View of the experimental apparatus for the melting of an ice plate

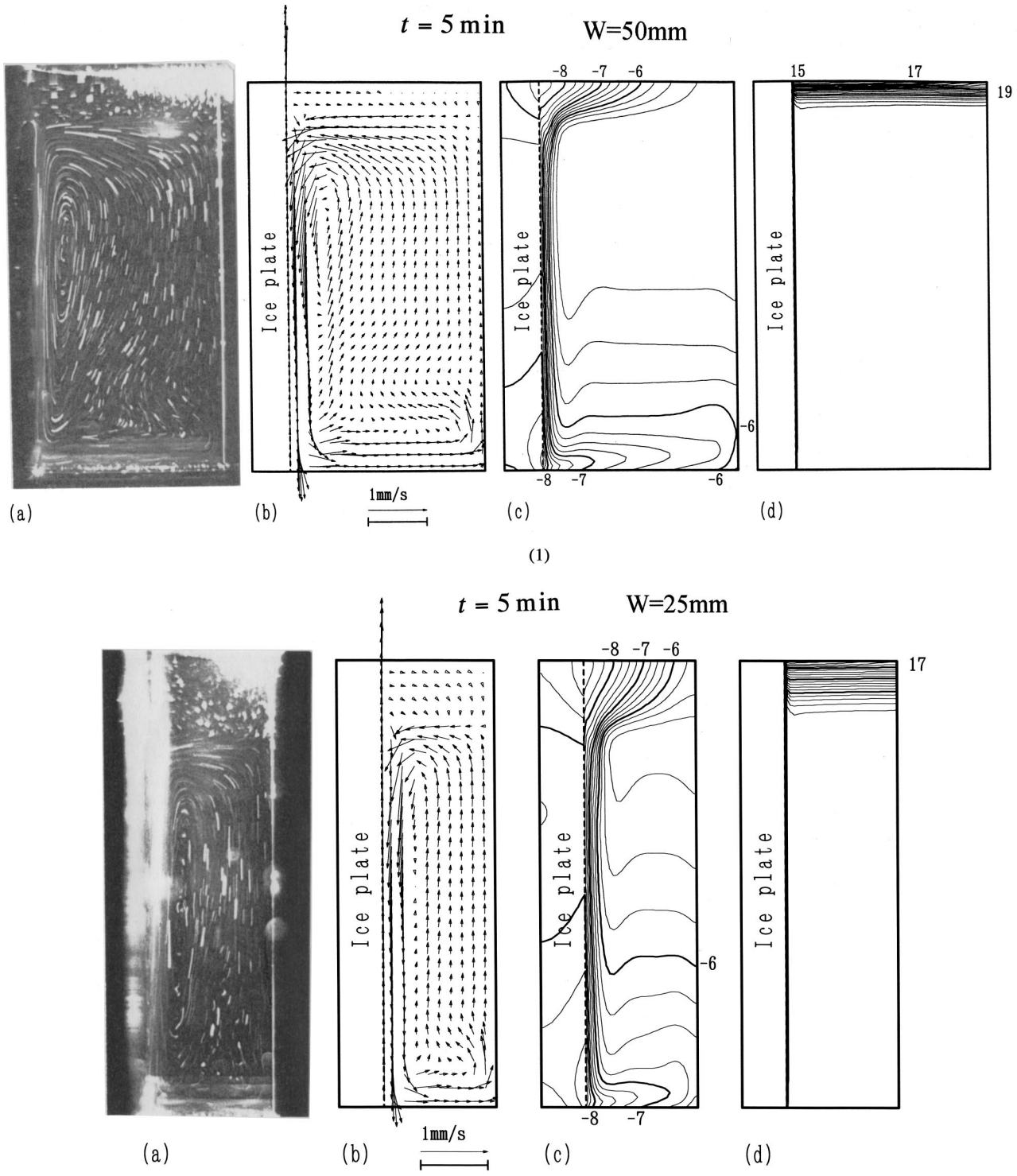

Fig. 3 (1), (2), and (3): (*a*) visual flow observation in the liquid and predicted results of (*b*) velocity vectors; (*c*) isotherms, and (*d*) concentration isopleths at $t=5$ min for (1) $W=50$ mm, (2) $W=25$ mm, and (3) $W=15$ mm ($H=100$ mm, $\delta=10$ mm, $C_i=20$ wt%, $T_{si}=T_{Li}=-5°C$)

Procedures and Materials. The test cell was filled with a calcium chloride aqueous solution of a prescribed initial concentration $C_i=0.2$ (20 wt%), and the liquid was adjusted to the initial temperature $T_{Li}=-5°C$. On the other hand, the temperature of the ice plate out of the test cell was adjusted to the initial temperature T_{Si}. After the ice plate temperature reached the initial temperature (i.e., $T_{Si}=T_{Li}=-5°C$), the ice plate was gently immersed into the liquid so as not to disturb the liquid. After a pre-selected time had passed, the ice plate was quickly pulled up and the nominal liquid stuck on the ice surfaces was wiped out with a blotting paper. Then the mass of the ice plate was measured to obtain the mean melting mass M.

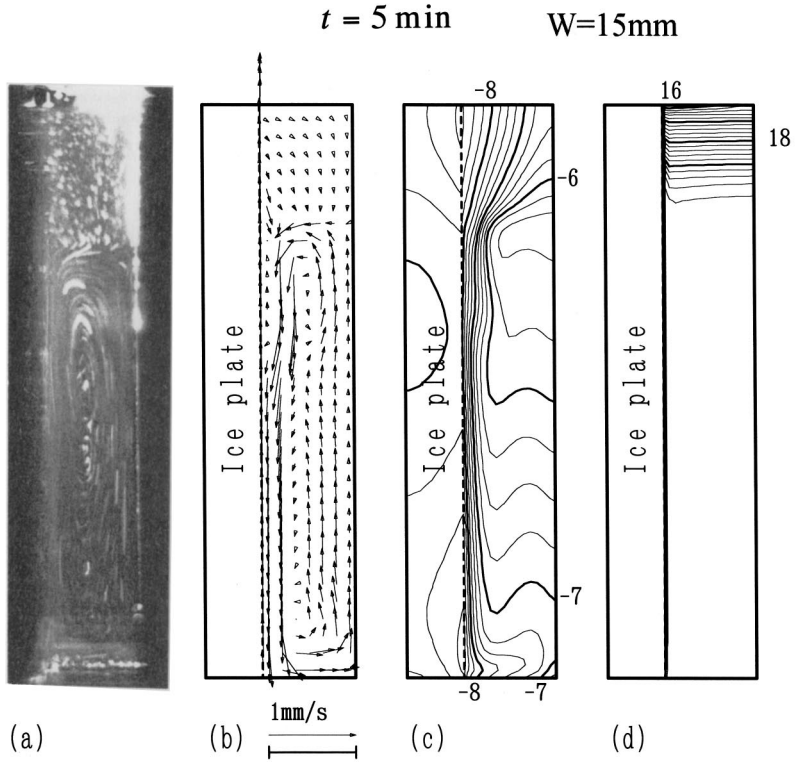

(3)

Fig. 3 (***continued***)

Two techniques for flow visualization were employed using powder milk tracers to visualize stream lines and a black ink solution to investigate the flow direction which revealed a very complicated double diffusive convection pattern in the melt liquid. Before the melting experiment began, a little powder milk was suspended in the liquid. A slit light sheet from a halogen lamp illuminated the cell from above during a 15 s interval just after a desired melting time had passed. A photograph was taken at the same time.

The liquid used in this experiment is a solution of a calcium chloride ($CaCl_2$) in water (H_2O) of a eutectic type. The liquidus line indicating the thermodynamic equilibrium relationship of temperature and concentration (T_F and C_F) have been in the previous studies [14,15]. The air bubble free ice plate used in this experiment was made of distilled and degasified water because rejected air bubbles from the melting front would disturb flow in the liquid. The ice plate was made flat by melting the surface of it with a weakly heated copper plate.

Results and Discussion

Flow in the Liquid With Visual Observations and Numerical Predictions. Figure 3(1), (2) and (3) shows (*a*) visual observations of natural convection in the liquid, and numerical predictions of (*b*) velocity vectors, (*c*) isotherms, and (*d*) isopleths of concentration for the case of (1) $W=50$ mm, (2) $W=25$ mm, and (3) $W=15$ mm. It is seen that the liquid temperature near the melting front decreases predominantly, which causes an increase in the liquid density, and therefore will act to move the liquid downward (negative buoyancy). On the other hand, the solute concentration near the melting front decreases due to the adding of melt water, which causes a decrease in the liquid density, and therefore acts to make the liquid unstable (positive buoyancy). However, the predominance of the buoyancy due to density/concentration decrease (i.e., $|\beta_C| \gg |\beta_T|$, see Table 1) causes the liquid to move upward. Eventually a very thin concentration boundary layer appears near the melting front as can be seen from the profiles of vertical velocity component v in Fig. 4. On the other hand, out of the concentration boundary layer a downward thermal convection appears with a counter-clock-wise circulation. Accordingly, low density and low temperature melt liquid rises up along the melting front and accumulates in the upper part of the

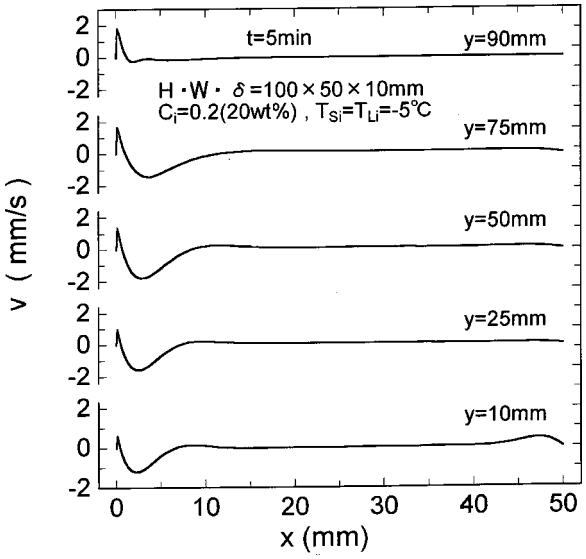

Fig. 4 Predicted profiles of the vertical velocity component v (*x*=0: melting front)

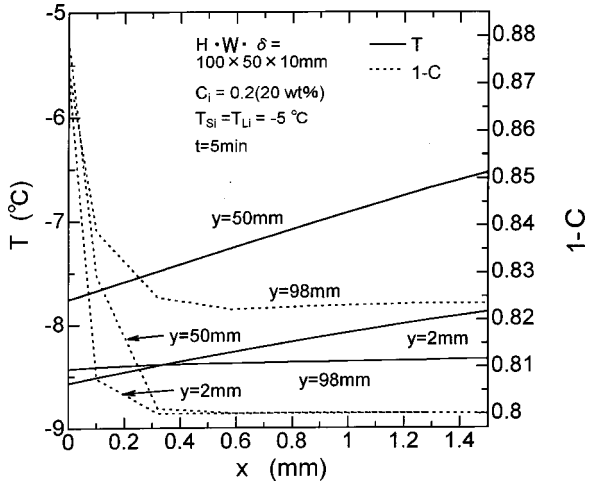

Fig. 5 Predicted profiles of temperature (T) and water concentration ($1-C$) near the melting front ($x=0$: melting front)

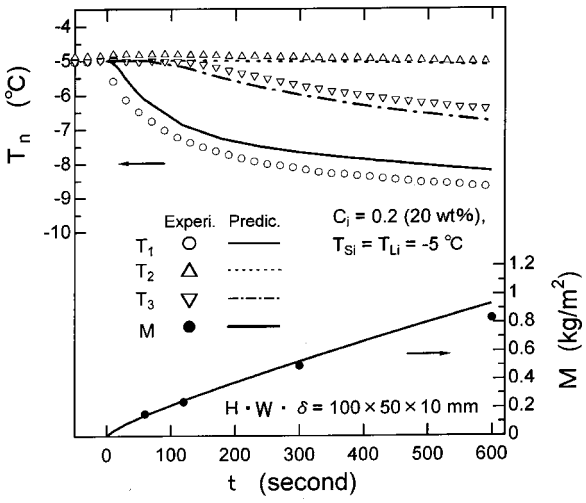

Fig. 6 Comparison of predictions and experiments for the temperature T_1 ($y_1=50$ mm), T_2 ($y_2=90$ mm), and T_3 ($y_3=10$ mm) and the mean melting mass M

liquid layer, which is seen as a stratified layer contaminated by the melt liquid. This contaminated stratified layer (i.e., stagnant region) is seen to be almost quiescent as can be seen in the flow visualization and velocity vectors. In the thermal convection layer under the stagnant region the concentration of the liquid retains almost the initial concentration while the temperature of it gradually decreases.

The liquid width W (i.e., liquid volume) will affect the development of the stagnant region. It is seen that the thickness of the stagnant region develops faster with decreasing W. This is mainly attributed to the decrease of the capacity of the liquid region to include the melt water. Moreover the temperature depression in the liquid becomes faster with decreasing W, and the intensity of flow becomes weaker with decreasing W.

Temperature and Concentration Profiles Near the Melting Front . Figure 5 shows the expanded profiles of temperature (T: solid line) and water concentration (1-C: dashed line) near the melting front with height from the bottom, y, as parameter. The concentration gradients are very steep compared to the temperature gradients, which are a typical feature appearing in double diffusive convection due to the high Lewis number Le. The profiles of concentration outside of the concentration boundary layer are almost uniform (horizontal). These typical profiles are very similar qualitatively to the diffusion model proposed by Nernst concerning a solid dissolution into a mixture (Moelwyn-Hughes [21]). The concentration gradient gradually decreases along the upward direction of the melting front. This behavior results as that the rising melt liquid in the concentration boundary layer becomes more water-rich due to the diffusion of melt water from the melting front.

Transient Temperature Depression in the Melting System and Mean Melting Mass. Figure 6 shows the comparisons of predictions and experiments for the transient temperature decrease in the melting systems and for the transient mean melting mass. Although the initial temperatures of both ice and liquid are the same (-5°C) as already explained, the tmeperature in the ice plate T_1 will decrease spontaneously. This typical behavior seems curious, however, it demonstrate the spontaneous melting of ice in a homogeneous mixture. The concentration gradient which appears near the melting front induces the melting of ice. At this time it is necessary to absorb the latent heat for melting from both the ice and liquid sides, and therefore a temperature gradient will appear at the melting front, and eventually the temperature of the ice plate decreases spontaneously. The Lewis number Le is very large, about 400 in this problem. This means that the rate of mass diffusion is very small compared to the rate of heat conduction. Therefore the melting of ice will be mainly dominated by mass diffusion. The temperature T_2 and T_3 begin to decrease gently after the decrease of T_1. The bottom temperature T_3 is lower than the top temperature T_2 due to the enhanced counter-clockwise rotation in the uncontaminated region. On the other hand, the mean melting mass M will increase monotonically during the melting process. It is seen that M marks about 1 kg/m^2 at $t=600$ s in spite of no heat supply from the liquid at the beginning of the melting.

Figure 7 shows the effect of the liquid width W on the mean melting mass M. The height of the ice plate (liquid depth) H is 100 mm. M is insensitive to W until about $t=120$ s. However, the effect of liquid width gradually increases during the melting process. This behavior is explained as follows. As can be seen from the flow visualizations and velocity vectors (Fig. 3), the stagnant region for small W will develop faster compared to a large W. This corresponds to a decrease of the region having an abrupt concentration gradient promoting the melting rate, so that will reflect a decrease of the melting rate.

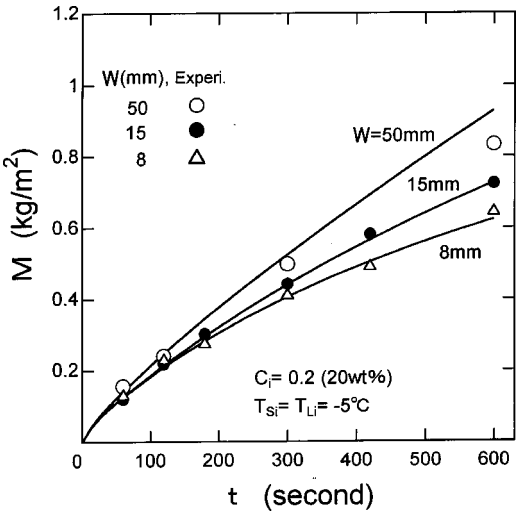

Fig. 7 Effect of the liquid width W on the mean melting mass M ($H=100$ mm, $\delta=10$ mm, $C_i=20$ wt%, $T_{si}=T_{Li}=-5$°C)

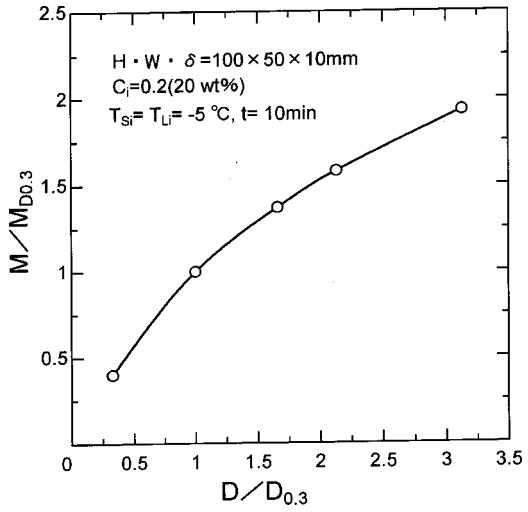

Fig. 8 Effect of the mass diffusion coefficient on the mean melting mass

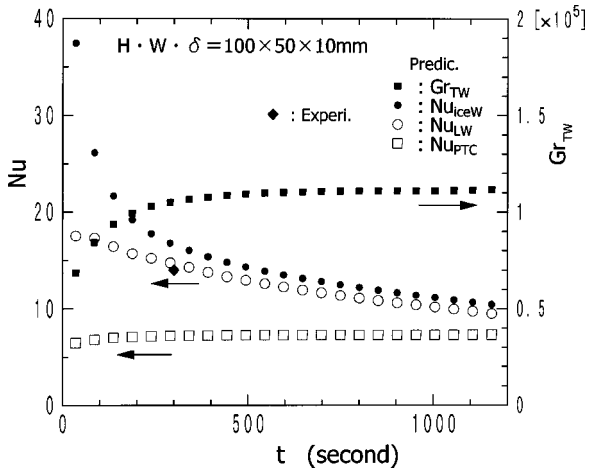

Fig. 9 Transient mean melting Nusselt numbers of Nu_{iceW} and Nu_{LW} and thermal Grashof number Gr_{TW} ($t<20$ min)

Effect of the Mass Diffusion Coefficient on the Mean Melting Mass. Figure 8 shows the effect of the mass diffusion coefficient rate $D/D_{0.3}$ on the mean melting mass rate $M/M_{D0.3}$, where $D_{0.3}=0.3\times10^{-9}$ m^2/s is adopted as a plausible estimation and $M_{D0.3}$ is the mean melting mass for $D_{0.3}$. If more exact data for D were available, Fig. 8 would yield a more precise relationship between the mean melting mass M and D.

The Mean Melting Nusselt Number. To compare with steady state heat transfer for pure water or other circumstances of double diffusive natural convection in a rectangular cavity, the present numerical calculations have been extended to till $t=1200$ s ($=20$ min).

Figure 9 shows the transient mean melting Nusselt numbers Nu_{iceW} and Nu_{LW} for $W=50$ mm, which are evaluated from q_{ice} and q_L respectively as defined by Eq. (4′). These are compared with the Nusselt number (Nu_{PTC}) of the pure thermal convection related by McAdams [22], (i.e., $N=0$), in a closed rectangular cavity. Just after the melting begins, both Nusselt numbers are relatively high due to the strong unsteady heat transfer near the melting front. Moreover Nu_{LW} is slightly lower than Nu_{iceW}. However, the difference in the Nusselt numbers becomes gradually smaller. This specific feature of the difference of Nu_{LW} and Nu_{iceW} is explained as follows. The appearance of a temperature gradient (i.e., q_S) in an ice plate will retard the ice melting into the pure water due to the positive temperature gradient (see Eq. (4)). On the other hand, the appearance of the temperature gradient (i.e., q_S) will promote the ice melting into mixtures in the present study due to the negative temperature gradient. This behavior is a prominent difference between ice melting into the pure water and ice melting into a mixture. In other words, the heat flux q_L should be used to evaluate the mean melting Nusselt number in the liquid in the early stage of melting. However, from the above discussions it can be used q_{ice} to evaluate the mean melting Nusselt number at the melting front after the developed melting. The experimental result (◆) in Fig. 9 is calculated from the results in Fig. 6 assuming $T_{Fm}=T_1$ and $T_{Rm}=(T_2+T_3)/2$ at $t=300$ s. The temperature difference of T_{Fm} and T_1 is small as about 0.3°C at $t=300$ s from the results of numerical prediction. This experiment should be compared with the Nu_{iceW} (●) because q_{ice} ($=h_f\dot{m}_m$) is used for evaluating Nusselt number. It is seen that the deviation among both Nusselt numbers is comparatively small. It would be noteworthy to have carried out a quantitative comparison of experiment and numerical solution for the mean melting Nusselt number under the actual melting conditions.

Table 2 indicates the numerical results of the mean melting Nusselt numbers for $t=20$ min evaluated for $l=H$ to compare to other results related to the present study. Han and Kuehn [23,24] reported the steady state double diffusive natural convection in a vertical rectangular enclosure experimentally and numerically. Their experimental results were not from melting ice but from an electrochemical technique. They reported the numerical result of $Nu_{LH}=16$ under the conditions $Gr_{TH}=8\times10^5$ and $H/W=4$. On the other hand, the present numerical results indicate $Nu_{LH}=14.19$ under the conditions of $Gr_{TH}=8.05\times10^5$ and $H/W=4$ as shown in Table 2.

Mergui and Gobin [16] proposed the following correlation for transient double diffusive convection with asymmetrical boundary conditions for $H/W=3$.

$$Nu_{QS}=0.322(1+N)^{-0.17}(Ra_T)^{0.25} \tag{9}$$

where, Nu_{QS} is the mean Nusselt number at the time $t=t_{QS}$, the time that the Nusselt numbers at the hot and cold walls (i.e., melting front) are equal. Estimating Nusselt number from Eq. (9) using the present conditions of $H/W=4$ and $Gr_{TH}=8.05\times10^5$ in Table 2 leads to $Nu_{QS}\cong10$ which is comparatively smaller than $Nu_{LH}=14.19$ in the present calculation and $Nu_{LH}=16$ in Han and Kuehn [24]. Another large difference for the Nusselt number appears between Mergui and Gobin [16] and the present. Their Nusselt number for double diffusive convection with ice melting is smaller than that for pure thermal convection (i.e., $N=0$). On the contrary, the present results show results opposite to their calculations as seen in Figs. 9.

The mean melting Nusselt number defined by Sammakia and Gebhart [7] for a vertical ice plate melting in saline water is the

Table 2 Numerical results after the developed melting at $t=20$ min ($l=H$)

W	Nu_{iceH}	Nu_{LH}	Sh_H	Gr_{TH}	Gr_{CH}	N	H/W
8	33.48	21.45	3759	199000	22400000	112	12.5
15	19.24	15.09	3945	545000	33500000	62	6.7
25	16.80	14.19	4133	805000	41300000	51	4
50	20.34	18.51	4511	895000	50900000	57	2

same as the present definition of Nu_{iceH} in Eq. (8). However, since the reference length in the Nusselt numbers are different from each other, it is difficult to compare heat transfer characteristics quantitatively at the melting front by using only the Nusselt numbers. To this difficulty, an idea will be proposed for a comparison of both heat transfer coefficients. The heat transfer coefficient of Sammakia and Gebhart is about 17.5 W/(m^2K) which is slightly larger than the present result of about 15 W/(m^2K). From the above consideration, the mean melting Nusselt number predicted by Mergui and Gobin is comparatively low, and might not reflect the actual ice melting behavior into mixtures.

The Mean Melting Sherwood Number. The Sherwood numbers Sh_H is about 100 for $Gr_{TH}=8\times10^5$ ($Gr_{CH}=10^5$ fixed) and $H/W=4$ in Han and Kuehn [24], and is about 140–160 for Rayleigh number $Ra_{CH}=4.2\times10^9$ and $H/W=3$ in Mergui and Gobin [16]. Their Sherwood numbers are very small compared with the present result of 4133 for $Gr_{TH}=8.05\times10^5$ in Table 2. This is mainly attributed to the fact that their model assumptions concerning the boundary conditions at the cold wall (i.e., melting front) do not account for phase change. The heat and mass balances in the melting front boundary conditions of Eqs. (4) and (5) should be used to predict the heat and mass transfer characteristics for the actual melting. As another reason of the difference between the Sherwood numbers, the present ice melting is mainly dominated by the concentration gradient with abrupt temperature decrease at the melting front in a strong unsteady state.

From the above discussion it is very difficult to establish the melting Nusselt and Sherwood numbers for the ice melting into mixtures in a steady state due to the development of the stagnant region and the abrupt change in the melting front temperature/concentration. The Nusselt and Sherwood numbers will also strongly change after ice melting begins. It is difficult to precisely estimate the transient melting mass from only the Nusselt and Sherwood numbers when the various melting conditions such as T_{Li}, T_{Si}, C_i, H/W, and δ will change. Therefore, it is necessary to more thoroughly investigate the problem experimentally and analytically to easily and precisely estimate the transient melting amount.

Concluding Remarks

The melting of a vertical ice plate immersed into a homogeneous calcium chloride aqueous solution was considered experimentally and numerically. The following can be concluded:

1 The ice melted spontaneously with decreasing temperature at the melting front even when there existed no initial temperature difference between ice and liquid.

2 The present two-dimensional numerical calculation applied to an ideal model predicted approximately the mean melting mass and the abrupt temperature decrease in the melting system within a comparatively short melting time of about $t=600$ s.

3 The liquid layer width W (i.e., aspect ratio) did not affect the melting rate within an early melting stage, however a small W (i.e., large aspect ratio) caused the melting rate to decrease during the melting process due to the abrupt devolution of the stagnant region.

4 The mean melting Nusselt number at the melting front was comparatively higher than that for pure thermal convection without change of phase in the early melting stage due to the mass diffusion dominated melting and strong unsteady state in the melting system.

5 The mean melting Sherwood number was numerically predicted to have a higher value compared to other results related to double diffusive natural convection in a rectangular cavity without change of phase.

Acknowledgments

The authors wish to acknowledge support for this study by the technical official T. Fujita, the under graduate students K. Kirihata, T. Oshima, and A. Sawaki.

Nomenclature

a = thermal diffusivity, m^2/s
c = specific heat, kJ/kg K
C = solute ($CaCl_2$) concentration (mass fraction), kg/kg
C_F = solute concentration at the melting front, kg/kg
D = mass diffusion coefficient, m^2/s
g = gravitational acceleration, m/s^2
Gr_C = concentration Grashof number
Gr_T = thermal Grashof number
h_D = mass transfer coefficient, m/s
h_f = latent heat for melting, kJ/kg
H = depth of the liquid layer, 100 mm (=height of an ice plate), mm
l = temporary reference length for W or H
Le = Lewis number (a/D)
$\dot{m}$ = melting mass per unit area and time (=melting rate), kg/m^2s
M = mean melting mass per unit area, kg/m^2
N = buoyancy ratio, Eq. (8)
Nu = mean Nusselt number
Nu_{PTC} = mean Nusselt number for pure thermal convection
p = pressure, N/m^2
Pr = Prandtl number
q_{ice} = total heat flux consumed to the ice melting ($=q_L+q_S=h_f\dot{m}_m$), kJ/m^2s
q_L = heat flux towards the melting front from liquid region, kJ/m^2s
q_S = heat flux towards the melting front from ice plate region, kJ/m^2s
Ra = Rayleigh number
Sh = mean Sherwood number
S_ϕ = source term
t = time, s
T = temperature, °C or K
T_1 = temperature in the middle ($y_1=H/2$) of an ice plate (see Fig. 1), °C or K
T_2 = temperature at the upper right side corner (y_2) (see Fig. 1), °C or K
T_3 = temperature at the lower right side corner (y_3) (see Fig. 1), °C or K
T_F = temperature at the melting front, °C or K
u = x-component velocity, m/s
u_j = velocity ($u_1=u$, $u_2=v$), m/s
v = y-component velocity, m/s
W = width of the liquid layer
x = horizontal coordinate ($x=0$ indicates the melting front), mm
x_j = coordinate ($x_1=x$, $x_2=y$)
Δx_F = the mesh size attached to the melting front, mm
y = vertical coordinate or distance from the bottom (see Fig. 1), mm

Greek Symbols

α = heat transfer coefficient, kJ/m^2s K
β_C = concentration expansion coefficient, $(kg/kg)^{-1}$
β_T = temperature expansion coefficient, K^{-1}
Γ_ϕ = general diffusion coefficient
δ = ice plate thickness in analysis (2 δ is in experiment), mm
λ = thermal conductivity, kJ/m s K
μ = viscosity, kg/m s
ν = kinematic viscosity, m^2/s
ρ = density, kg/m^3

ϕ = dependent variables (u, v, T, C)

Subscript

C = concentration
F = melting front
H = height
i = initial
L = liquid
LU = lucite plate
m = mean
mix = mixture (aqueous solution)
r = reference value (initial value)
R = interface between liquid and vertical styrofoam plate
S = solid (=ice)
ST = styrofoam
T = temperature
W = width
Φ = ice (S), lucite plate (LU), styrofoam (ST)

References

[1] Griffin, O. M., 1973, "Heat, Mass, and Momentum Transfer During the Melting of Glacial Ice in Sea Water," ASME J. Heat Transfer, **95**, pp. 317–323.
[2] Marschall, E., 1977, "Free-Convection Melting on Glacial Ice in Saline Water," Lett. Heat Mass Transfer, **4**, pp. 381–384.
[3] Huppert, H. E., and Turner, J. S., 1980, "Ice Blocks Melting Into a Salinity Gradient," J. Fluid Mech., **100**, pp. 367–384.
[4] Josberger, E. G., and Martin, S., 1981, "A Laboratory and Theoretical Study of the Boundary Layer Adjacent to a Vertical Melting Ice Wall in Salt Water," J. Fluid Mech., **111**, pp. 439–473.
[5] Carey, V. P., and Gebhart, B., 1982, "Transport Near a Vertical Ice Surface Melting in Saline Water, Some Numerical Calculations," J. Fluid Mech., **117**, pp. 379–402.
[6] Carey, V. P., and Gebhart, B., 1982, "Transport Near a Vertical Ice Surface Melting in Saline Water, Experiments at Low Salinities," J. Fluid Mech., **117**, pp. 403–423.
[7] Sammakia, B., and Gebhart, B., 1983, "Transport Near a Vertical Ice Surface Melting in Water of Various Salinity Levels," Int. J. Heat Mass Transf., **26**, pp. 1439–1452.
[8] Johnson, R. S., and Mollendorf, J. C., 1984, "Transport From a Vertical Ice Surface Melting in Saline Water," Int. J. Heat Mass Transf., **27**, pp. 1928–1932.
[9] Sugawara, M., Inaba, H., Nishimura, H., and Mizuno, M., 1987, "Melting of Horizontal Ice Layer From Above by Combined Effect of Temperature and Concentration of Aqua-Solvent," Waerme- Stoffuebertrag., **21**, pp. 227–232.
[10] Beckermann, C., and Viskanta, R., 1988, "Double-Diffusive Convection Due to Melting," Int. J. Heat Mass Transf., **31**, pp. 2077–2089.
[11] Schütz, W., and Beer, H., 1992, "Melting of Ice in Pure and Saline Water Inside a Square Cavity," Chem. Eng. Process., **21**, pp. 311–319.
[12] Fukusako, S., Tago, M., Yamada, M., Kitayama, K., and Watanabe, C., 1992, "Melting Heat Transfer From a Horizontal Ice Cylinder Immersed in Quiescent Saline Water," ASME J. Heat Transfer, **114**, pp. 34–40.
[13] Sugawara, M., and Sasaki, S., 1993, "Melting of Snow With Double Effect of Temperature and Concentration," ASME J. Heat Transfer, **115**, pp. 771–775.
[14] Sugawara, M., and Fujita, T., 1997, "Melting of an Ice Layer With Double Effect of Temperature and Concentration (2nd Report: Development of Numerical Predictions With Flow Visualization)," Trans. Jpn. Soc. Mech. Eng., Ser. B, **63**, pp. 2784–2792.
[15] Sugawara, M., and Irvine, T. F., 2000, "The Effect of Concentration Gradient on the Melting of a Horizontal Ice Plate From Above," Int. J. Heat Mass Transf., **43**, pp. 1591–1601.
[16] Mergui, S., and Gobin, D., 2000, "Transient Double Diffusive Convection in a Vertical Enclosure With Asymmetrical Boundary Conditions," ASME J. Heat Transfer, **122**, pp. 598–602.
[17] Carslaw, H. S., and Jaeger, J. C., 1959, *Conduction of Heat in Solids*, 2nd ed., Oxford at the Clarendon Press, p. 284.
[18] Eckert, E. R. G., and Drake, R. M., 1972, *Analysis of Heat and Mass Transfer*, McGraw-Hill Book Company, pp. 718–719.
[19] Patankar, S. V., 1980, *Numerical Heat Transfer and Fluid Flow*, Hemisphere, New York.
[20] *Hand Book of Air Conditioning System Design*, Part 4, 1965, McGraw-Hill Book Company, pp. 32–35.
[21] Moelwyn-Hughes, E. A., 1947, *The Kinetics of Reaction in Solution*, 2nd ed., Oxford at the Clarendon Press, pp. 367–377.
[22] McAdams, W. H., 1954, *Heat Transmission*, 3rd ed., McGraw-Hill Book Company.
[23] Han, H., and Kuehn, T. H., 1991, "Double-Diffusive Natural Convection in a Vertical Rectangular Enclosure-I. Experimental Study," Int. J. Heat Mass Transf., **34**, pp. 449–459.
[24] Han, H., and Kuehn, T. H., 1991, "Double Diffusive Natural Convection in a Vertical Rectangular Enclosure-II. Numerical Study," Int. J. Heat Mass Transf., **34**, pp. 461–471.

Surface Temperature Measurement of Semi-Transparent Ceramics by Long-Wavelength Pyrometry

Frank E. Pfefferkorn
School of Mechanical Engineering,
Purdue University,
West Lafayette, IN 47907-1288

Frank P. Incropera
College of Engineering,
University of Notre Dame,
Notre Dame, IN 46556

Yung C. Shin
School of Mechanical Engineering,
Purdue University,
West Lafayette, IN 47907-1288

A procedure using a long-wavelength pyrometer is developed for the measurement of surface temperatures on materials that are semitransparent at shorter wavelengths, and specific application is made to a dense zirconia ceramic (Mg-PSZ) undergoing laser-assisted machining (LAM). The pyrometer operates in a waveband between 11 and 14 μm, and a detailed description of measurement uncertainties is provided. The largest uncertainties relate to knowledge of the surface emissivity and the large temperature gradients generated by the LAM process. Repeatability of the measurements is demonstrated, and a parametric study of three LAM parameters reveals expected trends.
[DOI: 10.1115/1.1527906]

Keywords: Ceramics, Heat Transfer, Laser, Measurement Techniques

Introduction

Increasingly, long-wavelength pyrometry is being considered for surface temperature measurements in applications of semitransparent materials characterized by large spatial and/or temporal variations. Applications include thermal barrier coatings, ceramic turbine blades, ceramic heat exchangers, and manufacturing processes. One such process involves the laser machining (LM) or laser-assisted machining (LAM) of ceramics. Laser machining uses intense heating to melt, evaporate, or sublimate material [1–3]. Laser-assisted machining increases material removal rates by utilizing a localized heat source to elevate the workpiece temperature prior to material removal with a traditional cutting tool [4–6]. At high temperatures the yield strength of ceramics can decrease below the fracture strength, changing the material deformation behavior from brittle to ductile [7] and enabling the use of a single point cutting tool to remove material at rates approaching those of metal cutting. For successful LM or LAM a narrow temperature range must be maintained at a specified location and time. This range is bounded at the low end by the minimum temperature required to change the mechanical behavior (LAM) or the phase (LM) of the ceramic and at the high end by temperatures and temperature gradients that cause thermal damage to unmachined portions of the workpiece.

Accurate temperature measurement during LAM and LM is needed to verify thermo-mechanical process models, elucidate physical phenomena, and for subsequent implementation of process control. Subsurface temperatures of material in the deformation zone associated with material removal determine how the material deforms or transforms and subsequently how it is removed. While such temperatures are extremely difficult to measure, they may be inferred by using surface temperature measurements with an appropriate thermo-mechanical model. Because the optimal window of operation may be narrow, accurate measurement of workpiece surface temperatures is required for successful control of the machining processes.

Pyrometry is well suited for measuring surface temperatures of a workpiece undergoing LM or LAM, and the approach of this study was adopted from an extensive assessment of alternative measurement techniques [8]. In fact, for LAM, rotation of the workpiece, a hostile machining environment and fast transients necessitate use of a pyrometer for surface temperature measurements.

A laser pyrometer was successfully used to measure surface temperature and emissivity in-situ during LAM of silicon nitride [9]. However, use of this pyrometer is restricted to opaque surfaces and is inappropriate for materials that are semitransparent in the spectral region of the measurements. Several ceramics, such as partially-stabilized zirconia (PSZ), mullite, and alumina are semitransparent at wavelengths up to 8 μm, and if pyrometry is to be used for surface temperature measurements, operation must be at longer wavelengths. The objective of this study is to develop a procedure which facilitates the use of long-wavelength pyrometry ($11<\lambda<14\ \mu$m) to measure the surface temperature of semitransparent ceramics, with special consideration given to a PSZ workpiece undergoing LAM.

Radiative Properties of Semitransparent Ceramics

The suitability of certain wavelengths for pyrometric surface temperature measurements is based on an effective measurement depth, $d_e=\kappa_\lambda^{-1}$, which corresponds to an optical depth of unity and the distance from the surface at which 63.2 percent of the transmitted component of the incident radiation is absorbed according to Beer's law [10,11]. A pyrometer targeted at the surface of a workpiece will collect radiation emitted by the volume of material corresponding to the area of the spot and the depth d_e, which should be small to reduce the effect of temperature variations associated with local temperature gradients. Soda lime silica glasses, for example, are generally considered opaque at wavelengths longer than 5 μm, at which $d_e=133\ \mu$m, and have an absorption peak for wavelengths near 10 μm with a large absorption coefficient ($\kappa_\lambda=968\ \text{mm}^{-1}$) at the CO_2 laser wavelength (10.6 μm) [12]. In the region immediately beyond this absorption peak ($\lambda>10\ \mu$m), the effective measurement depth does not exceed $d_e=4\ \mu$m, making this region well suited for pyrometry [12].

The upper extent of the transmission range for pure, monocrystalline alumina is 5 μm [13], and radiative property measurements of a commercial alumina (99 wt.% $Al_2O_3+SiO_2$, CaO, MgO; polycrystalline; 1.8 percent porosity) [14] confirm an increase in the extinction coefficient for $\lambda>5\ \mu$m. However, for pyrometric

Contributed by the Heat Transfer Division for publication in the JOURNAL OF HEAT TRANSFER. Manuscript received by the Heat Transfer Division February 5, 2002; revision received September 9, 2002. Associate Editor: S. T. Thynell.

Table 1 Comparison of zirconia ceramics used in radiative property studies

	Makino et al. [14]	Tsukuma [17]	Wahiduzzaman and Morel [18]	PSZ used in this study
Composition	ZrO_2>85 wt. %, Y_2O_3, SiO_2, Al_2O_3	82.8 mol% ZrO_2, 10 mol% TiO_2, 7.2 mol% Y_2O_3	76 % ZrO_2, 24 % ceria	ZrO_2, 4 mol% MgO
Processing	sintered, 1600–1700°C, 1 atm, air	sintered, 1630°C, 7 h, O_2 then HIP, 1500°C, 100 MPa, 0.5 h, Ar	plasma sprayed	iso-pressed, sintered at 1 atm
Grain Size	0.1–3.0 μm	100–200 μm	-	50 μm
Porosity	-	-	-	2.7% closed
Phase Content	-	cubic	-	4.2 mol% monoclinic
Waveband Studied	0.5–33 μm	0.3–10 μm	⩽20 μm	0.5–33 μm (literature review)
Semi-transparent	$\lambda<5$ μm	$\lambda<8$ μm	$\lambda<5$ μm	$\lambda<8$ μm (assumed)
Opaque	$\lambda>5$ μm	$\lambda>8$ μm	$\lambda>5$ μm	$\lambda>8$ μm (assumed)

measurements, alumina should only be considered opaque for $\lambda > 8$ μm, at which $d_e = 40$ μm. Since transmittance data for mullite indicate a sharp decrease at $\lambda \approx 5$ μm [15,16], it is reasonable to assume that its spectral absorptivity increases with wavelength beyond 5 μm, such that an acceptably small value of d_e exists for $\lambda > 10$ μm.

Makino et al. [14] determined that fully-dense, sintered zirconia exhibits strong absorption above 5 μm, where its optical properties are represented by the complex index of refraction, $n_{c,\lambda} = n_\lambda - ik_\lambda$, and k_λ is the extinction coefficient. Makino et al. found that, for $\lambda < 5$ μm, scattering (at grain boundaries, inclusions, or pores) is more significant than absorption and that, above 7 μm, scattering vanishes as the size of the scattering centers decreases relative to λ. Hence, absorption of radiation at longer wavelengths ($\lambda > 7$ μm) depends more on material composition and crystal structure than on physical characteristics such as grain size, porosity, and glassy phase content, which vary significantly with the manner in which the ceramic is processed.

Tsukuma [17] considered a 0.73 mm thick, titania-yttria-zirconia ceramic that was processed by isostatic pressing and had a spectral transmissivity greater than 60 percent in the visible spectrum, but was opaque above 8μm. Wahiduzzaman and Morel [18] considered 2.5-mm thick thermal-barrier-coatings of plasma-sprayed zirconia and found them to be "highly opaque" beyond 5 μm.

The foregoing results suggest that, while variations in chemical composition and processing can significantly affect the radiative properties of zirconia in the visible and near-infrared spectra, all of the materials become opaque above some cutoff wavelength. The results for zirconia ceramics are summarized in Table 1, from which it is concluded that the optical properties do not vary significantly for $\lambda > 8$ μm. Accordingly, the index of refraction, n_λ, and the extinction coefficient, k_λ, (Fig. 1) measured by Makino et al. [14] for $\lambda > 8$ μm may be assumed to apply to the PSZ of this study (Table 1).

Using the extinction coefficient, k_λ, determined by Makino et al. [14], an absorption coefficient, $\kappa_\lambda = 4\pi k_\lambda / \lambda$, may be calculated, which, in turn, can be used to determine the effective measurement depth, d_e. Variation of d_e with wavelength for the spectrum associated with the long-wavelength pyrometer of this study is shown in Fig. 2. The results indicate that a pyrometer operating in the range $11 < \lambda < 14$ μm will largely receive radiation from a surface layer whose thickness is less than approximately 15 μm.

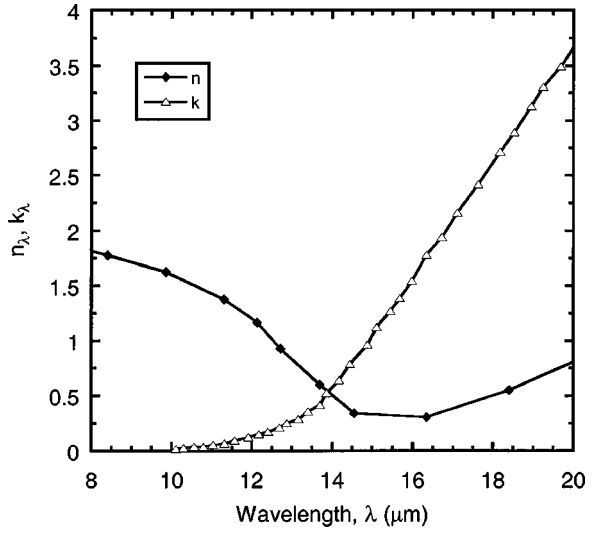

Fig. 1 Spectral complex index of refraction for PSZ [14]

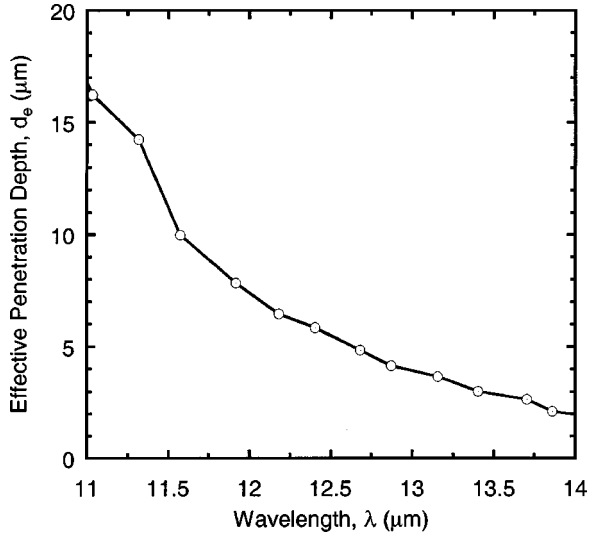

Fig. 2 Effective measurement depth, d_e, at which 63.2 percent of spectral radiation is absorbed in PSZ

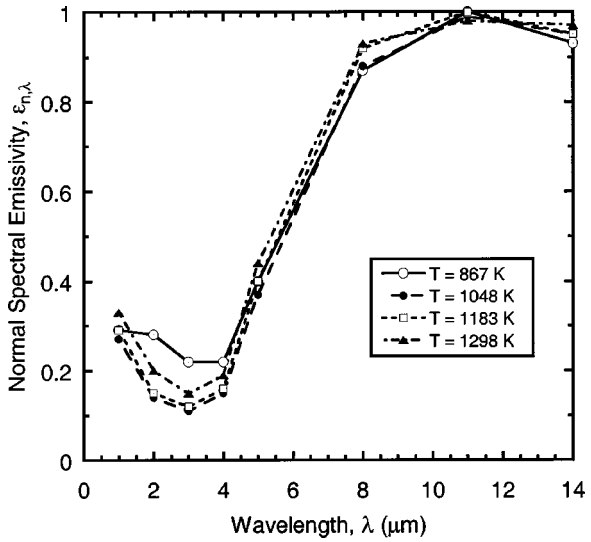

Fig. 3 Normal spectral emissivity of as-sintered PSZ ($1<\lambda<15$ μm) [19]

To use a long-wavelength pyrometer for surface temperature measurement, the surface emissivity must be known. From Fig. 3 it is seen that the normal spectral emissivity of PSZ is approximately 0.95 for $11<\lambda<14$ μm [19]. The lack of data for contrasting as-sintered, machined, and polished surfaces requires the use of this emissivity for all experimental surface conditions. However, since the primary contribution to the uncertainty in the measured temperature is due to the emissivity, it would be beneficial to measure the actual emissivity of a sample to minimize the uncertainty in the surface temperature.

It is important to remember that, since the objective of pyrometry is to infer the surface temperature from emitted radiation, radiation emitted from a volume below the surface and detected by the measurement device can affect the result. Therefore, a target may be considered opaque if the effective measurement depth, d_e, is small enough to yield negligible temperature variations due to temperature gradients normal to the surface. However, the requirement is less stringent for a laser-heated surface, since temperatures decrease sharply with depth and any radiation detected from beneath the surface will not strongly affect the measurement. In contrast, when the laser is turned off, the surface cools rapidly and the maximum temperature is located below the surface. The measured temperature will then be affected by radiation emitted from the hot region beneath the surface, if d_e is not smaller than the distance of the hot region from the surface, and will exceed the actual surface temperature.

Experimental Procedures

Long-Wavelength Pyrometer. The long-wavelength pyrometer of this study is a special design developed to the authors' specifications by the Williamson Corporation.[1] It is a "single wavelength" sensor using a thermopile detector to measure radiation between 11 and 14 μm. The pyrometer can measure temperatures from 500 to 1500°C, collecting 93 percent of the detected energy from a 2 mm diameter target at an optimum focal distance of 162 mm. A small glass window centered on a germanium lens allows passage of a visible laser beam through the optics to align the target on the workpiece surface. The lens is shrouded by a protective sleeve with an aperture that does not obstruct the pyrometer's field of view (Fig. 4). Compressed air is introduced into the protective sleeve, and a nozzle directs an air jet across the aperture. Because the focal length of the pyrometer is only 162 mm and there is a protective aperture with an air screen halfway between the lens and the surface, there is little opportunity for machining debris to absorb or scatter radiation within the field of view.

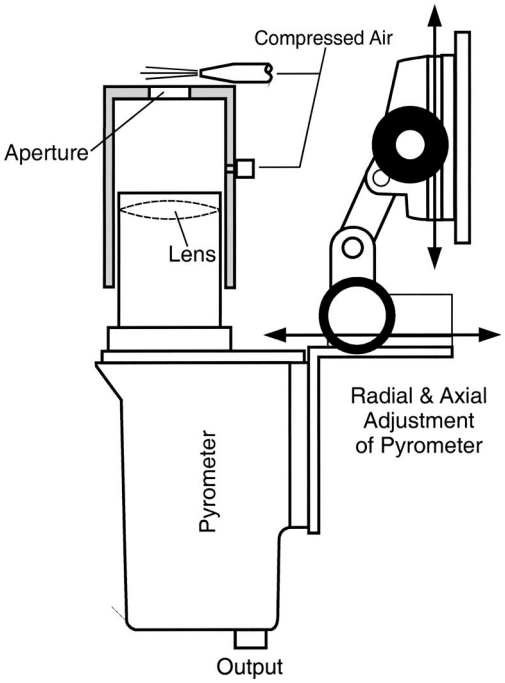

Fig. 4 Schematic of long-wavelength pyrometer with protective aperture, air screen, and positioning stage

The pyrometer was designed with a waveband between 11 and 14 μm to avoid the CO_2 laser wavelength (10.6 μm), to operate in a spectral range where PSZ is opaque ($\lambda>8$ μm), to have a small target size, and to achieve an acceptable signal-to-noise ratio. The requirements of a small target size and operation at long wavelengths result in a low infrared signal. To achieve an acceptable signal-to-noise ratio and temperature resolution, a broad waveband is needed to provide a sufficiently strong infrared signal and the amplification circuit has a low-pass cut-off frequency of 3 Hz [11,20]. The desired waveband is achieved by superimposing two wide band-pass filters, each with 80 percent transmittance between half power wavelengths of 8.047–13.708 μm and 11.391–15.368 μm. The germanium lens also filters energy and has a spectrally dependent transmissivity curve that influences the effective wavelength of the device. The protective sleeve (Fig. 4) shields the lens from machining debris and acts as a radiation shield to protect the pyrometer from thermal loading.

The optics (germanium) used for focusing energy in the 11–14 μm waveband limit the smallest achievable target size to a diameter of approximately 2 mm, and the energy detected by the pyrometer can be partitioned into concentric rings. The center circle of radius $r=0.52$ mm provides 68.5 percent of the signal. Another 16.5 percent of the detected energy originates from the ring between $r=0.52$ mm and $r=0.66$ mm, and approximately 8.3 percent of the signal originates from the ring between 0.66 mm and 1.015 mm. Because the target imaged by the pyrometer during laser-assisted machining (LAM) is characterized by large axial temperature gradients on the surface of the workpiece, the temperature reported by the pyrometer is a weighted average of values in the field of view.

Assuming a uniform surface temperature and emissivity in the target spot, the output of the radiation detector, S, is

$$S=R_\lambda Q=R_\lambda \varepsilon_\lambda I_{\lambda,b}(\lambda,T)A_t\omega\Delta\lambda\,\tau_{\lambda,t} \tag{1}$$

where R_λ is the spectral responsivity of the detector, Q is the radiant energy reaching the detector, ε_λ is the spectral emissivity

[1]Williamson Temperature Sensor TEMPMATIC 4900S-C-22-FOV8″/200-SWL-LA-NSO177-10C-110V, Williamson Corp., Concord, MA.

at the effective wavelength, $I_{\lambda,b}$ is the Planck function evaluated at the surface temperature and effective wavelength, A_t is the target area with the pyrometer positioned perpendicular to the surface, ω is the solid angle formed by the lens and the target, $\Delta\lambda$ is the bandwidth, and $\tau_{\lambda,t}$ is the total transmissivity, which accounts for signal attenuation by the optical elements between the target and the detector. The spectral responsivity, R_λ, describes the sensitivity of the detector to energy at different wavelengths and is defined as the ratio of the voltage output to the incident radiation. Substituting the Planck distribution

$$I_\lambda(\lambda,\varepsilon,T)=\frac{\varepsilon_\lambda C_1}{\lambda^5[\exp(C_2/\lambda T)-1]} \tag{2}$$

into Eq. (1) and solving for the unknown temperature, it follows that

$$T=\frac{C_2}{\lambda\cdot\ln\left[\dfrac{C_1\cdot R_\lambda\cdot A_t\cdot\omega\cdot\Delta\lambda\cdot\tau_{\lambda,t}}{\lambda^5}\cdot\dfrac{\varepsilon_\lambda}{S}+1\right]} \tag{3}$$

Equation (3) uses the detector output, S, and the emissivity, ε_λ, to determine the true surface temperature. With $\varepsilon_\lambda=1$, Eq. (3) may be expressed as

$$T_b=\frac{C_{c,2}}{\ln(C_{c,1}/S+1)} \tag{4}$$

where $C_{c,1}$ and $C_{c,2}$ are calibration constants that combine terms in Eq. (3). The constants in Eq. (4) can be determined with a black body calibration source, where any uncertainty in the source emissivity and temperature can affect the uncertainty in the calibration constants. The pyrometer was calibrated by the manufacturer, and this uncertainty is embedded in the manufacturer's documented accuracy.

Because the pyrometer uses a wide band-pass (11–14 μm), an effective wavelength, λ_e, is used to characterize the surface emissivity of the band and thus determine the surface temperature from Eq. 4 [11]. The effective wavelength may be obtained from an expression of the form

$$\varepsilon_\lambda(\lambda_e)E_{gl,b}(\lambda_e,T)=\frac{\displaystyle\int_{11}^{14}\varepsilon_\lambda(\lambda)E_{\lambda,b}(\lambda,T)\tau_{\lambda,t}(\lambda)R_\lambda(\lambda)d\lambda}{\displaystyle\int_{11}^{14}\tau_{\lambda,t}(\lambda)R_\lambda(\lambda)d\lambda} \tag{5}$$

where the total spectral transmissivity is the product of transmissivities for the two filters and the lens, $\tau_{\lambda,t}=\tau_{\lambda,f1}\tau_{\lambda,f2}\tau_{\lambda,1}$. For this analysis it is assumed that the spectral responsivity, R_λ, is independent of all variables except wavelength. Since the pyrometer uses a thermopile detector with a spectrally flat responsivity [11], R_λ cancels out of Eq. (5). Because the blackbody emissive power and the surface emissivity depend on temperature, the effective wavelength is also temperature dependent. An effective wavelength of $\lambda_e=12.388$ μm at 1000°C is obtained iteratively by numerically integrating the right-hand-side of Eq. (5) and applying the secant method. Since the spectral transmissivity of the filters is approximately uniform over the designated waveband, λ_e is influenced only by the spectral transmissivity of the lens, and variations of the spectral emissivity (Fig. 3) and emissive power with wavelength and temperature.

Laser-Assisted Machining. The LAM experiments are conducted using a 1.5 kW (continuous wave) CO_2 laser, whose beam delivery is integrated with a computer numerically controlled (CNC) lathe. The laser optics are attached to the lathe turret that provides translation in the axial and radial directions of the workpiece, and axial translation of the laser optics is synchronized with that of the cutting tool during LAM. The laser power setting is manually controlled and adjusted before each experiment, while all functions of the lathe are controlled by a computer. The CO_2 laser power reaching the workpiece is calibrated with a digital calorimeter[2] for values in the range from 200 to 2200 W.

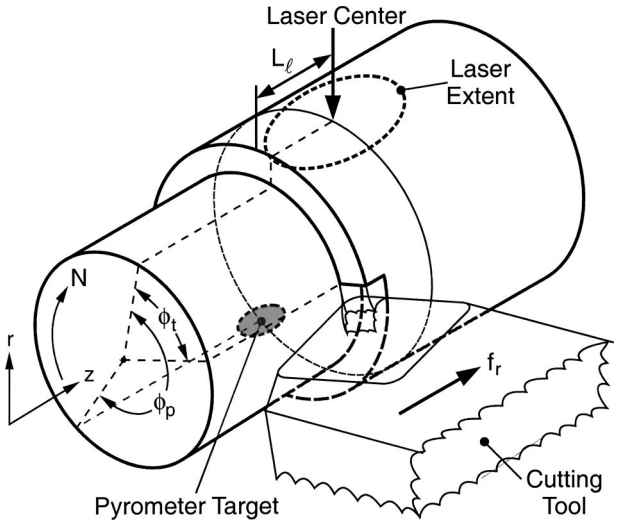

Fig. 5 Schematic of pyrometer location with respect to the workpiece, laser and cutting tool (ϕ_t=55 deg, ϕ_p=220 deg, L_l=1.6 mm, N=800 rpm, f_r=16 mm/min)

The pyrometer is mounted beneath the workpiece on a bracket connected to the axial translation stage of the lathe and moves with the laser beam and cutting tool in the axial (z) direction (Fig. 5), thereby measuring the surface temperature at a fixed distance from the cutting zone and the laser-impingement location. The angles between the pyrometer target and laser center, $\phi_p=212$ deg, the laser center and tool, $\phi_t=55$ deg, and the laser center and vertical, $\phi_L=10$ deg, are fixed. The laser center leads the cutting tool in the axial direction ($L_l=1.6$ mm) to allow enough time for energy to penetrate radially. Data are recorded at 1 kHz by a PC-based data acquisition system, and measured temperatures are based on the arithmetic average of five hundred data points.

A LAM experiment consists of two phases: a preheat phase in which the laser irradiates the end of the rotating workpiece without axial translation of the laser or the cutting tool and a material removal phase in which the laser and cutting tool move axially along the workpiece. The preheat phase allows an acceptable machining temperature to be achieved at the depth-of-cut before material removal is initiated.

Nominal experimental operating conditions correspond to a laser power, $P_l=200$ W, a beam diameter, $D_l=4.0$ mm, a laser-tool lead, $L_l=1.6$ mm, a depth-of-cut, $d=0.5$ mm, a feed rate, $f_r=16$ mm/min, a spindle speed, $N=800$ rpm, and a preheat time, $t_p=(6+1.9)$ s. The first component of t_p is the time during which the laser is stationary and heating the rotating workpiece, while the second component is the duration of axial translation before the cutting tool engages the workpiece. A compressed air jet is concentric with the laser beam and exits the laser nozzle to protect the optics. Material removal is performed with a square polycrystalline cubic boron nitride (PCBN) tipped cutting tool (Kennametal grade KD120, SPGN120308). The as-received Mg-PSZ workpieces have been pre-ground with an average surface roughness of 0.3 μm measured parallel to the axis of symmetry and are 15.0 mm in diameter by 63.8 mm long.

[2]Model 30C Digital Power Probe, Optical Engineering® Inc., Santa Rosa, CA

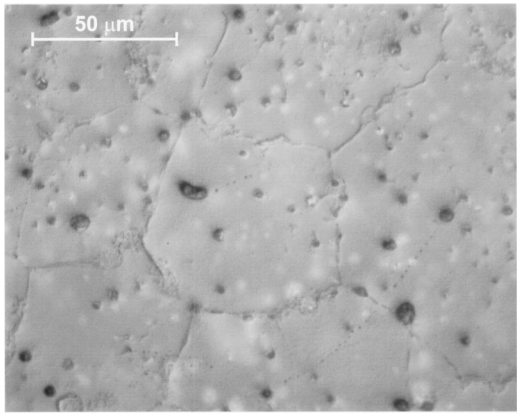

Fig. 6 Optical differential image contrast (DIC) micrograph of polished and etched Mg-PSZ

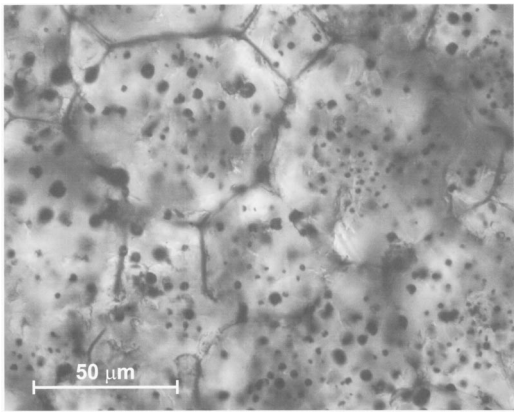

Fig. 7 Transmitted light micrograph of polished Mg-PSZ thin section (30μm thick)

Specific Features of Mg-PSZ. The Mg-PSZ used in this study is milky white in color, has an effective density of $\rho_e = 5770\ \mathrm{kg/m^3}$, and contains 4 mol% MgO. From X-ray diffraction performed on the as-received material, the monoclinic phase content was determined to be 4.2 mol% with the remainder comprised of tetragonal and cubic phases. As shown in Figs. 6 and 7, the samples of this study have closed pores, and the porosity may be quantified by measuring the area ratio of visible pores in optical micrographs. The pore area ratio was measured over a sufficient number of micrographs to insure that the calculated porosity did not change with additional measurements and hence that its value closely approximated the volume porosity. The results from six micrographs of 200× and 500× magnification were averaged to obtain a volume porosity of approximately 4.4 percent.

The optical micrograph of Fig. 6 was obtained by using the Senarmont differential image contrast (DIC) feature of a Zeiss Axiotech on a sample mechanically polished with 1 μm diamond paste and etched in 48 percent HF solution for 5 minutes. Differential image contrast is based on the interference of two slightly offset polarized beams and shows minute elevation differences in a relief-like fashion. The grain size is approximately 50 μm with little grain boundary phase and an abundance of pores, which is typical of commercially available Mg-PSZ ceramics [21,22]. The pores are visible as the dark areas (depressions) in Fig. 6, while the white spots are believed to be caused by pores just below the surface. This premise is based on the assumption that a significant amount of light incident on these locations is totally reflected. Partially-stabilized zirconia has a refractive index of $n=2$ [14], and assuming that a closed pore below the surface is filled with air or another gas ($n\sim1$), the critical angle for total reflection of light incident on the PSZ-pore interface can be determined from the Fresnel Equations. The critical angle for light travel through PSZ and incident on an air pocket is 30 deg. Since the DIC micrograph in Fig. 6 is generated by changing the angle of the light incident on the sample surface, the white spots are likely caused by light reflected from a PSZ-pore interface. Because it is not known at what height the pores in Fig. 6 intersect the surface, it is impossible to quantify the pore size distribution. Another view of the pore size distribution and density is shown in a light transmission micrograph of a polished thin section of 30 μm thickness (Fig. 7). The larger black circles indicate pores that exist throughout the 30 μm thick sample, while the smaller spots may be either pores or tetragonal precipitates in the cubic matrix.

Measurement Uncertainty

Factors that contribute to the total uncertainty in the measured temperature relate to conditions associated with the surface itself, the measurement device, and the environment. The largest sources of experimental uncertainty are incomplete knowledge of the surface emissivity and the coupled influence of the size of the imaged area and the large surface temperature gradients.

The workpiece surface is characterized by large axial temperature gradients, caused by the material's low thermal diffusivity, and small circumferential gradients, due to the high rotational speed and the associated advection of energy. Due to the large axial temperature gradients, the uncertainty in the target position contributes to uncertainty in the recorded temperature. This uncertainty was estimated numerically by predicting a weighted average of the temperature of the target as a function of its displacement from a nominal location that is axially centered on, but 212 degrees from the laser spot [8]. Because circumferential temperature gradients are comparatively small, the uncertainty in the circumferential positioning of the pyrometer target ($\pm$2.24 deg) has a negligible effect on the temperature measurement.

Since, the pyrometer views a 2 mm diameter area containing large axial temperature gradients, an area-weighted average temperature is utilized for the three energy collection regions identified previously. The average is double-weighted by the surface area within a region (e.g., $A_{CS,1\text{-}W1}$) and the percentage of the total energy collected from that region (e.g., W_1, W_2, W_3) and is expressed as

$$T_{\text{average}}=\frac{A_{CS,1-W,1}W_1T_1+A_{CS,2-W,1}W_1T_2+\ \ldots\ +A_{CS,N-W,3}W_3T_N}{A_{CS,1-W,1}W_1+A_{CS,2-W,1}W_1+\ \ldots\ +A_{CS,N-W,3}W_3} \tag{6}$$

The region temperatures are determined from a three-dimensional, unsteady heat transfer model for partially stabilized zirconia (PSZ) undergoing laser-assisted machining (LAM) [8,23], with the diffusion approximation used to model internal radiative transfer for the semitransparent portion of the spectrum ($\lambda>8\ \mu$m) and the workpiece treated as opaque for $\lambda>8\ \mu$m. For the prescribed LAM conditions, predictions of the temperature field yielded a position uncertainty of $\delta T_{\text{pos}}\approx+21/-52°\text{C}$ at T

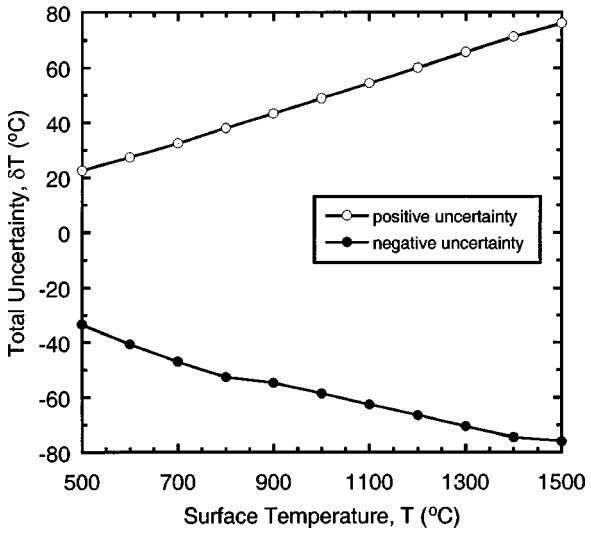

Fig. 8 Total (asymmetric) uncertainty in measured temperature as a function of surface temperature

$=1000°C$ for a ± 0.25 mm uncertainty in the axial location of the target. The difference between the positive and negative uncertainty limits is due to asymmetry of the axial temperature distribution about the center of the target.

The effect of uncertainty in the surface emissivity on the measured temperature may be determined by differentiating the Planck distribution (Eq. 2) with respect to temperature and emissivity and combining the results to obtain

$$\frac{\delta T}{T} = \frac{\delta \varepsilon_\lambda}{\varepsilon_\lambda} \cdot \frac{\lambda T[\exp(C_2/\lambda T)-1]}{C_2 \exp(C_2/\lambda T)} \tag{7}$$

At long wavelengths, such as the effective wavelength of $\lambda_e = 12.4\ \mu$m, the sensitivity of the temperature to uncertainties in the emissivity is approximately proportional to wavelength. From published data for the emissivity (Fig. 3), a conservative estimate of its uncertainty is $\delta\varepsilon_\lambda = +0.03/-0.05$ about $\varepsilon_\lambda = 0.97$. If an uncertainty of $\delta\varepsilon_\lambda/\varepsilon_\lambda = -0.05$ is used in Eq. (7), the uncertainty in temperature is $\delta T_{em} = -26°C$ at $T = 1000°C$. Because the spectral emissivity of PSZ in the pyrometer's waveband is relatively insensitive to wavelength and temperature (Fig. 3), a constant value of δT_{em} is used.

Equation (5) is used to determine the effective wavelength, which in turn is used to determine the emissivity and true surface temperature from the measured signal (Eq. 3). Differentiating Eq. (2) with respect to temperature and wavelength and combining the results, the following expression is obtained for the uncertainty in temperature due to uncertainty in the effective wavelength.

$$\frac{\delta T}{T} = \frac{\delta \lambda_e}{\lambda_e}\left\{1 - 5 \cdot \frac{\lambda_e T}{C_2} \frac{[\exp(C_2/\lambda_e T)-1]}{\exp(C_2/\lambda_e T)}\right\} \tag{8}$$

Uncertainty in the effective wavelength is a function of uncertainties in the spectral dependence of emissivity, transmissivity, and responsivity, as well as surface temperature through its effect on the shape of the black body emissive power (Eq. 5). The resultant uncertainty in the effective wavelength, $\delta\lambda_e = \pm 0.006\ \mu$m at $\lambda_e = 12.388\ \mu$m, contributes an uncertainty in the measured temperature of $\delta T_\lambda = \pm 1.4°C$ at $T = 1000°C$.

The uncertainty in the distance between the lens and the surface is negligible and has no effect on the temperature measurement. The pyrometer was calibrated by the manufacturer, and uncertainties in the calibration constants are embedded in the manufacturer's documented accuracy of 0.75 percent of full scale, or $\delta T_{\text{int}} = 0.0075(1500\text{-}500)°C = 7.5°C$.

Assuming all uncertainties to be independent and random, the total uncertainty in temperature, δT, may be expressed as [24]

$$\delta T = \sqrt{\left(\frac{\partial T}{\partial \varepsilon_\lambda}\delta\varepsilon_\lambda\right)^2 + \left(\frac{\partial T}{\partial z}\delta z\right)^2 + (\delta T_{\text{int}})^2 + \left(\frac{\partial t}{\partial \lambda_e}\delta\lambda_e\right)^2} \tag{9}$$

From the foregoing results for the component uncertainties $(\delta T_{em}; \delta T_{\text{pos}}; \delta T_{\text{int}}; \delta T_\lambda)$, the total uncertainty in the measured surface temperature has been calculated as a function of temperature and the results are shown in Fig. 8. The total uncertainty exceeds the internal accuracy of the pyrometer (as specified by the manufacturer) because the pyrometer is not used in an ideal or fully characterized environment. The total uncertainty could be significantly reduced by reducing uncertainties in the emissivity and target position, and by reducing the size of the pyrometer target.

Results

Multiple experiments were performed for the prescribed (nominal) operating conditions to ascertain repeatability of the temperature measurements, and the results, as shown in Fig. 9, are within a 95 percent confidence interval. The axial and circumferential positions of the cutting tool, laser spot, and pyrometer target are all fixed with respect to each other by physical stops or shims. The laser power is calibrated before each series of tests and is adjusted with an accuracy of ± 2 W of the reading. As a CNC part program is used to control the tool movement, spindle speed, preheat time, and laser shutter, it is unlikely that any inaccuracy in the timing actions or rate of movement will have a measurable effect on the process. The most probable contributions to the variations among the data sets are variations in the workpiece properties and/or forced convection cooling by the impinging air jet from the laser nozzle. Although a constant emissivity is used by the pyrometer to determine the surface temperature (Fig. 3), the emissivity data were collected under quasi-equilibrium conditions involving slow heating and cooling cycles in controlled atmospheres. In contrast, the surface of the workpiece is undergoing dynamic heating at high rates, which may induce variations in the emissivity that have been shown to cause significant variations in the measured temperature. Although small variations in the chemical composition of zirconia ceramics can alter their radiation properties, the properties are weakly dependent on chemical composition or microstructure for wavelengths greater than approximately 8 μm [14]. However, radiation properties can vary significantly with composition at near infrared wavelengths [14,17,18], where the majority of energy transferred by internal radiation would be

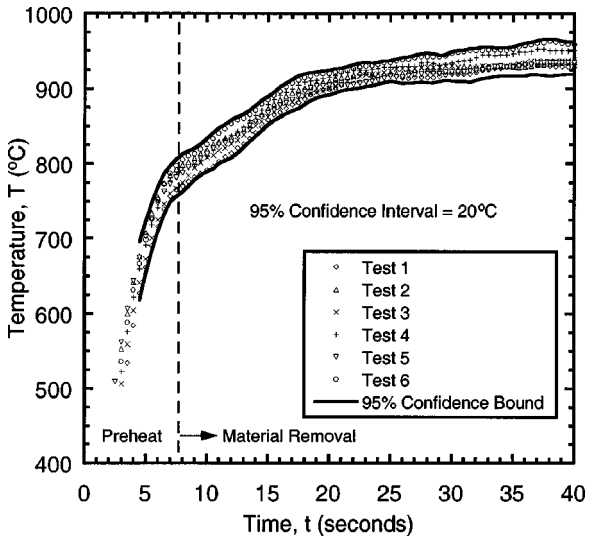

Fig. 9 Repeatability of surface temperature measurement under nominal operating conditions

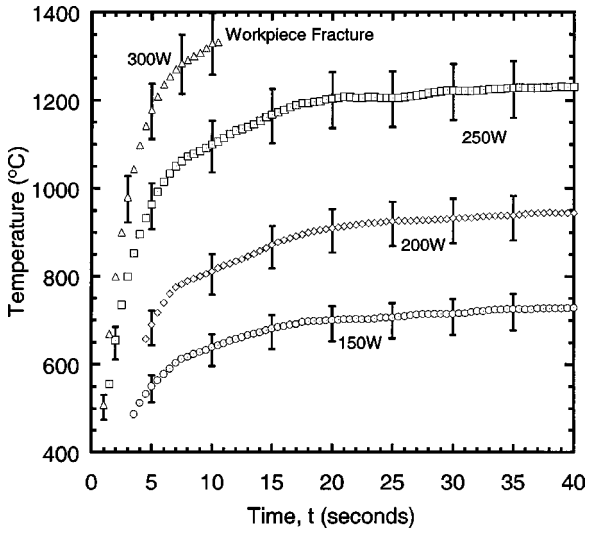

Fig. 10 Effect of laser power on temperature history at the pyrometer location

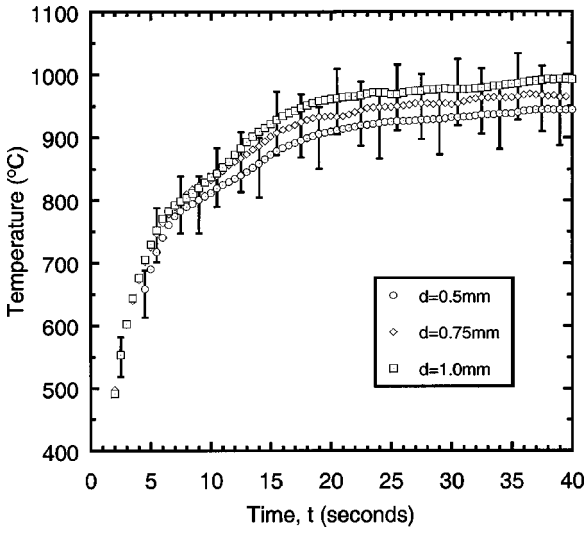

Fig. 12 Effect of depth-of-cut on temperature history

found. Such variations would influence internal heat transfer, thereby changing the workpiece surface temperature.

To determine a confidence interval for temperature measurements during LAM, the standard deviation, σ_x, for six temperature histories (during nominal operating conditions) was determined at each discrete time. If the scatter of the data about the average temperature at each time is random, it can be said with 95 percent confidence that a measurement will fall within a band $\pm 2\sigma_x = \pm 20°C$. The 95 percent confidence interval is shown by the solid lines in Fig. 9 and represents the precision of the temperature measurement. The scatter in the data may be caused by slight variations in measurement procedures and/or other experimental conditions such as variations in material properties. However, as the 95 percent confidence interval lies within the total measurement uncertainty (Fig. 8), the source of the scatter cannot be determined and it is not statistically significant.

Previous investigations of LAM for silicon nitride and mullite ceramics have shown the laser power, P_l, feed rate, f_r, and depth-of-cut, d, to have the most significant influence on temperature [5,6,9,25,26]. The results of varying these parameters for PSZ are shown in Figs. 10 through 12, respectively.

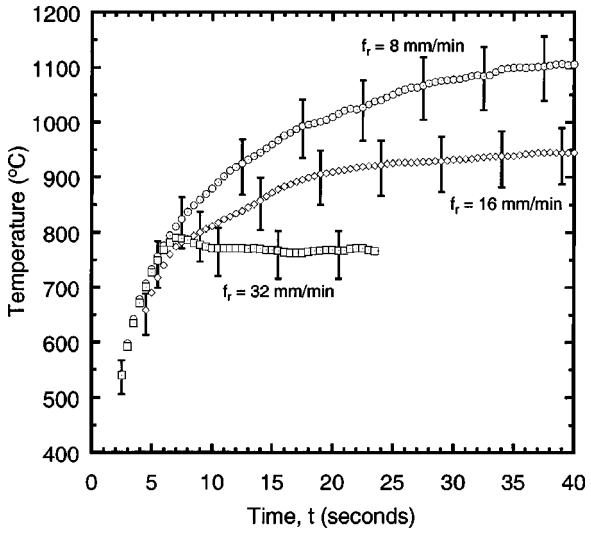

Fig. 11 Effect of feed rate on temperature history

Figure 10 shows the effect of laser power on the surface temperature at the pyrometer's measurement location (Fig. 5). The energy deposited in the workpiece increases with laser power, and there is almost a linear relationship between the power and the temperature achieved 20 seconds into the process, after which quasi-steady conditions are achieved. At 300 W the workpiece fractured at a location ahead of the cutting zone due to thermally induced stresses resulting from large temperature gradients. Hence, PSZ has an upper limit of heating which is dictated by temperature gradients and resulting thermal stresses.

The feed rate controls the amount of energy deposited per unit distance traversed by the laser, and its effect is shown in Fig. 11. The different durations are due to traversal of a workpiece of fixed axial length (10 mm) at different feed rates. The amount of energy deposited per distance and time decreases with increasing feed rate, and quasi-steady temperatures at the end of the cut for feed rates of 8 and 32 mm/min are approximately 1120°C and 760°C, respectively. The three tests in Fig. 11 were performed at a constant laser power of 200 W, beam diameter of 4 mm, and laser-tool lead of 1.6 mm. In actual machining, it is not desirable to increase the feed rate without also increasing the laser power to achieve a desired machining temperature. However, as already demonstrated there are limits to increasing the laser power due to an attendant increase in temperature gradients and the potential for thermal fracture of the workpiece.

Increasing the depth-of-cut d is an important means of achieving a higher material removal rate and therefore an important parameter in the LAM process. Figure 12 shows the effect of d, with the smallest value, $d = 0.5$ mm, corresponding to the nominal condition. The data indicate an increase in the measured temperature with increasing depth-of-cut, but the uncertainty exceeds differences in the data, thereby indicating statistical equivalence of the results. Therefore, any definitive conclusion concerning the effect of depth-of-cut on the temperature field is dependent on reducing the uncertainty in the temperature measurement.

Conclusions

Dense zirconia ceramics are to varying degrees semitransparent below approximately 8 μm, and radiative properties in this waveband depend strongly on composition, processing, and microstructure. However, zirconia ceramics, as well as alumina, mullite, and silica glasses, have large extinction coefficients above approxi-

mately 8 μm, where they are essentially opaque. In principle, a pyrometer operating in this waveband may therefore be used to measure surface temperatures.

The objective of this study has been to develop and evaluate a pyrometric measurement technique for semitransparent ceramics at high temperatures, with special attention given to the wavelength interval from 11 to 14 μm and to an application involving laser-assisted machining (LAM) of fully-dense Mg-PSZ. The long wavelengths associated with the interval are dictated by the need to avoid the wavelength associated with CO_2 laser emission (10.6 μm), as well as by the need to insure a spectral region where PSZ is opaque. The long-wavelength pyrometer considered in this study has been shown to be sensitive to uncertainties in surface emissivity and geometrical positioning, which manifests the influence of large temperature gradients within the target spot. The total uncertainty associated with these effects ranges from $-33/+22$°C at a surface temperature of 500°C to $-59/+49$°C at 1000°C. Temperature measurements made in LAM of Mg-PSZ have been shown to be repeatable with a 95 percent confidence interval and well within the total measurement uncertainty. A parametric study of the effects of laser power, feed rate, and depth-of-cut show expected trends.

It is concluded that a long-wavelength pyrometer can be used to accurately measure the surface temperature of dense zirconia ceramics, as well as other semitransparent ceramics, if the surface emissivity may be accurately determined and optical resolution provides a surface area small enough to encompass small temperature variations.

Acknowledgments

Support of this work by the National Science Foundation under Grant No. 9802047-CTS and 0115172-DMI, the Purdue Research Foundation, and the School of Mechanical Engineering at Purdue University through the Laura Winkelman and Ingersoll-Rand fellowships, is gratefully acknowledged.

Nomenclature

A_t = target area [m^2]
C_1 = first radiation constant [$=2hc_o^2=1.191\times10^8$ W·μm^4·m^{-2}]
C_2 = second radiation constant [$=hc_o/k=1.439\times10^4$ μm·K]
c_o = speed of light in vacuum [$=2.998\times10^8$ m/s]
D_l = beam diameter [mm]
d = depth-of-cut [mm]
d_e = effective measurement depth [m]
$E_{\lambda,b}$ = black body emissive power [W·m^{-2}·μm^{-1}]
f_r = feed rate [mm/min]
h = universal Planck constant [$=6.6256\times10^{-34}$ J·s]
I_λ = radiation intensity [W·m^{-2}·sr^{-1}·μm^{-1}]
k = extinction coefficient, and universal Boltzmann constant [$=1.3805\times10^{-23}$ J/K]
L_l = laser-tool lead [mm]
N = spindle speed [rpm]
n = refractive index
n_c = complex index of refraction
P_l = laser power [W]
Q = energy incident on detector [W]
R = responsivity [V/W]
r = radius [mm]
S = signal from pyrometer [V]
T = temperature [K]
t_p = preheat time [s]
z = axial direction [m]

Greek Symbols

δx = uncertainty in x [units of x]
ε = emissivity
κ = absorption coefficient [m^{-1}]
λ = wavelength in vacuum [μm]
ρ = density [kg·m^{-3}]
σ_x = standard deviation
τ = transmissivity [m^{-1}]
ϕ_L = laser angle to vertical [deg]
ϕ_p = laser-pyrometer angle [deg]
ϕ_t = laser-tool angle [deg]
ω = solid angle [sr]

Subscripts

b = black body
e = effective
t = total
λ = spectral

References

[1] Solomah, A. G., 1993, "Laser Machining of Silicon Nitride Ceramics," in *International Conference on Machining of Advanced Materials*, S. Jahanmir, ed., Gaithersburg, MD, NIST special publication 847, pp. 543–547.
[2] Morita, N., 1993, "Crack-Free Processing of Hot-Pressed Silicon Nitride Ceramics Using Pulsed YAG Laser," in *International Conference on Machining of Advanced Materials*, S. Jahanmir, ed., Gaithersburg, MD, NIST Special Publication 847, pp. 517–524.
[3] Hügel, H., Wiedmaier, M., and Rudlaff, T., 1995, "Laser Processing Integrated into Machine Tools—Design, Application, Economy," Opt. Quantum Electron., **27**(12), pp. 1149–1164.
[4] König, W., and Zaboklicki, A. K., 1993, "Laser-Assisted Hot Machining of Ceramics and Composite Materials," in *International Conference on Machining of Advanced Materials*, S. Jahanmir, ed., Gaithersburg, MD, NIST Special Publication 847, pp. 455–463.
[5] Lei, S., Shin, Y. C., and Incropera, F. P., 2001, "Experimental Investigation of Thermo-Mechanical Characteristics in Laser Assisted Machining of Silicon Nitride Ceramics," ASME J. Manuf. Sci. Eng., **123**, pp. 639–646.
[6] Rozzi, J. C., Pfefferkorn, F. E., Shin, Y. C., and Incropera, F. P., 2000, "Experimental Evaluation of the Laser Assisted Machining of Silicon Nitride Ceramics," ASME J. Manuf. Sci. Eng., **122**(4), pp. 666–670.
[7] Lei, S., Shin, Y., and Incropera, F., 2000, "Deformation Mechanisms and Constitutive Modeling for Silicon Nitride Undergoing Laser-Assisted Machining," Int. J. Mach. Tools Manuf., **40**(15), pp. 2213–2233.
[8] Pfefferkorn, F. E., 2002, "Laser-Assisted Machining of Zirconia Ceramics," Ph.D. thesis, Purdue University, West Lafayette, IN.
[9] Pfefferkorn, F. E., Rozzi, J. C., Incropera, F. P., and Shin, Y. C., 1997, "Surface Temperature Measurement in Laser-Assisted Machining Processes," Exp. Heat Transfer, **10**(4), pp. 291–313.
[10] von Allmen, M., and Blatter, A., 1995, *Laser-Beam Interactions with Materials: Physical Principles and Applications*, 2nd ed., Springer, Berlin.
[11] DeWitt, D. P., and Nutter, G. D., 1988, eds., *Theory and Practice of Radiation Thermometry*, J. Wiley & Sons, New York, p. 1138.
[12] Rubin, M., 1985, "Optical Properties of Soda-Lime Silica Glasses," Sol. Energy Mater., **12**, pp. 275–288.
[13] Smakula, A., 1962, "Synthetic Crystals and Polarizing Materials," Opt. Acta, **9**, pp. 205–222.
[14] Makino, T., Kunitomo, T., Sakai, I., and Kinoshita, H., 1984, "Thermal Radiation Properties of Ceramic Materials," Heat Transfer-Jpn. Res., **13**(4), pp. 33–50.
[15] Prochazka, S., and Klug, F. J., 1983, "Infrared-Transparent Mullite Ceramics," J. Am. Ceram. Soc., **66**, pp. 874–880.
[16] Aksay, I. A., Dabbs, D. M., and Sarikaya, M., 1991, "Mullite for Structural, Electronic, and Optical Applications," J. Am. Ceram. Soc., **74**, pp. 2243–2358.
[17] Tsukuma, K., 1986, "Transparent Titania-Yttria-Zirconia Ceramics," J. Mater. Sci. Lett., **5**, pp. 1143–1144.
[18] Wahiduzzaman, S., and Morel, T., 1989, "Modeling of the Effect of Translucence of Engineering Ceramics on Heat Transfer in Diesel Engines," ASME Paper 89-HT-1,
[19] Touloukian, Y. S., and DeWitt, D. P., 1972, *Thermal Radiative Properties of Nonmetallic Solids*, Plenum Publishing, New York.
[20] Larrick, T. F., 1999, Williamson Corporation, personal communication.
[21] Standard, O. C., and Sorell, C. C., 1998, "Densification of Zirconia—Conventional Methods," Kvant. Elektron. (Moscow), **153–154**, pp. 251–300.
[22] Chaim, R., Heuer, A. H., and Aronov, V., 1990, "Surface Microstructure Changes on Laser Treatment of MgO-Partially-Stabilized Zirconia," J. Am. Ceram. Soc., **73**(6), pp. 1519–23.
[23] Pfefferkorn, F. E., Incropera, F. P., and Shin, Y. C., 1999, "Transient, Three-Dimensional Heat Transfer Model for Partially Stabilized Zirconia Undergoing

Laser-Assisted Machining,'' in *ASME International Mechanical Engineering Congress and Exposition*, Nashville, TN, HTD-Vol. 364-3, pp. 197–209.
[24] Taylor, J. R., 1997, An *Introduction to Error Analysis: The Study of Uncertainties in Physical Measurements*, University Science Books, Sausalito, CA.
[25] Rozzi, J. C., Incropera, F. P., and Shin, Y. C., 1998, ''Transient Thermal Response of a Rotating Cylindrical Silicon Nitride Workpiece Subjected to a Translating Laser Heat Source: II—Parametric Effects and Assessment of a Simplified Model,'' ASME J. Heat Transfer, **120**(4), pp. 907–915.
[26] Rebro, P. A., Shin, Y. C., and Incropera, F. P., 2001, ''Laser-Assisted Machining of Reaction Sintered Mullite Ceramics,'' in *ASME International Mechanical Engineering Congress and Exposition*, New York, NY, CD#3, MED-23341, ASME, New York.

Backward Monte Carlo Simulations in Radiative Heat Transfer

Michael F. Modest
e-mail: mfm6@psu.edu
Fellow ASME,
Department of Mechanical and Nuclear Engineering,
Penn State University,
University Park, PA 16802

Standard Monte Carlo methods trace photon bundles in a forward direction, and may become extremely inefficient when radiation onto a small spot and/or onto a small direction cone is desired. Backward tracing of photon bundles is known to alleviate this problem if the source of radiation is large, but may also fail if the radiation source is collimated and/or very small. In this paper various implementations of the backward Monte Carlo method are discussed, allowing efficient Monte Carlo simulations for problems with arbitrary radiation sources, including small collimated beams, point sources, etc., in media of arbitrary optical thickness. [DOI: 10.1115/1.1518491]

Keywords: Heat Transfer, Monte Carlo, Radiation, Scattering

Introduction

The ''standard'' Monte Carlo method for radiative heat transfer, as presented in various textbooks and review articles [1–3] is a ''forward'' method, i.e., a photon bundle is emitted and its progress is then followed until it is absorbed or until it leaves the system. The method can easily simulate problems of great complexity and, for the majority of problems where overall knowledge of the radiation field is desired, the method is reasonably efficient. However, if only the radiative intensity hitting a small spot and/or over a small range of solid angles is required, the method can become terribly inefficient. Consider, for example, a small detector (maybe 1 mm × 1 mm in size) with a small field of view (capturing only photons hitting it from within a small cone of solid angles) monitoring the radiation from a large furnace filled with an absorbing, emitting and scattering medium. In a standard Monte Carlo simulation one would emit many photon bundles within the furnace, and would trace the path of each of these photons, even though only a very small fraction will hit the detector. It may take many billion bundles before a statistically meaningful result is achieved—at the same time calculating the intensity field everywhere (and without need): clearly a very wasteful procedure. Obviously, it would be much more desirable if one could just trace those photon bundles that eventually hit the detector.

This idea of a backward tracing solution, sometimes also known as *reverse Monte Carlo* has been applied by several investigators [4–10]. All of these investigations have been somewhat limited in scope, looking at light penetration through nonemitting oceans and atmospheres [4–6], computer graphics [7,8], reflecting boundaries [9], and emitting media [10]. All the aforementioned papers have dealt with large light sources (in volume and/or solid angle range), making a backward simulation straightforward. A number of other methods to overcome the inefficiency of standard Monte Carlo implementations in problems with small sources and/or detector have appeared in the Nuclear Engineering literature, e.g., [11–13].

It is the purpose of the present study to give a comprehensive formulation for backward Monte Carlo simulations in the area of radiative heat transfer, capable of treating emitting, absorbing and anisotropically scattering media, media with diffuse or collimated irradiation (with large or small footprints), media with point or line sources, etc. In addition, the method will be described in terms of standard ray tracing (bundles of fixed energy) as well as using energy partition (bundles attenuated by absorption) [1] (also called ''absorption suppression'' by Walters and Buckius [3]).

Contributed by the Heat Transfer Division for publication in the JOURNAL OF HEAT TRANSFER. Manuscript received by the Heat Transfer Division October 18, 2001; revision received June 10, 2002. Associate Editor: R. Skocypec.

Theoretical Development

Similar to the development of Walters and Buckius [10], we will start with the principle of reciprocity described by Case [14]. Let $I_{\lambda 1}$ and $I_{\lambda 2}$ be two different solutions to the radiative transfer equation for a specific medium,

$$\hat{\mathbf{s}}\cdot\nabla I_{\lambda j}(\mathbf{r},\hat{\mathbf{s}}) = S_{\lambda j}(\mathbf{r},\hat{\mathbf{s}}) - \beta_\lambda(\mathbf{r}) I_{\lambda j}(\mathbf{r},\hat{\mathbf{s}}) + \frac{\sigma_{s\lambda}(\mathbf{r})}{4\pi}\int_{4\pi} I_{\lambda j}(\mathbf{r},\hat{\mathbf{s}}')\Phi_\lambda(\mathbf{r},\hat{\mathbf{s}}',\hat{\mathbf{s}})\,d\Omega', \quad j=1,2, \tag{1}$$

subject to the boundary condition

$$I_{\lambda j}(\mathbf{r}_w,\hat{\mathbf{s}}) = I_{w\lambda j}(\mathbf{r}_w,\hat{\mathbf{s}}), \quad j=1,2, \tag{2}$$

where $\mathbf{r}$ is a vector pointing to a location within the medium, $\hat{\mathbf{s}}$ is a unit direction vector at that point, S is the local radiative source, β is the extinction coefficient, σ_s the scattering coefficient, Φ is the scattering phase function, and Ω denotes solid angle. The principle of reciprocity states that these two solutions are related by the following identity:

$$\int_A\int_{\hat{\mathbf{n}}\cdot\hat{\mathbf{s}}>0} [I_{w\lambda 2}(\mathbf{r}_w,\hat{s})I_{\lambda 1}(\mathbf{r}_w,-\hat{\mathbf{s}}) - I_{w\lambda 1}(\mathbf{r}_w,\hat{\mathbf{s}})I_{\lambda 2}(\mathbf{r}_w,-\hat{\mathbf{s}})](\hat{\mathbf{n}}\cdot\hat{\mathbf{s}})\,\delta\Omega\,dA = \int_V\int_{4\pi}[I_{\lambda 2}(\mathbf{r},-\hat{\mathbf{s}})S_{\lambda 1}(\mathbf{r},\hat{\mathbf{s}}) - I_{\lambda 1}(\mathbf{r},\hat{\mathbf{s}})S_{\lambda 2}(\mathbf{r},-\hat{\mathbf{s}})]\,d\Omega\,dV, \tag{3}$$

where A and V denote integration over enclosure surface area and enclosure volume, respectively, and $\hat{\mathbf{n}}\cdot\hat{\mathbf{s}}>0$ indicates that the integration is over the hemisphere on a point on the surface pointing into the medium.

In the Backward Monte Carlo scheme, the solution to $I_{\lambda 1}(\mathbf{r},\hat{\mathbf{s}})$ [with specified internal source $S_{\lambda 1}(\mathbf{r},\hat{\mathbf{s}})$ and boundary intensity $I_{w\lambda 1}(\mathbf{r}_{\lambda 1},\hat{\mathbf{s}})$] is found from the solution to a much simpler problem $I_{\lambda 2}(\mathbf{r},\hat{\mathbf{s}})$. In particular, if we desire the solution to $I_{\lambda 1}$ at location $\mathbf{r}_i$ (say, a detector at the wall) into direction $-\hat{\mathbf{s}}_i$ (pointing out of the medium *into* the surface), we choose $I_{\lambda 2}$ to be the

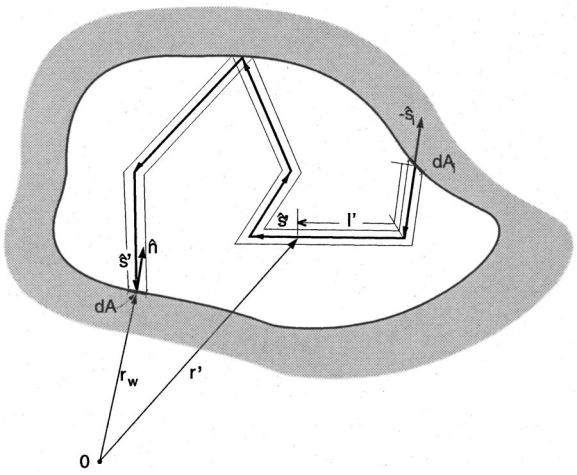

Fig. 1 Typical ray path in a backward Monte Carlo simulation

solution to a collimated point source of unit strength located also at $\mathbf{r}_i$, but pointing into the opposite direction, $+\hat{\mathbf{s}}_i$. Mathematically, this can be expressed as

$$I_{w\lambda 2}(\mathbf{r}_w,\hat{\mathbf{s}})=0, \tag{4a}$$

$$S_{\lambda 2}(\mathbf{r},\hat{\mathbf{s}})=\delta(\mathbf{r}-\mathbf{r}_i)\,\delta(\hat{\mathbf{s}}-\hat{\mathbf{s}}_i), \tag{4b}$$

where the δ are Dirac-delta functions for volume and solid angles, defined as

$$\delta(\mathbf{r}-\mathbf{r}_i)=\begin{cases}0, & \mathbf{r}\neq\mathbf{r}_i,\\ \infty, & \mathbf{r}=\mathbf{r}_i,\end{cases} \tag{5a}$$

$$\int_V \delta(\mathbf{r}-\mathbf{r}_i)\,dV=1, \tag{5b}$$

and similarly for solid angle. If the infinitesimal cross-section of the source, normal to $\hat{\mathbf{s}}_i$, is dA_i, then this results in an $I_{\lambda 2}$ intensity at $\mathbf{r}_i$ of

$$I_{\lambda 2}(\mathbf{r}_i,\hat{\mathbf{s}})=\frac{\delta(\hat{\mathbf{s}}-\hat{\mathbf{s}}_i)}{dA_i}. \tag{6}$$

As the $I_{\lambda 2}$ light beam travels through the absorbing and/or scattering medium, it will be attenuated accordingly.

Substituting Eqs. (4) into Eq. (3) yields the desired intensity as

$$I_{\lambda 1}(\mathbf{r}_i,-\hat{\mathbf{s}}_i)=\int_A\int_{\hat{\mathbf{n}}\cdot\hat{\mathbf{s}}>0} I_{w\lambda 1}(\mathbf{r}_w,\hat{\mathbf{s}})I_{\lambda 2}(\mathbf{r}_w,-\hat{\mathbf{s}})(\hat{\mathbf{n}}\cdot\hat{\mathbf{s}})\,d\Omega\,dA + \int_V\int_{4\pi} S_{\lambda 1}(\mathbf{r},\hat{\mathbf{s}})I_{\lambda 2}(\mathbf{r},-\hat{\mathbf{s}})\,d\Omega\,dV. \tag{7}$$

While the $I_{\lambda 2}$ problem is much simpler to solve than the $I_{\lambda 1}$ problem, it remains quite difficult if the medium scatters radiation, making a Monte Carlo solution desirable. Therefore, we will approximate $I_{\lambda 1}$ as the statistical average over N distinct paths that a photon bundle emitted at $\mathbf{r}_i$ into direction $\hat{\mathbf{s}}_i$ traverses, as schematically shown in Fig. 1, or

$$I_{\lambda 1}(\mathbf{r}_i,-\hat{\mathbf{s}}_i)=\frac{1}{N}\sum_{n=1}^{N} I_{\lambda 1n}(\mathbf{r}_i-\hat{\mathbf{s}}_i), \tag{8}$$

where the solution for each $I_{\lambda 1n}$ is found for its distinct statistical path (with absorption and scattering occurrences chosen exactly as in the forward Monte Carlo method). Along such a zig-zag path of total length l from $\mathbf{r}_i$ to $\mathbf{r}_w$, consisting of several straight segments pointing along a local direction $\hat{\mathbf{s}}'(\mathbf{r}')$, $I_{\lambda 2}$ is nonzero only over an infinitesimal volume along the path, $dV=dA_i l$, and an infinitesimal solid angle centered around the local direction vector $-\hat{\mathbf{s}}=\hat{\mathbf{s}}'(\mathbf{r}')$. At its final destination on the enclosure surface, the beam of cross-section dA_i illuminates an area of only $dA=dA_i/(-\hat{\mathbf{s}}'(\mathbf{r}_w)\cdot\hat{\mathbf{n}})$, so that Eq. (7) simplifies to

$$I_{\lambda 1n}(\mathbf{r}_i-\hat{\mathbf{s}}_i)=I_{w\lambda 1}(\mathbf{r}_w,-\hat{\mathbf{s}}'(\mathbf{r}_w))\exp\left[-\int_0^l \kappa_\lambda(\mathbf{r}')dl'\right] + \int_0^l S_{\lambda 1}(\mathbf{r}',-\hat{\mathbf{s}}'(\mathbf{r}'))\exp\left[-\int_0^{l'}\kappa_\lambda(\mathbf{r}'')dl''\right]dl', \tag{9}$$

where $\int_0^{l'} dl''$ indicates integration along the piecewise straight path, starting at $\mathbf{r}_i$, and κ_λ is the local absorption coefficient. It is seen that $I_{\lambda 1n}(\mathbf{r}_i,-\hat{\mathbf{s}}_i)$ consists of intensity emitted at the wall into the direction of $-\hat{\mathbf{s}}'(\mathbf{r}'_w)$ (i.e., along the path toward $\mathbf{r}_i$), attenuated by absorption along the path, and by emission along the path due to the source $S_{\lambda 1}$, in the direction of $-\hat{\mathbf{s}}'(\mathbf{r}')$ (also along the path toward $\mathbf{r}_i$), and attenuated by absorption along the path, between the point of emission, $\mathbf{r}'$, and $\mathbf{r}_i$. This result is intuitively obvious since it is the same as the symbolic solution to the standard radiative transfer equation (RTE) [1], except that we here have a zig-zag path due to scattering and/or wall reflection events.

If we trace a photon bundle back toward its point of emission, allowing for intermediate reflections from the enclosure wall (as indicated in Fig. 1), then, at the emission point $\mathbf{r}_w$, $I_{w\lambda 1}=\epsilon_\lambda \mathbf{I}_{b\lambda}(\mathbf{r}_w)$, where ϵ_λ is the local surface emittance (assumed to be diffuse here), and $I_{b\lambda}$ is the blackbody intensity or Planck function. And, if the internal source of radiation is due to isotropic emission, then, comparing the standard RTE [1] with Eq. (1) we find $S_{\lambda 1}(\mathbf{r}',-\hat{\mathbf{s}}')=\kappa_\lambda(\mathbf{r}')I_{b\lambda}(\mathbf{r}')$. Thus,

$$I_{\lambda n}(\mathbf{r}_i,-\hat{\mathbf{s}}_i)=\epsilon_\lambda(\mathbf{r}_w)I_{b\lambda}(\mathbf{r}_w)\exp\left[-\int_0^l \kappa_\lambda(\mathbf{r}')dl'\right] + \int_0^l \kappa_\lambda(\mathbf{r}')I_{b\lambda}(\mathbf{r}')\exp\left[-\int_0^{l'}\kappa_\lambda(\mathbf{r}'')dl''\right]dl', \tag{10}$$

where the subscript "l" has been dropped since it is no longer needed. Equation (10) may be solved via a standard Monte Carlo simulation or using the energy partitioning scheme described by Modest [1] and Walters and Buckius [3]. For the standard method scattering lengths l_σ are chosen as well as an absorption length l_κ. The bundle is then traced backward from $\mathbf{r}_i$ unattenuated [i.e., the exponential decay terms in Eq. (10) are dropped], until the total path length equals l_κ or until the emission location $\mathbf{r}_w$ is reached (whichever comes first). Thus,

$$I_{\lambda n}(\mathbf{r}_i,-\hat{\mathbf{s}}_i)=\begin{cases}\displaystyle\int_0^{l_\kappa}\kappa_\lambda(\mathbf{r}')I_{b\lambda}(\mathbf{r}')dl', & l_\kappa<l,\\ \epsilon_\lambda(\mathbf{r}_w)I_{b\lambda}(\mathbf{r}_w)+\displaystyle\int_0^l \kappa_\lambda(\mathbf{r}')I_{b\lambda}(\mathbf{r}')dl', & l_\kappa\geq l\end{cases}. \tag{11}$$

If energy partitioning is used only scattering lengths are chosen and $I_{\lambda n}$ is found directly from Eq. (10).

Radiative Fluxes. If radiative flux onto a surface at location $\mathbf{r}_i$ over a finite range of solid angles is desired, the flux needs to be computed using the statistical data obtained for $I_{\lambda n}(\mathbf{r}_i,-\hat{\mathbf{s}}_i)$. For example, for a detector located at $\mathbf{r}_i$ with opening angle $\theta_{\max}$ one obtains

$$q_{\text{det}} = \int_0^{2\pi} \int_0^{\theta_{\max}} \epsilon'_\lambda(\theta,\psi) I_{\lambda \text{in}}(\theta,\psi) \cos\theta \sin\theta d\theta d\psi$$

$$= \frac{1}{2} \int_0^{2\pi} \int_{\cos^2\theta_{\max}}^{1} \epsilon'_\lambda(\theta,\psi) I_{\lambda,\text{in}}(\theta,\psi) d(\cos^2\theta) d\psi$$

$$\simeq \pi(1-\cos^2\theta_{\max}) \sum_{n=1}^{N} \epsilon'_\lambda(\hat{\mathbf{s}}_n) I_{\lambda n}(-\hat{\mathbf{s}}_n), \tag{12}$$

where the directions $\hat{\mathbf{s}}_n$ need to be picked uniformly from the interval $0 \leq \psi \leq 2\pi$, $\cos^2\theta_{\max} \leq \cos^2\theta \leq 1$. The azimuthal angle ψ_n is found in standard fashion from $\psi_n = 2\pi R_\psi$, while θ_n is found from

$$R_\theta = \frac{\int_{\cos^2\theta_n}^{1} d\zeta}{\int_{\cos^2\theta_{\max}}^{1} d\zeta} = \frac{1-\cos^2\theta_n}{1-\cos^2\theta_{\max}} = \frac{\sin^2\theta_n}{\sin^2\theta_{\max}},$$

$$\text{or} \quad \theta_n = \sin^{-1}(\sqrt{R_\theta} \sin\theta_{\max}), \tag{13}$$

where R_θ and R_ψ are random numbers picked uniformly from $0 \leq R \leq 1$. If the detector is of finite dimension, points distributed across the surface are chosen like in a forward Monte Carlo simulation.

Collimated Irradiation. Backward Monte Carlo is extremely efficient if radiative fluxes onto a small surface and/or over a small solid angle range are needed. Conversely, forward Monte Carlo is most efficient if the radiation source is confined to a small volume and/or solid angle range. Both methods become extremely inefficient, or fail, if radiation from a small source intercepted by a small detector is needed. For collimated irradiation (and similar problems) backward Monte Carlo can be made efficient by separating intensity into a direct (collimated) and a scattered part, as outlined in Chapter 16 of [1]. Thus, letting $I(\mathbf{r},\hat{\mathbf{s}}) = I_d(\mathbf{r},\hat{\mathbf{s}}) + I_s(\mathbf{r},\hat{\mathbf{s}})$, results in a direct component, attenuated by absorption and scattering,

$$I_d(\mathbf{r},\hat{\mathbf{s}}) = q_{\text{coll}}(\mathbf{r}_w)\, \delta(\hat{\mathbf{s}}-\hat{\mathbf{s}}_0) \exp\left[-\int_{\mathbf{r}\to\mathbf{r}'} (\kappa+\sigma_s) ds' \right], \tag{14}$$

which satisfies the RTE without the inscattering term. This leads to a source term in the RTE for the scattered part of the intensity, due to (first) scattering of the collimated beam, of

$$S_{\lambda 1}(\mathbf{r},\hat{\mathbf{s}}) = \sigma_s(\mathbf{r}) \frac{q_{\text{coll}}(\mathbf{r}_w)}{4\pi} \exp\left[-\int_0^{l_c} (\kappa_\lambda + \sigma_{s\lambda}) dl'_c \right] \Phi(\mathbf{r},\hat{\mathbf{s}}_0,\hat{\mathbf{s}}), \tag{15}$$

where q_{coll} is the collimated flux entering the medium at $\mathbf{r}_w$, traveling a distance of l_c toward $\mathbf{r}$ in the direction of $\hat{\mathbf{s}}_0$, and the scattering phase function $\Phi(\mathbf{r},\hat{\mathbf{s}}_0,\hat{\mathbf{s}})$ indicates the amount of collimated flux arriving at $\mathbf{r}$ from $\hat{\mathbf{s}}_0$, being scattered into the direction of $\hat{\mathbf{s}}$. Therefore, the diffuse component of the intensity at $\mathbf{r}_i$ is found immediately from Eq. (9) as

$$I_{\lambda n}(\mathbf{r}_i, -\hat{\mathbf{s}}_i) = \int_0^{l} S_{\lambda 1}(\mathbf{r}', -\hat{\mathbf{s}}') \exp\left[-\int_0^{l'} \kappa_\lambda dl'' \right] dl', \tag{16}$$

with $S_{\lambda 1}$ from Eq. (15). As before, Eq. (16) may be solved using standard tracing [picking absorption length l_κ, and dropping the exponential attenuation term in Eq. (16)] or energy partitioning [using Eq. (16) as given].

Point and Line Source. Backward Monte Carlo also becomes inefficient if the radiation source comes from a very small surface or volume and/or if the source is unidirectional. The trick is again to break up intensity into a direct component (intensity coming directly from the source without scattering or wall reflections), and a multiply-scattered and reflected part. Again, we let I_d satisfy the radiative transfer equation without the inscattering term, or,

$$\hat{\mathbf{s}} \cdot \nabla I_d(\mathbf{r},\hat{\mathbf{s}}) = S_d(\mathbf{r},\hat{\mathbf{s}}) - \beta(\mathbf{r}) I_d(\mathbf{r},\hat{\mathbf{s}}), \tag{17}$$

which has the simple solution

$$I_d(\mathbf{r},\hat{\mathbf{s}}) = \int S_d(\mathbf{r}',\hat{\mathbf{s}}) \exp\left[-\int_{\mathbf{r}\to\mathbf{r}'} (\kappa+\sigma_s) ds' \right] ds, \tag{18}$$

where the main integral is along a straight path from the boundary of the medium to point $\mathbf{r}$ in the direction of $\hat{\mathbf{s}}$. For example, if there is only a simple point source at $\mathbf{r}_0$ with total strength Q_0, emitting isotropically across a tiny volume δV, Eq. (18) becomes

$$I_d(\mathbf{r},\hat{\mathbf{s}}) = \frac{Q_0}{4\pi|\mathbf{r}_0-\mathbf{r}|^2} \exp\left[-\int_{\mathbf{r}_0\to\mathbf{r}} (\kappa+\sigma_s) ds' \right] \delta(\hat{\mathbf{s}}-\hat{\mathbf{s}}_0), \tag{19}$$

where $\hat{\mathbf{s}}$ is a unit vector pointing from $\mathbf{r}_0$ toward $\mathbf{r}$, and use has been made of the fact that

$$\delta V = \delta A \;\; \delta s = \frac{\delta\Omega_0 \delta s}{|\mathbf{r}_0-\mathbf{r}|^2}, \tag{20}$$

where $\delta\Omega_0$ is the solid angle, with which δV is seen from $\mathbf{r}$. Equation (19) can be used to calculate the direct contribution of Q_0 hitting a detector, and it can be used to determine the source term for the RTE of the scattered radiation as

$$S_1(\mathbf{r},\hat{\mathbf{s}}) = \frac{\sigma_s(\mathbf{r})}{4\pi} \int_{4\pi} I_d(\mathbf{r},\hat{\mathbf{s}}') \Phi(\mathbf{r},\hat{\mathbf{s}}',\hat{\mathbf{s}}) d\Omega'$$

$$= \frac{\sigma_s(\mathbf{r}) Q_0}{16\pi^2|\mathbf{r}_0-\mathbf{r}|^2} \exp\left[-\int_{\mathbf{r}_0\to\mathbf{r}} (\kappa+\sigma_s) ds' \right] \Phi(\mathbf{r},\hat{\mathbf{s}}_0,\hat{\mathbf{s}}). \tag{21}$$

The rest of the solution proceeds as before, with $I_n(\mathbf{r}_i, -\hat{\mathbf{s}}_i)$ found from Eq. (16).

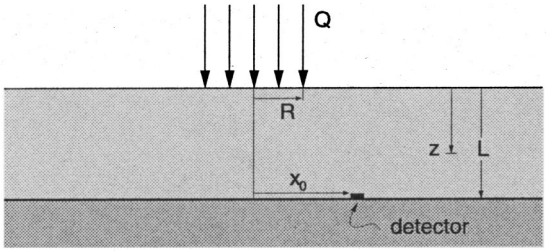

Fig. 2 One-dimensional slab with normally incident collimated irradiation

Sample Calculations

Isotropically Scattering, Nonabsorbing Medium With Collimated Irradiation. As a first example we will consider a one-dimensional slab $0 \leq z \leq L = 1$ m of a gray, purely isotropically scattering medium ($\sigma_s = 1\ \text{m}^{-1} = \text{const}$; $\Phi = 1$), bounded at the top ($z = 0$) by vacuum and at the bottom ($z = L$) by a cold, black surface. Collimated irradiation of strength $Q = 100$ W is normally incident on this nonreflecting layer, equally distributed over the disk $0 \leq r \leq R = 0.1$ m, as shown in Fig. 2. A small detector 2 cm $\times$ 2 cm in size, with an acceptance angle of $\theta_{\max}$ is located on the black surface at $x = x_0 = 0.2$ m, $y = 0$. The object is to determine the flux incident on the detector for varying acceptance angles, comparing forward and backward Monte Carlo implementations. In all simulations the number of photon bundles was doubled again and again until a relative variance of less than 2 percent of the desired quantity was achieved.

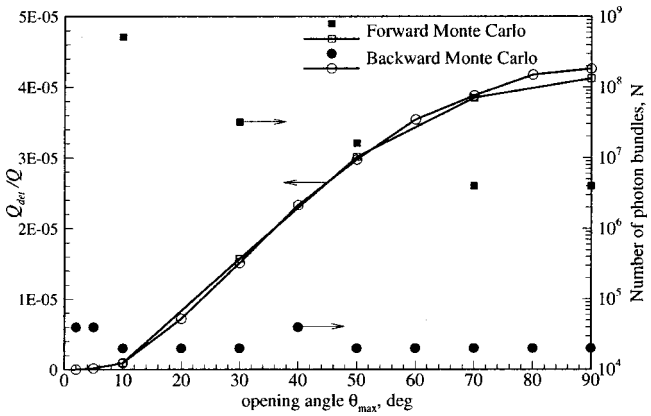

Fig. 3 Detector fluxes and required number of photon bundles (to achieve relative variance less than 2 percent) for one-dimensional slab with normally incident collimated irradiation

In a Forward Monte Carlo simulation emission points across the irradiation disk for N bundles are chosen, and emission is always into the $\hat{\mathbf{s}}=\hat{\mathbf{k}}$ or z-direction. Each bundle carries an amount of energy of Q/N and travels a distance of

$$l_\sigma=\frac{1}{\sigma_s}\ln\frac{1}{R_\sigma}, \tag{22}$$

before being scattered into a new direction, where R_σ is a random number picked uniformly from $0\leqslant R_\sigma\leqslant 1$. For isotropic scattering the incident direction is irrelevant and one may set the new direction to that given for isotropic emission. The bundle is then traced along as many scattering paths as needed, until it leaves the layer ($z<0$, or $z>L$). If the bundle strikes the bottom surface ($z=L$), incidence angle ($\hat{\mathbf{s}}\cdot\hat{\mathbf{k}}>\cos^2\theta_{\max}$?) and location ($x$, y on detector?) are checked and a detector hit is recorded, if appropriate. Results are shown in Fig. 3. As the detector's acceptance angle increases, more photon bundles are captured. Obviously, this results in a larger detector-absorbed flux. However, it also increases the fraction of statistically meaningful samples, decreasing the variance of the results or the number of required photon bundles to achieve a given variance. Here all calculations were carried out until the variance fell below 2 percent of the calculated flux, and the necessary number of bundles is also included in the figure. For the chosen variance about 4×10^6 bundles are required for large acceptance angles, rising to 512×10^6 for $\theta_{\max}=10$ deg. Results are difficult to obtain for $\theta_{\max}<10$ deg. Similar remarks can be made for detector area: as the detector area decreases, the necessary number of bundles increases. Modeling a more typical detector 1 mm$\times$1 mm in size would almost be impossible.

In a Backward Monte Carlo simulation, since no direct radiation hits the detector ($x_0>R$), the scattered irradiation is calculated from Eqs. (16) and (15) with $q_{\text{coll}}=Q/\pi R^2$ as

$$I_n(\mathbf{r}_i,-\hat{\mathbf{s}}_i)=\int_0^l\frac{\sigma_s Q}{4\pi^2R^2}e^{-\sigma_s z}H(R-r(l'))dl', \tag{23}$$

where l consists of a number of straight-line segments, for which $dl'=dz'/\cos\theta$, and H is Heaviside's unit step function. Therefore,

$$I_n(\mathbf{r}_i,-\hat{\mathbf{s}}_i)=\frac{\sigma_s Q}{4\pi^2R^2}\sum_j\int_{z_{1j}}^{z_{2j}}e^{-\sigma_s z}\frac{dz}{s_{zj}}$$
$$=\frac{Q}{4\pi^2R^2}\sum_j\frac{e^{-\sigma_s z_{1j}}-e^{-\sigma_s z_{2j}}}{s_{zj}}, \tag{24}$$

where $s_{zj}=\cos\theta_j$ is the z-component of the direction vector for the j^{th} segment, and z_{1j} and z_{2j} are the z-locations between which the segment lies within the cylindrical column $r\leqslant R$ (note that some segments may lie totally inside this column, some partially, and some not at all). Starting points distributed across the detector are chosen as in forward Monte Carlo, and a direction for the backward trace is picked from Eq. (13). Again, a scattering distance is found from Eq. (22), after which the bundle is scattered into a new direction. However, rather than having fixed energy, the backward-traveling bundles accumulate energy according to Eq. (24) as they travel through regions with a radiative source. The total flux hitting the detector is calculated by adding up bundle energies according to Eq. (12). Results are included in Fig. 3, and are seen to coincide with forward Monte Carlo results to about one variance or better (discrepancy being larger at large $\theta_{\max}$, since the *absolute* variance increases). However, the number of required bundles remains essentially independent of opening angle at about 20,000 (and, similarly, independent of detector area). Since the tracing of a photon bundle requires essentially the same cpu time for forward and backward tracing, for the problem given here the backward Monte Carlo scheme is up to 25,000 times more efficient than forward Monte Carlo.

Absorbing/Scattering Medium With Collimated Irradiation. Expanding on the previous example, for an acceptance angle of $\theta_{\max}=10$ deg, we will now assume that the medium absorbs as well as scatters radiation, using absorption coefficients of $\kappa_\lambda=1\ \text{m}^{-1}$ and $\kappa_\lambda=5\ \text{m}^{-1}$. Forward as well as backward Monte Carlo will be used, and also both standard ray tracing as well as energy partitioning.

Forward Monte Carlo—Standard Ray Tracing. The solution proceeds as in the previous example, except that also an absorption length l_κ is chosen similar to Eq. (22). If the sum of all scattering paths exceeds l_κ, the bundle is terminated.

Forward Monte Carlo—Energy Partitioning. The solution proceeds as in the previous example, except the energy of each bundle hitting the detector is attenuated by a factor of $\exp(-\kappa l)$, where l is the total (scattered) path that the bundle travels through the layer before hitting the detector.

Backward Monte Carlo—Standard Ray Tracing. The solution proceeds as in the previous example, except for two changes. First, the local scattering source must be attenuated by absorption of the direct beam, and Eq. (24) becomes

$$I_n(\mathbf{r}_i,-\hat{\mathbf{s}}_i)=\frac{\sigma_s Q}{4\pi^2R^2}\sum_j\int_{z_{1j}}^{z_{2j}}e^{-(\kappa+\sigma_s)z}\frac{dz}{s_{zj}}$$
$$=\frac{\omega Q}{4\pi^2R^2}\sum_j\frac{e^{-\beta z_{1j}}-e^{-\beta z_{2j}}}{s_{zj}}, \tag{25}$$

where ω and β are scattering albedo and extinction coefficient, respectively. And again, an absorption length l_κ is chosen, and the addition in Eq. (25) is stopped as soon as the total path reaches l_κ or the bundle leaves the layer (which ever comes first).

Backward Monte Carlo—Energy Partitioning. Again, the scattering source must be attenuated as in Eq. (25), but the exponential attenuation term in Eq. (16) must also be retained. Thus,

$$I_n(\mathbf{r}_i,-\hat{\mathbf{s}}_i)=\frac{\sigma_s Q}{4\pi^2R^2}\int_0^l e^{-\beta z(l')-\kappa l'}H(R-r(l'))dl', \tag{26}$$

where the integrand contributes only where the source is active ($r\leqslant R$), but attenuation of the bundle takes place everywhere ($l'=$total distance along path from $\mathbf{r}_i$ to $\mathbf{r}'$). The rest of the simulation remains as in the previous case. Results are summarized in Table 1. As expected, if standard ray tracing is employed, the number of required bundles grows exponentially if the absorption coefficient becomes large, both for forward and backward Monte Carlo. While backward Monte Carlo retains its advantage (indeed, the forward Monte Carlo simulation for $\kappa_\lambda=5\ \text{m}^{-1}$ could only be

Table 1 Comparison between four different Monte Carlo implementations to calculate irradiation onto a detector from a collimated source

κL	Forward MC—Standard		Forward MC—Energy partitioning		Backward MC—Standard		Backward MC—Energy partitioning	
	Q_{det}/Q	$N\times10^{-6}$	Q_{det}/Q	$N\times10^{-6}$	Q_{det}/Q	$N\times10^{-6}$	Q_{det}/Q	$N\times10^{-6}$
0	9.22×10^{-6}	512	9.22×10^{-6}	512	9.17×10^{-6}	0.02	9.17×10^{-6}	0.02
1	2.66×10^{-6}	512	2.70×10^{-6}	512	2.56×10^{-6}	0.08	2.59×10^{-6}	0.02
5	2.54×10^{-8}	16,384*	2.93×10^{-8}	512	2.77×10^{-8}	5.12	2.79×10^{-8}	0.02

*Variance of 5% (all other data have variance of 2%)

carried out to a variance of 5 percent), the relative growth of required bundles appears to be worse for backward Monte Carlo. If energy partitioning is employed, the number of bundles remains unaffected by the absorption coefficient for both, forward and backward Monte Carlo.

Isotropically Scattering, Nonabsorbing Medium With Internal Point Source. In a final example a point source of strength $Q_0=100$ W, located at $x_0=y_0=0$, $z_0=0.5L$ will be considered for a purely scattering medium. Again, flux hitting the detector will be compared using forward and backward Monte Carlo methods.

The forward Monte Carlo simulation is almost identical to that of the first example, except that all photon bundles are now emitted from a single point, but into random directions. In the backward Monte Carlo simulation, the detector flux again consists of a direct and a scattered component and, again, the direct component is zero, this time because all direct radiation hits the detector at an angle larger than the acceptance angle. The I_n are then found from Eqs. (21) and (16) as

$$I_n(\mathbf{r}_i,-\hat{\mathbf{s}}_i)=\frac{\sigma_s Q}{16\pi^2}\sum_j\int_{l_{\sigma,j}}\frac{e^{-\sigma_s|\mathbf{r}_0-\mathbf{r}|}}{|\mathbf{r}_0-\mathbf{r}|^2}dl', \tag{27}$$

where the $l_{\sigma,j}$ are the straight paths the bundle travels between scattering events. Equation (27) must be integrated numerically, and this can be done using a simple Newton-Cotes scheme; here no optimization of the quadrature was attempted, except that—away from the source—the number of integration points was minimized for small l_σ (large σ_s). Alternatively, the integral can be obtained statistically from

$$I_n(\mathbf{r}_i,-\hat{\mathbf{s}}_i)=\frac{\sigma_s Q}{16\pi^2}\sum_j\frac{l_{\sigma,j}}{M}\sum_m\frac{e^{-\sigma_s|\mathbf{r}_0-\mathbf{r}_m|}}{|\mathbf{r}_0-\mathbf{r}_m|^2}, \tag{28}$$

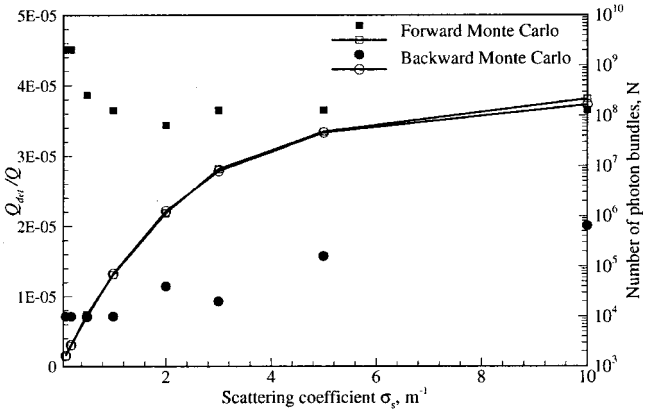

Fig. 4 Detector fluxes and required number of photon bundles (to achieve relative variance less than 2 percent) for one-dimensional slab with internal point source

where the $\mathbf{r}_m$ are M random locations chosen uniformly along path $l_{\sigma,j}$. Results for detector flux as function of scattering coefficient are shown in Fig. 4.

For small values of σ_s the number of photon bundles required to achieve a relative variance of 2 percent is much smaller for the backward Monte Carlo method, as expected, since the volume with secondary scattering (i.e., the Source S_1) is relatively large, and the detector is small. However, as σ_s increases, the size of the secondary scattering volume decreases, and backward Monte Carlo becomes less and less efficient. For both methods large σ_s mean smaller $l_{\sigma,j}$, leading to increased tracing effort for each individual bundle. Numerical integration via Eq. (28) was generally much more efficient than Newton-Cotes quadrature, with $M=1$ usually being sufficient (since the integral is evaluated so many times). However, for large σ_s this method became inefficient, requiring many photon bundles to achieve a 2 percent relative variance. In addition, *all* methods became inefficient for $\sigma_s>10\ \text{m}^{-1}$.

Summary

A comprehensive formulation for backward Monte Carlo simulations, capable of treating emitting, absorbing and anisotropically scattering media, media with diffuse or collimated irradiation (with large or small footprints), media with point or line sources, etc., has been given. The basic backward Monte Carlo simulation of Walters and Buckius [3] was reviewed and was extended to allow for collimated irradiation, point sources, and other sources of small volume/area and/or small solid angle range. In addition, the method was extended to allow standard ray tracing (bundles of fixed energy) as well as energy partitioning (bundles attenuated by absorption). Sample results for radiation hitting a small detector show that forward Monte Carlo methods degrade rapidly with shrinking detector size and acceptance angle. Backward Monte Carlo, on the other hand, is unaffected by detector size, but requires a relatively large radiation source, which—in the case of collimated irradiation or point sources—needs to be created artificially by separating direct and scattered radiation. Even for relatively large detectors/opening angles, using backward Monte Carlo can result in several orders of magnitude lesser computer effort, and becomes the only feasible method for very small detectors. Similarly, using energy partitioning in strongly absorbing media also reduces numerical effort by orders of magnitude for, both, forward and backward Monte Carlo simulations.

Nomenclature

A = area, m^2
I = radiative intensity, W/m^2 sr
l = geometric length, m
$\hat{\mathbf{n}}$ = unit surface normal
N = number of photon bundles
q = radiative heat flux, W/m^2
$\mathbf{r}$ = position vector
R = random number
$\hat{\mathbf{s}}$ = unit direction vector
S = radiative source, W/m^3 sr

T = temperature, K
V = Volume, m^3

Greek Symbols

β = extinction coefficient, cm^{-1}
ϵ = surface emittance
λ = wavelength, μm
Φ = scattering phase function
κ = absorption coefficient, cm^{-1}
Ω = solid angle, sr
σ_s = scattering coefficient, cm^{-1}
θ, ψ = incidence angles, rad

Subscripts

b = blackbody emission
j = path identifier
n = bundle identifier
w = wall
λ = spectral

References

[1] Modest, M. F., 1993, *Radiative Heat Transfer*, McGraw-Hill, New York.
[2] Siegel, R., and Howell, J. R., 1992, *Thermal Radiation Heat Transfer*, 3rd ed., Hemisphere, New York.
[3] Walters, D. V., and Buckius, R. O., 1992, ''Monte Carlo Methods for Radiative Heat Transfer in Scattering Media,'' in *Annual Review of Heat Transfer*, **5**, Hemisphere, New York, pp. 131–176.
[4] Gordon, H. R., 1985, ''Ship Perturbation of Irradiance Measurements at Sea: 1—Monte Carlo Simulations,'' Appl. Opt., **24**, pp. 4172–4182.
[5] Collins, D. G., Blättner, W. G., Wells, M. B., and Horak, H. G., 1972, ''Backward Monte Carlo Calculations of the Polarization Characteristics of the Radiation Emerging From Spherical-Shell Atmospheres,'' Appl. Opt., **11**, pp. 2684–2696.
[6] Adams, C. N., and Kattawar, G. W., 1978, ''Radiative Transfer in Spherical Shell Atmospheres—I. Rayleigh Scattering,'' Icarus, **35**, pp. 139–151.
[7] Nishita, T., Miyawaki, Y., and Nakamae, E., 1987, ''A Shading Model for Atmospheric Scattering Considering Luminous Intensity Distribution of Light Sources,'' Comput. Graph., **21**, pp. 303–310.
[8] Sabella, P., 1988, ''A Rendering Algorithm for Visualizing 3D Scalar Fields,'' Comput. Graph., **22**, pp. 51–58.
[9] Edwards, D. K., 1983, ''Numerical Methods in Radiation Heat Transfer,'' in *Proc. Second National Symposium on Numerical Properties and Methodologies in Heat Transfer*, Shih, T. M., ed., Hemisphere, pp. 479–496.
[10] Walters, D. V., and Buckius, R. O., 1992, ''Rigorous Development For Radiation Heat Transfer In Nonhomogeneous Absorbing, Emitting And Scattering Media,'' Int. J. Heat Mass Transf., **35**, pp. 3323–3333.
[11] Cramer, S. N., 1996, ''Forward-Adjoint Monte Carlo Coupling With No Statistical Error Propagation,'' Nucl. Sci. Eng., **124**(3), pp. 398–416.
[12] Serov, I. V., John, T. M., and Hoogenboom, J. E., 1999, ''A Midway Forward-Adjoint Coupling Method for Neutron and Photon Monte Carlo Transport,'' Nucl. Sci. Eng., **133**(1), pp. 55–72.
[13] Ueki, T., and Hoogenboom, J. E., 2001, ''Exact Monte Carlo Perturbation Analysis by Forward-Adjoint Coupling in Radiation Transport Calculations,'' J. Comput. Phys., **171**(2), pp. 509–533.
[14] Case, K. M., 1957, ''Transfer Problems and the Reciprocity Principle,'' Rev. Mod. Phys., **29**, pp. 651–663.

Surface Energy Variation Effect on the Onset of Thermocapillary Instability of a Thin Liquid Layer Heated from the Side

Lin Wu
Department of Electrical Engineering,
Princeton University,
Princeton, NJ 08540

Kang Ping Chen
e-mail: k.p.chen@asu.edu
Department of Mechanical & Aerospace Engineering,
Arizona State University,
Tempe, AZ 85287-6106

A general interfacial energy balance equation taking into account surface energy variation is derived for viscous two-layer flows. Application of this interfacial energy equation to a thin liquid layer heated from one side using a one-layer model shows that thermocapillary induced surface energy variation has a tendency to stabilize the system, resulting in an increase in the critical Marangoni number for the onset of thermocapillary instability. Thermocapillary induced surface energy variation tends to decrease the temperature of hot surface spots and increase the temperature of cold surface spots through an absorb-release mechanism. This absorb-release mechanism increases the free surface's capability to convect thermal energy from hot spots to cold spots and thus redistributes the disturbance energy evenly across the free surface. This new stabilizing effect becomes stronger at high surface temperature and at high surface dilatation rate.
[DOI: 10.1115/1.1527909]

Keywords: Convection, Film, Heat Transfer, Instability, Interface, Surface Tension

1 Introduction

Thermocapillary convections in thin liquid layers subject to a temperature gradient normal or parallel to the layer have been studied extensively since the pioneering experiments of Bénard [1]. Block [2] showed experimentally that if the liquid layer is thin enough (thinner than 1 mm), the convective motions observed by Bénard in a thin layer heated from below were actually driven by the surface tension gradient due to the variation of surface tension with temperature, and not by the thermal instability of a heavy fluid on top of a light fluid analyzed by Rayleigh [3]. The mechanism for the classical Bénard-Marangoni convection of a thin static liquid layer with a free surface heated from below or cooled from above was analyzed by Pearson [4]. When a random hot spot appears at the free surface as the temperature is disturbed, surface tension, which usually is a monotonically decreasing function of temperature, pulls fluid away from the hot spot in all directions. To conserve mass, hotter fluid directly beneath the hot spot will rise to replace old colder fluid and heat up the hot spot even further. Thus, if the vertical temperature gradient is large enough, the hot spot will be maintained, and consequently the disturbance will start a circulatory motion in the form of the well known Bénard cells. Smith and Davis [5] extended the problem to include temperature gradients in both directions, parallel to the free surface and normal to the free surface. They identified two types of instabilities, one in the form of stationary longitudinal rolls and the other in the form of traveling hydrothermal waves.

Classical theories, however, ignored the effect of surface energy variation due to thermocapillarity in the interfacial energy balance equation. Chen [6] showed that this thermocapillary-induced surface energy variation effect can have a measurable influence on the critical Marangoni number for the onset of Bénard convection cells at room temperatures. In this paper, we will first derive an interfacial energy balance equation applicable to general two-layer flows. We will then examine the effect of thermocapillary-induced surface energy variation on the onset of thermocapillary instabilities for a thin liquid layer heated from one side. The analysis shows that surface energy variation has a tendency to stabilize the system, causing a non-negligible increase in the critical Marangoni number for the onset of thermocapillary instability in this system. No influence on the direction of propagation of the disturbance waves is found, however. A mechanism for the stabilizing effect of surface energy variation will also be explored.

Contributed by the Heat Transfer Division for publication in the JOURNAL OF HEAT TRANSFER. Manuscript received by the Heat Transfer Division March 5, 2002; revision received September 17, 2002. Associate Editor: G. P. Peterson.

2 Interfacial Energy Balance Equation for Two-Layer Flows

The general interfacial energy balance equation at the interface between two immiscible viscous fluids can be derived following Joseph and Renardy [7]. For a region V enclosing the fluid-fluid interface Σ (see Fig. 1), the equation of energy balance in integral form can be written as

$$\frac{d}{dt}\int_v \rho\left(e+\frac{|\mathbf{u}|^2}{2}\right)dv+\frac{d}{dt}\int_\Sigma U^s d\Sigma = -\int_{\partial v}\mathbf{q}\cdot\mathbf{n}_{12}dS+\int_{\partial v}\mathbf{u}\cdot\mathbf{t}dS+\int_v \rho\mathbf{u}\cdot\mathbf{g}dV+\int_{\partial\Sigma}\sigma\tau\cdot\mathbf{u}_\Sigma dl \tag{1}$$

where ρ is the fluid density, $\mathbf{u}$ is the fluid velocity, e is the specific internal energy of the fluid, U^S is the surface internal energy per unit area (surface specific internal energy), $\mathbf{q}$ is the heat flux vector, and $\mathbf{t}$ is the traction. V_1, V_2, $V(V=V_1+V_2)$ are the control volumes with boundaries ∂V_1, ∂V_2, ∂V, respectively. Σ is the interface between V_1 and V_2, and $\mathbf{n}_{12}$ is the outward unit normal pointing from 1 to 2 at the interface, τ is the unit tangential vector of Σ at $\partial\Sigma$, and $\mathbf{u}_\Sigma$ is the velocity of the interface.

Application of the divergence theorem, surface divergence theorem as well as surface transport theorem (Joseph, [8]) to equation (1) gives

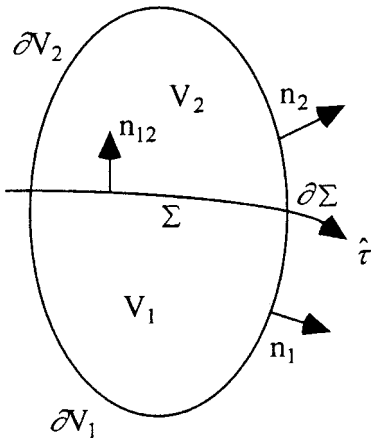

Fig. 1 Control volume with an interface. V_1, V_2 are two material volumes with surfaces ∂V_1, ∂V_2 and an interface Σ in between. $\partial\Sigma$ is the boundary of Σ. n_1, n_2 are outward normal vectors on ∂V_1 and ∂V_2 respectively. n_{12} is the normal vector on Σ pointing from 1 to 2. $\hat{\tau}$ is a tangential vector of Σ on $\partial\Sigma$.

$$\int_V\left[\rho\frac{d}{dt}\left(e+\frac{|\mathbf{u}|^2}{2}\right)+\mathrm{div}\,\mathbf{q}+\mathrm{div}(\mathbf{Tu})-\rho\mathbf{u}\cdot\mathbf{g}\right]dV$$
$$=\int_\Sigma\left\{-m\left[\left[e+\frac{|\mathbf{u}|^2}{2}\right]\right]+[[\mathbf{q}]]\cdot\mathbf{n}_{12}-[[\mathbf{u}\cdot\mathbf{Tn}_{12}]]\right\}d\Sigma$$
$$-\frac{d}{dt}\int_\Sigma(U^S-\sigma)d\Sigma-\int_\Sigma\left[\frac{D_S\sigma}{Dt}-\mathbf{u}\cdot\nabla_{II}\sigma-2H\sigma\mathbf{u}_\Sigma\cdot\mathbf{n}_{12}\right]d\Sigma \tag{2}$$

where m is the mass flux across the interface,

$$m=\rho_1(\mathbf{u}_\Sigma-\mathbf{u}_1)\cdot\mathbf{n}_{12}=\rho_2(\mathbf{u}_\Sigma-\mathbf{u}_2)\cdot\mathbf{n}_{12}. \tag{3}$$

The jump in any physical quantity f across the interface Σ is defined as

$$[[f]]=f_1-f_2, \tag{4}$$

where f_1 is the property of fluid 1 at Σ, f_2 is the property of fluid 2 at Σ, respectively. $\mathbf{T}$ is the Cauchy stress tensor, and $2H$ is the sum of the mean curvature of the interface. The surface convective derivative is

$$\frac{D_S}{Dt}=\frac{\partial}{\partial t}+u_\Sigma\cdot\nabla_{II}, \tag{5}$$

and the surface gradient operator

$$\nabla_{II}=\nabla-\mathbf{n}_{12}(\mathbf{n}_{12}\cdot\nabla). \tag{6}$$

Since V is arbitary, the interfacial energy balance equation is therefore given by

$$-m\left[\left[e+\frac{|\mathbf{u}|^2}{2}\right]\right]+[[\mathbf{q}]]\cdot\mathbf{n}_{12}-[[\mathbf{u}\cdot\mathbf{Tn}_{12}]]+\left\{\frac{D_s}{Dt}(U^s-\sigma)-\mathbf{u}\cdot\nabla_{II}(U^s-\sigma)+\nabla_{II}\cdot[(U^s-\sigma)\mathbf{u}_\Sigma]\right\}-\left[\frac{D_s\sigma}{Dt}-\mathbf{u}\cdot\nabla_{II}\sigma-2H\sigma\mathbf{u}_\Sigma\cdot\mathbf{n}_{12}\right]=0. \tag{7}$$

The interfacial momentum balance equation is (Joseph and Renardy, [7])

$$m[\![\mathbf{u}]\!]+[\![\mathbf{T}]\!]\mathbf{n}_{12}=\nabla_{II}\sigma+2H\sigma\mathbf{n}_{12}. \tag{8}$$

Inner product (8) with $\mathbf{u}_\Sigma$ and subtract the result from (7) gives

$$[[\mathbf{q}]]\cdot\mathbf{n}_{12}=m\left[\left[e+\frac{|\mathbf{u}-\mathbf{u}_\Sigma|^2}{2}\right]\right]+[[(\mathbf{u}-\mathbf{u}_\Sigma)\cdot\mathbf{Tn}_{12}]]+\frac{D_sU^s}{Dt}+(\mathbf{u}_\Sigma-\mathbf{u})\cdot\nabla_{II}(U^s-\sigma)+(U^s-\sigma)\nabla_{II}\cdot\mathbf{u}_\Sigma. \tag{9}$$

Equation (9) is the general interfacial energy balance equation for two-layer flow of immiscible fluids.

A special form of the interfacial energy balance equation was obtained by Chen [6] for thermocapillary flows. For thermocapillary flows, surface tension depends on temperature only, $\sigma=\sigma(\theta)$, the thermodynamic relation between the surface specific internal energy and temperature (Hirschfelder et al.[9])

$$U^S=-\theta^2\frac{d}{d\theta}\left(\frac{\sigma}{\theta}\right)=\sigma-\theta\frac{d\sigma}{d\theta} \tag{10}$$

can be used to further simplify the interfacial energy equation (9) to

$$[[\mathbf{q}]]\cdot\mathbf{n}_{12}=m\left[\left[e+\frac{|\mathbf{u}-\mathbf{u}_\Sigma|^2}{2}\right]\right]+[[(\mathbf{u}-\mathbf{u}_\Sigma)\cdot\mathbf{Tn}_{12}]]-\theta\frac{d^2\sigma}{d\theta^2}\frac{D_s\theta}{Dt}-\theta\frac{d\sigma}{d\theta}\nabla_{II}\cdot\mathbf{u}_\Sigma. \tag{11}$$

When there is no interfacial mass transfer, $m=0$, $\mathbf{u}=\mathbf{u}_\Sigma$, the interfacial energy balance equation for thermocapillary flow becomes

$$[[\mathbf{q}]]\cdot\mathbf{n}_{12}=-\theta\frac{d^2\sigma}{d\theta^2}\frac{D_s\theta}{Dt}-\theta\frac{d\sigma}{d\theta}\nabla_{II}\cdot\mathbf{u} \tag{12}$$

Equation (12) shows that the heat flux across a fluid-fluid interface is not continuous if surface energy varies with temperature. The first and the second terms on the right-hand-side of Eq. (12) represent the change of the surface specific internal energy with temperature and the surface internal energy increase due to surface dilatation, respectively. Thus, the interfacial energy balance equation for a *one-layer* model for thermocapillary flow with no condensation/evaporation is

$$\mathbf{q}\cdot\mathbf{n}=-\theta\frac{d^2\sigma}{d\theta^2}\frac{D_s\theta}{Dt}-\theta\frac{d\sigma}{d\theta}\nabla_{II}\cdot\mathbf{u}+h(\theta-\theta_{\mathrm{air}})+Q_0, \tag{13}$$

where h is the thermal conductance of the surface, θ_{air} is the ambient air temperature, Q_0 is the prescribed heat flux across the surface. In contrast to the classical theories, the interfacial energy balance Eq. (13) shows that, in general, thermocapillary convections depend on the absolute temperature of the interface, not just the temperature difference across the liquid layer as in the classical theories. The thermodynamic state of the interface plays a role in determining the convection induced by thermocapillarity. In the remainder of the paper, we will examine the surface energy variation effect on the thermocapillary convection for a thin layer heated from one side.

3 Governing Equations for the Onset of Thermocapillary Instability in a Thin Liquid Layer Heated From the Side

Consider the thermocapillary flow of a thin liquid layer heated from the side with a constant temperature gradient $d\theta/dx=-b(<0)$ imposed parallel to the layer (Fig. 2). The thin liquid layer has a mean depth of d and is bounded by passive gas at the top and an insulating solid plane surface at the bottom. The film thickness d is much larger than the mean free path of the liquid molecules so that the continuum approximation holds. At the mean time, the film is thin enough so that surface tension force dominates over the gravitational force (under normal gravitational field, this requires the film to be thinner than 1 mm). The liquid is Newtonian, incompressible with a constant density ρ, dynamic viscosity μ, kinematic viscosity v, thermal conductivity k, thermodiffusivity κ, and unit thermal surface conductance h. To simplify the analysis, the liquid-gas interface is assumed to be nondeformable. This assumption is justified when the crispation number $C=\mu\kappa/d\sigma$, which is a measure of the deformability of the free surface, is vanishingly small. Deformability of the free

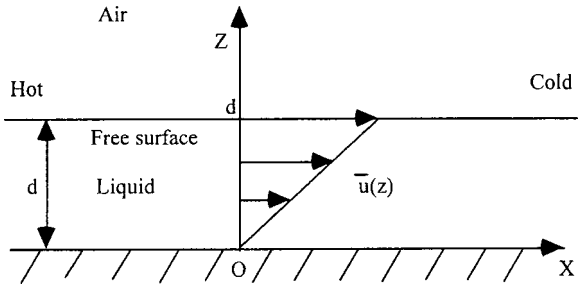

Fig. 2 The configuration of the one layer system horizontally unbounded. A constant temperature gradient is imposed in the positive *x* direction. Surface tension gradient drives the fluid to move in the direction shown with a linear basic state velocity profile.

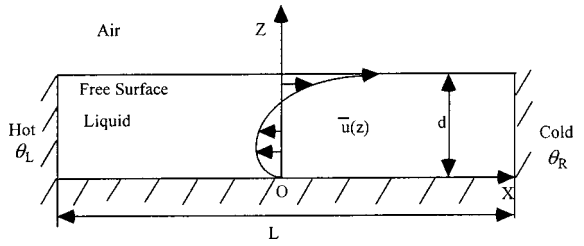

Fig. 3 The configuration of the one layer system horizontally bounded ($d/L \ll 1$). A constant temperature gradient is imposed in the positive *x* direction. Surface tension gradient drives the fluid to move in the direction shown. A parabolic basic state velocity profile approximates the core region away from the ends when the aspect ratio L/d is very large.

surface has relatively small effect on thermal instability (Smith, [10]), particularly for finite wavelength disturbances. Surface deformability introduces an additional instability mode in the long wave range, and this type of instability is excluded by the nondeformable assumption used here. The two basic state considered here are the linear flow and the return flow (Figs. 2, 3). The linear flow models an unbounded thin layer and the return flow approximates the flow in the core region of a thin layer confined in a large aspect ratio slot (Fig. 3).

For most common fluids in mild temperature range, surface tension varies nearly linearly with temperature. Thus, the surface tension temperature relation is frequently approximated as a linear function:

$$\sigma = \sigma_0 - \gamma(\theta - \theta_0), \tag{14}$$

where θ_0 is a reference temperature and σ_0 is the value of the surface tension at this reference temperature. In the dynamic thermocapillary layer problem considered in this study, θ_0 is the basic state free surface temperature at $x=0$ and σ_0 is the surface tension at θ_0, $\gamma = -d\sigma/d\theta$ at $\theta = \theta_0$ and γ is positive for most common fluids (examples for which γ is negative include ethyl *p*-azoxybenzoate, and ethyl *p*-ethoxybenzalamino-α-methylcinnamate, see Harkins, [10]).

The governing equations are the continuity equation, the incompressible Navier-Stokes equations, and the energy equation. Since the liquid layer considered is very thin, gravitational effect is neglected in the formulation. Length, velocity, temperature difference $\theta - \theta_0$ (θ_0 is the free surface temperature at $x=0$), time, pressure, surface tension are scaled with d, $\gamma bd/\mu$, bd, $\mu/\gamma b$, γb, σ_0. The controlling parameters are: Marangoni number $\mathrm{Ma} = \gamma bd^2/\mu\kappa$, Prandtl number $\mathrm{Pr} = \nu/\kappa$, and Biot number $\mathrm{Bi} = hd/k$.

The dimensionless linear and return flow solutions of the basic state are given by (Smith and Davis, [5])

$$\bar{u} = \bar{u}'(1)z + \frac{1}{2}\bar{u}''(1)(z^2 - 2z), \tag{15}$$

$$\bar{v} = \bar{w} = 0, \tag{16}$$

$$\bar{p}_x = \bar{u}''(1), \tag{17}$$

$$\bar{\theta} = -\bar{u}'(1)x + \mathrm{Ma}\bar{u}'(1)\left\{\frac{1}{24}\bar{u}''(1)(1-z^4) + \frac{1}{6}[\bar{u}'(1) - \bar{u}''(1)](1-z^3)\right\}, \tag{18}$$

where

$$\bar{u}'(1) = 1, \quad \bar{u}''(1) = 0, \tag{19}$$

corresponds to the linear flow solution, and

$$\bar{u}'(1) = 1, \quad \bar{u}''(1) = 1.5 \tag{20}$$

corresponds to the return flow solution.

To study the hydrodynamic stability of the basic states, we perturb the velocity field, temperature field and pressure field to

$$(u,v,w) = (\bar{u}+\tilde{u}, \bar{v}+\tilde{v}, \bar{w}+\tilde{w}), \tag{21}$$

$$\theta = \bar{\theta} + \tilde{\theta}, \tag{22}$$

$$p = \bar{p} + \tilde{p}, \tag{23}$$

where overbars stand for the basic state quantities and tilts stand for the perturbation quantities. To study the onset of instability, we assume that these perturbations are infinitesimally small, and the governing equations can be linearized to obtain the linearized perturbation equations. We will only list the dimensionless linearized interfacial energy balance equation for the perturbations here, since all other equations are standard and can be found in, say, Smith and Davis [5]. The dimensionless linearized interfacial energy balance equation for the perturbation field is

$$\frac{\partial\tilde{\theta}}{\partial z} + \mathrm{Bi}\tilde{\theta} = \left[\Gamma - \frac{\gamma^2 bd}{k\mu}\bar{u}'(1)x\right]\frac{\partial\tilde{w}}{\partial z}, \tag{24}$$

where the dimensionless parameter Γ is given by

$$\Gamma = \frac{\theta_0\gamma^2}{\mu k}, \tag{25}$$

which measures the importance of the surface energy variation due to surface dilatation relative to the energy conducted to the surface from the bulk.

The second term in the bracket on the right hand side of the Eq. (24) prevents the use of normal mode, since its coefficient is a function of *x*. However, if

$$x \ll \frac{k\mu}{\gamma^2 bd\bar{u}'(1)}, \tag{26}$$

the second term in the bracket on the right hand side of (24) can be neglected and the normal mode decomposition can be used. Condition (26) limits the approximation to situations where the liquid layer depth is small or the surface temperature θ_0 is large. Under this approximation, the linearized surface energy equation for the perturbation becomes

$$\frac{\partial\tilde{\theta}}{\partial z} + \mathrm{Bi}\tilde{\theta} = \Gamma\frac{\partial\tilde{w}}{\partial z}. \tag{27}$$

The normal mode equations can be obtained by writing $\tilde{u}(x,y,z) = \hat{u}(z)e^{i(\alpha x + \beta y - \delta t)}$, with α being the wave number in the *x* direction, β the wave number in the *y* direction, and δ the growth rate of the disturbances. Other perturbation quantities are decomposed into similar normal modes. If the imaginary part of δ

Table 1 The value of $\Gamma/\gamma^2=\theta_I/\mu k$ for Organic compounds at normal temperature

Organic compounds			
Material (θ_I)	Dynamic viscosity μ (dyne·cm^{-2})	Thermal conductivity k ($\times 10^4$ erg·cm^{-1} s^{-1}°K^{-1})	$\theta_I/\mu k$ (dyne^{-2} cm^2°K^{-2})
Acetaldehyde (20°C)	0.0022	1.71	7.788
Acetone (15°C)	0.00337	1.90	4.576
Allyl alcohol (30°C)	0.011	1.80	1.53
Benzene (20°C)	0.00652	1.58	2.84
Benzene (60°C)	0.00392	1.51	5.63
Ethyl alcohol (20°C)	0.012	1.67	1.46
Ethyl iodide (30°C)	0.00543	1.11	5.03
Heptane (30°C)	0.00386	1.40	5.60
Hexane (50°C)	0.00248	1.37	9.5
Pentane (20°C)	0.00240	1.35	9.04
Propyl chloride (40°C)	0.00291	1.25	8.6

is greater than zero, random disturbance will grow with time and the system is unstable to infinitesimal disturbances. Disturbance equations in normal-mode form are:

$$\left[D^2-(\alpha^2+\beta^2)-i\alpha\frac{\mathrm{Ma}}{\mathrm{Pr}}\overline{u}+i\frac{\mathrm{Ma}}{\mathrm{Pr}}\delta\right]\hat{u}=i\alpha\hat{p}+\frac{\mathrm{Ma}}{\mathrm{Pr}}D\overline{u}\hat{w}, \tag{28}$$

$$\left[D^2-(\alpha^2+\beta^2)-i\alpha\frac{\mathrm{Ma}}{\mathrm{Pr}}\overline{u}+i\frac{\mathrm{Ma}}{\mathrm{Pr}}\delta\right]\hat{v}=i\beta\hat{p}, \tag{29}$$

$$\left[D^2-(\alpha^2+\beta^2)-i\alpha\frac{\mathrm{Ma}}{\mathrm{Pr}}\overline{u}+i\frac{\mathrm{Ma}}{\mathrm{Pr}}\delta\right]\hat{w}=D\hat{p}, \tag{30}$$

$$\left[D^2-(\alpha^2+\beta^2)-i\alpha\,\mathrm{Ma}\,\overline{u}+i\,\mathrm{Ma}\,\delta\right]\hat{\theta}=\mathrm{Ma}\,\overline{\theta}_x\hat{u}+\mathrm{Ma}\,\overline{\theta}_z\hat{w}, \tag{31}$$

$$D\hat{w}+i\alpha\hat{u}+i\beta\hat{v}=0, \tag{32}$$

where the differential operator $D=d/dz$. The boundary conditions in normal mode forms are:

at $z=0$,

$$\hat{u}=\hat{v}=\hat{w}=D\hat{\theta}=0; \tag{33}$$

at $z=1$,

$$\hat{w}=0, \tag{34}$$

$$D\hat{u}+i\alpha\hat{\theta}=0, \tag{35}$$

$$D\hat{v}+i\beta\hat{\theta}=0, \tag{36}$$

$$D\hat{\theta}+Bi\,\hat{\theta}=\Gamma D\hat{w}. \tag{37}$$

A Chebyshev collocation method (Orszag and Kells [11]) is used to discretize the system of ordinary differential equations, and the resulting generalized matrix eigenvalue problem is solved using IMSL's eigensolver. The numerical code is fully validated by reproducing the results of Smith and Davis [5].

4 Results and Discussion

Since the Squire's theorem does not hold for this problem (Smith and Davis, [5]), three-dimensional disturbances have to be considered. With fixed values of Pr and Bi, there is a minimum Marangoni number corresponding to a particular pair of α and β for the onset of thermocapillary instability. A cylindrical coordinate in the α and β plane is introduced:

$$\alpha=r\cdot\cos\phi, \tag{38}$$

$$\beta=r\cdot\sin\phi, \tag{39}$$

where

$$r=\sqrt{\alpha^2+\beta^2}, \tag{40}$$

$$\tan\phi=\beta/\alpha. \tag{41}$$

At each wave propagation angle ϕ, we change over all wave numbers r to find the smallest Marangoni number in this fixed direction. Because there is a symmetry about the x-axis, we only need to consider 0 deg $\leqslant\phi\leqslant$180 deg.

The effect of the surface energy variation on the thermocapillary instability is controlled by the parameter Γ. $\Gamma=0$ corresponds to the classical theories where no such effect is considered. In Table 1 and 2, values of Γ/γ^2 for some organic and inorganic compounds at representative temperatures are listed. To obtain the value for Γ, the value of surface tension temperature gradient γ is needed. $\Gamma=0.0176$ for water at 20°C, and $\Gamma=0.074$ for acetone at 20°C. Since the value of Γ is directly proportional to the surface temperature, it is not entirely unreasonable to use the values of $\Gamma=0.1$, or 0.2 in our calculation for the purpose of illustrating the effect of surface energy variation.

The stability of the linear flow is considered first. At small Prandtl number, the disturbance takes the form of span-wise ($\phi\approx$90 deg) traveling hydrothermal wave (Smith and Davis, [5]). Figure 4 shows that the minimum Marangoni number occurs at $\phi=83$ deg, $\phi=97$ deg for Pr=0.5, Bi=0. Figure 4 clearly shows that surface energy variation has a stabilizing effect on the system with the critical Marangoni number being raised from 20.04 for $\Gamma=0$ to 20.27 for $\Gamma=0.1$. There is no change in the propagation angle for the most dangerous disturbance, however. There is also a symmetry about the axis $\phi=90$ deg. This symmetric property of the neutral stability curves holds for both the linear flow and the return flow to be considered next.

When the Prandtl number is large, the disturbance takes the form of longitudinal rolls (Smith and Davis, [5]). Figure 5 shows that when Pr=∞, Bi=0, the most dangerous angle is 90 deg. At $\phi=90$ deg, the critical Marangoni number is 15.48 for $\Gamma=0$, and

Table 2 The value of $\Gamma/\gamma^2=\theta_I/\mu k$ for Inorganic compounds at normal temperature

Inorganic compounds			
Material (θ_I)	Dynamic viscosity μ (dyne·cm^{-2})	Thermal conductivity k ($\times 10^4$ erg·cm^{-1} s^{-1}°K^{-1})	$\theta_I/\mu k$ (dyne^{-2} cm^2°K^{-2})
Water (20°C)	0.01	5.97	0.49

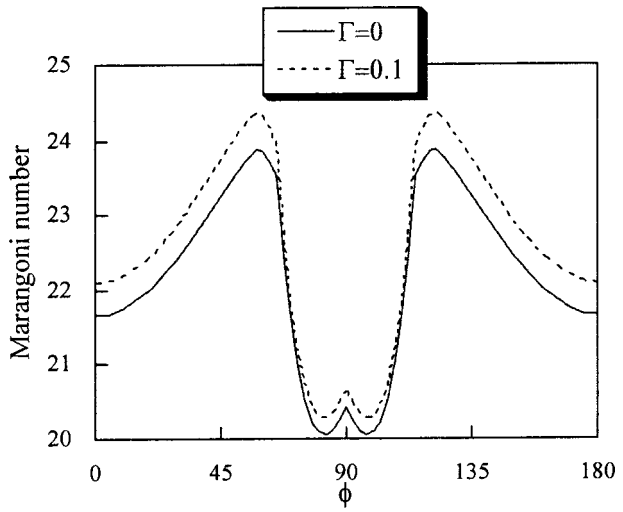

Fig. 4 The effect of the parameter Γ on the minimum Marangoni number at each direction ϕ for the linear flow solution with Pr=0.5, Bi=0. At ϕ=83 deg, 97 deg, Ma_c=20.04, for Γ=0, and Ma_c=20.27, for Γ=0.1.

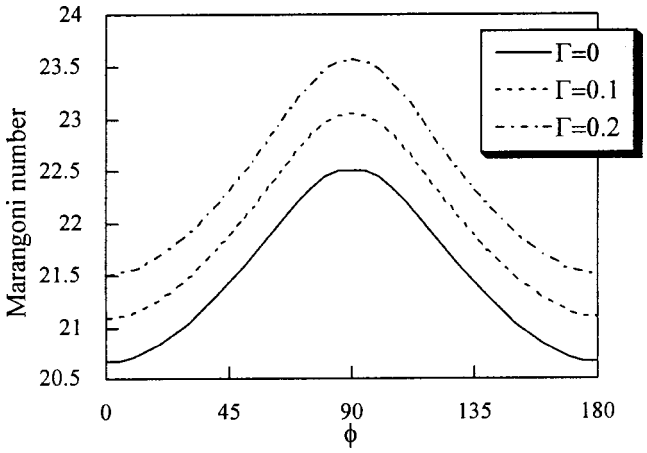

Fig. 6 The effect of the parameter Γ on the minimum Marangoni number at each direction ϕ for the linear flow solution with Pr=1, Bi=0. At ϕ=0 deg, 180 deg, Ma_c=20.67, for Γ=0, and Ma_c=21.09, for Γ=0.1, Ma_c=21.50, for Γ=0.2.

15.68 for Γ=0.1. At ϕ=0°, the critical Marangoni number is 20.63 for Γ=0 and 21.07 for Γ=0.1.

As stated by Smith [12], there is a narrow range of Prandtl number around 1, for which the preferred mode takes the form of stream-wise traveling wave. In Fig. 6, our calculation shows that ϕ=0 deg corresponds to the minimum Marangoni number. Since there is a symmetry about ϕ=90 deg, ϕ=180 deg also corresponds to the minimum Marangoni number. This means that the preferred mode travels both upstream and downstream at the same time. The critical Marangoni number increases from 20.67 for Γ=0 to 21.09 for Γ=0.1, and to 21.50 for Γ=0.2. Surface energy effect, however, does not change the direction of propagation of the most dangerous mode.

Similar stabilizing effect due to the surface energy variation on the onset of instability for the return flow solution is also observed. In Fig. 7, the critical Marangoni number as a function of the propagation angle ϕ is plotted for Pr=1, Bi=0. The most dangerous angles are 55 deg and 125 deg. There is an increase of 0.85 in the critical Marangoni number when Γ is increased from 0 to 0.1. In Fig. 8, similar stabilizing effect is observed when the Prandtl number is increased to 10, with an increase in the minimum critical Marangoni number from 273.76 to 275.16 for the most dangerous angles 20 deg and 160 deg when Γ is increased from 0 to 0.1.

The physical mechanism of the stabilizing effect due to surface energy variation can be explored with the aid of Fig. 9. Figure 9 is a sketch of the instantaneous streamlines of the disturbance flow, which is periodic in the horizontal direction. Since the surface is non-deformable, $\hat{w}=0$ everywhere along the free surface. Fluids are pulled away from the hot spot A and driven towards the cold spot B. To conserve mass, fluid underneath the hot spot A move upward toward point A, and the fluid underneath the cold spot B move downward away from point B. Thus, $d\hat{w}/dz<0$ near point A and $d\hat{w}/dz>0$ near point B. The linearized interfacial energy balance for the disturbance in normal mode form (Eq. (37)) is:

$$D\hat{\theta}+\mathrm{Bi}\hat{\theta}=\Gamma D\hat{w}. \tag{42}$$

The sign of the second term on the left-hand side of the equation is positive at the hot spot A, and negative at the cold spot B. Physically, the second term on the left-hand side of (42) represents the surface heat loss/gain to/from the environment. The environment obtains energy from the hot spot A and feeds energy to the cold spot B through heat conduction. This cooling/heating mecha-

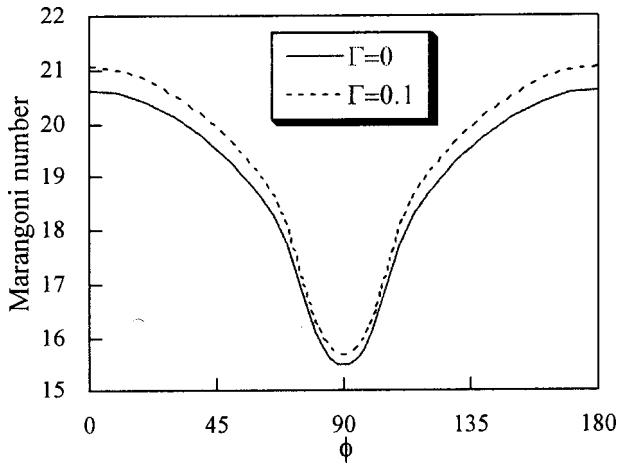

Fig. 5 The effect of the parameter Γ on the minimum Marangoni number at each direction ϕ for the linear flow solution with Pr=∞, Bi=0. At ϕ=90 deg, Ma_c=15.48, for Γ=0, and Ma_c=15.68, for Γ=0.1.

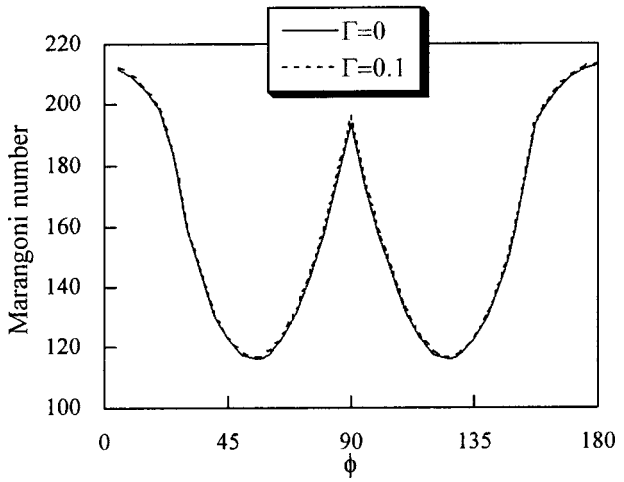

Fig. 7 The effect of the parameter Γ on the minimum Marangoni number at each direction ϕ for the return flow solution with Pr=1, Bi=0. At ϕ=55 deg, 125 deg, Ma_c=116.01, for Γ=0, and Ma_c=116.85, for Γ=0.1.

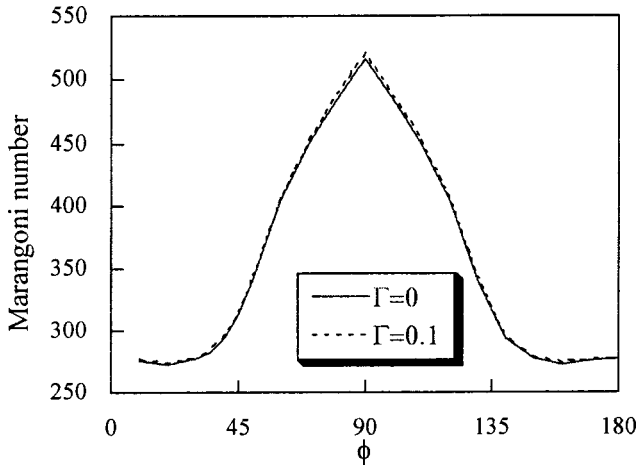

Fig. 8 The effect of the parameter Γ on the minimum Marangoni number at each direction ϕ for the return flow solution with Pr=10, Bi=0. At ϕ=20 deg, 160 deg, Ma_c=273.76, for Γ=0, and Ma_c=275.16 for Γ=0.1.

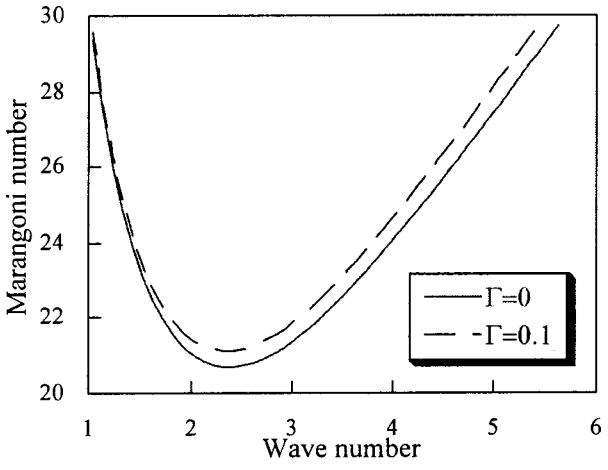

Fig. 10 The neutral stability curves for the linear flow solution with Pr=1, Bi=0, at the most dangerous directions ϕ=0 deg, 180 deg. The stabilizing effect of Γ increases with the wave number.

nism from the environment thus has a tendency to stabilize the system. Because the new dimensionless parameter Γ is a positive constant, the surface energy variation term on the right hand side of (42) is negative near point A, and positive near point B. Since the surface energy variation term on the right hand side of (42) always have the opposite sign to the second term on the left hand side, surface energy variation has the same stabilizing effect on the system.

The simple fact that surface energy increases with temperature means that the surface absorbs energy at high temperature locations and releases energy at low temperature locations. Thus, the physical origin for the stabilizing effect of the surface energy variation due to thermocapillarity is that the free surface absorbs energy in the region where there is an upflow, which corresponds to a hot spot at the free surface where the free surface is stretched, and releases energy in the region where there is a downflow, which corresponds to a cold spot at the free surface where free surface shrinks. In other words, the surface energy variation of the free surface tends to decrease the temperature of the hot spot and increase the temperature of the cold spot through an absorb-release mechanism. As a result, the surface energy variation has a tendency to suppress temperature disturbance at interface and this has a stabilizing effect. The parameter Γ is a measure of the capability of the free surface to absorb/release energy. Since Γ is directly proportional to the base state temperature of the free surface, the free surface can absorb more energy at a hot spot and release more energy at a cold spot at higher base state surface temperature. Thus, the new stabilizing effect due to surface energy variation is stronger at larger values of Γ.

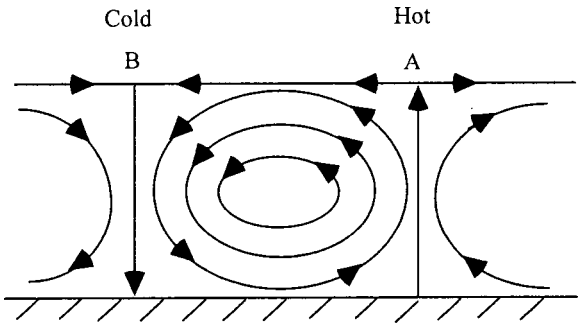

Fig. 9 Sketch of disturbance flow streamlines. Arrows indicate disturbance flow directions.

The above mechanism for the stabilizing effect of the surface energy variation due to thermocapillarity shows that surface energy variation will have a stronger stabilizing effect if the system has stronger upflow or downflow, which corresponds to a larger stretching or shrinking rate of the interface. This can be seen from Fig. 10 and Figure 11. The two figures show that, for both the linear flow and return flow, the stabilizing effect increases with wave number. The reason for this is that large wave number corresponds to circulation cells with decreasing width, which in turn means stronger vertical velocity disturbance, and as a result, the stabilizing effect of the surface energy variation will be stronger. Figures 12 and 13 show the stabilizing effect of Γ on the linear flow and the return flow as a function of Prandtl number. The stabilizing effect is stronger when Prandtl number is greater than 0.1.

The free surface in the base state is planar for the case studied in this paper. Thus, there is no surface dilatation in the base state. When there is surface dilatation in the base state, an additional term $\theta\gamma\nabla_{II}\cdot\mathbf{U}$ will appear at the right hand side when the surface energy balance equation (13) is linearized, where $\nabla_{II}\cdot\mathbf{U}$ is the surface dilatation of the base state and θ is the surface disturbance temperature. If surface dilatation $\nabla_{II}\cdot\mathbf{U}$ is strong, which can occur when the convection slot is not shallow, then this extra term could

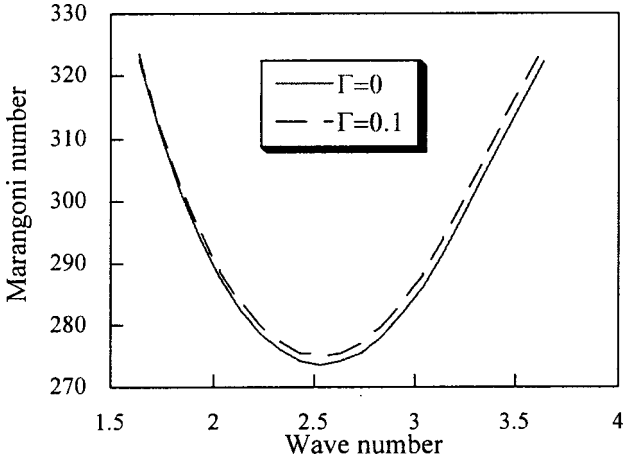

Fig. 11 The neutral stability curves for the return flow solution with Pr=10, Bi=0, at the most dangerous directions ϕ=20 deg, 160 deg. The stabilizing effect of Γ increases with the wave number.

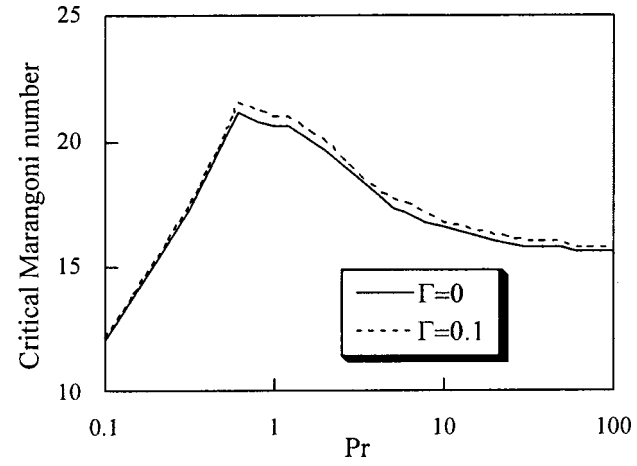

Fig. 12 The stabilizing effect of Γ on the critical Marangoni number corresponding to the most dangerous direction as a function of the Prandtl number for the linear flow with Bi=0

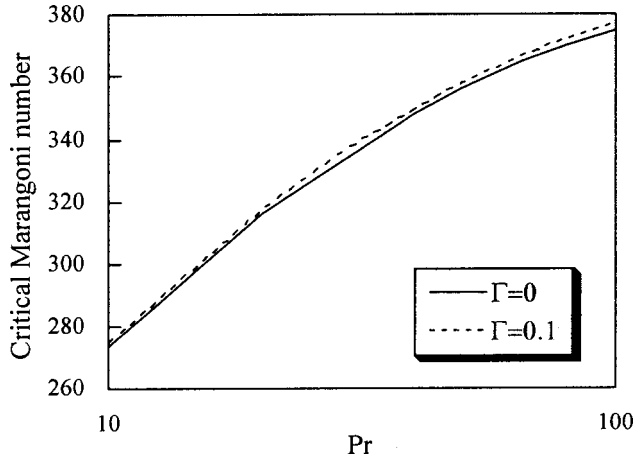

Fig. 13 The stabilizing effect of Γ on the critical Marangoni number corresponding to the most dangerous direction as a function of the Prandtl number for the return flow with Bi=0

contribute strongly to the stability problem. This aspect of the surface energy variation effect has not yet been investigated.

5 Conclusions

An interfacial energy balance equation taking into account surface energy variation has been derived for general two-layer flows of two immiscible fluids with or without evaporation/condensation. When this energy balance equation is applied to thermocapillary flows, it is found that, in general, the convective motion of thermocapillary flow caused by instability depends on the absolute temperature as well as the dilatation of the free surface, not just the temperature gradient in normal or horizontal direction as in the classical theories. Studies on the thermocapillary flows for a thin liquid layer heated from one side show that the surface energy variation due to thermocapillarity has an nonnegligible stabilizing effect on the onset of thermocapillary instabilities. The increase in the critical Marangoni number for the onset of thermocapillary instability increases with the parameter Γ. The critical Marangoni number is increased by about 1 for $\Gamma=0.1$, which is not uncommon for liquid organic compounds at room temperature. The direction of the propagation of the most dangerous disturbance wave, however, is not affected by this surface energy variation effect.

A physical mechanism for the stabilizing effect due to the surface energy variation is explored. The free surface tends to absorb energy from the system in the region with an upflow, which corresponds to a hot spot at the free surface where the free surface is stretched, and release energy in the region with a down flow, which corresponds to a cold spot at the free surface where the free surface shrinks. This absorb-release mechanism redistributes the disturbance energy evenly across the interface. As a result, higher disturbance energy is required to destabilize the system.

Nomenclature

ρ = fluid density
$\mathbf{u}$ = fluid velocity
e = specific internal energy of the fluid
U^S = surface internal energy per unit area (surface specific internal energy)
$\mathbf{q}$ = heat flux vector
$\mathbf{t}$ = traction
V_1, V_2, $V(V=V_1+V_2)$ = the control volumes with boundaries ∂V_1, ∂V_2, ∂V, respectively
Σ = interface between V_1 and V_2
$\mathbf{n}_{12}$ = outward unit normal pointing from 1 to 2 at the interface
τ = the unit tangential vector of Σ at $\partial\Sigma$
$\mathbf{u}_\Sigma$ = the velocity of the interface
h = thermal conductance of the surface
θ_{air} = ambient air temperature
Q_0 = prescribed heat flux across the surface
m = mass flux across the interface
μ = dynamic viscosity
ν = kinematic viscosity
k = thermal conductivity
κ = thermodiffusivity
C = $\mu\kappa/d\sigma$, the crispation number
θ_0 = the basic state free surface temperature at $x=0$
σ = surface tension
σ_0 = the surface tension at θ_0,
γ = $-d\sigma/d\theta$ at $\theta=\theta_0$
Ma = $\gamma b d^2/\mu\kappa$ (Marangoni number)
Pr = ν/κ (Prandtl number)
Bi = hd/k (Biot number)
Γ = $\theta_0\gamma^2/\mu k$

References

[1] Bénard, H., 1900, "Les Tourbillons Cellulaires dans une Nappe Liquide," Rev. Gen. Sciences Pure Appl., **11**, pp. 1309–1328.
[2] Block, M. J., 1956, "Surface Tension as the Cause of Bénard Cells and Surface Deformation in a Liquid Film," Nature, **178**, pp. 650–651.
[3] Lord, Rayleigh, 1916, "On Convection Currents in a Horizontal Layer of Fluid, When the Higher Temperature is on the Under Side," Philos. Mag., **32**, pp. 529–546.
[4] Pearson, J. R. A., 1958, "On Convection Cells Induced by Surface Tension," J. Fluid Mech., **4**, pp. 489–500.
[5] Smith, M. K., and Davis, S. H., 1983, "Instabilities of Dynamic Thermocapillary Liquid Layer. Part 1. Convective Instabilities," J. Fluid Mech., **132**, pp. 119–144.
[6] Chen, K. P., 1997, "Interfacial Energy Balance Equation for Surface-Tension-Driven Bénard Convection," Phys. Rev. Lett., **22**, pp. 4395–4397.
[7] Joseph, D. D., and Renardy, Y. Y., 1992, *Fundamentals of Two-Fluid Dynamics*, **1**, Springer-Verlag, New York.
[8] Joseph, D. D., 1976, *Stability of Fluid Motions(II)*, Springer-Verlag, New York.
[9] Hirschfelder, J. O., Curtiss, C. F., and Bird, R. B., 1954, *Molecular Theory of Gases and Liquids*, John Wiley & Sons, New York.
[10] Harkins, W. D., 1952, *The Physical Chemistry of Surface Films*, Reinhold Publishing, New York.
[11] Orszag, S. A., and Kell, L. C., 1980, "Transition to Turbulence in Plane Poisuille and Plane Coutte Flow," J. Fluid Mech., **96**, pp. 159–205.
[12] Smith, M. K., 1986, "Instability Mechanisms in Dynamic Thermocapillary Liquid Layers," Phys. Fluids, **29**, pp. 3182–3186.

Heat Transfer of Impacting Water Mist on High Temperature Metal Surfaces

N. Sozbir[1]

Y. W. Chang

S. C. Yao
e-mail: scyao@cmu.edu

Department of Mechanical Engineering,
Carnegie Mellon University,
Pittsburgh, PA 15213

Experimental studies were conducted to reveal the heat transfer mechanism of impacting water mist on high temperature metal surfaces. Local heat transfer coefficients were measured in the film-boiling regime at various air velocities and liquid mass fluxes. The test conditions of water mist cover the variations of air velocity from 0 to 50.3 m/s, liquid mass flux from 0 to 7.67 kg/m^{2}s, and surface temperature of stainless steel between 525°C and 500°C. Radial heat transfer distributions were measured at different liquid mass fluxes. The tests revealed that the radial variation of heat transfer coefficients of water mist has a similar trend to the air jet cooling. At the stagnation point, heat transfer coefficient increases with both the air velocity and the liquid mass flux. The convective air heat transfer is consistent with the published correlation in the literature. The heat transfer contribution due to the presence of water increases almost linearly with the liquid mass flux. The total heat transfer coefficient can be established as two separable effects, which is the summation of the heat transfer coefficient of air and of liquid mass flux, respectively. This study shows that with a small amount of water added in the impacting air jet, the heat transfer is dramatically increased. The Leidenfrost temperature under water mist cooling was also measured. The Leidenfrost temperature increased with both the air velocity and the liquid mass flux. [DOI: 10.1115/1.1527913]

Keywords: Boiling, Cooling, Droplet, Heat Transfer, Sprays

Introduction

Traditionally water sprays have been used extensively in metallurgical industries for the cooling of high temperature metals at film boiling. Sprays are made of large drops, in the order of 100 μm or larger, and operated at high mass flux to give high heat transfer rates. However, the heat transfer distribution frequently is not uniform and water utilization efficiency is low.

Recently, more and more industrial processes use water mist for cooling. Water mist contains small droplets, in the order of or less than 100 μm, and carries co-flowing air which are entrained or are used for atomization. The mass flux of water mist is low and therefore, the heat transfer rate is not as high as sprays; however, the water mist provides relatively uniform heat transfer and has high water usage efficiency. Furthermore, both water and air flow rates can be adjusted to provide a wide range of heat transfer variations. Due to these advantages, water mists are used preferably for cooling of thin metal sheets and for tempering of glass at high temperature film boiling conditions. Water mists have also been proposed for the cooling of electronics at nucleate boiling conditions.

At the film boiling regime, the impacting droplets of water mist will contact with surface for a very short period of time; however, the resulting heat transfer is significant. The contact heat transfer mechanisms include the convection in the layer of vapor underneath the droplets and transient homogeneous nucleation at the point of droplet-surface contact. In additional to the droplet contact heat transfer, there is radiation from the surface and convection to the flowing air on the surfaces. Due to the droplet-surface contacts, material properties and roughness also influence the heat transfer.

When water mist cooling is applied to surfaces at low temperatures, nucleate boiling occurs. Many researchers have studied mist heat transfer at this condition. Typically, the recent ones are Graham and Ramadhyani [1], Lee et al. [2] and Yang et al. [3]. However, studies of mist impingement on surfaces at high temperature film boiling regime are limited. Pedersen [4] studied water droplets impinging upon a heated surface at 1800°F. His data of 200 to 400 μm droplets showed that the approaching velocity is the major parameter affecting droplet heat transfer and that surface temperature has minor effect on heat transfer. Choi and Yao [5] investigated an impacting spray experimentally. An impulse-jet liquid spray system and a solid particle spray system were compared. The effects of air convective were revealed. Nishio and Kim [6] reported the heat transfer of dilute spray impinging on hot surfaces. The report focused on the effects of the rebound motion and sensible heat of droplets on heat transfer in the high temperature region. A simple model was developed to predict the heat flux distribution of a dilute spray impinging on a hot surface. They assumed that the droplet number flow rate of the spray is small that the heat transfer of each droplet is independent.

Ideally, for the impaction cooling of water mist at high surface temperature, the heat transfer contribution of air and water could be separable and independent. An attempt was made by Deb and Yao [7], who modeled the spray cooling by considering droplet impingement heat transfer and air convective heat transfer separately. The overall heat transfer is considered as the summation of these two contributions in addition to radiation cooling. However, no experimental verification was reported in terms of parametric study of these factors to validate this idea directly. In the present study, experiments were conducted on stainless steel disks at the high temperatures to verify these separable effects. Local heat transfer coefficients were measured in film boiling regime. The air flow and water flow are controlled independently and the operational conditions included pure air and water mist at different liquid mass fluxes. As a result, the air and water effects are revealed independently and parametrically. The Leidenfrost temperature was obtained at various air velocities and liquid mass fluxes. Sozbir and Yao [8] investigated a water mist cooling for glass tempering experimentally. Very high velocity air jet impingement was applied during the cooling process of glass tempering. The heat transfer of multiple water mist jets on glass was

[1]Visiting Assistant Professor from Sakarya University, Turkey

Contributed by the Heat Transfer Division for publication in the JOURNAL OF HEAT TRANSFER. Manuscript received by the Heat Transfer Division October 17, 2002; revision received September 3, 2002. Associate Editor: C. T. Avedisian.

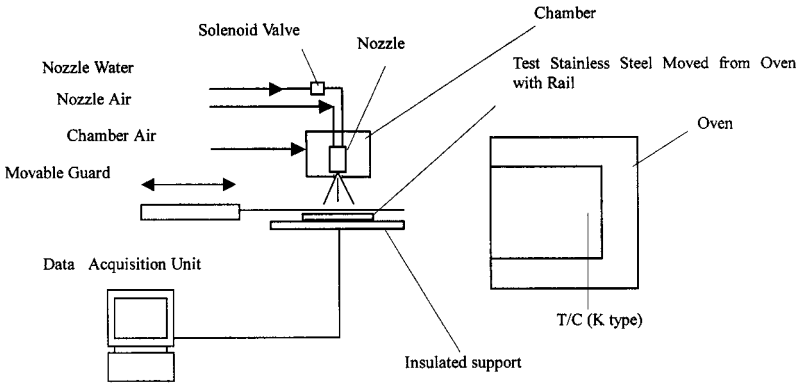

Fig. 1 Schematic of experimental apparatus

studied. The mist cooling demonstrates a definitive saving on the use of high-pressure air. When using mist cooling, the energy requirements of the system are significantly lowered.

Experimental Approach

Experimental Apparatus and Procedure. The experimental apparatus consisted of an air atomizer nozzle, air flow system, liquid supply system, oven, test plate, and a data acquisition unit. A schematic diagram of the system is shown in Fig. 1. The air atomizer nozzle producing the mist flow is depicted schematically in Fig. 2(*a*). It consists of a commercial air-atomizing nozzle (Spraying Systems Co., Air Atomizing, 1/8 J, Full Cone, Round Spray, and Spray Set-up No. SU11), and an air chamber. As shown in Fig. 2(*b*), the chamber contains three air inlets and a pressure gauge. Upstream of the water line is a solenoid on-off valve. At the bottom of air chamber, there is an opening of 7.9 mm diameter. Typically, the air atomizer produces a solid cone of mist at a flow rate of 22.7 cm^3/min (0.006 gpm). The droplet volume median diameter is about 20 μm, when applied with 96.5 kPa (14 psig) air pressure and 68.9 kPa (10 psig) water pressure. The total spray angle was about 13 deg [9].

The schematic of water mist jet impingement is shown in Fig. 3. Before the experiments were carried out, the local flow conditions were measured at a distance of 40 mm from the nozzle. This distance affects the air velocity and drop mass flux. The approaching velocity of impinging pure air was measured by TSI Air Velocity Meters (Velocicalc, Model 8345/8346). The total air supply flow rate in the system was measured with a rotameter. The local liquid mass flux, *G*, was measured directly using a small cylindrical catcher. The total water supply flow rate in the system is measured with a rotameter.

The test plate was made of stainless steel (SS304) with 101.6 mm in diameter, and 1 mm in thickness. To minimize the effect of surface oxidization, the test plates were cleaned with emery paper and liquid cleaner before each test to remove the oxide depositions. Plates are changed regularly after a few tests. To measure the temperature-time history of test plate during cooling, three bare thermocouple wires (Type K) with 0.1778 mm in diameter were spot welded to the backside of the plates. The wires are insulated using ceramic beads. The backside of the plate was insulated with a shallow cavity at room temperature. The temperature variations in time were recorded using a digital data acquisition system (SP 2030, DAS 08/EXP 16).

At the beginning of the experiment, the test plate was heated to an initial temperature about 815°C–870°C (1500°F–1600°F) in the oven. The water mist from the nozzle was turned on and the plate was taken out from the oven to put on the insulated cavity and underneath the shutter, which protect the plate from spray impingement. After the shutter was suddenly removed by the actuation of an air cylinder, the mist impinged on the heated surface.

Data Reduction

Throughout the test, the heated plate was positioned horizontally. It was found that the heat loss at the backside is mainly the radiation. The temperature difference between the front side and the backside through the cooling transient was estimated to be within 10°C. For a stainless steel plate of 1 mm thickness, the

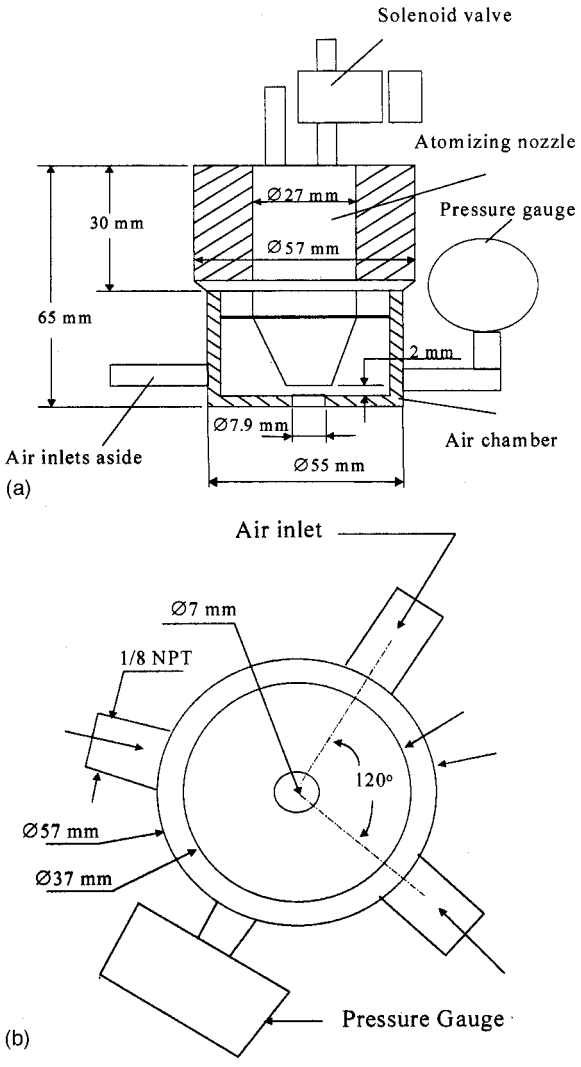

Fig. 2 (*a*) Schematic of experimental nozzle; and (*b*) top view of the nozzle.

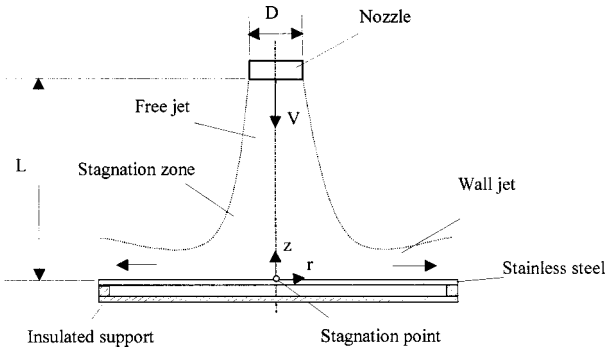

Fig. 3 Schematic of surface impingement model for air convection prediction

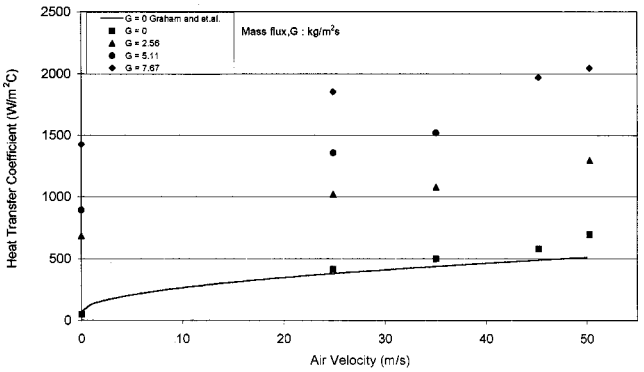

Fig. 4 Experimental result of heat transfer coefficient at 500°C to 525°C

calculated Biot number, based on plate thickness is in the range from 0.05 to 0.11, therefore, it is reasonable to assume a lumped condition to evaluate the surface heat flux, and the inversed conduction method was not necessary. Thus, the temperature measured at the backside was used to represent the mean temperature of the plate during a transient.

The data were taken at a time step of 0.02 seconds. Only the data between 525°C and 500°C (which is beyond the Leindenfrost temperature and drops do not wet the surface) are used to evaluate the heat transfer at various conditions. In fact, this temperature range is also important to the glass tempering and steel rolling processes. Considering the negligible radial conduction over the thin plate a lumped system can be applied to any specific region during cooling. The average heat transfer coefficient was calculated by

$$mC_p(dT/dt) = hA(T_w - T_a) + \varepsilon\sigma 2A(T_w^4 - T_s^4) \tag{1}$$

where m is the disk mass, C_p is the specific heat of the disk, h is the convective heat transfer coefficient, A is the disk heat transfer area at one side, T_w is the disk surface temperature, T_a is the air temperature, T_s is the surrounding temperature (which is close to T_a), ε is the emissivity, and σ is the Stefan-Boltzman constant. The value of emissivity used in the evaluation of radiation heat transfer (from front and back sides of disk) is obtained from cooling tests without mist or forced air-cooling. Natural convective cooling heat transfer is evaluated and use in Eq. (1) to deduce the emissivity at this condition. Generally, radiative heat loss is in order of 10–15 percent of the overall heat transfer during mist cooling in the present study.

Experimental Uncertainty

The measurement error of the air velocity is within 0.1 m/s, the water mass flux is within 0.1 kg/m^{2}s and the thermocouple reading is within 0.4 percent.

The thickness of stainless steel test plate is 1 mm, and the temperature difference between front side and backside during cooling is estimated to be within 10°C. The cooling data, taken between 525 and 500°C, are used to evaluate the change in temperature with time, dT/dt, as given in Eq. (1). Since this is well within the film-boiling regime, the rate of change in temperature is steady. Therefore, all the consistent errors, such as the assumption of lumped approach, will not affect dT/dt and the results of data reduction. This also reduces the possible error because the inversed conduction is not used. The estimated error of the deduced heat transfer coefficient is therefore in the order of 0.4 percent due to the uncertainty of thermocouples readings.

Another possible source of error comes from the calibration of surface emissivity during the pure air-cooling tests. Considering a 5 percent error of the natural convection formula, the resulting error on the estimated emissivity will be order of 7 percent. When this emissivity is used in equation (1), an estimated error on heat transfer coefficient will be order of 0.85 percent. Combine this data reduction uncertainty with the thermocouple reading uncertainty, the overall uncertainty of heat transfer coefficient is in the order of 1 percent.

Results and Discussion

Air Convection Cooling. The experimental results of air convective cooling without droplets are compared with existing correlations at stagnation point in the literature. Although the heat transfer of laminar round jet has been reported by Incropera and Dewitt [10] and Martin [11], the configuration of the nozzle used in Graham and Ramadhyani [1] is most relevant to the present study. They reported the three-dimensional stagnation point Nusselt number $\mathrm{Nu}_{a,o}$ as:

$$\mathrm{Nu}_{a,o} = \mathrm{Re}_D^{0.5}\mathrm{Pr}^{0.4} \tag{2}$$

When the Reynolds number, Re_D, and stagnation point Nusselt number, $\mathrm{Nu}_{a,o}$ are based on jet velocity and air nozzle diameter then

$$\mathrm{Nu}_{a,o} = h_{a,o}D/k_a \tag{3}$$

$$\mathrm{Re}_D = VD/\nu \tag{4}$$

where V is the air velocity at the exit of the jet.

The variation of heat transfer coefficient with air velocity is presented in Fig. 4. The experimental heat transfer data of pure air jet (liquid mass flux, G, is zero, solid curve in Fig. 4) are compared to the summation of results from Eq. (2) and radiation heat transfer. Good agreement is shown. The calculated h is about 15 percent below the data. The discrepancy is likely due to the free stream turbulence that enhances the heat transfer of the jet [12]. A similar observation has been addressed in Ref. [7] where a 15 percent free stream turbulence intensity induced 25 percent heat transfer enhancement. The reason for the present data showing a higher level of heat transfer is possibly due to the free stream turbulence in the air jet, which is induced by the complex internal geometry of the air passage in the nozzle, as shown in Fig. 2(a). Considering this, the present data of pure air-cooling is compatible with the general expectation.

Water Mist Cooling. Figure 4 presents the variation of heat transfer coefficient for mist cooling with air velocity at various liquid mass fluxes, G. The data indicate that the heat transfer coefficient increases strongly with the liquid mass flux. When air velocity increases, heat transfer coefficient also increases.

Since the liquid mass flux is the primary factor affecting the heat transfer coefficient, the heat transfer coefficient was replotted against the liquid mass flux in Fig. 5, where the lines are a curve fit to the data. Quantitatively, the heat transfer coefficients improve dramatically with the presence of mist. For example, at 25 m/s air velocity, a small liquid mass flux of 2.56 kg/m^{2}s will

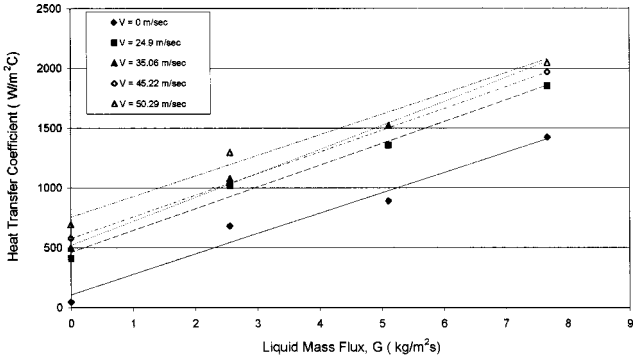

Fig. 5 Heat transfer coefficient against the liquid mass flux

increase the heat transfer to more than double of air convection only. It is also observed that the heat transfer coefficient increases almost linearly with the liquid mass flux.

It is interesting to identify the respective effects of air jet and liquid mass flux in water mist cooling. Therefore, the difference between the total heat transfer data and the pure air data, which is the summation of air jet convective heat transfer and the radiative heat transfer, is used to determine the heat transfer coefficient due to the water mist only. The water mist heat transfer coefficient is then presented with respect to the liquid mass flux in Fig. 6. The figure indicates that the heat transfer contribution of water increases monotonically with the water mass flux. When the mass flux is small the relationship is rather linear. When the mass flux increases the effect is slightly less than linear, which is likely due to the interference effect of drops on surface heat transfer. This occurs when the spray density increases and drops are not having independent heat transfer because frequently the local surface temperature does not fully recover before another drop impact to a same point. Also the jet velocity does not influence significantly to the water mist heat transfer. In other words, droplet velocity has a relatively minor effect to the heat transfer of mist. This has also been reported in Ref. [5, 7] before. This possibly due to the increase of velocity may increase the droplet deformation during an impact, but decrease the time duration of the interaction. These two effects tend to compensate each other when considering their effect on the heat transfer results. To correlate the primary of liquid mass flux, this water mist heat transfer coefficient can be represented as:

$$h_{\text{mist}} = 284 G^{0.8} \tag{5}$$

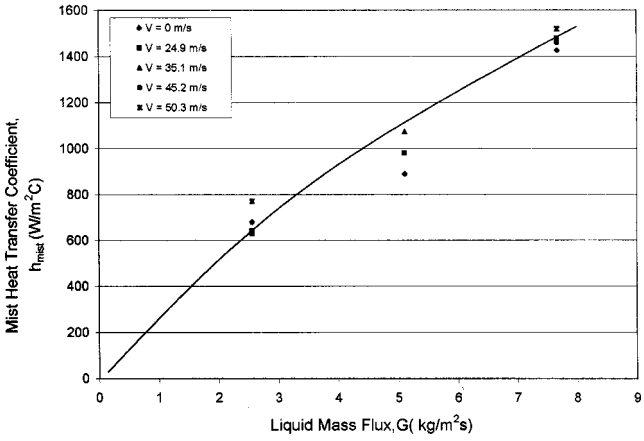

Fig. 6 The difference of total and air heat transfer coefficient against the liquid mass flux

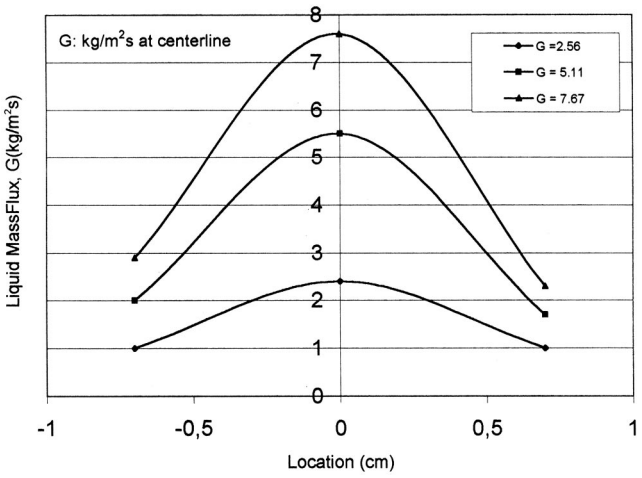

Fig. 7 Radial spray liquid mass flux distributions ($V = 35$ m/s)

Where h_{mist} is water mist heat transfer coefficient in W/m^2°C and G is liquid mass flux in kg/m^{2}s.

The relationship can be written in non-dimensional form as:

$$\text{Nu}_{\text{mist}} = 194\, \text{Re}_l^{0.8} \tag{6}$$

where

$$\text{Nu}_{\text{mist}} = h_{\text{mist}} D / k_l \tag{7}$$

$$\text{Re}_l = GD / \mu_l \tag{8}$$

It is noticed that the nozzle orifice diameter, D, is taken as the characteristic length to be consistent with the air convection formulation.

Accordingly, the overall heat transfer of the dilute mist flow, without considering the radiation, can be predicted as the summation of air and water mist components in the form of

$$h_{\text{conv}} = h_{a,o} + h_{\text{mist}} \tag{9}$$

Where the $h_{a,o}$ can be evaluated from Eq. (2) and h_{mist} from Eq. (6). Therefore, for water mist cooling at film boiling condition, the convective heat transfer of air and liquid mass flux can be accounted for separately.

Radial Distributions. The radial distribution of water mist heat transfer is important for the quality control during the cooling processes of metal and glass sheets. The radial water mass flux distribution of the spray was measured using several of small tubes to catch the spray deposition directly. A typical result is shown in Fig. 7 at different flow rates. The resulting radial heat transfer distribution at different liquid mass fluxes is shown in Fig. 8. All the data are at a constant air velocity of 35 m/s. The locations of thermocouples are at center, 16.93 and 33.87 mm from the center stagnation point. In Fig. 8, the heat transfer coefficients at different radial locations are normalized by the heat transfer of mist flow at the stagnation point as described in Eq. (9). The figure indicated that the normalized radial heat transfer distribution of water mist is also very close to that of the pure air jet case. This is possibly due to the small size of water mist drops ($\sim$20 μm). It appears that since the droplets are entrained with the air, the deposition and mist heat transfer distributions are similar to the pure air flow case.

Leidenfrost Temperature. The experimental results of the Leidenfrost temperature, T_{LF} at the center stagnation point of the plate are given with respect to the liquid mass flux, G, in Fig. 9. The Leidenfrost temperature is defined as the temperature associated with minimum heat flux on the film-boiling curve. Since the

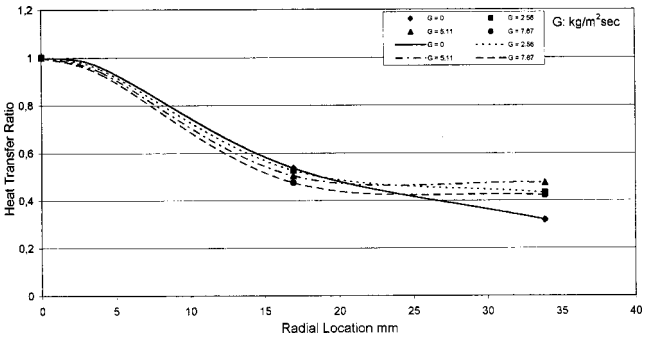

Fig. 8 Heat transfer distributions on the radial direction of a single jet (V=35 m/s)

plate is only 1 mm thick and the cooling process takes only 2 ~3 seconds, the effect of radial conduction is negligible. The data indicates that the Leidenfrost temperature increases for larger values of liquid mass flux. These trends are similar to that reported by Ishigai [13], and Hoogedoorn [14]. However, the present experiment indicates that the Leidenfrost temperature also increases with increasing air velocity (for water mist cooling). At higher air velocity, the droplets impact on surface with more momentum, and induce the quenching easier. As a result, the Leidenfrost temperature is also higher.

Conclusions

Experimental studies were conducted to reveal the heat transfer of dilute water mist on high temperature metal surfaces. Local heat transfer coefficients were measured in film boiling regime at various air velocities and liquid mass fluxes. Radial heat transfer distributions were also studied. The Leidenfrost temperature against the air velocity and the liquid mass flux was discussed. The major conclusions from the study are as follows:

1. With a small amount of water in the air jet, the heat transfer is dramatically increased. The water mist heat transfer coefficient increases with both the air velocity and the liquid mass flux. Mist and air heat transfer are independent.
2. The convective air heat transfer is consistent with the predictions based on correlation in the literature.
3. Mist heat transfer increases almost linear with the water mass flux. The velocity effect is small.
4. The overall convective heat transfer coefficient can be viewed as two separable elements, which is the summation of the heat transfer coefficients of air and of liquid mass flux, respectively. For a general prediction, Eq. (9) can be used where Eqs. (2) and (6) can be applied.
5. The normalized radial distribution of mist flow heat transfer is similar to that of pure air jets.
6. The Leidenfrost temperature increases with both the air velocity and the liquid mass flux.

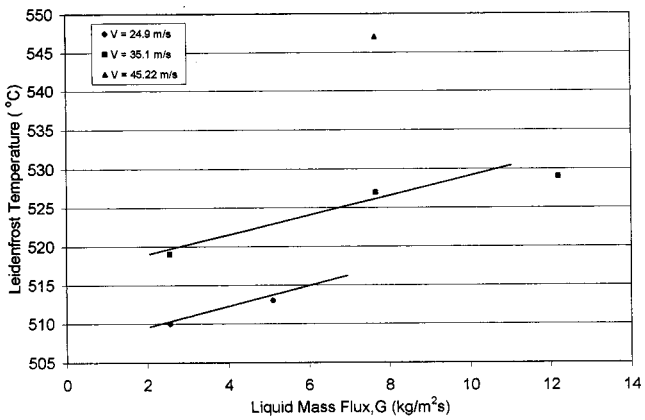

Fig. 9 Variation of Leidenfrost temperature with liquid mass flux

Acknowledgment

The authors wish to thank Pilkington North America, Inc. for the financial support of this study. The technical guidance and advice of Mr. T. A. Dunifon, Mr. B. Thomas and Dr. A. C. Woodward are gratefully appreciated.

Nomenclature

A = area, m^2
Bi = Biot number
C_p = constant pressure specific heat, kJ/kgK
D = nozzle opening diameter, m
G = liquid mass flux, kg/m^2 sec
h = heat transfer coefficient, $W/m^2°C$
k = conductivity, W/m°C
m = mass, kg
Nu = Nusselt number
Pr = Prandtl number
Re = Reynolds number
T = temperature, K, °C
t = time, sec
V = air velocity, m/s
ε = emissivity
μ = dynamic viscosity, Pa s
σ = Stefan-Boltzman constant, $W/m^2 K^4$

Subscript

a = air convective cooling
D = nozzle opening diameter
LF = Leidenfrost
l = water
o = stagnation point
s = surrounding
w = wall

References

[1] Graham, K. M., and Ramadhyani, S., 1996, "Experimental and Theoretical Studies of Mist Jet Impingement Cooling," ASME J. Heat Transfer, **118**, pp. 343–349.
[2] Lee, S. L., Yang, Z. H., and Hsyua, Y., 1994, "Cooling of a Heated Surface by Mist Flow," ASME J. Heat Transfer, **116**, pp. 167–172.
[3] Yang, J., Chow, L. C., and Pais, M. R., 1996, "Nucleate Boiling Heat Transfer in Spray Cooling," ASME J. Heat Transfer, **118**, pp. 668–671.
[4] Pedersen, C. O., 1969, "An Experimental Study of the Dynamics Behavior and Heat Transfer Characteristics of Water Droplets Impinging upon a Heated Surface," Int. J. Heat Mass Transf., **13**, pp. 369–380.
[5] Choi, K. J., and Yao, S. C., 1987, "Mechanisms of Film Boiling Heat Transfer of Normally Impacting Spray," Int. J. Heat Mass Transf., **30**, pp. 311–318.
[6] Nishio, S., and Kim, Y. C., 1987, "Heat Transfer of Dilute Spray Impinging on Hot Surface—Simple Model Focusing on Rebound Motion and Sensible Heat of Droplets," Int. J. Heat Mass Transf., **41**, pp. 4113–4119.
[7] Deb, S., and Yao, S. C., 1989, "Analysis on Film Boiling Heat Transfer of Impacting Sprays," Int. J. Heat Mass Transf., **32**, pp. 2099–2112.
[8] Sozbir, N., and Yao, S. C., 2002, "Investigation of Water Mist Cooling for Glass Tempering System," ASME International 6th *Biennial Conference on Engineering Systems Design and Analysis (ESDA 2002)*, Istanbul, Turkey, July 8–11.
[9] *Industrial Spray Products*, Spraying Systems Co., Catalog 60, Wheaton, IL.
[10] Incropera, F. P., and DeWitt, D. P., 2001, *Fundamental of Heat and Mass Transfer*, 5th ed., Wiley, New York.
[11] Martin, H., 1977, "Heat and Mass Transfer Between Impinging Jets and Solid Surfaces," Adv. Heat Transfer, **13**, pp. 1–60.
[12] McCormick, D. C., Test, F. L., and Lessman, R. C., 1984, "The Effect of Free-Stream Turbulence on Heat Transfer from a Rectangular Prism," ASME J. Heat Transfer, **106**, pp. 268–275.
[13] Ishigai, S., Nakanishi, S., and Ochi, T., 1979, "Mist Cooling of a Hot Surface," *16th National Heat Transfer Symposium of Japan*, (in Japanese), pp. 316.
[14] Hoogendoorn, C. J., and den Hond, R., 1974, "Leidenfrost Temperature and Heat Transfer Coefficients for Water Sprays Impinging on a Hot Surface," *Proc. of 5th International Heat Transfer Conference*, **4**, Tokyo, pp. 135–138.

Effect of Pressure, Subcooling, and Dissolved Gas on Pool Boiling Heat Transfer From Microporous Surfaces in FC-72

K. N. Rainey
e-mail: rainey@lanl.gov
Los Alamos National Laboratory,
P.O. Box 1663, MS-P940,
Los Alamos, NM 87545-1663

S. M. You
e-mail: you@uta.edu
The University of Texas at Arlington,
Department of Mechanical and Aerospace Engineering,
Box 19023,
Arlington, TX 76019-0023

S. Lee
e-mail: seri.lee@intel.com
Intel Corporation,
Desktop Architecture Lab,
JF2-54,
2111 N.E. 25th Avenue,
Hillsboro, OR 97124-5961

The present research is an experimental study of the effects of pressure, subcooling, and non-condensable gas (air) on the pool nucleate boiling heat transfer performance of a microporous enhanced and a plain (machine-roughened) reference surface. The test surfaces, 1-cm^2 flat copper blocks in the horizontal, upward facing orientation, were immersed in FC-72. The test conditions included an absolute pressure range of 30–150 kPa, a liquid subcooling range of 0 (saturation) to 50 K, and both gas-saturated and pure subcooling conditions. Effects of these parameters on nucleate boiling and critical heat flux (CHF) were investigated. Results showed that, in general, the effects of pressure and subcooling on both nucleate boiling and CHF were consistent with the prevailing trends in the literature. For the present heater geometry, the effects of dissolved gas on the boiling performance were generally small, however, as the dissolved gas content increased (through either increased pressure or subcooling) more of the nucleate boiling curve was affected (enhanced). The enhancement of CHF from increased liquid subcooling was greater for the microporous surface than the plain surface. Correlations for both nucleate boiling and CHF were also presented. [DOI: 10.1115/1.1527890]

Keywords: Boiling, Cooling, Enhancement, Gaseous, Heat Transfer

Introduction

The continual advancement of microelectronic chip designs in the electronics industry is creating the need for better, more efficient heat dissipation than conventional (single-phase) cooling schemes can provide. One possible solution that has received much attention is to utilize boiling heat transfer for heat dissipation. Currently, the most promising fluids for this type of cooling scheme are dielectric, highly-wetting fluids such as 3M's Fluorinerts. In order to develop a reliable cooling scheme utilizing boiling heat transfer, the effects of pressure, subcooling, and dissolved gas on the nucleate boiling heat transfer performance of these highly-wetting fluids must be known.

It has long been known that increased pressure improves the nucleate boiling performance (increased heat transfer coefficients). The nucleate boiling data of Nishikawa et al. [1] with various Freons and Watwe et al. [2] with FC-72 confirm this behavior for highly-wetting fluids. Using Han and Griffith's [3] theory, Nishikawa et al. [1] attributed this behavior to an increase in the range of cavity radius that may be activated at a given wall superheat with increased pressure (increased active nucleation site density). Nishikawa et al. also found that this caused the enhancement effectiveness of increased surface roughness to diminish at higher pressures. You et al. [4] and Watwe et al. [2] have shown that Rohsenow's [5] well-known nucleate boiling correlation predicts the effect of pressure reasonably well for highly-wetting fluids. With regard to the critical heat flux (CHF), Morozov [6] showed that the CHF increases with increasing pressure up to about one-third of the critical pressure and then decreases. Bar-Cohen and McNeil [7] and Watwe et al. [2] have shown that Zuber's [8] well-known CHF correlation predicts the effects of pressure reasonably well for highly-wetting fluids. In addition, You et al. [9] observed that increased pressure significantly reduced the incipient superheat in FC-72.

In fully-developed nucleate boiling, subcooling has been found to have little or no effect on the boiling performance [10]. You et al. [4] and later Watwe et al. [2] confirmed this behavior for FC-72. However, subcooling has been found to have a significant effect in the isolated bubble regime, particularly with small heating surfaces [4,11,12]. With regard to CHF, it has been observed that CHF significantly increases with increased subcooling showing a strong dependence [13,14]. Elkassabgi and Lienhard [13] also observed that at very high levels of subcooling the CHF became virtually constant (reached a maximum value). For incipience superheat behavior, there are conflicting reports in the literature. Both Normington et al. [15] and Phadke et al. [16] observed increased incipience superheat with increased subcooling in highly-wetting fluids, however, You et al. [9] observed a negligible effect of subcooling on incipience in FC-72.

The highly-wetting fluids used in electronics cooling research typically can absorb large amounts of non-condensable gases. FC-72, for example, can absorb about 48 percent by volume of air at standard conditions. Therefore, a thorough examination of the effects of dissolved gases on the boiling performance is needed. McAdams et al. [17] reported a strong enhancement of the boiling curve at low heat fluxes (partially-developed nucleate boiling) but only a weak effect at high heat fluxes (fully-developed nucleate boiling). Similar observations have been made by Pike et al. [18], Behar et al. [19], and O'Connor et al. [11]. Additionally, Watwe and Bar-Cohen [20] saw no effect of dissolved gas on the nucleate boiling performance in FC-72. Hong et al. [12] observed a significant effect of dissolved gas on the nucleate boiling curves of small wires in FC-72; however, they found that the effect disappeared at high heat fluxes and for large surfaces. Watwe and Bar-Cohen [20] observed no effect of dissolved gas on CHF. Hong et al. [14] observed a dependence of CHF on dissolved gas only for small heaters when length-scale effects are significant. With regard to

Contributed by the Heat Transfer Division for publication in the JOURNAL OF HEAT TRANSFER. Manuscript received by the Heat Transfer Division December 1, 2001; revision received September 26, 2002. Associate Editor: V. K. Dhir.

incipience, You et al. [9] and later O'Connor et al. [11] observed that at high dissolved gas concentrations, the incipience superheat was reduced.

Although the effects of pressure, subcooling, and dissolved gas on the nucleate boiling performance have been studied for plain surfaces, very little research has been done to determine if the effect of these parameters on enhanced surfaces is the same. The objective of the present work is to investigate the effects of pressure, subcooling, and dissolved gas (air) on the pool boiling heat transfer performance of a microporous enhanced surface and a plain reference surface and develop correlations for nucleate boiling and CHF. Testing was performed using a 1-cm^2 test surface in FC-72 at 30, 60, 100 and 150 kPa absolute pressures and subcoolings of 0 (saturated), 10, 30, and 50 K. In addition, a comparison was made between pure subcooling and gas-saturated conditions at 100 kPa. The results of this study are intended to aid in the design of future electronic cooling schemes involving boiling heat transfer.

Experimental Apparatus and Procedure

Test Facility. The pool boiling test facility used for the present work is shown in Fig. 1. The main test chamber was a stainless steel pressure vessel, 406 mm high and 154 mm in diameter. An internal water-cooled condenser and three band heaters located on the sides and bottom of the chamber were used for bulk fluid temperature control. The power to the three band heaters was controlled with an external temperature controller to maintain a set bulk fluid temperature. A cartridge heater was located in the bottom of the test chamber to provide additional heating/stirring during the degassing process. The test chamber was insulated with 15-mm thick foam insulation. A Type-T thermocouple was placed within the test chamber to measure the bulk liquid temperature. Both test heater assemblies were mounted to the stainless steel support bar within the test chamber (that can accommodate two test heaters). The auxiliary tank above the test vessel was used only for the pure subcooled testing. A cartridge heater was used during degassing and to maintain saturation conditions in the auxiliary tank for the pure subcooled tests. An external, water-cooled condenser was used during the degassing process and atmospheric testing to prevent loss of test liquid. The test liquid surface was maintained at approximately 15 cm above the test heater for the saturated and gas-saturated cases and at approximately 75 cm for the pure subcooled cases. A pressure transducer located in the auxiliary tank was used to measure the internal pressure.

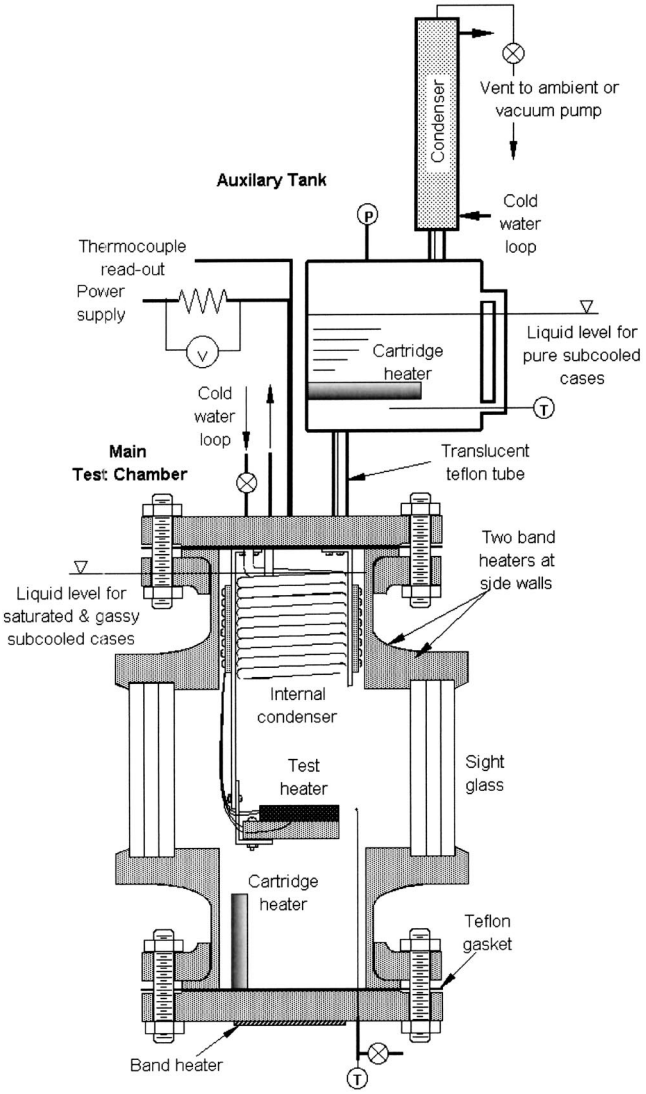

Fig. 1 Schematic of test apparatus

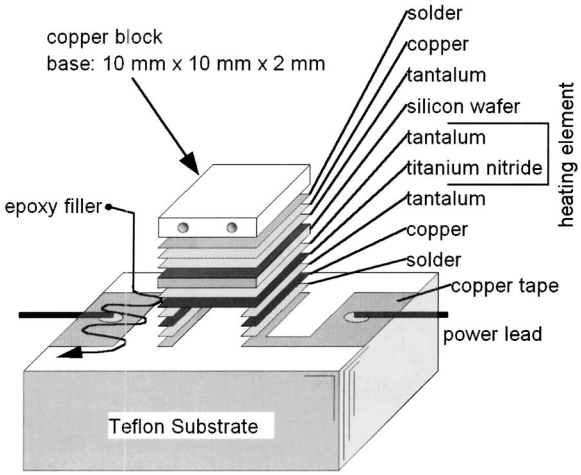

Fig. 2 Test heater design

The electrical circuit used to supply power to the test heater consisted of a computer controlled DC power supply connected in series with a shunt resistor and the test heater. The measured voltage across the test heater and the current determined from the measured voltage across the shunt resistor were used to calculate the heat flux applied to the test heater. All test data were measured with a computer controlled data acquisition system.

Test Heaters. The test heater design is shown in Fig. 2. The heating element was a two-layer thin metal film of tantalum and titanium nitride. The heating element was sputtered onto a 0.5 mm thick silicon nitride coated silicon wafer along with copper for solder connections. The total heating element electrical resistance was about 20 Ω. The heating element side of the wafer was soldered to copper tape for the power lead connections while the other side of the wafer was soldered to the copper block. The copper blocks were machined from solid pieces of copper using a high-speed steel slitting saw blade in the same manner as Rainey and You's [21] plain flat test surface. The copper block dimensions were 10 mm×10 mm×2 mm, and it contained two thermocouple wells centered in the base surface and spaced 5 mm apart and 5 mm deep. The copper/heater assembly was attached to a Teflon substrate (10-mm thick) using a 3M epoxy (1832L-B/A, thermal conductivity ≈0.067 W/m-K). The completed test heater was then mounted in a Lexan frame and surrounded by epoxy to generate a flush-mounted heating surface. The surface condition of the plain heater was ''machine-roughened.'' All the surfaces were cleaned with hydrochloric acid and acetone prior to testing.

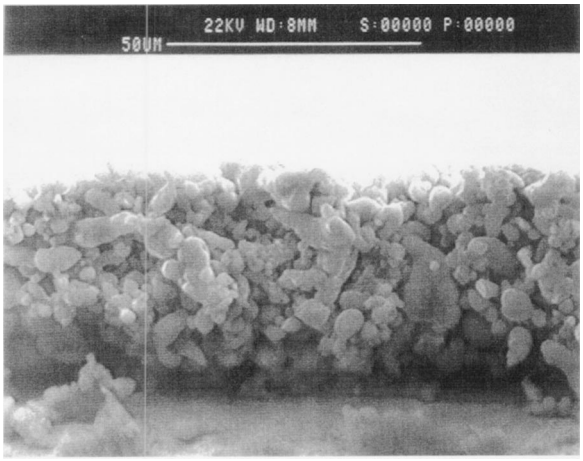

Fig. 3 SEM Photo of ABM microporous coating (side view)

For the microporous coated test heater, the coating used was the ABM coating introduced by Chang and You [22]. The microporous coating technique was previously developed by O'Connor and You [23], further refined by Chang and You [22,24], and patented by You and O'Connor [25]. The coating, shown in Fig. 3, is a surface treatment technique used to increase vapor/gas entrapment volume and active nucleation site density by forming a porous structure of about 0.1–1 μm size cavities. The ABM coating was named from the initial letters of its three components: Aluminum particles/Devcon Brushable Ceramic epoxy/Methyl-Ethyl-Keytone (M.E.K.). The mixture of the three components was drip-coated over the surface using a paintbrush. After the carrier (M.E.K.) evaporated, the resulting layer consisted of microporous structures with aluminum particles (1 to 20 μm in diameter) and a binder (Devcon Brushable Ceramic), having a thickness of $\approx$50 μm. The microporous coating provides no significant increase of the heat transfer surface area. Detailed descriptions of the coating are provided by O'Connor and You [23] and Chang and You [22,24].

Test Procedure. The test fluid, FC-72, is a highly-wetting dielectric perfluorocarbon produced by the 3M Industrial Chemical Products Division. FC-72 has been determined to be a good candidate fluid for immersion cooling applications because it is chemically stable/inert, dielectric, and has a relatively low boiling point ($T_{sat}=56°C$ at atmospheric pressure). Prior to all testing, the test chamber was heated to the test liquid's saturation temperature using the three band heaters and the cartridge heater. Once at saturation temperature, the test liquid was boiled vigorously for at least two hours to remove dissolved gases. All of the test surfaces were tested in the horizontal, upward facing orientation. The test matrix consisted of studies on different subcooling and pressure conditions (Table 1).

Saturated Cases. The fluid level for the saturation cases was maintained in the test chamber at about 15 cm above the test surface. After degassing, the external condenser was turned off. With the system still open to ambient, some of the test liquid was allowed to escape in order to push out any trapped air at the top of the condenser. After about 15 minutes, the valve at the top of the external condenser was closed. A vacuum pump was temporarily connected to the top of the external condenser to further make sure that all trapped air at the top of the condenser was removed. The measured temperature and pressure readings within the test chamber were checked against the FC-72 saturation curve to ensure that all non-condensables had been removed. The desired system pressure was then established by controlling the bulk fluid temperature using the internal condenser and three band heaters. After the desired pressure was obtained and stabilized, testing began. For the saturated tests at atmospheric pressure, a simpler procedure was used. Instead of the closed system approach above, the external condenser was left on and open to ambient (same procedure used by [21]).

Table 1 Test Matrix

Pressure, P_{sys} (kPa)	Subcooling, ΔT_{sub} (K)			
	0 (sat.)	10	30	50
30	X^1	X^1	...	...
60	X^1	X^1	X^1	...
100	X^2	X^2	X^2	...
150	X^1	X^{1}*	X^{1}*	X^{1}*

[1]gas-saturated only
[2]both pure subcooling and gas-saturated
*microporous surface only

Gas-Saturated Cases. The fluid level for the gas-saturated cases was maintained in the test chamber at about 15 cm above the test surface. After degassing, the external condenser was turned off and the valve at the top of the condenser was closed. The desired bulk fluid temperature was then established using the internal condenser and three band heaters. Once the desired temperature was obtained and stabilized, the valve at the top of the condenser was repeatedly cracked opened until the system stabilized at the desired pressure (the valve was then left closed during testing). This procedure produces a gas-saturated initial condition [12]. Although the gas content was not measured, it could be estimated from the relation $P_g=P_{sys}-P_v$, where P_{sys} is measured and $P_v=P_{sat}(T_{bulk})$. Testing then commenced. For the gas-saturated cases at atmospheric pressure, the external condenser was left on and open to ambient conditions.

Pure Subcooled Cases. In the present study, the pure subcooled testing was only performed at atmospheric pressure. The fluid level for the pure subcooled cases was maintained in the auxiliary tank at about 75 cm above the test surface. After degassing, the fluid in the auxiliary tank was maintained at saturation conditions for all of the pure subcooled testing to prevent regassing the subcooled fluid in the test chamber. With the system still open to ambient conditions, the desired bulk fluid temperature in the test chamber was then established using the internal condenser and three band heaters. Once the desired temperature was obtained and stabilized, testing began.

Boiling Curves. After the proper fluid conditions were obtained and stabilized, two consecutive boiling curves were generated for each test surface. Identical boiling curves for each surface assured the consistency and repeatability of the data. There was a two-hour delay between runs to allow the heater and test section to return to steady-state. Heat flux was controlled by voltage input. After each voltage change (heat-flux increment), a 15-second delay was imposed before initiating data acquisition. After the delay, the computer repeatedly collected and averaged 125 base surface temperature measurements over 15 seconds until the temperature difference between two consecutive averaged temperature measurements for all thermocouples was less than 0.2 K. The test heater at this point was assumed to be at steady-state. After reaching steady state, the heater surface and bulk fluid temperatures were measured and the heat flux was calculated. For heat flux values greater than $\approx$80 percent of CHF, instantaneous surface temperature was monitored for 45 seconds after each increment to prevent heater burnout. Each instantaneous surface temperature measurement was compared with the previous steady-state surface temperature measurement. If a temperature difference larger than 20 K was detected, CHF was assumed and the power shut off. The CHF value was computed as the steady-state heat flux value just prior to power supply shutdown plus half of the increment.

Experimental Uncertainty. The stability of the bulk fluid temperature was maintained within a maximum variation of ± 0.34 K and system pressure was maintained within a maximum variation of ± 1.7 kPa. Uncertainties for the heat-flux and temperature measurements were estimated for the present heater based on the method of Kline and McClintock [26]. Substrate conduction losses were estimated based on the values reported by O'Connor and You [23], whose heater had a similar construction as the present one. Taking into account both measurement and substrate conduction errors, the uncertainty in heat flux was estimated as 16 percent at 0.5 W/cm^2 and 6 percent at 16 and 80 W/cm^2. In addition, temperature measurement uncertainty was estimated considering thermocouple calibration error, temperature correction for the embedded thermocouples, and thermocouple resolution error. The uncertainty for temperature measurement was ± 0.4 K.

Results and Discussion

The effects of pressure and subcooling on the boiling heat transfer performance in FC-72 were investigated on two different test surfaces: plain (machined roughened) and microporous. All testing were performed under increasing heat flux conditions and in the horizontal, upward facing orientation, as listed in Table 1. The pure subcooled testing was only performed at 100 kPa. The gas-saturated plain surface data at 150 kPa were not included in the present analysis due to excessive surface oxidation during testing.

Reference Boiling Curves. Figure 4 illustrates the saturated nucleate boiling curves of the plain and microporous surfaces at atmospheric pressure. For comparison, the highly polished plain surface of Chang and You [27], the machine-roughened surface of Rainey and You [21], and the microporous (ABM) surface of Chang and You [22] are included. The single-phase natural convection data of all of the surfaces exhibit comparable heat transfer coefficients (indicating equivalent surface areas), hence showing negligible effects due to surface microstructures. The incipient superheat values of the present surfaces are comparable with those of Rainey and You [21] and Chang and You [22] and show the same decreasing trend with increased ''surface roughness'' as previously reported by Rainey and You [21]. O'Connor and You [23] attributed the decrease in incipient superheat for their microporous coating compared to plain surfaces primarily to the presence of larger embryonic bubble diameters produced by increased vapor/gas entrapment in the microstructure. For the plain surfaces, the rougher surface of the machine-roughened surfaces is expected to have larger cavities (larger embryonic bubble sizes) than the highly polished surface and thus exhibit decreased incipient superheats.

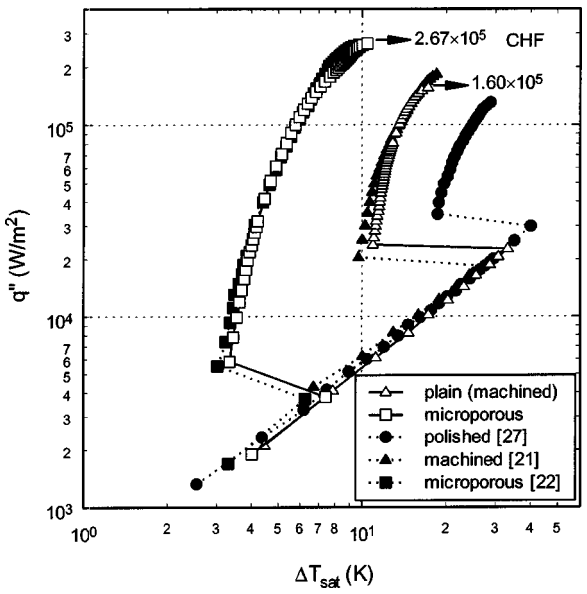

Fig. 4 Reference saturated boiling curves at $P_{sys}=100$ kPa

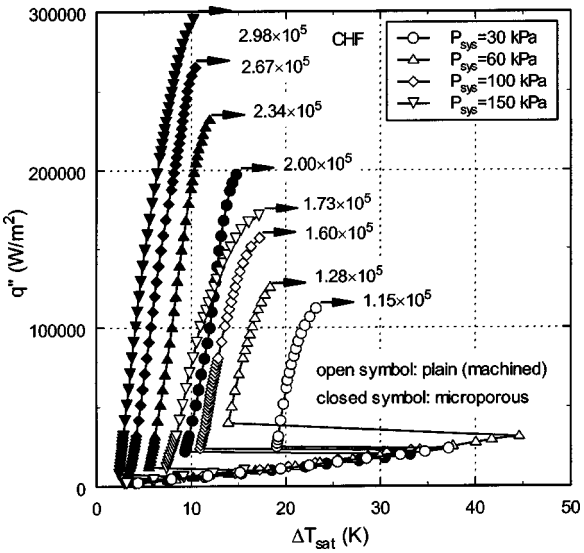

Fig. 5 Pressure effect for plain and microporous saturated boiling curves

The surface microstructure effect on nucleate boiling heat transfer and CHF can be clearly seen in Fig. 4. The nucleate boiling curves of the three types of surfaces in Fig. 4 show significant increases in heat transfer coefficient relative to increasing surface roughness as previously reported by Rainey and You [21], and is believed to be a direct result of increased active nucleation site density. The results of Honda et al. [28] also appear to show this same trend. The CHF values for the present plain and microporous surfaces (shown in Fig. 4) were comparable to the CHF values of 18.8 W/cm^2 reported by Rainey and You [21] for their machine-roughened surface and 26.3 W/cm^2 reported by Chang and You [22] for their microporous surface. For reference, Chang and You [27] reported a CHF value of 13.2 W/cm^2 for the highly polished surface shown in Fig. 4.

Effect of Pressure. Figure 5 illustrates the effect of system pressure on the saturated nucleate boiling curves of the plain and microporous surfaces. In general, the incipient superheat increased with decreasing pressure for both surfaces similar to the observations of You et al. [9]. This means that at low pressures, excessive incipient superheats may be encountered, even with enhanced surfaces. (With regard to electronics cooling, excessive incipient superheats will cause thermal stress on electronic components during boiling initiation and can increase the risk of transitioning directly to film boiling from single-phase convection.) The effect of pressure on the nucleate boiling performance is consistent with the prevailing trend in the literature of increased heat transfer coefficient with increased pressure [1,2,4,29]. In addition, the difference in the nucleate boiling performance between the plain and microporous surfaces appears to decrease with increased pressure. The CHF values also show a significant increasing trend with increased pressure (discussed later), which is consistent with the trends in the literature [2,6,7,29]. From Fig. 5, it appears that the effects of pressure are consistent for both the plain and microporous surfaces.

An additional observation about the shape of the boiling curves in Figs. 4 and 5 is worth noting. According to Rohsenow's [5] well-known nucleate boiling correlation, the majority of the nucleate boiling curve should be ''linear'' when plotted in log-log

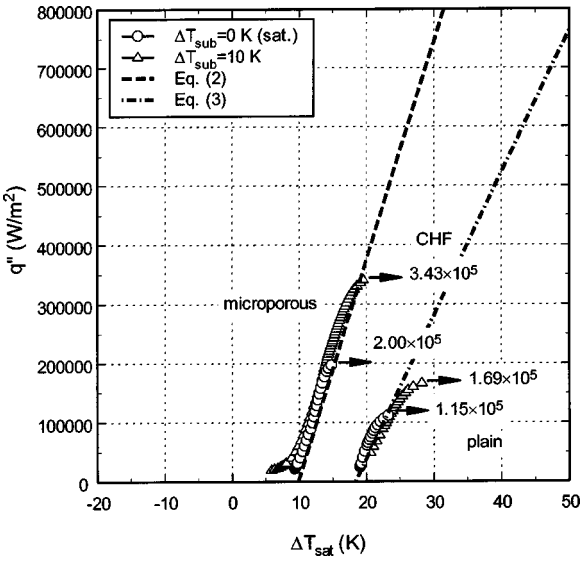

Fig. 6 Gas-saturated boiling curves at $P_{sys}=30$ kPa

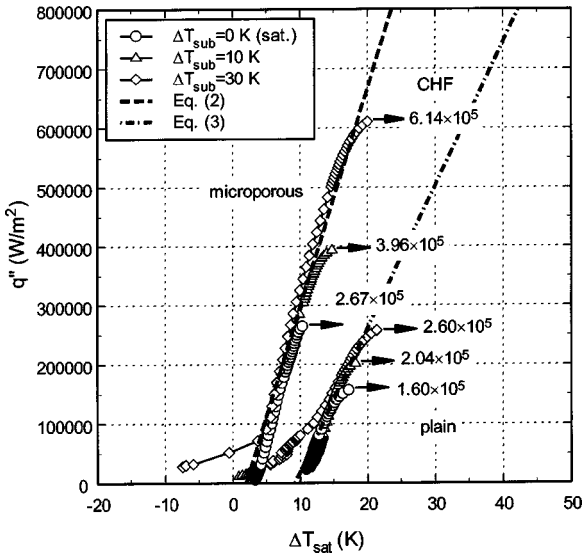

Fig. 8 Gas-saturated boiling curves at $P_{sys}=100$ kPa

scale. From the boiling curves in Figs. 4 and 5, it is observed that the boiling curves would not be well characterized by Rohsenow's correlation (discussed later).

Effect of Liquid Subcooling. For the present work, the subcooling level is defined as $T_{sat}(P_{sys})-T_{bulk}$. P_{sys} equals the fluid vapor pressure, P_v, only for pure subcooled cases while for the gas-saturated cases; P_{sys} equals the sum of the fluid vapor and non-condensable gas partial pressures or $P_{sys}=P_v+P_g$ [12]. Figures 6–9 illustrate the effects of liquid subcooling at all four tested system pressures for both the plain and microporous surfaces. The single-phase convection data have been removed for clarity. The most prominent feature in all of the figures is how the fully developed nucleate boiling curves collapse onto a single line regardless of the subcooling level. This is consistent with the prevailing trend on subcooling effect in the literature [10]. As subcooling increases, the bubble departure diameters and frequencies decrease [30] which reduces the amount of heat transferred through latent heat and microconvection. However, increased subcooling also decreases the superheated liquid layer thickness [31] which increases natural convection heat transfer and increases Marongoni convection heat transfer [32]. These combined effects are seen to result in relative insensitivity of the nucleate boiling curve to liquid subcooling. The results of Honda et al. [28] and Mudawar and Anderson [29] also show this behavior. The effect of the dissolved gas can be seen as an enhancement of the low heat flux boiling performance, which is discussed in the next section.

Gas-Saturated Versus Pure Subcooling. Before discussing the dissolved gas effect, some terminology needs to be clarified. The term ''gas-saturated'' is used in the present work to describe the initial condition of the fluid as being saturated with non-condensable gas (air). The term ''gassy subcooled'' is used in the present work to describe the fluid condition near the heater surface during boiling, which contains an indeterminable amount of dissolved gas; in other words, a condition that is somewhere between gas-saturated and pure subcooled. The term ''pure subcooled'' naturally refers to a completely degassed, subcooled fluid condition. Figure 10 compares gas-saturated and pure subcooled nucle-

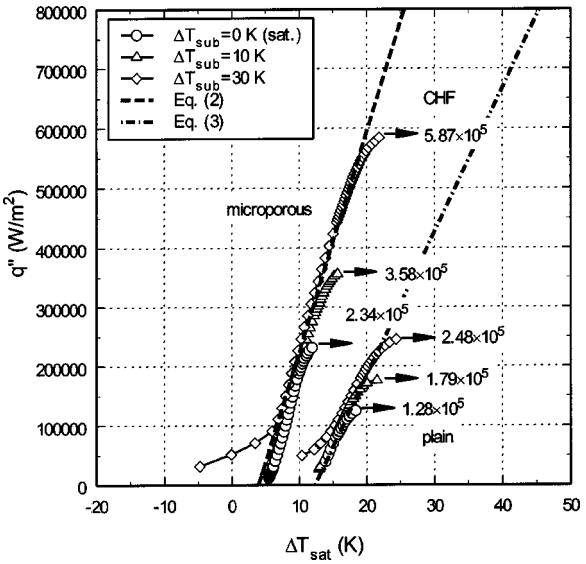

Fig. 7 Gas-saturated boiling curves at $P_{sys}=60$ kPa

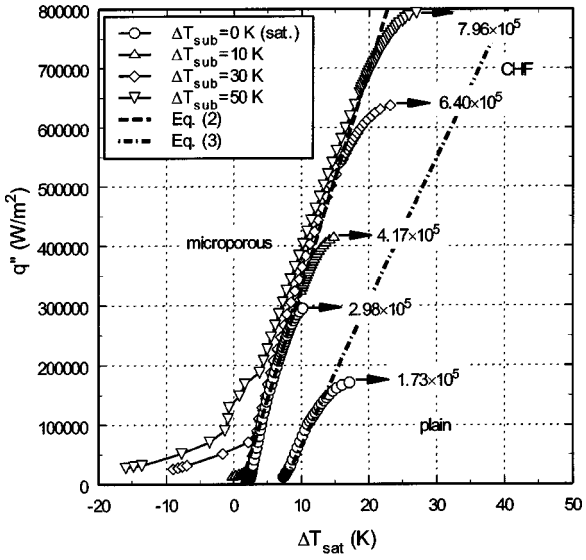

Fig. 9 Gas-saturated boiling curves at $P_{sys}=150$ kPa

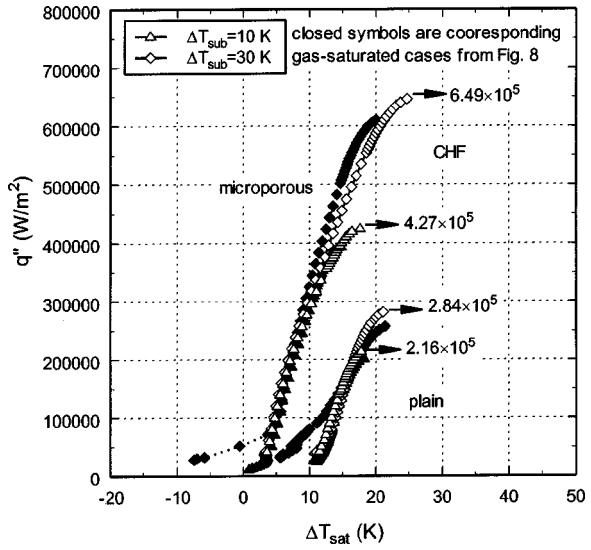

Fig. 10 Comparison of pure subcooled and gas-saturated boiling curves at $P_{sys}=100$ kPa

ate boiling curves at atmospheric pressure. The single-phase convection data have been removed for clarity. In general, incipient superheats were reduced from the pure subcooled values, which is consistent with the observations of You et al. [9] and O'Connor et al. [11]. This suggests that the dissolved air enhances heat transfer at low heat fluxes just after incipience but not at higher heat fluxes. For comparison, the boiling curve data of Honda et al.'s [28] 1-cm^2 S (smooth silicon surface) and EPF (rough silicon surface) surfaces are plotted in Fig. 11 and show similar dissolved gas behavior as that of the present data in Fig. 10. Honda et al. tested their surfaces with both ''degassed'' (pure subcooled) and ''gas dissolved'' (gas-saturated with air) fluid conditions in FC-72 at atmospheric pressure. O'Connor et al. [11] also observed this behavior. You et al. [4] attributed the enhancement of heat transfer from gas-saturated cases to a larger number of active nucleation sites due to the gas partial pressure within the nucleating bubbles. An increase in the gas partial pressure within the bubbles would reduce the required vapor pressure (and hence

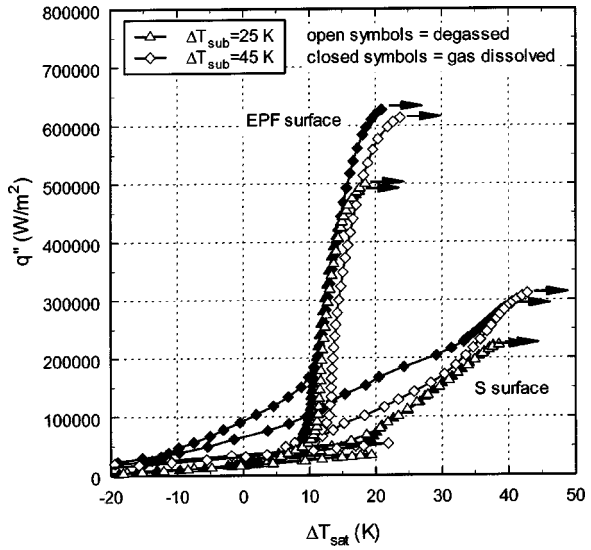

Fig. 11 Comparison of degassed (pure subcooled) and gas dissolved (gas-saturated) boiling curves of Honda et al.'s [28] *S* and EPF surfaces in FC-72 at atmospheric pressure

the wall temperature) required to activate the nucleating bubbles. This would shift the nucleate boiling curve to the left as seen in the low heat flux regions of Fig. 10. As the heat flux is increased, the nucleate boiling curves merged in Fig. 10 showing little effect of the dissolved air on the nucleate boiling performance. Honda et al.'s [28] data in Fig. 11 also show this behavior. Hong, et al. [12] explained this behavior as due to depletion of the dissolved gas near the heater surface creating a gassy subcooled condition. This depletion of dissolved gas near the heated surface provides an identical nucleate boiling situation with the pure subcooled case. Additionally, You et al. [4] observed that the dissolved gas enhancement on nucleate boiling increased with increasing gas content. As dissolved gas concentration increases, the gas-depleted liquid layer becomes re-gassed more efficiently. This would explain the increased effect of dissolved air on the nucleate boiling curves with increasing gas partial pressure, which is observed in Figs. 6–9 (the dissolved air content increases with increasing pressure and subcooling).

The CHF values of the gas-saturated cases were almost the same with the pure subcooled values as shown in Fig. 10. Watwe and Bar-Cohen [20] also saw no effect of dissolved air on CHF for their 1-cm^2 heater in FC-72. Honda et al.'s [28] data shown in Fig. 11 also show little effect of the dissolved gas on CHF. Using small wire heaters, Hong et al. [14] observed that the pure subcooled CHF values were higher than the gas-saturated CHF values for small wire diameters but the effect diminished as the wire diameter increased. The depletion of dissolved gas near the heater surface is most likely greater for larger heaters (less effective dissolved gas transport to the heater surface), which would produce CHF values closer to the pure subcooled values as was observed for the present heaters.

Correlation of Nucleate Boiling Curves. From the results presented thus far, it is concluded that, for a given fluid and heater combination within the present range of conditions, the nucleate boiling performance is essentially a function of pressure and surface microstructure. Although Rohsenow's [5] power-law correlation has been found to predict the effects of pressure well [2,4], the authors found that the present data are better correlated with a linear fit. The boiling curves should follow a straight line when plotted in log-log format (power-law) as proposed by Rohsenow. However, as can be seen from Figs. 5–9, the major portion of the boiling curves for both the plain and microporous surfaces are linear. The reason for the failure of Rohsenow's correlation to adequately describe the present data may be due to length-scale/heater size effects; however, more study is needed before any conclusions can be made.

From the above discussion, it was decided to correlate the present data in Figs. 5–9 with a linear equation in the following form:

$$q'' = a \cdot \Delta T_{sat} - b \cdot P_{sys}^{c} \tag{1}$$

The constants *a*, *b*, and *c* were determined by fitting the linear portions of the nucleate boiling data from Figs. 5–9. The low heat flux data that were affected by the dissolved air as well as the bending portion of the boiling curves near CHF were removed prior to fitting Eq. (1) to the data. The slope, *a*, in Eq. (1) was found by averaging the slopes of each individual boiling curve at all pressures. Once the slope was fixed for each surface condition (plain or microporous), the *y*-intercepts were found for each pressure and correlated using a power-law fit. From this procedure, the present saturated and gas-saturated data are well correlated by the following equations:

$$\text{Plain:} \quad q'' = 2.42\times 10^4 \cdot \Delta T_{sat} - 3.11\times 10^6 \cdot P_{sys}^{-0.571} \tag{2}$$

$$\text{Microporous:} \quad q'' = 3.71\times 10^4 \cdot \Delta T_{sat} - 3.22\times 10^7 \cdot P_{sys}^{-1.32} \tag{3}$$

Equations (2) and (3) are plotted as thick dashed lines in Figs. 6–9. As can be seen in Figs. 6–9, Eq. (1) models the effect of pressure for both the plain and microporous surfaces in the present

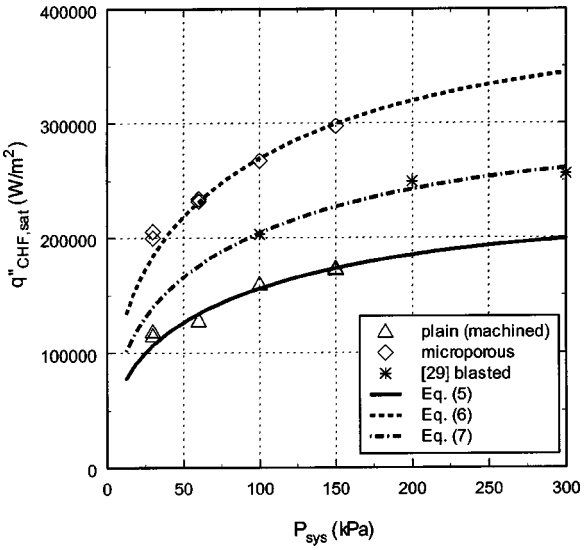

Fig. 12 Effect of Pressure on saturated CHF

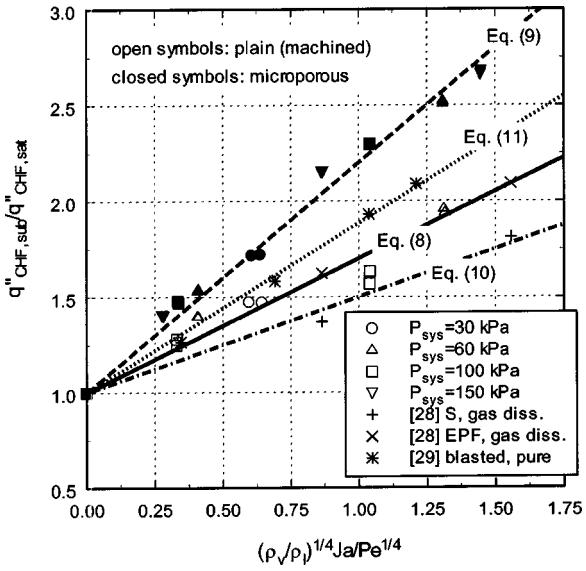

Fig. 13 Effect of subcooling on CHF (gas-saturated)

range of test conditions quite well. It is also interesting to note that although the boiling curve data of Honda et al.'s enhanced EPF surface in Fig. 11 qualitatively appear to show a similar linear type trend to the present data, their smooth S surface (which appears to be much smoother than the present plain surface) boiling curve data appear to follow a more power-law type trend.

Critical Heat Flux. From the CHF values shown in Figs. 4–9, it was observed that there are three parameters, which affect CHF: pressure, subcooling, and surface microstructure. With regard to the effects of pressure, Bar-Cohen and McNeil [7] and Watwe et al. [2] observed that Zuber's [8] correlation given by:

$$q''_{\mathrm{CHF},Z}=(\pi/24)h_{lv}\rho_v^{1/2}[g\sigma(\rho_1-\rho_v)]^{1/4} \tag{4}$$

predicts the effects of pressure in the present range of test conditions reasonably well. However, Zuber's correlation does not take into account the effects of surface microstructure. It was found that simply multiplying Eq. (4) by an empirically determined constant to account for the effects of surface microstructure in the present study worked quite well. From the observations of Rainey and You [21], the empirical constant is most likely directly related to the active nucleation site density just before CHF. Figure 12 illustrates the effect of pressure on CHF for the saturated plain and microporous cases. The data from both boiling curve runs at each condition are shown along with the modified Zuber correlation given by:

$$\text{Plain}\quad q''_{\mathrm{CHF,sat}}=1.03\cdot q''_{\mathrm{CHF},Z} \tag{5}$$

$$\text{Microporous}\quad q''_{\mathrm{CHF,sat}}=1.78\cdot q''_{\mathrm{CHF},Z} \tag{6}$$

For comparison, Mudawar and Anderson's [29] CHF data (1.61-cm^2 vapor blasted flat surface in saturated FC-72), which is also shown in Fig. 12, appears to follow the following modified Zuber correlation:

$$q''_{\mathrm{CHF,sat}}=1.35\cdot q''_{\mathrm{CHF},Z} \tag{7}$$

With regard to the effects of subcooling on CHF, Ivey and Morris' [36] correlation is widely used, however, the authors found that Inoue et al.'s [37] correlation fit the present data better which is given by:

$$\text{Plain}\quad q''_{\mathrm{CHF,sub}}=q''_{\mathrm{CHF,sat}}[1+0.70(\rho_v/\rho_1)^{1/4}\,\mathrm{Ja/Pe}^{1/4}] \tag{8}$$

$$\text{Microporous}\quad q''_{\mathrm{CHF,sub}}=q''_{\mathrm{CHF,sat}}[1+1.20(\rho_v/\rho_1)^{1/4}\,\mathrm{Ja/Pe}^{1/4}] \tag{9}$$

Figure 13 illustrates the effects of subcooling on CHF for the plain and microporous surfaces at all tested pressures. As can be seen in Fig. 13, Eqs. (8) and (9) correlate the present data quite well. Interestingly, the final form of the equation is very similar to Elkassabgi and Lienhard's [13] low subcooling region correlation (their correlation is obtained by setting the exponent on the density ratio to 0). An interesting observation from Fig. 13 is that the microporous surface exhibits a greater enhancement from increased subcooling than the plain surface. The microporous surface has a much higher active nucleation site density than the plain surface and thus smaller departing bubble diameters [22,23]. For comparison, the CHF data from Honda et al. [28] and Mudawar and Anderson [29] are also shown in Fig. 13. Honda et al.'s S surface data appear to be well correlated by:

$$q''_{\mathrm{CHF,sub}}=q''_{\mathrm{CHF,sat}}[1+0.50(\rho_v/\rho_1)^{1/4}\,\mathrm{Ja/Pe}^{1/4}] \tag{10}$$

while their enhanced EPF surface data appear to follow the present plain surface correlation given by Eq. 8. Mudawar and Anderson's vapor blasted surface data under pure subcooled conditions appear to be well correlated by:

$$q''_{\mathrm{CHF,sub}}=q''_{\mathrm{CHF,sat}}[1+0.88(\rho_v/\rho_1)^{1/4}\,\mathrm{Ja/Pe}^{1/4}] \tag{11}$$

Conclusions

The effects of pressure and subcooling on the pool boiling heat transfer performance of a microporous enhanced and a plain (machine-roughened) reference surface were investigated. The heating surfaces were horizontal, upward facing 1-cm^2 (1 cm×1 cm) copper surfaces and were submerged in FC-72. The test matrix included an absolute pressure range of 30 to 150 kPa and liquid subcooling levels up to 50 K. The major conclusions of this study are:

- The effect of pressure on nucleate boiling and CHF shows the same trend for both the plain and microporous enhanced surfaces for the present range of test conditions. As pressure increases, nucleate boiling performance and CHF increase while incipience wall superheat decreases.
- The effect of liquid subcooling on fully developed nucleate boiling performance was found to be generally negligible which is consistent with the prevailing trends in the literature. For gassy

subcooling, however, the dissolved gas caused a reduction in incipient superheat and an enhancement of nucleate boiling heat transfer at low heat fluxes just after incipience. In addition, as the amount of dissolved gas increased (through either increased pressure or subcooling), more of the nucleate boiling curve was affected (enhanced).

• A linear-type correlation was found to better fit the present nucleate boiling data than the well-known Rohsenow [5] correlation. The reason for the failure of Rohsenow's correlation to adequately model the nucleate boiling behavior may be due to length-scale/heater size effects; however, more study is needed before any conclusions can be made. The present nucleate boiling data for both the plain and microporous surfaces (including the effects of pressure) were well correlated by Eq. (1).

• The effect of liquid subcooling on CHF was found to be consistent with the trends in the literature, however, the microporous surface showed greater enhancement with increased subcooling than the plain surface. The dissolved gas had virtually no CHF. By combining Eqs. (4)–(9), the present CHF data are well correlated for the effects of pressure and subcooling.

Acknowledgments

The Desktop Architecture Lab group of Intel Corporation supported this study. The authors extend their thanks to the 3M Industrial Chemical Products Division for the donation of FC-72 test liquid.

Nomenclature

a,b,c = constants
c_p = specific heat capacity, [J/kg-K]
g = gravitational acceleration, [m/s^2]
h_{lv} = latent heat of vaporization, [J/kg]
q'' = heat flux, [W/m^2]
Ja = volumetric Jacob number, $\mathrm{Ja} \equiv (\rho_1 c_p \Delta T_{\mathrm{sub}})/(\rho_v h_{lv})$
Pe = effective Péclet number, $\mathrm{Pe} \equiv \sigma^{3/4}/(\alpha \rho_v^{1/2}(g(\rho_1-\rho_v))^{1/4})$
P = absolute pressure, [kPa]
T = temperature, [K]
ΔT_{sat} = surface superheat; $T_w - T_{\mathrm{sat}}(P_{\mathrm{sys}})$, [K]
ΔT_{sub} = liquid subcooling; $T_{\mathrm{sat}}(P_{\mathrm{sys}}) - T_{\mathrm{bulk}}$, [K]
α = thermal diffusivity, [m^2/s]
ρ = density, [kg/m^3]
σ = surface tension, [N/m]

Subscripts

bulk = bulk liquid
CHF = critical heat flux
g = non-condensable gas (air)
l = saturated liquid
sat = saturated conditions
sub = subcooled conditions
sys = system or total
v = saturated vapor
w = heater surface (wall)
Z = CHF prediction of Zuber [8]

References

[1] Nishikawa, K., Fujita, Y., Ohta, H., and Hidaka, S., 1982, "Effects of System Pressure and Surface Roughness on Nucleate Boiling Heat Transfer," Memoirs of the Faculty of Engineering, Kyushu University, **42**(2), pp. 95–111.
[2] Watwe, A. A., Bar-Cohen, A., and McNeil, A., 1997, "Combined Pressure and Subcooling Effects on Pool Boiling From a PPGA Chip Package," ASME J. Electron. Packag., **119**, pp. 95–105.
[3] Han, C. Y., and Griffith, P., 1965, "The Mechanism of Heat Transfer in Nucleate Boiling-Part I," Int. J. Heat Mass Transf., **8**, pp. 887–904.
[4] You, S. M., Simon, T. W., and Bar-Cohen, A., 1990, "Experiments on Nucleate Boiling Heat Transfer with a Highly-Wetting Dielectric Fluid: Effects of Pressure, Subcooling and Dissolved Gas Content," *Cryogenic and Immersion Cooling of Optics and Electronic Equipment*, HTD-Vol. 131, pp. 45–52.
[5] Rohsenow, W. M., 1962, "A Method of Correlating Heat Transfer Data for Surface Boiling of Liquids," ASME J. Heat Transfer, **74**, pp. 969–975.
[6] Morozov, V. G., 1961, "An Experimental Study of Critical Heat Loads at Boiling of Organic Liquids on a Submerged Heating Surface," Int. J. Heat Mass Transf., **2**, pp. 252–258.
[7] Bar-Cohen, A., and McNeil, A., 1992, "Parametric Effects on Pool Boiling Critical Heat Flux in Dielectric Liquids," *Proceedings of the Engineering Foundation Conference on Pool and External Flow Boiling*, ASME, Santa Barbara, CA, pp. 171–175.
[8] Zuber, N., 1959, "Hydrodynamic Aspects of Boiling Heat Transfer," AEC Report No. AECU-4439, Physics and Mathematics.
[9] You, S. M., Simon, T. W., and Bar-Cohen, A., 1990, "Experiments on Boiling Incipience with a Highly-Wetting Dielectric Fluid: Effects of Pressure, Subcooling and Dissolved Gas Content," *Heat Transfer, Proceedings of the International Heat Transfer Conference*, Hemisphere, New York, pp. 337–342.
[10] Carey, V. P., 1992, *Liquid-Vapor Phase-Change Phenomena*, Taylor and Francis.
[11] O'Connor, J. P., You, S. M., and Chang, J. Y., 1996, "Gas-Saturated Pool Boiling Heat Transfer From Smooth and Microporous Surfaces in FC-72," ASME J. Heat Transfer, **118**, pp. 662–667.
[12] Hong, Y. S., Ammerman, C. N., and You, S. M., 1997, "Boiling Characteristics of Cylindrical Heaters in Saturated, Gas Saturated, and Pure-Subcooled FC-72," ASME J. Heat Transfer, **119**, pp. 313–318.
[13] Elkassabgi, Y., and Lienhard, J. H., 1988, "Influences of Subcooling on Burnout of Horizontal Cylindrical Heaters," ASME J. Heat Transfer, **110**, pp. 479–486.
[14] Hong, Y. S., Ammerman, C. N., and You, S. M., 1998, "Effects of Length Scale, Subcooling, and Dissolved Gas Content on the Pool Boiling Critical Heat Flux of Cylindrical Heaters," *Proceedings of the 11th International Heat Transfer Conference*, Kyongju, Korea, pp. 389–394.
[15] Normington, P. J. C., Mahalingam, M., and Lee, T. Y. T., 1992, "Thermal Management Control Without Overshoot Using Combinations of Boiling Liquids," IEEE Trans. Compon., Hybrids, Manuf. Technol., **15**(5), pp. 806–814.
[16] Phadke, N. K., Bhavnani, S. H., Goyal, A., Jaeger, R. C., and Goodling, J. S., 1992, "Re-Entrant Cavity Surface Enhancement for Immersion Cooling of Silicon Multichip Packages," IEEE Trans. Compon., Hybrids, Manuf. Technol., **15**(5), pp. 815–822.
[17] McAdams, W. H., Kennel, W. E., Minden, C. S., Carl, R., Picornell, P. M., and Dew, J. E., 1949, "Heat Transfer at High Rates to Water with Surface Boiling," Ind. Eng. Chem., **41**(9), pp. 1945–1953.
[18] Pike, F. P., Miller, Jr., P. D., and Beatty, Jr., K. O., 1955, "Effect of Gas Evolution on Surface Boiling at Wire Coils," Chem. Eng. Prog., Symp. Ser., No. 17, **51**, pp. 13–19.
[19] Behar, M., Courtaud, M., Ricque, R., and Semeria, R., 1966, "Fundamental Aspects of Subcooled Boiling with and without Dissolved Gasses," *Proceedings of the 3rd International Heat Transfer Conference*, **IV**, pp. 1–11.
[20] Watwe, A. A., and Bar-Cohen, A., 1996, "Nucleate Pool Boiling and Critical Heat Flux in Gas-Saturated Dielectric Coolants," *Proceedings of the 2nd European Thermal-Sciences and 14th UIT National Heat Transfer Conference*, Rome, Italy, pp. 1631–1638.
[21] Rainey, K. N., and You, S. M., 2000, "Pool Boiling Heat Transfer From Plain and Microporous, Square Pin Finned Surfaces in Saturated FC-72," ASME J. Heat Transfer, **122**(3), pp. 509–516.
[22] Chang, J. Y., and You, S. M., 1997, "Enhanced Boiling Heat Transfer from Micro-Porous Surfaces: Effects of a Coating Composition and Method," Int. J. Heat Mass Transf., **40**(18), pp. 4449–4460.
[23] O'Connor, J. P., and You, S. M., 1995, "A Painting Technique to Enhance Pool Boiling Heat Transfer in FC-72" ASME J. Heat Transfer, **117**(2), pp. 387–393.
[24] Chang, J. Y., and You, S. M., 1997, "Boiling Heat Transfer Phenomena from Micro-Porous and Porous Surfaces in Saturated FC-72," Int. J. Heat Mass Transf., **40**(18), pp. 4437–4447.
[25] You, S. M., and O'Connor, J. P., 1998, "Boiling Enhancement Paint," U.S. Patent #5814392.
[26] Kline, S. J., and McClintock, F. A., 1953, "Describing Uncertainties in Single-Sample Experiments," Mech. Eng. (Am. Soc. Mech. Eng.), **75**(1), pp. 3–8.
[27] Chang, J. Y., and You, S. M., 1996, "Heater Orientation Effects on Pool Boiling of Micro-Porous-Enhanced Surfaces in Saturated FC-72," ASME J. Heat Transfer, **118**(4), pp. 937–943.
[28] Honda, H., Takamastu, H., and Wei, J. J., 2002, "Enhanced Boiling of FC-72 on Silicon Chips With Micro-Pin-Fins and Submicron-Scale Roughness," ASME J. Heat Transfer, **124**(2), pp. 383–390.
[29] Mudawar, I., and Anderson, T. M., 1990, "Parametric Investigation Into the Effects of Pressure, Subcooling, Surface Augmentation and Choice of Coolant on Pool Boiling in the Design of Cooling Systems for High-Power-Density Electronic Chips," ASME J. Electron. Packag., **112**, pp. 375–381.
[30] Yin, C. P., Yan, Y. Y., Lin, T. F., and Yang, B. C., 2000, "Subcooled Flow Boiling Heat Transfer of R-134a and Bubble Characteristics in a Horizontal Annular Duct," Int. J. Heat Mass Transf., **43**(11), pp. 1885–1896.
[31] Wiebe, J. R., and Judd, R. L., 1971, "Superheat Layer Thickness Measurements in Saturated and Subcooled Nucleate Boiling," ASME J. Heat Transfer, **93**(4), pp. 455–461.
[32] Marek, R., and Straub, J., 2001, "The Origin of Thermocapillary Convection in Subcooled Nucleate Pool Boiling," Int. J. Heat Mass Transf., **44**(3), pp. 619–632.
[33] Nishikawa, K., Fujita, Y., Uchida, S., and Ohta, H., 1984, "Effect of Surface Configuration on Nucleate Boiling Heat Transfer," Int. J. Heat Mass Transf., **27**, pp. 1559–1571.

[34] Lienhard, J. H., 1985, ''On the Two Regimes of Nucleate Boiling,'' ASME J. Heat Transfer, **107**, pp. 262–264.
[35] Rainey, K. N., and You, S. M., 2001, ''Effects of Heater Orientation on Pool Boiling Heat Transfer from Microporous Coated Surfaces,'' Int. J. Heat Mass Transf., **44**(14), pp. 2589–2599.
[36] Ivey, H. J., and Morris, D. J., 1966, ''Critical Heat Flux of Saturation and Subcooled Pool Boiling in Water at Atmospheric Pressure,'' *Proceedings of the 3rd International Heat Transfer Conference*, Vol. III, Chicago, IL, pp. 129–142.
[37] Inoue, T., Kawae, N., and Monde, M., 1998, ''Effect of Subcooling on Critical Heat Flux During Pool Boiling on a Horizontal Wire,'' Heat and Mass Transfer, **33**(5–6), pp. 481–488.

Experimental Study on Frost Structure on Surfaces With Different Hydrophilicity: Density and Thermal Conductivity

Jongmin Shin
Chief Research Engineer
e-mail: shinjm@lge.com

Alexei V. Tikhonov
Visiting Research Scientist
e-mail: tikhonov@lge.com

Cheolhwan Kim
Senior Research Engineer
e-mail: cheolhkim@lge.com

DA Research Laboratory,
LG Electronics Company,
391-2, Ga Eum Jeong Dong, Changwon,
Kyoung Nam,
641-711 Republic of Korea

An experimental study has been conducted to investigate the effects of surface energy on frost formation. Test samples with three different surfaces of which dynamic contact angles (DCA) were 23, 55, and 88 deg were installed in a wind tunnel and exposed to a humid airflow. The airflow Reynolds number, humidity, the air and the cold plate temperatures were maintained at 9000, 0.0042 kg/kg′, +12 and −22°C, respectively. The thickness and the mass of frost layer were measured and used to calculate frost density while heat flux and temperature profile were measured to obtain thermal conductivity. Exact positions of thermocouple junctions were verified by means of visualization system in order to increase accuracy. Results showed that frost density and thermal conductivity increase with time. The surface with a lower DCA showed a higher frost density and thermal conductivity during a two-hour test, but minor differences have been found after two hours of frost generation. Empirical correlations for thickness, mass deposition, density and thermal conductivity were proposed as the functions of test time and surface energy. [DOI: 10.1115/1.1518496]

Keywords: Heat Transfer, Low Temperature, Plasma, Plate, Properties

1 Introduction

Frosting is a well-known and undesirable in most technical applications phenomenon, which occurs on cold surface when water vapor in surrounding air adheres to the surface through mass transfer. Frost layer adversely affects the performance of devices due to the increase of the pressure drop in frosted air passages and the decrease of overall thermal efficiency. The performance of refrigerating unit under frost deposition gradually decreases and defrost process is required for the improvement of its performance. Traditionally applied electric heaters for frost removal by melting increase energy consumption, while temperature rise may decrease freshness of foods inside refrigerators. These days there are no clear and reliable measures to prevent frost formation and the designers of the equipment, operating under frost deposition, should account frost in their works. Thus it is impossible to suppress water vapor mass transfer, efforts to increase frost density and thermal conductivity by frost structure modification may be considered as promising.

Frost formation depends on air velocity, air humidity, air temperature, cold surface temperature and surface energy. Numerous researchers had studied influences of ambient conditions and wall temperatures on frost growth, while few works had been performed to investigate the effect of surface energy on frost formation and reported results were contradictionary. Meanwhile changing of surface energy is a very attractive way to modify frost properties. Nikulshina et al. [1], Seki et al. [2], and Hoke et al. [3] found that denser frost layer was formed on a lower energy surface, than on a higher one, i.e., on hydrophobic rather than on hydrophilic. It is believed that different shapes of frozen droplets on surfaces with different energies are the main reason for formation of various frost structures. Frost visualizations made by Tao et al. [4] and Hoke et al. [3] confirmed predictions about larger diameter of water droplets formed on hydrophilic surface during initial period of frost formation when condensed water droplets turned into ice. Yoshiyuki and Akiko [5] studied the performance of heat exchanger after the anti-frosting surface treatment of fins in order to extend the defrost cycle time of air cooler. A special coating made of water-repellent resin and inorganic particles was developed in order to create hydrophobic surface. As a result, compressor operating time between defrost processes was increased twice compared to a conventional air cooler with the same cooling performance. Ryu and Lee [6] studied frost formation in fin-and-tube heat exchangers with different surface energies and came to contrary conclusion. They found frost thickness for hydrophilic heat exchanger became thinner with smaller airside pressure drop, than that of a conventional aluminum heat exchanger. However, frost mass accumulated on hydrophilic heat exchanger was larger than that on conventional one. It implies that denser frost was formed on a hydrophilic heat exchanger. Unfortunately, hydrophilic heat exchanger lost its advantages rapidly with the increase of relative humidity, because thick frost layer reduced the influence of surface energy on further ice particles deposition.

Frost thermal conductivity and layer thickness are most important parameters for the design work and both are functions of frost density. That is why very often all frost properties are measured during test studies simultaneously. A review of literatures indicates that frost thermal conductivity may change as much as ten times during frost layer growth as confirmed by Yonko and Sepsy [7], Hayashi et al. [8], Deitenberger [9], Seki et al. [2], Auracher [10], and Sahin [11]. Designers may employ literature data on frost properties, because they are under investigation for more than half a century, but different expressions give various results for the same input conditions. Moreover, influence of dynamic contact angle (DCA), i.e., the quantitative characteristic of surface hydrophilicity, is hidden.

Objectives of the present study on frost phenomenon are: (1) to investigate the effect of surface energy on frost thickness, mass, density and thermal conductivity; and (2) to develop test technique and obtain local values of frost thermal conductivity.

Contributed by the Heat Transfer Division for publication in the JOURNAL OF HEAT TRANSFER. Manuscript received by the Heat Transfer Division September 4, 2001; revision received July 19, 2002. Associate Editor: J. G. Georgiadis.

2 Experimental Apparatus

The schematic diagram of experimental set-up is shown in Fig. 1(*a*). It consisted of three independent parts: a psychrometric chamber, a coolant supply loop and a wind tunnel with test sample. The psychrometric chamber included an air-handling unit with compressors, a 10 kW humidifier and 7 kW heaters and an air-sampling unit. Three compressors with the capacity of 1.5, 2.5 and 4.0 kW were available, and appropriate one could be selected to provide the desirable chamber temperature within $+5\sim+20$°C with RH from 40 to 80 percent. Airflow humidity was controlled at two points: at the entrance of the wind tunnel and after the test sample. For this purpose dry and wet air temperatures were measured by platinum resistance temperature sensors, RTD (100 Ω, CHINO), with the accuracy of ±0.05°C. Airflow velocity was obtained according to ASHRAE standard [12] employing nozzle and pressure drop measurements along it. Blower at the rear part of the wind tunnel was connected to power supply through controller and an inverter in order to control fixed rotations per minute of the motor and, therefore, constant volume airflow rate during the whole test run.

The wind tunnel was made of a transparent acrylic material with thickness and length of 10 mm and 1500 mm, respectively. It had inlet mesh for smoothening of airflow. Airflow passage cross section of 120 mm×300 mm was divided in the middle by 20 mm thick acrylic plate with the test sample. Frost deposited on the both sides of the sample. The coolant supply loop contained a stainless steel bath with heaters and heat exchanger connected to a low-temperature refrigerating unit. Such a design provided maintenance of constant coolant temperature in the range from −30 to −5°C with the accuracy of ±0.2°C. A stainless steel pump and a mass flow meter were used to obtain constant coolant flow rate. The coolant was the mixture of water and ethylene glycol by 50 to 50 percent in weight.

Test sample had simple design as shown in Fig. 1(*b*): two thin plates with known DCA were embracing thick one, which was made by welding method from aluminum alloy. The length of test sample in airflow direction was 100 mm, and its width and thickness were 300 mm and 20 mm, respectively. To provide coolant flow there were four rectangular channels with cross sectional area of 10×10 mm^2 inside internal thick plate. Also ten grooves were engraved on its both surfaces for installation of 0.127 mm diameter T-type thermocouples (TT-T-36, OMEGA). After installation thermocouples were covered by thermal paste (D-500, DOTITE) with thermal conductivity of 30 W/(m K). Then two thin external plates made of aluminum alloy on which frost deposited during a test run were attached to the central plate. On each side of test sample there were five thermocouples and the averaged value of their readings was assumed to be the cold plate temperature. Grooves did not intact external plates and no influence of thermocouples installation on frost deposition was expected therefore. Uncertainty in temperature measurements was within ±0.05°C, but uncertainty for averaged surface temperature was ±0.4°C due to temperature glide between coolant entrance and exit.

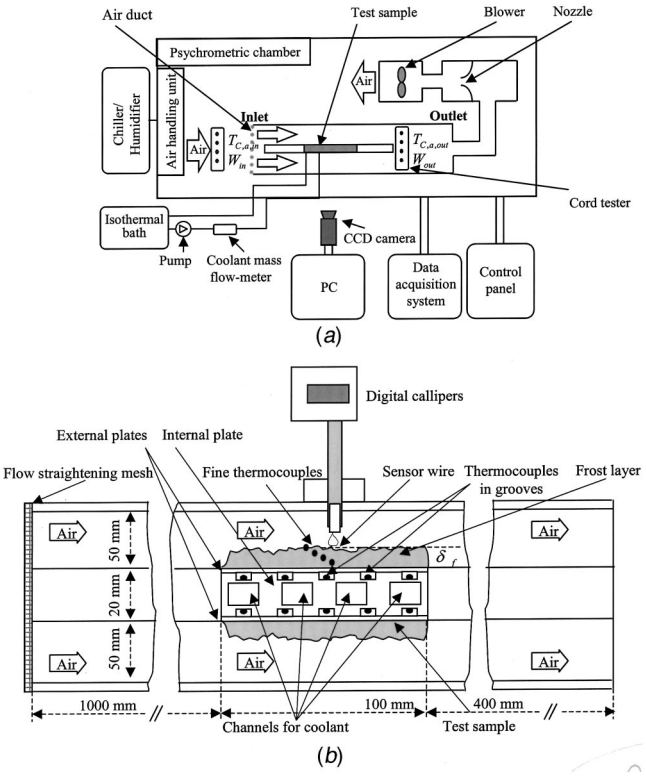

Fig. 1 Schematic diagram of test apparatus: (*a*) setup, and (*b*) design of the test sample with location of thermocouples and design of the sensor for frost thickness acquisition

The sample was jointed to coolant loop with one-touch fittings and coolant temperature at the inlet and outlet of the sample was controlled by RTD for future heat flux calculations. Cooling system provided the maintenance of cold surface temperature in the range of $-25\sim-5$°C. At the beginning of every test run plate temperature was equal to room one and then decreased rapidly as cold coolant flows through the inside channels of test sample. Finally, it had reached the desired level within a minute.

Four fine thermocouples (COCO-001, OMEGA) with 25 μm diameter electrodes were used for acquisition of temperature profile along the frost layer for frost thermal conductivity measurements. They were located in different points within 4 mm above the cold surface as shown in Fig. 1(*b*) and visualization system consisted of CCD camera (VX-1, SONY) with 25 times magnifying lens and computer was employed to confirm their exact positions. Locations of thermocouples were obtained repeatedly five times at the beginning of every test run and averaged value was employed during test data processing. The moment when junction would be covered by frost particles was under control by means of visualization system and when less than 50 percent of junction surface were in direct contact with the frost structure temperature measurements were assumed to be not reliable and were excluded from future data processing. All temperature sensors of the experimental set-up were connected to a hybrid recorder (HR2400, YOKOGAWA), which was a part of data acquisition system of IBM compatible personal computer with possibility to obtain and save data every 3 sec.

For frost thickness acquisition was applied sensing method with non-standard device consisting of acrylic basement and digital caliper with the 25 μm diameter wire as a sensor as shown in Fig. 1(*b*). In present study maximum detected value was assumed to be a frost layer thickness, and it was obtained for the central area of the sample within the circle of 20 mm in diameter. The process of measurement and the moment of touching were also controlled by the same visualization system. Acquisitions of frost thickness with the accuracy of ±0.03 mm were conducted for 30, 45, 60, 120, 180, and 240 minutes. Frost images were taken by CCD camera. Simultaneously the weight of the sample with deposited frost was obtained with the help of precision scale (TP-2KS, OHAUS) after frost deposition; then it was dried by fan and weighed again to calculate pure frost mass deposited. The accuracy of the measurements was ±0.00001 kg.

Three types of plates with known dynamic contact angles (DCA) were tested: aluminum plate coated with lacquer with DCA equal to 88 and aluminum plates treated by means of a new advanced plasma polymerization technology suggested by Koh et al. [13] for improvement of surface wettability. During polymerization the hydrophilic ions were moving in electric field towards the surface until they became tightly linked with it. Hydro-

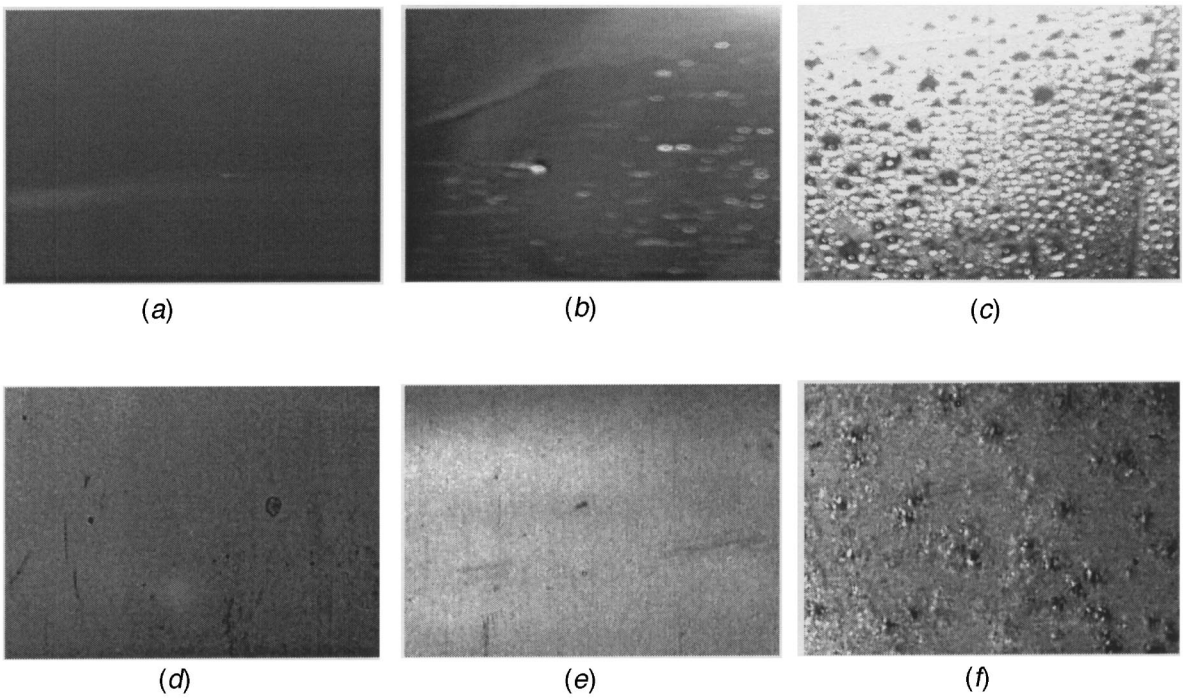

Fig. 2 Flow patterns on different surfaces ((*a*), (*b*), and (*c*)—water spray results; (*d*), (*e*), and (*f*)—initial frost after 2 min of generation): (*a*) DCA=23 deg (uniform: water forms a thin film on the surface, which can't be observed); (*b*) DCA=55 deg (pools: water forms small pools on the surface); (*c*) DCA=88 deg (droplets: water in a form of small droplets can be observed on the surface); (*d*) DCA=23 deg (uniform: frost deposits as a thin film); (*e*) DCA=55 deg (nearly uniform: few frost crystals have large dimensions); and (*f*) DCA=88 deg (rough: fronts layer obviously contains large crystals).

philic particles attracted water molecules and distributed them uniformly along the surface, making therefore the whole surface hydrophilic. After modification surfaces had DCA equal to 23 and 55. The advanced DCA was measured according to the Wilhelm plate method by means of SIGMA 70 (KSV, 77000B). During measurements test sample was moved into water with constant velocity downward to the gravity direction. The tangential angle of the water to the surface made during this period is called the advancing DCA. All forces acting on the sample, such as the gravity, buoyancy of the sample, surface tension and the force of sustain the test sample should be in equilibrium. Advancing DCA can be calculated during processing of test data. Shin et al. [14] described entire test procedure in details. Figure 2 illustrates the behavior of sprayed water and initial frost after 2 min on the surfaces with different DCA. A lot of individual droplets can be distinguished on the surface with DCA=88, while they were combined together on the surface with DCA=55 and, finally, turned into uniform water film on the surface with DCA=23. Similar trend was observed for frosting: large crystals were usual for the surface with lacquer coating, but uniform frost was on plasma treated one with DCA equal to 23.

Table 1 Test conditions

Air	Inlet dry bulb temperature, °C	12.0
	Inlet wet bulb temperature, °C	7.0
	Air velocity, m/s	1.57
	Air Reynolds number	9000
	Relative humidity, %	48.1
	Absolute humidity, kg/kg'	0.0042
Plate	Surface temperature, °C	- 22
	Advanced DCA, degree	23, 55 and 88
Water + Ethylene glycol	Flow rate, kg/s	0.0139
	Mass concentration ratio	50: 50

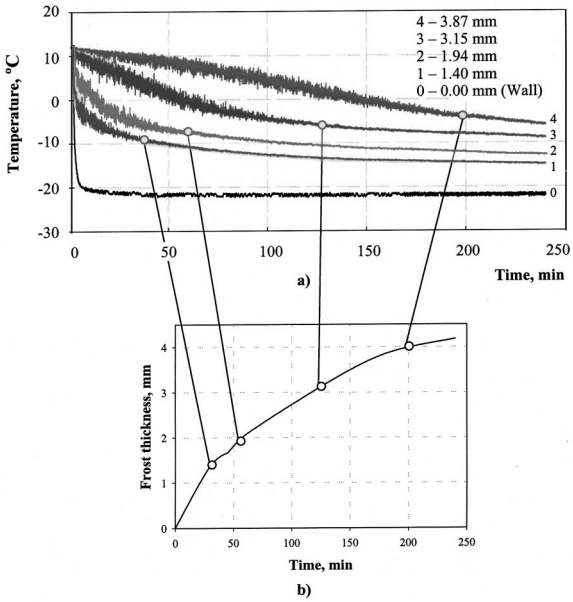

Fig. 3 Results of direct temperature measurements: (*a*) temperature distribution inside frost layer during frost deposition on the surface with DCA=88 deg, (*b*) test data on frost thickness versus time

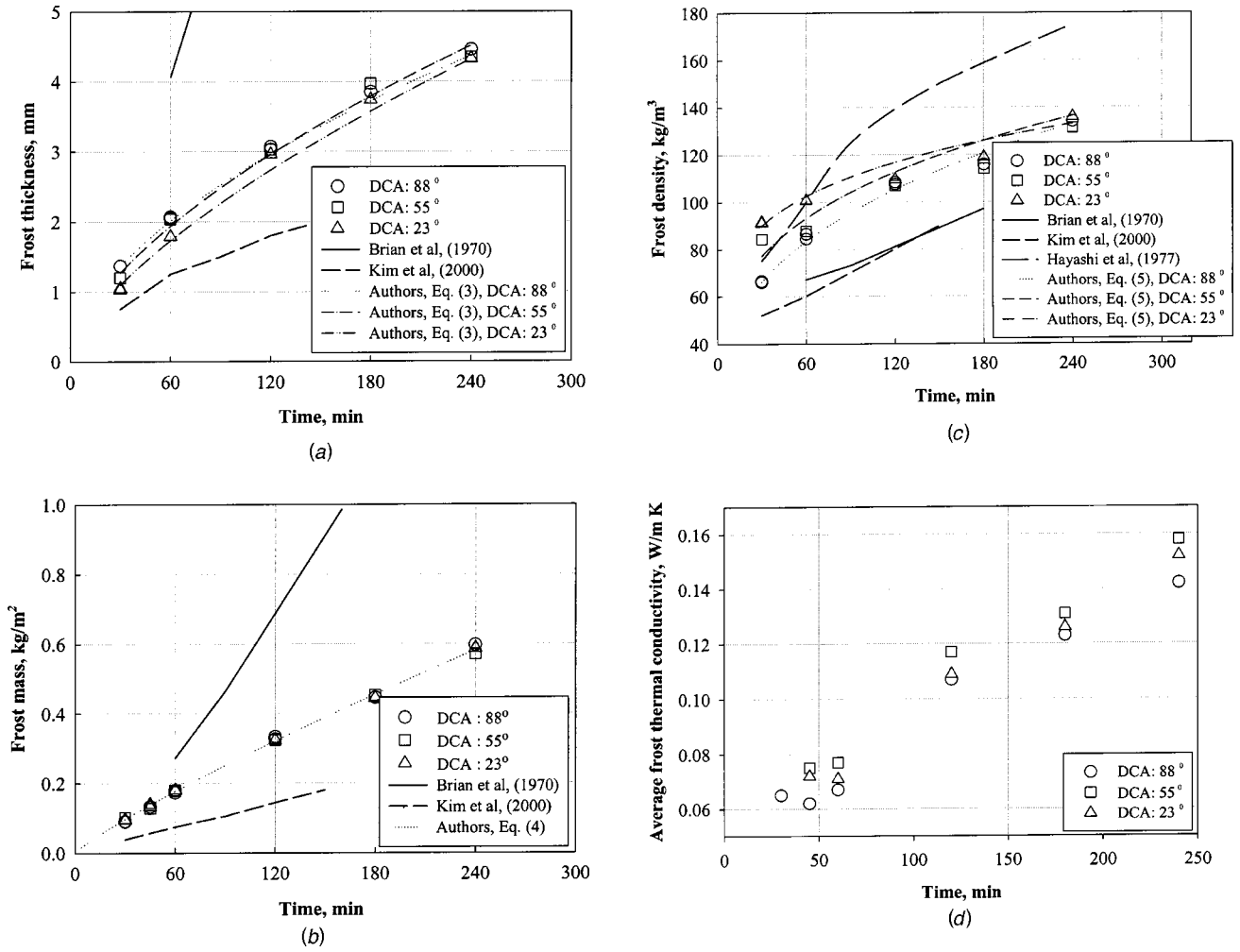

Fig. 4 Frost test results: (*a*) thickness, (*b*) mass deposition, (*c*) density, and (*d*) thermal conductivity

Test conditions are summarized in Table 1. Ambient conditions were similar to those in which evaporators of home refrigerators operate.

Measuring techniques from literatures for frost properties acquisition are given in Appendix 1 for comparison.

3 Processing of Test Data and Uncertainties of Measurements

Frost thickness and mass were obtained by direct measurements with uncertainty for the thinnest frost layer of 1.03 mm as ±2.4 percent. Deposited frost mass was calculated as a mass divided by sample area and for the smallest frost mass of 5.46 g uncertainty was ±0.18 percent. Further division by frost layer thickness would give frost density with uncertainty ±2.5 percent.

Effective frost thermal conductivity was obtained by steady-state method based on Fourier equation. Frost layer was assumed as a plain wall with certain temperatures at the boundaries. Heat flux rate was obtained by means of thermal balance equation for coolant, while frost surface temperature was measured by fine thermocouples located as described above. The following equations were applied for calculations:

$$k_f = \frac{q}{[(T_{fr,s} - T_p)/\delta_f]}, \tag{1}$$

$$q = \frac{C_{p,\text{cool}} \dot{m}_{\text{cool}} (T_{C,\text{cool,out}} - T_{C,\text{cool,in}})}{A}. \tag{2}$$

Two values of effective thermal conductivity were obtained in present study: average and local. For applied calculations and for comparison with available literature data the average value of thermal conductivity was found. For better understanding of frost deposition phenomena local values of thermal conductivity were under investigation and frost layer was divided into sublayers, formed by each two neighboring thermocouples. Maximum number of the sublayers was four when frost layer exceeded 4 mm. For any thin sublayer thermal conductivity was assumed to be constant and was obtained by means of same equations (1) and (2).

Temperature measurements were most crucial for thermal conductivity calculations. Typical temperatures versus time dependences for thermocouples located inside the frost structure and in the cold plate are shown in Fig. 3. Position of every thermocouple junction was carefully measured before every test run with the help of the same measuring tool as for frost thickness acquisition. Thermocouples' readings were very unstable until the most part of the junction was completely covered by frost. Therefore air movement beside rough frost—air interface should be considered as developed turbulent flow with vortices and extremely thin laminar sublayer. Location of thermocouple in parallel to the cold surface was the only way to conduct accurate temperature measurements. Plate temperature was measured by thermocouple located in the plate just below these four fine thermocouples.

Coolant flow parameters were recorded and processed simultaneously with heat flux versus time dependence as a result. Uncer-

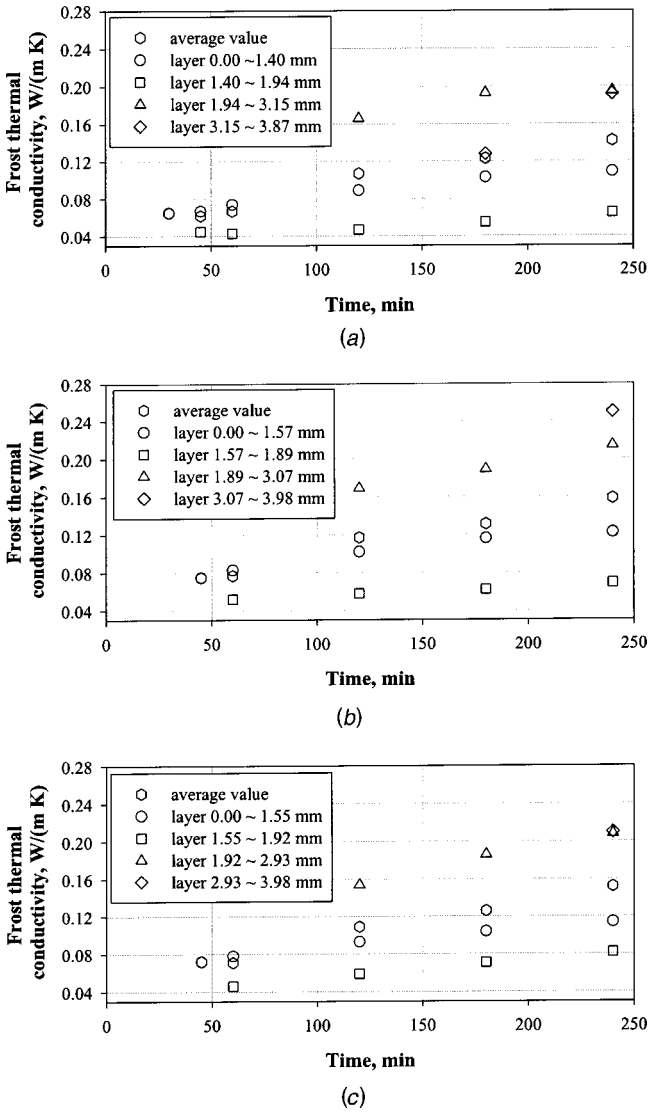

Fig. 5 Distribution of local frost thermal conductivities along the frost layer during 240 min test run. (*a*) DCA=88 deg, (*b*) DCA=55 deg, (*c*) DCA=23 deg.

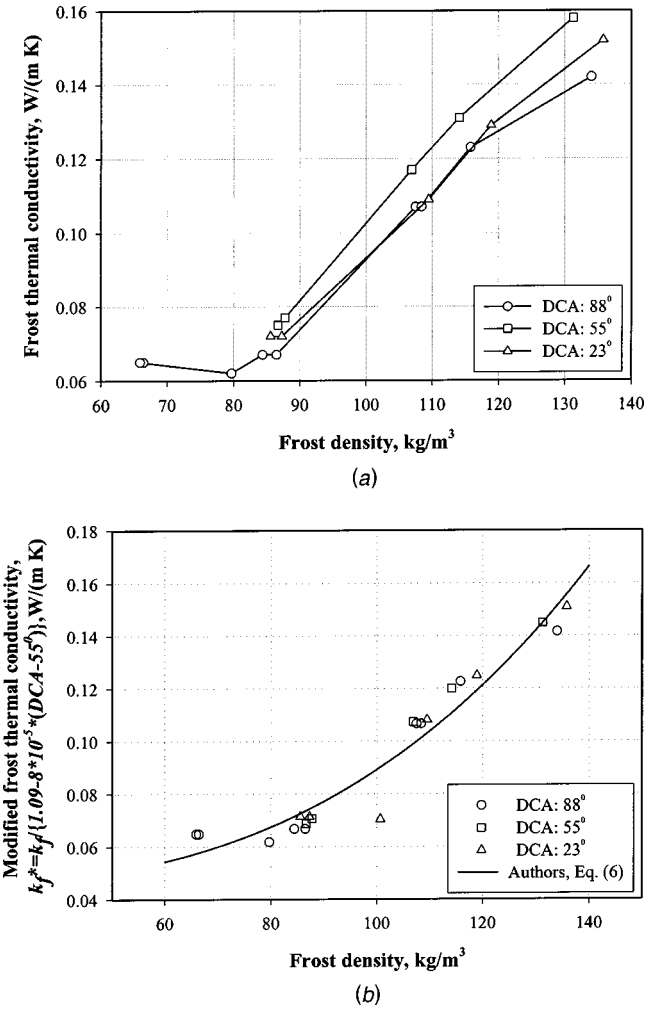

Fig. 6 Average frost thermal conductivity: (*a*) results of experiments and (*b*) correlation of test data

tainty in coolant temperature drop measurements was ± 0.02°C and for coolant flow rate measurements it was ± 0.0002 kg/s. The uncertainty of measurements of the lowest heat flux was within ± 4.8 percent.

Uncertainty for thermal conductivity values was ± 5 percent.

Measurements of ambient conditions were provided with the following accuracy: for relative airflow humidity uncertainty was ± 0.5 percent and for volume flow rate it was ± 0.02 m^3/min.

4 Experimental Results

4.1 Frost Thickness. Figure 4(*a*) shows frost thickness as the function of test time and DCA. The current test data are enclosed between results obtained by Brian et al. [15] and by Kim et al. [16]. Frost thickness rapidly increases with the increase of test time within 60 minutes, and then its slope turns to be gentle. It looks that frost layer begins to grow relatively faster on a higher DCA surface. The frost thickness on the surface with 23 deg of DCA makes up only 76 percent compared to that with 88 deg of DCA after 30 min. of frost deposition, but increases up to 97 percent after 120 min. Same trend occurs for the 55 degrees of DCA surface. Minor differences in frost thickness among surfaces have been found after 120 minutes.

The shapes of frost generated on different surfaces after 2 minutes of test time are shown in Figs. 2(*d*)–(*f*). Regular and very small crystals are generated on the low DCA surface, while irregular and large crystals are generated on the 88 deg of DCA surface. It seems that the difference comes from micro droplet generation. During first few moments of frost deposition, dropwise condensation occurs on the high DCA surface as was shown in Fig. 2(*c*). During further formation of a frost layer mass transfer beside the large ice crystals becomes more intensive than that of the other frost-air interface. This happens due to the difference in thermal conductivity between ice and frost, which, in turn, results in lower temperatures of large crystals. Larger temperature difference between crystal surface and bulk air is a reason of larger water vapor concentration difference, which is a driving force for mass transfer. Therefore the irregularity of the frost thickness on a higher DCA surface is increasing with time. In contrast, wider and more filmwise-looking droplets are generated on a lower DCA surface at the initial stage. They may cover almost the whole surface easily and accelerate uniform crystal growth from the very beginning of frost formation. Meanwhile the frost on the surface with the high DCA continues to grow. Frost itself has sufficient thermal resistance and with its growth, frost surface temperature becomes nearly uniform accelerating, in turn, uniform frost deposition. Frost layer irregularity, inherent to initial crystal growth period, is decreasing. Minor differences in frost thickness among surfaces can be found after 120 minutes.

Equation (3) represents relation between frost thickness and influential factors such as test time and DCA of the surface. The

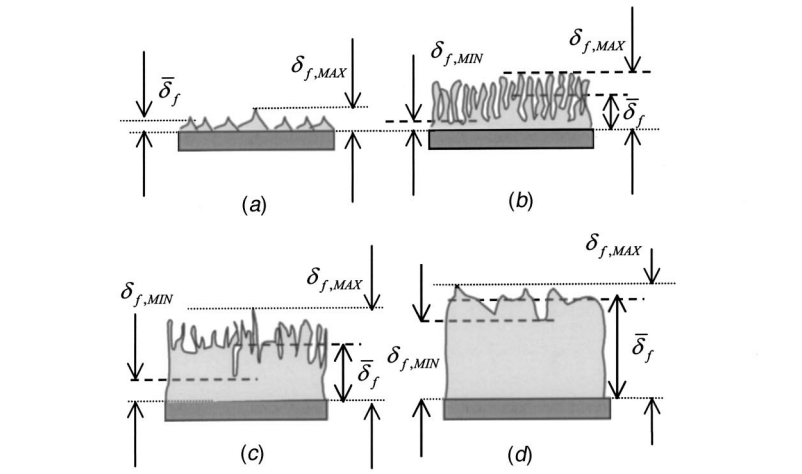

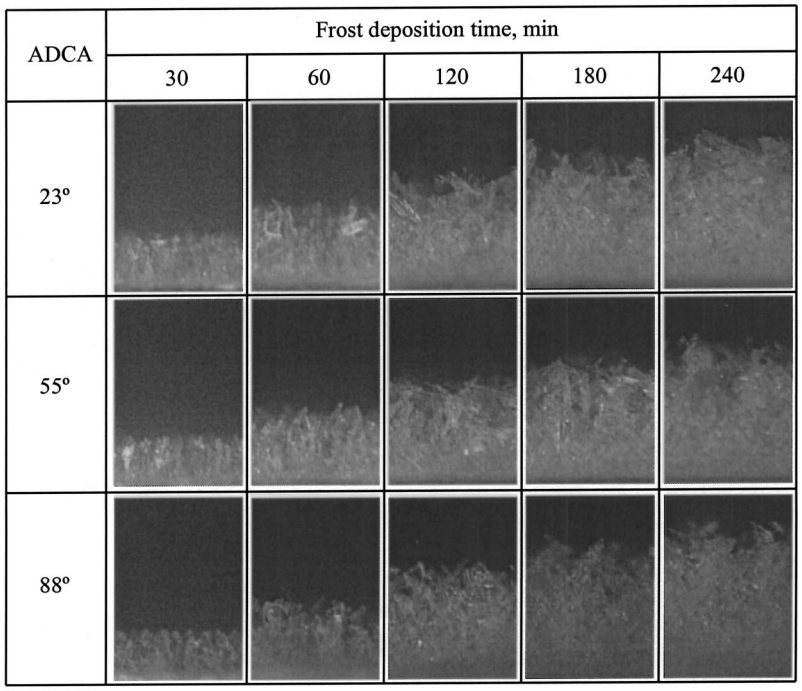

(e)

Fig. 7 Typical frost profiles: (*a*) droplet freezing, (*b*) crystal growth period or frost columns growth, (*c*) three-dimensional growth of frost structure, (*d*) seepage period, and (*e*) images of frost structure for 30, 60, 120, 180 and 240 min of frost deposition on surfaces with different DCA

measured values of frost thickness were correlated by the Eq. (3) with the accuracy of ± 6.5 percent for 90 percent of test data.

$$\delta_f = (0.0852 + 0.00134 \cdot \mathrm{DCA}) \cdot t^{(0.6954 - 0.00154 \cdot \mathrm{DCA})} \quad (3)$$

4.2 Frost Mass. Figure 4(*b*) shows frost mass according to test time and DCA. Frost mass linearly increases with time and test data are in agreement with Brian et al. [15] and Kim et al. [16]. Frost mass deposition on investigated surfaces does not differ sufficiently and it may be concluded that mass transfer coefficient is not a function of DCA.

For the frost mass 90 percent of test data are correlated with the accuracy of ± 6.3 percent with the values calculated by means of Eq. (4).

$$m_f = 0.0052 \cdot t^{0.861} \quad (4)$$

4.3 Frost Density. Figure 4(*c*) represents frost density with regard to test time and DCA. Frost density increases with the increase of test time, and the results are larger than test data obtained by Brian et al. [15] and Kim et al. [16], but lower than that received by Hayashi et al. [8]. However, Hayashi et al. maintained slightly larger airflow humidity during their tests.

Denser frost is formed on a lower DCA surface at the initial stage of frost generation, but it becomes nearly the same as frost generated on high DCA surface after 120 min. Frost density data for 55 deg of DCA surface lies in the middle of them. It seems that the strong effect of DCA on frost density continues for 120 min. from the beginning of frost deposition, and then effect of surface energy becomes weaker. However till the end of four hours test run frost layer on 23 deg of DCA surface remains slightly denser, than that on other surfaces.

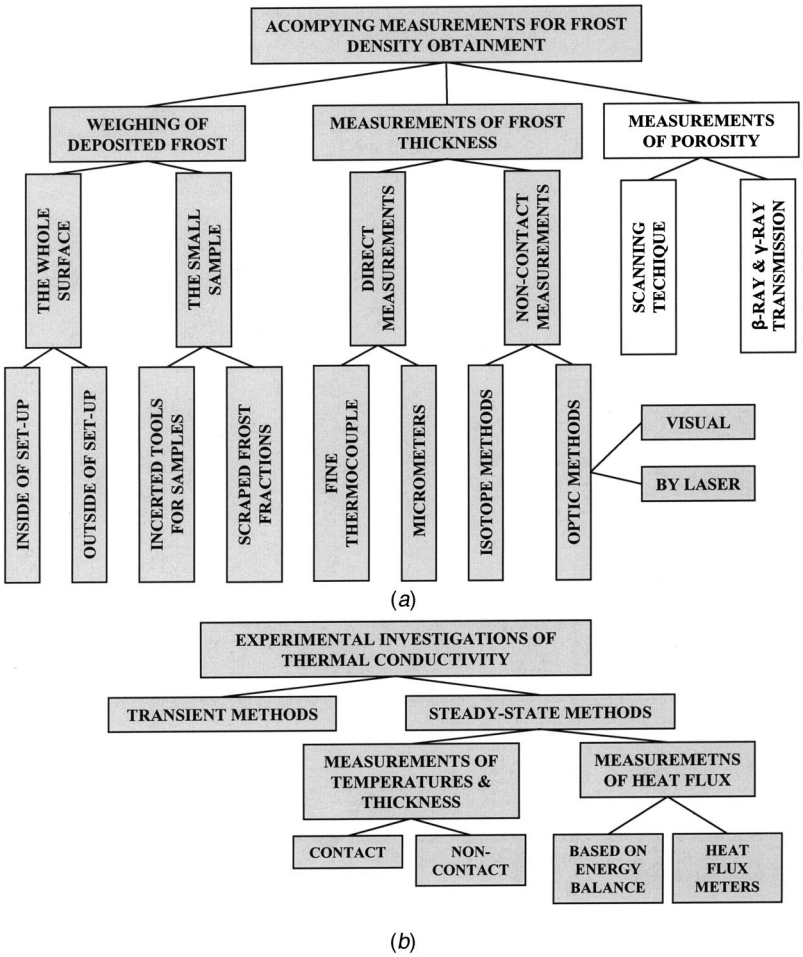

Fig. 8 Classification of test methods for frost properties study: (*a*) for frost density, and (*b*) for frost thermal conductivity

Analysis of frosting phenomenon shows that during initial period of frost formation the shape of micro droplets depends on surface energy and the process of frost growth is affected by DCA. It means that growth of crystals is going in different ways and is strictly controlled by surface energy. But when frost thickness reaches some certain level and frost-air interface will be distanced from cold surface itself, frost formation will be rather affected by environmental conditions than by any surface characteristics.

Average frost density is correlated with test time and DCA with the accuracy of ± 10.4 percent for 90 percent of test data by means of Eq. (5).

$$\rho_{f,\mathrm{ave}} = (109.53 - 45.54 \cdot \log \mathrm{DCA}) \cdot t^{0.0479 \cdot \mathrm{DCA}^{0.4357}} \qquad (5)$$

4.4 Frost Thermal Conductivity. Test data for average frost thermal conductivity versus time are presented in Fig. 4(*d*). Present test method provides measurements of effective heat transfer coefficient described by Hayashi et al. [8]. It is generally believed that thermal conductivity strongly depends on frost density. However in present investigations thermal conductivity for frost layers on surfaces with different DCA show smaller difference than density do during first two hours of frost growth: 15 percent and 39 percent, respectively. The reason may be found in the specific structure of frost during initial period of frost growth on surfaces with low DCA. Ice crystals, forming the frost layer, have different shapes, but they are still located in a same manner—separately. At the beginning convection and diffusivity contribute to heat transfer, but influence of the conductance is very small due to high porosity of frost matrix. Later, after two hours of frost formation, the layer may be still porous, but structure is changing and becoming more complicated due to frost particle formation in all directions. At that moment the role of frost matrix and conductance become more important for heat transfer.

After two hours of frost deposition differences in frost densities are decreasing as may be seen in Fig. 4(*d*). However thermal conductivity values are always higher for plasma-modified surfaces. This phenomenon should be also explained by differences in frost structure: surfaces with lower DCA provide formation of the frost layer with larger contact areas between frost particles and internal contact thermal resistances for such a type of a structure are reduced. One may also see that average effective thermal conductivity had increased by nearly four times after four hours of frost deposition and this tendency was observed for surfaces with different DCA.

Analysis of Fig. 5(*a*)–5(*b*) shows, that lowest local frost thermal conductivity will be for the thin layer second from the wall and higher values will be for the layer beside the cold wall and for the outer layer. Difference between thermal conductivities along the frost layer is about three times and it remains the same during all frost growth period, if seepage regime does not occur as it was in present study. For every layer thermal conductivity increases by 30~50 percent after four hours of frost growth, but initial distribution does not change: inside layers have smaller thermal conductivity than embracing ones. This phenomenon is caused by peculiarities of frost deposition mechanism and may be explained

in a following way. Closely beside the wall the densest frost sublayer with frozen droplets of pure water is located and, respectively, frost thermal conductivity is the highest; but next sublayer is formed on a previous one, like on the basement, and it consists of a large number of thin ice columns with differences in shape. The second layer should have high porosity and due to its intermediate location water vapor supply from moist air is hampered; that is why its thermal conductivity is relatively small. Outside frost sublayer has the highest thermal conductivity when frost deposits on plasma-modified surface with DCA=55 deg. For surfaces with DCA=23 and 88 deg there are the same values for the third and the fourth sublayer. It should be mentioned, that only after four hours of frost deposition frost layer exceeds 4 mm level and it was possible to use the readings of the forth thermocouple.

For average frost thermal conductivity the small decrease was detected during initial period of frost growth as may be seen in Fig. 4(*d*) and Fig. 6(*a*). This phenomenon needs more thorough investigations, but it is insignificant for the equipment operating in humid environment for the long time. Finally, for all test data the average frost conductivity was correlated by the following expression with the accuracy of ±10 percent for 90 percent of test data (Fig. 6(*b*)).

$$k_{f,\mathrm{ave}} = C_{\mathrm{DCA}} \cdot (0.0448 + 4.426 \cdot 10^{-8} \cdot \rho_f^3), \tag{6}$$

where $C_{\mathrm{DCA}} = 1.09 - 8 \cdot 10^{-5} \cdot (\mathrm{DCA} - 55)^2$.

Equation (6) may be applied for surfaces with the values of DCA within 23~88 deg.

5 Conclusions

In the present study, the effects of test time and DCA on frost properties for fixed test conditions were investigated. All measurements were accompanied by visual observations in order to confirm exact positions of sensors and increase accuracy. Results were in proper agreement with literature data.

High DCA surface showed the presence of irregular and rough crystals during the initial period of frost deposition, which resulted in high frost thickness and low frost density. On the contrary, low DCA surface showed uniform and regular crystals resulting in low frost thickness and high density. The surface characteristics played an important role during initial stage, but the effect became weaker as frost grew. Finally, environmental conditions dominated the frost growth after 120 min. of test time.

Values of average and local effective frost thermal conductivities were obtained by means of indirect test methods. It was found that variation of local thermal conductivity along the frost layer was significant. Frost layers close to the plate surface and to frost-air interface had highest thermal conductivity while for inside ones it was two or three times smaller. Such a difference remained constant during the whole test run, though absolute values of frost thermal conductivity were growing.

Nomenclature

A = cross sectional area, m^2
A_{sample} = area of the sample, m^2
C_p = specific heat during isobaric process, J/(kg K)
D_H = hydraulic diameter, $D_H = 4 \cdot A/P$, m
DCA = dynamic contact angle, degrees
Fo = Fourier number from Mao et al. [21]
L_{sub} = latent heat of sublimation, J/kg
k = frost thermal conductivity, W/(m K)
p = pressure, Pa
P = perimeter, m
R = Ideal gas constant, J/(K kg)
RH = relative humidity, percent
Re = Reynolds number, $\mathrm{Re} = D_H u/\upsilon_a$
t = test time, minutes
T_C = temperature, C
$T_{t,p}$ = temperature of water triple point, 273.16 K
u = velocity, m/s
W = absolute air humidity, kg/kg′
x = distance from front edge of the plate, m

Greek Symbols

α = void fraction
δ = thickness, mm
ρ = density, kg/m^3
ν = kinematic viscosity, m^2/s

Subscript

a = air
at = atmosphere
ave = average value
C = mark the process occur due to conductivity
col = ice column
comp = composite
cool = coolant
D = mark the process occur due to diffusivity
f = frost
fr,s = frost surface
g = gas
i = ice
in = inlet
out = outlet
p = plate
par = orientation of frost crystals is parallel to the plate
perp = orientation of frost crystals is perpendicular to the plate
w = water vapor
st = standard conditions: atmospheric pressure is 101.3 kPa and temperature is 0 deg. Celsius

Appendix 1

Frost Properties Measurements. In spite of years of frosting studies and numerous test techniques researchers didn't come to

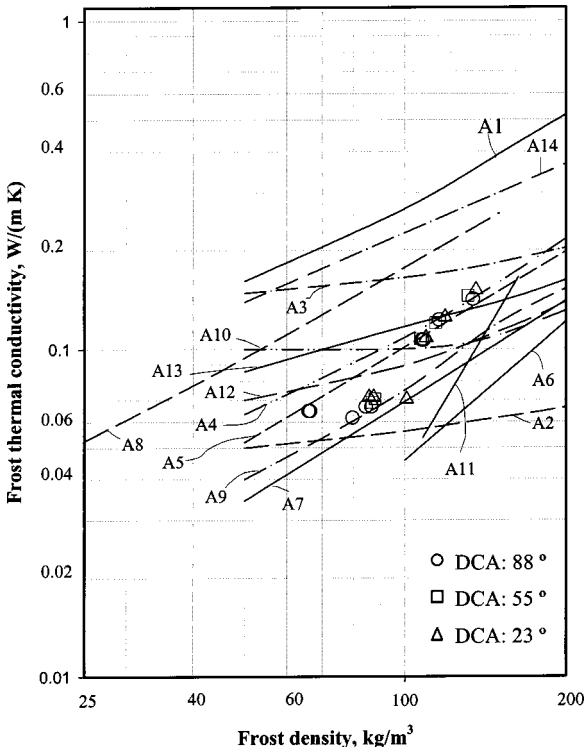

Fig. 9 Comparison of present test data on frost thermal conductivity verses frost density with predictions based on literature expression

Table 2 Expressions from literature

N	Equations	Density limits	References.
A1	$k_f = k_a \cdot \alpha_a + k_i \cdot (1-\alpha_a)$	Continuous ice phase in frost	Deitenberger, 1983
A2	$\frac{1}{k_f} = \frac{C_1}{k_{par}} + \frac{1-C_1}{k_{perp}}$, $\begin{cases} \frac{1}{k_{perp}} = \frac{(1-\alpha_i)}{k_a} + \frac{\alpha_i}{k_i} \\ k_{par} = (1-\alpha_i)\cdot k_a + \alpha_i \cdot k_i \end{cases}$	Simplified from Auracher, 1983.	Le Gall et al, 1997
A3	$k_f = 0.132 + 3.13\cdot 10^{-4}\rho_f + 1.6\cdot 10^{-7}\rho_f^2$	50 ~400 kg/m^3	Lee et al, 1997
A4	$k_f = 0.024248 + 0.00072311\rho_f + 0.000001183\rho_f^2$	< 573 kg/m^3	Yonko and Sepsy, 1967
A5	$k_f = 0.001202\rho_f^{0.963}$	< 500 kg/m^3	O'Neal and Tree, 1985
A6	$k_f = -8.71\cdot 10^{-3} + 4.39\times 10^{-4}\cdot \rho_f + 1.05\times 10^{-6}\cdot (\rho_f)^2$	50 ~ 680 kg/m^3	Ostin and Anderson, 1991
A7	$k_f = \frac{0.202\cdot \rho_f \cdot (1-\rho_f/1860)}{E - 0.189\cdot \rho_f}$ E=204 for Re<2600; E=295 for Re>5200; E=218 for Re=3000.	< 500 kg/m^3	Oscarsson et al, 1990
A8	$k_f = 3.6\times 10^{-15}\cdot [T_f]^{5.44} + 3.22\times 10^{-13}\cdot \left(\frac{\rho_f}{1000} - 0.025\right)\cdot [T_f]^{4.84}$	25 ~ 130 kg/m^3 Modified to SI	Brian et al, 1970
A9	$k_f(T) = 0.131\cdot 10^{-6}\cdot (1-\alpha_{col})\cdot \frac{L_{sub}\, p_{at}\, p_{st}}{T_{st}^{1.94} R_a^{\,2} T^{1.06}} \times \exp\left[\frac{L_{sub}}{R_a}\left(\frac{1}{T_{st}} - \frac{1}{T}\right)\right] + 1.202\cdot 10^{-3} \times \alpha_{col}\cdot (\rho_{col})^{0.963} + (1-\alpha_{col})(1.0465 + 0.017T)\cdot 10^{-5}$ Average $\frac{1}{\overline{k_f}} = \frac{1}{\delta_f}\int_0^{\delta_f} \frac{1}{k_f(T)}\,dy$	20 ~ 250 kg/m^3	Sahin, 2000
A10	$k_f = \alpha_i \cdot k_i + (1-\alpha_i)\cdot k_{comp}$ $\frac{k_g}{k_{comp}} = 1 - (\frac{6s}{\pi})^{0.333}[1 - (\frac{a^2-1}{a})\ln(\frac{a+1}{a-1})]$ $a = \{1 + \frac{4}{\pi(\frac{k_i}{k_g} - 1)(\frac{6s}{\pi})^{0.666}}\}$ $s = \frac{\rho_f - \rho_g}{\rho_i - \rho_g}$ $D = 0.086\frac{10000}{p}(\frac{T}{273})^{0.666}$ $k_g = k_a + \frac{D}{R_a T}(\frac{p}{p-p_w})\frac{dp_w}{dT}\cdot L_{sub}$	< 450 kg/m^3	Hayashi et al, 1977
A11	$k_f = 0.011\times k_i \times \left(\frac{x}{D_H}\right)^{-0.37} \times (W)^{2.044} \times \left(\frac{273.16 - T_p}{T_a - T_p}\right)^{0.216} \times \mathrm{Re}_{D_H}^{1.093} \times Fo^{0.699}$	< 200 kg/m^3, turbulent	Mao et al, 1992
A12	$k_f = k_C + k_D$ $k_C = \frac{1}{\frac{C_1}{k_{perp}} + \frac{1-C_1}{k_{par}}}$ $k_D = \frac{\rho_i - \rho_f}{\rho_i - 0.58\cdot \rho_f}\cdot L_{sub}\cdot 1.958\cdot 10^{-9}\,\frac{p_{st}}{p}\left(\frac{T}{T_{st}}\right)^{-1.28} \times \exp\left(24.02 - \frac{6145}{T}\right)$ $C_1 = 0.042 + 0.42\cdot 0.995^{\rho_f}$	50 ~ 800 kg/m^3	Auracher, 1987
A13	$k_f = func(\rho_f, T_f)$, $\overline{k_f} = \int_{T_p}^{T_{fr.s}} k_f \cdot dT/(T_{fr.s} - T_p)$,*	50 ~ 550 kg/m^3	Deitenberger, 1983
A14	$k_f = \frac{0.0085\cdot \rho_f^{0.7}\cdot t^{0.01}\cdot (1000\cdot W)^{0.3}}{1.66 - 0.205\cdot u_a + 0.045\cdot u_a^2}$	50 ~ 250 kg/m^3	Kim et al, 2000

*Deitenberger [9] gives detailed description of this expression in his original paper.
Data from Refs. [23–26] included in table.

Table 3 Reliability regions for expressions from literature

Eq.	$T_{C,p}$, °C	$W(RH)$ kg/kg' (%)	$T_{C,a}$, °C	u_a, m/s	Re	$\frac{\Delta k_f}{k_f}$
A3	-15	50 ~ 80 %	+ 25	0.5 ~ 2.0		20 %
A4	-7.8 ~ -30	0.007 ~ 0.0161	+21.1 ~ + 22.8			20 %
A5	-14 ~ -28	0.007 ~ 0.014	+ 15 ~ + 30		5700 ~ 13900	20 %
A6	- 6.5 ~ -19.9	31.1 ~ 75.1 %	+20.3 ~ + 21.2	3.0		30 %
A7	N/a	N/a	N/a		2600 ~ 22000	20 %
A8	- 9 ~ - 17	0.0035 ~ 0.005	+ 1 ~ + 34	4.0~10.0	5100 ~ 14700	10 %
A9	- 5 ~ - 25	0.003 ~ 0.007	+ 13 ~ + 23		2500 ~ 6000	30 %
A10	- 5.1~ - 18.6	0.002 ~ 0.010	+ 25	2.0 ~ 6.0		30 %
A11	- 5 ~ - 15	0.004 ~ 0.010	+ 15 ~ + 23	1.15~2.67	3000 ~ 7000	10 %
A12	- 5 ~ - 50	Assumed to be universal for large range of ambient conditions				20 %
A13	- 5 ~ - 193					50 %
A14	- 15 ~ - 25	60 ~ 80 %	+ 15 ~ + 25	1.0 ~ 3.0		5 %

Equations (A1) and (A2) may be applied to any conditions, if air or ice void fractions are given and C_1 is known.

the consensus about what frost thickness should be considered as actual frost layer height. As shown in Fig. 7 frost surface is very complicated and inconvenient for measurements. Meanwhile layer thickness effects accuracy of all frost properties and comparing of test data from literatures becomes a difficult task. Another problem is related to the choice of the parameter to be maintained as constant value during a test: plate temperature or heat flux rate. If constant value of heat flux is maintained, the cold plate temperature will change due to changes of the frost thermal resistance. Whereas if cold plate temperature is constant, the heat flux rate will be changeable due to the same reason. This dilemma is usually decided in favor of constant plate temperature, because operation conditions of real refrigerating equipment are characterized by more or less stable temperature of saturated refrigerant and, consequently, stable temperature of the evaporator. Experimental methods for frost studies are classified in Fig. 8.

Frost Layer Thickness. Available methods are divided into contact and noncontact ones equally applied by the researchers. Noncontact methods look more promising for application to frost thickness measurements and based on different techniques including gamma and beta rays or lasers. Unfortunately their application needs additional study of the method itself due to sensitivity to tests conditions and even after calibration the reliability of noncontact methods is the main concern. Besant et al. [17] employed laser beam technique with the laser beam directed in parallel to the frost surface. During measurements part of the beam was occluded by the frost and average layer thickness along the laser beam was obtained. Calibration of the system was provided by substitution of a knife-edge for the frosted surface and adjusting of the micrometer over the laser beam. The reported accuracy was 25 μm for laser beam with 2 mm in diameter. Method was recommended for application during the initial stage of frost growth and was suitable to obtain the height of the large frost crystals. Air was motionless during measurements.

Simple contact method based on touching of the frost surface by fine thermocouple as a sensor was described by Hayashi et al. [8] and Takura et al. [18]. The contact between fine thermocouple junction and frost surface, i.e., the moment of ''touching,'' was controlled by visualization system. Dependence on frost roughness for accuracy is a weak point of the method.

Frost Density. To obtain frost density mass and volume of the deposited frost should be known. Methods for mass acquisition differ by frost samples and conditions of weighing. Usual practice is interruption of frost test for measurements. Rarely, as Ostin and Anderson [19] did, sample was weighed during a test run with weighing machine being a part of the test set up. In some studies a mass of small sample scratched from the surface was measured, as Takura et al. [18] described, whereas Mao et al. [20,21] employed more complicated technique with fourteen removable discs installed into the cold plate at different downstream positions in order to investigate how frost distributes along a plate. At the end of every test run discs were carefully removed and accumulated frost was analyzed.

Frost Temperature. Frost surface temperature is employed in calculations of thermal conductivity as one of the boundary conditions. Some researchers assume it to be equal to zero deg in Celsius or to water triple point temperature, as Mao et al. [21] did, but such an assumption looks reliable for relatively high temperatures of cold plate with thick frost layer and airflow temperatures above zero degrees in Celsius while for other conditions it may be not true.

Several ways are accessible to measure frost-air interface temperature. Kim et al. [16] employed non-contact measuring system. However error related to uncertain frost emissivity values is a weak point of test methods based on radiant heat measurements and the unknown value of frost roughness aggravates the uncertainty of the results. Direct measurements of frost temperature, described in the studies of Yonko and Sepsy [17], Biguria and Wenzel [22], Brian et al. [15], Hayashi et al. [8], Ostin and Anderson [19], were provided by thermocouples as sensors and they were believed to be enough reliable if fine ones were used. The absence of temperature gradients beside junctions was essential for accuracy. For rough frost contact temperature measurements

depend on the position of the junction: when only small part of it was in a contact with frost particles the reliability of readings was low.

To obtain temperature of the cold plate all researchers used thermocouples.

Heat Flux. Heat flux is another important parameter for frost thermal conductivity calculations based on Fourier equation. Heat may be removed from the cold surface by coolant or by thermoelectric unit and that fact determines the methods for heat flux acquisition. The designs of the experimental set-ups with coolant supposed calculations of heat flux through energy balance equation based on inlet and outlet temperatures at the coolant side together with its mass flow rate. Examples of this approach may be found in studies by Yonko and Sepsy [7], Hayashi et al. [8], where also heat lost through insulation was obtained. In case of thermoelectric cooling heat flux meters should be applied, as Mao et al. [21] did in their studies on frosting phenomenon.

Frost Thermal Conductivity. Only few researchers, like Ostin and Anderson [19], applied transient method based on unsteady state temperature measurements inside the frost layer, while others, like Yonko and Sepsy [7], Biguria and Wenzel [22], Brian et al. [15], Hayashi et al. [8], and Mao et al. [21], conducted steady-state temperature measurements along the frost layer and acquisition of heat flux through the frost layer with further calculations of frost thermal conductivity. All steady-state methods, regardless to various test technique employed, suppose acquisition of frost surface temperature and thickness, cold plate temperature and heat flux with further calculations by means of Fourier equation. The transient methods are attractive due to their short duration. Constant or impulse heat flux was applied to a frost sample and temperatures in one or several points of the sample as a response were monitoring. Frost thermal conductivity was obtained by substitution of temperature values into expressions obtained from calibration tests with reference materials.

Appendix 2

Comparison of Frost Thermal Conductivity With Literatures. Test data on average effective frost thermal conductivity from present study was compared with the predicted by correlations from literature and the results are shown in Fig. 9. All corresponding correlations are collected in Table 2 and their reliability ranges are presented in Table 3. Equations (*A*4), (*A*5), and (*A*9) match present test data with the accuracy about $\pm 20 \sim 30$ percent. Unsatisfactory agreement with Eqs. (*A*1) and (*A*2) confirms assumption that not only conductance is responsible for heat transportation within frost layer.

References

[1] Nikulshina, D. G., Popova, E. M., Dol'skaya, V. I., Izotov, V. N., Luchin, V. A., and Starikh, Y. V., 1979, "The Study of the Influence of Hydrophobic Coating on Thermal and Aerodynamic Characteristics of Air Coolers," *Kholodilnaya Technika (Refrigerating Technique)*, **6** (in Russian), pp. 28–30.

[2] Seki, N., Fukusako, S., Matsuo, K., and Uemura, S., 1984, "Incipient Phenomena of Frost Formation," Bull. JSME, **27**(233), pp. 2476–2482.

[3] Hoke, J. L., Georgiadis, J. G., and Jacobi, A. M., 2000, "The Interaction Between the Substrate and Frost Through Condensate Distribution," *Technical report*, University of Illinois, Urbana-Champaign, p. 135.

[4] Tao, Y. X., Mao, Y., and Besant, R. W., 1994, "Frost Growth Characteristics on Heat Exchanger Surfaces: Measurement and Simulation Studies," *Fundamentals of Phase Change: Sublimation and Solidification*, HTD—Vol. 288, ASME, New York; pp. 29–38.

[5] Yoshiyuki, T., and Akiko, I., 1992, "Anti-Frosting Heat Exchanger," *National Technical Report*, **38**(1), pp. 108–113.

[6] Ryu, S. G., and Lee, K. S., 1999, "A Study on the Behavior of Frost Formation According to Surface Characteristics in the Fin-Tube Heat Exchanger," J. Air-Conditioning and Refrigerating, **11**(3) (in Korean), pp. 377–383.

[7] Yonko, J. D., and Sepsy, C. F., 1967, "An Investigation of the Thermal Conductivity of Frost While Forming on a Flat Horizontal Plate," ASHRAE Trans., **73**, Part 1, Paper No 2043, pp. 1.1–1.11.

[8] Hayashi, Y., Aoki, A., Adachi, S., and Hori, K., 1977, "Study of Frost Properties Correlating with Frost Formation Types," Trans. ASME J. Heat Transfer, **99**(**5**), pp. 239–245.

[9] Deitenberger, M. A., 1983, "Generalized Correlation of the Water Frost Thermal Conductivity," Int. J. Heat Mass Transf., **26**(4), pp. 607–619.

[10] Auracher, H., 1987, "Effective Thermal Conductivity of Frost," *Proceedings of the Int. Symp. of Heat and Mass Transfer in Refrigeration*, Dubrovnik, pp. 285–301.

[11] Sahin, A. Z., 2000, "Effective Thermal Conductivity of Frost During the Crystal Growth Period," Int. J. Heat Mass Transf., **43**, pp. 539–555.

[12] ASHRAE Standard, 1992, "Standard Method for Laboratory Airflow Measurements," ANSI/ASHRAE 41.2–1987 (RA 92), p. 32.

[13] Koh, S., Han, S., Song, S., Choi, W., and Jung, H., 1995, "Improving Wettability of Polycarbonate (PC) and Adhesion with Aluminum by Ar^+ Ion Irradiation," J. Mater. Res., **10**(6), pp. 2390–2397.

[14] Shin, J. M., Lee, N. G., Han, S. J., and Ha, S. C., 2001, "The Effect of Water Contact Angles of the Fin Surfaces of the Fin-and-Tube Heat Exchangers on the Water Hold-Up," J. Air-Conditioning and Refrigerating, **13**(6), pp. 490–496.

[15] Brian, P. L., Reid, R. C., and Shah, Y. T., 1970, "Frost Deposition on Cold Surfaces," Ind. Eng. Chem. Fundam., **9**(3), pp. 375–380.

[16] Kim, Y. C., Jhee, S., and Lee, K. S., 2000, "An Experimental Study of Frost Growth According to Environmental Parameters on a Flat Plate," *Proceedings of SAREK*, pp. 98–103.

[17] Besant, R. W., Rezkallah, K. S., Mao, Y., and Falk, J., 1990, "Measurements of Frost Thickness Using a Laser Beam and Light Meter," ASHRAE Trans., **96**, pp. 519–522.

[18] Takura, I., Saito, H., and Kishinami, K., 1983, "Study on Properties and Growth Rate of Frost Layers on Cold Surface," Trans. ASME J. Heat Transfer, **105**, p. 895–901.

[19] Ostin, R., and Anderson, S., 1991, "Frost Growth Parameters in a Forced Air Stream," Int. J. Heat Mass Transf., **34**(4/5), pp. 1009–1017.

[20] Mao, Y., Besant, R. W., and Rezkallah, K. S., 1991, "A Method of Measuring Frost Density Using Flush-Mounted Removable Discs," ASHRAE Trans. **97**(1), pp. 26–30.

[21] Mao, Y., Besant, R. W., and Rezkallah, K. S., 1992, "Measurements and Correlations of Frost Properties With Airflow Over the Flat Plate," ASHRAE Trans. **98**, pp. 65–78.

[22] Biguria, G., and Wenzel, L. A., 1970, "Measurements and Correlations of Water Frost Thermal Conductivity and Density," Ind. Eng. Chem. Fundam., **9**(1), pp. 129–139.

[23] Lee, K. S., Kim, W. S., and Lee, T. H., 1997, "A One-Dimensional Model for Frost Formation on a Cold Flat Surface," Int. J. Heat Mass Transf., **40**(18), pp. 4359–4365.

[24] Le Gall, R., Grillot, J. M., and Jallut, C., 1997, "Modeling of Frost Growth and Densification," Int. J. Heat Mass Transf., **40**(13), pp. 3177–3187.

[25] O'Neal, D. L., and Tree, D. R., 1985, "A Review of Frost Formation in Simple Geometry," ASHRAE Trans., **91**, pp. 267–281.

[26] Oscarsson, S. P., Krakow, K. I., and Lin, S., 1990, "Evaporator Models for Operation With Dry, Wet, and Frosted Finned Surfaces: Part 1—Heat Transfer and Fluid Flow Theory," ASHRAE Trans., **96**(1), pp. 373–380.

[27] Tao, Y. X., Besant, R. W., and Mao, Y., 1993, "Characteristics of Frost Growth on a Flat Plate During the Early Growth Period," ASHRAE Trans., **99**, pp. 746–753.

Observations of Early-Stage Frost Formation on a Cold Plate in Atmospheric Air Flow

Chin-Hsiang Cheng
e-mail: cheng@ttu.edu.tw

Keng-Hsien Wu

Department of Mechanical Engineering,
Tatung University,
Taipei, Taiwan 10451,
R.O.C.

The present study is conducted to investigate the frost formation on a cold plate in atmospheric air flow by means of experimental and theoretical methods. In order to provide observations for the early stage of the frost growth process, a microscopic image system is used to record the pattern and the thickness of the frost layer per five seconds after the onset of frost formation. In this study, a multiple-step ascending frost growth pattern caused by melting of frost crystals at the frost surface has been observed. Effects of velocity, temperature and relative humidity of air (V, T_a, and ϕ) are studied, and the surface temperature of the cold plate (T_w) is also varied. The considered ranges of these dominant variables are: $2 \leqslant V \leqslant 13$ m/s, $20 \leqslant T_a \leqslant 35°C$, 40 percent $\leqslant \phi \leqslant 80$ percent, and $-13 \leqslant T_w \leqslant -2°C$. The theoretical model presented by Cheng and Cheng [22] for predicting the frost growth rate during the frost layer growth period is verified. Results show that the predictions of frost growth rate by the model agree with the experiment data, especially for the frost layer growth period. [DOI: 10.1115/1.1513576]

Keywords: Heat Transfer, Mass Transfer, Melting, Phase Change, Refrigeration

Introduction

Frost formation on a cold plate has considerable practical relevance; however, the formation of frost could be desirable or undesirable depending on individual cases. For example, it is in general undesirable to have frost layer formed in the air-conditioning systems since the frost formation on the heat transfer surfaces not only results in additional thermal resistance but also leads to additional pressure drop. As reported by Emery and Siegel [1], a 50 to 75 percent decrease in heat transfer and a substantial increase in pressure drop are caused by frost formation on a compact heat exchanger. In addition, recent results provided by Su [2] also show a similar trend.

In the past several decades, a number of studies have been performed to investigate the process of frost formation [3]. However, since the frost formation process is really involved, even in the idealized cases of a humid air over a flat cold plate, a detailed physical picture for the frost formation is still not clear. For example, data provided by the previous studies [4–8] concerning the air velocity effects on frost formation are not in agreement. Schneider [4] and Şahin [5] found that the frost thickness is independent of the air velocity, whereas Lüer and Beer [6] found that a higher air velocity may cause an increase in average frost thickness, especially for the downstream region in a parallel-plate channel. O'Neal and Tree [7,8] observed that the frost growth rate increases with air velocity only as Reynolds number is less than 15,900. At a Reynolds number higher than this value, the frost growth shows no dependence on the Reynolds number. In addition, it is noted that even for the air temperature effects, inconsistencies between the existing reports are also found. Şahin [5] and Lüer and Beer [6] observed a thinner and denser frost layer at a higher air temperature. However, O'Neal and Tree [7] found no difference in the frost thickness in a three-hour experiment.

Secondly, during the frost formation process, the amount of water vapor of the atmospheric air approaching the frost layer is approximately divided into two parts [9–11]. One part of the water vapor enters the existing frost layer for solidification and increases the density throughout the frost layer. The other part rests on the surface of frost layer, and the solidification of this part of water vapor increases the frost thickness. Therefore, both the density and the thickness of the frost layer increase with time; however, the transient variation of the mass fractions of these two parts of water vapor is still not completely clear. In addition, based on the observations provided by Hayashi et al. [12] for frost crystal structure and variation in frost thickness and density, the frost formation process can be subdivided into three periods: (1) crystal growth period, (2) frost layer growth period, and (3) frost layer full growth period. Lately, two possible frost growth patterns, monotonic and cyclic, were reported by Östin and Andersson [13]. The cyclic frost growth is attributed to the frost melting on the frost surface that indicates the beginning of the frost layer full growth period described by Hayashi et al. [12]. However, since the evidence of pattern visualization or the quantitative information is lacking, further investigation of the frost growth periods is definitely necessary.

So far, the frost formation process is usually treated as a phenomenon of large time constant and hence, in these existing studies the frost growth data were recorded typically at a sampling rate of 15 to 30 minutes per sampling for a rather long duration (say, 2 to 5 h). However, based on the existing information, it may be concluded that the frost formation process consists of a number of periods having different features and characteristics. The frost structure could experience a transition between one period and another in a short period of time; therefore, a long-duration measurement with a sampling rate of 15 to 30 min per sampling would not provide enough information for the rapid changes in the state of the frost layer. This probably is one of the causes for the lack of detailed information regarding the frost growth periods. Therefore, in the present study, a microscopic image system has been built up to observe the frost growth pattern and measure the frost thickness per five seconds after the onset of frost formation. The application of this system can help avoid any omission for the rapid changes in seconds, which are highly expected during the early stage. Thus, the cyclic frost growth [12] can be further investigated in this study.

On the other hand, information about the frost layer has also been collected by theoretical methods. A number of reports have been presented for the growth of the frost layer during different periods. The theoretical models are developed based on the mass

Contributed by the Heat Transfer Division for publication in the JOURNAL OF HEAT TRANSFER. Manuscript received by the Heat Transfer Division November 1, 2001; revision received June 13, 2002. Associate Editor: P. S. Ayyaswamy.

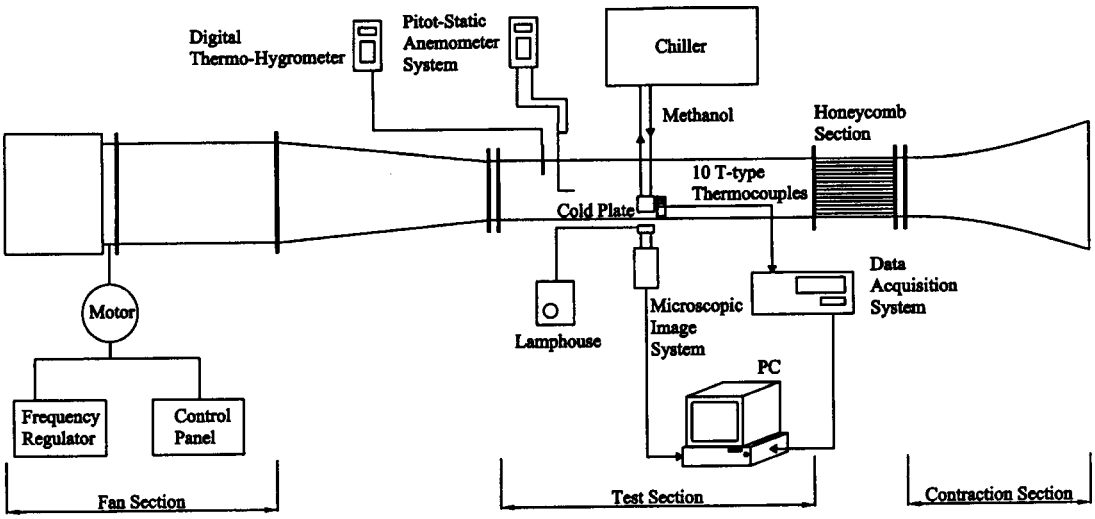

Fig. 1 Experiment system

and energy balance principles and normally consist of a set of ordinary or partial differential equations (ODEs or PDEs) plus required property relations. The models proposed by Jones and Parker [10], Meng et al. [14], Sami and Duong [15], Padki et al. [16], and Sherif et al. [17] are several cases dealing with ODEs. Tao and coworkers [18,19] presented a two-stage frost formation model which is referred to a PDE model. Chen et al. [20] proposed a numerical model for predicting the frost growth on plate-fin heat exchangers by treating the frost growth as a porous media that is transient, one-dimensional and including transient, two-dimensional heat conduction in the fins. In comparison with the experiments, either the ODE or PDE kind of models leads to satisfactory results [21] and provides a sufficient amount of data not easily obtainable with measurements. Recently, Cheng and Cheng [22] proposed an ODE-kind theoretical model which can be used to predict the frost growth rate on the surface of a flat plate with varying surface temperature. More recently, the model due to Cheng and Cheng [22] has been improved and extended to the analyses of frost formation for a stationary or oscillating cylinder by Fang [23]. In this study, the theoretical model due to Cheng and Cheng [22] is further verified using the obtained experimental data.

Four dominant variables are considered herein: the air velocity (V) and temperature (T_a) are varied within the ranges $2 \leqslant V \leqslant 13$ m/s and $20 \leqslant T_a \leqslant 35$°C, respectively; relative humidity of air (ϕ) ranges from 40 percent to 80 percent; and temperature of the cold plate (T_w) is varied from -13 to -2°C. Selection of these ranges is based on two reasons. Firstly, the ranges of the environmental variables are related to the applications in the modern air-conditioning systems. As a matter of fact, similar ranges have been taken into account in a number of the existing studies. Therefore secondly, the phenomena observed in this study may be compared with those reported in these existing studies.

Experimental Apparatus and Procedure

Experimental Apparatus. The experiment system in this study consists of a wind tunnel, a chiller, a cold plate and cooling unit assembly, the microscopic image system, an image processor, a data acquisition system for temperature measurement, a thermo-hygrometer, and a pitot-static anemometer system. The layout of the experiment system is given in Fig. 1. Experiments are performed in the test section of a suction-type open-loop wind tunnel. The wind tunnel has a length of 5.5 m and consists of a contraction section, a honeycomb section, the test section, and a fan section. The test section of the wind tunnel, which has a 300 mm×300 mm cross section and a length of 1.6 m, is made with Plexiglas plate of 10 mm thickness so that the frost layer can be clearly observed by the microscopic image system. The entrance contraction and the honeycomb sections are placed in front of the test section. The honeycomb section contains about 2000 subchannels, each with a length-to-diameter ratio of 34. The air velocity may be varied in the range of 0 to 20 m/s by means of a frequency regulator connected with the fan motor.

The chiller is used to provide a circulation of the low-temperature working fluid for cooling purpose. The working fluid, methanol, can be cooled down to lowest -20°C by the chiller and then is circulated to the cold plate and the cooling unit assembly. The cold plate is made of copper (C1220) with surface roughness of 0.57 μm. The length and the width of the cold plate are both fixed at 56 mm, and the thickness is 6 mm. The cold plate is mounted on a cooling unit, through which the low-temperature methanol is circulated. The cooling unit is also made of Plexiglas whose thermal conductivity is sufficiently low so as to reduce the heat transfer to the cooling unit from the surrounding. The cold plate is aligned with the bottom surface of the test section, and its lateral faces are insulated by a bakelite layer. Figure 2(a) shows the design of the cold plate and cooling unit assembly. The temperature of the cold plate is measured by eight T-type thermocouples installed at eight different locations uniformly distributed in the cold plate. All the thermocouple probes are placed at the same level of 3 mm beneath the surface of the cold plate. Temperature data are recorded by a data acquisition system (Model No. NetDAQ 2640A, FLUKE). The thermocouple wires are inserted into the cold plate from its lateral faces and connected to the data acquisition system from under the bottom face of the test section to eliminate possible disturbance to the air flow. Figure 2(b) shows the planar locations of the eight thermocouples installed in the cold plate. The uniformity of the temperature distribution on the cold plate surface has been observed based on the temperature data measured by the eight thermocouples. In addition, two T-type thermocouples are mounted at the inlet and the exit of the cooling unit to measure the inlet and exit temperatures of methanol. The temperature data recorded by the data acquisition system are transferred to a personal computer for further analysis.

The microscopic image system consists of a CCD camera (Model No. IK-624F, TOSHIBA), a zoom/enlarging lens unit (Model No. 29-95-92, OPTEM), and a luminescence house/annular illuminator unit (Model No. 29-60-02/29-60-31, OPTEM). The CCD camera and the zoom/enlarging lens unit, which is at maximum of 158× magnification, are mounted by the side of the test section for taking the photographs of the frost

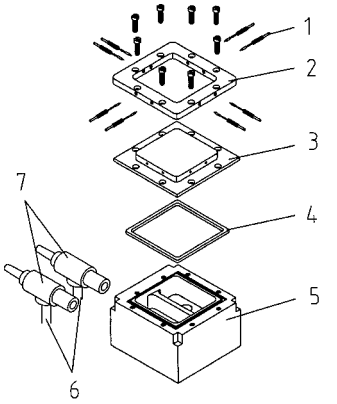

No.	Item
1	T-type thermocouples (×8)
2	Bakelite layer
3	Cold plate
4	O-ring
5	Cooling unit
6	T-type thermocouples (×2)
7	Inlet/Exit valve

(*a*)

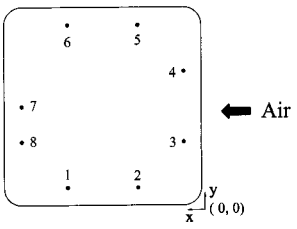

Node	Coordinate (mm)
1	(38, 5)
2	(18, 5)
3	(5, 18)
4	(5, 38)
5	(18, 51)
6	(28, 51)
7	(51, 28)
8	(51, 18)

(*b*)

Fig. 2 Cooling assembly: (*a*) cold plate and cooling unit; and (*b*) locations of thermocouples

formation per five seconds from outside. The annular illuminator unit provides luminescence light for observation, having no appreciable thermal radiation to the frost layer. A personal computer, equipped with a color PCI frame grabber, receives the images taken by the microscopic image system. The images are analyzed with an image processor (MATROX software, Inspector version 2.1). A software-based microscale having 150 pixels in 1 mm is developed by the image processor. A 1 mm objective microruler manufactured by OLYMPUS is used as a standard ruler for calibrating the microscale having a resolution of 1/150 mm per pixel scale in both *x* and *y*-directions. Therefore, as the number of pixel scales occupied by the area of the frost layer is determined with the image processor, the thickness of the frost layer can then be calculated.

The experiment system is placed in a laboratory room, and the conditions of the room air are controlled and varied by an air-conditioning system. The relative humidity and the temperature of the room air are continuously monitored by a thermo-hygrometer. Meanwhile, the relative humidity and temperature of the incoming air over the cold plate are measured by using another thermo-hygrometer. The temperatures measured by the meters are compared with those measured by *T*-type thermocouples to ensure the accuracy of the measurement. The relative uncertainty of the relative humidity measurement reaches a maximum ± 5 percent as the relative humidity ranges from 30 to 50 percent. The uncertainty of the temperature measurement is ± 0.1°C for full range.

The pitot-static anemometer system consists of a pitot-static probe and a differential pressure transducer. The pitot tube (1/8 in. diameter, DWAYER) is mounted in the downstream area of the test section to reduce possible interference with the air flow. The differential pressure signal developed in the pitot tube is transmitted to the differential pressure transducer, and there this signal is converted to air velocity by performing a mathematical conversion. The resolution and accuracy of the differential pressure transducer used in this study are 0.01 mmH_2O and ± 0.2 percent at full range, respectively. Note that the pitot-static probe is designed to measure velocities in steady-state flow conditions and small air velocity (less than 1.0 m/s) is not measured accurately since the magnitude of the differential pressure developed by the pitot tube is small. In this study, the air velocity is varied between 2 and 13 m/s, located in the valid range.

Table 1 Uncertainty analysis for measured variables

Variable	Typical value x	Uncertainty* δx	Relative uncertainty δx/x
V	2.0～5.0 m/s	0.1 m/s	2%
	10.0～20.0 m/s	0.4 m/s	2%
ϕ	30%～50 %	2 %	5%
	50%～90%	2%	2%
T_a	20～35℃	1.0℃	-
T_w	-13～-2℃	1.0℃	-
T_i	-20～0℃	0.1℃	-
T_o	-20～0℃	0.1℃	-
x_s	0～2.5 mm	0.007 mm	0.3%

* All values are estimated with 95 percent confidence.

Uncertainty Analysis. An uncertainty analysis has been carried out and the results are summarized in Table 1. Uncertainty may be caused by many sources. In this study, these sources are basically divided into four categories: environment-control uncertainty, calibration uncertainty, measurement uncertainty, and data acquisition uncertainty. The uncertainty interval for each measured variable is estimated with a 95 percent confidence using the concepts proposed by Kline and McClintock [24] and Moffat [25]. It is observed in Table 1 that the relative humidity of air contributes by far the largest relative uncertainty in the entire experiment, especially for the cases of lower relative humidity. For the relative humidity ranging from 30 to 50 percent, the relative uncertainty of the relative humidity measurement reaches a maximum ± 5 percent; however, only 2 percent is found for the relative humidity higher than 50 percent. The relative uncertainty of the relative humidity measurement is mainly caused by the uncertainties of the environmental condition control and the accuracy of the measurement instrument. The values listed in Table 1 involve all significant uncertainty sources and may be treated as the safest estimation of the uncertainty.

In addition, the relative uncertainty of air velocity measurement is approximately 2 percent for full range in this study. This value is partially contributed by the uncertainty of thermal properties of air. The thermal properties of air (e.g., air density) can be determined from numerous existing handbooks. However, the data from different existing sources are somewhat scattered, and moreover, the uncertainty of temperature measurement could actually produce error in the determination of the properties. Thus, the uncertainty of the thermal properties of air may be treated as a combination of a random uncertainty of the scattered data and fixed uncertainty caused by the error of temperature measurement. Note that the uncertainty of air density can propagate into the determination of air velocity since the air velocity is calculated by

$$V = \sqrt{\frac{2\Delta P}{\rho_a}} \tag{1}$$

where ρ_a is the air density and ΔP represents the pressure difference detected by the pitot tube.

According to Eq. (1), it is found that the uncertainty of air velocity is a function of the uncertainties of the differential pres-

sure measurement and the air density. The combining uncertainty is calculated by applying the methods described by Moffat [25]. The magnitudes of the uncertainties of these variables are basically reasonable and acceptable since in experiment some unpredictable uncertainties may always exist inevitably. As a matter of fact, the uncertainty of the benchmark experimental data may vary by 10 percent, as reviewed by Cheng et al. [26].

Results and Discussion

Frost Pattern. Figure 3 shows the photographs for the frost growth at different instants for the case at $V=2.5$ m/s, $T_a=26.5°C$, $\phi=41$ percent, and $T_w=-7.2°C$. The crystal growth period is first observed. Frost layer at the location of 30 mm from the leading edge of the cold plate is brought into focus of the microscopic system. The images are recorded per five sec; however, to save space only the photographs at several instants are provided in this figure. Small, isolated crystal columns grow in the direction perpendicular to the cold plate in a short period of time after start. In this period, the structure of the frost crystals is like a forest of trees, and the isolated columns grow at approximately the same rate while no homogeneous frost layer is found. At the end of the crystal growth period (about 60 sec from start for this case), a thin frost layer covering the surface is formed. Then, the thickness and the density of the frost layer both increase with time. The extent of the frost layer increases while new frost crystal columns continue to appear on top of the thin frost layer, and the density of the frost layer is increased by the formation of crystal branches stemming from the crystal columns. This period is referred to as the frost layer growth period. Note that for the case considered in Fig. 3, the tree-like crystal column structure is always found at the frost surface during the frost layer growth period. In Fig. 3, the frost formation process covers both the crystal growth and the frost layer growth periods. However, the frost layer full growth period is not reached within 30 min.

When the air velocity (V) is elevated greatly and the temperature of the cold plate becomes lower, a different pattern of frost layer may be seen during frost formation process. As displayed in Fig. 4, for $V=6.0$ m/s, $T_a=27.3°C$, $\phi=44$ percent, and $T_w=-10.2°C$, a denser frost layer is formed on the cold plate surface. Obviously, both the frost thickness and density are increased based on the visual inspection on Fig. 4. In a short time a frost layer composed of the frost crystals and their branches covers the cold plate, and this implies a shorter crystal growth period in this case. Next, in the frost layer growth period, a smooth, uniform frost layer grows gradually. The tree-like crystal column structure is still found at the frost surface, and the frost layer looks like a dry, porous-medium layer. For this case, the frost layer growth ends at about 20 min. After this time, the thickness of the frost layer does not change significantly until the frost surface begins to melt. The melting at the frost surface is attributed to the increase

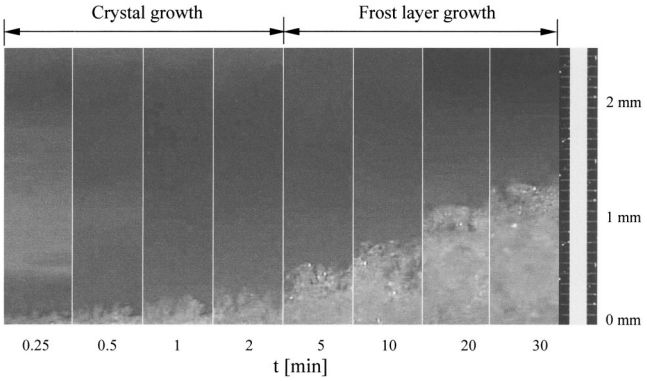

Fig. 3 Frost growth, for $V=2.5$ m/s, $T_a=26.5°C$, $\phi=41$ percent, and $T_w=-7.2°C$

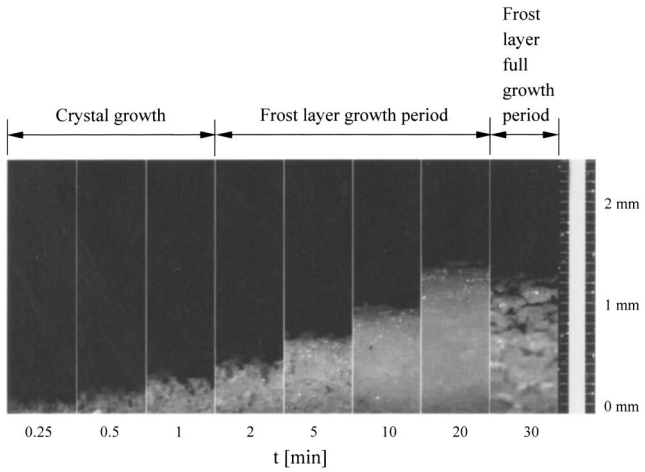

Fig. 4 Frost growth, for $V=6.0$ m/s, $T_a=27.3°C$, $\phi=44$ percent, and $T_w=-10.2°C$

in frost surface temperature due to the frost growth. As the frost surface temperature reaches the melting point of frost, the melting starts. The melted water initially stays at the frost surface with the support of surface tension, and then suddenly penetrates into the frost layer. The water penetrating into the frost layer may cause a slight collapse of the frost crystals in the neighboring areas and may be frozen to form an ice layer. The penetration of water into the layer causes a sudden increase in the frost layer density and a sudden decrease in its thermal resistance, and then the frost formation on the frost surface occurs again. The process of melting, freezing, and frost formation can be repeated several times for the duration of a test. Therefore, the frost layer grows in a multiple-step ascending manner. The environmental variables have profound influence on the frost layer pattern. For some certain cases, the frost layer may become ''wet'' under intense melting. The period with multiple-step ascending frost growth due to melting and freezing of water is known as the frost layer full growth period. The above observations basically confirm the experimental results provided in the previous reports [12,13] for the frost layer full growth period. In Fig. 4, the photograph at $t=30$ minutes clearly shows the frost layer wetted by the melting water.

Frost Thickness. Figure 5 shows the effects of the surface temperature of the cold plate on frost thickness. In this case, the velocity, temperature, and relative humidity are held constant at $V=4.2$ m/s, $T_a=27.3°C$, and $\phi=41$ percent. Decreasing the cold

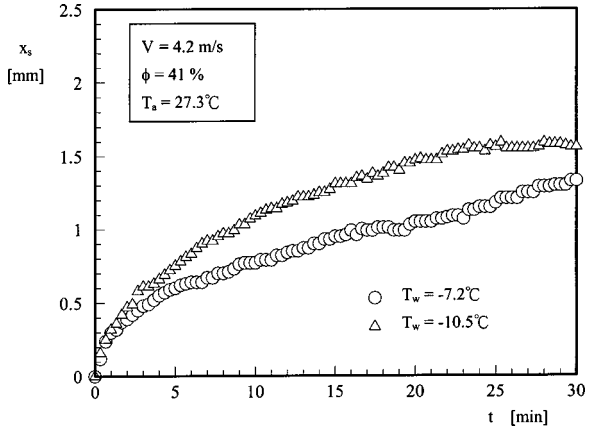

Fig. 5 Effects of cold plate surface temperature on frost thickness, for $V=4.2$ m/s, $T_a=27.3°C$, and $\phi=41$ percent

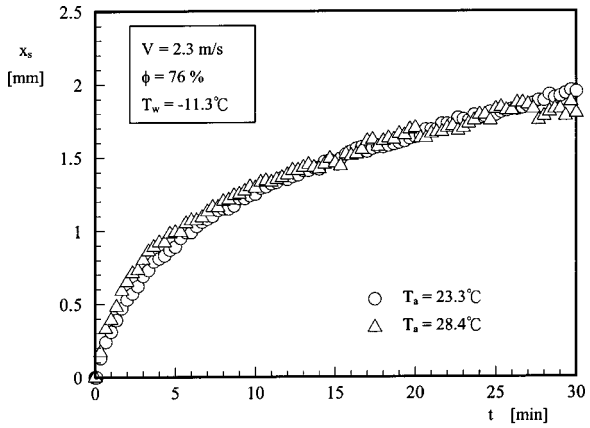

Fig. 6 Effects of air temperature on frost thickness, for $V = 2.3$ m/s, $\phi = 76$ percent, and $T_w = -11.3°C$

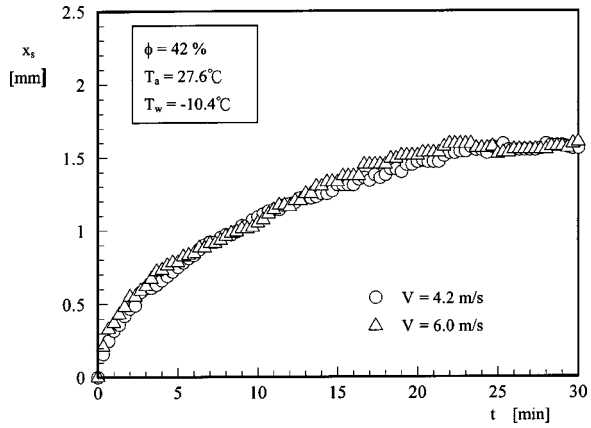

Fig. 8 Effects of air velocity on the frost thickness, for $T_a = 27.6°C$, $\phi = 42$ percent, and $T_w = -10.4°C$

plate surface temperature from $-7.2°C$ to $-10.5°C$ leads to a significant increase in frost thickness. For the case at $T_w = -7.2°C$, the frost thickness is 1.35 mm at $t = 30$ min, whereas for the case at $T_w = -10.5°C$, it reaches 1.56 mm during the test. The same tendency has been reported in Refs. [5], [6], [13].

Figure 6 conveys the effects of air temperature on the frost thickness, for the case at $V = 2.3$ m/s, $\phi = 76$ percent, and $T_w = -11.3°C$. The inconsistencies between the existing reports concerning the air temperature effects have been noted earlier. In Fig. 6, one observes only small difference in the frost thickness between the data obtained at $T_a = 23.3°C$ and $T_a = 28.4°C$. The comments for the results would be given in three aspects. Firstly, the water vapor with higher air temperature arriving at the frost surface may not be cooled immediately to a temperature below the

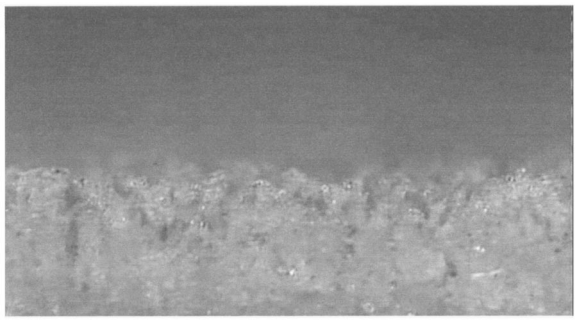

(*a*)

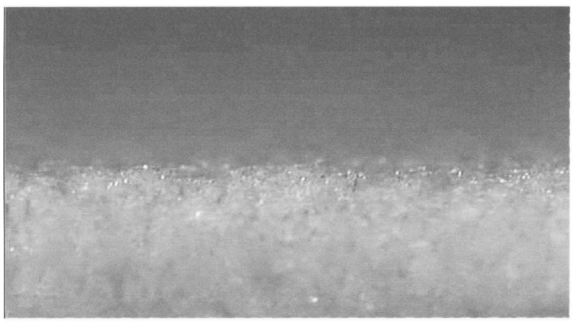

(*b*)

Fig. 7 Effects of air temperature on the structure of frost layer for $V = 2.3$ m/s, $\phi = 76$ percent, and $T_w = -11.3°C$. Photographs are taken at $t = 8$ min. (*a*) $T_a = 23.3°C$; and (*b*) $T_a = 28.4°C$.

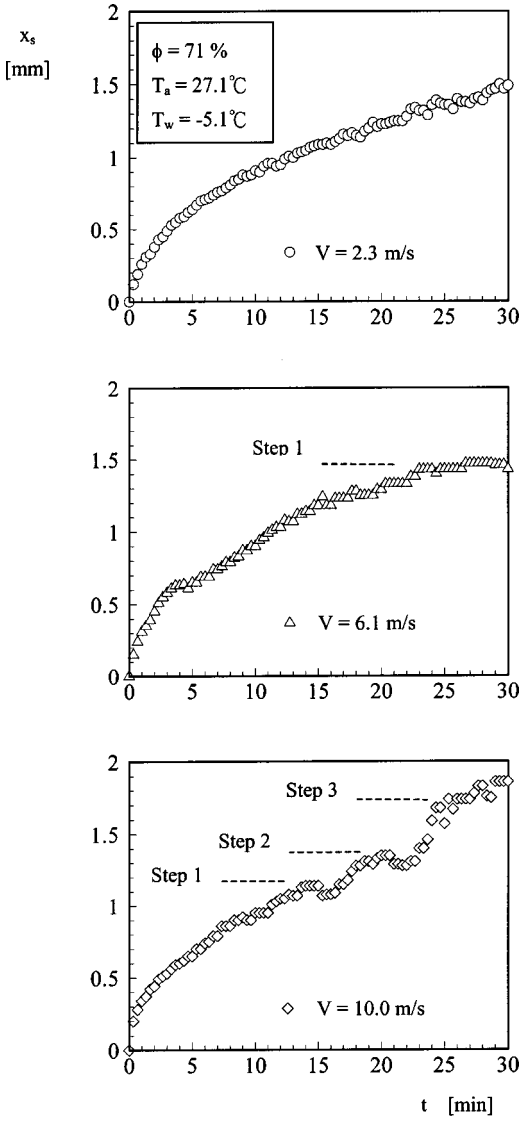

Fig. 9 Effects of air velocity on the frost thickness of the multiple-step ascending frost layer, for $T_a = 27.1°C$, $\phi = 71$ percent, and $T_w = -5.1°C$

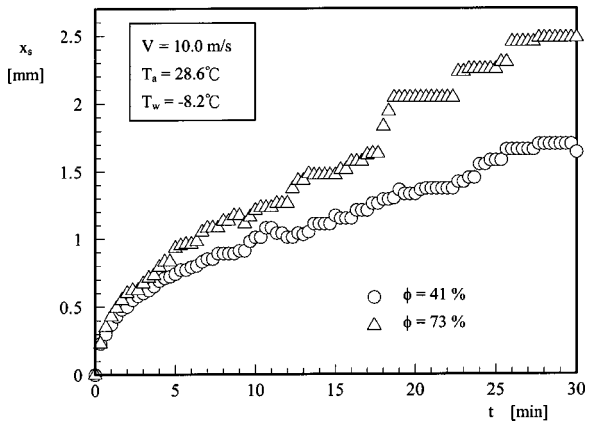

Fig. 10 Effects of relative humidity on frost thickness, for $V=10.0$ m/s, $T_a=28.6°C$, and $T_w=-8.2°C$

freezing point; therefore, the water vapor may not be deposited on the frost surface to increase the frost thickness but enter the frost layer for solidification. This could cause higher density but no remarkable difference in frost layer thickness. Figure 7 shows evidence illustrating the effects of the air temperature on the frost density for the same cases. In this figure, a denser frost layer is clearly seen at a higher air temperature.

Secondly, a higher air temperature causes a higher frost surface temperature; therefore, melting of the crystal columns and branches formed at the frost surface is easier to occur. When the air temperature is further elevated, the multiple-step ascending feature becomes more remarkable. Visual inspection based on the images recorded shows that melting at the frost surface leads to the multiple-step ascent. Thirdly, in Fig. 6, the values of the relative humidity of air are held constant for the cases considered. Hence, an increase in air temperature always comes along with an increase in the moisture content of the air. In this aspect, the frost thickness seemingly has a tendency to increase particularly when melting of water does not occur. All these factors lead to a complicated nature of the frost that may cause these inconsistencies found in the literature.

Data provided by the previous studies [4–8] regarding the air velocity effects on frost formation are also not in agreement. However, it can be expected that the heat and mass transfer to the frost layer may increase with the air velocity and therefore, either the frost density or the frost thickness will be elevated by increasing the air velocity. For those cases with an increasing air velocity which do not have a significant increase in the frost thickness, there is always a significant increase in the frost density, and vice versa. For example, in Fig. 8, the frost thickness data for $T_a=27.6°C$, $\phi=42$ percent, and $T_w=-10.4°C$ exhibit only slight dependence on the air velocity. However, a denser frost layer has been visually observed for the case at a higher air velocity, $V=6.0$ m/s.

Also lied in Fig. 8 is that a higher air velocity makes the frost layer full growth period appear earlier. This can be recognized based on the observation of the melting of the frost. To provide further insight into the effects of air velocity on frost melting, Fig. 9 shows the experimental results for the history of the frost thickness at various air velocities. Other environmental variables are fixed $T_a=27.1°C$, $\phi=71$ percent, and $T_w=-5.1°C$. At $V=2.3$ m/s, only the monotonic ascending frost layer is seen. When the air velocity is increased to 6.1 m/s, the frost layer full growth period can be clearly observed at about $t=30$ min. For the case at $V=10.0$ m/s a three-step ascending pattern is observed, and the frost layer becomes wet after the point marked step 1. A slight decrease of frost thickness may be found after each step due to the collapse of frost layer caused by the penetration of melted water. The feature of the multiple-step ascending frost is recorded per

Table 2 Theoretical model presented by Cheng and Cheng [22]

Frost thickness:

$$\frac{dx_s}{dt}=\frac{h_M(\omega_a-\omega_s)}{x_s\cdot 147.55\exp[0.227(T_s-273.15)](dT_s/dx_s)+\rho_f}$$

Frost surface temperature:

$$T_s=\frac{1}{2}\frac{x_s\Delta h}{k_f}\left[h_M(\omega_a-\omega_s)+\rho_f\frac{dx_s}{dt}\right]+\frac{h_H(T_a-T_s)}{k_f}x_s+T_w$$

Effective frost conductivity:

$$k_f=8.49\times10^{-17}\bar{T}_f^{5.44}+6.86\times10^{-14}(\bar{\rho}_f-0.025)\bar{T}_f^{4.84}$$

Effective frost density:

$$\rho_f=650\exp[0.227(T_s-273.15)]$$

Heat transfer coefficient:

$$Nu=0.664\,Re^{1/2}Pr^{1/3}$$

Mass transfer coefficient:

$$h_M=h_H/c_{pm}\quad\text{(Lewis number = 1)}$$

Specific heat:

$$c_{pm}=c_p+\omega_a c_{pv}$$

Vapor pressure at frost surface:

$$\ln P_{ws}=C_1/T_s+C_2+C_3T_s+C_4T_s^2+C_5T_s^3+C_6T_s^4+C_7\ln T_s$$

five sec, and it is found that the sampling rate is able to avoid any omission for the rapid changes taking place in a test.

Figure 10 depicts the effects of relative humidity of the air on the frost thickness, for $V=10.0$ m/s, $T_a=28.6°C$, and $T_w=-8.2°C$. It is noted that as the moisture content of the air increased, there is a corresponding increase in the frost thickness. In addition, the multiple-step ascending frost growth pattern is observed clearly as ϕ is elevated to 73 percent.

Comparison Between Experimental and Theoretical Data. The measurement data of frost growth are compared with those predicted by the theoretical model proposed by Cheng and Cheng [22] so as to verify the validity of the model. This model was developed based on the mass and the energy conservation laws, and was expressed in form of ordinary differential equations as-

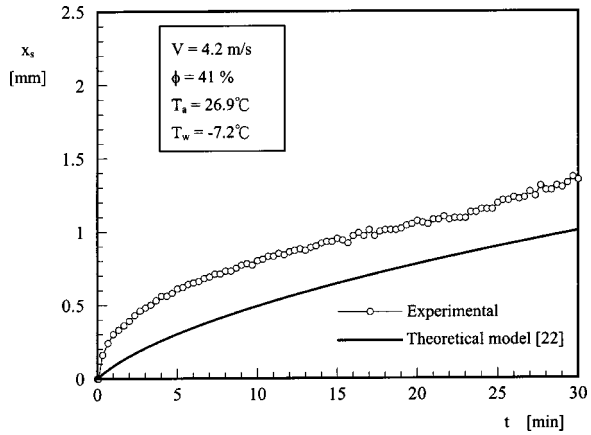

Fig. 11 Comparison in frost thickness between the experimental data and the theoretical predictions by Cheng and Cheng [22], for $V=4.2$ m/s, $T_a=26.9°C$, $\phi=41$ percent, and $T_w=-7.2°C$

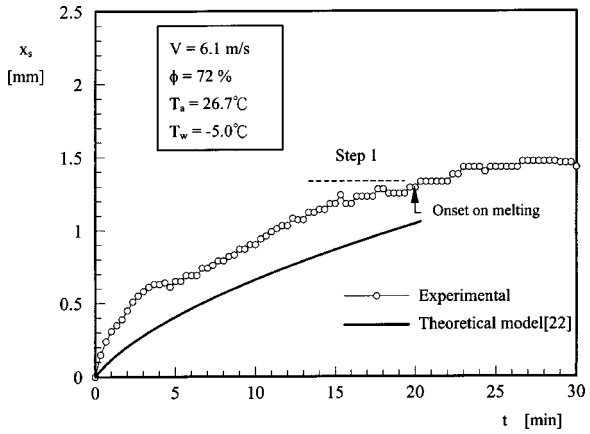

Fig. 12 Comparison in frost thickness between the experimental data and the theoretical predictions by Cheng and Cheng [22], for $V=6.1$ m/s, $T_a=26.7°C$, $\phi=72$ percent, and $T_w=-5.0°C$

sociated with necessary property relations. General description and further details of this model is available in [22]; therefore, the development of this model is not addressed herein. The mathematical expressions of the model are listed in Table 2. Note that the differential equations may be discredited into finite-difference form, and the numerical solutions for the histories of frost thickness, frost density, and frost surface temperature can be obtained under various environmental conditions. The numerical computation is terminated either when the freezing point temperature of water is reached (that is, beginning of melting) or the duration of the experiments is exceeded.

Figure 11 shows the results of comparison for $V=4.2$ m/s, $T_a=26.9°C$, $\phi=41$ percent, and $T_w=-7.2°C$. The experimental data exhibit a monotonic ascending pattern in the frost thickness growth, and no melting occurs in 30 min. The numerical predictions basically exhibit a same trend. In this figure, the discrepancy between the experimental and the numerical data is nearly constant and independent of time, especially in the frost layer growth period. Not surprisingly, the model is not able to provide accurate results for the early stage of the frost formation (that is, the crystal growth period), in which the cold plate is covered by the separate, isolated crystal columns, not a uniform frost layer. The predicted values of the frost thickness are lower than the experimental data from the beginning. This is because in the early crystal growth period a larger portion of the cold plate surface is really exposed to the air and thus results in smaller thermal and mass resistances to the heat and mass transfer.

Figure 12 shows the comparison between the experimental and the theoretical data for the case with one-step ascending patterns. For the case considered in this figure, the numerical computation is automatically terminated exactly before onset of melting, which is marked with "step 1" in this figure. This implies that the theoretical model can accurately simulate the trend of the increasing frost surface temperature and predict the onset time of melting.

Additional information for the relative performance of the theoretical model has been further investigated by comparing with other ODE-kind models proposed by Jones and Parker [10] and Sherif et al. [17], based on the same set of property relations. The results are available in Ref. [22].

Concluding Remarks

In this study the frost formation on a cold plate has been investigated by means of the experimental and theoretical methods. Experimental observations are performed for the early stage of the frost growth process. A microscopic image system has been built up for recording the frost growth pattern and measuring the thickness of the frost layer at a sampling time interval of 5 second in order to avoid any omission for the rapid changes in the tests. The microscopic image system is designed that the fragile, porous frost layer may be observed without destruction. The images of the frost layer are recorded and the thickness is measured with an image processor on a personal computer. A software-based micrometer having 150 pixels in 1 mm is used to measure the frost layer thickness. Meanwhile, a theoretical model has been developed in order to provide deeper insight into the heat and mass transfer characteristics of the frost layer. Comparison between the experimental data and the theoretical predictions has been made, and then relative performance of this model has also been investigated.

Based on the data recorded per five sec a multiple-step ascending pattern has been observed for the duration of 30 min for some particular cases. In the previous studies, the frost growth was recorded typically at a sampling time interval of 15 to 30 min during a 2 to 5 h frost formation process. Therefore, these rapid changes in the state of the frost layer could not be observed. In the present study, however, it is found that the frost layer may exhibit a multiple-step ascending pattern in no more than 30 min. It means that in a short time the frost layer is possible to reach the frost layer full growth period under some certain environmental conditions, especially for the cases at higher air temperature, higher air humidity, or higher air velocity.

The multiple-step ascending pattern of the frost layer is evidently caused by the melting of frost crystals at the frost surface. The melted water penetrates into the frost layer, stops the frost layer from growing up, and causes a densification. It is only when the thermal resistance is reduced due to the densification that the frost layer starts to grow again. The process of melting, freezing, and frost formation can be repeated several times in 30 min, and thus results in multiple-step ascending growth.

The inconsistencies among the previous studies regarding the air temperature and velocity effects on the frost thickness are probably caused by the complicated nature of the frost formation process. However, any conclusion drawn from the existing information should not neglect the role of frost density.

Comparisons between the predictions by the theoretical model due to Cheng and Cheng [22] and the experimental data show that the model is useful in predicting the frost growth rate for the frost layer growth period as well as the onset of frost melting. However, as expected, for the crystal growth period, the numerical predictions of the frost growth rate are in general lower than the experimental data.

Nomenclature

c_{pa} = specific heat of dry air [J/(kg·K)]
c_{pm} = specific heat of atmospheric air [J/(kg·K)]
c_{pv} = specific heat of water vapor [J/(kg·K)]
h = latent heat of solidification of water vapor [J/kg]
h_H = heat transfer coefficient [W/(m^2·K)]
h_M = mass transfer coefficient [kg/(m^2·s)]
Δh = latent heat of solidification for vapor [J/kg]
k = thermal conductivity [W/(m·K)]
$\dot{m}_t$ = total mass flux of water vapor [kg/(m^2·s)]
$\dot{m}_d$ = mass flux of water vapor increasing frost density [kg/(m^2·s)]
$\dot{m}_s$ = mass flux of water vapor increasing frost thickness [kg/(m^2·s)]
Nu = Nusselt number
Pr = Prandtl number
P_t = atmospheric pressure [N/m^2]
P_{vs} = partial pressure of saturated water vapor [N/m^2]
q_t = total heat flux [W/m^2]
Re = Reynolds number
t = time [s]
T = temperature [K] or [°C]
V = velocity [m/s]

x_s = frost thickness [mm]

Greek Symbols

ρ = density [kg/m^3]
ϕ = relative humidity [percent]
ω = humidity ratio [kg_v/kg_{dryair}]

Subscripts

a = atmospheric air
f = frost
o = exit of cooling unit
s = frost surface
w = surface of cold plate

References

[1] Emery, A. F., and Siegel, B. L., 1990, ''Experimental Measurements of the Effects of Frost Formation on Heat Exchanger Performance,'' Proceedings of AIAA/ASME Thermophysics and Heat Transfer Conference, *Heat and Mass Transfer in Frost and Ice Packed Beds and Environmental Discharges*, Armilli, R. V., Beasley, D. E., and Sengupta, S., eds., ASME HTD-Vol. 139, pp. 1–7.

[2] Su, Y. P., 2001, ''Study of Thermofluid Characteristics of Plate and Louvered Finned-and-Tube Heat Exchangers under Frosting Conditions,'' Master Thesis (advisor: Yan, W. M.), Huafan University, Taipei, Taiwan, June 2001.

[3] Yonko, J. D., and Sepsy, C. F., 1967, ''An Investigation of the Thermal Conductivity of Frost While Forming on a Flat Horizontal Plate,'' ASHRAE Trans., **73**, Part I, pp. I1.1–I1.9.

[4] Schneider, H. W., 1978, ''Equation of the Growth Rate of Frost Forming on Cooled Surface,'' Int. J. Heat Mass Transf., **21**, pp. 1019–1024.

[5] Şahin, A. Z., 1994, ''An Experimental Study on the Initiation and Growth of Frost Formation on a Horizontal Plate,'' Exp. Heat Transfer, **7**, pp. 101–119.

[6] Lüer, A., and Beer, H., 2000, ''Frost Deposition in a Parallel Plate Channel under Laminar Flow Conditions,'' Int. J. Therm. Sci., **39**, pp. 85–95.

[7] O'Neal, D. L., and Tree, D. R., 1984, ''Measurement of Frost Growth and Density in a Parallel Plate Geometry,'' ASHRAE Trans., **90**, pp. 278–290.

[8] O'Neal, D. L., and Tree, D. R., 1985, ''A Review of Frost Formation in Simple Geometries,'' ASHRAE Trans., **91**, pp. 267–281.

[9] Brian, P. L. T., Reid, R. C., and Shah, Y. T., 1970, ''Frost Deposition on Cold Surfaces,'' Ind. Eng. Chem. Fundam., **9**, pp. 375–380.

[10] Jones, B. W., and Parker, J. D., 1975, ''Frost Formation with Varying Environmental Parameters,'' ASME J. Heat Transfer, **97**, pp. 255–259.

[11] Sami, S. M., and Duong, T., 1989, ''Mass and Heat Transfer during Frost Growth,'' ASHRAE Trans., **95**, pp. 158–165.

[12] Hayashi, Y., Aoki, A., Adachi, S., and Hori, K., 1977, ''Study of Frost Properties Correlating with Frost Formation Types,'' ASME J. Heat Transfer, **99**, pp. 239–245.

[13] Östin, R., and Andersson, S., 1991, ''Frost Growth Parameters in a Forced Air Stream,'' Int. J. Heat Mass Transf., **34**, pp. 1009–1017.

[14] Meng, F., Gao, W., and Pan Y., 1987, ''Growth Rate of Frost Formation Through Sublimation—A Porous Medium Physical Model for Frost Layer,'' Proceedings of the 1985 International Symposium on Heat Transfer, *Heat Transfer Science and Technology*, Wang, B. X., ed., Hemisphere, Washington, pp. 584–593.

[15] Sami, S. M., and Duong, T., 1989, ''Mass and Heat Transfer during Frost Growth,'' ASHRAE Trans., **95**, pp. 158–165.

[16] Padki, M. M., Sherif, S. A., and Nelson, R. M., 1989, ''A Simple Method for Modeling the Frost Formation Phenomenon in Different Geometries,'' ASHRAE Trans., **95**, pp. 1127–1137.

[17] Sherif, S. A., Raju, S. P., Padki, M. M., and Chan, A. B., 1993, ''A Semi-Empirical Transient Method for Modeling Frost Formation on a Flat Plate,'' Int. J. Refrig., **16**, pp. 321–329.

[18] Tao, Y.-X., and Besant, R. W., 1993, ''Prediction of Spatial and Temporal Distributions of Frost Growth on a Flat Plate Under Forced Convection,'' ASME J. Heat Transfer, **115**, pp. 278–281.

[19] Tao, Y.-X., Besant, R. W., and Rezkallah, K. S., 1993, ''A Mathematical Model for Predicting the Densification and Growth of Frost on a Flat Plate,'' Int. J. Heat Mass Transf., **30**, pp. 353–363.

[20] Chen, H., Thomas, L., and Besant, R. W., 2000, ''Modeling Frost Characteristics on Heat Exchanger Fins: Part I. Numerical Model,'' ASHRAE Trans., **106**, pp. 357–367.

[21] Chen, H., Thomas, L., and Besant, R. W., 2000, ''Modeling Frost Characteristics on Heat Exchanger Fins: Part II. Model Validation and Limitation,'' ASHRAE Trans., **106**, pp. 368–376.

[22] Cheng, C. H., and Cheng, Y. C., 2001, ''Predictions of Frost Growth on a Cold Plate in Atmospheric Air,'' Int. Commun. Heat Mass Transfer, **28**, pp. 953–962.

[23] Fang, C. S., 1997, ''Predictions of Frost Growth and Heat Transfer Coefficient on Surface of an Oscillating Cylinder,'' Master thesis, (advisor: Cheng, C. H.), Tatung University, Taipei, Taiwan, June 1997.

[24] Kline, S. J., and McClintock, F. A., 1953, ''Describing Uncertainties in Single-Sample Experiments,'' Mech. Eng. (Am. Soc. Mech. Eng.), **75**, pp. 3–8.

[25] Moffat, R. J., 1988, ''Describing the Uncertainties in Experimental Results,'' Exp. Therm. Fluid Sci., **1**, pp. 3–17.

[26] Cheng, C. H., Chen, H. N., and Aung, W., 1997, ''Experimental Study of the Effect of Transverse Oscillation on Convection Heat Transfer from a Circular Cylinder,'' ASME J. Heat Transfer, **119**, pp. 474–482.

Effects of Varying Geometrical Parameters on Boiling From Microfabricated Enhanced Structures

C. Ramaswamy
IBM Corporation,
Hopewell Junction, NY 12533

Y. Joshi
G. W. Woodruff School of Mechanical Engineering,
Georgia Institute of Technology,
Atlanta, GA 30332

W. Nakayama
ThermTech International,
Kanagawa, Japan 255-0004

W. B. Johnson
Laboratory for Physical Sciences,
College Park, MD 20740

The current study involves two-phase cooling from enhanced structures whose dimensions have been changed systematically using microfabrication techniques. The aim is to optimize the dimensions to maximize the heat transfer. The enhanced structure used in this study consists of a stacked network of interconnecting channels making it highly porous. The effect of varying the pore size, pitch and height on the boiling performance was studied, with fluorocarbon FC-72 as the working fluid. While most of the previous studies on the mechanism of enhanced nucleate boiling have focused on a small range of wall superheats (0–4 K), the present study covers a wider range (as high as 30 K). A larger pore and smaller pitch resulted in higher heat dissipation at all heat fluxes. The effect of stacking multiple layers showed a proportional increase in heat dissipation (with additional layers) in a certain range of wall superheat values only. In the wall superheat range 8–13 K, no appreciable difference was observed between a single layer structure and a three layer structure. A fin effect combined with change in the boiling phenomenon within the sub-surface layers is proposed to explain this effect.
[DOI: 10.1115/1.1513575]

Keywords: Boiling, Electronics, Enhancement, Experimental, Heat Transfer, Microstructures

Introduction

Enhanced structures are often used to improve the two-phase heat transfer, over plain surfaces. For example, heat exchangers and process equipment use tubes with engineered features on the walls that promote boiling/condensation and improve the performance significantly (see Thome [1] and Webb [2]). In electronics cooling, the heat source area is typically around 1–4 cm^2, and the space around the heat source is limited. Employing an enhanced structure can provide a sufficiently large heat transfer area (per unit volume) in this constrained space. Hence, the use of enhanced structures for electronics cooling is a very attractive option.

A few authors have investigated two-phase heat transfer (pool boiling) from enhanced structures, for electronics cooling. Noteworthy among them are Oktay [3], Nakayama et al. [4] and Mudawar and Anderson [5]. A sketch of the enhanced surfaces developed by these authors, with heat fluxes achieved in pool boiling, is shown in Fig. 1. The sketch shows that, in general, there are two ways of fabricating the enhanced structures, sintering metallic particles and using grooved/machined plates with very small features (0.1–0.8 mm). This study focuses on the latter category and hence all future discussions in this paper are relevant to that.

Geometrical features of the enhanced structures play an important role in their boiling performance. A few studies have addressed this by conducting systematic parametric experiments. Nakayama et al. [6] developed boiling enhancement structures by soldering a thin copper sheet to a copper substrate containing rectangular channels. The copper sheet was then pierced to form pores of different diameter on top of the channels (see Fig. 2). Their studies on the effect of pore diameter revealed an optimum value for best thermal performance, which was a function of the wall superheat and working fluid. The working fluids in their study were water, R-11 and liquid nitrogen. For example, in an earlier study by Nakayama et al. [7], a pore diameter of 140 μm was found to result in best performance for wall superheats more than 2 K in water. For wall superheats below 2 K, a pore diameter of 80 μm resulted in better performance than 140 μm.

Arshad and Thome [8] conducted experiments with surfaces similar to Nakayama et al. [7]. They tested three different channel cross-sections—circular, rectangular and triangular (see Fig. 2). They obtained best performance with water as the working fluid for a pore diameter of 250 μm, which is slightly different from the pore diameter of 180 μm obtained by Nakayama et al. [7]. The channels with triangular cross-section had the best performance at low heat fluxes, but dried out at intermediate heat fluxes. Ma et al. [9] carried out parametric experiments on grooved surfaces covered with fine mesh screens and a thin brass sheet with pores of different diameters (see Fig. 2). Using a combination of a 40-mesh screen and a plate having 160 μm diameter pores provided the best performance in water (9 W/cm^2 at a wall superheat of 1 K). They also tested grooves of different cross-section—triangular, rectangular and pentagonal. Their experiments showed that the triangular grooves performed better than the rectangular grooves for heat fluxes greater than 8 W/cm^2.

Recently, Chien, and Webb [10] carried out a detailed parametric study on an integral fin tube with a copper foil soldered on top. The copper foil was then pierced to form pores. The effect of varying the pore diameters (120–280 μm) for different pore pitches (0.7–3.0 mm), on saturated boiling from R-123 and R-11 was examined. The results, in a wall superheat range of 0–3 K show an optimum pore size of 230 μm, for which the heat transfer coefficients were highest. However, beyond a wall superheat of 3 K, a pore size of 280 μm resulted in a higher heat transfer coefficient than pore size of 230 μm. Their data suggest that with an increase in the wall superheat, the optimum pore size increases. A larger pore pitch (fewer number of pores/cm) resulted in a higher heat transfer coefficient, for a pore size of 230 μm and 280 μm.

Contributed by the Heat Transfer Division for publication in the JOURNAL OF HEAT TRANSFER. Manuscript received by the Heat Transfer Division May 2, 2001; revision received June 11, 2002. Associate Editor: G. P. Peterson.

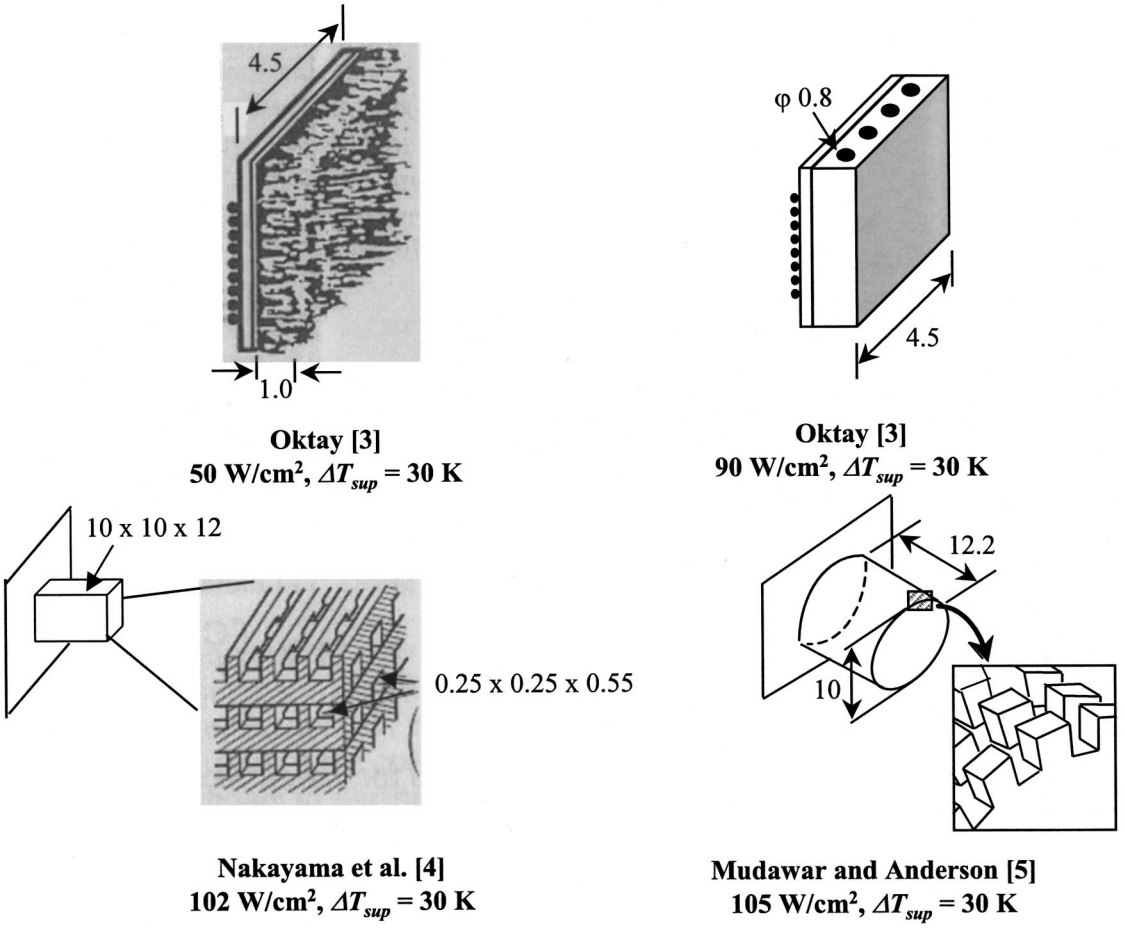

Fig. 1 Enhanced structure in electronics cooling, using FC-72 as the working fluid

However, beyond approximately 2 W/cm^2, this trend reversed and a smaller pore pitch (more pores/cm) resulted in better performance. For a pore size of 120 μm, a smaller pore pitch resulted in higher heat transfer coefficients at all heat fluxes. From the data one can conclude that beyond a heat flux of 2 W/cm^2, a larger number of pores/cm will result in higher heat dissipation.

The above mentioned studies [7–10] are limited to a wall superheat in the range 0–4 K. For the fluids used in electronics cooling (fluorocarbons or FC family), wall superheats as high as 30 K are possible under normal operation. For example, for FC-72 the saturation temperature at atmospheric pressure is approximately 56°C and the maximum allowable chip temperatures may

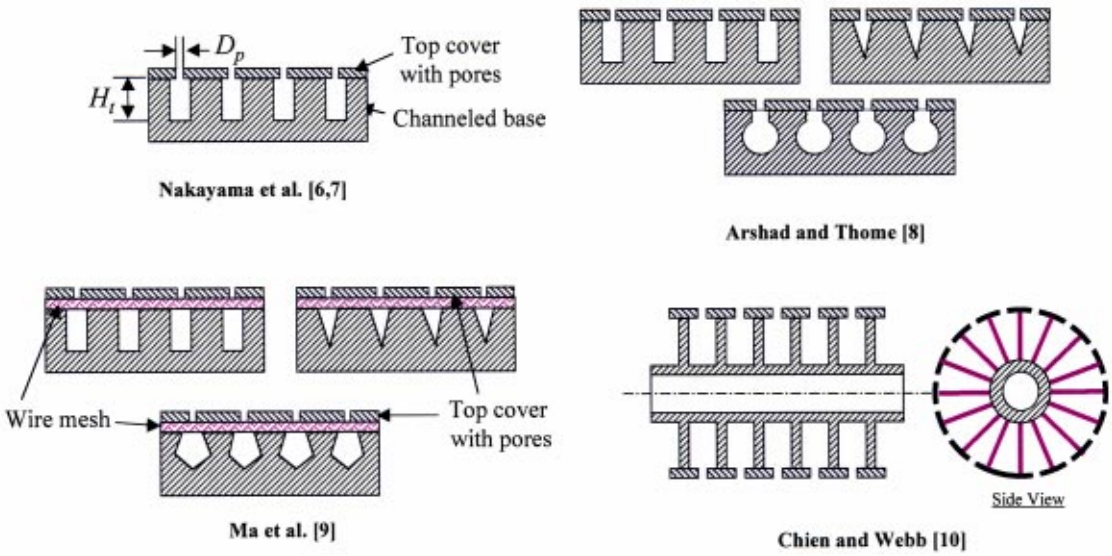

Fig. 2 Cross-sectional view of structures used by authors for parametric study

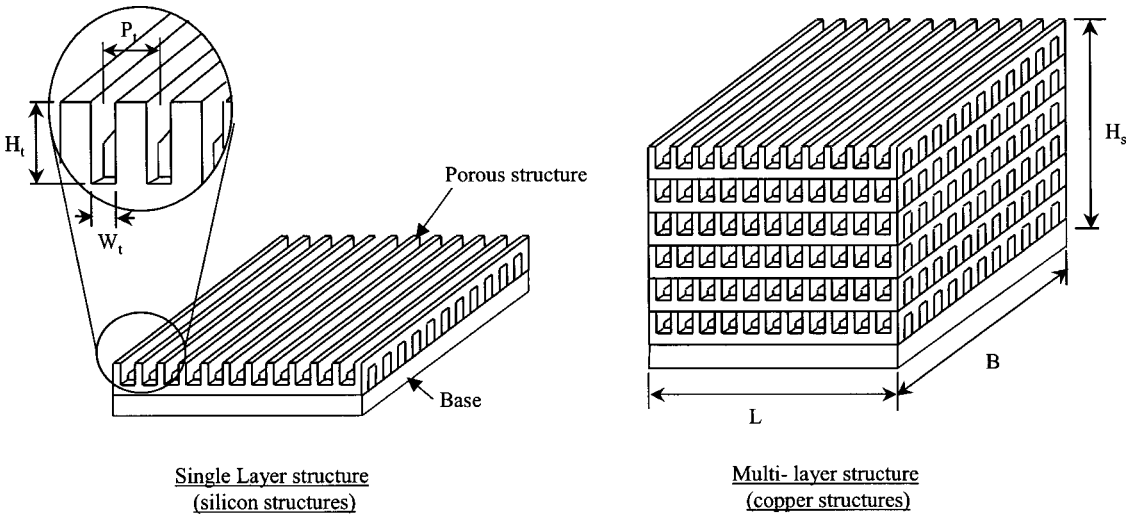

Fig. 3 Enhanced structures employed in this study (silicon and copper)

be on the order of 85°C. It is necessary to understand the effect of the geometry of surface enhancement features at these wall superheat levels. The current investigation aims at studying the effect of varying some of the geometrical parameters, of an enhanced structure, in the wall superheat range 4–30 K, with FC-72 as the working fluid. The enhanced structure used in this study was similar to one used by Nakayama et al. [4] and has a structured array of pores (more details in next section). The particular structure was chosen because the dimensions can be optimized in a systematic fashion, which is one of the goals of this study. The effect of stacking multiple layers of the enhanced structures on the boiling performance was also studied and the results are included here. A one-dimensional model to predict the effect of stacking was developed and the predictions compared to the experimental results.

Enhanced Structures

A sketch of the enhanced structure, which was the focus of this study, is shown in Fig. 3. The structures have an array of rectangular channels cut on either side of a substrate and aligned at an angle of 90 deg to each other. The depth of the channels is more than half the thickness of the substrate, resulting in the channels intersecting at discrete locations to provide square pores. In this study, silicon and copper substrates were used to fabricate the enhanced structures. The advantage of using silicon is that the enhanced structures can be directly bonded on the passive side of a silicon chip (or die), resulting in a lower thermal resistance and eliminating coefficient of thermal expansion (CTE) mismatch.

Two methods of fabrication, compatible with integrated circuits microfabrication techniques, were used for silicon—wet etching and wafer dicing. In wet etching, a silicon wafer with ⟨110⟩ crystal orientation was patterned using photolithography and then etched using a 40 percent KOH solution. In wafer dicing, a high-speed saw, with diamond impregnated nickel blades, was used to mill the channels one at a time. The width of the channels was varied using blades of different thickness. This resulted in pores of different sizes. The structures thus fabricated were then bonded to a silicon base plate using thin aluminum foil (2 μm), sandwiched between the two and annealed at 570°C. Silicon forms a eutectic with aluminum at this temperature, forming a permanent bond.

Copper has been used in many of the previous studies and is also included in the present study. The individual copper structures were first fabricated using wire electro-discharge machining. Several layers, depending on the required stack height, were then dip soldered (63Pb-37Sn) and bonded together at 200°C. A more detailed discussion on these techniques is presented in Ramaswamy et al. [11] and Ramaswamy [12].

The enhanced structures with multiple layers resulted in geometrical features that are different from previous studies [7–10] in that they are three-dimensional and the bubble dynamics may be very different compared to a single layer structure. Structures with different channel size, pitch and height were used in the current study and the geometrical details are listed in Table 1.

Experimental Setup

A schematic of the test facility is shown in Fig. 4(*a*). The test set-up consists of evaporator and condenser sections separated by flexible PFA (poly-fluoro-alkoxy) tubing with an internal diameter of 3.2 mm. This provides a thermosyphon loop with the condenser placed at a higher elevation compared to the evaporator for liquid return by gravity. Figure 4(*b*) shows a detailed sketch of the evaporator section which consists of a plexiglass enclosure (12.7 mm thick walls) of outside dimensions 50 mm×50 mm×40 mm. The heater assembly consists of an Omega cartridge heater embedded into a square copper rod (1.1 cm^2 cross sectional area). Omegatherm® ''201'' high thermal conductivity, high temperature paste was applied between the heater and the copper rod for good contact. The copper rod was insulated with plexiglass and additional Styrofoam insulation to minimize heat loss. The enhanced structure was soldered to one end of this heater assembly.

Four copper-constantan sheathed thermocouples (0.08 mm diameter) were embedded at the center of the copper rod starting from 4 mm below the boiling surface at intervals of 4 mm. These

Table 1 Three-dimentional enhanced structures employed in the current study

Structure Identification Number	Channel Width (W_t) μm	Channel Pitch (P_t) mm	Channel Height (H_t) mm	Layer Thickness (mm)	Material
C-0.27-0.63	270	0.63	0.55	0.85	Copper
C-0.20-0.5	200	0.5	0.55	0.85	Copper
S-0.32-0.7-D	320	0.7	0.26	0.51	Silicon
S-0.20-1.0-W	200	1.0	0.26	0.50	Silicon
S-0.20-0.7-D	200	0.7	0.26	0.51	Silicon
S-0.20-0.5-W	200	0.5	0.26	0.50	Silicon
S-0.15-2.1-D	150	2.1	0.26	0.51	Silicon
S-0.15-1.4-D	150	1.4	0.26	0.51	Silicon
S-0.15-0.7-D	150	0.7	0.26	0.51	Silicon
S-0.15-0.5-W	150	0.5	0.26	0.50	Silicon
S-0.12-0.7-D	120	0.7	0.26	0.51	Silicon
S-0.09-0.7-D	90	0.7	0.26	0.51	Silicon

D - wafer dicing
W - wet chemical etching

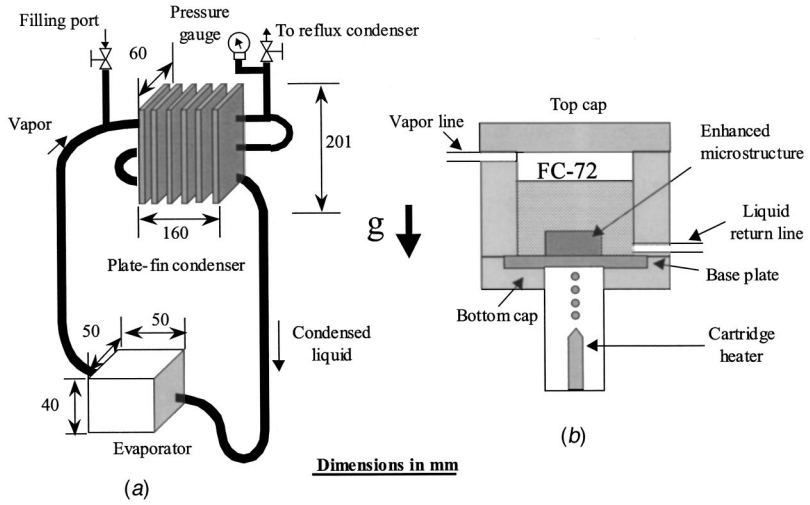

Fig. 4 (*a*) Schematic of the thermosyphon loop; and (*b*) detailed view of the evaporator

thermocouples were used to calculate the heat flux at the base of the enhanced structure (1 cm^2) by a one-dimensional heat conduction analysis. Pool temperature in the evaporator section was measured using an embedded copper-constantan thermocouple of 0.08 mm diameter. The thermocouple measurements were acquired using a National Instruments data acquisition system interfaced to a personal computer and controlled using LabVIEW software.

Power to the heater was supplied by a Fisher Scientific Variac (0-140V). Voltage taps were placed on the heater lead wires very near the sheath. This provided precise measurement of voltage drop across the heater. A precision resistor ($1\Omega \pm 0.01\Omega$) was connected in series to the power supply to measure the line current. A Fluke 87 True RMS multimeter measured the voltages.

A plate fin condenser was employed with the fin spacing of 6 mm optimized for operation in natural convection. A Robinair pressure gauge (-101 kPa to 0.8 MPa) was attached to the loop near the exit of the condenser to monitor the loop pressure during leak test of the set-up (in vacuum and under pressure). An ice cooled spiral tube reflux condenser was used to trap any vapor leaving the condenser. It also provided a vent for the system to maintain it at atmospheric pressure throughout the tests.

Experimental Procedure

Every experimental run was preceded by a degassing operation. The vent valve (Fig. 4(*a*)) was opened and a heat input of 70 W was supplied to the heater (to start vigorous boiling). Boiling was sustained for about one hour and then the system was allowed to cool down for two hours. The vent valve was kept closed during this period. The system reached room temperature by this time in all the runs. Before commencement of the test runs, the valve was again opened to ensure atmospheric conditions inside the system at all heat input levels. This procedure ensured that the dissolved gas concentration of non-condensibles was uniform, if not zero, in all the runs.

The initial heat input was set at 1 W and incremented in steps of 1 W until boiling was observed. Subsequently, the increments were increased to 2.5 W and beyond 20 W, to 10 W (in all cases the boiling was well established before reaching 20 W). The temperatures were monitored continuously and the heat input incremented after the system reached steady state (defined by a rise of less than 0.2 K in a span of 10 minutes). The temperatures were then recorded at two-second intervals for one minute. The averaged values were used to calculate the temperature gradient and the heat input to the enhanced structure. The tests were continued until the temperature at the base of the enhanced structure exceeded 85°C, a limit for most commercial electronics. Finally, the heat input was decremented through the same values, as it was incremented, until cessation of boiling.

Measurements and Uncertainty Analysis

The voltage measurement uncertainty was specified by the instrument manufacturer as 0.7 percent of the reading. The precision resistor used to measure the line current was accurate to 1 percent. The thermocouples and the National Instruments data acquisition system were calibrated against a precision mercury thermometer at ice point to an uncertainty of 0.1 K. Uncertainty estimates for derived quantities were made using the Kline and McClintok [13] technique. These estimates included the uncertainties due to resolution of instruments and placement of the thermocouples. The maximum uncertainty in the electrical power input was ± 1.4 percent. As a result of the linear curve fit of the temperature data, from the inline thermocouples, the maximum uncertainty in the heat flux was ± 13.6 percent (mostly contributed by the uncertainty in the location of thermocouples in the copper rod). The uncertainty in the wall superheat values was ± 0.12 K.

Results and Discussion

Effect of Pore Size. The pore diameter in this study is defined as the diameter of a circle that is inscribed inside the square pore. The pore diameter (D_p) was varied from 90 μm to 320 μm, with the pitch (P_p) fixed at 0.7 mm (13 pores/cm). The results are presented in Fig. 5. As the pore size (and hence the channel width) was increased the heat transfer performance improved. The improvement is easily discernible at low to intermediate heat fluxes ($4-20$ W/cm^2). However, at the higher heat fluxes the performance is very similar for all pore sizes. At a wall superheat of 10 K, the improvement in heat dissipation is approximately 4 percent, 20 percent, 35 percent, and 45 percent for a pore size of 120 μm, 150 μm, 200 μm, and 320 μm respectively (relative to 90 μm). At a wall superheat of 30 K, however, the improvement is only 3.3 percent, 4.2 percent, 5 percent, and 5.5 percent in the same order of pore sizes (relative to a size of 90 μm). In the heat flux range of $35-40$ W/cm^2, the difference in the wall superheat values for all the pore sizes was within 0.5 K. Hence, the effect of channel size is considered negligible for these high heat fluxes. The enhancement in heat dissipation for the different pore sizes, for selected values of wall superheats, is listed in Table 2.

Chien and Webb [10] found that a pore size of 280 μm resulted in higher heat transfer coefficients than a pore size of 230 μm and

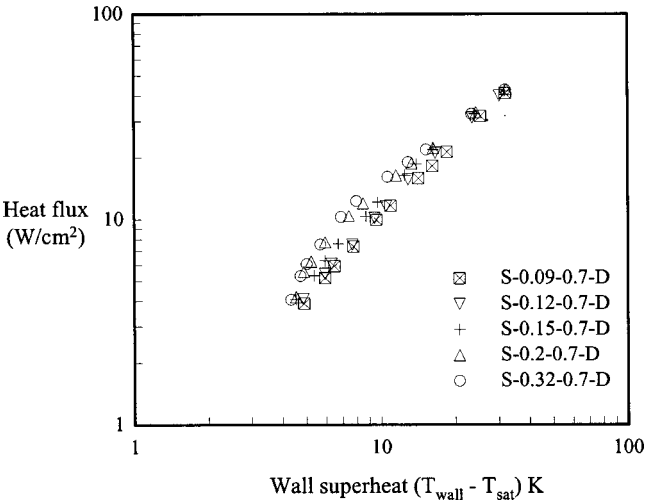

Fig. 5 Effect of pore size on boiling heat transfer (P_p = 0.7 mm)

120 μm, beyond a wall superheat of 3 K. The results from the current study also show that a larger pore size results in a higher heat flux, beyond a wall superheat of 4 K.

Nakayama et al. [6] hypothesized three modes of boiling from enhanced structures (Fig. 6). Their study suggests that as the heat flux is increased, the interior channels would dry out and the boiling mechanism can be expected to be very similar to that from plain surfaces. Under these conditions varying the channel size would not result in any significant change in the total heat dissipated. The data from the current study suggest that in the heat flux range 35–40 W/cm^2, the interior channels may be devoid of liquid and hence are not contributing to the heat dissipation.

Table 2 Relative enhancement (percent) in heat dissipation for different pore sizes (P_p=0.7 mm, H_s=1.2 mm)

ΔT_{sup} (K)	D_p = 120 μm	D_p = 150 μm	D_p = 200 μm	D_p = 320 μm
5	5.9	17.9	45.6	50.0
10	4.0	19.8	35.2	44.9
15	12.0	19.5	23.2	28.0
20	11.2	15.0	15.6	19.6
25	6.9	8.9	8.9	10.6
30	3.2	4.2	4.7	5.3

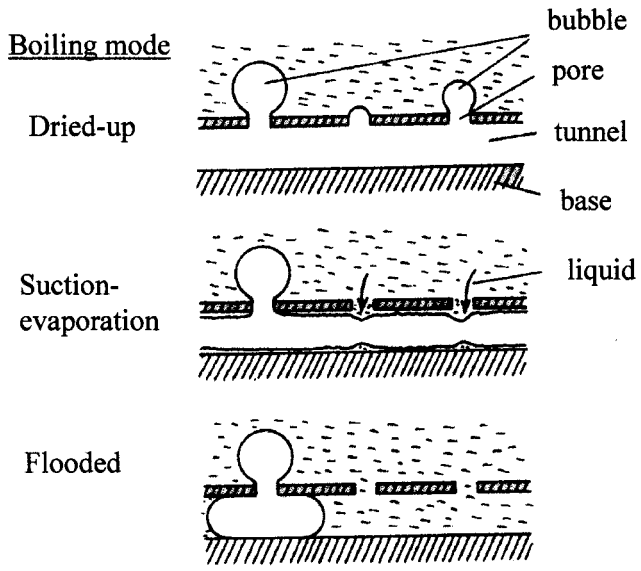

Fig. 6 Possible modes of boiling (Nakayama et al., [6])

Effect of Pore Pitch. The effect of varying the pore pitch was studied for two different pore sizes—150 μm and 200 μm. The pitch was varied from 0.5 mm to 2.1 mm for a fixed pore size of 150 μm, and from 0.5–1.0 mm for a pore size of 200 μm. The results for a pore size of 150 μm are shown in Fig. 7. As the pore pitch was decreased from 2.1 to 0.5 mm, a significant improvement in the heat dissipation resulted. At a wall superheat of 10 K, this improvement is 14 percent, 127 percent, and 186 percent for a pitch of 1.4, 0.7, and 0.5 mm respectively (relative to a pore pitch of 2.1 mm). The number of pores/cm^2 is 16, 36, 169, and 361 for a pore pitch of 2.1, 1.4, 0.7, and 0.5 mm respectively. Clearly, the number of pores increases significantly as the pitch is reduced and this provides additional sites for bubble generation. Also, the area for liquid flow into the channels increases resulting in a possible increase in the latent heat transfer inside the channels.

At higher heat fluxes (>30 W/cm^2), the improvement in the heat dissipation is less, although still discernible. The enhancement data for the different pore pitches are listed in Table 3 for selected wall superheat values. For a wall superheat of approximately 15 K, the structure with a pitch of 1.4 mm had lower heat dissipation compared to one with 2.1 mm. Visual observation showed that for the latter structure, the entire channel network (on the external surface) was contributing to boiling instead of just the pores. The latter structure was fabricated using a wafer dicing saw and the channel walls were not very smooth and the boiling from the pores quickly spread to the entire channel. Repetitive experiments showed the same phenomenon. For the structure with 1.4 mm pitch, this spreading occurred at a wall superheat of approximately 17 K, and the performance exceeded that with a pitch of 2.1 mm. Visual observation also showed that this phenomenon

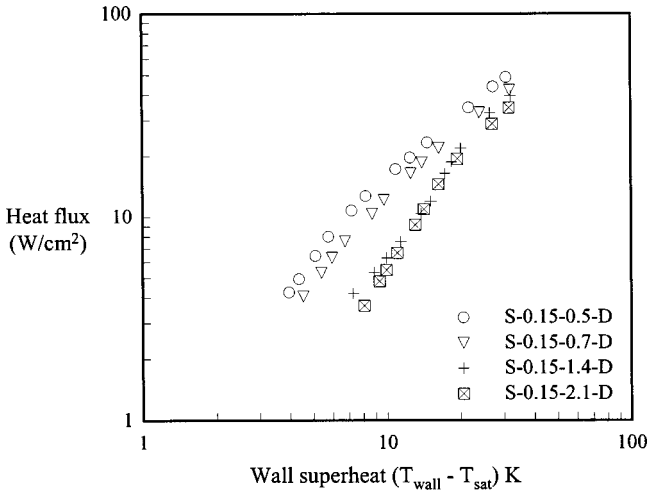

Fig. 7 Effect of pore pitch on boiling heat transfer (D_p = 0.15 mm)

Table 3 Relative enhancement (percent) in heat dissipation for different pore pitches (D_p=150 μm and 200 μm, H_s = 1.2 mm)

ΔT_{sup} (K)	D_p = 150 μm			D_p = 200 μm	
	P_p = 1.4 mm	P_p = 0.7 mm	P_p = 0.5 mm	P_p = 0.7 mm	P_p = 0.5 mm
10	14.0	127.1	185.9	46.6	99.1
15	-4.2	63.0	93.2	41.0	76.8
20	7.8	34.3	58.4	20.3	41.1
25	15.0	29.0	52.1	13.2	27.7
30	14.5	23.5	46.8	7.6	21.7

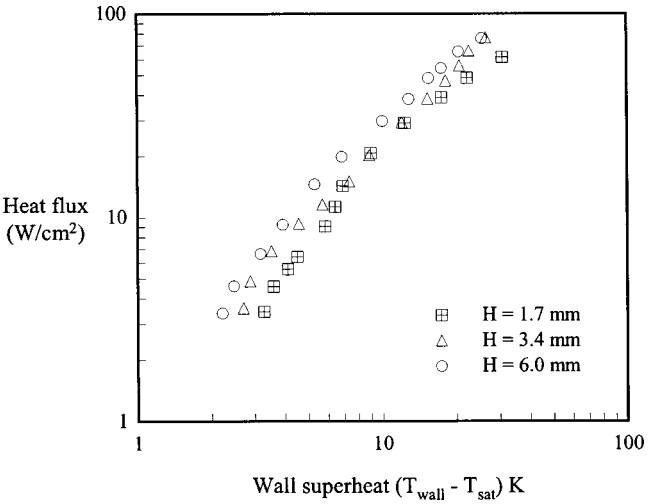

Fig. 8 Effect of varying stack height (H_s) on boiling heat transfer (for 'C-0.2-0.5')

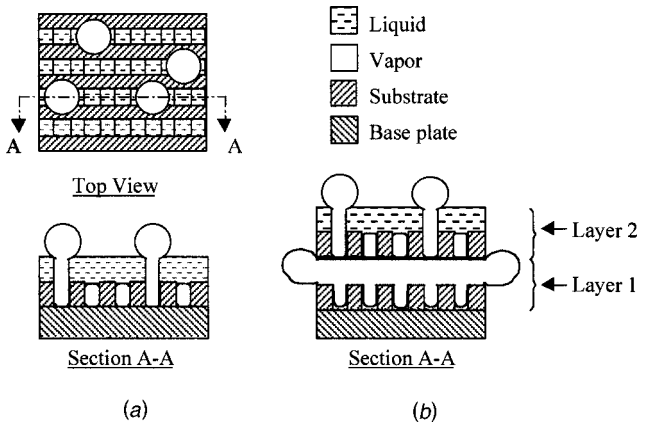

Fig. 9 Liquid and vapor distribution in the channels (*a*) single layer structure; and (*b*) two-layer structure

occurred only after all the pores had become active for either structure. The effect of varying the pore pitch, for a pore size of 200 μm, shows a similar trend. The data are listed in Table 3.

For a pore size of 120 μm, Chien and Webb [10] found that a smaller pore pitch resulted in higher heat transfer coefficients at all heat fluxes. However, for larger pore sizes, an opposite effect was observed. It was hypothesized that for the larger pore sizes the channels were actually flooded and that could have resulted in the lower heat transfer coefficients. In the current study, the heat fluxes tested were much higher and hence the mode of operation is hypothesized as "suction-evaporation" (see Fig. 6). This would result in a trend similar to that of the 120 μm pore size observed by Chien and Webb [10].

Effect of Stack Height. The effect of varying the number of layers was studied for two different structures (C-0.2-0.5 and C-0.27-0.63). For both structures, the individual layers were 0.85 mm thick. The number of layers tested was 1, 3, and 6 (for both structures). Both structures had a base plate 0.85 mm thick, resulting in a stack height of 1.7, 3.4, and 6.0 mm respectively. The results for the structure "C-0.2-0.5" are shown in Fig. 8. The curves show an improvement in the heat dissipation with additional layers (increase in stack height). For a stack height of 3.4 mm, the improvement is significant at low wall superheats (40 percent at 5 K), reducing at intermediate wall superheats (3 percent at 10 K) and once again rising at higher wall superheats (37.9 percent at 30 K), compared to a single layer structure (height of 1.7 mm). The results for a stack height of 6.0 mm also show a reduction in the enhancement with an increase in the wall superheat upto 10 K and beyond that an increase. The improvement in the heat dissipation for the structures with a height of 3.4 mm and 6.0 mm at selected wall superheat values is presented in Table 4. The values clearly confirm the trend described above. The results for structure "C-0.27-0.63" are similar to that of "C-0.2-0.5".

Table 4 Relative enhancement in heat dissipation for different stack heights for structure 'C-0.2-0.5' and 'C-0.27-0.63' (compared to H_s=1.7 mm)

ΔT_{sup} (K)	C-0.2-0.5		C-0.27-0.63	
	H_s = 3.4 mm	H_s = 6.0 mm	H_s = 3.4 mm	H_s = 6.0 mm
5	40.2	82.8	19.4	67.4
10	3.8	29.1	-8.8	26.2
15	8.7	35.4	2.9	34.5
20	20.5	44.1	23.6	45.4
25	37.9	40.9	35.9	47.9

The improvement in heat dissipation for the three-layer and six-layer structures, relative to a single layer structure, at select wall superheat values, are listed in Table 4.

Two factors could have contributed to this observed effect. One of the factors is a phenomenological difference between boiling from the sub-surface layers and that from the top layer. For a single layer structure, the postulated vapor and liquid distributions are shown in Fig. 9(*a*). The top channels are open to the liquid pool and hence the liquid flows into the bottom channels through all the pores (at the intersection of the channels and at the open ends of the channels). Assuming that the mode of boiling is suction-evaporation, bubbles initiate at the pores when the pressure inside the bottom channels exceeds the breakthrough pressure ($4\sigma/D_p$). For a two-layer structure, the hypothesized vapor and liquid distributions are shown in Fig. 9(*b*). The figure shows that both the top and bottom channels of layer "1" are now filled with vapor. At the internal pores, bubbles will not initiate as the pressure on both sides of the pores is same and there is no liquid-vapor interface. Also for layer "1" the liquid intake is only through the open end of the channels. This will result in lesser liquid supply compared to the single-layered structure and hence the evaporation inside the channels can be expected to be lesser. This in turn will reduce the bubble generation rate at the open ends of the channels and hence lesser contribution to the total heat flux. For layer "2" of the two-layer structure the distribution is similar to that for a single-layer structure and hence bubble formation will be similar to the single layer structure. In other words, adding more layers need not result in a proportional increase in the heat dissipation. Extending this hypothesis to a multi-layer structure ("*n*" layers), all the sub-surface layers ("1"–"$n-1$") will behave similar to layer "1" described above and the top most layer ("*n*") will behave similar to a single layer structure.

The other factor is the fin effect caused by the finite thermal conductivity of the structure. As explained in the former section adding layers does not increase the effective area of heat transfer proportionally. This will result in fin efficiency less than one, which will further reduce the heat dissipation from the structure. A simple one-dimensional model was used to evaluate this effect (for details see Ramaswamy [12]). Experimental results of a one-layer structure were used to deduce the heat transfer coefficient at different wall superheat values. The heat transfer coefficients were then used to predict the heat transfer contribution from each layer of multi-layered structures (three and six layer) based on the local wall superheat values. Although the model was simplistic for a complicated phenomenon like boiling, it showed a weak dependence of the heat dissipated on the fin efficiency (finite thermal conductivity of the structure).

Nakayama et al. [14] developed a two-dimensional transient model for solving the heat conduction equation, for the enhanced

structures used in their study. Heat transfer coefficients were evaluated from the experimental data of a one-layer structure. These heat transfer coefficients were then used in the model. The evaporation inside the channels was modeled using a volumetric heat sink term in the energy equation. Although the use of a volumetric heat sink term seems more accurate for modeling the evaporation inside the channels, it requires knowledge of the latent heat transfer component of the total heat dissipated. For the current study only the total heat dissipated is known and hence a simpler one-dimensional model was used.

Conclusions

The salient results of the parametric study on boiling from the enhanced structure are as follows:

1 The heat dissipation increases with an increase in the pore size (for the same pore pitch). In the range of pore sizes tested (90–320 μm), the largest pore size resulted in maximum heat dissipation. The effect is more prominent at low to intermediate wall superheats (4–12 K). However, at a wall superheat of 30 K, all the pore sizes resulted in similar performance.

2 The effect of pore pitch on heat transfer performance was found to be more significant. With a reduction in pitch (and hence addition of more channels/cm) the heat dissipation increased significantly. This was investigated for a pore size of 150 μm and 200 μm and both sizes showed a similar trend. Again, the effect is more prominent at low to intermediate wall superheats. However, unlike the pore size study, the effect of pitch was easily discernible even at a wall superheat of 30 K.

3 The study on varying the stack height showed that the heat dissipation does not always go up because of addition of multiple layers. The increase in heat dissipation is proportional to increase in area at low wall superheats (4–6 K) and at high superheats (25–30 K). Around a wall superheat of 10 K, which corresponded to beginning of fully developed boiling, the heat dissipation from a three-layer stack was found to be almost same as that of a single-layer stack. Two possible factors were outlined to explain this effect. A one-dimensional fin model was evaluated to show the weak dependence of the heat dissipated on the fin effect of a multi-layer structure.

Acknowledgments

This work was performed while the authors were at the University of Maryland, College Park. The authors would like to acknowledge support of this work through the members of CALCE Electronic Products and Systems Center and the Defense Advanced Research Projects Agency contract N00164-99-C-0039 and Semiconductor Research Corporation Contract 99-NJ-649.

Nomenclature

A_c = cross-sectional area of structure (m^2)
A_{ex} = total external surface area (m^2)
B = width of the structure (m)
D_p = pore size (m)
g = acceleration due to gravity, (9.81 m/s^2)
h_{av} = heat transfer coefficient (W/m^2-K)
h, h_i = local heat transfer coefficient (W/m^2-K)
H_s = total stack height (m)
H_t = channel depth (m)
k = thermal conductivity (W/m-K)
L = length of the structure (m)
P_c = perimeter of the enhanced stack (m)
P_p = pore pitch (m)
P_t = channel pitch (m)
q'' = heat flux (W/m^2)
Q = heat dissipation (W)
T_{sat} = saturation temperature of liquid, FC-72 (K)
T_{wall} = temperature at base of enhanced stack (K)
W_t = channel width (m)
z = dimension perpendicular to the enhanced structure base (m)

Greek Symbols

ΔT_{sup} = wall superheat, $T_{wall}-T_{sat}$ (K)
$\Delta T_{sup\,i}$ = local wall superheat, T_i-T_{sat} (K)
θ = referenced temperature, Eq. 3 (K)
σ = surface tension (N/m)

References

[1] Thome, J. R., 1990, *Enhanced Boiling Heat Transfer*, Hemisphere Publishing, NY.
[2] Webb, R. L., 1994, *Principles of Enhanced Heat Transfer*, John Wiley & Sons, NY.
[3] Oktay, S., 1982, "Departure From Natural Convection (DNC) in Low-Temperature Boiling Heat Transfer Encountered in Cooling Microelectronic Devices," *Proceedings of the 7th International Heat Transfer Conference*, **4**, Hemisphere Publishing, NY, pp. 113–118.
[4] Nakayama, W., Nakajima, T., and Hirasawa, S., 1984, "Heat Sink Studs Having Enhanced Boiling Surfaces For Cooling Microelectronic Components," ASME Paper No. 84-WA/HT-89.
[5] Mudawar, I., and Anderson, T. M., 1993, "Optimization of Enhanced Surfaces for High Flux Chip Cooling by Pool Boiling," ASME J. Electron. Packag., **115**, pp. 89–100.
[6] Nakayama, W., Daikoku, T., and Nakajima, T., 1982, "Effects of Pore Diameters and System Pressure on Saturated Pool Nucleate Boiling Heat Transfer from Porous Surfaces," ASME J. Heat Transfer, **104**, pp. 286–291.
[7] Nakayama, W., Daikoku, T., Kuwahara, H., and Nakajima, T., 1980, "Dynamic Model of Enhanced Boiling Heat Transfer on Porous Surfaces, Part I: Experimental Investigation," ASME J. Heat Transfer, **102**, pp. 445–450.
[8] Arshad, J., and Thome, J. R., 1983, "Enhanced Boiling Surfaces: Heat Transfer Mechanism and Mixture Boiling," *Proceedings of ASME-JSME Thermal Engineering Joint Conference*, **1**, ASME Publications, New York, NY, pp. 191–917.
[9] Ma, T., Liu, X., Wu, J., and Li, H., 1986, "Effects of Geometrical Shapes and Parameters of Re-entrant Grooves on Nucleate Pool Boiling Heat Transfer From Porous Surfaces," *Proceedings of the 8th International Heat Transfer Conference*, **4**, Hemisphere Publishing, NY, pp. 2013–2018.
[10] Chien, L.-H., and Webb, R. L., 1998, "A Parametric Study of Nucleate Boiling on Structured Surfaces, Part II: Effect of Pore Diameter and Pore Pitch," ASME J. Heat Transfer, **120**, pp. 1049–1054.
[11] Ramaswamy, C., Joshi, Y., Nakayama, W., and Johnson, W. B., 1999, "Compact Thermosyphons Employing Microfabricated Components," Microscale Thermophys. Eng., **3**(4), pp. 273–282.
[12] Ramaswamy, C., 1999, "A Compact Two-Phase Thermosyphon Employing Microfabricated Boiling Enhancement Structures," Ph.D. dissertation, University of Maryland at College Park, MD.
[13] Kline, S. J., and McClintock, F. A., 1953, "Describing Uncertainties in Single Sample Experiments," Mech. Eng. (Am. Soc. Mech. Eng.), **75**, pp. 3–8.
[14] Nakayama, W., Nakajima, T., Ohashi, S., and Kuwahara, H., 1989, "Modeling of Temperature Transient of Microporous Studs in Boiling Dielectric Fluid After Stepwise Power Application," *Heat Transfer in Electronics*, R. K. Shah, ed., ASME HTD—Vol. 111, ASME, New York, pp. 17–23.

M. Alex Kramer
Research Assistant

Miles Greiner
Professor
e-mail: greiner@unr.edu

Mechanical Engineering Department,
University of Nevada,
Reno, NV 89557

J. A. Koski
Principal Member of Technical Staff

Carlos Lopez
Member of Technical Staff

Sandia National Laboratories,
Albuquerque, NM 87185-0717

Ahti Suo-Anttila
Innovative Technology Solutions Corporation,
Albuquerque NM 87110-4162

Measurements of Heat Transfer to a Massive Cylindrical Calorimeter Engulfed in a Circular Pool Fire

A large-scale experiment was performed to measure heat transfer to a massive cylindrical calorimeter engulfed in a 30 minute circular-pool fire. This test simulated the conditions of a truck-sized nuclear waste transport package in a severe fire. The calorimeter inner surface temperature and the flame environment emissive power were measured at several locations as functions of time. An inverse heat conduction technique was used to estimate the net heat flux to the calorimeter. Tall porous fences surrounded the test facility to reduce the effect of wind on the fire. Outside the fences, 2.9 m/s winds blew across the calorimeter axis at the beginning of the test but decreased with time. The wind tilted and moved the fire so that the initial flame environment emissive power was substantially less on the windward side than the leeward side. The calorimeter became more uniformly engulfed as the winds decreased. The maximum heat flux to the calorimeter was 150 MW/m^2 on the leeward side at the beginning of the fire, and generally decreased with time. The local variations of calorimeter temperature and heat flux were closely related to the local flame environment emissive power. [DOI: 10.1115/1.1527905]

Keywords: Experimental, Fire, Heat Transfer, Radiation

Introduction

Large radioactive materials transport packages must withstand severe fire conditions without releasing their contents. Regulations describing a 30 minute fully engulfing fire test that is used for licensing these packages are contained in Title 10, Part 71 of the Code of Federal Regulations, known as 10CFR71 [1], and International Atomic Energy Agency ST-1 [2]. Cask design studies, transportation risk and safety studies, and regulatory analyses all require computational tools to predict the response of packages to both regulatory and historically based accident conditions. Since these analyses require multiple fire simulations, the computational tools must be rapid as well as accurate.

The Container Analysis Fire Environment (CAFE) computer code is currently under development at Sandia National Laboratories as a tool for package design and risk studies [3]. It uses computational fluid dynamics simulations and a number of fire and radiation models to calculate heat transfer from large fires to massive engulfed objects. CAFE may be linked to finite element analysis (FEA) programs that calculate the internal response of a package to the fire. The velocity boundary conditions required in CAFE's fluid dynamics simulator are chosen based on heat transfer data from full-scale fire experiments. CAFE's accuracy is based on experimental data and so it cannot be considered a fully predictive fire model. However, it will be a valuable tool for rapidly interpolating between benchmarked conditions, making it useful for design and risk studies. Its usefulness will be increased after it has been benchmarked against a variety of fire conditions.

Numerous large-fire tests have been performed on transportation packages over the past 20 years. However, most of these tests evaluated regulatory compliance and were not designed to quantify heat transfer [4]. A small number of large-scale fire tests were performed to measure heat transfer from fires to massive objects [5–7]. These tests concentrated on how thermal mass and surface temperature affect heat transfer, and how the cold object surface influences the fire environment. However these objects were not the same general size and shape as transport casks. Moreover, the tests did not measure heat transfer as functions of location over the entire object.

The goal of the current experiment was to measure heat transfer versus time and location to a massive cylindrical calorimeter engulfed in a pool fire. The calorimeter is roughly the same size as a high level nuclear waste package transported by tractor-trailer truck. The fire was designed to comply with the 10CFR71 regulations used to license such packages. These data will be used to adjust the CAFE fire model [8] and to develop engineering models for radiant heat transfer in large fires [9].

Experimental Method

The 10CFR71 regulations specify that a transport package under test must be suspended one meter above a hydrocarbon fuel pool, and that the pool must extend horizontally between 1 and 3 m beyond the object [1]. Moreover, the wind conditions must be sufficiently calm so that the object will be engulfed in a fire environment characterized by a temperature of at least 800°C and emissivity of at least 0.9 for 30 minutes. Figure 1 shows plan views of the experiment test facility that was designed to comply with these conditions. It is located at the Sandia National Laboratories Burn Site and its orientation relative to compass directions is shown in the figure.

The experiment was designed with the intention of *eliminating* wind effects. Tests were performed during early morning periods when the winds are generally light. Figure 1(*a*) shows that sixteen 6 m (20 ft) high fences were placed in a 24.4 m (80 ft) diameter circle around the facility to reduce the effect of wind. Each barrier formed a *V*-shape with the apex pointing toward the fire. Each wind barrier was constructed from chain link fencing with aluminum strips woven into each slot (the area porosity of the fencing was less than 20 percent). The bottoms of the wind fences were 0.3 m above the ground and the fences were separated from each other by one-meter gaps. These gaps were used so that the barriers would not disrupt the natural inward flow of air toward the fire. Measurements for a slightly different wind fence arrangement show that the wind speed inside the barriers without fire is roughly half that outside the fences.

Contributed by the Heat Transfer Division for publication in the JOURNAL OF HEAT TRANSFER. Manuscript received by the Heat Transfer Division October 12, 2001; revision received September 9, 2002. Associate Editor: J. P. Gore.

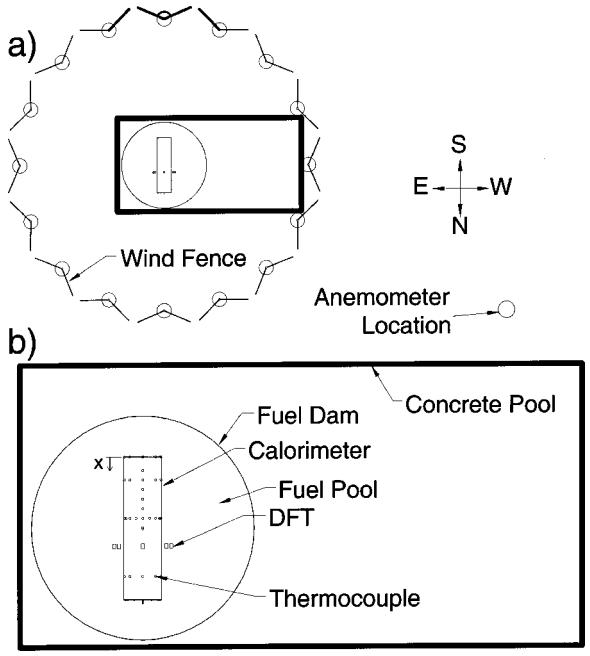

Fig. 1 Plan view of the experimental test facility: (*a*) wind fences, anemometer location, and compass directions; and (*b*) calorimeter instrumentation, water and fuel pools

The wind direction and speed were monitored with propeller type anemometers attached to wind vanes. The measurements were taken outside of the wind fences due to the high temperatures inside the barriers. The anemometers were located 30 m (100 ft) to the northwest of the fire pool, with the intention of measuring the wind speed independent of the fire effects. Measurements were performed at heights of 3.0 m (10 ft) and 6.1 m (20 ft) above the ground. The manufacturer's stated accuracy of the anemometers was ± 0.3 m/s, and wind data were collected at 15 second intervals.

Even though wind barriers were employed and the wind speeds were low, the Results section of this paper shows that the external winds had a significant effect on the measured heat transfer to the calorimeter. Additional wind measurement locations would have better characterized the external environment than the two used in this experiment. However, the current wind measurements do characterize the general trends of the external environment and are therefore useful for benchmarking and adjusting fire simulation codes.

Figure 1(*b*) shows that the calorimeter was located above a 9 m wide, 18 m long, and 1 m deep, water-filled concrete pool. A 7.16 m (23.5 ft) diameter sheet metal fuel dam (seen in Fig. 3) contained JP-8 fuel floating on the water in a circle. The calorimeter was a 3800 kg (8400 lb) carbon steel pipe of length $L=4.6$ m (15 ft), diameter $D=1.2$ m (4 ft), and wall thickness $W=2.54$ cm (1 in). Two caps, 2.54 cm (1 in) thick, were fastened to each end. The south end cap was penetration welded to the cylindrical body while the north end cap was bolted to allow access to the interior.

The calorimeter was supported horizontally 1 m above the center of the fuel pool. The minimum horizontal distance between the calorimeter end caps and the edge of the fuel pool was 1.22 m and the maximum distance from the sides to the pool edge was 2.97 m. These distances are in compliance with the 10CFR71 regulations. The structure supporting the calorimeter above the pool was constructed from 10 cm square cross section steel tubing. It was designed to contact the calorimeter at six locations. The support stand was insulated and water-cooled during the tests.

The small circles in Fig. 1(*b*) show the locations where thermocouples were fastened to the *interior* surface of the calorimeter. Each thermocouple was a Chromel/Alumel (type *K*) wire pair, sheathed in inconel tubing, insulated with MgO, and was ungrounded. They were attached to the interior surface of the calorimeter with spot welded nichrome metal strips. A 2.54 cm-thick layer of Thermal Ceramics Kaowool insulation was placed next to the interior surface and standard fiberglass filled the remaining volume. To avoid shunting errors the thermocouple lead wires were insulated from the metal calorimeter walls by placing them inside the Kaowool insulation. The instrumentation wire bundle exiting the calorimeter was exposed to the fire environment. To further avoid shunting errors, the bundle was insulated and water-cooled during the tests. Its temperature was measured and never exceeded 40°C.

Most of the thermocouples were arranged in four rings. Using the *x*-coordinate system shown in Fig. 1(*b*) ($x=0$ is at the inner surface of the south end cap), the rings were located at $x=0$, 0.73, 1.96, and 3.78 m. The rings at the end cap, south, and north ($x=0$, 0.73, and 3.78 m) had eight thermocouples equally spaced around the interior circumference. The central ring at $x=1.96$ m had 16 thermocouples. In addition to these rings, five thermocouples were placed in a line along the top at $x=0.43$, 1.04, 1.35, 1.65, and 2.26 m. Two more were attached to the south end cap in a vertical line, each 19.5 cm from the center of the cap. A thermocouple was used to monitor the temperature of the center of the calorimeter insulation. Detailed diagrams of thermocouple locations are provided in Kramer et al. 2000 [10].

Six of the thermocouples were randomly selected and calibrated at 30, 500, and 1100°C. All six were certified to have error limits that are the greater of ± 1.1°C or 0.4 percent of their reading. Only a small portion of this uncertainty was found to be random in nature [11]. Each thermocouple was connected to a signal conditioner (electronic ice-point/amplifier) whose output was read by a 12-bit computer data acquisition system. The temperature input resolution for this system was ± 0.4°C. Temperatures were recorded at 5 second intervals. Each data point represents the average of 300 samples taken over one second. This averaging reduced random errors that can be caused by radio frequency interference.

Small rectangles in Fig. 1(*b*) marked ''DFT'' show locations where eight Directional Flame Thermometer (DFT) fixtures were placed outside of the calorimeter [12,13]. These devices are designed to measure the radiant heat flux they receive from their environment. The DFT's were located above, to the west, below and to the east of the calorimeter (angular positions $\theta=0$, 90, 180, and 270 deg, respectively) at axial position $x=2.82$ m. At each of these locations, two fixtures were placed 15.25 cm (6 in) and 30.5 cm (12 in) from the outside surface of the calorimeter.

Each DFT fixture is a cylinder-shaped object that has thin stainless steel foils on the end caps. In this experiment, the foils face the north and south directions (parallel to the calorimeter axis). The foils have thermocouples attached to the interior surface, and the interior volume of the fixture is filled with insulation. The foils rapidly approach thermal equilibrium with the radiant heat flux they receive from their surroundings. The measured temperature T_{DFT} is used to determine the emissive power the DFT receives from its environment, $E_{\mathrm{DFT}} \approx \sigma T_{\mathrm{DFT}}^4$ (corrections are made for phase lag in an unsteady environment [13]).

In the current paper we only report results from the south-facing DFT sensing foils that are located 15.25 cm from the calorimeter surface. Figure 1(*b*) shows that the south-facing foils are exposed to the environment outside the central thermocouple ring at $x=1.96$ m. The DFT emissive power E_{DFT} is only a good indication of flame emissive power E_{Flame} when the DFT is fully engulfed in optically thick flames. If it is not engulfed, then it is exposed to the external environment or the calorimeter surface and E_{DFT} can be significantly less than E_{Flame}.

Two tests were performed on August 24th and 25th, 2000. The calorimeter exhibited a blotchy rusted surface before the first test. The extreme heat and oxidation that occurred during that test left

the surface a nearly even gray color with regions of soot, and this was the initial condition for the second test. Two different reflectometers, covering the infrared and near infrared spectrums were used to measure the emissivities of the gray and soot covered regions. The soot yielded a surface emittance of 0.9–0.94, while the gray regions had a measured emittance of 0.8–0.85. A dominant mode of heat transfer in pool fires is radiation [7], and the surface emissivity affects this transport. The results of the second test are therefore described in this paper because its initial surface properties are better known than those of the first test.

Results

Before the test was initiated 5110 liters (1350 gal) of JP-8 fuel was placed on top of the water in the fuel dam. This corresponds to a 12.7 cm (5 in) deep layer. The fuel was ignited at the edge of the pool using a torch and the flames spread slowly across the pool. Roughly 2 minutes was required before the calorimeter was fully engulfed. The time scale was set to $t=0$ when the fire first engulfed the calorimeter. The fire lasted until $t=34$ minutes. The burning rate of the fuel was not measured as a function of time, however nearly all of it was consumed during the 34 minute fire.

Figure 2 shows the wind speed measured outside the fences. Traces are included for data measured 3.0 and 6.1 m above the ground, and for a two-minute window average of both sets of measured data. The wind came from the east for the first 24 minutes of the test. If the direction inside the fence is the same as that outside, then this corresponds to the wind blowing across the calorimeter axis. There was a lull between $t=24$ and 27 minutes. After $t=27$ minutes the wind came from the south (parallel to the calorimeter axis). The wind speeds at the higher and lower elevations are close to each other. They both exhibit oscillations with periods between one and seven minutes and amplitudes of roughly 0.5 m/s. The wind speed had its highest value at the beginning of the test, 2.9 m/s (6.5 mph), and generally decreased with time. The average wind speed throughout the test was 1.02 m/s.

Figure 3 shows two photographs taken during the fire. Both pictures show that the flames neck inward with increasing height above the ground. Figure 3(*a*) was taken during a time of low wind. We see that the end cap of the calorimeter is not engulfed even though the fuel pool extends 1.2 m beyond it. An observer standing directly east of the calorimeter took Fig. 3(*b*). It was taken during a period when the wind was blowing away from the observer and across the calorimeter axis. At this time a large portion of the eastern side of the calorimeter is not engulfed. Figure 2 shows that the wind blew across the calorimeter for much of the test. This suggests that the west side of the calorimeter was engulfed in flames for a greater fraction of time than its east side.

Figure 4 shows two-minute window-averaged DFT emissive power versus time for regions near the west, bottom, east and top of the calorimeter (θ=0, 90, 180, 270 deg). The emissive power

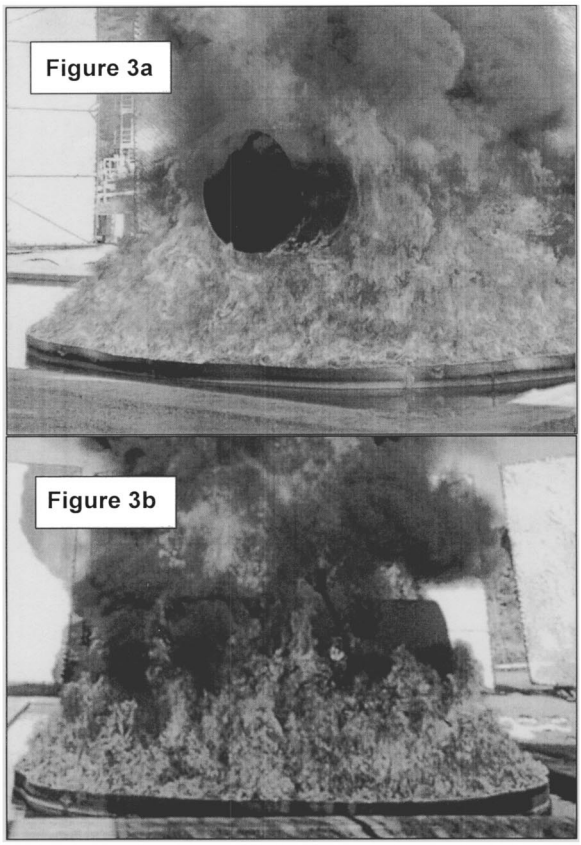

Fig. 3 Fire photographs (*a*) low wind, and (*b*) slight crosswind

was essentially zero at all locations before the fire was lit. The west side emissive power increased very rapidly after the fire was ignited. After $t=4$ minutes it reached a steady state level that averaged roughly 200 kW/m^2 with peaks as high as 230 kW/m^2. Oscillations with periods between 5 and 7 minutes and amplitudes between 15 and 30 kW/m^2 persisted throughout the test. The period of these oscillations is similar to that of the window-averaged wind speed shown in Fig. 2.

The west-side emissive power appears to decrease slightly during the last 6 minutes of the test, after the wind died down and then shifted direction. The higher emissive power during the first 24 minutes suggests the presence of a recirculation zone. Efficient air/fuel mixing in this zone may have increased the effective fire

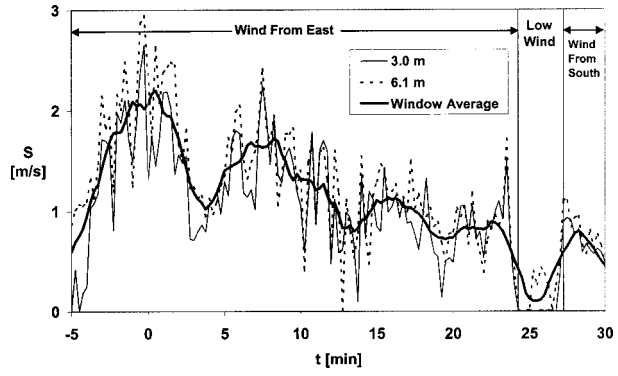

Fig. 2 Outside-fence wind speed versus time

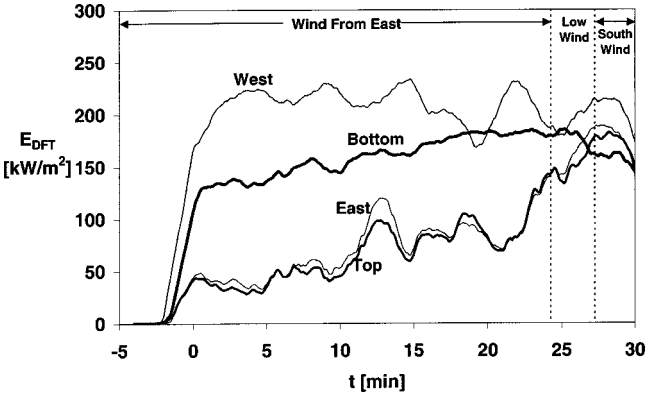

Fig. 4 Environment emissive power versus time at θ=0, 90, 180, and 270 deg measured by south facing DFT's at x = 1.96 m

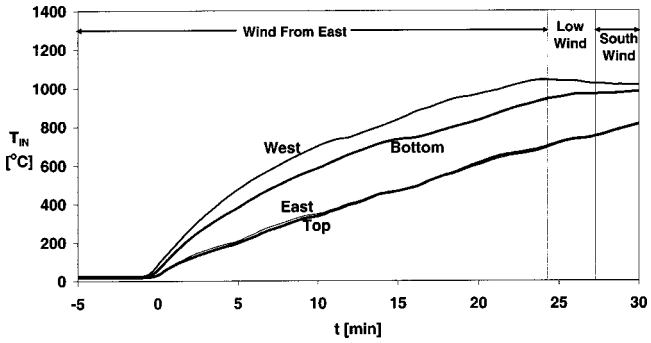

Fig. 5 Measured inner surface temperature versus time for θ=0, 90, 180, and 270 deg at x=1.96 m

temperature relative to the levels that existed during the last 6 minutes of the fire when there was no crosswind.

The emissive power near the bottom of the calorimeter rose from 120 to 180 kW/m^2 during the period $t=1$ to 25 minutes. It then dropped during the last five minutes of the test, after the wind shifted. The lower emissive power at the end of the test suggests that a fuel-vapor rich zone formed between the fuel pool and the calorimeter. Combustion in such a vapor dome is limited by the lack of sufficient oxygen. This vapor dome may not have existed at earlier times due to the stronger cross winds. The temporal oscillations at the bottom were smaller than they were on the west side. This may be because the bottom was more sheltered from unsteady wind effects than the upper portions of the calorimeter.

The emissive powers measured near the top and east regions of the calorimeter were very similar to each other throughout the fire. They were between 40 to 50 kW/m^2 for the first 10 minutes of the fire, significantly lower than the other locations. During this period, the outside-fence wind speed was greater than 1.2 m/s. This may have tilted the flames so that the east and top portions of the calorimeter were only intermittently engulfed. The emissive power levels exhibit a spike during the period $t=11$ to 14 minutes, corresponding to a time when Fig. 2 shows a dip in the wind speed. From $t=10$ to 24 minutes the emissive power grew from 50 to 140 kW/m^2, as the wind speed decreases from 1.2 to 0 m/s. The emissive power at these locations grew very rapidly after $t=24$ minutes when the wind stopped blowing across the calorimeter. The low crosswind condition may have allowed the top and east side to be more continuously engulfed in flames. Finally, the top and east side emissive powers exhibited oscillations that were similar to those at the west side of the calorimeter.

High values of emissive power appear to indicate periods when a location is engulfed in thick flames. Seen as a whole, Fig. 4 shows that the calorimeter was much more uniformly engulfed at the end of the fire test (when the winds were light) than it was at the beginning. Comparing Fig. 4 with the wind data in Fig. 2 shows that the emissive power on the east (windward) side of the calorimeter *increased* as the wind speed decreased. However, the west (leeward) side emissive power was *not* strongly affected by wind speed.

Figure 5 shows inner surface temperature versus time at the west, bottom, east and top locations of the calorimeter central section ($x=1.96$ m). Before the fire was lit the calorimeter temperature was essentially uniform at 20±2°C. The fire was ignited at $t=-2$ minutes, and the interior temperature started rising at $t=-40$ seconds. After $t=0$, when the calorimeter was first engulfed, the west and bottom were significantly hotter than the east and top locations, especially for the first 24 minutes. This is consistent with the flame emissive powers reported in Fig. 4. The temperature of the west side began to decrease at $t=24$ minutes. This corresponds to the time when the wind stopped blowing across the calorimeter. In general, the slope of each temperature-versus-time curve is proportional to the local heat flux. However, the slope of all four curves briefly level off (drop to zero) as they approach 750°C. This is caused by the latent heat of the Curie solid-to-solid phase change, which mild steel experiences at this temperature.

Figure 6 shows polar plots of the inner surface temperature as a function of angular location ($\theta=0$ is at the top of the calorimeter) at times $t=1$, 5, 10, 20, and 30 minutes. Plots are presented for the end cap, south, central and north cross-sections, at $x=0$, 0.73, 1.96, and 3.78 m, respectively. While the temperatures were highest at the central section, the profile shapes were similar at each axial station. Moreover, the temperature at all locations increased with time. The following discussion is focused on the central section. The temperature distribution is asymmetric, especially for the first 10 minutes. The west side and bottom (between $\theta=45$ deg and $\theta=225$ deg) were always hotter than the east side and top. This is consistent with the relative values of the local emissive power reported in Fig. 4. For the first 20 minutes the temperature rise rate was fairly uniform within this leeward (western) region, indicating that the heat transfer rate was fairly uniform. The temperature rise rate in the last 10 minutes of the test, after the wind shifted, was much lower than it was between $t=10$ and 20 minutes.

The temperature rise rate on the eastern (windward) side was much slower during the first 10 minutes of the test than it was on the western (leeward) side. However, the rise in the east side temperature was much more rapid after $t=10$ minutes, when its environment emissive power began to increase rapidly. Finally, the temperature data shows that the leeward side (from $\theta=45$ deg to $\theta=225$ deg) received 94 percent more energy during the first 10 minutes of the fire than the windward side, and 51 percent more energy during the first 20 minutes. However, at $t=30$ minutes, after the wind shifted, the energy absorbed by the west side was only 22 percent more than the east side.

Figure 7 shows the variation of inner surface temperature with dimensionless axial location x/L at $t=20$ minutes. Profiles are shown for lines along the top, west, bottom and east sides of the calorimeter, $\theta=0$, 90, 180, and 270 deg, respectively. The temperatures were highest at the center and drop off as the end caps are approached (the north end cap at $x/L=1$ was not instrumented). At the south end cap the edge of the fire pool extended only 1.2 m from the calorimeter. As seen in Fig. 3(*a*) the flames sloped inward from the pool edge and did not engulf the end caps, allowing them to remain cooler than the rest of the calorimeter. The temperature profiles at the west side and bottom are fairly uniform over the central 60 percent of the calorimeter, while the profiles at the east side and top drop off more rapidly. This suggests that the flame region was narrower on the top and east than it was on the bottom and west.

The Sandia One-Dimensional Direct and Inverse Thermal (SODDIT) computer code [14] was used in conjunction with the interior temperature measurements to calculate the heat flux to the calorimeter exterior surface as a function of time and location. The inputs to SODDIT are the measured inner surface temperature $T_{IN}(t_i)$ at equally spaced times $t_i=im\Delta t$, the measured calorimeter diameter D and wall thickness W, and its measured material properties (temperature-dependent specific heat $c_p(T)$ and thermal conductivity $k(T)$, and a temperature-independent value of the density ρ). In the expression for the evaluation times $t_i=im\Delta t$, Δt is the measurement time interval, $i=1,2,3\ldots$, and the integer m designates the fraction of data points that are skipped ($m=1$ uses all the data, $m=4$ uses ever fourth data point). For the current work, $\Delta t=5$ sec and $m=4$.

SODDIT uses a one-dimensional conduction model along with sensitivity coefficients and the future-time method to determine the outer surface heat flux $q''_{OUT}(t_i)$ and temperature $T_{OUT}(t_i)$ at times t_i. In the current work the number of future times in the SODDIT calculation was set to 4. SODDIT was used to calculate the exterior surface heat flux and temperatures for locations that are in proximity to all the thermocouples shown in Fig. 1(*b*) ex-

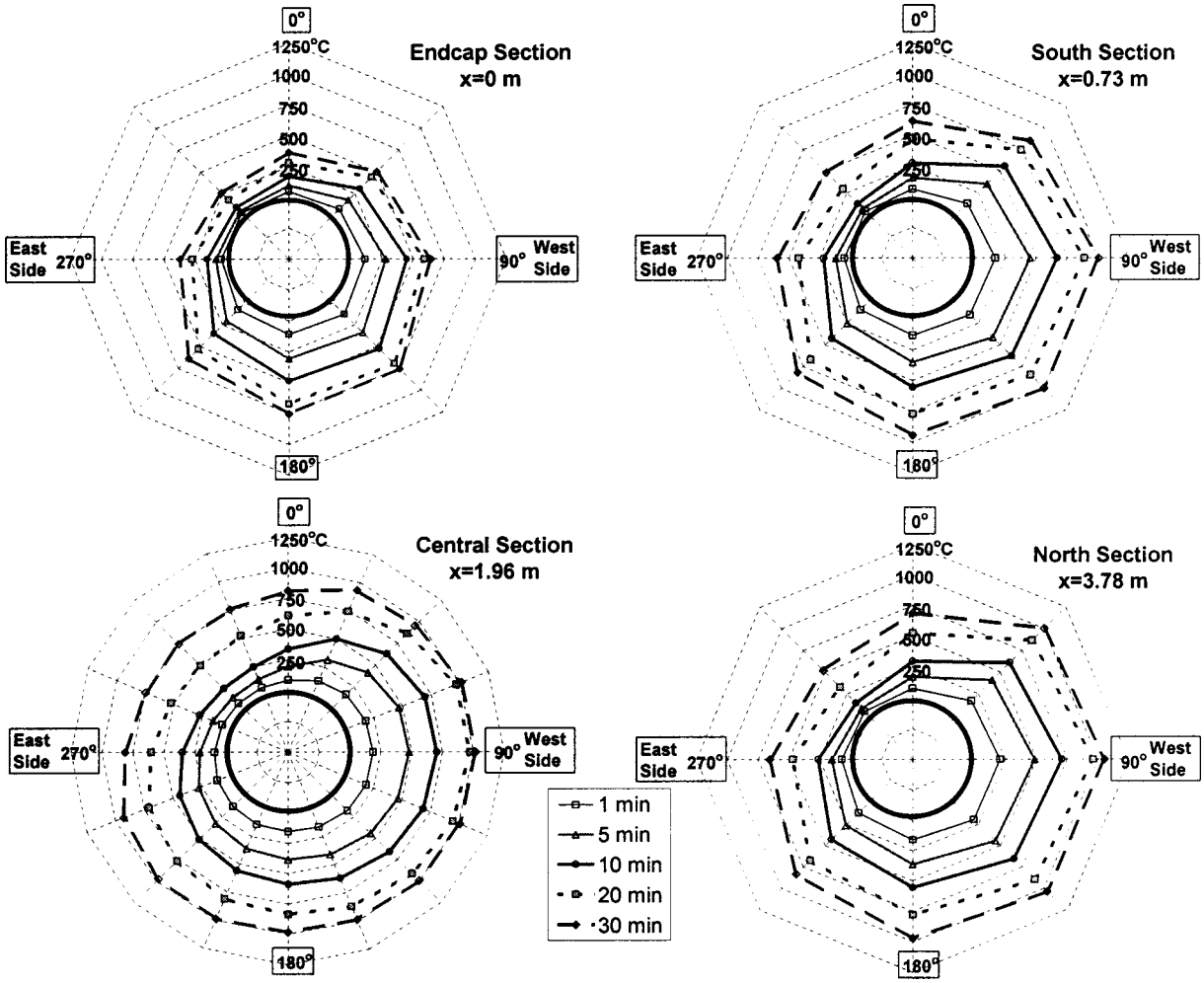

Fig. 6 Measured inner surface temperature T_{IN} versus angular position and time for $x=0$, 0.73, 1.96, and 3.78 m

cept those near the south end cap (at $x=0$). SODDIT was not used near the end cap because the conduction in this region is clearly not one-dimensional.

The calorimeter steel thermal diffusivity $\alpha=k/\rho c_P$ was measured as a function of temperature using the laser pulse diffusivity technique. Differential scanning calorimetry was used to measure the specific heat c_P as a function of temperature. The room temperature density ρ was determined from the dimensions and mass of a small cylindrical sample. The 95 percent confidence-level uncertainties of the thermal conductivity, specific heat, density and wall thickness were estimated to be ± 11.2 percent, ± 5 percent, ± 0.75 percent, and ± 3.5 percent of their respective measured values. The measured effective specific heat exhibited a spike in the temperature range 726–768°C. This spike was caused by the latent heat of the Curie solid-solid phase change. The uncertainty in the effective specific heat is much greater in this temperature range than it is at higher and lower temperatures.

Figure 8 illustrates the use of the SODDIT computer code to

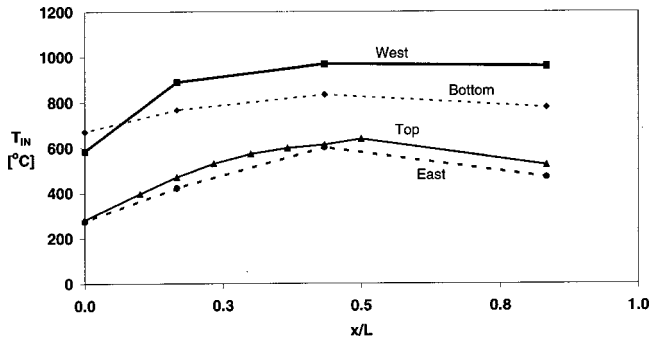

Fig. 7 Measured inner surface temperature versus axial location at $t=20$ min for $\theta=0$ deg, 90 deg, 180 deg, and 270 deg

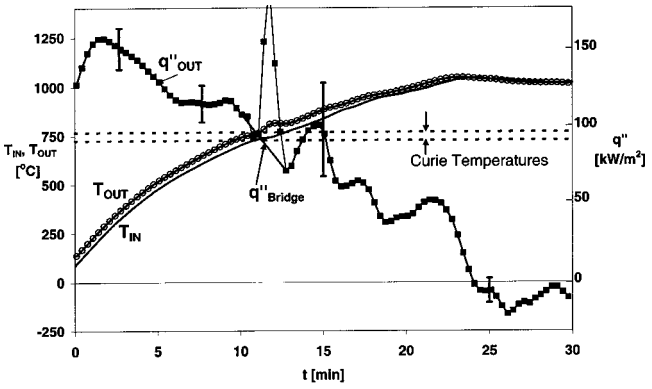

Fig. 8 SODDIT-calculated exterior surface heat flux and temperature, and the measured inner surface temperature versus time for $\theta=90$ deg at $x=1.96$ m. The Curie-bridge is also shown.

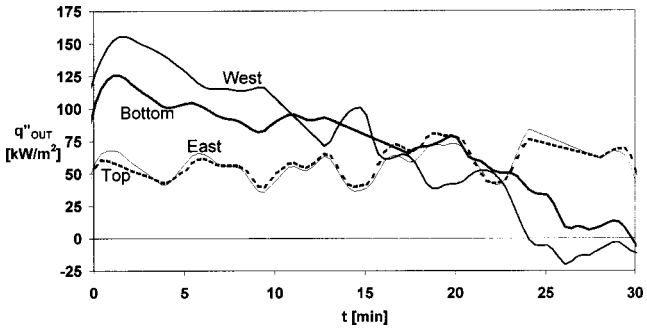

Fig. 9 SODDIT-calculated exterior surface heat flux versus time for θ=0, 90, 180, and 279 deg at x=1.96 m

quantify the time dependent heat flux to the west side (θ=90 deg) of the central ring (x=1.96 m). The solid line marked T_{IN} shows the measured interior surface temperature (also shown in Fig. 5). The line with open circles marked T_{OUT} is the SODDIT-calculated exterior surface temperature outside the location where T_{IN} was measured (θ=90 deg, x=1.96 m). Two horizontal dashed lines show the temperature range of the Curie phase change (726–768°C) for the calorimeter steel. The line with square symbols is the SODDIT-calculated net heat flux to the exterior surface of the calorimeter, q''_{OUT}. Positive values of q''_{OUT} indicate heat transfer from the fire to the calorimeter.

During the time that the inner surface temperature is rising (t=0 to 24 minutes), the net heat flux is from the fire to the calorimeter ($q''_{OUT}>0$). The direction of the heat transfer causes the exterior temperature T_{OUT} to be greater than the interior value, T_{IN}. We see that the outer surface temperature first passes into the Curie range at t=9 minutes and the inner surface temperature does not pass out of that range until t=13 minutes. The SODDIT-predicted heat flux exhibits a sharp oscillation between time t=11 and 13 minutes. These oscillations are caused by the inaccuracy of the effective specific heat in the Curie temperature range. In this work, we ignore the SODDIT predicted heat flux during the time period when the calorimeter is within the Curie temperature range. We use a linear bridge between the SODDIT predictions at the beginning and end of this period. In this paper the Curie-bridge technique is applied to the heat flux data whenever the inner or outer surface temperatures are within the Curie range.

Simulations with the linked CAFE/Finite Element Analysis system were used to evaluate the ability of SODDIT with the Curie bridge to calculate an 80 second window-average of the applied heat flux [11,15]. The estimated 95 percent confidence level uncertainty of the SODDIT-calculated heat flux is less than ±15

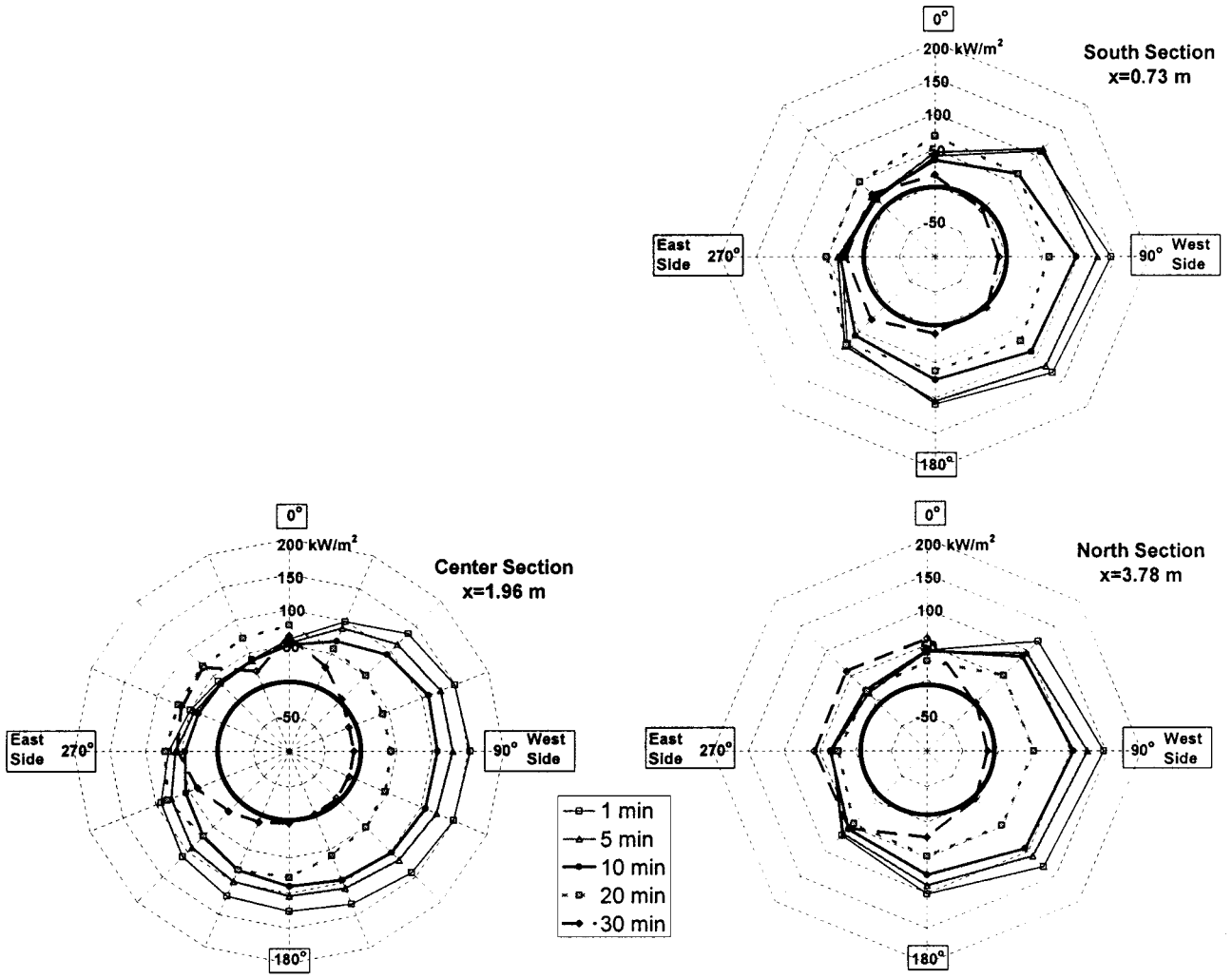

Fig. 10 SODDIT-calculated exterior surface heat flux q''_{OUT} versus angular position and time for x=0.73, 1.96, and 3.78 m

kW/m^2 when the calorimeter temperature is not inside the Curie range (726°C to 768°C). The uncertainty is considerably higher when the calorimeter temperature is inside that range. The error bars in Fig. 8 show the 95 percent confidence level uncertainty at $t=3$, 7, 15, and 25 min.

Figure 9 shows net SODDIT-calculated heat flux q''_{OUT} versus time at $\theta=0$, 90, 180, and 270 deg for the central section ($x=1.96$ m). The heat flux values at the west side and bottom of the calorimeter are high at the beginning of the fire, when the calorimeter is relatively cold. They decrease with time as the calorimeter surface temperatures increase. The heat flux on the east side and top of the calorimeter exhibit oscillations. However, their levels are roughly constant with time. Although the surface temperatures at these locations were rising with time, the flame emissive power shown in Fig. 4 was also rising. This is the reason the *net* heat flux at these locations remained nearly constant. Figure 4 also shows that the fire environments at the top and east locations were very similar. This caused the net heat fluxes at the two locations (shown in Fig. 9) to be very similar. All four traces in Fig. 9 exhibit low frequency unsteadiness with oscillatory periods between 4 and 7 minutes. The oscillatory amplitude on the west, east and top are all around 12 kW/m^2, while the amplitude on the bottom is somewhat lower. These oscillatory periods and amplitudes are consistent with the flame emissive powers described in Fig. 4.

Figure 10 shows polar plots of net heat flux to the calorimeter as a function of angular position at times $t=1$, 5, 10, 20, and 30 minutes. Plots are presented for the south, central and north cross-sections at $x=0.73$, 1.96, and 3.78 m respectively. SODDIT was not used to find the heat flux at the end caps since conduction in that region is clearly not one-dimensional. The heat flux profiles are similar at all three cross sections. On the west side of the calorimeter ($\theta=22.5$ deg to 202.5 deg) the heat flux decreases at each successive time shown in the figure. The heat flux is negative (from the calorimeter to the environment) in the region $\theta=45$ deg to 135 deg at the end of the fire when the wind direction shifted. For the first ten minutes of the fire, the heat flux on the east side of the calorimeter is substantially less than it is on the west side. Moreover, the east side heat flux is essentially constant during that period of time. It then *increased* in the region $\theta=270$ deg to 0 deg after that region became more continuously engulfed in flames.

Conclusion

A large-scale experiment measured heat transfer to a massive pipe calorimeter suspended in a circular JP-8 pool fire for 30 minutes. These conditions approximated a truck-sized nuclear waste transport package in a regulatory test. Tall, porous fencing surrounded the outdoor test facility. The fencing was designed to reduce the effect of wind while allowing a natural indraft of air. The speed and direction of the wind were measured as functions of time at two elevations outside the barriers. The calorimeter inner surface temperature and the flame environment emissive power were also measured at several locations as functions of time. The net window-average heat transfer rate to the calorimeter was determined using an inverse heat conduction technique.

Winds with an outside-fence speed of 2.9 m/s blew across the calorimeter axis at the beginning of the test but decreased with time. The average speed during the test was 1.02 m/s. Even with the wind barriers, the winds tilted and moved the fire so that the initial flame environment emissive power on the windward side was substantially less than the leeward side. The calorimeter became more uniformly engulfed as the winds decreased. The maximum calculated heat flux to the calorimeter was roughly 150 MW/m^2 on the leeward side at the beginning of the fire, and generally decreased with time. The local and temporal variations of calorimeter temperature and heat flux were closely related to the local environment emissive power, which, in turn, was affected by the wind.

The current data are well suited for benchmarking and adjusting the Container Analysis Fire Environment (CAFE) computer code, which is intended for use in design and risk analyses of massive nuclear waste transport packages. The benchmarked version of CAFE can be linked to a finite element analysis model of a transport package and then used to determine package response for the wind conditions that existed during the current test. CAFE can be used for other wind conditions after additional benchmarking experiments have been performed.

Acknowledgments

The US Department of Energy funded this work under DOE/EPSCoR Grant DE-FG02-98ER45715. The authors would like to thank W. R. Jacoby, Rodney Oliver, Terrence Aselage, and A. R. Mahoney for their valuable help and expertise.

Nomenclature

c_p = calorimeter effective thermal conductivity
D = calorimeter diameter
E_{DFT} = emissive power measured by a directional flame thermometer (DFT)
E_{Flame} = emissive power of the flames
i = integer index, 1,2,3 . . .
k = calorimeter thermal conductivtiy
L = calorimeter length
m = inverse of the fraction of measured data points used in SODDIT analysis
q''_{OUT} = calorimeter outer surface heat flux
t = time after the calorimeter is fully engulfed
Δt = measurement time interval
T_{Flame} = local flame temperature
T_{IN} = calorimeter inner surface temperature
T_{OUT} = calorimeter outer surface temperature
S = Outside-fence wind speed
W = calorimeter wall thickness
x = axial coordinate ($x=0$ is at the south end of the calorimeter)
α = calorimeter thermal diffusivity, $k/\rho c_p$
ρ = calorimeter density
θ = angular coordinate around calorimeter ($\theta=0$ is at the top of the calorimeter)
σ = Stefan-Boltzmann constant

References

[1] U.S. Nuclear Regulatory Commission, 2001, "Packaging and Transportation of Radioactive Material," *Code of Federal Regulations*, Title 10, Part 71.
[2] International Atomic Energy Agency, 1985, "Regulations for the Safe Transport of Radioactive Material," Safety Series No. 6, IAEA, Vienna.
[3] Suo-Anttila, A. J., Koski, J. A., and Gritzo, L. A., 1999, "CAFE: A Computer Tool for Accurate Simulation of the Regulatory Pool Fire Environment for Type B Packages," *Proceedings of the ASME Pressure Vessels and Piping Conference*, August 1–5, 1999, Boston, MA.
[4] Nuclear Packaging Inc., 1989, "Safety Analysis Report for the TRUPACT-II Shipping Package," Docket Number 71-9218.
[5] Gregory, J. J., Keltner, N. R., and Mata, Jr., R., 1989, "Thermal Measurements in Large Pool Fires," ASME J. Heat Transfer, **111**, pp. 446–454.
[6] Koski, J. A., Gritzo, L. A., Kent, L. A., and Wix, S. D., 1996, "Actively Cooled Calorimeter Measurements and Environment Characterization in a Large Pool Fire," Fire Mater., **20**(2), pp. 69–78.
[7] Nakos, J. T., and Keltner, N. R., 1989, "The Radiative-Convective Partitioning of Heat Transfer to Structures in Large Pool Fires," Heat Transfer in Radiation, Combustion, and Fires, R. K. Shah, ed., **106**(2), pp. 381–3878.
[8] Ju, H., Greiner, M., and Suo-Anttila, A., 2001, "Computer Simulations of a Generic Truck Cask in a Regulatory Fire Using the Container Analysis Fire Environment (CAFE) Code," Int. J. of Radioactive Materials Transport, 13, pp. 35–40.
[9] Kramer, M. A., Greiner, M., and Koski, J. A., 2001, "Radiation Heat Transfer to the Leeward Side of a Massive Object Suspended Over a Pool Fire," presented at the *2001 International Mechanical Engineering Congress and Exposition*, November 11–16, 2001, New York, Paper No. IMECE2001/HTD-24250.
[10] Kramer, M. A., Greiner, M., Koski, J. A., Lopez, C., and Suo-Anttila, A. J., 2000, "Design of an Experiment to Measure Heat Transfer to a Massive Ob-

ject Engulfed in a Full Scale Regulatory Fire,'' *Proc. 2000 ASME Pressure Vessels and Piping Conference*, Seattle WA, July 23–27.
[11] Kramer, M. A., Greiner, M., Koski, J. A., and Lopez, C., ''Uncertainty of Heat Transfer Measurements in an Engulfing Pool Fire,'' presented at the Symposium on Thermal Measurements: The Foundation of Fire Standards, ASTM Committee E05 on Fire Standards, Dallas Texas, December 3, 2001.
[12] Koski, J. A., 2000, ''Measurement of Temperature Distributions in Large Pool Fires with the use of Directional Flame Thermometers,'' *Proc. 2000 ASME Pressure Vessels and Piping Conference*, Seattle WA, July 23–27.
[13] Blanchat, T. K., Humphries, L. L., and Gill, W., May 2000, ''Sandia Heat Flux Gauge Thermal Response and Uncertainty Models,'' issued by Sandia National Laboratories, SAND2000-1111, 45 pages.
[14] Blackwell, B. F., Douglass, R. W., and Wolf, H., 1987, ''A User's Manual for the Sandia One-Dimensional Direct and Inverse Thermal (SODDIT) Code,'' issued by Sandia National Laboratories, SAND85-2478, 136 pages.
[15] Kramer, M. A., 2001, ''Measurements of Heat Transfer to a Massive Cylindrical Object Engulfed in a Regulatory Pool Fire,'' M.S. thesis, University of Nevada, Reno, NV.

Analytical and Experimental Study of Combustion and Heat Transfer in Submerged Flame Metal Fiber Burners/Heaters

S. A. Leonardi

R. Viskanta
e-mail: viskanta@ecn.purdue.edu

J. P. Gore

School of Mechanical Engineering,
Purdue University,
West Lafayette, IN 47907-1288

A theoretical model has been developed to predict the thermal performance of inert, direct-fired, woven-metal fiber-matrix porous radiant burner. The local chemical heat release was modeled by a detailed mechanism, and convection heat transfer between the gas and the solid phases in the burner was described by an empirical heat transfer coefficient. The solid matrix was modeled as a gray medium, and the discrete ordinates method was used to solve the radiative transfer equation to calculate the local radiation source/sink in the energy equation for the solid phase. The fully coupled nature of the calculations without external specification of flame location represents a key advance over past efforts towards modeling of porous radiant burners, because for a given mass flow rate the actual heat loss from the flame determines its position and is not a free parameter. The calculated results for the burner surface temperature, the gas exhaust temperature and the radiation efficiency for a single layer Fecralloy burner were compared with experimental data from this laboratory and reasonable agreement was obtained for a range of operating conditions. [DOI: 10.1115/1.1527910]

Keywords: Combustion, Flame, Heat Transfer, Radiation

1 Introduction

Gas fired radiant burners are used in a number of manufacturing processes such as paper drying and finishing, powder and paint curing, baking, textile drying and polymer thermal processing. Interest in gas-fired radiant burners/heaters for materials processing and manufacturing applications is increasing due to their desirable characteristics of high radiant heating rates and minimal pollutant emissions [1,2,4–6]. There are two types of porous gas burners: 1) those with the flames anchored at the surface and 2) those with flames submerged (embedded) in the solid matrix [1,2]. The surface flame type burners are limited to a firing rate of about 300 kW/m^2 and have modest radiant efficiencies. Submerged flame burners, like the reticulated ceramic burners, may have higher radiant efficiencies and firing rates [5]. However, the mechanical properties of the ceramics are poor under demanding thermal cycling; metal fiber burners with flames embedded in the fiber matrix have potentially similar thermal performance as the reticulated ceramic heaters with increased durability. Air and fuel are mixed prior to entering the fiber matrix leading to premixed combustion. A large surface area to volume ratio of the matrix results in effective convective heat transfer between the gaseous reactants and combustion products and the solid. The matrix is at a higher temperature in the preheat region due to radiation and conduction heat transfer upstream from the reaction zone. The incoming fuel air mixture is preheated and the ranges of flammability and flame stability may be substantially extended [3,4].

Recent reviews of past work on radiant burners are available [2,6] and need not be repeated here. The emphasis in these reviews is on porous burners using reticulated ceramics for the pads. Reports on burners using woven metal fibers for pads are fewer. Pioneering work in modeling a sintered metal fiber burner was done by Golombok et al. [7]. In addition to the highly refractory properties (i.e., ability to endure both the high temperatures and the thermal cycling associated with the burner operation), metal fiber structure enhances the emittance of the burner [8]. Using a 22 μm diameter Fecralloy fiber mat with a porosity of 80 percent (empirically determined to yield close to optimum performance, according to the authors), the authors developed a one-dimensional model with single-step chemistry and obtained stable flames with firing rates in the range 100 to 700 kW/m^2. The main feature of the model was the consideration of anisotropic effective solid thermal conductivity resulting from the fiber arrangement. Internal radiation was included by means of an enhanced conductivity and the model equations were simplified using the method of activation energy asymptotics (i.e., the reduction of the burner to a sequence of boundary value problems). The reaction zone thickness and solid temperature were varied iteratively until the asymptotic boundary conditions at the exit were satisfied. Similar studies [9,10] modeled combustion in high-porosity isotropic burners made of alumina and silica fibers, and the role of the thermal conductivity in controlling the flame speed and stability was emphasized. One study [9] identified an increase in the thermal conductivity as a reason for an increase in the flame speed and a net decrease in radiant efficiency. Because of this, Golombok et al. [7] suggested that the relatively low effective conductivity of a metal fiber burner was of great interest in enhancing performance.

Another numerical study of the heat transfer characteristics of a porous radiant burner was performed by Tong and Sathe [11] using a one-dimensional conduction, convection and radiation model. The combustion was modeled as a spatially dependent heat generation, and the lack of thermal equilibrium between the gas and solid phases was accounted for by using separate energy equations for the two phases. The solid matrix was assumed to emit, absorb, and scatter radiant energy, and the spherical harmonics approximation was used to solve the radiative transfer equation. The authors found that for a given rate of heat generation, large optical thicknesses and high volumetric heat transfer coefficients were desirable for maximizing the radiant output. Furthermore, low solid thermal conductivities (in agreement with the

Contributed by the Heat Transfer Division for publication in the JOURNAL OF HEAT TRANSFER. Manuscript received by the Heat Transfer Division February 26, 2001; revision received September 4, 2002. Associate Editor: R. Skocypec.

studies described above), scattering albedos and flow velocities, and high reflectivities produced the highest radiant output in their parametric calculations.

A different formulation for the heat transport in a fiber burner was developed by Andersen [12]. The model accounted for heat transfer by conduction in the fibers as well as in the gas, and the radiation inside the fibrous material was modeled by the two-flux formulation, i.e., isotropic scattering was not assumed. Conduction was not modeled, rather the solid conductivity was used as the effective conductivity, but the main limitation was that a prescribed heat release function for combustion inside the fibrous layer was used instead of fully coupling the heat transfer and the chemical reactions. The reported predictions were only of a qualitative nature.

Hsu and Matthews [13] first identified the necessity of using detailed chemical kinetics. Prior researchers had simulated the gas-phase reactions using single-step chemistry [10] or simulated the combustion process as a prescribed heat source [11,12], but Hsu and Matthews [13] made predictions using both single-step and multi-step kinetics mechanisms. They concluded that it was essential to use multi-step kinetics if accurate predictions of the temperature distributions, energy release rates, total energy release, and composition profiles and emissions were sought. The authors showed that single-step kinetics was adequate for predicting all the flame characteristics except the pollutant emissions for the very lean conditions ($\Phi \approx 0.5$) under which equilibrium favors the more complete combustion process dictated by global chemistry. However, for higher equivalence ratios the errors were significant. For $\Phi = 1.0$, the error in the peak gas temperature could be hundreds of degrees.

Rumminger et al. [14] developed a one-dimensional model for simulating a reticulated ceramic burner operation. The model employed multistep chemistry and used a two-flux approximation for radiative transfer. The authors assumed complete combustion at a downstream boundary. The results are compared to measurements of gas temperatures above the burner. Uncertainties in the porous medium properties and effects of solid surface on chemistry were highlighted. The main distinction of the present work from that of Hsu and Matthews [13] and those cited in References [2] and [6] is that the location of the flame in the porous solid is not prescribed and that more realistic properties as well as transport coefficients are being used. Henneke and Ellzey [15] have carried out a transient analysis of flame propagation in a 52.2 cm thick porous bed using complete methane-air chemistry and were able to predict flame propagation direction to a fixed location with good accuracy.

The purpose of this paper is to report on a combustion/heat transfer model for predicting the thermal performance and temperature distributions in a metal fiber, woven-matrix porous radiant burner/heater using a detailed methane chemistry model [16]. The model predictions for the thermal performance of the burner are compared with the experimental results from a radiant heater with a novel design using Fecralloy for the burner pad [17–19].

2 Analysis

2.1 Model Description and Assumptions. A schematic of a one-dimensional radiant burner and the relevant heat transfer modes are shown in Fig. 1. A mixture of gas and air enters an inert porous material on the left ($x=0$). The material consists of a homogeneous matrix, comprised of one or more layers. The chemical reactions take place within the solid and the flame is anchored at a location that is not known *a priori*, but rather determined by the interaction of conduction, convection, advection, radiation and chemical energy release due to combustion. As the chemical energy is released in the gas phase, a fraction of the heat is transferred from the gas to the solid by convection and in its turn energy is radiated by the solid.

An approach involving a fixed flame location cannot be used for radiant burner pads, because for a fixed flow rate the flame position along with the heat loss is a solution to the coupled equations. A fixed flame position approach can be used in deep porous reactors [2,15], because the heat loss reaches a value that is independent of flame position in such cases.

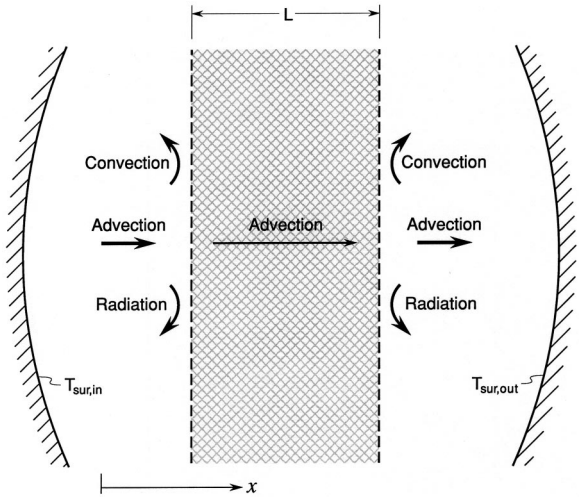

Fig. 1 Schematic of a one-dimensional porous burner. The relevant heat transfer modes are indicated with arrows; advection by the gas; convection and radiation from the faces; conduction (two phases), convection, radiation and chemical release inside the solid domain.

A number of assumptions are needed to cast the problem in a form suitable for a relatively simple numerical solution. The main interest is in obtaining the performance of the burner in steady-state operation and not during transients. The idealizations used in this study are: (1) The burner is considered to be very large in directions perpendicular to the inlet velocity so that one-dimensional flow and heat transfer can be assumed. This is a very good assumption since the flame zone is much thinner than the non-axial dimensions of the porous medium. Visual observations and photographic images [17,18] reveal clearly that the temperature over the entire face of the burner was uniform; (2) Combustion gases behave as ideal gases and Dufour and Soret effects are neglected; (3) The processes are steady, the flame is one-dimensional and heat losses to the sides of the burner are negligible in comparison to the heat release; (4) Homogeneous chemical reaction takes place only in the gas phase, no surface (catalytic) reactions are considered; (5) Inlet velocities are small and they remain small enough, in spite of the acceleration due to the property changes and heat release, for the flow to be laminar so that the process is isobaric; (6) Solid and gas phases are not in thermal equilibrium, i.e., there is a net exchange due to convection within the matrix. The volumetric heat transfer coefficient is considered to be constant throughout the porous pad, i.e., not a function of the local gas velocity; (7) The solid matrix is considered spectrally gray and its thermophysical and radiative properties are taken as constant; (8) The pore dimensions are small, therefore, the gas opacity is also small particularly in relation to the porous matrix opacity, and hence the gas phase can be considered as radiatively non-participating; and (9) The index of refraction of the medium is assumed to be unity.

Note that simplifications have not been made regarding the chemical reactions, which can include any number of elementary steps and intermediate species. A discussion of the chemical kinetics treatment is given in the next subsection.

2.2 Model Equations. The equations governing a steady, isobaric, one-dimensional (constant area) flame propagation inside a porous material may be written (included here only for completeness) using the aforementioned assumptions as follows [6]:

Continuity.

$$\dot{m} = \rho_g u A \tag{1}$$

The heater area, A, is considered to be unity in this one-dimensional formulation.

Species ($k=1, \ldots, K$)

$$\rho_g u \frac{dY_k}{dx} - \frac{d}{dx}(\rho_g Y_k V_k) - \dot{\omega}_k W_k = 0 \tag{2}$$

Energy for Gas

$$\rho_g c_{pg} u \frac{dT_g}{dx} - \frac{d}{dx}\left(k_g \frac{dT_g}{dx}\right) + \sum_{k=1}^{K} \rho_g Y_k V_k c_{pk} \frac{dT_g}{dx} + \sum_{k-1}^{K} \dot{\omega}_k h_k W_k - h_v (T_g - T_s) = 0 \tag{3}$$

Energy for Solid

$$\frac{d}{dx}\left(k_s \frac{dT_s}{dx}\right) - \frac{d\mathcal{F}}{dx} + h_v (T_g - T_s) = 0 \tag{4}$$

Radiative Transfer

$$\frac{d\mathcal{F}}{dx} = \kappa\left[4\sigma T_s^4 - 2\pi \int_{-1}^{1} I(x,\mu) d\mu\right] = 0 \tag{5}$$

Equation of State

$$\rho_g = \frac{p W_g}{\mathcal{R} T} \tag{6}$$

Equation (2) states the balance between (from left to right) advection, diffusion and source (or sink) for each of the K species. In the gas energy equation, Eq. (3), the balance between convection, conduction, interdiffusion, heat release and convection to the solid phase is enforced. The solid energy equation, Eq. (4), accounts for the balance between conduction, convection to the gas phase and radiation. Note that these equations are tightly coupled. The same convection term, $h_v(T_g - T_s)$, appears as a source in the gas energy equation and as a sink in the solid energy equation. The generation term for the k species (last term in the left-hand-side of Eq. (3), $\dot{\omega}_k W_k$) multiplied by the enthalpy of that species, h_k, is included in the gas energy balance. Additionally, the mass continuity equation, Eq. (1) is coupled to all species and gas energy balances through the advection terms.

In order to close the system of differential equations (Eqs. (1) to (6)), it is necessary to model the source terms. The net chemical production rates, $\dot{\omega}_k$, of each species results from a competition between all of the chemical reactions involving that species. The PREMIX code [20] and the CHEMKIN package were modified to solve the above partial differential equations. The details of program modifications are described by Leonardi [17].

The chemical kinetics was simulated assuming that each reaction proceeded according to the law of mass action and that the forward rate coefficient, k_f, were in the modified Arrhenius form:

$$k_f = a_1 T^{a2} \exp\left(-\frac{\varepsilon}{\mathcal{R} T}\right) \tag{7}$$

The details of the chemical reaction equations and the thermochemical properties are found in the user's manual for CHEMKIN [21].

The constants a_1, a_2 and ε for the Arrhenius expressions were obtained from the GRI-Mech 2.11 mechanism [16]. GRI-Mech 2.11 is a compilation of 277 elementary chemical reactions and associated rate coefficient expressions and thermochemical parameters for the 49 species in the reactions. It differs from the version 1.2 release in that it includes nitrogen chemistry relevant to natural gas chemistry and reburning. More recently, an updated version of the kinetics rates has been released in GRIMech 3.0. However, the changes involved do not affect the present results significantly.

In CHEMKIN, the thermophysical properties of the individual species, such as thermal conductivity and diffusion coefficient, are evaluated using Stockmayer potentials. An extended Euken-Hirshfelder correction for polyatomic species was also included. A more detailed description can be found in Kee et al. [22]. The gas mixture thermal conductivity was determined from the individual component conductivities by means of an empirical combination averaging formula as done by Mathur et al. [23].

2.3 Radiative Transfer. The radiative transfer equation which allows calculation of the radiation intensity appearing in Eq. (5) is needed to close the problem. Emission, absorption and scattering are treated by performing an energy balance on the radiative energy emitted, absorbed, scattered out from a direction **s** (out-scattering) and scattering into the direction **s** (in-scattering). The radiative transfer equation can be solved using the discrete ordinates method [24]. For a set of N discrete directions the integrodifferential equation for radiative transfer can be expressed as

$$\mu_i \frac{dI(x,\mu_i)}{dx} = \kappa(x) I_b(x) - \beta(x) I(x,\mu_i) + \frac{\sigma(x)}{4\pi} \sum_{j=1}^{N} w_j p(\mu_i, \mu_j) I(x,\mu_i,\mu_j), \quad i = 1,2,\ldots,N \tag{8}$$

with $\beta = \kappa + \sigma$. The N equations are subject to the boundary conditions on the face of the burner

$$I(x_L,\mu_i) = (1-\phi)\rho_L I_b(T_{\text{sur}}) + (1-\phi)\left[\varepsilon_L I_b(x_L) + \frac{\rho_L}{\pi} \sum_{\hat{n}\cdot\hat{s}_j} w_j p(\mu_i,\mu_j) I(x,\mu_i,\mu_j)\mu_j\right], \quad \mathbf{n}\cdot\mathbf{s}_j > 0 \tag{9}$$

A similar equation holds for the right face of the burner/heater.

Equation (8) together with the boundary conditions given by Eq. (9) constitute a set of N simultaneous, first-order, linear ordinary differential equations for the unknown intensities in the discretized directions. If scattering is present ($\sigma \neq 0$), the equations are coupled in such a way that generally an iterative solution scheme is necessary. The computational details are given elsewhere [17].

2.4 Boundary Conditions. Boundary conditions are needed for the dependent variables: mass flow rate, $\dot{m}$, species concentrations, Y_k, gas temperature T_g and solid temperature, T_s. The mass flow rate, $\dot{m}$, is a known constant determined by the desired firing rate and equivalence ratio. The gas temperature at the inlet is found enforcing that all the heat conducted upstream is advected back into the (left) computational domain:

$$\dot{m} c_{\text{pg}} (T_l - T_{\text{in}}) = k_{gl} \left.\frac{dT}{dx}\right|_1 \tag{10}$$

Note that a simple Dirichlet boundary condition (as in the original PREMIX code) does not work properly due to unaccounted heat losses. The temperature gradient at the inlet is not zero in some cases (especially at low firing rates), and the fixed-temperature boundary condition results in energy conducted upstream that does not return into the computational domain.

The species concentrations boundary conditions at the cold boundary are determined by a balance between advection and diffusion which corresponds to specifying the mass flux fractions, $Y_k + \rho_g Y_k V_k A/\dot{m}$, for all species. These quantities are zero for all species except CH_4, O_2 and N_2.

Vanishing gradients are imposed for the gas temperature and the mass fractions at the outlet boundary (beyond the front face of the burner), except for O_2 and N_2 which are set to values corresponding to the ambient atmospheric conditions to allow for back-diffusion.

The solid faces (both on the left and right) are subjected to convective heat transfer to the gas and also exchange radiation with the surroundings. The effect of the reduction of the solid surface area due to porosity is accounted for in the convection and conduction terms. However, since the fibers are of small dimensions and thus relatively optically thin, the entire area (and not only the fraction $1-\phi$) is considered to exchange thermal radiation with the surroundings. This also accounts for radiative losses from the fibers that are one or two layers deep into the surface

$$(1-\phi)\left[h_L(T_g-T_s)+k_s\frac{dT_s}{dx}\right]_L=\varepsilon_L\sigma(T_s^4-T_{\text{sur,in}}^4)_L \quad (11)$$

$$(1-\phi)\left[h_R(T_g-T_s)+k_s\frac{dT_s}{dx}\right]_R=\varepsilon_R\sigma(T_s^4-T_{\text{sur,out}}^4)_R \quad (12)$$

Note that in writing Eq. (12) absorption of radiation emerging from the solid matrix by the gases as well as emission and self-absorption of radiation by the combustion products upstream of the outlet has been neglected. Of course, neglect of radiation from the gases would lead to underprediction of the solid temperature near the right boundary. The neglect is justified on the basis that the pad is effectively opaque and the radiation emerging from it is much more intense than emitted by the optically thin gases (CO_2 and H_2O) at a lower temperature than the pad. This physical situation is unlike to that in deep porous burners [13,15] or where the flame is anchored at the face of the burner [14]. Therefore, because uncertainties in the model input parameters and the small opacity of the combustion products the preheating of the solid matrix by the gases is neglected. Any preheating of the right face of the matrix by the gases can be simulated by arbitrarily increasing the surrounding temperature, $T_{\text{sur,out}}$.

The thermal coupling between the solid and gas phases is affected through the volumetric heat transfer coefficient h_v. The coefficient cannot be predicted for the complex, irregular geometries of fibrous materials. This parameter plays an important role in determining the nature of the solution; therefore, these data were obtained through experimentation [17].

2.5 Method of Solution. The PREMIX computer program modifications, the solution strategy and the computer program validation are given by Leonardi [17].

The solution of the model equations requires specifying the properties of the solid and the composition of the fuel stream. For this purpose, a single 0.2 cm thick Fecralloy layer was considered as the flame support material which started at $x=0.2$ cm and ended at $x=0.4$ cm. The computational domain extends up to $x=0.5$ cm. For plotting purposes, however, the inlet plenum (i.e., the initial 0.2 cm) is not included. This is done in order to show in more detail the remainder of the computational domain where the changes actually occur. The gas-only region (from $x=0$ to $x=0.2$ cm) serves to model the inlet plenum. The incoming fuel mixture was selected to be of an equivalence ratio of 1.1, which resulted in relatively fast computations (5 to 10 CPU hours on an IBM 6000 machine) due to the lack of the complex HC and NO chemistry of richer flames and allowed a study of the effects of partial premixing.

The numerical solution of the model equations to the desired tolerance (absolute tolerance of 10^{-9}, relative tolerance of 10^{-4}, assuring four digits of accuracy) required using 67 mesh points for the gas phase: 45 points were used for the upstream preheat and flame zone, seven for the two-phase region after the flame and the remaining 13 for the downstream gas-only zone. The solution in the solid domain needed 54 points. It is interesting to note that there is a region with a relatively high accumulation of mesh points at the exit of the domain (at the right) due to the presence of a second (diffusion) flame, and the need of matching the imposed Dirichlet boundary condition that specifies the O_2 and N_2 concentrations there. Further details of the adaptive grid refinement and computations are provided by Leonardi [17].

Numerically the problem considered is much more challenging than that analyzed by Henneke and Ellzey [15] who considered filtration combustion in a packed bed. The metal fiber woven pad (2–4 mm thick) was two orders of magnitude (versus 52.2 cm) thinner than the one considered by them. Stabilization of the flame inside the thin layer was a major difficulty of the numerical simulations, because, as already discussed, the location of the flame cannot be fixed *a priori*. The authors recognize that the function of the packed bed porous burner is to convert efficiently chemical energy to thermal energy of the gases and not to convert chemical energy to radiant energy.

Table 1 Mechanical and thermophysical characteristics of Frecralloy* metal fiber mat used for the burner pad

Characteristic or Property	NIT100S	NIT200S
Density, ρ (kg/m^3)	540	600
Specific heat, c_p (J/kg K)	432 (333 K)	422 (333 K)
Thermal conductivity, k (W/m K)	0.13	0.13
Fiber diameter, d (μm)	35	35
Emittance, ε (−)	0.65	0.65
Porosity, ϕ (−)	0.91	0.91

*Accotech Corp., Marietta, GA 30067

3 Experimental Methods

A diffuser based housing provided a uniformly distributed fuel air mixture to the 30 cm×30 cm square burner with the porous woven fibrous metal (Fecralloy, NIT200S) pad flame support layer. The physical and thermophysical characteristics of the Fecralloy woven pad used are summarized in Table 1. Fecralloy is a refractory steel which has a very good oxidation resistance even at temperatures above 1000°C. The detailed description of the novel experimental burner, instrumentation and instrument arrangement is given elsewhere [16–18]. Methane gas was used as fuel, and the fuel firing rates ranged form 170 to 340 kW/m^2. The equivalence ratios were in a narrow range ($0.9\leqslant\Phi\leqslant1.1$) and were confined to values expected for the operating conditions of the burner/radiant heater. Here, only the burner surface and exhaust temperature measurements are discussed.

The difference in radiation efficiency for different positions of the radiation flux detector was less than 0.5 percent, indicating the reaction uniformity across the surface. The experimental uncertainty obtained by error propagation of an estimated maximum 10 percent error in fuel flow setting and a 3 percent error in the radiometer readings was less than 5 percent for all conditions [17]. The experimental uncertainty in radiation efficiency measurements was estimated to be ±2 percent.

3.1 Burner Surface Temperature Measurements. Radiation thermometers (Ircon Ultimax and Raytec Raynger) calibrated in the ranges 40–400 C, 0–540 C and 500–2800 C were used to measure the apparent burner surface temperature. The surface temperature determined by the radiometer is based on the heat flux measured by the radiometer which results from emission of radiation at various locations within the porous material and not just at the surface. Further, the participating combustion gases absorb a portion of the flux. Therefore, the temperatures indicated by the radiometers are only approximate representations of the apparent surface temperature. The temperatures reported here were also verified by comparison with measurements of the burner surface spectral radiation intensity obtained with spectral radiometers. These data allow elimination of the interference from the absorbing species using selection of a wavelength band around

3.8 μm wavelength for the determination of the apparent solid surface temperature. These data showed that the errors in the surface temperature data caused by gas band absorption were less than 50K for the present conditions.

3.2 Exhaust Gas Temperature and Spectral Intensity. Measurements of the exhaust gas temperature in the neighborhood of the strong thermal radiation field emitted by the burner surface is usually a difficult problem from the experimental point of view. It is not possible to use a simple thermocouple because the radiation corrections become significant and prone to uncertainty. More sophisticated methods are necessary and an up-to-date discussion is available [17].

In this study, a fast infrared array spectrometer (FIAS) to simultaneously measure spectral radiation intensities over the 1.8 to 4.9 μm wavelength range was used. The range covers two important bands of CO_2 and one important band of H_2O radiation. Radiation from the flame (the detector is placed in such a way that its line of view is parallel to the burner surface to avoid the direct radiation from the solid matrix) is directed and dispersed over a staggered 160-element linear array PbSe detector. A tuning fork chopper at a fixed frequency of 390 Hz is used. During each chopper cycle ten scans are initiated over the 160-pixel linear array PbSe detector. Ji et al. [25] report the details about the instrumentation, including specifications and calibration procedure. Once the gas emission spectrum is available (see Ref. [19] for a sample spectrum form the FIAS), species concentrations and temperature were calculated using an inverse iterative procedure. A narrow band analysis in RADCAL [26] was used for an inverse iterative procedure. A more recent radiation model [27] does not improve the results [28]. Recently, Ji et al. [28] compared several adiabatic turbulent lean premixed flame temperatures with this measured procedure. Based on their success, the temperature of the exhaust gases for the present study was measured using the same procedure. The heater was mounted in a horizontal position (facing upwards to allow the hot gases plume to rise from the solid surface). The measurement location was within the view angle at a distance of approximately 2.5 cm from the burner to minimize the entrainment of (cold) room air. Emission spectra were acquired for several firing rates and equivalence ratios [17,19].

4. Results and Discussion

4.1 Flame Location. Depending on the operating conditions, the radiant burner flame stabilizes within the porous matrix or above its surface. The transition from an embedded flame to a surface anchored flame occurs both at the lowest firing rates and at the highest firing rates. The latter limit is based on the incoming reactant velocity being greater than the adiabatic and super adiabatic flame speed attainable in this configuration. This limit was not observed in the present experiments and computations. The surface flame at the lower limit firing rates occurs because the heat released is not sufficient to sustain the energy transferred to the solid matrix. This limit was observed both in the present experiments and the present computations. The surface flame stabilization was observed to occur at a firing rate of around 100 kW/m^2 in the experiment while the computations showed the surface flame at a much higher firing rate of 220 kW/m^2. It is encouraging that an inherent instability was at least qualitatively captured by the computations. However, in view of the vast differences in the applicable physical process in the two flame regimes, further comparison between the measurements and the predictions are limited to the embedded flame regime.

Visual observations and photographic images [17,18] showed that the flame was embedded inside the porous matrix and the pad was uniform in appearance over the entire face. This suggests that heat losses from the edges of the housing were small, and the process of combustion and heat transfer could be treated as one-dimensional inspite of some heat losses from the outside of the housing walls.

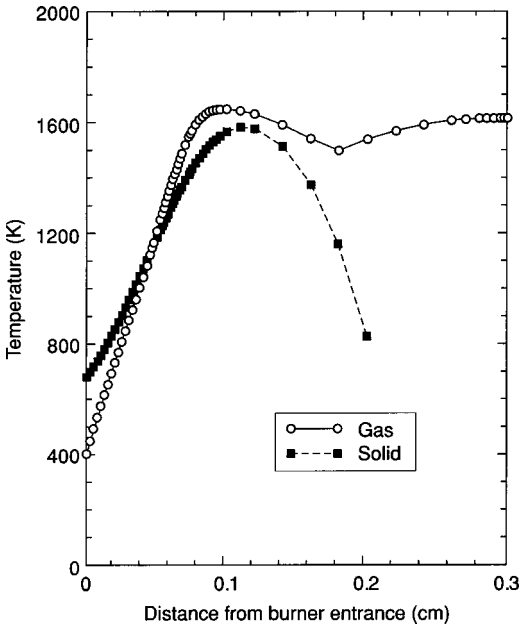

Fig. 2 Calculated gas and solid matrix temperature distributions inside the porous radiant burner/heater

4.2 Temperature Distributions in Gas and Solid Phases. The relevant model parameters are: porous matrix thickness, $L = 0.002$ m; volumetric (average) heat transfer coefficient, $h_v = 1 \times 10^6$ W/m^3 K [16]; extinction coefficient, $\beta = 200$ m^{-1}; scattering coefficient, $\sigma = 20$ m^{-1}; phase function, $p(\mu', \mu) = 1$ (isotropic scattering); heat transfer coefficient at faces, $h = 50$ W/m^2 K. The physical characteristics and the thermophysical properties of the NIT200S Fecralloy metal fiber woven pad used in the experiments are summarized in Table 1. Discrete ordinate equations were carried up to order 4 (S_4-approximation); symmetric and non-symmetric S_2 were not accurate enough and higher (than S_4) order approximations did not improve the accuracy of the solution. Downstream O_2 concentration was assumed to be 0.2 and the surrounding temperature was selected to be 400 K based on the effects of hot gases. Note that the concept of "surface" for a fibrous material can be ambiguous and often requires a clearer definition. It can refer to the whole surface of the material, or only the fraction of the area occupied by the uppermost layer of fibers. The former definition is used here to define the radiation boundary.

Figure 2 depicts the calculated gas and solid temperature distributions inside the burner and the gas space above or in front of it, depending on the burner orientation. The temperature profile of the gas shows a rapid, quasi-linear increase at the burner entrance. It peaks at the flame location ($x \approx 0.09$ cm, a premixed flame) and then decreases since the combustion gases transfer energy to the solid. These losses are larger than the still ongoing chemical heat release. The gas temperature past the peak is higher than the solid temperature. Heat is transferred from the hot gas to the solid preflame region by both solid conduction and radiation. In this region energy is then transferred from the solid back to the gas to preheat the gas. In the post-peak region the solid looses heat by radiation across the front face and its temperature drops. After leaving the solid matrix, the gas temperature rises again, mainly due to the continued oxidation of CO and H_2 (diffusion flame). The premixed flame inside a porous burner is considerably thicker than a free flame, mainly because the preheating takes place over a broader region.

The temperature distribution in the solid matrix is approximately parabolic, with a subtle inflection point near the entrance of the burner, where the gas temperature, initially low, reaches the

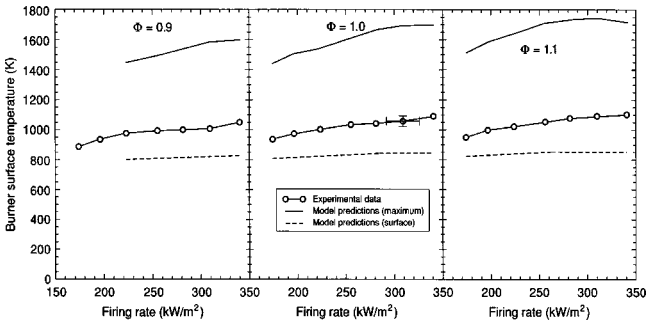

Fig. 3 Comparison of the predicted and measured burner surface temperatures for different fuel inlet mixtures

temperature of the solid. Peak temperatures of the solid matrix are reached some distance downstream of the maximum gas temperature at about $x \approx 0.12$ cm.

In the entrance region ($x < 0.05$ cm) the porous solid is at a higher temperature than the gas mixture and preheats it. The gas temperature increases at a faster rate than the solid matrix temperature because of the heat transfer from the reaction zone. A local maximum in the gas temperature occurs at $x \approx 0.08$ cm, indicating that the trend is reversed, i.e., the temperature of the solid increases faster. There is another local extremum in the gas temperature (in this case, a minimum) at $x \approx 0.18$ cm, after which the temperature difference between the gas and the solid increases significantly corresponding to the region near the burner face, where the solid matrix temperature decreases due to radiative output (even though the hot gases are still transferring energy to the solid by convection). Exit temperature difference between the gas and the solid is about 700 K.

4.3 Solid Surface Temperature. The predictions of the surface temperature of the solid matrix are plotted together with the experimental data obtained from the radiometric measurements in Fig. 3 for equivalence ratios of $\Phi = 0.9$, 1.0, and 1.1. For all inlet mixtures, the surface temperatures increase with an increase in the firing rate, and the simulations capture this trend. Note that the predicted "surface" temperature (i.e., the temperature of the last grid point of the solid matrix) is always about 200 K below the data, but the data always lie between the calculated surface and maximum temperatures. As mentioned earlier, the experimental technique relies on comparing the radiant flux emitted by the burner to that of a blackbody. The fact that the measurements are in between the calculated surface and maximum temperatures is indicative of radiation being emitted not only from the surface but partly from the bulk of the matrix. The concept of a "surface" is not straightforward for a porous medium.

4.4 Temperature of the Exhaust Gases. A comparison between the model predictions and the experimental exit gas temperature data for the single-layer Fecralloy burner is shown in Fig. 4 for equivalence ratios of $\Phi = 0.9$, 1.0, and 1.1. The general trends in all cases is that the gas temperature increases with increasing firing rate since the flame temperature increases and its location is almost constant. The model predictions tend to capture this general behavior with a few exceptions discussed below.

For the rich flame ($\Phi = 1.1$), the numerical results present initially a steep gradient, but the increase in the gas temperature moderates (and eventually decreases) at the highest firing rates. This particular deviation from the general trend at the higher end of the firing range can be explained by realizing that the reaction zone stabilizes further away from the burner face, deeper inside the solid matrix; and the peak flame temperature increase is not enough to compensate for the additional convective heat losses (since the hot gases are in contact with the porous medium for a longer time).

Relatively good agreement is observed for the stoichiometric

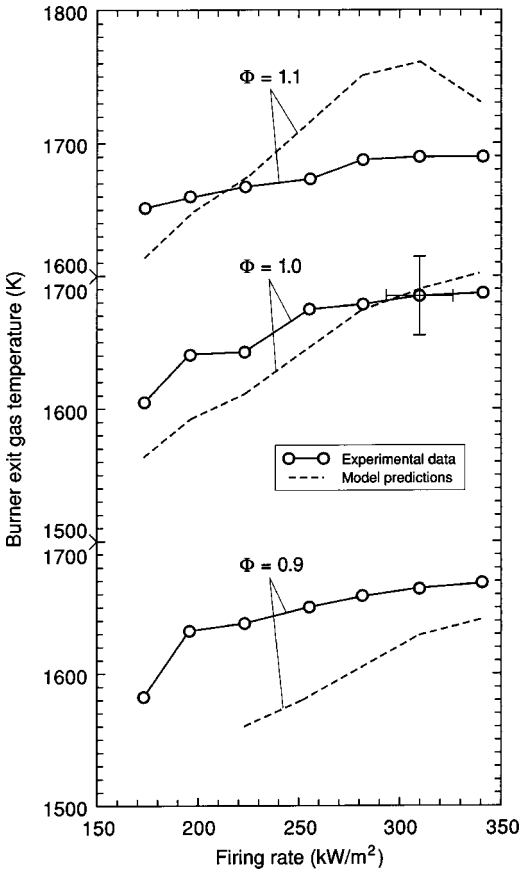

Fig. 4 Comparison of the predicted and measured exit gas temperatures for different fuel inlet mixtures

case ($\Phi = 1.0$) where data and the predictions are identical at the firing rate of 300 kW/m^2. On the other hand, the lean mixture case ($\Phi = 0.9$) shows that the gas temperature is somewhat underpredicted for firing rates between 220 and 340 kW/m^2. Below this range (not shown in the figure), the calculated results are much higher than the data since the computer program predicts that the flame stabilizes outside the solid matrix instead of within the pad. Therefore, the heat losses from the gas phase become considerably smaller [18].

4.5 Radiation Efficiency. A comparison of measured and predicted radiation efficiency as a function of the firing rate is shown in Fig. 5. The estimated experimental uncertainty in the determination of the gas firing rate (FR) and the efficiency are indicated by the bars. At a lower firing rate range, up to 225 kW/m^2, there was an increase in the efficiency for all inlet mixture and configuration combinations indicating that heat losses from the burner housing to the surroundings were significant. Additionally, effects of more incomplete chemistry at the lower temperatures can have an impact. At higher firing rates the radiation efficiency was approximately constant in the range of 18–26 percent. However, the numerical predictions show that the firing rate at which the maximum occurs decreases slightly with increasing equivalence ratio, from 310 kW/m^2 for $\Phi = 0.9$ to 280 kW/m^2 for$=1.1$ as shown in Fig. 5.

It was observed that the burners with the thicker flame support pad (double Fecralloy layer) had higher radiation efficiency than their thinner counterparts at the same operating conditions. This performance increase was probably a combination of two factors: a longer gas mixture residence time in the high temperature region resulting in more complete combustion, and an effective increase in pad volume allowing for a larger fraction of thermal radiation emission since radiation is emitted not only from the surface but

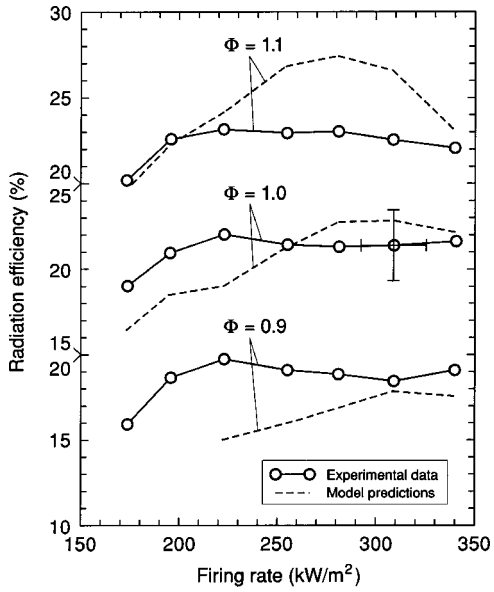

Fig. 5 Comparison of the predicted and measured radiation efficiency for different fuel inlet mixtures

also from within the semitransparent material. Radiation efficiency for the double-layer burner was about 2 percent to 3 percent higher when using the single-layer burner.

Finally, for both single- and double-layer burners, the radiation efficiency increased when increasing the equivalence ratio (in the studied range $\Phi=0.9$ to 1.1, i.e., near stoichiometric conditions). The same trend was noted for all firing rates. This observation agrees with the fact that the maximum adiabatic flame temperature occurs not at stoichiometric, but rather at a slightly rich equivalence ratio as a consequence of both the heat of combustion and the heat capacity of the product declining beyond $\Phi=1.0$. For equivalence ratios between $\Phi=1.0$ and $\Phi(T_{max})$, the heat capacity decreases more rapidly than the heat of combustion [29]. In addition, the need for oxygen from the surroundings pushes the flame towards the surface leading to lower losses by self-absorption.

The results were consistent with those obtained with commercial metal-fiber burners. Singh [30] performed extensive measurements using industrial burners and obtained similar radiation efficiency results for stoichiometric and 10 percent excess air inlet mixtures at firing rates beyond 225 kW/m^2. Radiation efficiency is predicted reasonably well for the stoichiometric mixture ($\Phi=1.0$). Agreement is not as good for rich ($\Phi=1.1$) and lean ($\Phi=0.9$) mixtures, being over and under predicted.

5 Conclusions

A one-dimensional model has been developed to predict the flame structure inside a metal-fiber, woven-matrix (Fecralloy) pad and the thermal performance of the porous burner. The chemical reactions were modeled using the GRI-Mech 2.11 mechanism. The key features of this model are that fully coupled heat transfer and combustion processes were modelled with realistic material property specifications. Based on the results obtained the following conclusions can be drawn:

- A surface flame (i.e., not submerged) was predicted for certain conditions such as a lean mixture at low firing rates. Even though the magnitude of the firing rate at which this transition occurred was not adequately reproduced, it is encouraging that the model captures this experimentally observed behavior. A drastic drop in radiation efficiency was predicted when the premixed flame moves outside the pad. This is in agreement with experimental measurements.
- The model predictions for global parameters (burner surface temperature, gas exit temperature and radiation efficiency) were compared with experimental data for three different equivalence ratios ($\Phi=0.9$, 1.0 and 1.1) for a wide range of firing rates (170 to 340 kW/m^2) and the two results were found to be consistent.
- Extensive parameter studies have been carried out to study the effects of the volumetric heat transfer coefficient, solid matrix emittance, effective thermal conductivity, extinction and scattering coefficients as well as firing conditions on the thermal performance, and the results are given elsewhere [17]. All of the burner operating conditions were found to play an important role in determining the combustion and thermal characteristics of the system.

Acknowledgments

The authors acknowledge useful discussions with Mr. Shyam Singh of SSEEI, Inc. and Dr. Kevin Krist of the Gas Research Institute. This work was supported, in part, by the Gas Research Institute under contract No. 5093-260-2659 to SSEEI, Inc. with Dr. Krist serving as the GRI Program Manager. We also thank Dr. Ozzie Missoum of Acotech Corporation for supplying the Fecralloy samples.

Nomenclature

A = cross sectional heater area
a_1 = pre-exponential coefficient in the modified Arrhenuis equation, Eq. (7)
c = specific heat
$\mathcal{E}$ = activation energy
$\mathcal{F}$ = radiative heat flux
FR = firing rate per unit area
h = heat transfer coefficient
h_v = volumetric heat transfer coefficient between gas and solid
I = intensity of radiation
I_b = Planck's function (integrated over spectrum)
L = burner pad thickness
m = mass flow rate per unit area
$\mathbf{n}$ = unit normal
k = thermal conductivity
$\mathcal{R}$ = universal gas constant
s = unit vector in given direction
T = temperature
u = velocity of the gas mixture
V = diffusion velocity
W = molecular weight
x = spatial coordinate (see Fig. 1)
Y = mass fraction
ε = emittance of burner pad
β = extinction coefficient
μ = dynamic viscosity or direction cosine ($\mu=\mathbf{n}\cdot\mathbf{s}$)
ρ = mass density or reflectance of burner pad
σ = scattering coefficient or Stefan-Boltzmann constant
Φ = equivalence ratio
ϕ = porosity
ω = single scattering albedo, σ/β
$\dot{\omega}$ = species production

Subscripts

L = left face of burner (boundary), see Fig. 1
b = blackbody
g = gas
in = inlet condition
k = solid
R = right face of burner (boundary), see Fig. 1
sur = surroundings
w = wall

References

[1] Viskanta, R., 1996, ''Interaction of Combustion and Heat Transfer in Porous Inert Media,'' *Transport Phenomena in Combustion*, S. H. Chan, ed., Taylor & Francis, Washington, DC, pp. 64–87.

[2] Howell, J. R., Hall, M. J., and Ellzey, J. L., 1996, ''Combustion of Hydrocarbon Fuels Within Porous Media,'' Prog. Energy Combust. Sci., **22**, pp. 121–145.

[3] Weinberg, R. J., 1986, ''Combustion in Heat Recirculating Rurners,'' *Advanced Combustion Methods*,'' F. J. Weinberg, ed., Academic Press, London, pp. 183–236.

[4] Hsu, P-F., Evans, W. D., and Howell, J. R., 1993, ''Experimental and Numerical Study of Premixed Combustion Within Homogeneous, Porous Ceramics,'' Combust. Sci. Technol., **90**, pp. 149–172.

[5] Mital, R., Gore, J. P., and Viskanta, R., 1997, ''A Study of the Structure of Submerged Reaction Zone in Porous Ceramic Radiant Burners,'' Combust. Flame, **111**, pp. 175–184.

[6] Viskanta, R., and Gore, J. P., 2000, ''Overview of Cellular Ceramics Based Porous Radiant Burners for Supporting Combustion,'' International Journal on Environmental Combustion Technology, **1**, pp. 167–203.

[7] Golombok, M., Prothero, A., Shirvill, L. C., and Small, L. M., 1991, ''Surface Combustion in metal Fibre Burners,'' Combust. Sci. Technol., **77**, pp. 203–223.

[8] Golombok, M., and Shirvill, L. C., 1990, ''Radiation Characteristics of Surface Combustion Burners,'' *Proceedings of EUROTHERM No. 17*, pp. 7–13.

[9] Sathe, S. B., Peck, R. E., and Tong, T. W., 1990, ''A Numerical Analysis of Heat Transfer and Combustion in Porous Radiant Burners,'' Int. J. Heat Mass Transf., **33**, pp. 1331–1338.

[10] Sathe, S. B., Peck, R. E., and Tong, T. W., 1990, ''Flame Stabilization and Multimode Heat Transfer in Inert Porous Media: a Numerical Study,'' Combust. Sci. Technol., **70**, pp. 93–109.

[11] Tong, T. W., and Sathe, S. B., 1991, ''Heat Transfer Characteristics of Porous Radiant Burners,'' ASME J. Heat Transfer, **113**, pp. 423–428.

[12] Andersen, F., 1992, ''Heat Transfer Model for Fiber Burners,'' Prog. Energy Combust. Sci., **18**, pp. 1–12.

[13] Hsu, P-F., and Matthews, R. D., 1993, ''The Necessity of Using Detailed Kinetics in Models for Premixed Combustion Within Porous Media,'' Combust. Flame, **93**, pp. 457–466.

[14] Rumminger, M. D., Dibble, R. W., Heberle, N. H., and Grossley, D. R., 1996, ''Gas Temperature Above a Porous Radiant Burner: Comparison of Measurements and Model Predictions,'' *Twenty-Sixth Symposium (International) on Combustion*, The Combustion Institute, Pittsburgh, pp. 1755–1762.

[15] Henneke, M. R., and Ellzey, J. L., 1999, ''Modeling of Filtration Combustion in a Packed Bed,'' Combust. Flame, **117**, pp. 832–846.

[16] Bowman, C., Hanson, R., Davidson, D. (Jr.), Lissianski, V., Smith, G., Golden, D., Frenklach, M., and Goldenberg, M., GRI-MECH 2.11, http://me.berkeley.edu/grimech.

[17] Leonardi, S. A., 2000, ''Partially-Premixed Combustion in Porous Radiant Burners,'' Ph.D. thesis, Purdue University, W. Lafayette, IN.

[18] Leonardi, S. A., Gore, J. P., and Viskanta, R., 2001, ''Experimental Investigation of Partially-Premixed Combustion in a Novel Porous Radiant Burner, *Proceedings of the 2001 National Heat Transfer Conference*, Bergman, T. L. and Panchal, C. B., eds., ASME, New York, **1**, pp. 915–921.

[19] Leonardi, S. A., Viskanta, R., and Gore, J. P., 2002, ''Radiation and Thermal Performance Measurements of Metal Fiber Burner,'' J. Quant. Spectrosc. Radiat. Transf., **73**, pp. 491–501.

[20] Kee, R., Grcar, J. F., Smooke, M., and Miller, J., 1985, ''A Fortran Program for Modeling Steady Laminar One-Dimensional Premixed Flames,'' Sandia National Laboratory Report SAND85-8240.

[21] Kee, R. J., Miller, J., and Jefferson, T., 1980, ''CHEMKIN: a General Purpose, Problem Independent, Transportable Fortran, Chemical Kinetic Program Package,'' Sandia National Laboratory Report SAND 80-8003.

[22] Kee, R., Warnatz, J., and Miller, J., 1983, ''A Fortran Computer Program Package for the Evaluation of Gas-Phase Viscosities, Conductivities and Diffusion Coefficients,'' Sandia National Laboratory Technical Report SAND83-8209.

[23] Mathur, S., Tondon, P. K., and Saxena, S. C., 1967, ''Thermal Conductivity of Binary, Ternary and Quaternary Mixtures of Rare Gases,'' Mol. Phys., **12**, pp. 569–579.

[24] Modest, M. F., 1993, *Radiative Heat Transfer*, McGraw-Hill Book Co., New York.

[25] Ji, J., Gore, J. P., Sivathanu, Y. R., and Lim, J., 2000, ''Fast Infrared Array Spectrometer Used for Radiation Flame Measurements of Lean Premixed Flames,'' paper presented at the 35th National Heat Transfer Conference, June 10–12, 2001, Anaheim, CA. (A copy of the paper can be obtained from the authors.)

[26] Grosshandler, W. L., 1993, ''RADCAL,'' Technical Report NIST-11402, National Institute of Science and Technology, Gaithersburg, MD.

[27] Soufiani, A., and Taine, J., 1997, ''High Temperature Gas Radiative Property Parameters of Statistical Narrow-Band Model for H_2O, CO_2 and CO, and Correlated K Model for H_2O and CO_2,'' Int. J. Heat Mass Transf., **40**, pp. 987–991.

[28] Ji, J., Sivathanu, Y. R., and Gore, J. P., 2000, ''Thermal Radiation Properties of Turbulent Lean Premixed Methane Air Flames,'' Proceedings of the Combustion Institute, **28**, pp. 391–398.

[29] Turns, S. E., 1996, *An Introduction to Combustion*, McGraw-Hill Book Co., New York.

[30] Singh, P., 1997, personal communication, Purdue University, W. Lafayette, IN.

Optimal Temperature and Current Cycles for Curing of Composites Using Embedded Resistive Heating Elements

A. Mawardi

R. Pitchumani
e-mail: r.pitchumani@uconn.edu

Composites Processing Laboratory,
Department of Mechanical Engineering,
University of Connecticut,
Storrs, CT 06269-3139

*Curing is an important and time consuming step in the fabrication of thermosetting-matrix composite products. The use of embedded resistive heating elements providing supplemental heating from within the material being cured has been shown in previous studies (Ramakrishnan, Zhu, and Pitchumani, 2000, J. Manuf. Sci. Eng., **122**, pp. 124–131; and Zhu and Pitchumani, 2000, Compos. Sci. Technol., **60**, 2699–2712.) to offer significant improvements in cure cycle time and cure uniformity, due to the inside-out curing. This paper addresses the problem of determining the temperature and electrical current cycles, as well as the placement configuration of the conductive mats, for time-optimal curing of composites using embedded resistive heating elements. A continuous search simulated annealing optimization technique is utilized coupled with a numerical process simulation model to determine the optimal solutions for selected process constraints. Optimization results are presented over a range of material systems and different numbers of conductive mats to assess the effects of materials reactivity on the optimal number of conductive mats.* [DOI: 10.1115/1.1527903]

Keywords: Composites Fabrication, Optimal Cure Cycles, Heat Transfer, Resin Transfer Molding, Resistive Heating

1 Introduction

Fabrication of thermosetting-matrix composites is accomplished by subjecting the resin-fiber mixture to a prescribed temperature cycle in order to initiate and sustain an irreversible crosslinking exothermic chemical reaction in the resin, called cure. The cure process causes the initial mixture to be transformed into a rigid component whose structural integrity is retained upon the withdrawal of the external temperature variation. The magnitude and time duration of the imposed temperature variation, referred to as the cure cycle, is an important process parameter affecting the temperature distribution and the progress of the crosslinking reaction (measured in terms of a degree of cure) within the composite.

Initially during the cure process, the temperature of the outer layers of the composite which are exposed to the cure temperature cycle increases more rapidly than that of the inner layers, and as the process progresses, the exothermic cure reaction may bring the temperatures of the inner layers to exceed those of the outer layers. Moreover, the heat released during the cure reaction may lead to excessively rapid rate of temperature increase, or the temperature within the material exceeding an allowable maximum value. Maintaining spatial homogeneity in the temperature and degree of cure distribution within the matrix, and maintaining the exotherm-induced maximum temperature and temperature gradient within allowable limits constitute the principal constraints governing the total time of the cure process.

Determination of cure cycles that lead to minimum cure time in practice has relied on trial-and-error or empirical procedure where either simulations based on numerical models or experimental trials are carried out for several candidate cure cycles (Pillai et al. [3]; Loos and Springer [4]; Han et al. [5]; Bogetti and Gillespie [6]; Ciriscioli et al. [7]). This approach does not warrant the best possible process parameters, and, in turn, leads to suboptimal manufacturing times and cost. A rigorous approach to determining the optimal cure cycle was reported by Rai and Pitchumani [8], in which an optimization problem was formulated over a numerical process model and solved using a nonlinear programming scheme. The results were reported for a wide range of resin materials and process constraints. It was shown that the constraints on temperature and cure homogeneity fundamentally limit the magnitude of the temperature ramps in the optimal cycles. This constitutes a fundamental limitation of the curing of composites using peripheral heating.

The foregoing limitation may be alleviated via an inside-out curing strategy, where the inner layers are also subjected to a heat source that allows them to cure in synchronization with the outer layers. Such a strategy provides for temperature and cure homogeneity through the composite cross section during the cure process, and in turn offers the potential to significantly reduce the cure time. One approach toward realizing volumetric internal heating is the use of microwave energy (Lee and Springer [9]; Thostensen and Chou [10]). This approach provides improvement to conventional curing; however, the problem of differential curing persists since the microwave energy attenuates with thickness.

The objective of inside-out curing may also be realized through the use of conductive carbon fibers as resistive heating elements embedded within the cross-section of the composite being cured. Ramakrishnan et al. [1] and Zhu and Pitchumani [2] investigated the approach numerically and experimentally for several resistive heating configurations and demonstrated improved temperature and cure homogeneity, and significant savings in the cure time. The investigation focused on a prescribed cure temperature cycle while varying the steady current supplied to the resistive heating elements. It may be envisioned that significant enhancement to the process could be realized through the use of a time varying current cycle, whereby the current supplied may be better tailored to accelerating the process. In this case, process design calls for determination of the optimal temperature and current variations during the process, which is the focus of the present study.

Contributed by the Heat Transfer Division for publication in the JOURNAL OF HEAT TRANSFER. Manuscript received by the Heat Transfer Division March 21, 2001; revision received August 12, 2002. Associate Editor: A. F. Emery.

Specifically, this paper considers the problem of determining the optimal cure temperature and current cycles so as to minimize the fabrication time while simultaneously satisfying constraints on (a) the maximum material temperature, $T_{\max}$, (b) the maximum temperature gradient, $\dot{T}_{\max}$, (c) the maximum temperature difference across the material, $\Delta T_{\max}$, and (d) the minimum degree of cure desired in the product, $\epsilon_{\min}$. The decision variables consist of the magnitude and duration of each stage of the temperature cycle prescribed in the peripheral heating, the magnitudes and durations of the stages of the electrical current cycles in the resistive heating elements, and the location of the heating elements within the laminates. The optimization problem is solved using a simplex search based simulated annealing algorithm, combined with a numerical process simulation model to obtain both objective function and constraints information. The optimization results are presented for selected process constraints on three different resin systems.

The paper is organized as follows: The process model development is presented in Section 2, followed by the formulation of the optimization problem in Section 3. Section 4 discusses the optimization results along with the parametric studies.

2 Process Model

Figure 1 shows a schematic description of a process configuration with embedded resistive heating elements. The configuration consists of a lay-up of resin saturated fiber layers placed between two tooling plates. Interspersed among the fiber layers are discrete layers of conductive-fiber mats, placed at specific locations across the thickness, where electrical current is passed through to produce resistive heating along those discrete planes within the cross section. Peripheral heating with prescribed temperature cycle is applied from the bottom plate, while the top plate surface is exposed to the surrounding allowing heat transfer through convection.

Heat transfer takes effect from the cure temperature cycle imposed on the bottom plate as well as from resistive heating elements embedded in the cross-section. The cure reaction proceeds simultaneously with the heating of the material, and the exothermic nature of the cure reaction generates heat which in turn helps to accelerate further reaction. The dominant physical phenomena in the process are (a) heat transfer associated with the heating from the bottom plate as well as volumetric heating due to the resistive heating at the conductive mats including the exothermic cure reaction, and (b) the chemical reaction leading the cure process.

Mathematical models for the process are formulated from energy conservation and chemical kinetics considerations. The energy transfer is assumed to be predominantly one-dimensional through the thickness of the layers (y-direction in Fig. 1), since the surface and resistive heating are uniform along the length-width plane of the layers. The governing equations may be written as [2]:

$$\frac{\partial[(\rho C)_i T]}{\partial t} = \frac{\partial}{\partial y}\left(k_i \frac{\partial T}{\partial y}\right) + \mathbf{f_i} C_{R0} H_R (1-v_i)\frac{\partial \epsilon}{\partial t} + \mathbf{g_i}\varphi_c \left(\frac{I}{A}\right)^2;$$

$$i = B, F, C, T;$$

$$\mathbf{f_B} = \mathbf{f_T} = 0, \quad \mathbf{f_F} = \mathbf{f_C} = 1; \quad \mathbf{g_B} = \mathbf{g_F} = \mathbf{g_T} = 0, \quad \mathbf{g_C} = 1 \qquad (1)$$

where C_{R0} is the initial concentration of the reactive resin, H_R is the heat of reaction due to cure, I is the current flowing through conductive layers with cross-sectional area A, $(\rho C)_i$ and k_i are the volumetric specific heat and the thermal conductivity of the i^{th} material, and the subscript i denotes the different material regions in the problem domain as follows: B is the base plate, F is the resin-saturated reinforcement fiber layers, C is the resin-impregnated conductive layers, and T is the top plate. The fiber volume fraction in the i^{th} material is denoted as v_i and has significance only for $i=F$ and C. The terms $\mathbf{f_i}$ and $\mathbf{g_i}$ are binary variables (having value of 0 or 1) and signify the presence or absence of the internal heat generation due to exothermic chemical reaction and the resistive heating at specific spatial locations, respectively. In the base plate and top plate regions, $\mathbf{f_B}=\mathbf{f_T}=\mathbf{g_B}=\mathbf{g_T}=0$ which denotes the absence of internal heat generation, implying a purely conductive heat transfer. In the resin-saturated reinforcement fiber layers region, $\mathbf{f_F}=1$ while $\mathbf{g_F}=0$ which reflects the presence of exothermic cure reaction in the region. Similarly, in the region of the resin-saturated conductive mats, $\mathbf{f_C}=\mathbf{g_C}=1$ the presence of heat generation resulted from chemical reaction and resistive heating combined. The terms T, t, and y are, respectively, the temperature, time and the distance from the bottom plate along the vertical axis. The electrical resistivity of the resin-saturated conductive mats, φ_C, is evaluated based on the relation between electrical resistivity and thermal conductivity according to Lorenz law [11],

$$\frac{\varphi_C}{\varphi_{CF}} = \frac{k_{CF}}{k_{CI}} \qquad (2)$$

where φ_{CF} and k_{CF} respectively denote the electrical resistivity and thermal conductivity of the pure conductive fiber material, while k_{CI} denotes the in-plane thermal conductivity of the resin-saturated conductive mat. In this study, the conductive mats are considered to be of the plain weave architecture, where the values of the in-plane and transverse thermal conductivities, k_{CI} and k_C, are obtained using the mosaic model proposed by Ning and Chou [12,13].

The rate of cure reaction, $\partial\epsilon/\partial t$, appearing in the energy equation, Eq. (1), is modeled using an empirical expression following the approach adopted in the literature [4,5]. The kinetics of an autocatalytic cure reaction is often described in terms of an Arrhenius type rate equation as follows:

$$\frac{\partial \epsilon}{\partial t} = \left[K_{10}\exp\left(-\frac{E_1}{RT}\right) + K_{20}\exp\left(-\frac{E_2}{RT}\right)\epsilon^m\right](1-\epsilon)^n \qquad (3)$$

where ϵ is the degree of cure, defined as the fraction of the initial resin concentration, C_{R0}, that has reacted, such that $\epsilon=0$ corresponds to unreacted initial mixture, while $\epsilon=1$ denotes completion of the cure reaction. The coefficients K_{10} and K_{20} are frequency factors, E_1 and E_2 are activation energies, and R is the universal gas constant, while m and n are empirical exponents. Equation (3) models the cure of many practical resin systems, including all of the resin systems used in this study. The exact values of the corresponding kinetic parameters are presented later in this paper.

The governing equations, Eqs. (1) and (3), are solved simultaneously, subject to the following initial and boundary conditions.

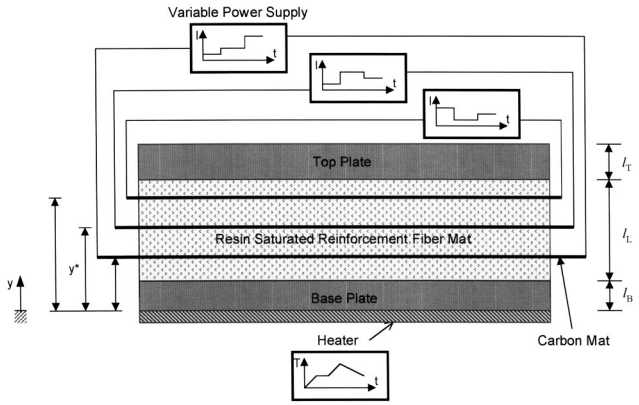

Fig. 1 A curing process configuration with embedded resistive heating elements

The initial temperature is set to be at the room temperature, T_0, while initially, the resin is completely unreacted, corresponding to $\epsilon = 0$. These conditions are stated as:

$$T(y,0) = T_0, \quad (0 \leqslant y \leqslant l_B + l_L + l_T)$$

$$\epsilon(y,0) = 0, \quad (l_B \leqslant y \leqslant l_B + l_L) \tag{4}$$

where l_B, l_L, and l_T are the thickness of the base plate, the laminate, and the top plate, respectively as shown on Fig. 1. The temperature at the bottom of the base plate corresponds to the prescribed temperature cycle, while convective heat transfer occurs at the exposed surface of the top plate. These boundary conditions can be expressed as:

$$T(0,t) = T_B(t) \tag{5}$$

$$-k_T \frac{\partial T}{\partial y}(l_B + l_L + l_T, t) = h_T T(l_B + l_L + l_T, t) - T_0 \tag{6}$$

A numerical simulator was created based on the model presented above. The governing equations along with their boundary conditions were solved using an implicit one-dimensional finite-difference scheme with a control volume formulation [14,15]. The mesh consisted of 50–59 numerical grids along the *y*-direction, depending on the number of embedded conductive mats, n_C; the time step Δt was determined such that the mesh Fourier number, $\alpha \Delta t / \Delta x^2$ based on the thermal diffusivity α of every material in the domain, was less then unity. The stopping criterion for the numerical simulation was based on one of two factors namely, all sections of the laminate attained a desired minimum degree of cure, or the end of the specified cure temperature cycle was reached; the corresponding time was the cure time for the process. In addition to the cure time, t_{cure} and the minimum degree of cure, $\epsilon_{\min}$, the process model also yielded the values for the maximum temperature, $T_{\max}$, the maximum temperature gradient, $\dot{T}_{\max}$, and the maximum temperature difference, $\Delta T_{\max}$, within the laminate during the process. These values were used as the constraints in the optimization problem described in the following section. The numerical simulator, therefore, constituted the basis of the optimization problem.

3 The Optimization Problem

The objective of the optimization is to determine the temperature cycles, current cycles, and the location of the conductive mats, for minimizing the time for curing composites using embedded resistive heating elements. The optimization is subject to physical constraints on the temperature-related parameters and the degree of cure during the process. The cure temperature cycles are expressed as a series of piecewise linear segments, as presented schematically in Fig. 2. A temperature cycle is represented by the end point temperatures T_i of each stage and the respective stage durations t_i. In this study, the temperature cycles consist of four stages, which provide for a reasonably accurate representation of cure temperature schedules yet maintaining the number of decision variables sufficiently small to minimize computational effort for the optimization. Additional stages may be introduced albeit at the computational expense associated with the increased number of decision variables in the optimization.

The cure temperature cycle is represented in the optimization problem in terms of 8 decision variables: the end-point temperatures of the four stages T_1, T_2, T_3, T_4, and their corresponding stage time durations t_1^T, t_2^T, t_3^T, and t_4^T. On the other hand, the current cycles are expressed as a series of three piecewise constant segments, as shown in Fig. 2, and are represented in terms of the stage currents I_1, I_2, I_3, and the respective stage durations t_1^I, t_2^I, t_3^I. However, the cure process requires that both temperature and current cycles complete at the same time: $\Sigma_i t_i^T = \Sigma_j t_j^I$. To achieve this requirement, the last stage duration of the current cycle, t_3^I, is chosen to be a dependent variable whose value can be

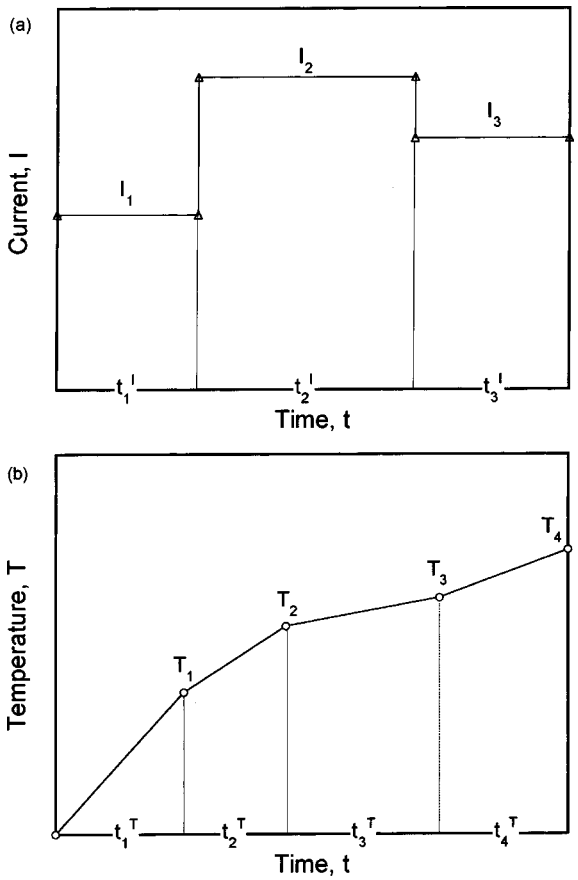

Fig. 2 Illustration of (*a*) the three-stage piecewise constant cure current cycle and (*b*) the four-stage piecewise linear curve temperature cycle considered in the study

calculated in terms of the other stage durations, as $t_3^I = \Sigma_i t_i^T - (t_1^I + t_2^I)$. Thus, in the optimization problem, t_3^I is not included as a decision variable, and the current cycle is represented in terms of 5 decision variables. Additionally, decision variables representing the locations of the conductive elements were also considered part of the design problem in this study. For a configuration with multiple embedded conductive elements, the study allows for different current cycles to be prescribed in each conductive element. Consequently, the number of decision variables is $8 + 6n_C$, which increases with the number of embedded conductive elements, n_C.

The objective function to be minimized is the cure time t_{cure} and the optimized variables are the parameters that comprise the temperature cycle $T_j(t_j^T)$, $j = 1, \ldots, 4$, the current cycle $I_k(t_k^I)$, $k = 1, \ldots, 3$, and the locations of the n_C conductive mat(s) y_i^*, $i = 1, \ldots, n_C$. Thus, the optimization may be written mathematically as:

$$\underset{T_j(t_j^T), I_k(t_k^I), y_i^*}{\text{Minimize}} \quad t_{\text{cure}} \tag{7}$$

subject to

$$g_1 = T_{\max} - T_{\text{crit}} \leqslant 0 \tag{8}$$

$$g_2 = \dot{T}_{\max} - \dot{T}_{\text{crit}} \leqslant 0 \tag{9}$$

$$g_3 = \Delta T_{\max} - \Delta T_{\text{crit}} \leqslant 0 \tag{10}$$

$$g_4 = \epsilon_{\text{crit}} - \epsilon_{\min} \leqslant 0 \tag{11}$$

where the subscripts max, min, and crit refer to the maximum, minimum, and critical values, respectively. The temperature-related constraints [Eqs. (8)–(10)] pertain to limiting the residual/

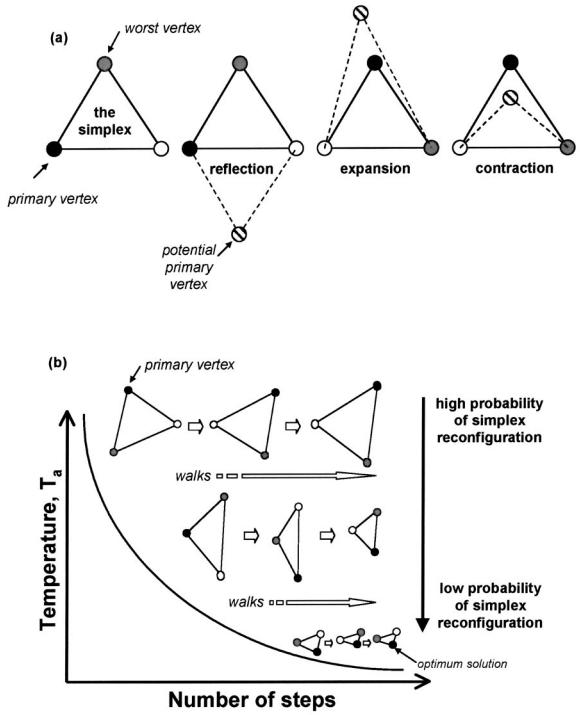

Fig. 3 Schematic diagram of simulated annealing optimization combined with simplex search algorithm

thermal stresses induced during processing, as well as to maintaining temperature and property homogeneity across the section. Constraint Eq. (11) ensures curing of composite to a desired minimum degree, ϵ_{crit}.

The optimization problem represented by Eqs. (7)–(11) was solved using the Nelder-Mead simplex method [16] combined with a simulated annealing technique to improve the effectiveness of the search [17]. The simplex method is an algorithm that performs continuous search for selecting a new point during an optimization iteration which guarantees objective function improvement. A simplex is defined as a convex hull of $N+1$ vertices in an N-dimensional space, representing the N decision variables that govern the objective function evaluation. The vertices are ranked, from best to worst, based the corresponding objective function evaluations, and the best vertex is defined as the primary vertex. Since a primary vertex represents a set of decision variables which corresponds to the lowest objective function evaluation, the finding of a new primary vertex constitutes an improvement to the objective function evaluation. Thus, the algorithm searches for a new simplex by replacing the worst vertex by a potential new primary vertex, through a set of predefined simplex movements, which include reflection, expansion, and contraction, illustrated in Fig. 3(*a*) for a two-dimensional simplex. The primary movement is the reflection of the worst vertex, while expansion and contraction are secondary movements dependent on the result of the reflection. If the reflection results in a new vertex that is better than the current primary vertex (i.e., has a lower objective function value), an expansion of the reflected simplex will follow, recognizing that a further movement of the new vertices in the direction of the reflection might lead to a much better vertex. If the reflection of the worst vertex does not lead to a new vertex that is better than the current primary vertex but still better than the next worst vertex, the new simplex is accepted. However, if the reflection of the worst vertex does not result in a vertex that is better than the next worst vertex, contraction of the original simplex is executed to reduce its size. Additional details on the Nelder-Mead algorithm, including parameter selection for the various movement and tie-breaking rules (if two vertices of equal objective function value are evaluated), may be found in Ref. [18].

In the Nelder-Mead method, the decision to accept or reject each movement is made based solely on the criterion of reducing the objective function value. This could potentially result in the entrapment of the solution in a local minimum. However, if the Nelder-Mead method were combined with a simulated annealing technique, the moves in the design exploration will be subject to a probabilistic acceptance criterion (the Metropolis equation), which offers a better opportunity to arrive at a global minimum. The optimization approach in the present application, therefore, uses a combined Nelder-Mead simplex method and simulated annealing algorithm, as discussed below.

Simulated annealing is an optimization technique which mimics the physical process of annealing (slow cooling) of metals [19], in which the molecules are free to move at high temperatures, but as the annealing temperature slowly decreases, the molecular movement becomes increasingly restricted before finally settling down to a configuration of the lowest energy state. Relating to the optimization problem, the molecular configuration represents the decision variables, while the energy state represents the objective function to be minimized. Starting at high temperature in the annealing schedule, an initial trial simplex undergoes reconfigurations based on the movements defined in the Nelder-Mead method. Each reconfiguration of the simplex is accepted based on an associated probability p, given by the Metropolis criterion [20]

$$p = \min\left(\exp\left[-\frac{E_{n+1} - E_n}{k T_a} \right], 1 \right) \tag{12}$$

where T_a is the annealing temperature, k is the Boltzmann constant, E_n is the objective function corresponding to the primary vertex prior to reconfiguration, and E_{n+1} is the objective function corresponding to the new primary vertex in the reconfigured potential simplex. If $E_{n+1} < E_n$, the probability of acceptance is unity, as per Eq. (12), which implies that a reconfiguration resulting in a lower objective function value is always accepted. In addition, Eq. (12) also allows for an occasional acceptance of an uphill move (i.e., $E_{n+1} > E_n$), based on the corresponding probability, p. The probability of accepting an uphill move is greater at higher annealing temperature T_a, while as T_a decreases the probability becomes progressively smaller.

A simplex reconfiguration following the foregoing procedure is defined as a walk. At every annealing temperature, T_a, a certain number of walks are executed before the temperature decreases according to the prescribed annealing schedule. Thus, the annealing schedule and the number of walks at each temperature constitute parameters of the simulated annealing optimization. The overall integration of the simulated annealing algorithm with the Nelder-Mead simplex method is presented in Fig. 3(*b*). Initially, at higher annealing temperature, the simplex undergoes reconfiguration at a higher probability according to Eq. (12), which in turn allows the simplex to explore more of the design domain. As the number of steps increases, the cumulative effect of the various simplex movements reduces the size of the simplex, and simultaneously, the annealing temperature also decreases, which reduces the probability of simplex reconfiguration. Near the end of the schedule, the low annealing temperature causes the probability of accepting an uphill move to be extremely low. The simplex movements continue until the algorithm reaches a stopping criterion, which is either the annealing schedule has been completed (in terms of a specified maximum number of walks), or the simplex reduces to a pre-determined infinitesimal size. The maximum number of walks can be determined in proportion to the number of decision variables [17], or by trial runs to yield an expected rate of convergence. At the stopping point, the decision variable values corresponding to the primary vertex of the simplex constitute the optimum solution.

The Nelder-Mead simplex method combined with simulated annealing is designed to solve non-linear unconstrained optimization. Since the optimization problem in hand has several constraints, g_k [Eqs. (8)–(10)], those constraints are incorporated using a penalty method [21] into an augmented objective function to be minimized, such that the optimization problem becomes unconstrained:

$$\underset{T_j(t_j^T),I_k(t_k^I),y_i^*}{\text{Minimize}} \quad t_{\text{cure}} + \sum_k \lambda_k \max(g_k,0) \tag{13}$$

where λ_k are the penalty coefficients, whose values were selected for each constraint equation g_k such that if the constraint was not satisfied the constraint penalty contributed, $\lambda_k g_k$ is equal to 100 times the expected value of the optimal cure time. If the constraint g_k is satisfied, $\max(g_k,0)$ evaluates to zero, since g_k is negative, and constraint g_k does not contribute to the penalty.

As described previously, the number of decision variables in the optimization problem varies depending on the number of conductive mats, n_C. For example, optimization of a process with one embedded carbon mat would require 14 decision variables: 8 variables representing temperature cure cycles, 5 variables representing one current cycle, and one variable for the location of the mat. Thus, the simplex is formed in a 14-dimensional space, and consisted of 15 vertices. The initial guess on the values of the decision variables corresponds to one of the vertices of the simplex, and the other 14 vertices are created by adding scaled basis unit vectors $\beta \mathbf{e}_{(\mathbf{n})}$—where β is a scaling factor, such that the hypersurfaces of the simplex are linearly independent of each other. The numerical process simulator is invoked to determine the augmented objective function corresponding to each vertex at every step of the optimization procedure. At the completion of the optimization algorithm, the primary vertex of the final simplex represents the optimal decision variables, and the corresponding objective function evaluation represents the optimal cure time, t_{cure}^*.

4 Results and Discussion

The optimization approach presented in the previous section was validated in two parts: First, the numerical simulation model, which forms the core of the framework, was validated with experimental data on a variety of resistive heating configurations. The validation results are presented in Ref. [2] and are not repeated here. Secondly, the optimization framework utilizing the process model was validated using the results presented in Ref. [2]. In their study, the process consisted of a fixed cure temperature cycle, and a steady current was used for the resistive heating. Parametric investigations were conducted by varying the number of embedded heating elements, and the resin kinetics parameters [for kinetics of the form in Eq. (3), but with $K_{10}=0$]. The parametric results were used to derive the optimum resistive heating configurations that minimized the cure time while satisfying constraints of the form in Eqs. (8)–(11). The results were expressed in terms of a dimensionless power density, P_d, defined as $P_d = (I_L^2 \varphi_C / T_0 k_L)(I/A)^2$, and dimensionless groups representing the kinetics parameters.

For the purpose of validation, the current cycle in the present formulation was taken to be a single stage, and the cure temperature cycle was fixed to be that used in Ref. [2]. Furthermore, the carbon mat locations were prescribed to be the values used in Ref. [2]. Thus, the decision variable in the optimization was reduced to only the stage current magnitude. The optimization framework was used to solve for the optimal steady current, for varying resin kinetics parameters, subject to the same critical values of the constraint parameters [Eqs. (8)–(11)] as in Ref. [2]. Figure 4 shows an example comparison of the variation of the optimal current, expressed as a dimensionless power density, P_d, with the Damköhler number, Da—a dimensionless group which signifies the ratio of the conduction time scale to the reaction time scale—defined as $\text{Da} = K_{20} l_L^2 / \alpha_L$, where α_L is the thermal diffusivity of the laminate. The plot corresponds to three embedded heating elements, and shows that the optimal dimensionless power density increases with the Damköhler number. Overall, the optimization results (markers in the plot) are seen to correspond closely to the results from Ref. [2] derived using parametric studies (shown as the dashed line).

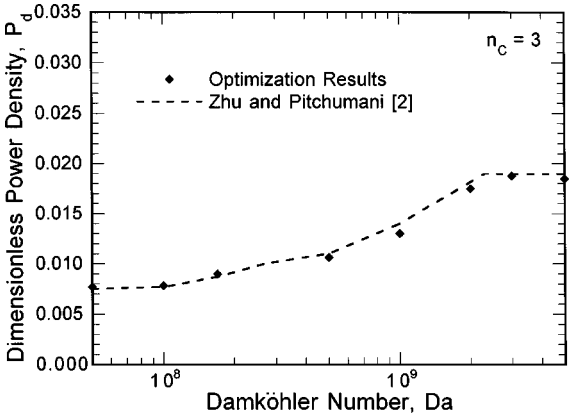

Fig. 4 Validation of the optimization results with the data from Ref. [2], for the resistive heating configuration using three carbon mats

With the validated optimization framework as basis, the optimization studies presented in this paper focus on three material systems: a fiberglass-epoxy resin system EPON 815 catalyzed with EPICURE-3274, an Owens-Corning fiberglass-polyester system with Percadox 16N and benzoyl peroxide initiator (OC-E701/P16N/BPO) and a polyester system, CYCOM-4102 of American Cyanamid Company. The embedded resistive heating elements are considered to be carbon mats, G-104, of Textile Technologies Inc. The reaction kinetics for the resin systems are summarized in Table 1, and the physical properties of the material systems are also available in the references cited in Table 1. The tooling plate considered in the study is made out of copper with volumetric specific heat $(\rho C)_T$ of 3439.2 kJ/m^3 K, and thermal conductivity (k_T) of 395.0 kW/m K.

Optimization runs are carried out for fixed number of carbon mats n_C, by initially supplying trial values of the cure temperature cycle, the current cycle through each carbon mat, and the location of the carbon mat(s) across the thickness. The critical values of the constraint used in the study are set to be identical for all material systems, as follows:

$$T_{\text{crit}} = 150°\text{C}; \quad \dot{T}_{\text{crit}} = 0.6°\text{C/s}; \quad \Delta T_{\text{crit}} = 69°\text{C}; \quad \epsilon_{\text{crit}} = 0.97 \tag{14}$$

These values typify those commonly required in practice. However, the effect of varying constraint values is also investigated later in this section. The optimization procedure is executed until the optimal cure time, and the corresponding temperature cycle, current cycles, and carbon-mat locations, have been found. Each optimization run was repeated for ten different initial trial solutions, and the optimum results corresponding to the least cure time value among the ten trial results was taken to be the global optimum solution. In most cases, it was observed that the global optimum solution was reached in several of the ten trials.

Figure 5 shows the optimal temperature cycles, in solid lines, and the optimal current cycles, in dashed lines, as well as the optimal locations of carbon mats (y^*) for curing a 1.27 cm-thick fiberglass/EPON-815/EPICURE-3274 system with different numbers of embedded carbon mats, n_C. The optimal cure time for the process without resistive heating is 1710 seconds (Fig. 5(*a*)). The optimal cure times for n_C carbon mats, $t_{n_C}^*$, nominally reduces as the number of carbon mats increases: 1002 seconds for 1 mat (Fig. 5(*b*)), 961 seconds for 2 mats (Fig. 5(*c*)), and 948 seconds for 3

Table 1 Kinetics model and parameters for systems used in the study

Material	Kinetics Model	Kinetic Parameters
CYCOM-4102 Pillai et al. [3]		$K_{10}=0\ \text{min}^{-1}$ $K_{20}=3.7\times10^{22}\ \text{min}^{-1}$ $E_1=0$ kJ/kmol $E_2=1.66\times10^5$ kJ/kmol $H_R=74.1$ kJ/kg $m=0.524;\ n=1.476$
OC-E701/P16N/BPO Han et al. [5]	$\frac{d\varepsilon}{dt}=(K_{10}e^{-E_1/RT}+K_{20}e^{-E_2/RT}\varepsilon^m)(1-\varepsilon)^n$	$K_{10}=5.69\times10^{12}\ \text{s}^{-1}$ $K_{20}=8.61\times10^8\ \text{s}^{-1}$ $E_1=1.07\times10^5$ kJ/kmol $E_2=7.51\times10^4$ kJ/kmol $H_R=200$ kJ/kg $m=0.58;\ n=1.42$
EPON-815/EPICURE-3274 Ramakrishnan et al. [1]		$K_{10}=0\ \text{s}^{-1}$ $K_{20}=4.18\times10^5\ \text{s}^{-1}$ $E_1=0$ kJ/kmol $E_2=55.92$ kJ/kmol $H_R=384$ kJ/kg $m=0.25;\ n=1.75$

mats (Fig. 5(*d*)). Compared to the optimal cure time without resistive heating, the presence of one carbon mats reduces the optimal cure time by about 41 percent, which is a significant improvement in the processing time. However, the cure time reduction by further addition of carbon mats is somewhat small in proportion to the actual cure time, thus implying that for EPON-815/EPICURE-3274, increasing the number of carbon mats beyond 1 is seen to be less economical considering the cost associated with the additional carbon mats. This points to one carbon mat being the practically optimal solution. The optimal location for the single carbon mat is at $y^*=1.22$ cm, which is near the top plate. For the cases with two and three carbon mats (Figs. 5(*c*) and 5(*d*), respectively), the optimal location of one of the carbon mats is also at the identical location, $y^*=1.22$ cm. This result confirms the intuitive notion that any additional heat source must be first located farthest from the peripheral heating to obtain the optimum solution.

The variation of the optimal number of carbon mats with the kinetic properties of the material system is examined by considering the OC-E701/P16N/BPO and CYCOM-4102 resin systems which exhibit faster kinetics relative to EPON-815/EPICURE-3274. Figures 6 and 7 present the results for OC-E701/P16N/BPO and CYCOM-4102, respectively. Without resistive heating the optimal cure times are 1172 seconds for OC-E701/P16N/BPO and 3012 seconds for CYCOM-4102 (Figs. 6(*a*) and 7(*a*)). Using one carbon mat, $n_C=1$, the optimal cure time reduces to 418 seconds for OC-E701/P16N/BPO and 742 seconds for CYCOM-4102, which constitute savings of 64 percent and 75 percent, respectively, compared to the respective cure times without resistive heating. The Figures show that as the number of carbon mats increases from $n_C=1$ (Figs. 6(*b*) and 7(*b*)) to $n_C=2$ (Figs. 6(*c*) and 7(*c*)), a significant further reduction in optimal cure time is achieved for both material systems: 334 seconds ($n_C=2$) for OC-E701/P16N/BPO, and 509 seconds ($n_C=2$) for CYCOM-4102. However, as the number of mats increases to $n_C=3$ (Figs. 6(*c*) and 7(*c*)), the cure time reduction becomes less relative to that of going from $n_C=1$ to $n_C=2$: 325 seconds for OC-E701/P16N/BPO and 487 seconds for CYCOM-4102, implying that two carbon mats can be considered the practically optimal configuration

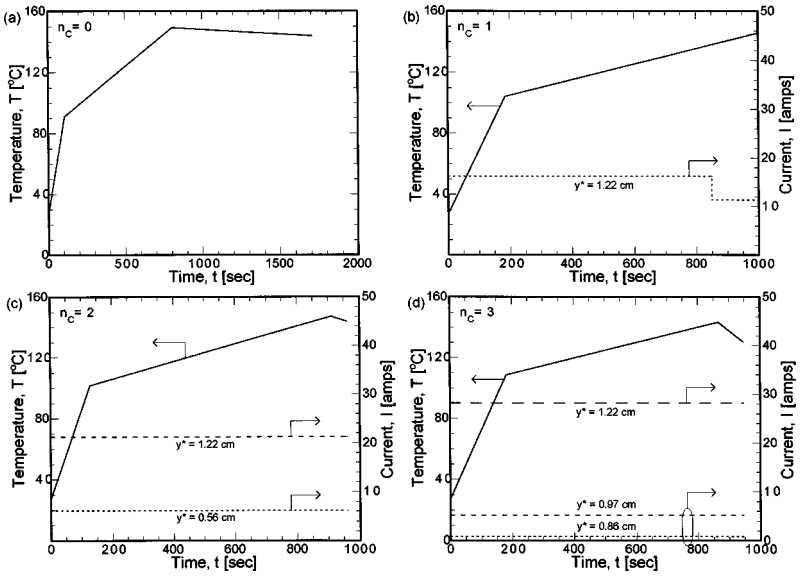

Fig. 5 Optimal temperature and current cycles for curing a 1.27 cm-thick EPON-815/EPICURE-3274 laminate embedded with (*a*) 0 carbon mat, (*b*) 1 carbon mat, (*c*) 2 carbon mats, and (*d*) 3 carbon mats

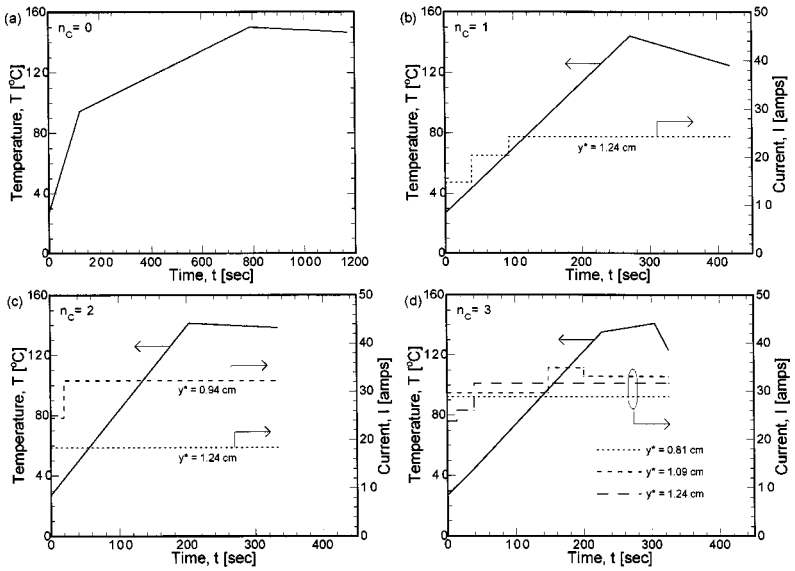

Fig. 6 Optimal temperature and current cycles for curing a 1.27 cm-thick OC-E701/P16N/BPO laminate embedded with (*a*) 0 carbon mat, (*b*) 1 carbon mat, (*c*) 2 carbon mats, and (*d*) 3 carbon mats

for both material systems. This result, together with the case of EPON-815/EPICURE-3274 discussed above, shows that as the reactivity of the material system increases, the optimal number of mats also increases. This trend was also reported based on parametric studies in Ref. [2].

It is worth examining the form of the optimal temperature cycles (solid lines) and the current cycles (dashed lines) relative to the constraints in the optimization. In the case of $n_C=1$, the gradual increase via multiple steps to higher current value in the current cycles shown in Figs. 6(*b*) and 7(*b*) may be attributed to the temperature gradient constraint which limits the sudden increase in temperature due to resistive heating by high current near the top surfaces. However, in the case of EPON-815/EPICURE-3274 in Fig. 5(*b*), the current stays constant at a lower value through the process before it drops at the end of the cure cycle, thereby satisfying all the constraints. In the multiple-carbon-mat cases, $n_C=2$ and $n_C=3$, the gradual increase in the current cycles does not exist due to additional heat sources inside the laminates which allows more homogeneous increase of temperature—thereby maintaining temperature difference below the critical value—throughout the laminate. This allows more heat to be supplied to the laminates since the beginning of the cycle without violating any constraint, thus enabling a faster cure process.

As discussed above, the critical values of the constraints affect closely the shape of the cure cycles and, in turn, the optimal cure time. Toward elucidating this effect further, studies were conducted to investigate the effect of the critical values of the constraints on the optimal cure temperature and current cycles. Figure 8(*a*) presents the result for a reference set of critical values for the case of curing a 1.27 cm-thick CYCOM-4102, while Figs. 8(*b*), 8(*c*), and 8(*d*) present the temperature cycles, in solid lines, and current cycles, in dashed lines, for different values of T_{crit}, ΔT_{crit},

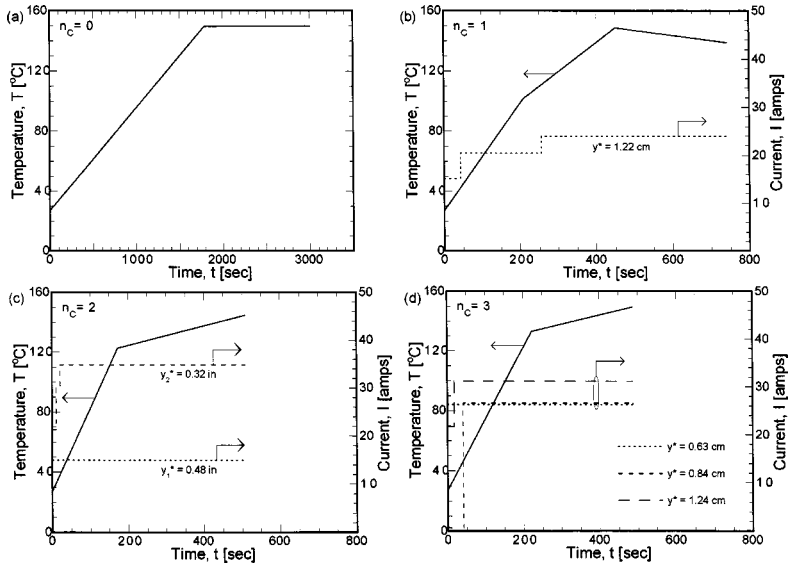

Fig. 7 Optimal temperature and current cycles for curing a 1.27 cm-thick CYCOM-4102 laminate embedded with (*a*) 0 carbon mat, (*b*) 1 carbon mat, (*c*) 2 carbon mats, and (*d*) 3 carbon mats

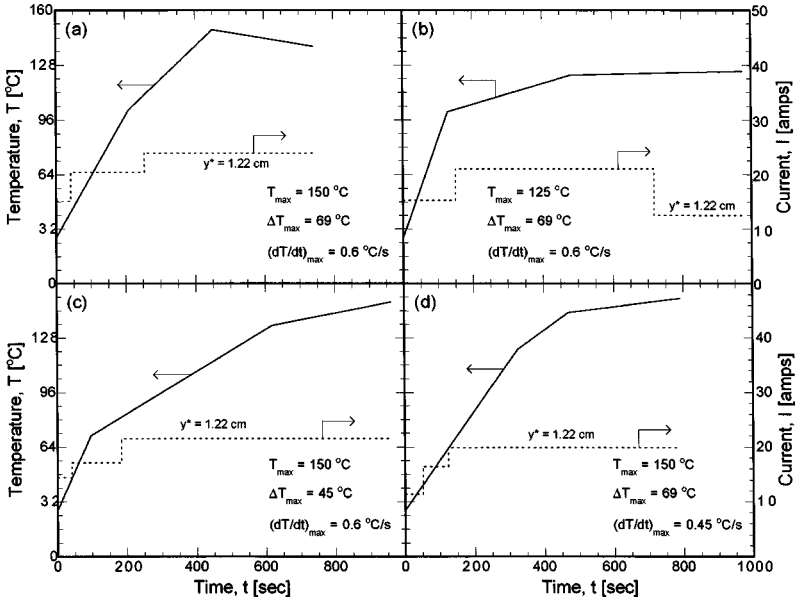

Fig. 8 Optimal temperature and current cycles for curing a 1.27 cm-thick CYCOM-4102 laminate embedded with 1 carbon mat for different critical values of constraints

and $\dot{T}_{\text{crit}}$, respectively. In all these cases, resistive heating using one carbon mat was considered. Figures 8(*a*) and 8(*b*) demonstrate that the optimal cure time increases as the critical temperature, T_{crit}, constraint is tightened. The corresponding temperature and current cycles demonstrate variations to accommodate the smaller value of critical temperature, highlighted by a step decrease in the current cycle at the end of the curing process. Figures 8(*c*) and 8(*d*) suggest that as the constraints of critical temperature difference and critical temperature gradient are tightened, the optimal cure time, $t^*_{n_C}$, increases as expected due the fact that as both constraints limit the rate of temperature increase, the cure process requires longer time to complete. Further, Fig. 8(*c*) shows that as the allowable temperature difference, ΔT_{crit} decreases, the optimal temperature cycle is adjusted to provide slower temperature ramps. Figure 8(*d*) also reveals that a smaller value of the allowable temperature gradient $\dot{T}_{\text{crit}}$ causes the current cycle to start from a lower initial value to avoid excessively rapid heating rate.

To further illustrate the effects of tighter constraints on the optimal curing process in the presence of resistive heating, the temperature history at selected locations within the laminate are presented in Fig. 9, which refers to a 1.27 cm-thick CYCOM-4102 system with one embedded carbon mat, $n_C=1$, at optimal location $y^*=1.22$ cm. Figure 9(*a*) shows the optimal current cycle (bold line) and the temperature history at three different locations across the thickness (thin lines), corresponding to a critical temperature, T_{crit}, of 150°C. The temperatures near the base plate ($y=0$ cm) are similar to the prescribed temperature cycle, as seen in Fig. 8(*a*). Without resistive heating element, the temperatures near the top surface ($y=1.27$ cm) would be lower than those at other locations within the laminate. However, the presence of a carbon mat near the top surface causes the temperatures in the middle of the laminate ($y=0.635$ cm) to be the lowest across the section, for this case considered. Figure 9(*a*) also verifies that the magnitude of the increase in the current cycle is governed by the temperature gradient constraint, since an increase in current cycle magnitude causes rapid temperature change near the carbon mat at that instant, as seen in the temperature history at $y=1.27$ cm, corresponding to various steps in the current cycle ($t\approx 50$ s and $t\approx 250$ s). Figure 9(*b*) presents the temperature history plot for critical temperature, $T_{\text{crit}}=125$°C, showing that a decrease in the magnitude of electrical current at the later stage of the curing process is necessary to avoid violating the critical temperature constraint. Near the top surface ($y=1.27$ cm), where the carbon mat is located, the temperature variation exhibits a brief reversal in the increasing trend to that of decreasing at the time the current

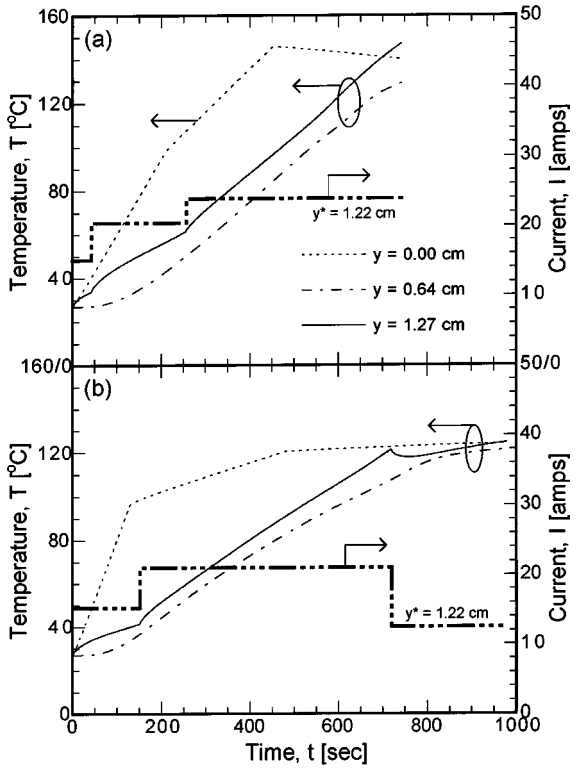

Fig. 9 Temperature history at various locations within the laminate during curing process using the optimal temperature and current cycles for a 1.27 mm-thick CYCOM-4102 laminate, for critical temperatures of: (*a*) 150°C and (*b*) 125°C

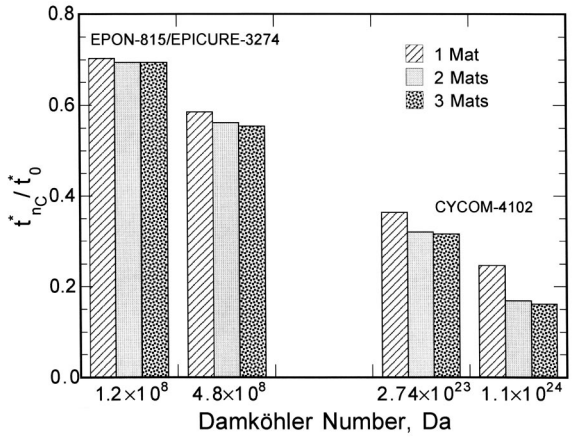

Fig. 10 Normalized optimal cure time as a function of dimensionless Damköhler number

magnitude is reduced, $t \approx 700$ sec, thereby allowing the process to continue without violating the constraint on maximum temperature.

Considering the issue of optimal number of mats, n_C^*, for different material systems, it is helpful to summarize the results as a function of the Damköhler number, Da. Figure 10 presents a summary of the optimal results for two different materials for which the kinetics model has only one pre-exponential factor and one activation energy (Table 1). The Damköhler number is defined based on this non-zero pre-exponential factor as $K_{20}l_L^2/\alpha_L$. The variation in the Damköhler number within each material system is obtained by changing the laminate thickness, whereas the variation of Da from one material system to another reflects the change in the pre-exponential factor. The *y*-axis of the plot represents the ratio between the optimal cure time for curing with n_C carbon-mats, $t^*_{n_C}$, and the optimal cure time without resistive heating, t_0^*, and is a measure of the savings in the cycle time due to resistive heating. The Figure shows that as Da increases, which corresponds to reduced reaction time scale relative to heat diffusion time scale, the value of the cure time ratio decreases, which translates to an increase in the savings in optimal cure time by using resistive heating. This may be attributed to the fact that as the reactivity of the resin increases, the presence of resistive heating elements helps expedite the curing process to a greater extent. The Figure further shows that as the number of mats increases, the optimal cure time decreases as also noted previously. It may be reasoned that while incorporation of additional carbon mats progressively reduces the optimal cure time, the savings in cure time has to be viewed relative to the cost/effort of inclusion of more heating elements. For larger values of Da, increasing the number of carbon mats from one to two significantly reduces the cure time, while the effect of increasing from two to three carbon mats is seen to be much less significant on the cure time savings, despite an absolute decrease in the optimal cure time. For smaller Damköhler numbers, Fig. 10 shows that even an increase in n_C from 1 to 2 offers less of savings in cure time.

In an attempt to determine the optimal number of carbon mats, n_C^*, a cost analysis in terms of both cure time and power usage comparison is presented in Fig. 11. The power consumption is calculated in this study as:

$$P_{n_C} = \sum_{i=1}^{n_C} \int_0^{t^*_{n_C}} I_i(t)^2 dt \tag{15}$$

The Figure presents, as a stacked bar plot, the normalized cure time savings, $\tau_{n_C} = (t_0^* - t^*_{n_C})/t_0^*$, and the normalized power savings, $P^*_{n_C} = (P_{\max} - P_{n_C})/P_{\max}$, for different number of carbon

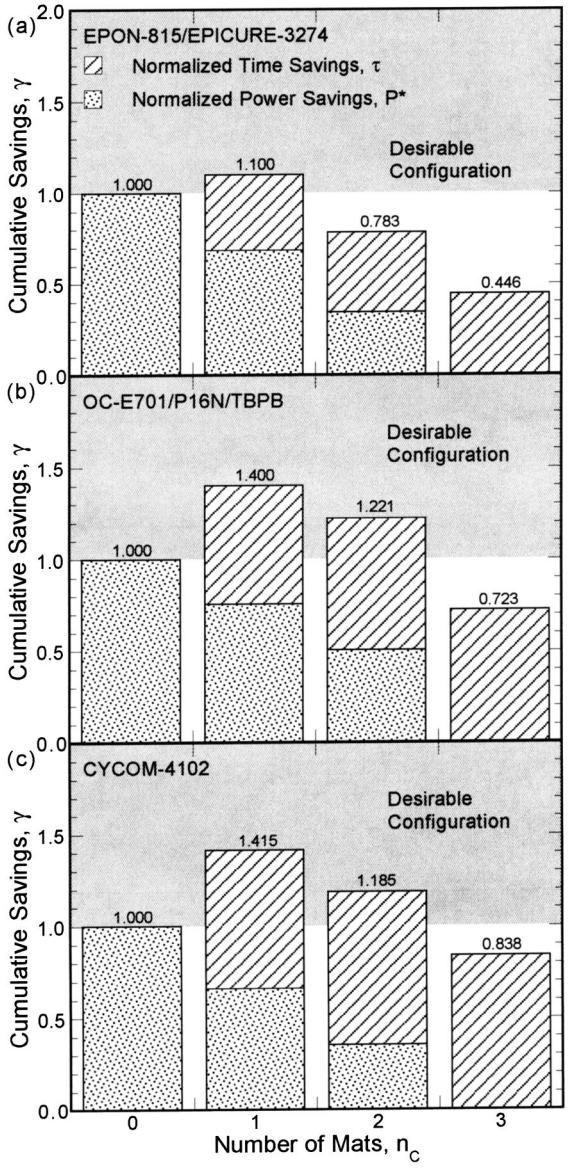

Fig. 11 Normalized cure time and power consumption savings as a function of number of carbon mats, for (*a*) EPON-815/EPICURE-3274, (*b*) OC-E701/P16N/BPO, and (*c*) CYCOM-4102

mats, n_C, for all material systems used in this study. The maximum power, $P_{\max}$, corresponds to the power consumption for $n_C = 3$ for each material system. The sum of the normalized cure time savings and the normalized power savings is referred to as the cumulative savings parameter, γ_{n_C}. For the processing without resistive heating ($n_C = 0$): $\tau_0 = 0$ and $P_0^* = 1$ independent of material system, which leads to $\gamma_0 = 1$. It follows that for the processing with resistive heating, it is desirable that the cumulative savings exceed that for the reference case of no resistive heating, i.e., $\gamma_{n_C} > \gamma_0$. Since $\gamma_0 = 1$, the region $\gamma_{n_C} > 1$ is identified in the plots as the desirable configuration for resistive heating. This region is indicated by the shaded area in Figs. 11(*a*)–11(*c*). Based on the consideration of time and power savings, Fig. 11 provides for deciding the number of carbon mats that constitutes the optimal configuration for each resin system. It is seen that the single carbon mat configuration offers the most cumulative savings for all the resin systems. Further, for EPON-815/EPICURE-3274 (Fig. 11(*a*)), one carbon mat is the only configuration that satisfies

$\gamma_{n_C} > 1$, while for OC-E701/P16N/BPO (Fig. 11(*b*)) and CYCOM-4102 (Fig. 11(*c*)), both one and two carbon mats satisfy the criterion. Since additional carbon mats always reduces the cure time, the optimal number of carbon mats n_C^* could be defined as the highest number of mats for which the cumulative savings exceeds that of the process without resistive heating. Thus, the optimal number of carbon mats for EPON-815/EPICURE-3274 is one, while for OC-E701/P16N/BPO and CYCOM-4102 two carbon mats constitute the optimal configuration. It may be noted from Fig. 10 that the CYCOM-4102 system corresponds to higher Damköhler number value in comparison to the EPON-815/EPICURE-3274 system for the same laminate thickness. The results in Fig. 11(*a*) and 11(*c*), therefore, suggest that the cumulative power and time savings, γ_{n_C}, increases with Damköhler number.

The paper presented a comprehensive discussion on the optimization of temperature and current cycles for curing process using resistive heating. The results in terms of optimal cure time, optimal current cycles along with optimal location and configuration provide a valuable reference for better process design. The optimization framework presented in the paper may be used to determine optimal temperature and current cycles for constraint values other than those used in the study, although the physical trends elucidated in this article are expected to be generally valid.

5 Conclusions

A systematic approach to optimization of a process for fabrication of thermosetting-matrix composites by the use of embedded resistive heating element was presented. The objective was to determine the optimal temperature cycles, electrical current cycles, and the conductive mats configuration so as to minimize the fabrication time subject to process constraints. A numerical model formed the basis of the optimization problem, which was solved using a combination of simulated annealing and simplex search algorithm. Optimal cure times, temperature and current cycles were presented for three material systems with different reaction kinetics. The optimal solutions are presented for various conductive mats configuration, as well as several process design constraints. The results showed that the approach of varying the current with time together with the cure temperature cycles leads to cure time reduction. In general, the cure time decreases as the number of mats increases, and for the material systems considered in the study, one or two carbon mats were shown to be the practical optimal configuration, based on an analysis incorporating the electrical power consumption of the resistive heating elements. The variation of the results with the resin kinetics and composite thickness were reported in terms of a non-dimensional Damköhler number, which showed that material systems with higher reactivity or larger thickness experienced greater cure time reduction by the additional resistive heating elements.

Acknowledgment

The study was funded by the National Science Foundation through Grant Nos. DMI-0119430 and CTS-0112822. The authors gratefully acknowledge the support.

Nomenclature

A = cross-sectional area of conductive mat
C_{R0} = initial concentration of the reactive resin [kg/m^3]
E_1, E_2 = activation energies in the kinetics model [kJ/mol]
E_n, E_{n+1} = energy states in simulated annealing
$\mathbf{f_i}$, $\mathbf{g_i}$ = binary variables
g_k = constraint values
h = heat transfer coefficient [W/m^{2}K]
H_R = heat of the cure reaction [kJ/kg]
I = electrical current [A]
k_{CI} = in-plane thermal conductivity of resin-saturated conductive mat
k_i = thermal conductivity of material i [W/mK]
K_{10}, K_{20} = pre-exponential factors in the kinetic model [s^{-1}]
l_i = thickness of material i [m]
m, n = empirical exponents in the kinetics model
n_C = number of carbon mats
p = probability factor in the Metropolis criterion
P^* = normalized electrical power savings
R = universal gas constant [kJ/mol K]
t = time [s]
T = temperature in the composite at any time t and spatial location y [K]
T_a = annealing temperature [K]
v_i = fiber volume fraction of material i
x, y = coordinate axes
y^* = optimal location of conductive mat [cm]

Greek Symbols

α = thermal diffusivity $k/\rho C$ [m^2/s]
γ = normalized cumulative savings
ϵ = degree of cure
φ_C = electrical resistivity of resin saturated conductive mat [Ohm/m^2]
φ_{CF} = electrical resistivity of pure conductive mat [Ohm/m^2]
ρC = volumetric specific heat [kJ/m^{3}K]
τ = normalized cure time savings

Subscripts

$*$ = optimal value
B = base plate
C = resin-impregnated conductive layer
F = resin-saturated fiber layer
L = laminate
T = tooling
crit = critical value
max = maximum value
min = minimum value
n_C = number of conductive mats

References

[1] Ramakrishnan, B., Zhu, L., and Pitchumani, R., 2000, "Curing of Composites Using Internal Resistive Heating," J. Manuf. Sci. Eng., **122**, pp. 124–131.
[2] Zhu, L., and Pitchumani, R., 2000, "Analysis of a Process for Curing Composites by the Use of Embedded Resistive Heating Elements," Compos. Sci. Technol., **60**, pp. 2699–2712.
[3] Pillai, V. K., Beris, A. N., and Dhurjati, P. S., 1994, "Implementation of Model-Based Optimal Temperature Profiles for Autoclave Curing of Composites Using a Knowledge-Based System," Ind. Eng. Chem. Res., **33**, pp. 2443–2452.
[4] Loos, A. C., and Springer, G. S., 1983, "Curing of Epoxy Matrix Composites," Journal of Composite Materials, **17**, pp. 135–169.
[5] Han, C. D., Lee, D. S., and Chin, H. B., 1986, "Development of a Mathematical Model for the Pultrusion Process," Polym. Eng. Sci., **26**, pp. 393–404.
[6] Bogetti, T. A., and Gillespie, J. W., 1991, "Two Dimensional Cure Simulation of Thick Thermosetting Composites," Journal of Composite Materials, **25**, pp. 239.
[7] Ciriscioli, P. R., Wang, Q., and Springer, G. S., 1992, "Autoclave Curing—Comparison of Model and Test Results," Journal of Composite Materials, **26**, pp. 90–103.
[8] Rai, N., and Pitchumani, R., 1997, "Optimal Cure Cycles for the Fabrication of Thermosetting-Matrix Composites," Polym. Compos., **18**, pp. 566–581.
[9] Lee, W. I., and Springer, G. S., 1984, "Microwave Curing of Composites," Journal of Composite Materials, **18**, pp. 387–409.
[10] Thostensen, E., and Chou, T.-W., 1998, "Microwave Accelerated Curing of Thick Composite Laminates," *Proceedings of the 13th American Society for Composite Conference*, Baltimore, MD, pp. 595–604.
[11] London, E. U., and Odishaw, H., 1991, *Handbook of Physics*, McGraw-Hill, New York, NY.
[12] Ning, Q., and Chou, T.-W., 1995, "A Closed-Form Solution for the Transverse Effective Thermal Conductivity of Woven Fabric Composites," Journal of Composite Materials, **29**, pp. 2280–2294.
[13] Ning, Q., and Chou, T.-W., 1995, "Closed-Form Solution for the In-Plane Effective Thermal Conductivity of Woven Fabric Composites," Compos. Sci. Technol., **55**, pp. 41–48.

[14] Patankar, S. V., 1980, *Numerical Heat Transfer and Fluid Flow*, Hemisphere, Washington, DC.
[15] Anderson, D. A., Tannehill, J. C., and Pletcher, R. H., 1984, *Computational Fluid Mechanics and Heat Transfer*, Hemisphere, Washington, DC.
[16] Nelder, J. A., and Mead, R., 1965, ''A Simplex Method for Function Minimization,'' Comput. J. (UK), **7**, pp. 308–313.
[17] Press, W. H., Flannery, B. P., Teukolsky, S. A., and Vettering, W. T., 1992, *Numerical Recipes in FORTRAN*, Cambridge University Press, New York, NY.
[18] Lagarias, J. C., Reeds, J. A., Wright, M. A., and Wright, P. E., 1998, ''Convergence Properties of the Nelder-Mead Simplex Method in Low Dimensions,'' SIAM J. Optim., **9**, pp. 112–147.
[19] Kirkpatrick, S., Gelatt, C. D., and Vecchi, M. P., 1983, ''Optimization by Simulated Annealing,'' Science, **220**, pp. 671–680.
[20] Metropolis, N., Rosenbluth, A., Rosenbluth, M., and Teller, A., 1953, ''Equation of State Calculations by Fast Computing Machines,'' J. Chem. Phys., **21**, pp. 1087–1092.
[21] Bertsekas, D. P., 1999, *Nonlinear Programming*, Athena Scientific, Belmont, MA.

Transient Thermal Modeling of In-Situ Curing During Tape Winding of Composite Cylinders

Jonghyun Kim

Tess J. Moon

John R. Howell

Department of Mechanical Engineering,
The University of Texas at Austin,
Austin, TX 78712

Fully-transient, two-dimensional, heat transfer analysis for the simultaneous tape winding and in-situ curing of composite cylinders is presented. During processing, the orthotropic composites are continuously wound onto an isotropic mandrel and cured simultaneously by infrared (IR) heating. To most efficiently and effectively consider the continual accretion of composite, the model is formulated within a Lagrangian reference frame in which the heating source rotates while the coordinate system and composite are stationary. This enables prediction of composite temperature and degree-of-cure history from the first to last layer. Separate heat conduction equations are formulated for both the mandrel and composite cylinder. The composite cylinder's outer surface is modeled as a moving boundary due to the accumulated layers. Exothermic heat generation due to the epoxy resin's chemical reaction is included as a function of temperature and degree of cure. Numerical simulations using a control-volume-based finite difference method are run for a common graphite/epoxy (AS4/3501-6) composite. The Lagrangian approach was found to more accurately predict the in-situ curing temperature and degree-of-cure histories than the previously used, quasi-steady-state Eulerian approaches, which underpredict thermal losses. The model and its computational implementation were verified using analytical solutions and actual experiments. During winding, the top layer's maximum temperature increases with total number of layers wound, demonstrating that a given incoming prepreg tape's temperature history evolves with time. Moreover, with appropriate mandrel preheating, the inner layers can reach a very high degree of cure by the end of the winding process, revealing that the mandrel's initial temperature has a significant effect on the composite's temperature and degree-of-cure history. Substantial increases in the winding speed have little or no effect on the composite's temperature history, but can significantly reduce the corresponding degree-of-cure. The development of structurally debilitating residual stresses are an important concern in selecting process parameters, such as winding speed and heating power. Taking advantage of the strong correlation between winding speed and IR heat flux, process windows can be used to guide the selection of manufacturing process parameters. These definitively show that there are thermodynamically imposed limits on how fast the cylinders may be wound and radiatively cured. [DOI: 10.1115/1.1527912]

Keywords: Manufacturing, Modeling, Porous Media, Processing, Radiation

1 Introduction

Polymer composites have demonstrated many benefits in aerospace applications since the 1950's. Polymer composites typically consist of polymer matrices reinforced with fibers. The fibers carry most of the loads applied to the composites. The functions of the polymers are to bind fibers together and to transfer the applied loads between the fibers. The fibers used in advanced composite materials include carbon, glass, kevlar and aramid. Carbon fibers have high specific strengths, while glass fibers are relatively inexpensive. Typical polymers are divided into thermoset, thermoplastic, or blended matrices. Thermoset matrices tend to have higher tensile and compressive strengths and lower melt viscosity, while thermoplastic matrices generally exhibit higher fracture toughness and higher service temperatures.

Polymer composite cylinders have a wide range of applications from large aircraft parts such as fuselages and wings to small sporting goods such as fishing rods, golf club shafts and tennis rackets. The performance of advanced polymer composites is well recognized due to their combination of light weight and high strength. However, high manufacturing costs prohibit the wide use of composite parts. Traditional autoclave curing involves long process time and severe temperature gradients in the parts. A great deal of attention is being paid to the development of manufacturing processes in order to reduce manufacturing costs. Some research is focused on automated processes, such as resin transfer molding [1], filament or tape winding [2] and tape laying [3].

In order to develop a manufacturing process, it is helpful to understand and simulate the fundamentals of the thermal process. Heat transfer analysis plays an important role in the study of the curing of thermoset composites. Process simulation using a heat transfer model is useful to determine appropriate thermal process conditions. Moreover, chemical reactions generate exothermic heat inside a thermoset composite during its cure. Since the exothermic reaction has a significant effect on the temperature distribution in the composites, the heat transfer analysis is coupled to the cure kinetics to calculate heat generation of the thermoset. The selection of a proper cure cycle is very important as it influences the mechanical properties and the cure characteristics of the composite material [4,5]. Therefore, a cure cycle for each application should be carefully selected.

For the fabrication of a large composite structure, it may not be possible to uniformly cure the entire part. Thick composite cylinders show delamination during curing processes and fiber buckling during post cure [6]. Even though the investigators in [6]

Contributed by the Heat Transfer Division for publication in the JOURNAL OF HEAT TRANSFER. Manuscript received by the Heat Transfer Division August 24, 2001; revision received September 6, 2002. Associate Editor: S. S. Sadhal.

made some suggestions for processing conditions, they are qualitative. Recommended cure cycles for a specific composite provided by the manufacturers are mostly for the manufacture of thin parts. Numerous studies report that there are significant gradients in temperature and degree of cure during the manufacture of thick thermoset composites [7]. This is believed to be the result of the exothermic reaction from thermosets and the relatively low conductivity in the transverse fiber direction. In order to reduce nonuniform distributions across the parts, the development of novel processing techniques is under way by many investigators using thermal modeling [8–11].

Several studies have demonstrated how to develop proper cure cycles especially for thick composites for traditional autoclave curing [12–16]. Yokota [12] investigated the effect of the time of pressure application using a dielectric viscosity monitoring technique. By generating the pressure application window, it was found that pressure should be applied between the completion of evolution of volatiles and the onset of resin gelation. Hjellming and Walker [13] developed an optimal, three-step cure cycle for thick composite cylinders to maintain low and uniform viscosity through the thickness during a consolidation period. They found that no simple scaling law exists for different thickness, i.e., the optimal cycle found in their study can be used only for cylinders with the same thickness. Martinez [14] used a cure cycle which adopted a decreasing temperature ramp during the peak of chemical reaction to avoid a temperature overshoot. Tang et al. [15] demonstrated that the layers are compacted from the layer close to a bleeder cloth and the compaction process propagates to the interior of the composite layers. They also showed that there is not enough compaction inside thick, thermoset-composite laminates. Twardowski et al. [16] performed a series of experiments to investigate the effects of process variables on processing concerns during the manufacture of thick laminates, including bagging materials, laminate thicknesses, initial degrees of cure and changes in thermal properties. They reported that glass fibers show higher temperature overshoot than carbon fibers due to their lower thermal conductivity.

Most thermal analyses for in-situ processing of thermoset composites were carried out based on one-dimensional analysis through the thickness of composites [8,11,17]. Burwasser and Springer [8] developed a model for electrothermal curing resulting from applying a current through the carbon fibers. Although the electrothermal curing during the winding process provided a reduced manufacturing time compared to traditional autoclave curing, no practical means were suggested on how to apply electrical power during winding. Also, electrical heating is good only for electrically conducting carbon fibers. Korotokov et al. [17] considered a simultaneous filament winding process for thermoset composites. The study was limited to a one-dimensional model in cylindrical coordinates on the assumption that layer winding time is small compared to representative curing time. Kim et al. [11] demonstrated a continuous curing process by intermittently supplying materials on a heated tool plate. Numerical results obtained from the one-dimensional model for the thick laminates showed that the manufacturing time required for continuous curing is shorter than that for autoclave curing.

Radiative heating of the surface layer during the winding process can provide energy to initiate the curing of the thermoset resin. However, in practice, circumferentially uniform radiant heating is not achieved during the winding process. Heat flux is limited to some portion of the surface area of the composite in the circumferential direction due to the space required for feeding the materials. A two-dimensional model is necessary for the case of non-uniform radiant heating around the mandrel even during the hoop-winding process. Chern et al. [9,10] developed a two-dimensional heat transfer model for the hoop winding process using in-situ infrared heating and verified their model through experiments. Volumetric radiation transfer was included in their model using the radiation transfer equation. Variable material properties such as thermal conductivity and thermal capacity were measured as a function of temperature and degree of cure and they are used in the model. However, the model does not include the thermal effect of the mandrel and is only useful for the outermost layers of composite cylinders. Kim et al. [18] investigated an in-situ curing process using a two-dimensional model with the assumption of a quasi-steady state; that is, each successive layer was assumed to undergo an identical repetitive process. They observed that the effect of the mandrel materials on the temperature distribution is insignificant, while the exothermic reaction is important. However, they found the assumption of quasi-steady state does not explain the true temperature and degree-of-cure history which is important in order to study the quality of final parts.

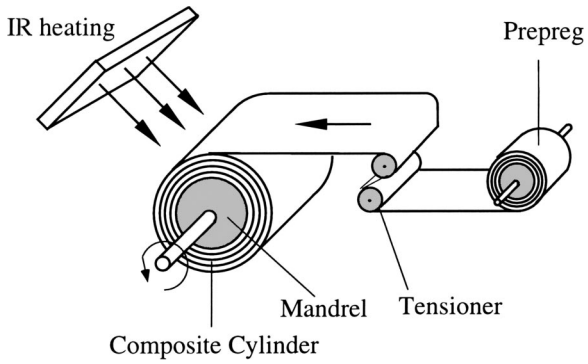

Fig. 1 Hoop winding while curing by in-situ infrared (IR) heating. Continuous fibers within the prepreg lie in the circumferential direction in the wound composite cylinder. Prepreg width is assumed to be equal to the cylinder length.

Figure 1 shows a schematic of the hoop winding process using in-situ curing. In the present study, AS4/3501-6 (carbon fiber/epoxy resin) prepreg is chosen due to its wide use in industry. Recommended for general purpose structural applications, the AS4/3501-6 prepreg is composed of unidirectional, continuous, PAN-based, AS4C carbon (graphite) fibers embedded in an amine-cured epoxy resin system. The epoxy resin, 3501-6, is a tetraglycidyl diamino diphenyl methane (TGDDM) with diaminodiphenylsulfone (DDS) catalyzed with boron trifluoride monoethylamine. 3501-6 was developed to operate in a temperature environment of up to 177°C (350°F).

In this paper, a fully-transient, two-dimensional, heat transfer model is established to simulate continuous, in-situ curing using infrared heating. The objective of this study is to predict the temperature history of an arbitrary material point cascading from the first to the last layer during in-situ curing using IR (infrared) heating. To achieve this objective, simulation of the thermal process during in-situ curing is performed with a moving boundary at the outer surface. The present heat transfer model considers hoop winding in a Lagrangian coordinate system to simplify the analysis; this model is used to investigate the temperature distributions within both the mandrel and composite cylinder. Also, the composite's degree of cure during the winding process is calculated using the Lagrangian temperature histories obtained from numerical analysis. The model's numerical results aid in the design of an infrared heating system necessary to achieve proper processing temperatures over a range of winding speeds. The temperature predictions at the end of the winding process are compared with the temperature distributions from the steady state approach.

2 Thermochemical Model

2.1 Assumptions and a Lagrangian Approach. The thermal analysis is based on an energy equation, coupled to the cure kinetics for the thermoset matrix. The heat transfer model is established in a Lagrangian coordinate system where the heat source is rotating while the coordinate system and the composite cylinder

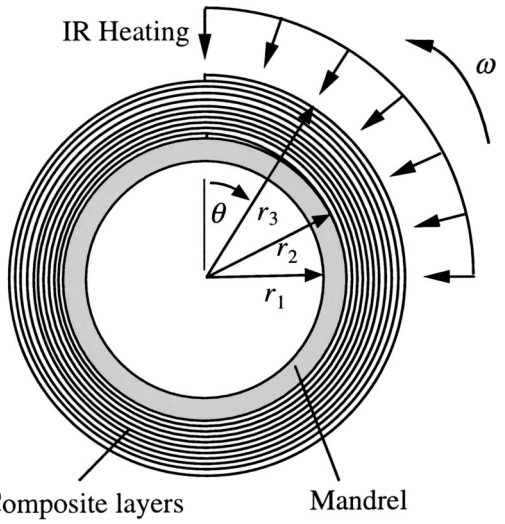

Fig. 2 Two-dimensional computational domain, composed of an isotropic mandrel and orthotropic, continuously wound, composite cylinder. Uniform radially-inward IR heating and negligible axial energy losses are assumed. Material accretion occurs at an effective laydown point $\theta_l(\tau)$ (Eq. (14)) in advance of the physical knit point at $\theta=0$; radiant preheating of the incoming tape occurs between $\theta_l(\tau)\leqslant\theta\leqslant 0$.

are stationary. Fig. 2 shows a schematic view of the heating condition and geometry of a composite cylinder being wound onto a mandrel. In the transient analysis, the heating system rotates instead of the mandrel to simplify the analysis (further explained later). The incident IR heat flux on the composite is considered to cover either a 90 deg or 180 deg angle in the results presented here, but this arbitrary parameter can be adjusted as necessary to mimic actual manufacturing conditions.

One of the critical issues during the development of the transient model is how to simulate the addition of material as the total number of wound layers increases. For the modeling of the moving laydown point during continuous winding, a Lagrangian coordinate system is employed here; the Lagrangian coordinate system describes the continuous winding better than the previously considered Eulerian coordinate system [10,18,19] by tracing the laydown point as it moves into the composite's interior with the addition of freshly wound prepreg. Moreover, the Lagrangian coordinate system is appropriate for the calculation of degree of cure as it focuses on the transient conditions within each material element.

It is necessary to temporally track the position of each material point when using the Lagrangian coordinate system. This requires a large amount of calculation and memory space to locate all the spatial positions as a function of time. To resolve this problem, a rotating heat source is considered, instead of the rotating mandrel and composite cylinder. By employing a Lagrangian coordinate system, each material element has its own temperature history in the transient analysis, which allows correct calculation of degree of cure. The outer surface's boundary condition becomes a function of time due to the composite cylinder's rotation. The laydown point moves circumferentially on the layer and is shifted up to a new layer at the end of each previous layer.

Thermal conductivity and thermal capacity are a function of temperature and degree of cure [20]. The numerical solution is obtained for the fully transient, two-dimensional heat transfer problem in cylindrical coordinates where the outer boundary of a hollow composite cylinder grows with the addition of fresh prepreg.

2.2 Formulation for a Transient Problem. Thermal analysis is performed in two dimensions (r and θ) under the assumption that axial energy losses are negligible (provided by guard heating, insulation or the cylinder's large length-to-diameter ratio). The computational domain of the heat transfer analysis for the hoop winding process is divided into two concentric regions: mandrel and composite. To determine the relative magnitude of important parameters, the governing equations are nondimensionalized, which also adds accuracy to the numerical computation by maintaining numerical values of the same order of magnitude. The nondimensional equations can be expressed:

Mandrel:

$$\mathrm{Hc}\cdot\frac{\partial\Theta}{\partial\tau}=\frac{1}{R}\frac{\partial}{\partial R}\left(R\frac{\partial\Theta}{\partial R}\right)+\frac{1}{R^2}\frac{\partial^2\Theta}{\partial\theta^2},\quad \text{for } R_1<R\leqslant R_2 \tag{1}$$

Composite:

$$\mathrm{CP}\cdot\frac{\partial\Theta}{\partial\tau}=\frac{1}{R}\frac{\partial}{\partial R}\left(K_1R\frac{\partial\Theta}{\partial R}\right)+\frac{Ai}{R^2}\frac{\partial}{\partial\theta}\left(K_2\frac{\partial T}{\partial\theta}\right)+\mathrm{Bi}\cdot\mathrm{Ch}\frac{d\alpha}{d\tau},\quad \text{for } R_2<R\leqslant R_3(\tau) \tag{2}$$

Reaction Rate:

$$\frac{d\alpha}{d\tau}=\frac{H_T}{H_U}\frac{d\beta}{d\tau} \tag{3}$$

where

$$\begin{aligned}\frac{d\beta}{d\tau}&=\mathrm{Da}\cdot\beta^m(1-\beta)^n,\quad \beta\leqslant\beta_{bp}\\ \frac{d\beta}{d\tau}&=\mathrm{Da}\cdot\frac{\overline{K}_2}{K_1}(1-\beta),\quad \beta>\beta_{bp}\end{aligned} \tag{4}$$

and β_{bp} is the isothermal degree of cure at the break point, i.e., transition between rate- versus diffusion-controlled cure kinetics [21].

The Biot number, $\mathrm{Bi}=h_{\mathrm{ref}}r_2/k_{1,\mathrm{ref}}$, appears in Eq. (2) due to the particular nondimensionalization chosen for the composite energy equation. All mandrel material properties are assumed constant, i.e., independent of temperature and direction. However, the composite structure is highly orthotropic due to significantly different thermal conductivities in the longitudinal and transverse fiber directions. The orthotropic composite's thermal conductivities and specific heat are expressed as a function of temperature and degree of cure, as given in [20]. The energy balance equation for the composite structure (Eq. (2)) includes a heat generation term due to the exothermic chemical curing reaction occurring in the thermoset resin. The cure kinetics for AS4/3501-6 prepreg (Eq. (3)) is used [21]. The parameter Da represents the ratio of conduction time scale to the reaction time scale [22]; it is a measure of how fast the cure reaction proceeds relative to thermal diffusion.

The nondimensional boundary conditions for the composite's top (outermost) surface and the mandrel's inner surface are listed in Eqs. (5)–(7), respectively. Meanwhile, periodic (matching) boundary conditions are employed at the location where the layers meet circumferentially; these are given in Eqs. (8)–(10) respectively.

$$K_1\frac{\partial\Theta}{\partial R}=\mathrm{Bi}[\alpha\cdot F_{d-\mathrm{lamp}}(\theta,\tau)\cdot\eta-(H+H_r)(\Theta-\Theta_\infty)-Ac(\Theta-\Theta_i)]\quad \text{at } R=R_3(\tau),\theta=\theta_l(\tau)\ \ (\text{laydown point}) \tag{5}$$

$$K_1\frac{\partial\Theta}{\partial R}=\mathrm{Bi}[\alpha\cdot F_{d-\mathrm{lamp}}(\theta,\tau)\cdot\eta-(H+H_r)(\Theta-\Theta_\infty)]\quad \text{at } R=R_3(\tau),\theta\neq\theta_l(\tau)\ \ (\text{other outer surface elements}) \tag{6}$$

$$\frac{\partial\Theta}{\partial R}=0\quad \text{at } R=R_1\ \ (\text{mandrel's inner surface}) \tag{7}$$

$$\Theta_{\theta=0}=\Theta_{\theta=2\pi};\quad \frac{\partial\Theta}{\partial\theta_{\theta=0}}=\frac{\partial\Theta}{\partial\theta_{\theta=2\pi}}\quad \text{at } \theta=0,\ 2\pi \text{ (mandrel)} \tag{8}$$

$$\Theta_{\theta=0,\ \text{layer}=n}=\Theta_{\theta=2\pi,\ \text{layer}=n+1}; \tag{9}$$

$$\frac{\partial\Theta}{\partial\theta}_{\theta=0,\ \text{layer}=n}=\frac{\partial\Theta}{\partial\theta}_{\theta=2\pi,\ \text{layer}=n+1}$$

$$\text{at } \theta=0,\ 2\pi \text{ (composite layers)} \tag{10}$$

Equation (5) applies for the element at the laydown point, i.e., the location where new materials are added to the composite cylinder; this material accretion is accounted for in the last term of Eq. (5). As the remainder of the outside surface elements do not involve material accretion, they are represented by Eq. (6).

The outermost layer's surface is heated by an infrared lamp and exposed to the surrounding ambient air. The boundary conditions that account for convection and emission heat losses are in Eqs. (5) and (6). A convective term, $\rho_c c_{P,c} V_t (T-T_i)$ (in dimensional form), describes the continuous material accretion at the laydown point; this term is necessary when the diffusion time scale is much smaller than the accretion time scale [17]. Emissive heat loss from the composite surface needs to be considered as the thermoset composite's processing temperature is very high relative to the ambient temperature and radiative loss is comparable to free convective heat transfer; the emissive heat loss term is linearized using the radiation heat transfer coefficient [23].

Periodic boundary conditions (Eq. (8)) are applied for the mandrel at $\theta=0$ and 2π. However, for each composite layer, the continuity conditions (Eqs. (9) and (10)) between the nth layer and the $(n+1)$th layer are applied due to continuous winding, i.e., each layer is connected at $\theta=0$. Finally, the mandrel's inner surface is assumed to be insulated (Eq. (7)).

The configuration factor $F_{d-\text{lamp}}(\theta,t)$ is used to vary the apparent heating area of the infrared lamp. In this study, infrared heating is assumed to be applied uniformly through either 90 deg or 180 deg about the composite cylinder. For example, for the 90 deg case, the configuration factor is set to: 1 for $0<\theta\leqslant 90$ deg; and 0 for 90 deg$<\theta\leqslant$360 deg. A variable heat transfer coefficient—a function of temperature, cylinder diameter and rotational speed—is used to estimate the convection heat transfer coefficients. The heat transfer around a rotating, heated cylinder is governed by two different mechanisms: natural convection due to temperature difference between the cylinder surface and ambient air; and forced convection due to the rotational motion. At the winding speeds used in this study (10–30 rpm), natural convection dominates the heat transfer; hence the relationship used is [23]:

$$h=\frac{0.456k_a}{r_3}[N_{\text{Ra}}]^{0.36}. \tag{11}$$

The initial conditions are listed in Eqs. (12)–(14).

$$\Theta=\Theta_{i,m} \quad \text{(mandrel)} \tag{12}$$

$$\Theta=\Theta_{i,c} \quad \text{at } \theta=\theta_l(\tau) \quad \text{(laydown point)} \tag{13}$$

$$\theta_l(\tau)=2\pi-\frac{\rho_c c_{P,\text{ref}}\omega r_2^2}{k_{1,\text{ref}}}\tau \tag{14}$$

The incoming tape's initial temperature is imposed at $\theta=\theta_l(\tau)$, the laydown point for the top layer; this condition permits flexibility in the analysis to examine the effect of preheating the incoming tape. Eq. (14) locates the moving, effective laydown point at the top layer at time τ, after the initiation of winding.

2.3 Solution Technique. The equations were discretized based on a control volume approach [24]. A modified, strongly implicit procedure (SIP) developed by Schneider and Zedan [25] is employed to solve the system of algebraic equations obtained from the discretization procedure. Stone [26] demonstrated that the SIP algorithm is not sensitive to the nature of the coefficient matrix by comparing cases with different ratios of conductivities in two orthogonal directions. Since a typical continuous fiber composite has about 10X higher thermal conductivity in the fiber rather than in the transverse-fiber direction, the SIP algorithm yields a more efficiently convergent solution to the conduction equation for many orthotropic composites.

One radial nodal point is used for each layer, whose thickness is 0.132 mm, while 20 nodes are used for the mandrel, whose thickness is 1 cm. Due to the mandrel's high thermal conductivity, 20 nodes were found to yield accurate, converged solutions. Doubling the number of nodes in the composite layers revealed no significant changes in the temperature distributions. The composite's degree of cure distributions are calculated by integrating Eq. (3) using the fourth order Runge-Kutta method.

The thermophysical properties of the AISI 304 stainless steel mandrel are taken to be: $\rho=7900$ kg/m,[3] $c_P=477$ J/kg·K and $k=16.6$ W/m·K [27]. Meanwhile, the temperature- and degree-of-cure-dependent specific heat and thermal conductivity of the AS4/3501-6 prepreg ($\rho=1800$ kg/m^3) are obtained from [10,20,28]. The prepreg's IR absorptivity α_a was measured as 0.87. Due to the resin's low surface reflectivity and embedded carbon fiber's high absorptivity, as well as the relatively small absolute temperature differences between emitted and absorbed radiation sources, the emissivity was assumed to be the same [29].

Verification of the model and computational implementation was accomplished by two independent comparison methods: by solving several simple thermal problems which have exact, analytical solutions [30]; and by actually winding several AS4/3501-6 cylinders instrumented with thermocouples [31–33].

3 Temperature and Degree-of-Cure Histories During Processing

The fully transient, two-dimensional model employing Lagrangian coordinates is used here to gain insights into the processing by investigating the process histories of temperature and degree of cure. The temperature distribution at the end of the winding obtained from the transient analysis is compared with that from the more restricted Eulerian analysis based upon the quasi-steady state assumptions [10,18,19].

Figure 3 shows the composite cylinder's temperature distributions from the top (or 100th) layer to the 20th inner (or 80th) layer with a winding speed of 10 rpm, an IR lamp heat flux of 48.6 kW/m^2, initial mandrel temperature of 480 K and mandrel diameter of 12.7 cm (5 in). The integer number on the x axis label represents the layer number. Values between integer layer numbers denote the angular location at each layer, e.g., 99.5 is the angular location at 180 deg for the 100th layer.

If there is no rotational motion, the maximum temperature occurs at the center of the heating area. With rotational motion, the maximum temperature is shifted to the exit of the heating area due to advection. Each layer is found to be divided by the temperature "valley" due to the relatively cold (room temperature, 25 K) incoming tape at the laydown point. The maximum temperature for the top layer occurs at 90 deg, which is the exit of the heating region. Quasi-steady state analysis predicts higher temperatures than the present, full transient analysis; in other words, quasi-steady state analysis significantly underestimates the heat loss at the composite's outer surface.

The composite's temperature evolutions during the winding process for two different initial mandrel temperatures, 430 and 480 K, are shown in Figs. 4 and 5, respectively. With only 10 layers wound, the middle layer's temperature distribution is affected by that of the top layer. However, by the time 50 layers are wound, the middle layer's temperature distribution is much less affected by that of the top layer and is, indeed, almost constant. This is due to the low transverse-fiber thermal conductivity in the composite cylinders's radial direction.

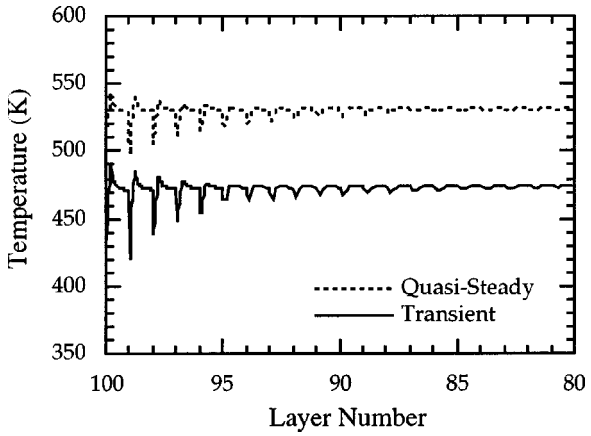

Fig. 3 Comparison of the temperature distributions in the top 20 layers of a composite cylinder wound from AS4/3501-6 prepreg predicted by the quasi-steady state [18] and current, fully transient approaches. Integer number on the *x* axis label represents the layer number. (Winding speed, 10 rpm; IR lamp heat flux, 48.6 kW/m^2; Initial mandrel temperature, 480 K; Mandrel diameter, 12.7 cm (5 in)).

The temperature distribution of the innermost layers is almost constant, as it is most affected by the temperature of the mandrel, which has a significantly larger heat capacity than the composite cylinder. Interestingly, the top layer's maximum temperature increases with the total number of layers wound, since the initial mandrel temperature is lower than the steady-state temperature for this given IR heat flux and winding speed. The lower initial mandrel temperature explains the 20 K increase in mandrel temperature by the end of winding process due to radial conduction to the mandrel from the hotter composite layers. The temperature history that an incoming prepreg tape goes through from the laydown point changes with time during winding, thus explaining the superiority of the transient thermal model over a quasi-steady state model for in-situ curing.

For the higher initial mandrel temperature, 480 K, shown in Fig. 5, the temperature distribution is uniform during the winding, except at initiation. Due to its high initial level, the mandrel temperature remains at steady state. Throughout the winding time, the radial temperature differences are less than 10 K, except for the layers near the top surface immediately under the heating region. Absent are the substantial radial temperature gradients typical of thick composites during autoclave curing [7]. These results demonstrate that the in-situ curing is an effective process to maintain a nearly uniform temperature distribution for arbitrarily thick composites.

Figures 6 and 7 illustrate the ply temperatures and advancement of the degree of cure within the first, 25th and 50th layers wound for an initial mandrel temperature of 430 K. The temperature fluctuations caused by the nonuniform, circumferential heating are smaller for the first layer wound than that for the 25th layer wound, reflecting the radial heat transfer from the relatively high thermal conductivity and capacitance mandrel. The temperature history of the 25th layer wound is higher than that of the first layer, due to the general increase of the processing temperature during the winding (Fig. 4).

The first layer's degree of cure is about 20 percent just as the 25th layer is wound; meanwhile, as the 50th layer is wound, the 25th layer's degree of the cure is approximately 25 percent. This seemingly small increase in degree of cure, though for exactly the same time period, is due to the general increase in processing temperature during the winding as progressively more layers are wound (see Fig. 4).

The degree of the cure of the first layer wound, i.e., that closest to the mandrel, is advanced to about 30 percent as the 50th layer

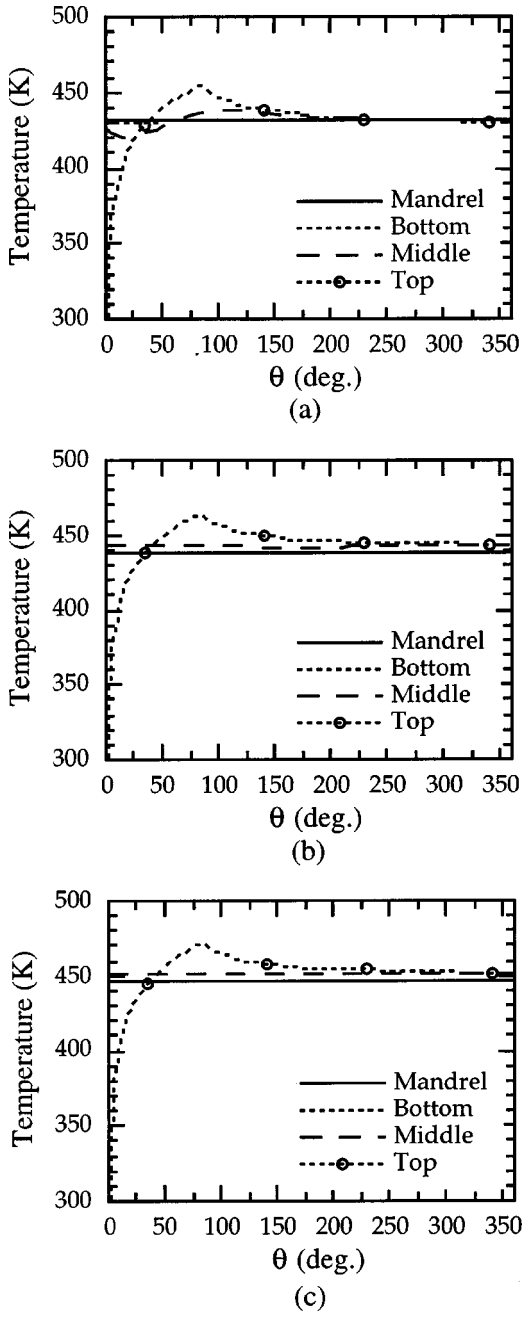

Fig. 4 Temperature evolutions during winding in the bottom, middle and top AS4/3501-6 prepreg layers and stainless steel mandrel after 10, 50, and 100 total layers are wound. (Winding speed, 10 rpm; IR lamp heat flux, 48.6 kW/m^2; Initial mandrel temperature, 430 K; Mandrel diameter, 12.7 cm (5 in).): (*a*) 10 layers wound; (*b*) 50 layers wound; and (*c*) 100 layers wound.

is wound. At the conclusion of the winding process, the degree-of-cure differences between layers decreases, i.e., a more uniform, through-thickness degree-of-cure distribution results due to the time available for the cure to approach completion within the inner layers. This is one distinct advantage that in-situ curing enjoys over autoclave curing, which often yields severe radial degree-of-cure gradients due to exothermic heat release in the epoxy matrix during curing, especially in the manufacture of thick structural components.

For comparison, Figs. 8 and 9 display the temperature and degree-of-cure results for the same parameter settings, except at the higher initial mandrel temperature of 480 K. For this case,

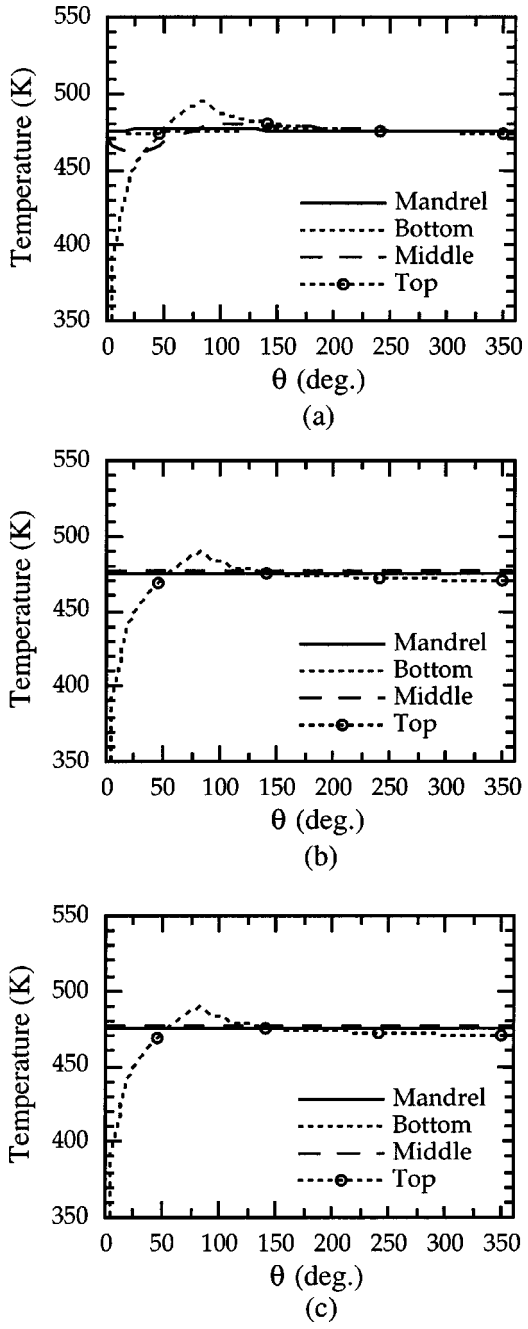

Fig. 5 Temperature evolutions during winding in the bottom, middle and top AS4/3501-6 prepreg layers and stainless steel mandrel after 10, 50, and 100 total layers are wound. (Winding speed, 10 rpm; IR lamp heat flux, 48.6 kW/m^2; Initial mandrel temperature, 480 K; Mandrel diameter, 12.7 cm (5 in).): (*a*) 10 layers wound; (*b*) 50 layers wound; and (*c*) 100 layers wound.

each wound layer has a similar temperature history. However, after the same winding time period, the degree of cure is less uniform in the cylinder wound on the higher-initial-temperature mandrel. This is due to the fact that the innermost layers attain high initial temperatures as a result of their contact (or close proximity) to the hot mandrel early in the winding process, which induces high reaction rates and rapid curing (illustrated in Fig. 9). From a practical perspective, by appropriately preheating the mandrel, the inner layers can reach a very high degree of cure by the end of the winding process.

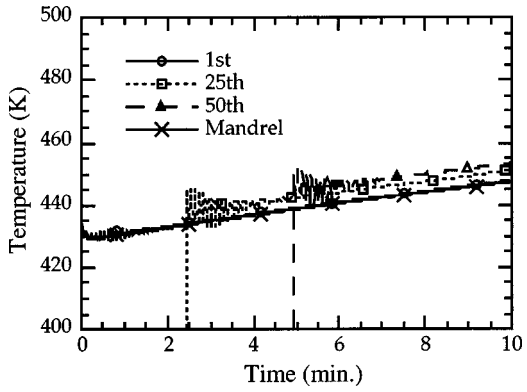

Fig. 6 Temperature histories in the 1st, 25th, and 50th wound layers of a composite cylinder wound from AS4/3501-6 prepreg. (Winding speed, 10 rpm; IR lamp heat flux, 48.6 kW/m^2; Initial mandrel temperature, 430 K; Mandrel diameter, 12.7 cm (5 in).)

4 Effects of Process Parameters and Process Window Development

The effect of initial mandrel temperature, IR heating region, and combination of IR power flux and winding speed upon the composite's temperature and degree of cure distributions are investigated. In addition, process windows, i.e., viable combinations

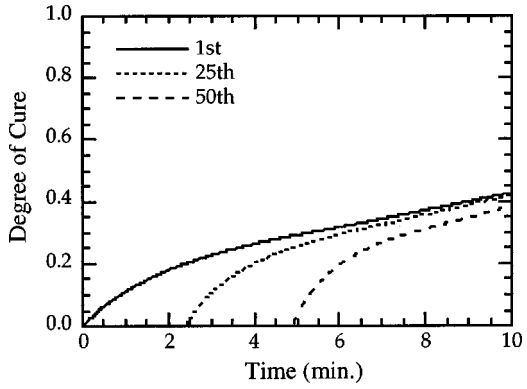

Fig. 7 Degree-of-cure evolutions in the 1st, 25th, and 50th wound layers of a composite cylinder wound from AS4/3501-6 prepreg. (Winding speed, 10 rpm; IR lamp heat flux, 48.6 kW/m^2; Initial mandrel temperature, 430 K; Mandrel diameter, 12.7 cm (5 in).)

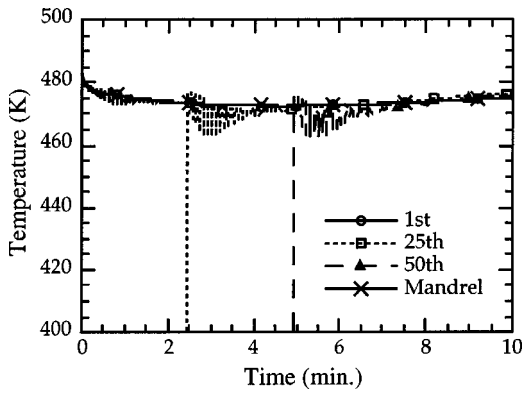

Fig. 8 Temperature histories in the 1st, 25th, and 50th wound layers of a composite cylinder wound from AS4/3501-6 prepreg. (Winding speed, 10 rpm; IR lamp heat flux, 48.6 kW/m^2; Initial mandrel temperature, 480 K; Mandrel diameter, 12.7 cm (5 in).)

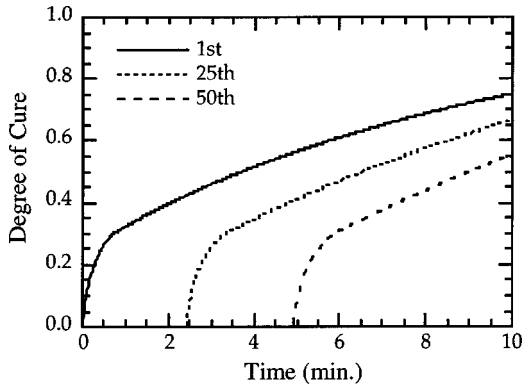

Fig. 9 Degree-of-cure evolutions in the 1st, 25th, and 50th wound layers of a composite cylinder wound from AS4/3501-6 prepreg. (Winding speed, 10 rpm; IR lamp heat flux, 48.6 kW/m^2; Initial mandrel temperature, 480 K; Mandrel diameter, 12.7 cm (5 in).)

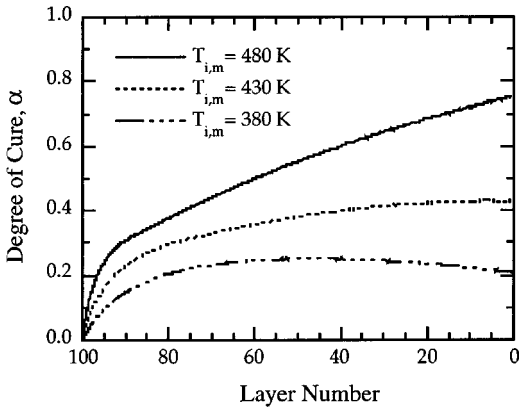

Fig. 11 Degree-of-cure distributions in the 100 layers of a composite cylinder wound from AS4/3501-6 prepreg for initial mandrel temperatures of 380, 430, and 480 K. (Winding speed, 10 rpm; IR lamp heat flux, 48.6 kW/m^2; Mandrel diameter, 12.7 cm (5 in).)

of manufacturing process parameters suitable to produce an acceptably cured part, are defined. A base reference case (100 prepreg layers wound at 10 rpm on a 480 K initial temperature mandrel having a 12.7 cm (5 in) diameter and heated by 48.6 kW/m^2 of radiant IR power) is used for comparison.

4.1 Effect of Initial Mandrel Temperature. Figure 10 displays the temperature distributions in the top 20 layers at the end of the 100-layer winding time for the three different initial mandrel temperatures: 380, 430, and 480K, assuming all other parameters are at their base reference state. Clearly, higher initial mandrel temperatures result in higher temperatures within the wound composite. If the mandrel has a lower initial temperature than the ''steady-state'' composite temperature for a given IR heat flux, winding speed and winding time, the mandrel effectively behaves like a heat sink, sapping energy from the composite winding.

Figure 11 shows the corresponding degree-of-cure distributions in the entire composite cylinder for the temperature profiles of Fig. 10. Remembering that the 380K-initial-temperature-mandrel composite demonstrates a more uniform, through-thickness temperature, it is not surprising that its first-wound layer's degree of cure is lower than that of the middle layer. Moreover, the first layer's curing time is longer than that of the middle layer (Fig. 4), since the latter experiences a higher processing temperature.

4.2 Effect of IR Heating Region. Figures 12 and 13 demonstrate the effect of the infrared heating region on the composite's temperature and degree-of-cure distributions by presenting the model results for two circumferential heating cases: one-quarter (or 90 deg) and one-half (or 180 deg) heating. In order to maintain approximately the same maximum processing temperature, distinct infrared heating powers must be used for each case: when the heating circumference is doubled, the heat flux is halved from 48.6 to 24.3 kW/m^2 for the same winding speed (10 rpm in this example). As might be expected, one-half heating produces slightly higher, but more uniform composite temperatures than those obtained from one-quarter heating. These two cases differ in the location of the maximum temperature: 90 deg and 180 deg for one-quarter and one-half heating, respectively. The final degree-of-cure distributions are almost identical, since the temperature histories are so similar. These results imply that the heating system design is relatively flexible and can be tailored based upon the characteristics of available IR lamp banks.

4.3 Correlation Between IR Heat Flux and Winding Speed Radiative power flux and winding speed combine to determine the net energy deposited onto the composite's surface. Proper combinations of heating power and winding speed can maintain the composite's processing temperature below the epoxy's degradation temperature T_{deg} =490 K for 3501-6 epoxy resin. The heating power for a given winding speed is found by running the numeri-

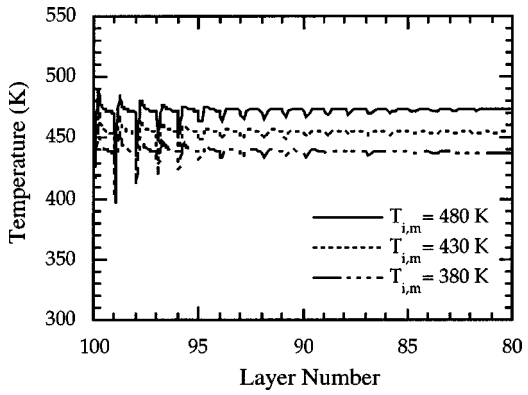

Fig. 10 Temperature histories in the top 20 layers of a composite cylinder wound from AS4/3501-6 prepreg for initial mandrel temperatures of 380, 430, and 480 K. (Winding speed, 10 rpm; IR lamp heat flux, 48.6 kW/m^2; Mandrel diameter, 12.7 cm (5 in).)

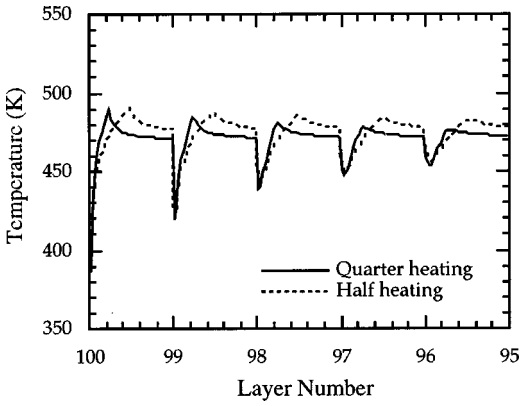

Fig. 12 Temperature distributions in the top 5 layers of a composite cylinder wound from AS4/3501-6 prepreg radiatively cured over one-quarter and one-half of its circumference. (Winding speed, 10 rpm; IR lamp heat flux, 48.6 kW/m^2; Mandrel diameter, 12.7 cm (5 in).)

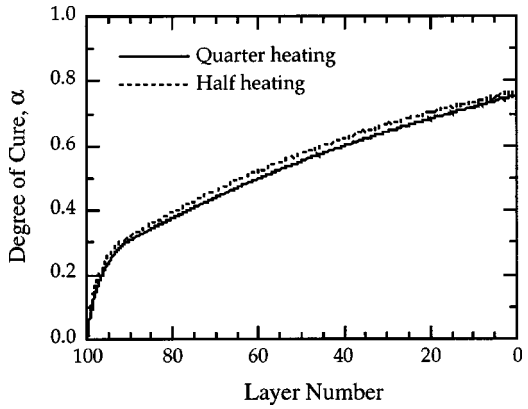

Fig. 13 Degree-of-cure distributions in top 100 layers a composite cylinder wound from AS4/3501-6 prepreg radiatively cured over one-quarter and one-half of its circumference. (Winding speed, 10 rpm; IR lamp heat flux, 48.6 kW/m^2; Mandrel diameter, 12.7 cm (5 in).)

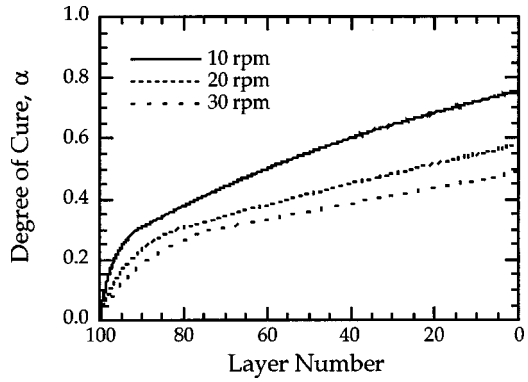

Fig. 15 Degree-of-cure distributions in top 100 layers a composite cylinder wound from AS4/3501-6 prepreg at the winding speeds of 10, 20, and 30 rpm. (Winding speed, 10 rpm; IR lamp heat flux, 48.6 kW/m^2; Mandrel diameter, 12.7 cm (5 in).)

cal model until this maximum temperature is reached; the resulting heating powers are 48.6, 84.0, and 114 kW/m^2 for 10, 20, and 30 rpm, respectively. As illustrated in Fig. 14, the resulting temperature distributions are strikingly similar for each case, except: in the immediate area of the heating region exit where the temperature profiles peak; and that higher winding speeds produce slightly more uniform circumferential temperature distributions. From a thermal perspective, changes in the winding speed yield subtle temperature differences as long as a proper heating power is provided.

Figure 15 shows the degree-of-cure distributions for the same three winding speeds. Interestingly, composites' maximum degree of cures are significantly different—in spite of the nearly identical processing temperatures. This is because a composite cylinder wound at 10 rpm is held at the processing temperature 3X longer than a comparable cylinder wound at 30 rpm, i.e., the total processing (therefore curing) time is inversely proportional to winding speed. As a result, composite cylinders wound at slower winding speeds require less extensive post-curing, which is typical of in-situ cured composites. To the extent that process-induced residual stresses are insignificant or irrelevant, high winding speeds can be combined with post-curing to increase the manufacturing throughput. However, in the more typical scenario in which residual stresses are significant contributors to reduced structural performance [32–36], winding speeds need to be more tightly controlled.

4.4 Process Window Development. Due to the strong correlation between winding speed and IR heat flux, appropriate combinations of these two parameters can be found to establish a process window [9,10,29] or set of manufacturing conditions which provide acceptable degrees of cure to achieve ''green'' strength (0.4–0.6) without degrading the epoxy resin (when $T \geqslant T_{deg}$). Figs. 16 and 17 depict the process windows for 90 deg heating of 12.7 cm (5 in) and 25.4 cm (10 in) mandrel-diameter composite cylinders, respectively. As the net heating area and linear winding speed both double with a corresponding doubling of the mandrel diameter, the net IR energy deposited at a given winding speed is independent of mandrel diameter, thus explaining the nearly identical process windows for these two different mandrel diameters. One also learns from these plots that there are thermodynamically imposed limits on how fast the cylinders may be wound (<20 rpm) and radiatively heated (<80 kW/m^2).

5 Conclusions

A fully-transient, two-dimensional, heat transfer model is established to investigate continuous, in-situ curing of a cylindrically wound composite of AS4/3501-6 prepreg, used due to the availability of necessary thermophysical and cure kinetics data. A Lagrangian approach, which traces each material point as it moves into the composite's interior, was found to more accurately predict the in-situ curing temperature and degree-of-cure histories than the previously used, quasi-steady-state Eulerian approaches,

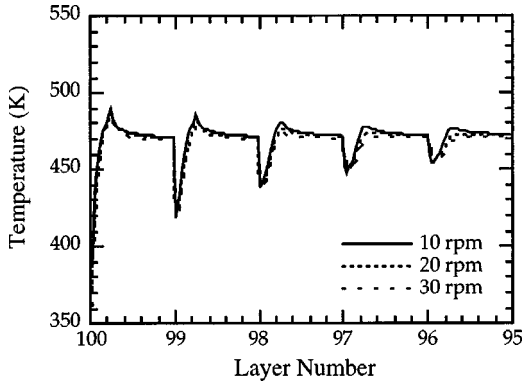

Fig. 14 Temperature distributions in the top 5 layers of a composite cylinder wound from AS4/3501-6 prepreg at the winding speeds of 10, 20, and 30 rpm. (Winding speed, 10 rpm; IR lamp heat flux, 48.6 kW/m^2; Mandrel diameter, 12.7 cm (5 in).)

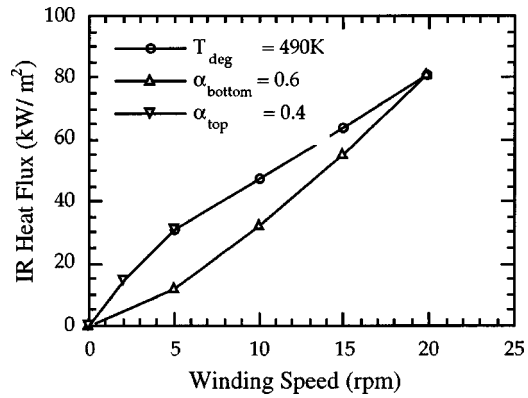

Fig. 16 Process window for a AS4/3501-6 prepreg composite cylinder wound on a 12.7 cm (5 in) diameter mandrel and radiatively cured over one-quarter of its circumference

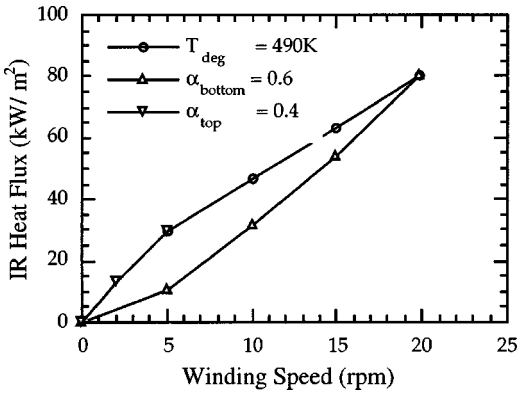

Fig. 17 Process window for a AS4/3501-6 prepreg composite cylinder wound on a 25.4 cm (10 in) diameter mandrel and radiatively cured over one-quarter of its circumference

which underpredict thermal losses. The model and its computational implementation were verified using analytical solutions and actual experiments.

During winding, the top layer's maximum temperature increases with total number of layers wound, demonstrating that a given incoming prepreg tape's temperature history evolves with time. Moreover, with appropriate mandrel preheating, the inner layers can reach a very high degree of cure by the end of the winding process, revealing that the mandrel's initial temperature has a significant effect on the composite's temperature and degree-of-cure history. Substantial increases in the winding speed have little or no effect on the composite's temperature history, but can significantly reduce the corresponding degree-of-cure. The development of structurally debilitating residual stresses is very often an important concern in selecting process parameters, such as winding speed and heating power.

Taking advantage of the strong correlation between winding speed and IR heat flux, process windows can be used to guide the selection of manufacturing process parameters. These definitively show that there are thermodynamically imposed limits on how fast the cylinders may be wound and radiatively cured.

Acknowledgments

The authors gratefully acknowledge the support of this research by: the U.S. Office of Naval Research through grant number ONR-N00014-92-J-1470 administered by Dr. Yapa D. S. Rajapakse; and the National Science Foundation through grant numbers DDM-9109592, DDM-9258413 and DDM-9311241, administered by Dr. Bruce Kramer; and the Texas Advanced Technology Program, grant number 1993-003658-359. Helpful discussions with Dr. B.-C. Chern are acknowledged, as is assistance in the literature survey and manuscript preparation by David J. Fowler and Mahan H. Mirza. Finally, ancillary support from the University of Texas at Austin's Bureau of Engineering Research is also acknowledged.

Nomenclature

Ai = ratio of anisotropic thermal conductivities, $k_{2,\mathrm{ref}}/k_{1,\mathrm{ref}}$
Ac = ratio of material accretion to convection loss, $\rho_c c_{P,c} V_t / h_{\mathrm{ref}}$
Bi = Biot number, $h_{\mathrm{ref}} r_2 / k_{1,\mathrm{ref}}$
Ch = ratio of heat of reaction to radiant heating input, $k_{1,\mathrm{ref}} \rho_r (1-\nu_f) H_U / \rho_c c_{P,\mathrm{ref}} r_2 \sigma T_{\mathrm{lamp}}^4$
CP = dimensionless specific heat of composite, $c_{P,c}/c_{P,\mathrm{ref}}$
c_P = specific heat, J/kg·K
Da = Damköhler number, $\rho_c c_{P,\mathrm{ref}} r_2^2 \overline{K_1} / k_{1,\mathrm{ref}}$
ΔE = activation energy for cure kinetics, J/mol
$F_{d-\mathrm{lamp}}$ = configuration factor from composite element to IR lamp
g = gravitational constant, 9.81 m/sec^2
H = dimensionless heat transfer coefficient, h/h_{ref}
H_r = dimensionless radiation heat transfer coefficient, h_r/h_{ref}
Hc = dimensionless specific heat of mandrel, $\rho_m c_{P,m}/\rho_c c_{P,\mathrm{ref}}$
H_T = heat of reaction for an isothermal scan at a temperature T, J/kg
H_U = ultimate heat of reaction, 4.227×10^5 J/kg
h = heat transfer coefficient, W/m^2·K
h_r = radiation heat transfer coefficient, $\varepsilon\sigma(T+T_\infty)(T^2+T_\infty^2)$
K_1 = dimensionless thermal conductivity in r direction, $k_1/k_{1,\mathrm{ref}}$
K_2 = dimensionless thermal conductivity in θ direction, $k_2/k_{1,\mathrm{ref}}$
$\overline{K_1}$, $\overline{K_2}$ = Arrhenius constants for cure kinetics, sec^{-1}
k = thermal conductivity, W/m·K
k_1, k_2 = thermal conductivity in r and θ directions, W/m·K
N_{Pr} = Prandtl number, $(\nu\rho c_P/k)_{\mathrm{air}}$
N_{Ra} = Rayleigh number, $[8gT_f^{-1}(T_3-T_\infty)r_3^3/\nu^2]\cdot N_{\mathrm{Pr}}$
n = cure reaction order
q = heat flux from IR lamp bank, $\sigma T_{\mathrm{lamp}}^4$
R = dimensionless radius or radial direction, r/r_2
r = radius or radial direction, m
r_1, r_2 = inner and outer radius of mandrel, m
r_3 = outer radius of composite cylinder, m
R = universal gas constant, 8.315 J/mol·K
T = temperature, K
T_f = film temperature, $(T_3(\tau)+T_\infty)/2$
t = time, sec
V_t = material accretion speed in the radial direction

Greek Symbols

α = degree of cure
α_a = absorptivity
β = isothermal degree of cure
β_{bp} = isothermal degree of cure at break point [21]
ε = emissivity
η = efficiency of IR lamp
Θ = dimensionless temperature, $h_{\mathrm{ref}}T/q_{\mathrm{lamp}}$
θ = circumferential angle, rad
ν = kinematic viscosity of air, m^2/sec
ν_f = fiber volume fraction
ρ = density, kg/m^3
σ = Stefan-Boltzmann constant, 5.670×10^{-8} W/m^2 K^4
τ = dimensionless time, $k_{1,\mathrm{ref}}t/\rho_c c_{P,\mathrm{ref}} r_2^2$
ω = angular speed of mandrel, rad/sec

Subscripts

1,2,3 = interfaces at r_1, r_2, r_3 (Fig. 2)
a = air
bottom = bottom
c = composite
deg = degradation
f = fiber
i = initial
l = laydown point
m = mandrel
r = resin
ref = reference temperature, 490 K
top = top
∞ = surrounding air

References

[1] Hayward, J. S., and Harris, B., 1990, ''Effect of Process Variables on the Quality of RTM Mouldings,'' SAMPE J., **26**, pp. 39–46.

[2] Kittelson, J. L., 1990, ''Tape Winding: A Logical Progression and Alternative to Filament Winding,'' SAMPE J., **26**, pp. 37–42.

[3] Sarrazin, H., and Springer, G. S., 1995, ''Thermochemical and Mechanical Aspects of Composite Tape Laying,'' J. Compos. Mater., **29**, pp. 1908–1943.

[4] Lee, S. Y., and Springer, G. S., 1988, ''Effects of Cure on the Mechanical Properties of Composites,'' J. Compos. Mater., **22**, pp. 15–29.

[5] Peters, W. M., and Springer, G. S., 1988, ''Effects of Cure and Sizing on Fiber-Matrix Bond Strength,'' J. Compos. Mater., **21**, pp. 157–171.

[6] Spencer, B. E., and Steele, L. F., 1984, ''Thick Wall Structures—Design and Manufacturing Techniques,'' 29th National SAMPE Symposium, pp. 80–91.

[7] Bogetti, T. A., and Gillespie, Jr., J. W., 1991, ''Two-Dimensional Cure Simulation of Thick Thermosetting Composites,'' J. Compos. Mater., **25**, pp. 239–273.

[8] Burwasser, J. T., and Springer, G. S., 1988, ''Electromechanical Curing of Filament Wound Composite Cylinders,'' J. Compos. Mater., **22**, pp. 81–100.

[9] Chern, B.-C., Moon, T. J., and Howell, J. R., 1995, ''Thermal Analysis of In-Situ Curing for Thermoset, Hoop-Wound Structures Using Infrared Heating: Part I—Predictions Assuming Independent Scattering,'' ASME J. Heat Transfer, **117**(3), pp. 674–680.

[10] Chern, B.-C., Moon, T. J., and Howell, J. R., 2002, ''On-Line Processing of Unidirectional Fiber Composites Using Radiative Heating: I. Model,'' J. Compos. Mater., **36**.

[11] Kim, C., Teng, H., Tucker, C. L., and White, S. R., 1995, ''The Continuous Curing Process for Thermoset Polymer Composites. Part 1: Modeling and Demonstration,'' J. Compos. Mater., **29**, pp. 1222–1252.

[12] Yokota, M. J., 1978, ''In-Process Controlled Curing of Resin Matrix Composites,'' SAMPE J., **14**(4), pp. 11–17.

[13] Hjellming, L. N., and Walker, J. S., 1989, ''Thermal Curing Cycles for Composite Cylinders with Thick Walls and Thermoset Resins,'' J. Compos. Mater., **23**, pp. 1048–1064.

[14] Martinez, G. M., 1991, ''Fast Cures for Thick Laminated Organic Matrix Composites,'' Chem. Eng. Sci., **46**, pp. 439–450.

[15] Tang, J., Lee, W. I., and Springer, G. S., 1987, ''Effects of Cure Pressure on Resin Flow, Voids, and Mechanical Properties,'' J. Compos. Mater., **21**, pp. 421–440.

[16] Twardowski, T. E., Lin, S. E., and Geil, P. H., 1993, ''Curing in Thick Composite Laminates: Experiment and Simulation,'' J. Compos. Mater., **27**, pp. 216–250.

[17] Korotokov, V. N., Chekanov, Y. A., and Rozenberg, B. A., 1993, ''The Simultaneous Progress of Filament Winding and Curing for Polymer Composites,'' Compos. Sci. Technol., **47**, pp. 383–388.

[18] Kim, J., Moon, T. J., and Howell, J. R., 1996, ''Effects of Process Variables on In-Situ Curing For Thick Composites Using Infrared Heating,'' ASME International Mechanical Engineering Congress and Exhibition, Vol. 96-WA/AMD-11, pp. 1–14.

[19] Chern, B.-C., Moon, T. J., and Howell, J. R., 1994, ''Modeling of Radiation-Initiated Cure-on-the-Fly of Epoxy-Matrix Composite Cylinders,'' J. Mater. Process. Manuf. Sci., **2**(4), pp. 373–390.

[20] Chern, B.-C., Moon, T. J., Howell, J. R., and Tan, W., 2002, ''New Experimental Data for Enthalpy of Reaction and Temperature- and Degree-of-Cure-Dependent Specific Heat and Thermal Conductivity of the Hercules 3501-6 Epoxy System,'' J. Compos. Mater., **36**(17), pp. 2061–2072.

[21] Kim, J., Moon, T. J., and Howell, J. R., 2002, ''Cure Kinetic Model, Heat of Reaction and Glass Transition Temperature of AS4/3501-6 Graphite/Epoxy Prepregs,'' J. Compos. Mater., **36**(21), pp. 2479–2498.

[22] Pitchumani, R., and Yao, S.-C., 1993, ''Non-Dimensional Analysis of an Idealized Thermoset Composites Manufacture,'' J. Compos. Mater., **27**, pp. 613–636.

[23] Etemad, G. A., 1955, ''Free-Convection Heat Transfer from a Rotating Horizontal Cylinder to Ambient Air With Interferometric Study of Flow,'' Trans. ASME, pp. 1283–1289.

[24] Patankar, S. V., 1980, *Numerical Heat Transfer and Fluid Flow*, Hemisphere Publishing Corporation, Washington.

[25] Schneider, G. E., and Zedan, M., 1981, ''A Modified Strongly Implicit Procedure for the Numerical Solution of Field Problems,'' Numer. Heat Transfer, **4**, pp. 1–19.

[26] Stone, H. L., 1968, ''Iterative Solution of Implicit Approximations of Multidimensional Partial Differential Equations,'' SIAM (Soc. Ind. Appl. Math.) J. Numer. Anal., **5**, pp. 530–559.

[27] Incropera, F. P., and DeWitt, D. P., 1990, *Introduction to Heat Transfer*, 2nd ed., John Wiley & Sons, New York.

[28] Chern, B.-C., Moon, T. J., and Howell, J. R., 1993, ''Measurement of the Temperature and Cure-Dependence of the Thermal Conductivity of Epoxy Resin,'' Exp. Heat Transfer, **6**, pp. 157–174.

[29] Chern, B.-C., Moon, T. J., and Howell, J. R., 2002, ''On-Line Processing of Unidirectional Fiber Composites Using Radiative Heating: II. Radiative Properties, Experimental Validation and Process Parameter Selection,'' J. Compos. Mater., **36**(16), pp. 1935–1965

[30] Kim, J., 1997, ''Thermal Modeling of In-Situ Curing of Composite Cylinders Using Infrared Radiation,'' Ph.D. dissertation, The University of Texas at Austin, Austin, TX.

[31] Kim, J., Moon, T. J., and Howell, J. R., 2002, ''In-Situ Curing of Helically-Wound Composite Cylinders: II. Materials Characterization and Experimental Validation,'' J. Compos. Mater., in press.

[32] Yee, K.-C., and Moon, T. J., 2003, ''Compressive Strengths of In-Situ Cured Graphite/Epoxy and Glass/Epoxy Composite Cylinders,'' J. Reinf. Plast. Compos., **22**(3), pp. 131–147.

[33] Yee, K.-C., and Moon, T. J., ''Assessment of In-Situ Cured Thermoset Composite Cylinders: Residual Stresses and Compressive Strength,'' Composites, Part A, to appear.

[34] Yee, K.-C., and Moon, T. J., 2002, ''Process-Induced Residual Stresses in a Continuously-Cured, Hoop-Wound Thermoset Composite Cylinder, II: Validation,'' J. Compos. Mater., in press.

[35] Kugler, D., and Moon, T. J., 2002, ''The Effects of Mandrel Material and Tow Tension on Defects and Compressive Strength of Hoop-Wound, On-Line Consolidated, Composite Rings,'' Composites, Part A, **33**(6), pp. 861–876.

[36] Yee, K.-C., and Moon, T. J., 2002, ''Plane Thermal Stress Analysis of an Orthotropic Cylinder Subject to an Arbitrary, Transient, Asymmetric Temperature Distribution,'' ASME J. Appl. Mech., **69**, pp. 632–640.

Mitigation of Particulate Fouling by Ozonation

Bang-Yenn Wu
e-mail: bywu@sitc.edu.tw
Assistant Professor
Department of Mechanical Engineering,
De-Lin Institute of Technology,
Taiwan, ROC

S. H. Chan
President
Office of the President,
Yuan-Ze University,
Taiwan, ROC

Heat transfer surface fouling introduces a major uncertainty into the design and operation of cooling water systems. Fouling caused by calcium carbonate ($CaCO_3$) typically occurs on heat transfer surfaces. Ozone has been successfully used for more than 90 years as a disinfectant in drinking water. Recently, it has been proposed to use ozone for cooling tower water treatment. In this research, the effectiveness of mitigation of calcium carbonate particulate fouling by ozone was studied systematically. The experimental results show that, at low Reynolds numbers, though the ozonation retards the initial calcium carbonate particulate fouling rate, the retardation led to a non-porous deposit layer and a higher asymptotic fouling resistance. However, at high Reynolds numbers, ozonation was found to reduce the asymptotic fouling resistance. [DOI: 10.1115/1.1518493]

Keywords: Fouling, Heat Transfer, Heat Exchangers, Particulate

Introduction

Fouling is a major unsolved problem in heat exchanger design. Fouling of heat exchanger increases capital expenditure, energy input and maintenance cost. Fouling by calcium carbonate is the most common deposition mechanism in cooling tower operation. The solubility of calcium carbonate in water decreases with increasing temperature. Hence, calcium carbonate fouling often occurs on heat exchanger surfaces. Many experimental studies and analytical modeling of $CaCO_3$ scaling in laminar falling film and turbulent shell-and-tube flows have been reported [1–9]. A review of recent advances can be found elsewhere [10].

Ozone has been used for water treatment for more than ninety years on European continent and proved to be quite successful in disinfection of water and wastewater. In recent years, ozone has been used in calcium carbonate fouling control. Several reports [11–15] showed that ozone can effectively prevent or eliminate calcium carbonate scaling. However, many opposite results [16–20] have shown otherwise in recent years.

Therefore the objective of our research is to investigate systematically over a broad range of Reynolds number the mitigation effect of ozonation on calcium carbonate scale formation in a well controlled environment. The first part of the study investigated the mitigation effect on molecular calcium carbonate scaling, while the present one on particulate calcium carbonate scaling. The result of the former has been reported elsewhere [21] and the latter is now given below.

Experimental Setup and Procedure

The experimental setup, shown in Fig. 1, was designed and built to investigate effects of ozone on calcium carbonate particulate fouling of a heat transfer surface in an open recirculating cooling system. Visual control in the fouling experiment was desirable. Thus, Excelon® R-4000 transparent, rigid PVC (Schedule 40) pipes and transparent Excelon® fittings were used in this setup. The annular test assembly consisted of an outer transparent Pyrex cylinder, 45.72 cm long with an inside diameter of 2.54 cm, and an inner heater rod 1.27 cm outer diameter and 12 cm long. The detail description of the experimental setup is given elsewhere [22].

In order to form calcium carbonate particles in advance, 47g calcium chloride, 41g sodium bicarbonate and 46g sodium chloride were added into the cooling tower basin. Many calcium carbonate particles were founded in the cooling tower basin. A filter (about 25 μm size filter paper) was installed in the inlet of the main test loop to prevent particles greater than 25 μm from reaching the test section. The water mixture was circulated through the annular test section to form calcium carbonate particulate fouling on the outer surface of the inner heater rod. Under the uniform heat flux condition used in this research, an instantaneous average heat transfer coefficient can be calculated from the measured temperatures and heat flux by

$$h_m = q_w/(T_w - T_b) \tag{1}$$

where q_w is heat flux input, T_w and T_b are temperature of the heater wall and bulk mixture, respectively. Hence, the following fouling resistance can be calculated by maintaining constant q_w and T_b.

$$R_f = (T_{w,f} - T_{w,c})/q_w \tag{2}$$

where subscripts f and c indicate fouling and clean tube conditions, respectively. In all experiments, 700 watts of heat load were used and the inlet water was at the room temperature, i.e., approximately at 24°C.

Experimental Results and Discussions

Several experiments have been carried out during this research. The initial thermal-hydraulic and chemical conditions of the experiments are given in Table 1. The uncertainties for the experimental data are listed in Table 2.

The solubility of calcium carbonate is a function of temperature, which can be expressed as [23]

$$-\log K_{sp} = 13453 - 3000/T - 0.0401T \tag{3}$$

At 25°C, the calcium carbonate solubility product (K_{sp}) is about $3.8*10^{-9}$ M^2. The ion addition in the experiments was around $9.64*10^{-3}M^2$, far exceeding the solubility product. Therefore, some of the chemical additions did not completely dissolve in the water solution and homogeneous crystallization occurred in the bulk solution. Besides, the impurity of the tap water and the additions of sodium chloride provided the sites where the heterogeneous crystallization occurs. Many insoluble calcium carbonate particles were found in the cooling tower basin. A filter (about 25 μm size) was installed in the inlet of the main test loop to prevent larger calcium carbonate particles from reaching the test section. But it did allow small particles to flow through this filter into the main test loop. This phenomenon was confirmed by the observation of the small particles in the working fluid passing through the test section and by the observation of a jump in fluid conductivity

Contributed by the Heat Transfer Division for publication in the JOURNAL OF HEAT TRANSFER. Manuscript received by the Heat Transfer Division January 15, 2002; revision received June 26, 2002. Associate Editor: C. H. Amon.

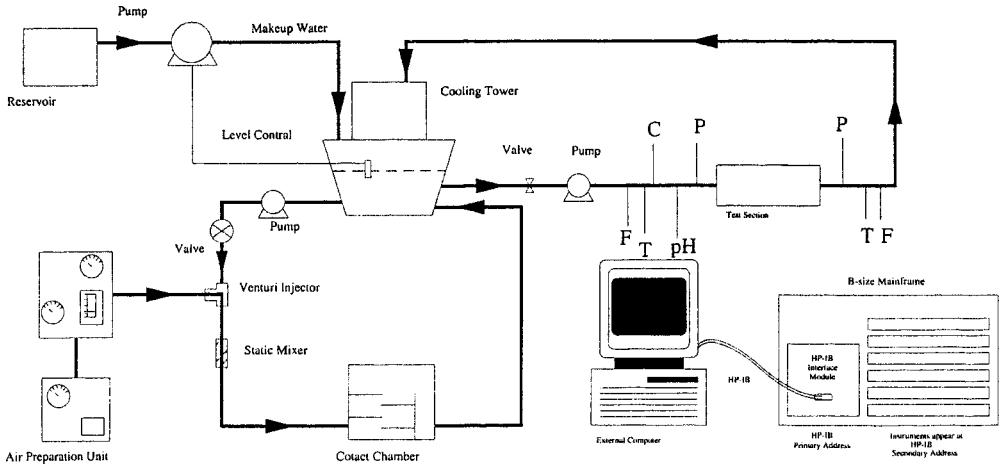

Fig. 1 Experimental setup

after the chemicals were added. Therefore, the particulate calcium carbonate fouling was assumed to be the dominant fouling mechanism in these experiments.

For particulate fouling, turbulent core motion and Brownian motion presumably caused the deposition of calcium carbonate particles on the heated tubular surface. No induction was observed for particulate fouling in all experiments (see Figs. 2–4), because small calcium carbonate particles settled on the surface which acted as seeding sites to bond other free particles.

Since the self-decomposition rate of ozone to oxygen increases with temperature, some of the dissolved ozone self-decomposed to oxygen in the vicinity of heater surface. In view that the solubility of ozone is thirteen (13) times that of oxygen, some self-decomposed oxygen could not dissolve in the solution near the heater surface. This insoluble oxygen generates small bubbles on the heater surface so that the gas layer acted to prevent calcium carbonate particles from settling on the surface. This retardation of settling decreases the initial fouling rate of particulate fouling. Figure 2 shows the fouling resistance curves with ozonation and without ozonation at Reynolds number 9400. The initial fouling rate with ozonation is $0.4*10^{-5}$ m^2-°C/W-hr, less than that without ozonation, $1.75*10^{-5}$ m^2-°C/W-hr. Similarly, the fouling resistance curves at Reynolds numbers 6000 and 7500 are shown in Figs. 3 and 4. The initial fouling rate with ozonation and without

Table 1 Initial experimental conditions

Test #	Re	T_{inlet} (°C)	O_3 (mg/l)	pH	Conductivity (mg/l)	P-alk[1]	T-alk[2]	Ca-Hard[3]
1-1	9400	24.3	X	7.5	3031	0	457	977
1-2	9400	23.6	0.47	8.3	3046	0	496	913
2-1	6000	24	X	7.9	3028	0	515	903
2-2	6000	24.2	0.31	8.2	3027	0	489	861
3-1	7500	24.1	X	8.0	3052	0	570	1028
3-2	7500	24	0.38	8.1	3055	0	594	1001

[1] Phenolphthalein Alkalinity (mg/l as $CaCO_3$), [2] Total Alkalinity (mg/l as $CaCO_3$),

[3] Calcium Hardness (mg/l as $CaCO_3$)

Table 2 Uncertainty data

Parameters	q (watt/m^2)	$T_{w,f}$ (°C)	$T_{w,c}$ (°C)	R_f (*10^{-4} m^2-°C/watt)
Uncertainty	137000±8000	100±1	90±1	0.73±0.11
Tolerance(%)	5.8	1.0	1.1	15.1

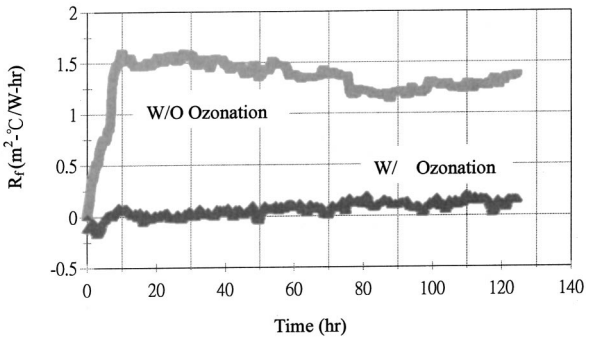

Fig. 2 Comparison of calcium carbonate particulate fouling curves with and without ozonation at Re=9400 (Test 1-1 and Test 1-2)

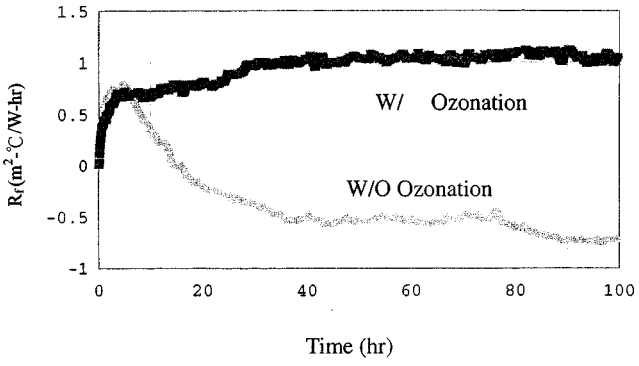

Fig. 3 Comparison of calcium carbonate particulate fouling curves with and without ozonation at Re=6000 (Test 2-1 and Test 2-2)

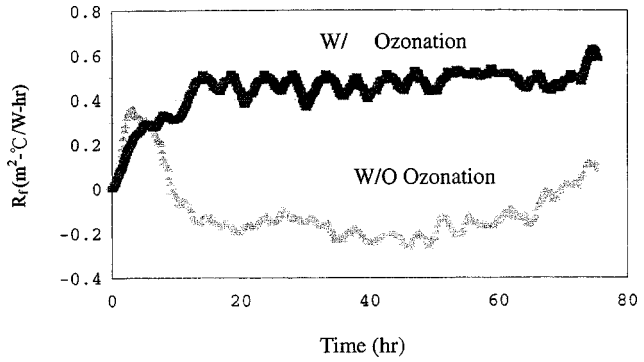

Fig. 4 Comparison of calcium carbonate particulate fouling curves with and without ozonation at Re=7500 (Test 3-1 and Test 3-2)

ozonation at Reynolds number 6000 were $1*10^{-5}$ m^2-°C/W-hr and $3*10^{-5}$ m^2-°C/W-hr, respectively, while at Reynolds number 7500, they were $0.44*10^{-5}$ m^2-°C/W-hr and $1.8*10^{-5}$ m^2-°C/W-hr with and without ozonation, respectively. These initial fouling rates are summarized and compared in Table 3. When ozonation was applied, even though the initial fouling rates were found to be less than that without ozonation for all experimental conditions test here, the final asymptotic values of fouling resistance were not necessary lower. The asymptotic value was found to be lower at a high Reynolds number of 9400 (Fig. 2), but was higher at the other lower Reynolds number conditions of 6000 (Fig. 3) and 7500 (Fig. 4). A possible explanation is given next.

The rate of ozone decomposition in water increases as pH increases. When pH increases (say, >8), ozone will decompose to the very short-lived hydroxyl free radical (HO·) as follows:

$$O_3 + OH^- \rightarrow HO_2^- + O_2$$

$$HO_2^- + O_3 \rightarrow O_3^- + HO_2$$

$$O_3^- + H_2O \rightarrow OH\cdot + O_2 + OH^-$$

As pH approaches 10, very little molecular ozone can be detected in solution. Bicarbonate (HCO_3^-) and carbonate (CO_3^{-2}) anions which can present in natural water are excellent scavengers (destroyers) of hydroxyl free radicals. Therefore, when the pH of recirculating water is high (say, >8) and the total alkalinity is high (>200 mg/l, see Table 1), ozone can decompose to hydroxyl free radicals, which in turn can react with bicarbonate or carbonate anions readily. This reaction destroys the original equilibrium state in the solution by changing the composition and properties of the solution, all of which can alter the heat transfer coefficient. In order to verify this heat transfer coefficient alteration by ozonation, another run to test the effects of ozonation without adding any chemicals on heat transfer coefficient of clean tube condition was carried out. First of all, the experiments without adding any chemicals and ozone were performed for several different Reynolds number conditions in the same experimental setup. From the recorded temperature readings and heat input, the heat transfer coefficients for different Reynolds numbers were calculated. Then, repeat those runs by adding ozone. For the range of the Reynolds numbers tested in fouling experiments, the average heat transfer coefficient with ozonation was found to be higher than the one without ozonation as illustrated in Fig. 5. Higher heat transfer coefficient means a lower surface temperature and hence a lower fouling resistance. Thus, the slower initial fouling rate (see Figs. 2–4) in the test run with ozonation as compared to that without ozonation can now be explained. It was caused by two primary effects: (1) Small bubbles formed on the heater surface due to the ozone solubility changed on heated surface. The bubble formation and departure break the laminar sublayer and enhance heat transfer. (2) The destruction of the original equilibrium state of the solution by hydroxyl free radicals due to decomposition of ozone at higher pH value.

The porosity of the deposition layer of calcium carbonate particles was also investigated. In reference to Table 3, the two highest initial fouling rates were for the test runs at Re=6000 and 7500 without ozonation. Experimentally, the deposition layers of these two runs were found to be porous in structure. As shown in Figs. 3 and 4, their initial fouling resistances increased rapidly but then decreased after six hours of operation. Eventually the fouling resistance was found to be less than zero, which means that the heat transfer equipment had a better heat transfer coefficient than the clean tube condition. The latter was likely caused by heat transfer enhancement due to the surface roughness of the deposit, which overshadowed the heat transfer reduction due to the formation of the porous deposit layer. In the corresponding test runs with ozonation, the fouling layers were found to be nonporous and their fouling resistances were increased to higher asymptotic values than those without ozonation (see Figs. 3 and 4). However, in the test runs at Re=9400 (Fig. 2), no porous deposits were observed either with or without ozonation. Both fouling resistance curves were found to increase with time. But the asymptotic value of the one with ozonation was found to be less than that without ozonation. It is noted that, for this ozonation run at Re=9400, the initial fouling rate is the slowest one (see Table 3) and the deposit layer was found to be the smoothest (nonporous). It is further noted that ozonation in this run was found to have a positive effect in mitigating the initial stage of the calcium carbonate particulate fouling. In reference to Table 3, it can also be alternately stated that, whether ozonation was executed or not, the experiments showed that a porous calcium carbonate deposit was formed when the initial fouling rate was equal to or greater than $1.8*10^{-5}$ m^2-°C/W-hr (Re≤7500). However, when the initial fouling rate equal to or less than $1.75*10^{-5}$ m^2-°C/W-hr (Re ≥9400), a nonporous calcium carbonate deposit layer was found.

Table 3 The initial fouling rate (m^2-°C/W-hr)

Reynolds number	6000	7500	9400
W/ Ozonation	$1*10^{-5}$	$0.44*10^{-5}$	$0.4*10^{-5}$
W/O Ozonation	<$3*10^{-5}$>	<$1.8*10^{-5}$>	$1.75*10^{-5}$

< > indicates that porous deposits were formed

Conclusions

Ozonation was found to reduce the initial fouling rate in calcium carbonate particulate fouling. This occurred because of the

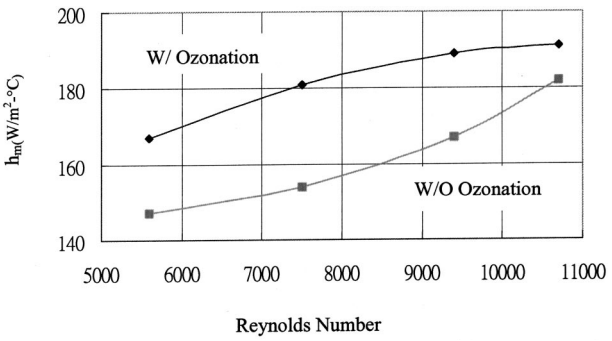

Fig. 5 Effects of ozonation on heat transfer coefficient for different Reynolds number

destruction of original equilibrium state by hydroxyl free radicals due to decomposition of ozone in high pH solutions, and because of a very thin oxygen layer on the heater surface by ozonation due to the solubility difference between ozone and oxygen. Moreover, calcium carbonate particulate fouling with ozonation did not form a porous deposit at Reynolds numbers of 6000, 7500, and 9400. At Reynolds numbers of 6000 and 7500 without ozonation, the rapid initial fouling rates led to porous calcium carbonate deposits, the roughness of which promoted better transfer effects than that with ozonation. Also ozonation was found to lead to a higher asymptotic fouling resistance in spite of the slower initial fouling rate. However, at higher Reynolds number of 9400, both test runs with and without ozonation did not form porous layers, and ozonation was found to reduce the asymptotic fouling resistance of calcium carbonate fouling.

Acknowledgments

The donation of the cooling tower by the Union Chemical Laboratories of the Industrial Technology Research Institute (ITRI) in Taiwan, the variac by Dr. Knudsen at Oregon University, the data acquisition system by Sundstrand Corporation and the loan of the test section by Ashland Company are appreciated. This project was sponsored by the U.S. National Science Foundation, grant no. CTS-9117230.

Nomenclature

h_m = average heat transfer coefficient, W/m^2-°C
K_{sp} = calcium carbonate solubility product, M^2
q_w = heat flux input, W
R_f = fouling rate, m^2-°C/W-hr
T_w = temperatures of the heater wall, °C
T_b = temperatures of bulk mixture, °C
$T_{w,f}$ = temperatures of the heater wal of fouling condition, °C
$T_{w,c}$ = temperatures of the heater wall of clean condition, °C

References

[1] Wahl, E. F., 1977, *Geothermal Energy Utilization*, John Wiley, New York.
[2] Taborek, J., Aoki, T., Ritter, R. B., Palen, J. W., and Kundsen, J. G., 1972, ''Predictive Method for Fouling Behavior,'' Chem. Eng. Prog., **68**(7), pp. 69–78.
[3] Cleaver, J. W., and Yates, B., 1976, ''The Effect of Re-entrainment on Particle Deposition,'' Chem. Eng. Sci., **31**, pp. 835–845.
[4] Hasson, D., Avriel, M., Resnick, W., Rozenman, T., and Windreich, S., 1968, ''Mechanism of Calcium Carbonate Deposition on Heat-Transfer Surfaces,'' Ind. Eng. Chem. Fundam., **7**(1), pp. 59–65.
[5] Hasson, D., and Perl, I., 1981, ''Scale Deposition in a Laminar Falling-Film System,'' Desalination, **37**, pp. 279–292.
[6] Sheikholeslami, R., and Watkinson, A. P., 1986, ''Scaling of Plain and Externally Finned Heat Exchanger Tubes,'' ASME J. Heat Transfer, **108**, pp. 147–152.
[7] Watkinson, A. P., and Martinez, O., 1975, ''Scaling of Heat Exchanger Tubes by Calcium Carbonate,'' ASME J. Heat Transfer, 504–508.
[8] Chan, S. H., and Ghassemi, K. F., 1991, ''Analytical Modeling of Calcium Carbonate Deposition for Laminar Falling Films and Turbulent Flow in Annuli: Part I—Formulation and Single-Species Model,'' ASME J. Heat Transfer, **113**, pp. 735–740.
[9] Chan, S. H., and Ghassemi, K. F., 1991, ''Analytical Modeling of Calcium Carbonate Deposition for Laminar Falling Films and Turbulent Flow in Annuli: Part II—Multi-Species Model,'' ASME J. Heat Transfer, **113**, pp. 741–746.
[10] Chan, S. H., 1992, ''Heat and Mass Transfer in Fouling,'' *Annual Review of Heat Transfer*, C. L. Tien, ed., **4**, pp. 363–399.
[11] Osgood, S., 1991, ''Ozonation of Cooling Tower Water: A Case Study,'' Water Conservation Unit, Oakland, CA.
[12] Pryor, A. E., 1991, ''Ozone Treatment of Cooling Water at a Gas Production Facility,'' Corrosion/91, Paper No. 583, NACE, TX.
[13] Grosz, G. A., and Batchlor, D. R., 1991, ''The Efficiency of Ozone for Cooling Tower Water Treatment,'' *Proceeding of the 10th Ozone World Congress*, International Ozone Association, Stamford, CT, **1**, pp. 357–370.
[14] Merritt, J. A., 1992, ''Update of Cooling Tower Ozonation at an Organic Chemical Manufacturing Facility,'' Technical Paper No. TP92-04, Cooling Tower Institute, Houston, TX.
[15] Gill, G., 1996, ''Eight Years of Continuous Cooling Tower Ozonation,'' Corrosion/96, Paper No. 496, NACE, Houston, TX.
[16] McGrane, W. K., 1992, ''Ozone Cooling Tower Treatment With and Without Mineral Removal,'' Ozone. Sci. Eng., **14**, pp. 231–244.
[17] Lawson, T. S., and Feltzin, A. E., 1992, ''Ozonation in a Carbon Dioxide Plant Cooling System,'' Corrosion/92, Paper No. 393, NACE Houston, TX.
[18] Burda, P. A., and Healey, B. A., 1993, ''Performance and Mechanisms of Cooling Tower Treatment by Ozone,'' Corrosion/93, Paper No. 488, NACE, Houston, TX.
[19] Rao, N. M., 1994, ''Towards Development of An Ozone Compatible Cooling Water Treatment,'' Corrosion/94, Paper No. 469, NACE, Houston, TX.
[20] Nasrazadani, S., and Chao, Tah Jin, 1994, ''Laboratory Evaluations of Ozone as a Scale Inhibitor for Use in Open Recirculating Cooling System,'' ASHRAE Research Project 765-RP Final Report, ASHRAE, Inc., Atlanta, GA.
[21] Wu, Bang-Yennhan, and Chan, S. H., 1997, ''Effects of Ozonation on Fouling of Heat Exchangers,'' *National Heat Transfer Conference*, Baltimore, MD.
[22] Wu, Bang-Yenn, 1996, ''Effects of Ozonation on Fouling of Heat Exchangers,'' Ph.D. thesis, University of Wisconsin-Milwaukee, Milwaukee, WI.
[23] Stumm, W., and Morgan, J. J., 1981, *Aquatic Chemistry: An Introduction Emphasizing Chemical Equilibria Natural Water*, John Wiley & Sons, New York.

Investigation on Convective Heat Transfer and Flow Features of Nanofluids

Yimin Xuan
e-mail: ymxuan@mail.njust.edu.cn

Qiang Li

School of Power Engineering,
Nanjing University of Science & Technology,
Nanjing 210094, China

An experimental system was built to investigate convective heat transfer and flow features of the nanofluid in a tube. Both the convective heat transfer coefficient and friction factor of the sample nanofluids for the turbulent flow are measured, respectively. The effects of such factors as the volume fraction of suspended nanoparticles and the Reynolds number on the heat transfer and flow features are discussed in detail. A new type of convective heat transfer correlation is proposed to correlate experimental data of heat transfer for nanofluids. [DOI: 10.1115/1.1532008]

Keywords: Convection, Enhancement, Experimental, Heat Transfer, Nanoscale

1 Introduction

With progresses of thermoscience and thermal engineering, many efforts have been devoted to heat transfer enhancement. Among them, application of additives to liquids is often involved. Since the flow media themselves may be the controlling factor of limiting heat transfer performance, solid additives are suspended in the base liquids in order to change transport properties, flow and heat transfer features of the liquids [1,2]. Besides describing chronological development in this field, Hetsroni and Rozenblit [3] investigated the thermal interaction between the particles-laden turbulent flow and a heated plate for a liquid-solid mixture consisting of water and polystyrene particles. Traditionally, solid particles of micrometer or millimeter magnitudes are mixed in the base liquid. Although the solid additives may improve heat transfer coefficient, practical application are limited because of the fact that the micrometer and/or millimeter-sized particles settle rapidly, clog flow channels, erode pipelines and cause severe pressure drops. The concept of nanofluids refers to a new kind of heat transport fluids by suspending nanoscaled metallic or nonmetallic particles in base fluids. Energy transport of the nanofluid is affected by the properties and dimension of nanoparticles as well as the solid volume fraction. Some experimental investigations have revealed that the nanofluids have remarkably higher thermal conductivities than those of conventional pure fluids and shown that the nanofluids have great potential for heat transfer enhancement [4–7]. Compared with the existing techniques for enhancing heat transfer by adding millimeter and/or micrometer-sized particles in fluids, nanofluids are expected to be ideally suited for practical application with incurring little or no penalty in pressure drop because the nanoparticles are so small that the nanofluid behaves like a pure fluid.

To apply the nanofluid to practical heat transfer processes, more studies on its flow and heat transfer feature are needed. Pak and Cho [8] performed experiments on turbulent friction and heat transfer behaviors of two kinds of the nanofluids. In their study, γ-Al_2O_3 and TiO_2 were dispersed in water, and the experimental results showed that the Nusselt number of the dispersed fluids increases with increasing the volume fraction of the suspended solid particles and the Reynolds number. Lee and Choi [9] applied the nanofluid as the coolant to a microchannel heat exchanger for cooling crystal silicon mirrors used in high-intensity X-ray sources and pointed out that the nanofluid dramatically enhances cooling rates compared with the conventional water-cooled and liquid-nitrogen-cooled microchannel heat exchangers.

It is expected that the main reasons of heat transfer enhancement of the nanofluids may be from intensification of turbulence or eddy, suppression or interruption of the boundary layer as well as dispersion or backmixing of the suspended nanoparticles, besides substantial augmentation of the thermal conductivity and the heat capacity of the fluid. Therefore, the convective heat transfer coefficient of the nanofluids is a function of properties, dimension and volume fraction of suspended nanoparticles as well as the flow velocity. The conventional convective heat transfer correlation of the pure fluid isn't applicable to the nanofluid. To understand the mechanism of heat transfer enhancement of nanofluids and to accelerate practical applications of the nanofluids, more investigations are needed on fundamental features of convective heat transfer and flow performance of the nanofluids. Based on one of the previous papers [10], this paper is aimed at studying the single-phase flow and heat transfer performance of the nanofluid in tubes for the turbulent flow and developing heat transfer correlation for the experimental data.

2 Experimental System

An experimental rig is built to study the flow and convective heat transfer feature of the nanofluid flowing in a tube. As shown schematically in Fig. 1, the experimental system mainly includes a reservoir tank, a pump, a pipe line, a test section, a cooler, and a fluid collection tank.

The reservoir tank of 5 Liter is manufactured of polymethylmethacrylate to reserve the nanofluid and to monitor the dispersion behavior and stability of the nanofluid. The cooler of 5.2 KW cooling capacity is used to keep a constant temperature of the nanofluid at the inlet of the test section. The flow rate is controlled with two adjusting valves, one at the main flow loop and the other at the by-bass line. A three-way valve is installed at the end of the main flow loop and it provides an access for the nanofluid from the reservoir tank into the fluid collection tank to measure the mass flow rate of the nanofluid. The test section is a straight brass tube of the inner diameter of 10 mm and the length of 800 mm. Eight thermocouples (K-type) are mounted at different places of the heat transfer test section to measure the wall temperatures and other two thermocouples are respectively located at the entrance and exit of the test section to read the bulk temperatures of the nanofluid. To obtain a constant-heat-flux boundary condition, the heat transfer test section is heated electrically by a DC power supply capable of delivering a maximum of 3.5 KW. The test section is thermally isolated from its upstream and downstream sections by plastic bushings to minimize the heat loss resulting

Contributed by the Heat Transfer Division for publication in the JOURNAL OF HEAT TRANSFER. Manuscript received by the Heat Transfer Division October 12, 2001; revision received September 25, 2002. Associate Editor: K. S. Ball.

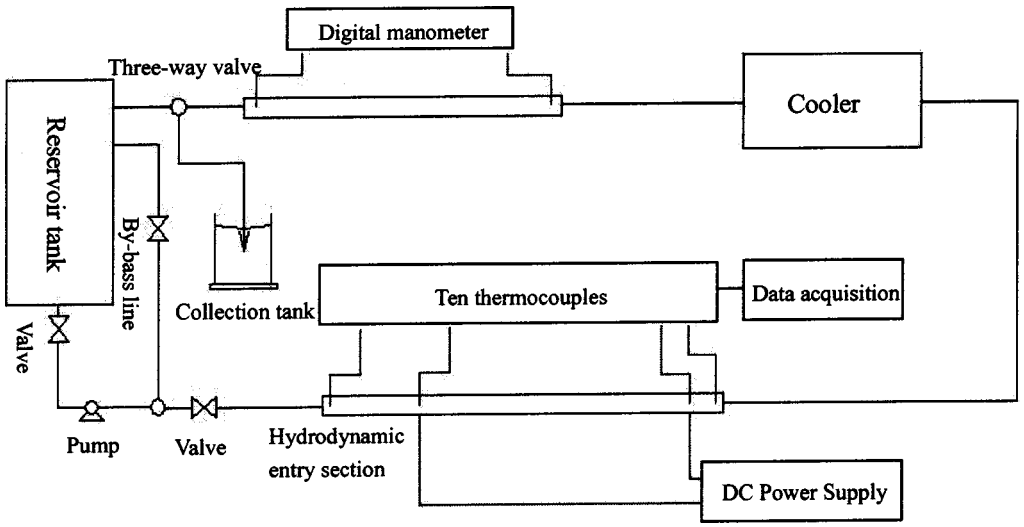

Fig. 1 The experimental system of the convective heat transfer feature for the nanofluid

from axial heat conduction. In order to minimize the heat loss from the test section to the ambient, the whole test section is thermally isolated on the outside with a layer of expanded pearl powder and a vacuum casing tube. The hydrodynamic entry section is long enough to accomplish fully developed flow at the entrance of the heat transfer test section. Two pressure transducers are installed at the both ends of the test section to measure the pressure drop of nanofluids.

During experimental runs, the tube wall temperatures, inlet and outlet temperatures of the sample nanofluid, mass flow rates and electric power inputs as well as the static pressures are measured. The measured Nusselt numbers of the nanofluid within the fully developed turbulent flow region are obtained from the following correlation

$$h_{nf}=\frac{q}{T_w-T_f} \tag{1}$$

$$\mathrm{Nu}_{nf}=\frac{h_{nf}D}{k_{nf}} \tag{2}$$

The transport properties of the nanofluid are calculated by using the mean value of the temperatures of the nanofluid at the inlet and outlet. Before measuring the convective heat transfer coefficient of nanofluids, the reliability and accuracy of the experimental system are estimated by using water as the working fluid. The results of estimation experiment are compared with the calculated values obtained from the well-known Dittus-Boelter equation [11]

$$\mathrm{Nu}=0.023\,\mathrm{Re}^{0.8}\mathrm{Pr}^{0.4} \tag{3}$$

As shown in Fig. 2, the good coincidence between the experimental results and the calculated values for water reveals that the precision of the experimental system is considerably high. The uncertainty of the experimental system is less than 4 percent.

Uncertainty of the experimental data may result from the measuring errors of parameters such as heat flux, temperature as well as flow rate. It can be defined as:

$$\left(\frac{\delta\mathrm{Nu}}{\mathrm{Nu}}\right)=\sqrt{\left(\frac{\Delta q}{q}\right)^2+\left(\frac{\Delta T}{T}\right)^2+\left(\frac{\Delta u}{u}\right)^2} \tag{4}$$

The error term $(\Delta q/q)$ arises from reading errors of direct electric current and voltage as well as heat loss from the experimental system to the ambient. The calibration results of energy balance revealed that experimental uncertainty of the heat flux is less than 3 percent in this experiment. The thermocouple is calibrated by using the thermostat and the measuring precision is of 0.1 percent. Flow rates are measured directly by weighing fluid and the measuring error of the flow rate is less than 1 percent. Therefore, uncertainty of the experimental data is less than 4 percent.

3 Convective Heat Transfer Experiment and Correlation

The sample nanofluids are prepared by mixing the nanostructured Cu particles below 100 nm diameter and deionized water. The details of preparation procedure of nanofluids are referred to the previous paper [7]. The nanofluids with different particle volume fractions are used in the experiment to investigate the effect of the nanoparticle concentration on the enhanced heat transfer performances of nanofluids, in which 0.3 percent, 0.5 percent, 0.8 percent, 1.0 percent, 1.2 percent, 1.5 percent, and 2.0 percent volume fraction Cu-water nanofluids are involved. Nanofluids with higher volume fractions of nanoparticles may be limited in practical application and consume much more solid particles. The Reynolds number Re varies between the range 10,000~25,000.

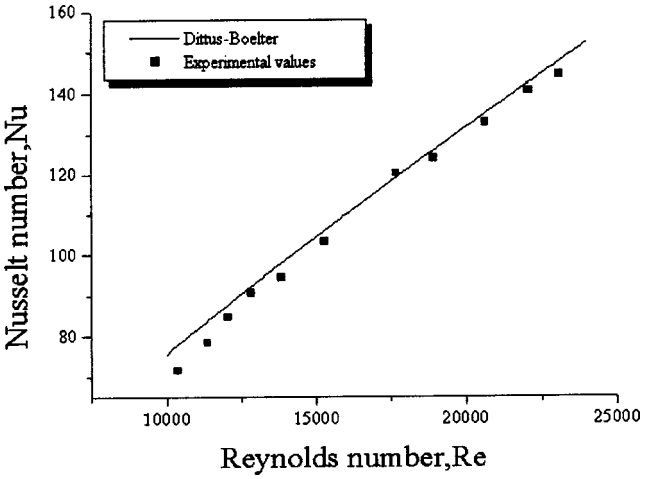

Fig. 2 Comparison between the measured Nusselt numbers of water and the calculated values with Eq. (3)

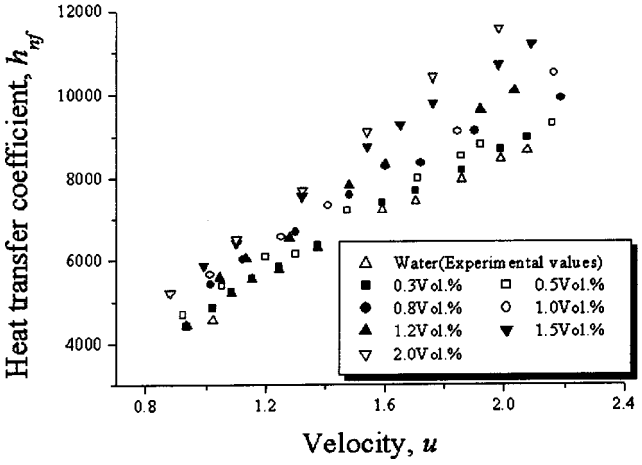

Fig. 3 Variation of heat transfer coefficient with velocity in the turbulent flow

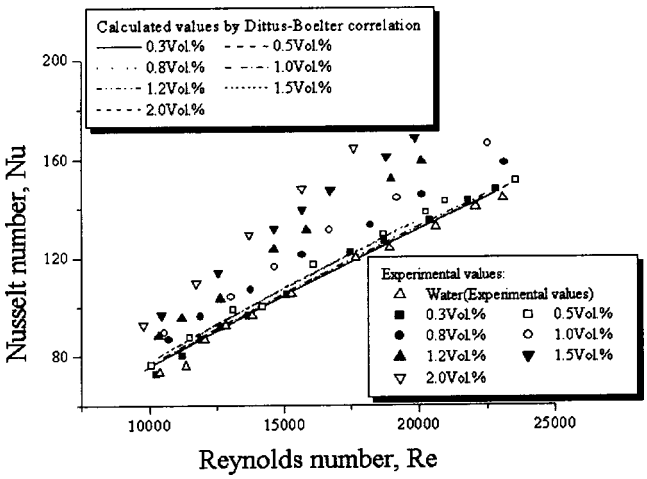

Fig. 4 The Nusselt numbers of nanofluids with the Reynolds numbers and the predicated values from the Dittus-Boelter correlation

As shown in Fig. 3, the convective heat transfer coefficient of the nanofluid increases with the flow velocity as well as the volume fraction of nanoparticles and it is larger than that of the base liquid (water) under the same flow velocity. It may be instructive to point out that proper selection of the particle volume fraction and of the couple pair of solid particles and base liquid are important for applying nanoparticles to heat transfer enhancement. In some cases, the viscosity of the dispersed fluid sharply increases with increasing the particle volume fraction and becomes much higher than that of the base liquid, so that higher volume fraction of the solid particles may suppress heat transfer enhancement of the suspension. Pak and Cho [8] studied heat transfer process of the suspensions consisting of water and metallic oxide particles such as γ-alumina (Al_2O_3) with mean diameter of 13 nm and titanium dioxide (TiO_2) with mean diameter of 27 nm and found that the convective heat transfer coefficient of the suspensions at a volume concentration of 3 percent was 12 percent smaller than that of pure water when compared under the condition of constant average velocity. The reason may be that both the suspensions have much higher viscosities than that of water, which suppresses flow turbulence. While preparing the nanofluid, therefore, it may be of importance to select the volume fraction, dimensions and material properties of the nanoparticles suspended in the base liquid.

Figure 4 illustrates variation tendency of the Nusselt numbers of the sample nanofluid with the volume fraction of nanoparticles and the Reynolds number Re. The experimental results indicate that the suspended nanoparticles remarkably improve heat transfer performance of the base fluid. Compared with water, the Nusselt number of the nanofluid is increased more than 39 percent for the nanofluid with the volume fraction 2.0 percent of Cu nanoparticles. The experimental results also indicate that the heat transfer feature of a nanofluid remarkably increases with the volume fraction of nanoparticles. The particle volume fraction is one of the main factors affecting the Nusselt numbers of the nanofluid. While the volume fraction of the Cu nanoparticles increases from 0.5 percent to 2.0 percent, for example, the ratio of the Nusselt number of the Cu-water nanofluid to that of water varies from 1.06 to 1.39 under the same Reynolds number.

As mentioned before, the nanofluid behaves more like a fluid than the conventional solid-fluid mixtures in which relatively larger particles with micrometer or millimeter orders are suspended. But the nanofluid is a two-phase fluid in nature and has some common features of the solid-fluid mixtures. The effects of several factors such as gravity, Brownian force, and friction force between the fluid and ultrafine solid particles, the phenomena of Brownian diffusion, sedimentation, and dispersion may coexist in the main flow of a nanofluid. This means that the slip velocity between the fluid and the suspended nanoparticles may not be zero, although the particles are ultrafine. Random movement of the suspended nanoparticles increases energy exchange rates in the fluid. The dispersion will flatten temperature distribution and makes the temperature gradient between the fluid and wall steeper, which augments heat transfer rate between the fluid and the wall. The enhanced heat transfer by the nanofluid may result from the following two aspects [10]: One is that the suspended particles increase the thermal conductivity of the two-phase mixture; another is that chaotic movement of ultrafine particles accelerates energy exchange process in the fluid. The comparison between the experimental results and the predicated values from the Dittus-Boelter correlation is shown in Fig. 4. The predicted results are obtained in such a way that all the transport properties involved in the Dittus-Boelter correlation are respectively replaced by the effective conductivity, viscosity and diffusivity of the nanofluid. Clearly, greater deviation between the experimental results and the predicted ones from the conventional correlation exists and such deviation increases with increasing the volume fraction of the suspended nanoparticles and the Reynolds number. For example, the discrepancy between both them is over 30 percent for Re $=17{,}600$ and $\phi=2.0$ percent. The Dittus-Boelter correlation failed to predict the dependency of the Nusselt number of the nanofluid on the volume fraction of nanoparticles because this correlation is valid only for the single-phase flow. It is improper to apply the Dittus-Boelter correlation to prediction the Nusselt number for the nanofluid even if the effective transport properties of the nanofluid are used, especially for the case that the volume fraction of the nanoparticles is larger than 0.5 percent. The values of the Nu number calculated from the Dittus-Boelter correlation just slightly change (as illustrated by the solid and dotted lines in Fig. 4), although the volume fraction of the nanoparticles varies from 0.3 percent to 2.0 percent. In fact, the experimental data of the Nu number do remarkably vary with the volume fraction of the nanoparticles (as shown by all the scattered points in Fig. 4).

A new approach needs to be tried to develop the heat transfer correlation for the nanofluid. In general, the Nusselt number Nu of a nanofluid may be expressed as follows:

$$\mathrm{Nu}_{nf}=f\left(\mathrm{Re},\mathrm{Pr},\frac{k_d}{k_f},\frac{(\rho c_p)_d}{(\rho c_p)_f},\right.$$

$$\left.\phi,\text{dimensions and shape of particles}\right) \qquad (5)$$

Table 1 The effective thermal conductivity and viscosity of the sample nanofluid

Transport properties	Volume fraction of nanoparticles						
	0.3%	0.5%	0.8%	1.0%	1.2%	1.5%	2.0%
k_{nf} (W/m·°C)	0.6054	0.615	0.6252	0.6306	0.633	0.663	0.702
$\upsilon_{nf}\times 10^6$ (m^2/s)	0.91	0.915	0.945	0.96	1.012	1.044	1.125

In the light of analysis and derivation presented in the previous paper [10], the following formula is proposed to correlate the experimental data for the nanofluid:

$$\mathrm{Nu}_{nf}=c_1(1.0+c_2\phi^{m_1}\mathrm{Pe}_d^{m_2})\mathrm{Re}_{nf}^{m_3}\mathrm{Pr}_{nf}^{0.4} \tag{6}$$

Compared with the heat transfer correlation for conventional single-phase flow, the volume fraction ϕ of suspended nanoparticles and the Peclet number are involved in the above expression. The Peclet number Pe describes the effect of thermal dispersion caused by microconvective and microdiffusion of the suspended nanoparticles. The case $c_2=0$ refers to zero thermal dispersion, which namely corresponds to the case of the pure base fluid. The particle Peclet number Pe_d in expression (6) is defined as

$$\mathrm{Pe}_d=\frac{u_m d_p}{\alpha_{nf}} \tag{7}$$

The Reynolds number of the nanofluid is defined as

$$\mathrm{Re}_{nf}=\frac{u_m D}{\upsilon_{nf}} \tag{8}$$

The Prandlt number Pr of the nanofluid is defined as

$$\mathrm{Pr}_{nf}=\frac{\upsilon_{nf}}{\alpha_{nf}} \tag{9}$$

To calculate this parameter, the thermal diffusivity of the nanofluid α_{nf} is defined as

$$\alpha_{nf}=\frac{k_{nf}}{(\rho c_p)_{nf}}=\frac{k_{nf}}{(1-\phi)(\rho c_p)_f+\phi(\rho c_p)_d} \tag{10}$$

Where, the thermal conductivity k_{nf} and the viscosity υ_{nf} are experimentally obtained and the experimental procedure is described in detail in reference [6]. Some experimental data are listed in Table 1.

From the whole ensemble of experimental data, the coefficient c_1 and c_2 as well as the exponent m_1, m_2, and m_3 in expression (6) can be determined by a proper data-reduction procedure. For a given flow velocity, a set of all these coefficients and exponents is fit for predicting heat transfer performance of nanofluids with different volume fractions of suspended nanoparticles. For a variety of volume fraction of suspended nanoparticles, for example, the Nusselt number Nu for the turbulent flow of nanofluids inside a tube are obtained as follows:

$$\mathrm{Nu}_{nf}=0.0059(1.0+7.6286\phi^{0.6886}\mathrm{Pe}_d^{0.001})\mathrm{Re}_{nf}^{0.9238}\mathrm{Pr}_{nf}^{0.4} \tag{11}$$

Figure 5 depicts the curves of the theoretical predictions of convective heat transfer coefficients of nanofluids from correlation (11). Obviously, there exists good coincidence between the results calculated from this correlation and the experimental ones. The discrepancy between both them falls below 8 percent. It reveals that formula (6) correctly incorporates the main factors of affecting heat transfer process of the nanofluid into in a simpler form and can be used to correlate experimental data of heat transfer coefficient of the nanofluid. Once all the coefficients and exponents in formula (6) have been determined by correlating experimental data of heat transfer for nanofluids, therefore, this formula can be used to predict the convective heat transfer coefficient for such suspensions with different volume fractions of nanoparticles in the turbulent flow.

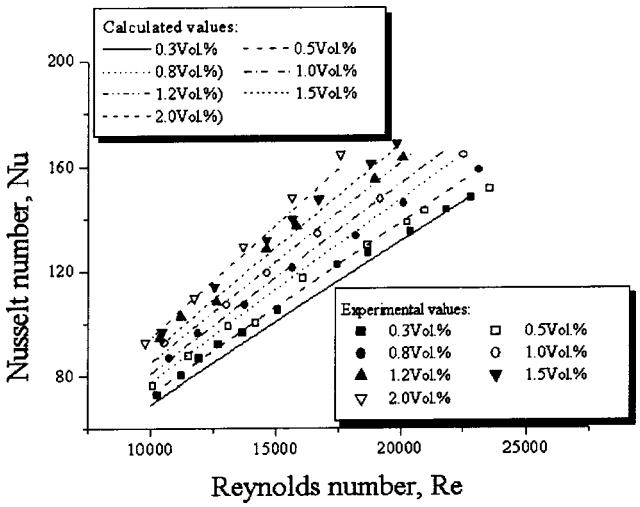

Fig. 5 Comparison between the measured data and the calculated values from correlation (11) for turbulent flow

4 Pressure Drop Experiment

It is necessary to learn the flow resistance of nanofluids besides the heat transfer enhancement feature in order to apply the nanofluid to practical cases. The pressure drops of the dilute suspensions consisting of water and Cu-nanoparticles in a tube are experimentally measured for the turbulent flow.

Four sample nanofluids with the volume fractions of nanoparticles 1.0 percent, 1.2 percent, 1.5 percent, and 2.0 percent are used in pressure drop test. Figure 6 illustrates the friction factors as a function of the Reynolds number for the turbulent flow. The friction factor of the pure water is also shown as a solid line in the figures. The friction factor is defined as

$$\lambda_{nf}=\frac{P_{nf}D}{L}\frac{2g}{u_m^2} \tag{12}$$

Obviously, the friction factors of the dilute nanofluids are almost equal to those of water under the same Reynolds number. Compared with water, no significant augmentation in pressure drop for the nanofluid is found in all runs of the experiment,

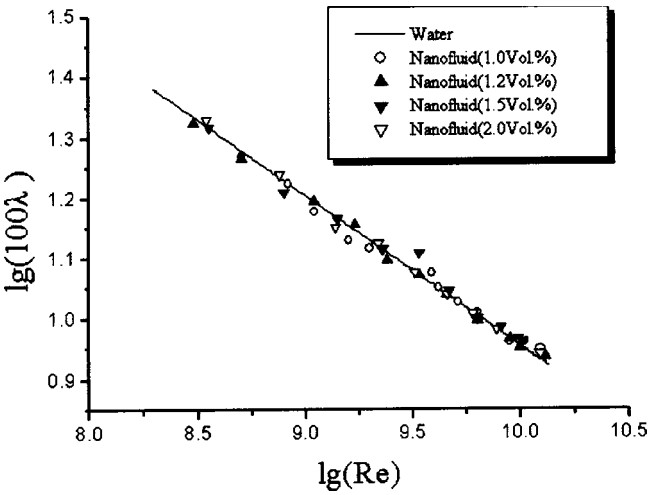

Fig. 6 The friction factors of nanofluids for the turbulent flow

which reveals that dilute nanofluids will not cause extra penalty in pump power. It implies that the friction factor correlation for the single-phase flow can be extended to the dilute nanofluids.

5 Conclusions

The convective heat transfer feature and flow performance of Cu-water nanofluids in a tube have experimentally been investigated. The suspended nanoparticles remarkably enhance heat transfer process and the nanofluid has larger heat transfer coefficient than that of the original base liquid under the same Reynolds number. The heat transfer feature of a nanofluid increases with the volume fraction of nanoparticles.

By considering the microconvection and microdiffusion effects of the suspended nanoparticles, a new type of the convective heat transfer correlation for nanofluids in a tube has been proposed as $\mathrm{Nu}_{nf}=c_1(1.0+c_2\phi^{m_1}\mathrm{Pe}_d^{m_2})\mathrm{Re}_{nf}^{m_3}\mathrm{Pr}_{nf}^{0.4}$. This correlation correctly takes the main factors of affecting heat transfer of the nanofluid into account.

On the other hand, the friction factor for the dilute nanofluids consisting of water and Cu-nanoparticles is approximately the same as that of water. The nanofluid with the low volume fraction of the suspended nanoparticles incurs almost no extra penalty of pump power.

Acknowledgment

This work has been supported by the National Science Foundation of China (Grant No. 59976012 and No. 50176018) and the Chinese Ministry of Education.

Nomenclature

d = nanoparticle diameter, m
D = inner diameter of the tube, m
g = acceleration of gravity, $\mathrm{m/s^2}$
h = heat transfer coefficient, $\mathrm{W/m^2K}$
k = thermal conductivity of the sample nanofluid, W/mK
L = length of the pressure drop test tube, m
Nu = Nusselt number
P = pressure drop, Pa
Pe = Peclet number
Pr = Prandtl number
q = heat flux, $\mathrm{W/m^2}$
Re = Reynolds number
T = temperature, °C
u = mean velocity, m/s
ϕ = volume fraction
α = thermal diffusivity, $\mathrm{m^2/s}$
υ = viscosity, $\mathrm{m^2/s}$

Subscript

d = particle
f = fluid
in = inlet
m = mean
out = outlet
nf = nanofluid
w = tube wall

References

[1] Liu, K. V., Choi, U. S., and Kasza, K. E., 1988, ''Measurements of Pressure Drop and Heat Transfer in Turbulent Pipe Flows of Particulate Slurries,'' report, Argonne National Laboratory ANL-88-15.

[2] Webb, R. L., 1993, *Principles of Enhanced Heat Transfer*, John Wiley & Sons, New York.

[3] Hetsroni, G., and Rozenblit, R., 1994, ''Heat Transfer to a Liquid-Solid Mixture in a Flume,'' Int. J. Multiphase Flow, **20**(4), pp. 671–689.

[4] Wang, X., Xu, X., and Choi, S. U. S., 1999, ''Thermal Conductivity of Nanoparticle-Fluid Mixture,'' J. Thermophys. Heat Transfer, **13**(4), pp. 474–480.

[5] Lee, S., Choi, S. U. S., Li, S., and Eastman, J. A., 1999, ''Measuring Thermal Conductivity of Fluids Containing Oxide Nanoparticles,'' J. Heat Transfer , **121**, pp. 280–289.

[6] Li, Q., and Xuan, Y., 2000, ''Experimental Investigation on Transport Properties of Nanofluids,'' *Heat Transfer Science and Technology 2000*, Wang Buxuan, ed., Higher Education Press, pp. 757–762.

[7] Xuan, Y., and Li, Q., 2000, ''Heat Transfer Enhancement of Nanofluids,'' Int. J. Heat Fluid Flow, **1**(21), pp. 58–64.

[8] Pak, B. C., and Cho, Y. I., 1998, ''Hydrodynamic and Heat Transfer Study of Dispersed Fluids with Submicron Metallic Oxide Particles,'' Exp. Heat Transfer, **11**, pp. 151–170.

[9] Lee, S., and S. U. S. Choi, 1996, ''Application of Metallic Nanoparticle Suspensions in Advanced Cooling Systems,'' *Recent Advances in Solids/Structures and Application of Metallic Materials*, L. Shinpyo, eds., PVP-Vol. 342/MD-vol. 72, ASME, New York, pp. 227–234.

[10] Xuan, Y., and Roetzel, W., 2000, ''Conceptions for Heat Transfer Correlation of Nanofluids,'' Int. J. Heat Mass Transf., **43**, pp. 3701–3707.

[11] Incropera, F. P., and DeWitt, D. P., 1996, *Introduction to Heat Transfer*, John Wiley & Sons, New York.

Scanning Thermal Wave Microscopy (STWM)

Ohmyoung Kwon[1]
e-mail: omkwon@wow.hongik.ac.kr

Li Shi

Arun Majumdar

Department of Mechanical Engineering,
University of California,
Berkeley, CA 94720

This paper presents a technique, scanning thermal wave microscopy (STWM), which can image the phase lag and amplitude of thermal waves with sub-micrometer resolution by scanning a temperature-sensing nanoscale tip across a sample surface. Phase lag measurements during tip-sample contact showed enhancement of tip-sample heat transfer due to the presence of a liquid film. The measurement accuracy of STWM is proved by a benchmark experiment and comparison to theoretical prediction. The application of STWM for sub-surface imaging of buried structures is demonstrated by measuring the phase lag and amplitude distributions of an interconnect via sample. The measurement showed excellent agreement with a finite element analysis offering the promising prospects of three-dimensional thermal probing of micro and nanostructures. Finally, it was shown that the resolving power of thermal waves for subsurface structures improves as the wavelengths of the thermal waves become shorter at higher modulation frequencies.
[DOI: 10.1115/1.1518492]

Keywords: Electronics, Heat Transfer, Microscale, Microstructures, Nanoscale, Nonintrusive Diagnostics

1 Introduction

This paper presents a new non-destructive evaluation (NDE) technique of imaging sub-surface structure on the sub-micrometer scale using thermal waves. Although the atomic force microscope (AFM) can examine surface structures with atomic resolution, it does not generally yield any sub-surface information. As three-dimensional micro and nanoengineered devices are developed in the future, the demand for the NDE technique of micro- and nanostructures is expected to grow. For example, with advances in integrated circuit (IC) manufacturing technology, the minimum feature size in ULSI circuits is becoming smaller and the number of layers is increasing. This trend poses challenges in the diagnosis and study of the reliability physics of ULSI circuits. Hence, there is a need for developing techniques to locate and characterize sub-surface defects in ULSI circuits buried in insulating materials.

The propagation of thermal waves in a solid can be used to study sub-surface structures at micro and nanometer scales. This is because thermal waves propagate at much slower speeds than sound waves which is commonly used in NDE at large scales. Hence, for a given frequency, the wavelengths of thermal waves are much shorter. When the surface of a one-dimensional semi-infinite medium is modulated in a sinusoidal manner, the temperature fluctuation in the medium is given as [1]

$$T(x,t) = T_0 \exp(-\sqrt{\omega/2\alpha}x)\cos(\omega t - \sqrt{\omega/2\alpha}x) \tag{1}$$

where x is the distance from the surface, T_0 is the amplitude of the surface temperature fluctuation, ω is the angular frequency, and α is the thermal diffusivity. From Eq. (1) the dispersion relation and the wavelength of plane thermal waves are given as

$$v = 2\sqrt{\pi\alpha f} \tag{2}$$

and

$$\lambda = 2\sqrt{\pi\alpha/f} \tag{3}$$

where v is the wave speed, f is the wave frequency, and λ is the wavelength. At 100 kHz, the wave speed in Pyrex glass is about 0.9 m/s and the wavelength is about 9 μm. Consequently, phase lag of 1 deg corresponds to 25 nm of distance. If one had to use ultrasonic waves of similar wavelengths, the frequencies required would be in the range of 0.1–1 GHz, which is difficult to operate. One must note, however, that the thermal waves decay exponentially and the decay length is on the order of the wavelength. Hence, features only a wavelength below a surface can be studied.

The phase lag and the amplitude of thermal waves depend on the thermal diffusivity of the medium and the wave frequency [1]. Using this principle, extensive work has been done to obtain the thermal properties of materials. This can be classified depending upon whether thermal waves were generated by electrical [2–4] or optical heating [5–7] and/or upon whether the phase lag and the amplitude were measured optically [5,6] or thermo-electrically [2,3,7]. In these works, the focus was on extracting the material properties and not for imaging. Therefore, most of the data were obtained at a single point.

There have also been many efforts undertaken to image subsurface structures using photoacoustic microscopy and photothermal wave microscopy [8]. Photoacoustic microscopy (PAM) uses photothermally generated acoustic waves to investigate subsurface structures and photothermal wave microscopy images thermal wave propagation and scattering by subsurface defects using probe beam. Thermoreflectance technique was also applied to image amplitude and phase lag distributions in a resistor heated by an alternating current [9]. The same technique was applied to perform reflectance microscopy on a biased MOSFET structure by scanning its gate surface [10]. Ocariz et al. [11] performed a theoretical study of the scattering of planar and spherical thermal waves by a buried single infinite cylinder. They also measured the amplitude and phase distributions using three different modulated photothermal techniques: thermoreflectance, infrared radiometry, and mirage [12,13]. The resolution of these techniques is diffraction limited by the wavelength of the probe beam, which is approximately 1 μm. To overcome this, STWM described here takes advantage of the high spatial resolution (~50 nm) of recently developed probes for the purpose of scanning thermal microscopy (SThM) [14].

Through a benchmark experiment, it is first shown that STWM can image thermal wave propagation with sub-micrometer resolution. Then, STWM is used to measure the amplitude and phase lag

[1]Current address: Department of Mechanical Engineering, Hong-ik University, Seoul, Korea 121-791.

Contributed by the Heat Transfer Division for publication in the JOURNAL OF HEAT TRANSFER. Manuscript received by the Heat Transfer Division December 17, 2001; revision received July 3, 2002. Associate Editor: D. Poulikakos.

distributions at different frequencies on a sample containing two levels of metal interconnect bridged by a via. A detailed study of the thermal wave propagation mechanism is performed by comparing the measurement and simulation results.

2 Instrumentation

Figure 1 shows the experimental setup and the structure of a SThM probe, whose fabrication details were published elsewhere [14]. A resistor in the sample with an AC bias is used as a periodic heat source. When the AC bias frequency is f, the heat generation frequency is $2f$ because the power is proportional to the square of the applied current for an Ohmic resistor. While scanning a SThM probe across the sample, the topographical data is obtained under controlled force contact of the atomic force microscope (AFM). The thermoelectric signal from the SThM probe is fed into the lock-in amplifier (LIA), which measures the amplitude and the phase lag of the thermoelectric signal at the heating frequency $2f$. The phase lag of the thermal wave is obtained by comparing the phase of the second harmonic of the AC bias applied and the phase of the thermo-electric signal from the probe. Therefore, three (topography, phase lag, amplitude) images can be obtained simultaneously for STWM.

3 Benchmark Experiment

3.1 Theoretical Analysis. To verify the accuracy of STWM, a test sample containing Al line heaters, shown in Fig. 2(*a*), was prepared. While scanning a SThM probe across the periodically heated Al line heater, the phase lag distribution around the heat source was obtained. The sample was also used to measure the thermal conductivity of Pyrex glass by the 3ω method [4], which is plotted in Fig. 2(*b*). The measured thermal conductivity was used in a theoretical analysis to predict the phase lag distribution around the periodically heated Al line. This was used as a benchmark to compare the phase lag distributions measured with STWM.

For an infinitesimally narrow line of a periodically steady heat source in an infinite medium, the AC temperature distribution is given as [1]

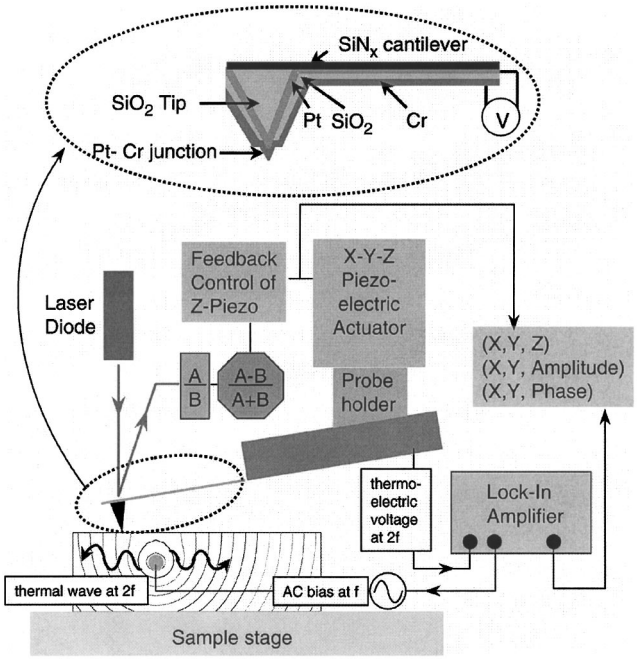

Fig. 1 Schematic diagram of the scanning thermal wave microscope

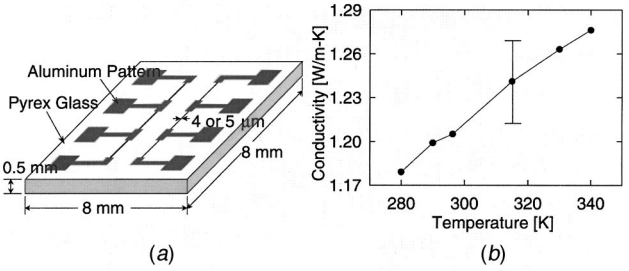

Fig. 2 (*a*) Schematic diagram of the test sample; (*b*) Measured thermal conductivity of Pyrex glass using the 3ω method (error bar shows ±3 percent range)

$$\theta(r)=\frac{Q_0}{2\pi k}K_0\left(\sqrt{\frac{\omega i}{\alpha}}r\right) \tag{4}$$

where Q_0 is the amplitude of periodic heat generation per unit length, k is the thermal conductivity of the substrate, ω is the angular frequency, i is the imaginary unit, α is the thermal diffusivity, and K_0 is a modified Bessel-function of the second kind of order zero. For the sample in Fig. 2(*a*), the Al resistor has a finite width of $2b$. The AC temperature distribution for the line heat source with finite width can be obtained by integrating Eq. (4) and is given as

$$\theta(x,y)=\frac{q_0}{\pi k}\int_{-b}^{b}K_0\left(\sqrt{\frac{\omega i}{\alpha}((x-\xi)^2+y^2)}\right)d\xi \tag{5}$$

where q_0 is the amplitude of the periodic heat generation per unit area. Amplitude and phase lag measurements using STWM should be compared to Eq. (5) to ensure the validity of this technique.

3.2 Phase Lag Variation Associated With Tip-Sample Point Contact. Before we can compare the phase lag distributions measured by STWM with theoretical predictions, it is important to understand the phase lag associated with the point contact of the SThM probe with the sample surface. Previous work has suggested that the dominant tip-sample heat transfer is through a liquid film bridge and that the thermal resistance is on the order of 10^5 K/W [15].

To closely examine the effect of the liquid film, the phase lag must be measured in real time as the probe is moved to and from the sample. Figure 3 shows the phase lag measured at 3.2 kHz and the cantilever deflection as a function of probe height. As the probe is lowered to the sample, the sensor is pulled down abruptly due to the short-range attraction caused by van der Waals force. This is indicated as the jump to contact. The tip-sample heat transfer is enhanced dramatically due to the liquid film and the phase lag decreases rapidly. The value for the phase lag is always negative by its nature. As the probe is moved further down towards the sample, the contact force increases as indicated by the upward cantilever deflection. However, the phase lag does not change appreciably, indicating that solid-solid conduction is insignificant.

When the probe is raised away from the sample, the sensor remains in contact with the sample due to the surface tension of the liquid film until the elastic force of the cantilever overcomes surface tension. At a cantilever deflection of about 30 nm, the cantilever snaps out of contact. The thermal contact through the liquid film is lost and heat conduction through the air dominates heat transfer. The phase lag is sharply increased by about 20 deg, indicating a large increase in tip-sample thermal resistance.

The above experiment shows there exists a liquid film bride between the tip and the sample, which enhances the tip-sample heat transfer dramatically. However, it does not give the value of the tip-sample phase lag. The tip-sample phase lag is related to the time constant of the thermal probe as well as to the tip-sample

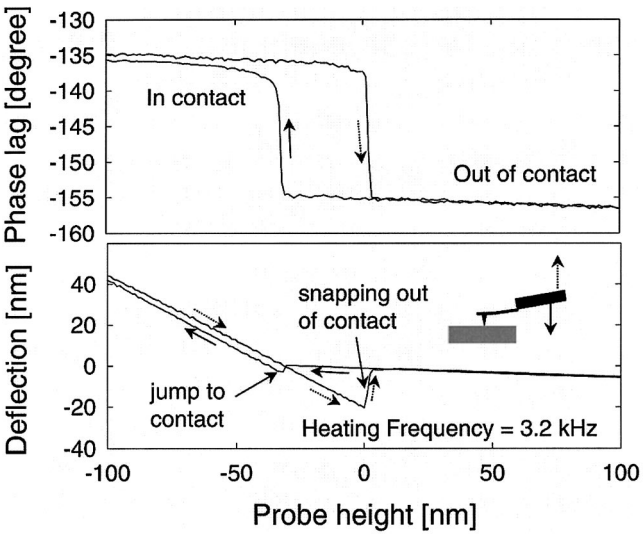

Fig. 3 Phase lag and deflection as a function of the probe height. The heating frequency is 3.2 kHz.

thermal resistance. Although very difficult, it is very important to measure the exact values of and reveal the quantitative relations between them. Further study on this topic is left for the future.

3.3 Phase Lag Variation During Scanning. When the tip is scanned across the sample, the measured phase lag is a sum of the actual phase lag of the wave propagated to the sample surface and that due to tip-sample contact resistance. If the phase lag caused by tip-sample contact resistance varies during the scanning, the interpretation of the measurement results can become very difficult. Therefore, it is important to compare the measurement result with the theoretical prediction directly and check whether the tip-sample phase lag remains constant during the scanning.

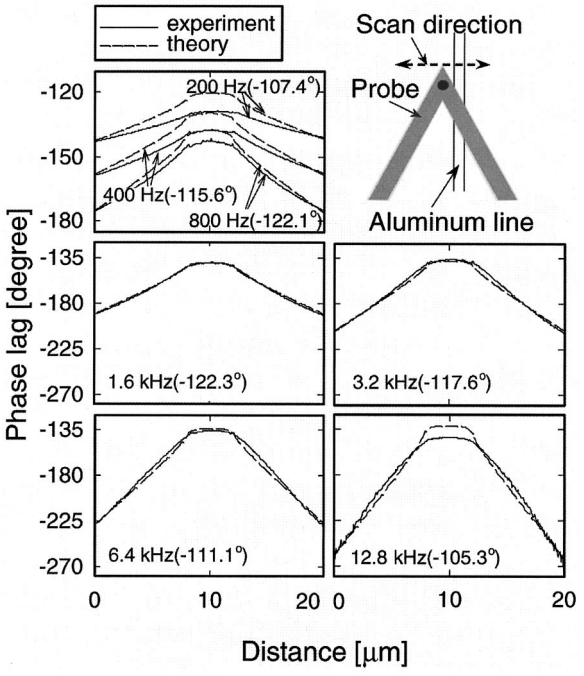

Fig. 4 Comparison between measured phase lag distributions and theoretical predictions as a function of position (symmetric scan). The offset added to the theoretically predicted value for each frequency is shown in the parentheses next to the heating frequency.

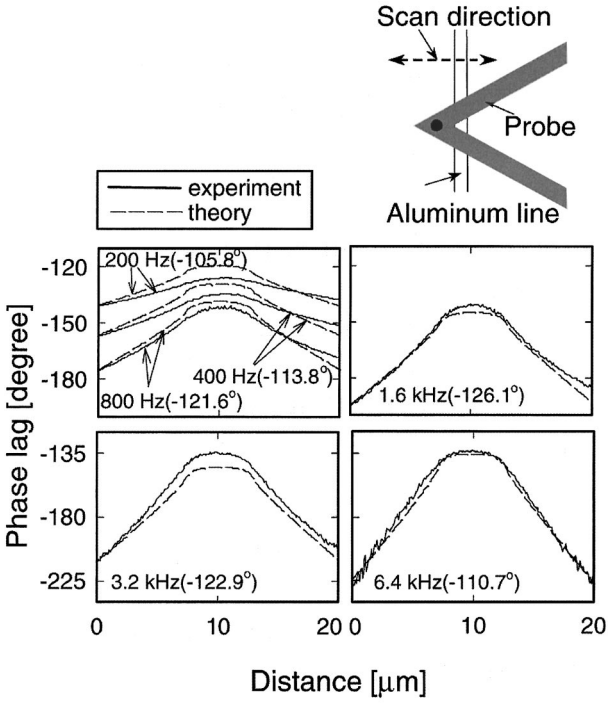

Fig. 5 Comparison between measured phase lag distributions and theoretical predictions as a function of position (asymmetric scan). The offset added to the theoretically predicted value for each frequency is shown in the parentheses next to the heating frequency.

One notable observation of the measurement results is that the phase lag distribution is affected by the orientation of the probe with respect to the aluminum heater. There are two such orientations, symmetric and asymmetric (see Figs. 4 and 5, respectively). The symmetric case will be explained in detail first.

The measurement results with a symmetric probe orientation are compared in Fig. 4. An offset value was added to the theoretically predicted value on the assumption that tip-sample phase lag remains constant but unknown during scanning. This assumption will be verified later. For the ease of comparison of the two values, the offset was chosen such that the measured and predicted phase lag distributions at a given frequency were equal at $x=0$ (see Fig. 4). The offset added to the theoretically predicted value for each frequency is shown in the parentheses next to the heating frequency. Although the data does not show good agreement with theory at low frequencies, the measured results approach theoretical predictions as the heating frequency is increased. The experiments summarized in Fig. 4 also demonstrate this behavior, showing excellent agreement between prediction and measurement at frequencies higher than 1.6 kHz. The small mismatch right on the aluminum heater at 12.8 kHz seems due to the fact that Eq. (5) does not take into account of surface topography and the finite thickness of the heater.

It is proposed that poor agreement at low frequency is caused by the frequency dependence of wave propagation paths other than tip-sample point contact. In order for the thermal waves propagated to the nitride cantilever through the air to affect the measurement, they must travel to the end of the silicon dioxide tip, where the thermocouple sensor is located (see Fig. 1). Hence, it can be argued that the effects of these waves will become insignificant if the penetration depth of the wave in silicon dioxide, δ_{th} is less than the probe height, H, i.e., $H > \delta_{th} = \sqrt{\alpha/\pi f}$. For a probe height, $H = 8\ \mu$m, the frequency when $\delta_{th} = H$ is 3.2 kHz.

The measurement results with an asymmetric probe orientation are shown in Fig. 5. The asymmetry is higher at lower frequencies and gradually reduces at higher frequencies, as shown in Fig. 5. This is because of the propagation of thermal waves to the nitride cantilever through the air at low frequencies. Accordingly, the influence of the waves propagated to the cantilever depends upon the cantilever shape and orientation, which leads to the asymmetry. Because the effect of the waves propagated to the cantilever reduces at higher frequency, agreement improves in this range.

The fact that phase lag distribution measurements are affected by the probe orientation at lower frequencies suggests that the disagreement between measurement and theory at lower frequencies is not caused by the variation of tip-sample phase lag, because probe orientation and tip-sample contact resistance are independent of each other. The agreement between phase lag distribution measurement results and theoretical predictions at high frequencies validates the assumption that tip-sample phase lag remains constant during scanning.

4 Phase Lag and Amplitude Measurement of Thermal Waves From Buried Heat Sources

Having demonstrated that STWM can measure phase lag distribution around an exposed heat source and that the tip-sample phase lag remains constant during scanning, the ultimate goal of the technique is to nondestructively evaluate sub-surface structure at sub-micrometer scale resolution. To demonstrate the effectiveness of the technique, a sample containing two levels of metal interconnect bridged by a via provided by Texas Instruments was used as the object of measurement. Optical micrographs of the sample are shown in Figs. 6(*a*) and (*b*).

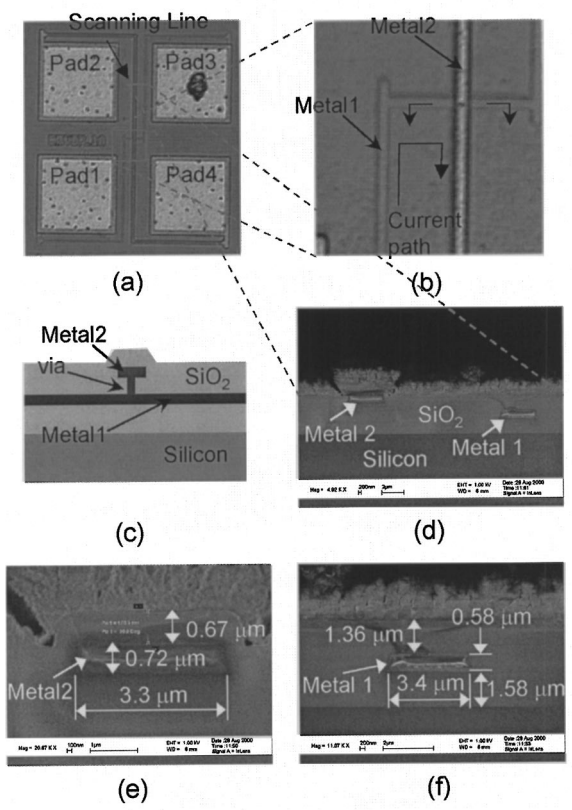

Fig. 6 VLSI via structure: (*a*) top view (optical micrograph); (*b*) scanned area (optical micrograph); (*c*) schematic diagram of cross-section; (*d*) the structure under the scanning line (electron micrograph); (*e*) the cross-sectional shape of Metal 2 (electron micrograph); and (*f*) the cross-sectional shape of Metal 1 (electron micrograph).

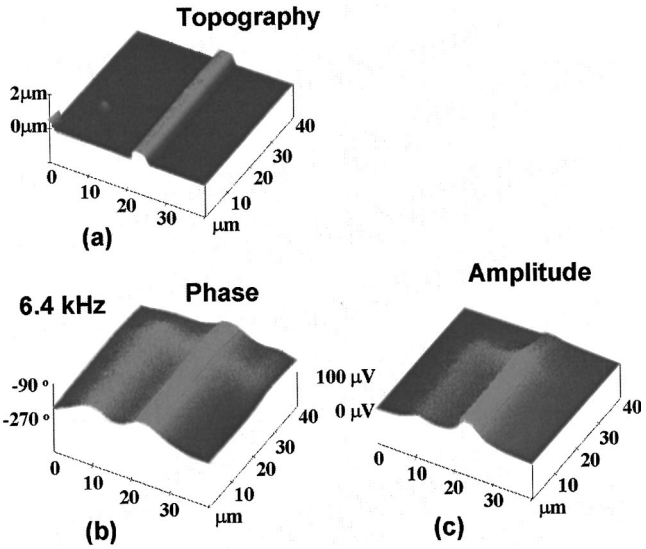

Fig. 7 Thermal wave imaging of a VLSI via structure: (*a*) Topography image; (*b*) phase lag image at 6.4 kHz; (*c*) amplitude image at 6.4 kHz.

To obtain an overall understanding of thermal wave propagation in the sample, the phase lag and the amplitude imaging were carried out. Figure 7 shows the imaging results at the frequency 6.4 kHz. To determine the location and the shape of the subsurface structure, topography, amplitude, and phase lag imaging results must be processed in a mathematically rigorous manner. This becomes a three-dimensional inverse boundary-value problem requiring mathematical proof of the existence and uniqueness of the solution. In this paper, a simpler two-dimensional case is dealt with in a quantitative manner.

The sample was cleaved after the measurement to determine the cross-sectional structure of the sample under the scanning line on which the probe was scanned. Figure 6(*d*) shows the overall structure of the cross section and Figs. 6(*e*) and (*f*) show the detailed configurations of Metal 2 and Metal 1, respectively. The cloudy features appearing on top of the silicon dioxide seem to be the material which was ablated by the focused laser beam and then deposited on the surface during the microgroove cutting process. Those cloudy features did not appear in the AFM imaging results before cleavage, as shown in Fig. 7(*a*). While surface topography due to Metal 2 is obvious, there is no bump due to Metal 1. Presumably, planarization took place after the silicon dioxide layer was deposited on Metal 1.

When thermal waves are generated by applying an AC bias across a metal line, the amplitude of the thermal wave is related to the electrical resistance of the metal line. The electrical resistances measured across every possible couple of contact pads showed that the electrical resistance of the via itself is approximately 0.3 Ω and that the electrical resistance of Metal 1 is nearly the same as Metal 2 and is about 12.4 Ω.

An AC bias was applied to three different pairs of contact pads separately: contact pads 2 and 3; 1 and 3; and 2 and 4. This was done to generate thermal waves from, both Metal 1 and Metal 2, Metal 1 only, and Metal 2 only, respectively. Comparing these cases, one could observe the effect of thermal wave interference. The range of thermal wave frequencies was from 2 kHz to 100 kHz.

Figure 8 shows phase lag distributions measured at three different wave generation modes for each frequency. At each thermal wave frequency the minima of phase lag occur at the points on the

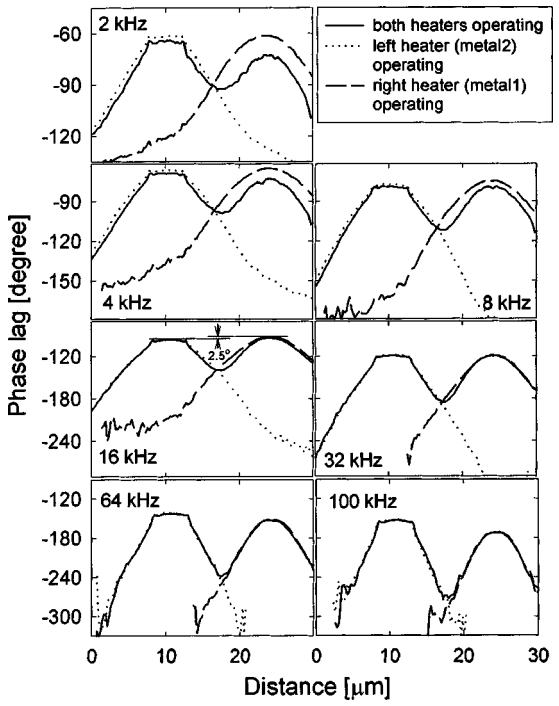

Fig. 8 Phase lag distributions measured at three different wave generation modes for each frequency

surface immediately above the heat sources. Evidently, this is because the distance between the heat source and the sensor is minimal at these points. It should be noted, however, that at lower frequencies the extremum values of phase lag with both heaters operating are different from those with each heater operating separately. For example, when both heaters are operating, r, the amplitude and ϕ, the phase lag on the surface right above the right heat source is given by

$$r\exp(i\phi)=r_l\exp(i\phi_l)+r_r\exp(i\phi_r) \tag{6}$$

where r_l and ϕ_l are the amplitude and the phase lag of the thermal wave from the left heat source, and r_r and ϕ_r are those from the right heat source. The phase lag of the thermal wave from the left heat source is relatively large because of the longer distance it travels, whereas its amplitude is reduced. Therefore, the right minimum of phase lag with both heaters operating is larger than that with right heater only operating.

The difference between the extremum values of phase lag with both heaters operating and those with each heater operating separately becomes almost negligible at higher frequencies. This is because thermal waves decay more rapidly when they travel at higher frequencies. Hence, the influence of remote wave sources becomes negligible at high frequency.

One peculiar point is that at 16 kHz the minimum of phase lag with the right heater operating is smaller by about 2.5 deg than that with the left heater operating (see Fig. 8). The reason for this is not obvious, as the right heater is buried deeper. Indeed, at 100 kHz the minimum of the phase lag with the right heater operating is larger by about 20 deg than that with the left heater operating. The interpretation of this phenomenon is not straightforward. To understand this and to check the validity of the measurement results, the phenomenon was simulated with a finite element method.

5 Finite Element Simulations

The computational domain used in the simulation is shown in Fig. 9. The geometry was built by measuring the sizes of each feature as accurately as possible from Fig. 6. Though an infinitely

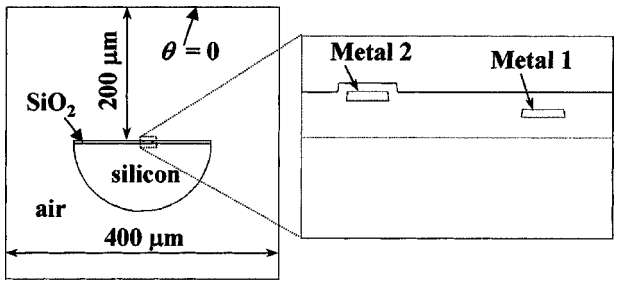

Fig. 9 Geometry used in the simulation

large domain should ideally be used, this is impossible in simulation. Hence, a sufficiently large domain was used instead in a way that the domain size was much larger than the decay length of the thermal waves.

The governing equation is given as

$$\rho c\omega i\theta=k\nabla^2\theta+g_0 \tag{7}$$

where ρ is density, c is specific heat, ω is the angular frequency of thermal wave, θ is complex temperature which represents both the amplitude and the phase lag, k is the thermal conductivity, and g_0 is the amplitude of periodic heat generation at frequency ω. Because the characteristic lengths of the features in the sample are much longer than the mean free paths of the electrons and phonons which are typically in the range of 5–10 nm at room temperature, Eq. (7) derived from the conventional Fourier heat conduction equation is still applicable. The properties of each subdomain were selected according to the materials. The amplitude of heat generation is zero except in Metal 1 and Metal 2. The boundary value of the complex temperature was arbitrarily chosen to be zero, because they are far away.

The equation was solved using the partial differential equation solver of MATLAB. Figure 10 shows the phase lag distributions calculated for three different wave generation modes for each fre-

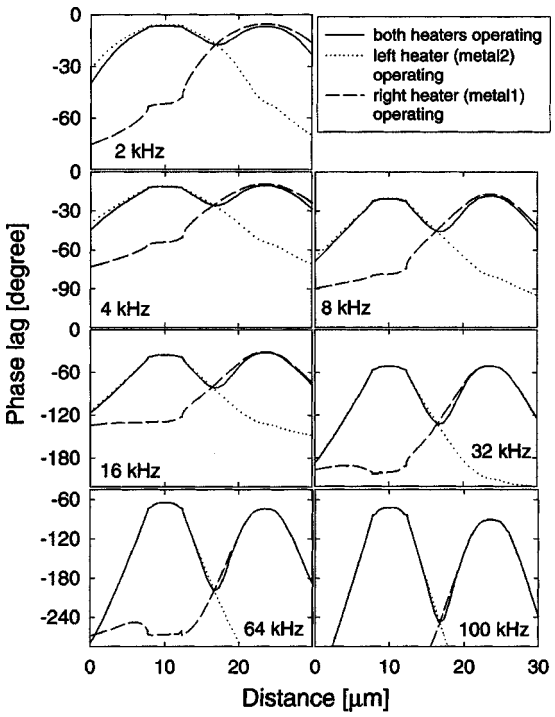

Fig. 10 Phase lag distributions calculated for three different wave generation modes for each frequency

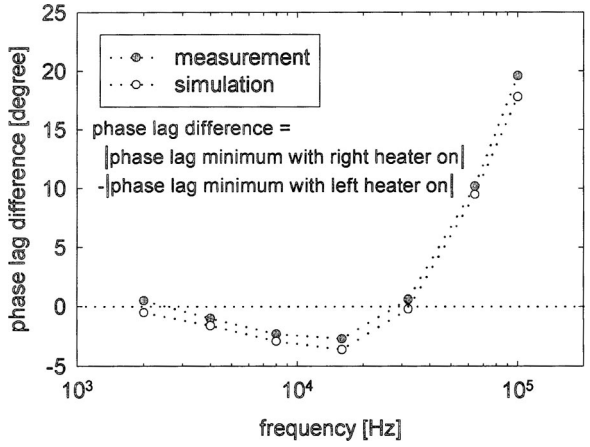

Fig. 11 The difference between minimum of phase lag with right heater operating and that with left heater operating at every wave frequency tested

quency. Compared with Fig. 10, with both heaters on, the measurement results in Fig. 8 gave a significantly higher peak on the right at 2 kHz and 4 kHz. This is due to the wave propagation paths other than tip-sample point contact, which also caused the poor agreement at relatively low frequencies in Figs. 4 and 5. As a result, the interference of the thermal wave from the left heat source becomes larger than the simulation results during the measurements.

The simulation showed that at 16 kHz the minimum of phase lag with the right heater operating is smaller by about 3 deg than that with the left heater operating. This was observed experimentally earlier in Fig. 8. Figure 11 shows the difference between the minimum of phase lag with the right heater operating and that with left heater operating at every wave frequency tested. The experiment and the simulation results match very closely. Clearly, the phase lag difference goes through a minimum. Using the analysis, it should be possible to explain this phenomenon by analyzing the simulation results, for which the data below the surface is readily available.

To help understand, the phase lag contours on the cross section at 16 kHz and 100 kHz were depicted in Fig. 12. The phase lag in the aluminum region where heat is generated is not zero. If the temperature oscillation in the aluminum region is used as the reference for the phase, the phase lag in the heat source region is zero by definition. However, what is used as the reference phase is the phase of heat generation, because the heat generation due to Joule heating is in phase with the second harmonic of the applied AC bias. Consequently, the phase lag in the heat source region is the phase difference between heat generation and temperature fluctuation. This phase lag is influenced by the thermal insulation around the heat source.

Figure 12 shows that at both 16 kHz and 100 kHz the phase lag of the left metal line is larger than that of the right metal line. The shapes of both heat sources are nearly the same, and, hence, their thermal mass should be as well. However, the thermal insulation of the metal lines is not. While both metal lines are embedded in a silicon dioxide film, metal line 1 is closer to the silicon substrate. The silicon substrate works like a heat sink because its thermal conductivity is two orders of magnitude higher than that of silicon dioxide. One the other hand, the air surrounding the region around the left heater works like a thermal insulator because its thermal conductivity is very low (~0.02 W/m-K). Therefore, the difference in phase lag of the metal lines arises from the difference in thermal insulation affected by the distance to the silicon substrate and the surface topography for this case.

The influence of thermal insulation explains why at 4, 8, and 16 kHz the minimum of phase lag measured on the surface due to the

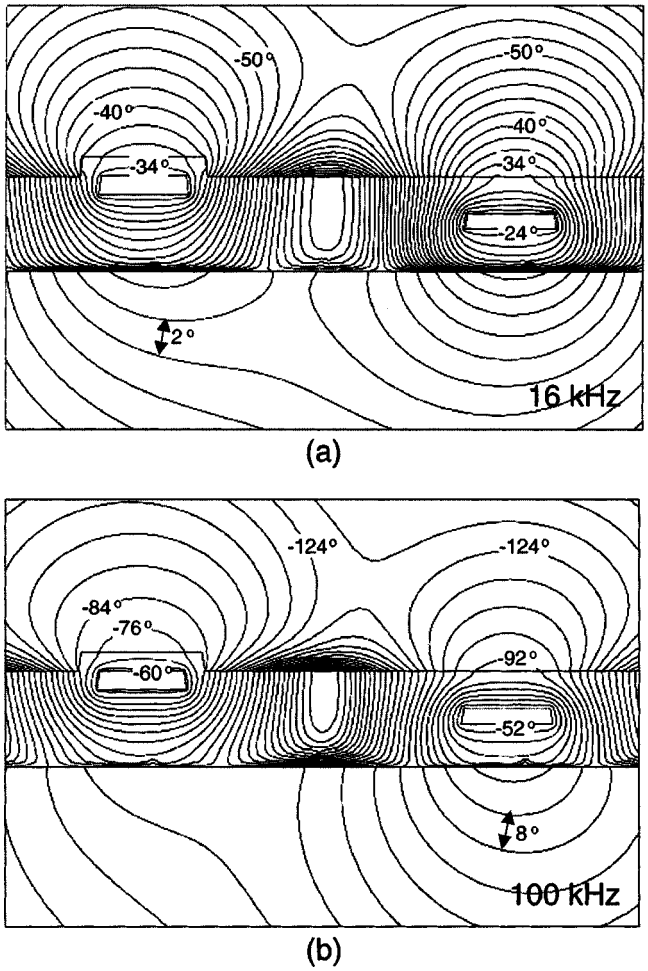

Fig. 12 Phase lag contours on the cross section: (*a*) At 16 kHz; (*b*) at 100 kHz

left heater is larger than the one due to the right heater, although the left heater is buried shallower than the right one. However, as frequency is increased, the phase lag due to the right heater measured on the surface becomes larger. The reason is as follows. At both frequencies, elliptical wave fronts propagate from the right heat source. Comparing the wave fronts, one can see that above and below the heat source the wave fronts are flatter at 100 kHz. This is due to the shorter wavelength at 100 kHz. The width of the heat source experienced by the wave becomes larger as the wavelength becomes shorter. Therefore, the shape of the wave front approaches that of a plane wave. The flatter shape of the wave fronts at shorter wavelengths results in more isophase lines between the right heat source and the surface. Therefore, at 64 kHz and 100 kHz, the phase lag due to the right heater measured on the surface becomes larger than the one due to the left heater, despite the influence of the thermal insulation.

6 Spatial Resolution

The phase lag gradient depends on the thermal diffusivity of the medium and the frequency of the thermal wave. For example, the phase lag gradient of a plane thermal wave is given by Eq. (8).

$$\frac{d\phi}{dx} = -\sqrt{\frac{\omega}{2\alpha}} \tag{8}$$

Typically, the range of the wave frequency used in STWM is from 1 to 100 kHz. In SiO_2, which is the most common insulating material used in integrated circuits, 1 degree of phase lag corre-

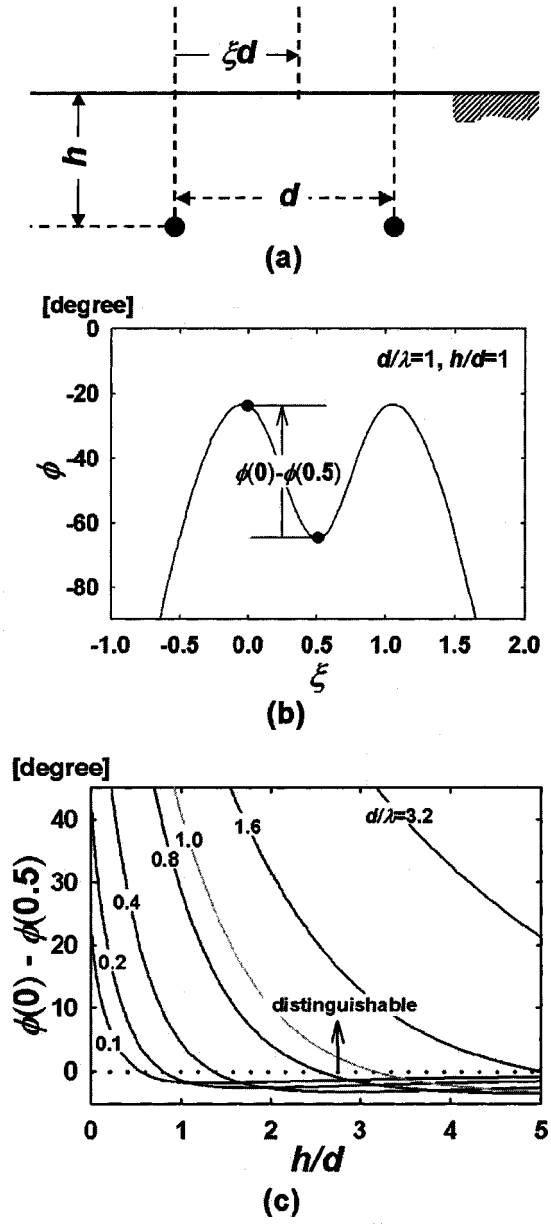

Fig. 13 (*a*) **Schematic diagram of two buried line heat sources;** (*b*) **Phase lag distribution on the surface with** $d/\lambda = h/d = 1$**;** (*c*) **phase lag difference between above a heat source and in the center of two heat sources,** $\phi(0) - \phi(0.5)$

sponds to 25 nm of distance at 100 kHz and 250 nm at 1 kHz. Therefore, even with the mildest phase lag gradient at 1 kHz, the phase lag corresponding to the spatial resolution of SThM probe ($\sim$50 nm) is about 0.2 deg, which is much larger than the phase measurement accuracy of lock-in ($\sim 10^{-3}$ deg). Hence, the spatial resolution of SThM probe rather than the phase measurement accuracy of a lock-in determines the spatial resolution of STWM imaging.

In order to retrieve subsurface information from STWM imaging results, one should understand the resolving power of thermal waves as well as the imaging resolution of STWM. For the two buried line heat sources shown in Fig. 13(*a*) the phase lag distribution on the surface can be obtained from the complex temperature distribution given by Eq. (9).

$$\theta(\xi) = 2\left(\frac{Q_0}{2\pi k}\right)\left[K_0\left(2\pi\frac{d}{\lambda}\sqrt{2i\left(\xi^2+\left(\frac{h}{d}\right)^2\right)}\right) + K_0\left(2\pi\frac{d}{\lambda}\sqrt{2i\left((1-\xi)^2+\left(\frac{h}{d}\right)^2\right)}\right)\right] \quad (9)$$

where Q_0 is the amplitude of periodic heat generation per unit length, k is the thermal conductivity of the substrate, d is the distance between the two heater, λ is the wavelength, h is the depth of the heaters, and K_0 is a modified Bessel-function of the second kind of order zero. In order to reveal the underlying physics more clearly, the equation was written with the nondimensional parameters such as the nondimensional coordinate, ξ, nondimensional distance between two heat sources, d/λ, and the nondimensional depth, h/d.

As an example, the phase lag distribution on the surface with $d/\lambda = h/d = 1$ is shown in Fig. 13(*b*). For this particular case, the minimum of phase lag between the two peaks above the two line heat sources clearly shows there are two independent buried heat sources. When there exist a phase lag minimum between the two heat sources, the phase lag difference, $\phi(0) - \phi(0.5)$ is positive and the two buried heat sources can be easily distinguished. However, depending on the depth of the heat sources and the distance between them, thermal diffusivity of the medium, and the wavelength, the phase lag difference can become negative. When the phase lag difference becomes negative, it is difficult to tell whether there are two independent buried heat sources.

In order to understand the resolving power of thermal waves, the phase lag difference between the one above a heat source and the other in the center of two heat sources, $\phi(0) - \phi(0.5)$ was plotted as a function of h/d and d/λ in Fig. 13(*c*). When the distance between two buried heaters is the same with the thermal wavelength, or when the nondimensional distance between two heat sources, $d/\lambda = 1$, the phase lag difference, $\phi(0) - \phi(0.5)$ becomes smaller as the nondimensional depth, h/d increases and eventually becomes negative at around $h/d = 3$. When the thermal wave length becomes relatively shorter than the distance between two buried heaters, for example, when the nondimensional distance between two heat sources, $d/\lambda = 1.6$, the phase lag difference, $\phi(0) - \phi(0.5)$ becomes negative at a deeper location, at around $h/d = 5$. Figure 13(*c*) shows that as the parameter, d/λ increases, the buried heat sources are distinguished more clearly. In other words, as the wavelengths of thermal waves become shorter, the resolving power of the thermal waves improves. However, it is not always desirable to use shorter wavelengths, because thermal waves decay more rapidly with the shorter wavelengths and sometimes become difficult to detect. Hence, depending on cases and imaging purposes, the wave frequency should be determined properly.

In summary, the imaging resolution of STWM is limited by the resolution of SThM probe and the resolving power of thermal waves for subsurface structures improves as the wavelengths of the thermal waves become shorter.

7 Conclusion

This paper presents a technique, scanning thermal wave microscopy (STWM), which can image the phase lag and amplitude of thermal waves at sub-micrometer scales. This technique would enable nondestructive evaluation (NDE) of buried micro and nanostructures. To understand the measurement mechanism of STWM, experiments on the nature of the tip-sample contact were performed. These experiments showed that the liquid film between the tip and the sample reduces tip-sample phase lag by enhancing tip-sample heat transfer. The measurement accuracy of STWM was demonstrated by a benchmark experiment, which also showed that the tip-sample phase lag remains constant during scanning.

The ultimate goal of STWM is NDE of sub-surface structure at nanometer scale resolution. To demonstrate the effectiveness of

the technique a sample containing two levels of metal interconnect bridged by a via was used. The phase lag and amplitude distributions were measured with wave frequencies up to 100 kHz. The comparison between measurements and finite element analysis validated both results. The finite element analysis results showed that the phase lag of the heat source is affected by thermal insulation and that the shape of the wave front depends upon the wave frequency. Finally, simple estimations of the imaging resolution of STWM and the resolving power of thermal waves for subsurface structures were given.

In this paper, only the imaging of active elements that can generate heat was dealt with. However, one can easily imagine that the technique can be extended to the imaging of passive elements that cannot generate heat. For example, a plane thermal wave traveling within a medium would be scattered by a buried structure with different thermal properties from the medium. By measuring the amplitude and phase lag distributions of the scattered thermal wave arriving at the surface, it would be possible to decide the location and shape of the structure.

Acknowledgments

The authors want to thank S. Huxtable for his help in measuring the thermal conductivity of Pyrex glass by the 3ω method. This work was supported by Engineering Program, Basic Energy Sciences, Department of Energy.

Nomenclature

d = distance between two buried heat sources [m]
g_0 = amplitude of periodic heat generation per unit volume [W/m^3]
f = wave frequency [s^{-1}]
h = depth of buried heat sources [m]
H = the height of the probe tip [m]
i = imaginary unit, $\sqrt{-1}$
k = thermal conductivity [W/m-K]
K_0 = modified Bessel-function of the second kind of order zero
q_0 = amplitude of periodic heat generation per unit area [W/m^2]
Q_0 = amplitude of heat generation per unit length [W/m]
r = radial coordinate [m]; amplitude of thermal wave [K]
t = time [s]
T = temperature [K]
T_0 = amplitude of temperature fluctuation [K]
v = wave speed [m/s]
x, y = coordinates in Cartesian system
α = thermal diffusivity [m^2/s]
δ_{th} = thermal penetration depth [m]
ϕ = phase lag [degree]
λ = wavelength [m]
θ = complex temperature which represents both amplitude and phase lag [K]
ρ = density [kg/m^3]
ξ = integration variable; nondimensional coordinate
ω = angular frequency [rad/s]

References

[1] Carslaw, H. S., and Jaeger, J. C., 1959, *Conduction of Heat in Solids*, Oxford University Press, Oxford.
[2] Murashov, V. V., and White, M. A., 1998, ''Apparatus for Dynamical Thermal Measurement of Low-thermal Conductivity Particulate Materials at Sub-Ambient Temperatures,'' Rev. Sci. Instrum., **69**, pp. 4198–4204.
[3] Araki, N., Yang, J., Tang, D., and Makino, A., 1998, ''Measurement of the Thermal Conductivity of Layered Film by Periodic Heating,'' High Temp.-High Press., **30**, pp. 321–326.
[4] Cahill, D. G., 1990, ''Thermal Conductivity Measurement from 30 to 750 K: The 3 omega Method,'' Rev. Sci. Instrum., **61**, pp. 802–808.
[5] Bhusari, D. M., Teng, C. W., and Chen, K. H., 1997, ''Traveling Wave Method for Measurement of Thermal Conductivity of Thin Films,'' Rev. Sci. Instrum., **68**, pp. 4180–4183.
[6] Czarnetzki, W., Wandelt, M., and Roetzel, W., 1996, ''Thermal Wave Analysis for Measurements of Thermal Diffusivity,'' IEEE Instrum. Meas. Technol. Conf., Brussels, Belgium, pp. 1195–1199.
[7] Stanimirovic, A. M., Maglic, K. D., Perovic, N. L., and Vukovic, G. S., 1998, ''Measurement of Thermal Diffusivity of Thin Films by the AC Calorimetric Method,'' High Temp.-High Press., **30**, pp. 327–332.
[8] Mandelis, A., 1987, *Photoacoutic and Thermal Wave Phenomena in Semiconductors*, North-Holland, New York.
[9] Voigt, P., Hartmann, J., and Reichling, M., 1996, ''Thermal Wave Imaging of Electrically Heated Microstructures,'' J. Appl. Phys., **80**, pp. 2013–2018.
[10] Batista, J. A., Mansanares, A. M., Silva, E. C., and Fournier, D., 1997, ''Photothermal and Electroreflectance Images of Biased Metal-Oxide-Semiconductor Field-Effect Transistors: Six Different Kinds of Subsurface Microscopy,'' J. Appl. Phys., **82**, pp. 423–426.
[11] Ocariz, A., Sanchez-Lavega, A., and Salazar, A., 1997, ''Photothermal Study of Subsurface Cylindrical Structures. I. Theory,'' J. Appl. Phys., **81**, pp. 7552–7560.
[12] Ocariz, A., Sanchez-Lavega, A., and Salazar, A., 1997, ''Photothermal Study of Subsurface Cylindrical Structures. II. Experimental Results,'' J. Appl. Phys., **81**, pp. 7561–7566.
[13] Terron, J. M., Sanchez-Lavega, A., and Salazar, A., 2000, ''Multiple Scattering Effects of Thermal Waves Two Subsurface Cylinders,'' J. Appl. Phys., **87**, pp. 7561–7566.
[14] Shi, L., Kwon, O., Miner, A., and Majumdar, A., 2001, ''Design and Batch Fabrication of Probes for Sub-100 nm Scanning Thermal Microscopy,'' J. Microelectromech. Syst., **10**(3), pp. 370–378.
[15] Luo, K., Shi, Z., Varesi, J., and Majumdar, A., 1997, ''Sensor Nanofabrication, Performance, and Conduction Mechanism in Scanning Thermal Microscopy,'' J. Vac. Sci. Technol. A, **15**, pp. 349–360.

Active Thermal Control of Distributed Parameter Systems With Application to Testing of Packaged IC Devices

Matthew Sweetland
Mem. ASME
e-mail: sweetlan@alum.mit.edu

John H. Lienhard V
Fellow ASME
e-mail: lienhard@mit.edu

W. M. Rohsenow Heat and Mass Transfer Laboratory,
Department of Mechanical Engineering,
Massachusetts Institute of Technology,
77 Massachusetts Avenue, Room 3-162,
Cambridge, MA 02139-4307

Active control of the die-level temperature is desirable during production testing of high power microprocessors, so as to ensure accurate performance classification. Such control requires that the controlling thermal load time-lead the dissipated thermal load and that it be modulated to account for the distributed thermal capacitance and resistance of the device packaging. The analysis in this paper demonstrates fundamental limits of temperature control for typical devices under test conditions. These limits are identified for specified control power to die power ratios. The effects of test sequence design and device package design on the temperature control limits are also examined. The theory developed can be applied to any thermal control problem where a conductive medium separates the control source from the location where control is desired.
[DOI: 10.1115/1.1527908]

Keywords: Conduction, Control, Electronics, Heat Transfer, Temperature

1 Introduction

All high-performance electronic devices are subject to a 100 percent functional test prior to being shipped by the manufacturer [1]. High power microprocessor devices are also subject to a classification test to determine the effective operating speed of the device. During this classification test, the goal of control is to keep the temperature of the die at a single set temperature while the device power is varied between 0 percent to 100 percent power in a predetermined test sequence. Temperature increases over the specified test temperature decrease the signal propagation speed within the device, and an excessive temperature rise above the test temperature can result in the device being classified in the wrong category (e.g., a 1 GHz device classified and shipped as a 950 MHz device). The manufacturer normally specifies a die-level test temperature range; a typical test temperature specification is 85°C−0°C/+3°C.

As microprocessor device powers have increased and device sizes have decreased, the power densities in packaged microprocessor devices have approached levels of 50 to 100 W/cm^2 [2–4]. With test sequences rapidly varying the device power at these power densities, active temperature control is essential to holding the die temperature within tolerance. Because the tests are being performed on packaged devices, thermal control cannot be applied to the die itself. Instead, control heating and cooling must be applied to some external part of the packaging. This separation of the control point from the die limits the achievable temperature control tolerances for given test sequences and device powers.

An estimate of the required control power is needed in the early design phases of temperature control systems for test equipment, so that the heating and cooling system capabilities can be specified. For this reason, an analysis of the packaged device by itself, without any consideration of the control system, is very useful in determining the required minimum heating and cooling capacities as well as in determining the effects of varying the test sequence design and package design on the thermal control limits. This paper develops such a model.

Contributed by the Heat Transfer Division for publication in the JOURNAL OF HEAT TRANSFER. Manuscript received by the Heat Transfer Division December 18, 2001; revision received September 9, 2002. Associate Editor: G. S. Dulikravich.

2 Mathematical Model

Semiconductor packaging encompasses a wide range of geometries, die architectures, and materials. In this paper, we consider the arrangement shown in Fig. 1. The device consists of a silicon die mounted on single or multiple interposer/interface layers. An integrated heat spreader (typically plated copper) is mounted on top of the die structure with a very thin layer of a thermal interface material or grease between the die and the heat spreader. The heat spreader area is typically much larger than the die area and provides a bonding surface for an external heat sink in the final device application. We consider situations in which the die's heat generation is essentially uniform over its area, with no large-scale variations.

Our focus is on temperature under test conditions. During testing, the packaged device is held in a test socket which is itself temperature controlled to the desired test temperature. The socket is thermally isolated from the test electronics [1,5].

Work by Viswanath et al. [6] and Sweetland [7] has shown that the thermal resistance between the die structure and the interposer layer is typically much higher than the thermal resistance between the die structure and the surface of the integrated heat spreader. For this reason, only the die and integrated heat spreader will be considered in the transient model (the interposer side of the die is considered adiabatic). If the architecture of a particular device allows non-negligible heat transfer to the interposer, the present results will provide an upper bound on the required control power and a conservative basis for design.

Several additional simplifying approximations can be made about the device under test and the operating conditions. The goal of this analysis is to determine the limits of temperature control under typical transient die power fluctuations, so only transient effects will be considered[1]. The system is initially taken to be one-dimensional. This is equivalent to neglecting the effect of *transient* lateral conduction in the integrated heat spreader; a correction factor for this approximation is given in a later section.

The interfacial resistance between the die and the integrated

[1]The steady state (DC) component of the temperature response of the system can be superimposed if needed.

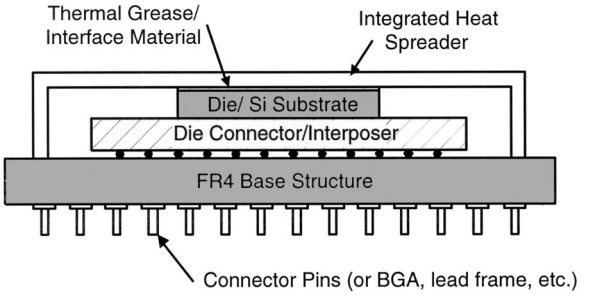

Fig. 1 Typical cross-section of a high power microprocessor device

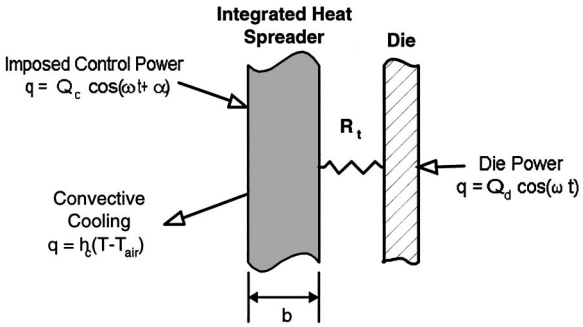

Fig. 2 Schematic diagram of simplified device for transient analysis. Q_c is the magnitude of the control input and α is the phase shift of the control input. Q_d is the magnitude of the die power profile.

heat spreader is assumed to be known. The heat capacitance of the interface material is neglected, since typical interface materials are thin relative to typical dies.

Temperature gradients within the die are taken to be small, effectively making the die a lumped object with uniform internal heat generation. At low frequencies, this approximation is easily justified because the thermal resistance of the interface layer is large compared to that of the die, unless the dies are very thick (>1500 μm). For higher frequencies, analysis of the unsteady conduction in the die, with heat generation confined to the face opposite the integrated heat spreader, shows that the die follows lumped response for the frequencies of importance to the die's thermal response. At sufficiently high frequencies, departures from lumped behavior occur but are associated with very small temperature variations [7]. We give a specific criterion later in the paper.

Based on these approximations, the physical system reduces to the model system shown in Fig. 2.

Various implementations of test-system temperature controls have been developed [7–9]. For the purposes of this paper, the control power is assumed to be a radiation source (a high power laser) whose power can be instantly adjusted. The front face of the integrated heat spreader is subjected to both this radiation and convective cooling. The convective conditions are constant[2], with thermal control being attained through modulation of the radiation source. This combined radiant heating/convection cooling thermal control system has the advantage that no additional thermal mass is placed in contact with the device under test, which greatly improves the transient response.

The transient part of the die test power sequence can be decomposed into component frequencies. The results will show that the control power required for a specified die temperature tolerance is a function of the test-sequence frequency. For this reason, the die power in the analysis will be assumed to be a sinusoidal signal at a fixed frequency and magnitude. Any desired test sequence can be reconstructed using sinusoids by superposition. A surface flux that provides the control power is also taken to be sinusoidal, having the same frequency but with some specified phase shift. It is important to note that the fluctuating (AC) control power is superposed on a larger, steady (DC) power so that the physical surface flux is always positive.

To start the transient analysis, only the temperature profile within the integrated heat spreader (IHS) will be considered. For mathematical convenience, that problem can be further decomposed into the two parts shown in Fig. 3. The first part is for the IHS with an adiabatic back face[3] and a front surface subject to convective cooling and the radiative control power profile (Fig. 3(*a*)). The second part is for the IHS with an imposed surface flux from the die on one face and convection on the other face (Fig. 3(*b*)). The two results are then combined using superposition. To maintain contact with the physical variables, we do not introduce a full nondimensionalization until the solution has been constructed, at the end of this section.

2.1 IHS Temperature Response to Control Input. The steady periodic transient response to the two cases in Fig. 3 can be calculated using a complex temperature approach [10]. Consider an infinite slab with one side adiabatic as shown in Fig. 3(*a*). The other face is subject to convective boundary conditions, an average heat transfer coefficient h_c with an air temperature $T_{\text{air}}=0$, and a control flux $Q(t)=Q_c\cos(\omega t)$. Using complex analysis methods, it is assumed that the solution to the temperature profile in the complex plane takes the form:

$$W=X(x)\cdot\tau(t) \tag{1}$$

where $\tau(t)=e^{i\omega t}$ and $i=\sqrt{-1}$ is the imaginary number. The conduction equation in the integrated heat spreader is

$$\frac{\partial^2 W}{\partial x^2}=\frac{1}{a_t}\frac{\partial W}{\partial t} \tag{2}$$

so with an assumed solution of form Eq. (1), this can be rewritten

$$\frac{d^2X}{dx^2}=\frac{i\omega}{a_t} \tag{3}$$

which has the general solution

$$X(x)=C_1\exp\left(-\sqrt{\frac{i\omega}{a_t}}x\right)+C_2\exp\left(\sqrt{\frac{i\omega}{a_t}}x\right) \tag{4}$$

The boundary conditions on Eq. (3) are as follows:

$$x=0 \quad \frac{dX}{dx}=0 \tag{5}$$

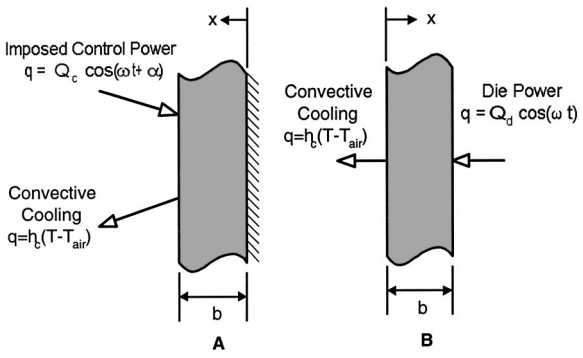

Fig. 3 Schematic drawing of decomposition for solution to transient temperature profile in integrated heat spreader

[2]Fixed air temperature and constant air flow rate.
[3]Die-side face is assumed adiabatic.

$$x=b \quad -k\frac{dX}{dx}+Q_c=h_cX \tag{6}$$

Use of the boundary condition at $x=0$ yields:

$$\frac{dX}{dx}=0=-\sqrt{\frac{i\omega}{a_t}}C_1+\sqrt{\frac{i\omega}{a_t}}C_2 \tag{7}$$

from which $C_1=C_2\equiv C$. The boundary condition at $x=b$ produces the expression:

$$h_cC[e^{-bL(i+1)}+e^{bL(i+1)}]+kC[e^{-bL(i+1)}-e^{bL(i+1)}]L(i+1)=Q_c \tag{8}$$

where $L\equiv\sqrt{\omega/2a_t}\,(\mathrm{m}^{-1})$. This equation must be solved for C. Expanding all exponential terms into complex sinusoids, Eq. (8) can be written as:

$$kL\cdot C(A+Bi)=Q_ce^{bL} \tag{9}$$

where

$$A=\left\{\frac{\mathrm{Bi}_{\mathrm{IHS}}}{bL}\cos(bL)(e^{2bL}+1)-[\cos(bL)+\sin bL]+e^{2bL}[\cos(bL)-\sin bL]\right\} \tag{10}$$

$$B=\left\{\frac{\mathrm{Bi}_{\mathrm{IHS}}}{bL}\sin(bL)(e^{2bL}-1)-[\cos bL-\sin(bL)]+e^{2bL}[\cos(bL)+\sin bL]\right\} \tag{11}$$

where $\mathrm{Bi}_{\mathrm{IHS}}=h_cb/k$ is the spreader Biot number and $bL=b\sqrt{\omega/2a_t}$ is a dimensionless frequency parameter. The Biot number is typically small compared to one. Equation (9) can now be solved for C by multiplying both sides through by the complex conjugate. Substituting the results into the original solution for X yields:

$$X=\frac{Q_ce^{bL}(A-Bi)}{kL(A^2+B^2)}[e^{-xL(i+1)}+e^{xL(i+1)}] \tag{12}$$

To find the solution to the temperature profile in the integrated heat spreader in the real domain, the real part of $Xe^{i\omega t}$ must be taken:

$$T(x,t)=\mathrm{Re}(Xe^{i\omega t})=\frac{Q_ce^{bL-xL}}{kL(A^2+B^2)}[A\cos(\omega t-xL)+B\sin(\omega t-xL)]+\frac{Q_ce^{bL+xL}}{kL(A^2+B^2)}[A\cos(\omega t+xL)+B\sin(\omega t+xL)] \tag{13}$$

2.2 IHS Temperature Response to Die Input. An identical approach can be used to find the temperature profile of the integrated heat spreader subject to heat input from the die, but with different boundary conditions. Using the coordinate system shown in Fig. 3(*b*), the boundary conditions are as follows:

$$x=0 \quad k\frac{dX}{dx}=h_cX \tag{14}$$

$$x=b \quad Q_d=k\frac{dX}{dx} \tag{15}$$

With Eq. (4) for X, the boundary condition at $x=0$ yields:

$$k\sqrt{\frac{i\omega}{a_t}}(C_2-C_1)=h_c(C_1+C_2) \tag{16}$$

This equation can be solved to express the new C_1 in terms of the new C_2:

$$C_1=C_2\frac{2(kL)^2-h_c^2+(2h_ckL)i}{h_c^2+2kh_cL+2(kL)^2} \tag{17}$$

in which $L=\sqrt{\omega/2a_t}$ as before. Defining

$$D=h_c^2+2kh_cL+2(kL)^2, \quad E=2(kL)^2-h_c^2, \quad F=2h_ckL \tag{18}$$

Eq. (17) can be written

$$C_1=C_2\frac{(E+Fi)}{D} \tag{19}$$

and the solution for X becomes

$$X=C_2\left[\frac{E+Fi}{D}\exp\left(-\sqrt{\frac{i\omega}{a_t}}x\right)+\exp\left(\sqrt{\frac{i\omega}{a_t}}x\right)\right] \tag{20}$$

Substitution of this expression into the boundary condition at $x=b$ produces

$$Q_d=C_2kL\left[(i+1)e^{bL}e^{bLi}-\frac{e^{-bL}}{D}(E+Fi)(i+1)e^{-bLi}\right] \tag{21}$$

which may be rearranged to

$$\frac{Q_d}{C_2kL}=e^{bL}[\cos(bL)-\sin(bL)]-\frac{e^{-bL}}{D}[G\cos(bL)+N\sin(bL)]+e^{bL}i[\sin(bL)+\cos(bL)]-\frac{e^{-bL}}{D}i[-G\sin(bL)+N\cos(bL)] \tag{22}$$

where

$$G=E-F \quad \text{and} \quad N=E+F. \tag{23}$$

With the following additional definitions

$$P=e^{bL}[\cos(bL)-\sin(bL)]-\frac{e^{-bL}}{D}[G\cos(bL)+N\sin(bL)] \tag{24}$$

$$R=e^{bL}[\sin(bL)+\cos(bL)]+\frac{e^{-bL}}{D}[G\sin(bL)-N\cos(bL)] \tag{25}$$

the solution for the constant C_2 may be written

$$C_2=\frac{Q_d(P-Ri)}{kL(P^2+R^2)} \tag{26}$$

The function X is therefore

$$X=\frac{Q_d(P-Ri)}{kL(P^2+R^2)}\left[\frac{(E+Fi)}{D}e^{-xL(i+1)}+e^{xL(i+1)}\right] \tag{27}$$

The solution for the temperature in the heat spreader is again found by solving for the real part of $Xe^{i\omega t}$. Setting

$$U=\frac{P\cdot E+R\cdot F}{D} \quad \text{and} \quad V=\frac{P\cdot F-E\cdot R}{D} \tag{28}$$

the final expression for the temperature of the heat spreader is

$$T(x,t)=\mathrm{Re}(Xe^{i\omega t})=\frac{Q_de^{-xL}}{kL(P^2+R^2)}[U\cos(\omega t-xL)-V\sin(\omega t-xL)]+\frac{Q_de^{xL}}{kL(P^2+R^2)}[P\cos(\omega t+xL)+R\sin(\omega t+xL)] \tag{29}$$

We note that P, R, U, and V depend on bL and $\mathrm{Bi}_{\mathrm{IHS}}$ only.

2.3 IHS Combined Temperature Response. The temperature response of the integrated heat spreader to concurrent control and die heat inputs is found using superposition. In particular, we seek the temperature on the face of the IHS that contacts the die. That temperature is obtained by adding the solution for the control input at $x=0$, Eq. (13), to the solution for the die input at $x=b$, Eq. (29), recalling that the x coordinates differ for the two solutions. A phase shift, α, must be added to the solution for the control input in order to calculate the required amplitude and phase lag of the control heat input for a desired IHS temperature; this simply means substituting $(\omega t+\alpha)$ for (ωt) in Eq. (13). After some algebra, the final temperature response on the die-side face of the IHS is:

$$T_{\mathrm{IHS}}=\frac{2Q_c e^{bL}}{kL(A^2+B^2)}\{[A\cos\alpha+B\sin\alpha]\cos(\omega t)+[B\cos\alpha - A\sin\alpha]\sin(\omega t)\}+\frac{Q_d e^{-bL}}{kL(P^2+R^2)}\{[U\cos(bL)+V\sin(bL)]\cos(\omega t)+[U\sin(bL)-V\cos(bL)]\sin(\omega t)\}+\frac{Q_d e^{bL}}{kL(P^2+R^2)}\{[P\cos(bL)+R\sin(bL)]\cos(\omega t)-[P\sin(bL)-R\cos(bL)]\sin(\omega t)\}. \quad (30)$$

From this result, for any specified power dissipation amplitude on the die Q_d and any desired IHS die-side temperature response T_{IHS}, the control power amplitude Q_c and phase shift α required can be calculated. For example, to obtain a constant temperature at the die contact point on the integrated heat spreader ($T_{\mathrm{IHS}}=0$, say), the magnitude and phase shift of the control signal are found by solving the equation:

$$\{PS_2\cdot[A\cos\alpha+B\sin\alpha]\cdot Q_c+PS_1\cdot e^{-bL}[U\cos(bL)+V\sin(bL)]+PS_1\cdot e^{bL}[P\cos(bL)+R\sin(bL)]\}\cos(\omega t)+\{PS_2\cdot[B\cos\alpha-A\sin\alpha]\cdot Q_c+PS_1\cdot e^{-bL}[U\sin(bL)-V\cos(bL)]+PS_1\cdot e^{bL}[R\cos(bL)-P\sin(bL)]\}\sin(\omega t)=0 \quad (31)$$

with

$$PS_1=\frac{Q_d}{kL(P^2+R^2)} \qquad PS_2=\frac{2e^{bL}}{kL(A^2+B^2)} \quad (32)$$

Since Eq. (31) must hold for any time t, the solution for Q_c and α may be obtained by requiring that coefficients of the sine and cosine terms of Eq. (31) vanish separately. This yields two equations which define Q_c as a function of α:

$$\left\{\frac{2e^{bL}[A\cos\alpha+B\sin\alpha]}{A^2+B^2}\right\}\cdot\frac{Q_c}{Q_d}=-\left\{\frac{e^{-bL}[U\cos(bL)+V\sin(bL)]+e^{bL}[P\cos(bL)+R\sin(bL)]}{P^2+R^2}\right\} \quad (33)$$

$$\left\{\frac{2e^{bL}[B\cos\alpha-A\sin\alpha]}{A^2+B^2}\right\}\cdot\frac{Q_c}{Q_d}=-\left\{\frac{e^{-bL}[U\sin(bL)-V\cos(bL)]+e^{bL}[R\cos(bL)-P\sin(bL)]}{P^2+R^2}\right\} \quad (34)$$

The solution to these simultaneous equations is the intersection point of a graph of the sine and cosine for Q_c as a function of α; a dimensional example is shown in Fig. 4. For a 10 Hz die power profile with a magnitude of $Q_d=10\ \mathrm{W/cm^2}$, the solution for the control power profile to obtain a constant temperature on the back face of the IHS is a 10 Hz control profile with a phase shift of $\alpha=226.1$ deg and an amplitude $Q_c=12.5\ \mathrm{W/cm^2}$.

In nondimensional terms, factors in braces in these equations depend only upon the dimensionless frequency parameter, bL, and the Biot number of the IHS, $\mathrm{Bi_{IHS}}$. Thus, the dimensionless control power required, Q_c/Q_d, is a function of (bL) and $\mathrm{Bi_{IHS}}$.

The solution for Q_c under given conditions can be used to generate the temperature profile in the IHS under steady periodic conditions. Figure 5 presents the temperature response in the IHS if only the die power profile is imposed, continuing the example begun in Fig. 4. As can be seen, the temperature of the IHS at the die interface fluctuates at 10 Hz, as does the convection side of the IHS. The maximum and minimum temperatures through the IHS are plotted in the bottom frame of Fig. 5. A phase shift occurs between the temperatures on the two faces, and the amplitude on the die side is slightly larger than the convection side.

If a control profile of magnitude $Q_c=12.5\ \mathrm{W/cm^2}$ and phase lag of $\alpha=226.1$ deg is applied to the convection side of the IHS, the resulting IHS temperature profile is shown in Fig. 6. As can be seen, the temperature variation at the die side contact face of the IHS can be reduced to zero by application of the control power profile.

2.4 Temperature Response of Die. The die normally has small thermal resistance and can be treated as isothermal for the frequencies of interest. Its temperature response is described by

$$m\cdot c_p\frac{dT_{\mathrm{die}}}{dt}=Q_d\cdot\cos(\omega t)-\frac{T-T_{BF}}{R_t} \quad (35)$$

where m is the mass of die per unit area and T_{BF} is the die-side surface temperature of the integrated heat spreader. This equation neglects the heat capacity of the thermal interface material between the die and the IHS. For ideal temperature control, where

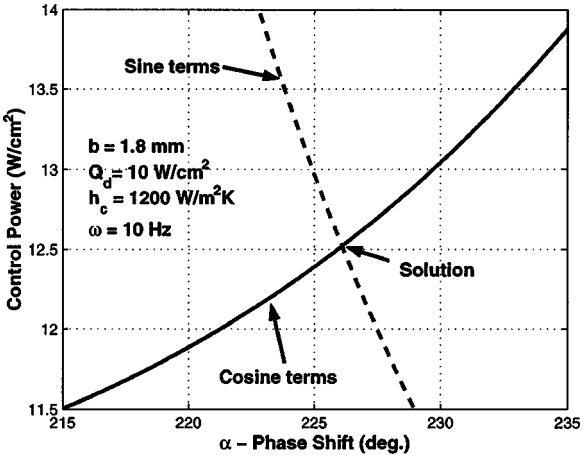

Fig. 4 Solution for phase shift and magnitude of control power profile

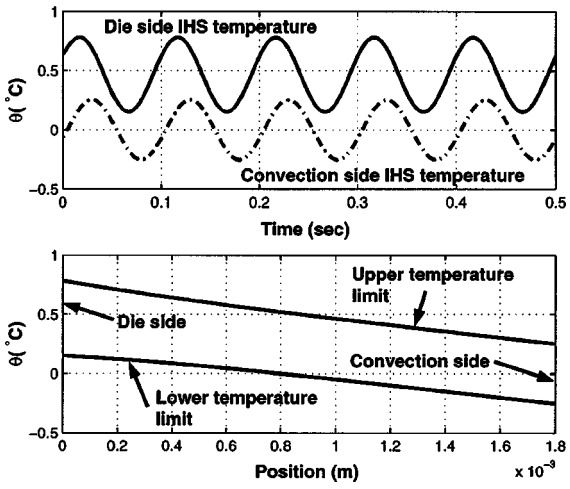

Fig. 5 Temperature response of IHS to a 10 Hz die power profile with $Q_d = 10$ W/cm^2. For this system, $h_c = 1200$ W/m^2 and the IHS is 1.8 mm thick.

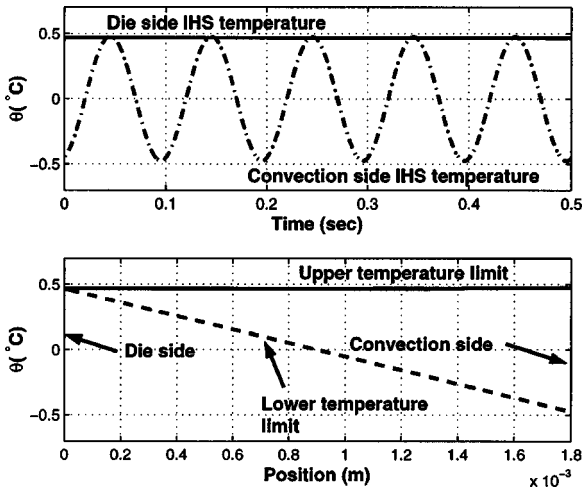

Fig. 6 Temperature response of IHS to a 10 Hz die power profile with $Q_d = 10$ W/cm^2 and a control power profile imposed on the front face

there is no change in die temperature, and taking the desired die temperature be zero[4], the equation for the IHS back face temperature becomes:

$$T_{BF} = -Q_d \cdot R_t \cos(\omega t) = Q_d \cdot R_t \cos(\omega t + \pi) \tag{36}$$

The second expression clearly shows that for ideal temperature control, the desired IHS back face temperature is 180 deg out of phase with the die power profile with a magnitude that depends on Q_d and the thermal interface resistance R_t. Returning to the example in Fig. 5, to obtain constant die temperature, the desired back-face temperature must be obtained by appropriate scaling of the control profile. To find this control profile, Eq. (31) must be solved, but instead of zero on the righthand side of the equation, the term $(-Q_d \cdot R_t \cos(\omega t))$ must be used. Again separating the sine and cosine terms, the solution for the power profile can be found.

The desired control profile phase shift to obtain a constant die temperature with a die power density of $Q_d = 10$ W/cm^2 is $\alpha = 283.42$ deg with a magnitude of $Q_c = 173.0$ W/cm^2. The phase shift calculated here is a phase lag between the die input and the control input, which may alternatively be regarded as a phase *lead* of 76.58 deg with the control power profile leading the die power profile. This is important when the analysis turns to control limits for a die power profile.

From these results, the temperature profile in the IHS can again be calculated, as in Fig. 7, which also shows the die power profile and the target temperature, T_{BF}. Although the target temperature can be again maintained, a significantly higher control power is required relative to the previous case (for which T_{BF} was held constant). The ratio of control power to die power has risen from 1.25 to 17.30. This is because the entire mass of the IHS must now be driven over a much wider temperature range. Similar calculations can be performed over the full range of frequencies and powers.

2.5 Control Profile Calculation With Specified Die Temperature Tolerance. The two previous analyses identify the control profile for the cases where the die temperature is constant (ideal control) or where the temperature of the back face of the IHS is held constant. To reach actual practice, we must go a step further and allow the die temperature to fluctuate within specified tolerance limits for a given die power profile (non-ideal control). We now adapt the previous analyses to obtain the control power profile for a varying die temperature.

In the light of Eqs. (35) and (36), we may assume that for non-ideal control, the back face temperature of the IHS has the form

$$T_{BF} = M \cdot R_t \cdot Q_d \cos(\omega t + \beta) \tag{37}$$

where the scaling factor M takes on a value between 0 and 1. Upon substituting Eq. (37) into Eq. (35) and integrating, we obtain

$$T_{\text{die}} = \frac{Q_d}{m c_p(\lambda^2 + \omega^2)} \{(1 + M\cos\beta)[\lambda\cos(\omega t) + \omega\sin(\omega t)] - \sin\beta[\lambda\sin(\omega t) - \omega\cos(\omega t)]\} \tag{38}$$

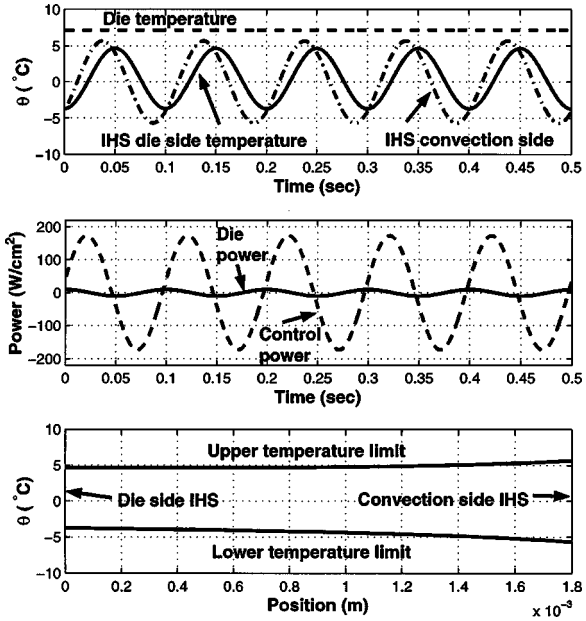

Fig. 7 IHS temperature profile for ideal control of die temperatures

[4]Any other desired die temperature can be used by adding a steady state offset to this solution.

where $\lambda \equiv 1/mc_pR_t$ ($1/\lambda$ is the lumped-capacity time constant associated with Eq. 35). Of interest here is the magnitude of the fluctuation of T_{die}. By setting this magnitude equal to the allowed tolerance ΔT of the die temperature, a relationship between the scaling factor M and the phase shift β is obtained:

$$M = -\cos\beta \pm \sqrt{\cos^2\beta - 1 + (mc_p\Delta T/2Q_d)^2(\omega^2+\lambda^2)} \quad (39)$$

The goal is to minimize M for a given die power profile, since a smaller value of M leads to a smaller required control power. Equation (39) can be differentiated with respect to β

$$\frac{dM}{d\beta} = \sin\beta \mp \frac{\cos\beta\sin\beta}{\sqrt{\cos^2\beta - 1 + (mc_p\Delta T/2Q_d)^2(\omega^2+\lambda^2)}} = 0 \quad (40)$$

This equation has two roots: $\beta=0$ and $\beta=\pi$. For the case $\Delta T = 0$, the solution must be $M=1$, not $M=-1$, so the correct root is $\beta=\pi$. Hence,

$$M = 1 - \frac{mc_p\Delta T}{2Q_d}\sqrt{\lambda^2+\omega^2} = 1 - \frac{\Delta T}{2Q_dR_t}\sqrt{1+\omega^2/\lambda^2} \quad (41)$$

which determines the magnitude of the fluctuation of T_{BF}.

One more issue must be addressed in order to find the required control power profile. The flux from the die into the heat spreader is no longer equal to the die power profile because some of the die power is taken up by the heat capacity of the die and stored in the form of a steady periodic die temperature change. From the preceding analysis, the die temperature profile is

$$T_{\text{die}} = \frac{Q_d(1-M)}{mc_p(\lambda^2+\omega^2)}[\lambda\cos(\omega t) + \omega\sin(\omega t)] \quad (42)$$

The heat flux from the die into the heat spreader, Q_{ds}, may be calculated from Eqs. (37) and (42)

$$Q_{ds} = \frac{T_{\text{die}} - T_{BF}}{R_t} = \left(\frac{Q_d\lambda(1-M)}{mc_pR_t(\lambda^2+\omega^2)} + MQ_d\right)\cos(\omega t) + \frac{Q_d\omega(1-M)}{mc_pR_t(\lambda^2+\omega^2)}\sin(\omega t) \quad (43)$$

$$Q_{ds} = Q_d\sqrt{\frac{\lambda^2+M^2\omega^2}{\lambda^2+\omega^2}}\cdot\cos(\omega t+\gamma) \equiv Q_{da}\cos(\omega t+\gamma)$$

where γ is given by

$$\gamma = \tan^{-1}\left[\frac{\omega\lambda(M-1)}{\lambda^2+M\omega^2}\right] \quad (44)$$

and the amplitude Q_{da} is defined as shown. The heat flux from the die into the integrated heat spreader is reduced in magnitude and shifted by a phase lag γ.

These revised solutions for the magnitude and phase shift of the flux and temperature at the die-side of the IHS can now be used in Eq. (30), by setting T_{IHS} in Eq. (30) to T_{BF} from Eq. (37) and setting Q_d in Eq. (30) to Q_{da} from Eq. (43). Upon separating the sine and cosine terms, there obtains:

$$\{PS_2\cdot[A\cos\alpha + B\sin\alpha]\cdot Q_c + PS_3e^{-bL}\cdot[U\cos(bL-\gamma) + V\sin(bL-\gamma)] + PS_3e^{bL}\cdot[P\cos(bL+\gamma) + R\sin(bL+\gamma)]\}\cos(\omega t) + \{PS_2\cdot[B\cos\alpha - A\sin\alpha]\cdot Q_c + PS_3e^{-bL}\cdot[U\sin(bL-\gamma) - V\cos(bL-\gamma)] - PS_3e^{bL}\cdot[P\sin(bL+\gamma) - R\cos(bL+\gamma)]\}\sin(\omega t) = -R_tM\cdot Q_d\cos(\omega t) \quad (45)$$

where PS_3 is defined as

$$PS_3 = \frac{Q_{da}}{kL(P^2+R^2)} \quad (46)$$

Equation (45) is solved in the same way as Eq. (31), by requiring that the sine and cosine terms vanish simultaneously:

$$\left\{\frac{2e^{bL}[A\cos\alpha + B\sin\alpha]}{A^2+B^2}\right\}\cdot\frac{Q_c}{Q_d}\cdot\frac{Q_d}{Q_{da}} = -M\cdot\frac{bL}{\text{Bi}_{ds}}\cdot\frac{Q_d}{Q_{da}} - \left\{\frac{e^{-bL}[U\cos(bL-\gamma) + V\sin(bL-\gamma)] + e^{bL}[P\cos(bL+\gamma) + R\sin(bL+\gamma)]}{P^2+R^2}\right\} \quad (47)$$

$$\left\{\frac{2e^{bL}[B\cos\alpha - A\sin\alpha]}{A^2+B^2}\right\}\cdot\frac{Q_c}{Q_d}\cdot\frac{Q_d}{Q_{da}} = -\left\{\frac{e^{-bL}[U\sin(bL-\gamma) - V\cos(bL-\gamma)] + e^{bL}[R\cos(bL+\gamma) - P\sin(bL+\gamma)]}{P^2+R^2}\right\} \quad (48)$$

where $\text{Bi}_{ds} \equiv b/(kR_t)$ is a Biot number for the die side of the IHS.

As previously noted, the coefficients (A,B,P,R,U,V) depend upon the dimensionless parameters bL and Bi_{IHS}. The factors Q_d/Q_{da}, M, and γ depend on the additional dimensionless groups $Q_dR_t/\Delta T$ and ω/λ. The latter parameter can be rewritten as

$$\frac{\omega}{\lambda} = (bL)^2\left(\frac{2a_tmc_pR_t}{b^2}\right) \equiv (bL)^2S \quad (49)$$

in which the dimensionless parameter S is the ratio of the lumped timescale of the die to the diffusion timescale of the IHS. We find, therefore, that the dimensionless control power Q_c/Q_d and phase shift α each depend upon five dimensionless variables: bL, Bi_{IHS}, Bi_{ds}, $Q_dR_t/\Delta T$, and S. Among these, only bL is dependent upon the signal frequencies used during testing. Thus, adjusting the range of bL selected in a test sequence most easily adjusts the required control power, since no redesign of the device or its packaging is required.

As a dimensional example, when $Q_d = 10\ \text{W/cm}^2$ and $\omega = 10$ Hz with $\Delta T = 4$ K, the required control power profile has a phase shift $\alpha = 277.2$ deg and a control magnitude of $Q_c = 63.05\ \text{W/cm}^2$. This performance is much better than for ideal temperature control where the control magnitude was found to be $173.0\ \text{W/cm}^2$. The resulting temperature profiles for the die and the back face of the IHS are shown in Fig. 8.

2.6 Model Confirmation. In order to provide an independent confirmation of the mathematical solution, an implicit finite difference model [11] of the die/heat spreader system was constructed. The details of this solution method will be outlined in a

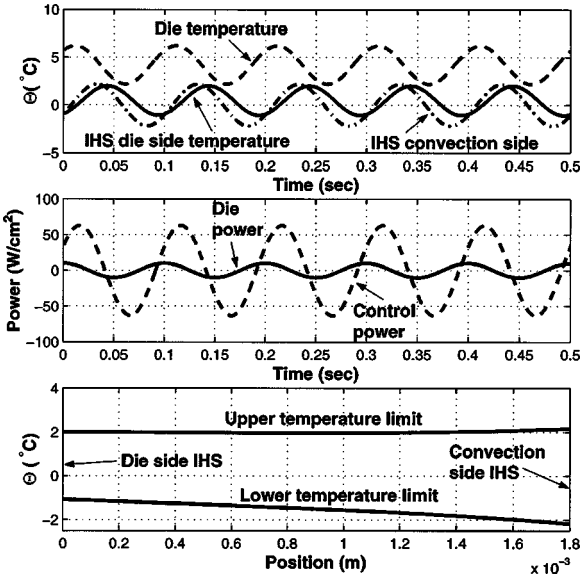

Fig. 8 Temperature profile for die and back-face of IHS for ω=10 Hz, Q_d=10 W/cm^2 and a tolerance ΔT=4 K

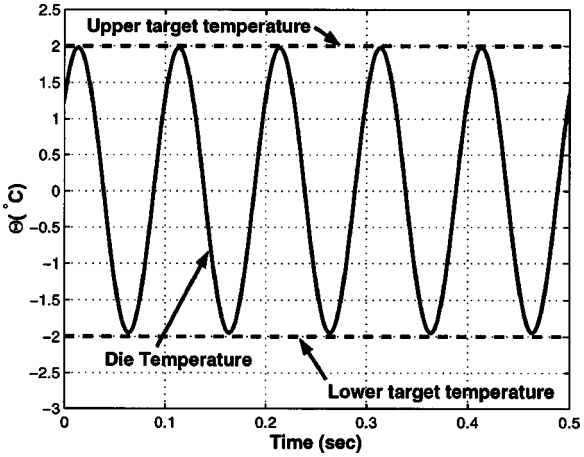

Fig. 9 Calculated die temperature using finite difference model to confirm analytic solution for control input. Target ΔT is 4 K with h_c=1200 W/m^{2}K, R_t=0.42 cm^{2}K/W, b=1.8 mm, and Q_d=10 W/cm^2.

later section, where the same method is used to estimate lateral conduction effects in the IHS. This approach is not very convenient for determining for the required control input magnitude and phase shift, but it is very useful for checking the analysis.

Figure 9 shows the die temperature as calculated from the finite difference model for a 10 Hz die power with $Q_d=10$ W/cm^2. The control input has $Q_c=63.05$ W/cm^2 and $\alpha=277.2$ deg, as predicted by the analysis for a tolerance of $\Delta T=4$ K. As can be seen, the finite difference model confirms that the predicted control input does control the die temperature to the desired level.

3 Control of Non-Sinusoidal Die Power Profile

Any periodic or finite length die power profile can be decomposed into a Fourier series of sinusoidal terms, each of which satisfies the analyses of the previous sections. The results can be superposed to find the temperature response for the actual die power profile. In any such decomposition, a steady (DC) component must also be added so that the power inputs are non-negative.

For example, a square-wave die power profile can be written as [12]

$$Q_{sq}(t)=\frac{4Q}{\pi}\sum_{n=1,3,5\ldots}\frac{1}{n}\sin\left(\frac{2n\pi t}{\tau}\right) \tag{50}$$

where Q is the amplitude of the square wave[5] and τ is its period. Each of these components can now be analyzed using the method developed previously in order to determine the required control input at each specific frequency. In order to do this, the temperature tolerance at each frequency must be specified in such a way that the total temperature tolerance of the die is maintained. For any specified total temperature tolerance, many solutions are possible; however, we desire the solution that minimizes control power required.

For example, suppose that desired total die temperature tolerance is $\Delta T=4$ K on a 5 Hz square-wave signal having $Q_d=10$ W/cm^2 and $h=1200$ W/m^{2}K. The control input may be broken down into an initial allowance of $\Delta T=1$ K for the first frequency component of the decomposition, 1 K for the second component, 1 K for the third, and 1 K for the fourth. For this initial guess, it can quickly be shown that the third and fourth components produce die fluctuations much lower than the target values of $\Delta T=1$ K, so that no control power is actually needed at these two frequencies. The required rms power for the two remaining frequencies is 57.2 W/cm^2. If the analysis is redone with $\Delta T=2$ K on the first and second components only, the required rms control power is 43.3 W/cm^2, and with $\Delta T=2.5$ K on the first frequency, 1.2 K on the second frequency, and 0.3 on the third frequency, the required rms control power is 32.0 W/cm^2. Multiple iterations are generally required to find the optimal solution; it is beyond our present scope to develop a systematic algorithm for these iterations. For the current example, an optimized result (Fig. 10) puts $\Delta T=2.3$ K on the first component (5 Hz), $\Delta T=1.0$ K on the third (15 Hz), and $\Delta T=0.7$ K on the fifth (25 Hz), requiring 29.0 W/cm^2 rms control power.

A similar analysis can be performed for power profiles of any shape. A triangular wave can be expressed as the Fourier series [12]

$$Q_{tr}(t)=\frac{8Q}{\pi^2}\sum_{n=1,3,5\ldots}\frac{(-1)^{(n-1)/2}}{n^2}\sin\left(\frac{2n\pi t}{\tau}\right) \tag{51}$$

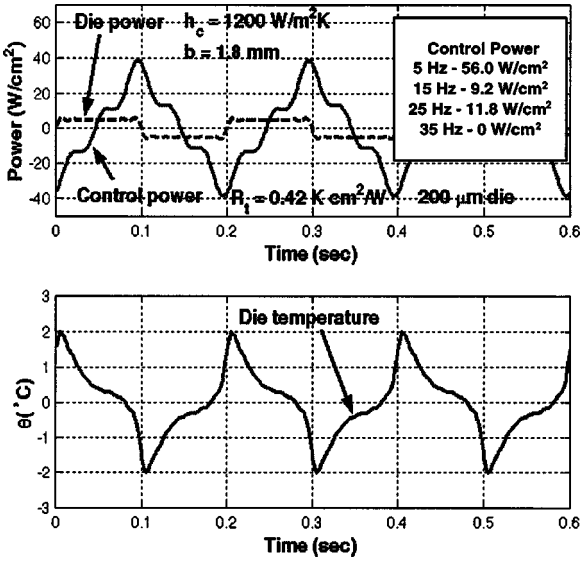

Fig. 10 Die and control powers and die temperature change, θ, for square-wave die power profile

[5]Half the peak to peak amplitude.

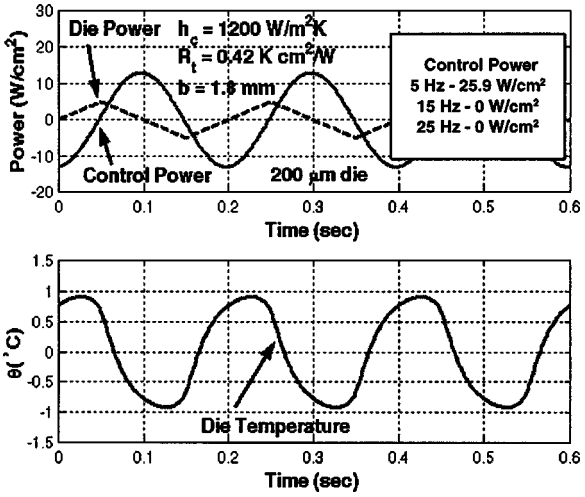

Fig. 11 Die and control powers and die temperature change, θ, for triangle-wave die power profile

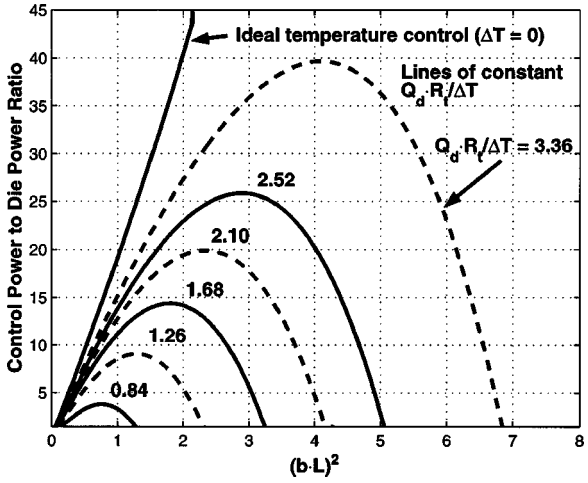

Fig. 12 Control power limits for specified die power amplitude, Q_d, and die temperature tolerance, ΔT, as a function of nondimensional die power frequency, $(bL)^2$

Using this decomposition, the control input for a desired level of die temperature control can be calculated. The solution in this case is fairly simple as only the first frequency term in the series requires control, so the entire ΔT tolerance can be applied to the first term. The results for a triangular wave decomposition are shown in Fig. 11.

Note the big difference in control power required between the triangular wave and square wave die power profiles. The square wave needs almost an 8:1 control to die power ratio to hold the die temperature within 4 K, whereas the triangular wave requires only a 2.4:1 ratio to hold a tighter tolerance of 2 K. Sudden changes in die power (as seen in a square wave) require much higher control power to hold a given temperature tolerance than do more slowly varying power profiles (such as the triangle wave).

4 Limits to Control for a Given Die Power Profile

A knowledge of the required control power profile for a given temperature tolerance in the die can be used to define the control limits for any given system. Specifically, for a given die power frequency and amplitude, if the control power is limited to some finite value then the die temperature can be controlled only to some minimum tolerance. Tighter temperature control is *not* possible for that level of control power.

Over a range of die power frequencies, the control power ratio, Q_c/Q_d, can be found for a given die temperature tolerance, scaled into the die power as $Q_d R_t/\Delta T$. By evaluating the control power ratio over a range of frequencies, we may define a control limit plot for a specified set of die conditions. Figure 12 shows such control limits over a range of dimensionless frequency, $(bL)^2$. In this graph, $\mathrm{Bi}_{\mathrm{IHS}}=0.0055$, $\mathrm{Bi}_{ds}=0.11$, and $S=0.76$, corresponding to a 200 μm thick die, a 1.8 mm thick copper IHS, $R_t=0.42\ \mathrm{cm^2K/W}$, and convective cooling through $h_c=1200\ \mathrm{W/m^2K}$. (Those values are typical of test conditions currently being developed [7].)

An expanded view of the same data is shown in Fig. 13. These figures illustrate the limits of control. There are three regions in Fig. 13, each representing a different region of operation. The area to the left of each curve represents a region where the temperature of the die can be controlled by applying the control power associated with that curve. The region to the right of the lines represents a region where the die power frequency is so high that no control is required to maintain the temperature tolerance limits on the die. The region contained under the curve is a regime where the specified control cannot be attained with the specified control power/die power ratio.

Figure 12 shows that any desired die flux to temperature tolerance ratio can be obtained with sufficient control power, so no theoretical limit to temperature control exists. On a practical level, however, power ratios over 3 or 4 quickly become impractical due to cooling requirements of the effective steady state heat load—the sum of the DC components of die power and control power. (Recall that this analysis was for the periodic components of the power profiles; in practice, both profiles also have steady components, since the instantaneous powers are never negative.)

These results lead to some very important points. The position of the lefthand sides of the curves are defined by the physical configuration of the heat spreader (thickness, conductivity, etc.), whereas the righthand sides are defined by the mass of the die, frequency of the die power profile, and thermal interface resistance between the die and the IHS. If the design of the IC device cannot be altered for thermal purposes, as is usually the case, a desired level of temperature control may instead be obtained by designing the circuit test sequence, for example, so that the die power profile always lies to the right side of the figure.

We may also evaluate the effect of design changes to the integrated heat spreader and thermal interface between the die and IHS. Changing the thermal resistance between the die and the IHS

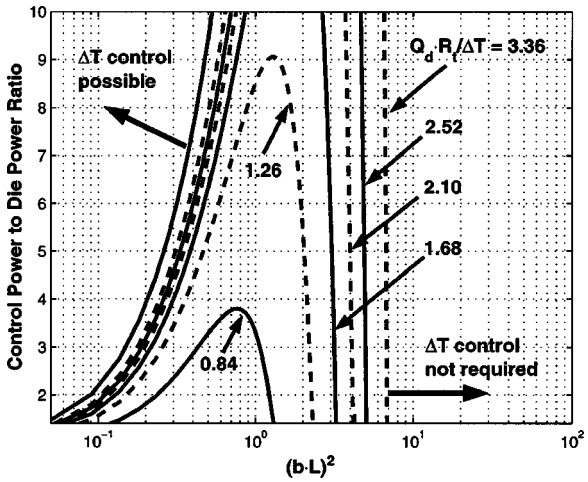

Fig. 13 Control power limits for specified die power amplitude, Q_d, and die temperature tolerance, ΔT, as a function of nondimensional die power frequency, $(bL)^2$

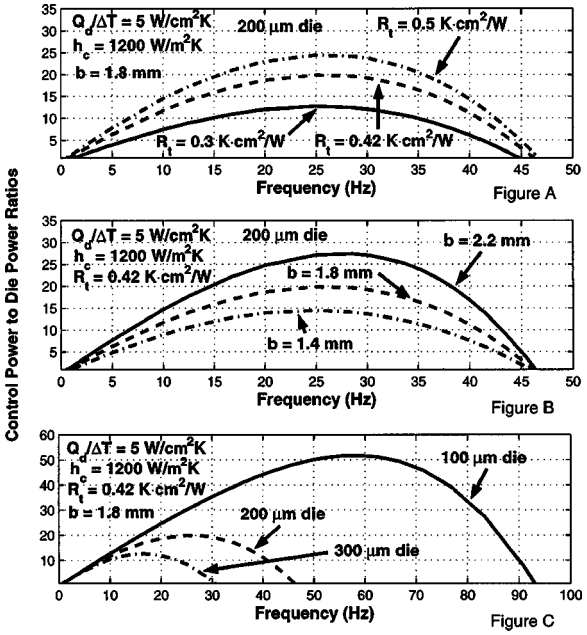

Fig. 14 Effect on control power limits of: (*a*) interfacial thermal resistance; (*b*) IHS thickness; and (*c*) die thickness.

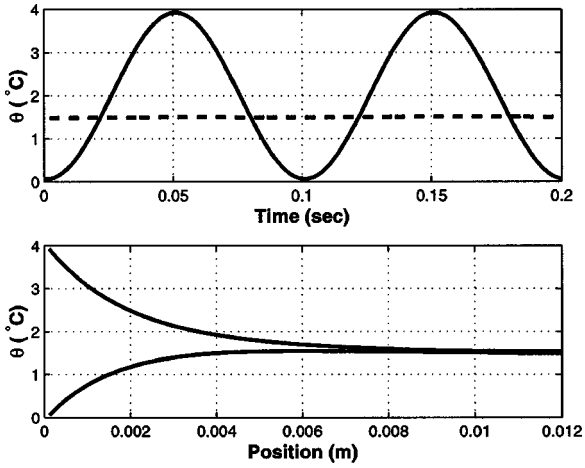

Fig. 15 Transient fin temperature profile for 10 Hz example. Top: temperature variation at base and tip of fin. Bottom: maximum/minimum temperature defect along the length of the fin.

can have a profound effect on the control limits at higher power ratios. This is seen in Fig. 14(*a*) for $Q_d/\Delta T = 5$ W/cm^{2}K. The effects of changing the thickness of the integrated heat spreader and the die are shown in Fig. 14(*b*) and Fig. 14(*c*), respectively. Changing the thickness of the die (and therefore its mass) has the largest impact on the control limits of the device. The increasing the thickness of the IHS also raised the power required for a given level of control. The effect of changing the convective transfer coefficient h_c is negligible, with no change observed when h_c varies from 500 W/m^{2}K to 2000 W/m^{2}K.[6]

4.1 Limitations of the Isothermal Die Approximation. The techniques used to analyze the IHS can also be applied to heat conduction in the die as a check on the lumped capacitance model for the die. The results of such analysis show that a die of thickness δ can be treated as isothermal for frequencies low enough that $\delta^2\omega/(2a_t) < 0.3$ to 0.4. For the baseline die considered here, that corresponds to frequencies of 200 to 300 Hz and $(bL)^2 < 30$ to 40. It must also be noted that the temperature variations associated with the higher frequencies tend to be quite small.

5 Lateral Conduction Effects in IHS

The function of the heat spreader is to act as a fin, conducting heat laterally away from the die. For the steady components of die power, the IHS will indeed function as a fin. For higher frequency components, however, the fin effect will be limited to a frequency-dependent thermal penetration length in the IHS near the die. Only the lower frequency components will have a sufficient penetration depth to influence the control response. In this section, we examine the effect of frequency-dependent lateral conduction on the control requirements.

The Biot number, $\mathrm{Bi}_{\mathrm{IHS}}$, for a typical heat spreader is very small, even at the highest h_c values considered here (e.g., $\mathrm{Bi}_{\mathrm{IHS}} = 0.009$ for $h_c = 2000$ W/m^{2}K and $b = 1.8$ mm). Thus, the thermal response of the parts of the spreader beyond the die can be modelled using the unsteady fin equation

$$\frac{\partial^2\Theta}{\partial x^2} + \frac{1}{A(x)}\frac{dA}{dx}\frac{\partial\Theta}{\partial x} - \frac{hP}{kA(x)}\Theta = \frac{1}{a_t}\frac{\partial\Theta}{\partial t} \tag{52}$$

where $\Theta = T - T_{\mathrm{air}}$, P is the perimeter subject to convection, $A(x)$ is the cross-sectional area, and a_t is the thermal diffusivity.

A square heat spreader with a square die can be broken into four identical quadrants, by symmetry. The cross-sectional area of the heat spreader can now be expressed as $A(x) = A_0 + 2\alpha \cdot b \cdot x$, where A_0 is the area of the fin along the line of contact with the die and $\alpha = 0.5$.

Equation (52) has been studied extensively, and analytical solutions have been reviewed by Aziz and Kraus [13]. In the present case, with variable cross-sectional area and time dependent boundary conditions, the equation will be solved using discrete methods. The two items of principal interest are the heat flux and the thermal penetration depth that result from a change in base temperature, with the latter corresponding to the temperature of the IHS directly over the die structure.

The base temperature is never uniform across the thickness of the heat spreader because the powers are time dependent (as shown in previous sections). Nevertheless, this temperature varies over a well specified range, and a bounding value can be used to examine the worst case losses into the fin-like parts of the IHS away from the die. The magnitude of the temperature variation in the IHS over the die can be taken from the previously determined IHS temperature profiles, such as Fig. 8.

Using an implicit finite difference method [11], the fin may be divided into the N sections shown in the inset in Fig. 16. The temperature of a fin section subject to time varying boundary conditions can be written as

$$\mathbf{A}\cdot\mathbf{T}^{i+1} = \mathbf{T}^{i} + \mathbf{F} \tag{53}$$

where $[\mathbf{T}^i]$ and $[\mathbf{T}^{i+1}]$ are arrays of the fin temperature at time step i and $i+1$ respectively. The details of the forcing function $[\mathbf{F}]$ and characteristic matrix $[\mathbf{A}]$ are standard, and will not be repeated here (see [7] for details). The temperature at time step $i+1$ is found by matrix inversion.

We used this approach to determine the temperature profile in the fin as a function of time subject to changing base temperature T_b^i. The fin was broken into 100 segments and the time step Δt was decreased by factors of two until successive changes in the time step produced results that varied by less than 0.01°C at all times.

The heat lost by conduction into the IHS away from the die is found by integrating the flux into the base area, A_0, over a full

[6]These values are typical of the air-jet array cooling we have implemented and measured in such systems. Small nozzle diameters, modest air pressures, and close nozzle-to-nozzle spacings are required.

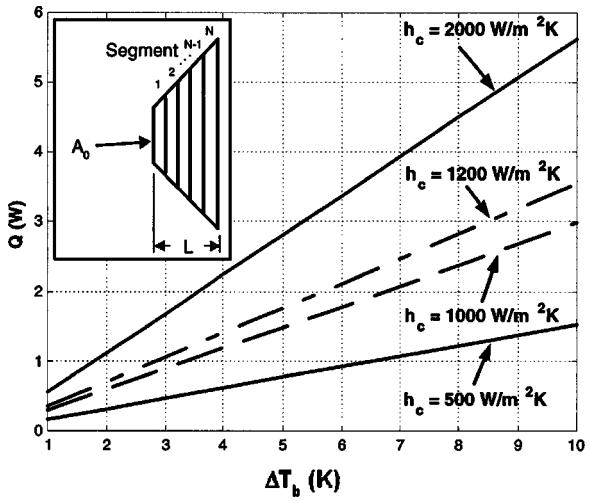

Fig. 16 Lateral conduction into IHS for various h_c: Q=cyclic lateral loss into IHS; ΔT_b=temperature fluctuation amplitude of IHS at die edge. Insert shows discretization of IHS for numerical solution.

period of the harmonic power variation. This heat may be viewed as lost control energy. For example, consider a 1 cm^2 die that has a 1.8 mm thick heat spreader measuring 3.4 cm by 3.4 cm. The temperature profile in the part of the IHS not above the die is shown in Fig. 15 for a 10 Hz base temperature variation having a peak-to-peak magnitude of 4 K with $h_c = 1200\,W/m^2K$. The cyclic heat loss is 0.36 W per fin segment, or 1.44 W for the entire heat spreader. Similar calculations have been done for a range of frequencies and for various h_c (Fig. 16).

The results of such analyses can be used in one of two ways to correct the control response for the lateral conduction losses. One approach is simply to add the control losses to the total control power. The second approach is to provide a control heat flux to an area of the heat spreader larger than the die, so as to minimize time-dependent lateral heat loss from the die (in the case of laser heating of the IHS, this amounts to over-illumination of the IHS). The second option is only really possible for higher frequency signals, because at lower frequencies the penetration depth is of the same order of magnitude as the width of the heat spreader. If the penetration depth is defined as the distance from the base of the fin to the point where the temperature fluctuation is less than 0.1°C, then the penetration depth for the temperature profile shown in Fig. 15 is 6.1 mm. Illuminating the die area covers 1.0 cm^2, illuminating the die area and a sufficient edge area to prevent lateral conduction effects on the die area requires illumination of 4.9 cm^2.

Similarly, the penetration depth for a 40 Hz signal is 3.4 mm with overillumination covering 2.8 cm^2; and at 100 Hz, the pentration depth is 2.1 mm with over-illumination covering 2.0 cm^2. Assuming the radiant intensity is uniform over the entire illuminated area, over-illumination requires 4.9 times more radiant power at 10 Hz, 2.1 times more at 40 Hz and 2.0 times the power at 100 Hz.

6 Conclusions

Time-leading temperature control in a distributed-parameter thermal system has been evaluated in one and two dimensions. A particular focus has been the testing of packaged, high-power, integrated circuits. The analysis identifies the control power required to bound the temperature variation of a system having time-dependent self-heating if control is by time-varying heat conduction to a position distant from the location being controlled.

The results may be very useful in the design of active thermal control systems for testing of electronic devices and for understanding the impact of electronic test-sequence designs and packaging design on the practical limits of temperature control. Three areas of operation for thermal control have been identified. At high frequencies, active control is not required because the temperature deviation without control is below the desired tolerance: steady (DC) cooling is all that is needed. At sufficiently low frequencies, thermal control can be obtained using a system's available control power. For intermediate frequencies, either control is not possible at the system's rated control power and desired temperature tolerance, or larger temperature deviations have to be accepted as a result of the system's limitation on control power.

This analysis can be applied to any situation where the temperature control source is separated from the active region where temperature control is desired, and should have value for systems other than electronics testing equipment.

Experimental tests of this analysis have been performed on prototype microprocessors, with good agreement [7]. These tests will be the subject of a future paper.

Acknowledgments

The authors would like to thank Teradyne Inc. for financial support of this work. The authors would also like to thank Andreas Pfahnl and Ray Mirkhani of Teradyne for their technical support of this work, as well as Pooya Tadayon at Intel Inc. for information and advice on testing conditions.

Nomenclature

$A(x)$ = cross-sectional area of IHS fin [m^2]
A_0 = base cross-sectional area of IHS fin [m^2]
A = mathematical constant, Eq. (10)
a_t = thermal diffusivity [m^2/s]
B = mathematical constant, Eq. (11)
Bi_{ds} = Biot number for die-side of IHS, b/kR_t
$\mathrm{Bi}_{\mathrm{IHS}}$ = Biot number for top side IHS, $h_c b/k$
b = integrated heat spreader thickness [m]
C, C_1, C_2 = mathematical constants
C_n = constant in infinite series
c_p = specific heat capacity at constant pressure [J/kg·K]
D, E, F = mathematical constants, Eq. (18) [$W^2/m^4 \cdot K^2$]
G = mathematical constant, Eq. (23) [$W^2/m^4 \cdot K^2$]
h_c = average convective transfer coefficient [$W/m^2 \cdot K$]
i = the imaginary number, $\sqrt{-1}$
k = thermal conductivity [W/m·K]
L = fin length [m]
L = unsteady diffusion scale in IHS, $\sqrt{\omega/2a_t}\,[m^{-1}]$
M = energy transfer correction factor, Eq. (39)
N = mathematical constant, Eq. (23) [$W^2/m^4 \cdot K^2$]
m = mass of die per unit area [kg/m^2]
P = mathematical constant, Eq. (24); or fin perimeter [m]
PS_1, PS_2 = mathematical constants, Eq. (32)
PS_3 = mathematical constant, Eq. (46)
Q_{sq} = square-wave die power density [W/m^2]
Q_{tr} = triangular wave die power density [W/m^2]
Q_d = die power density [W/m^2]
Q_{da} = corrected die power density [W/m^2], Eq. (43)

Q_c = control power density [W/m^2]
R = mathematical constant, Eq. (25)
R_t = thermal contact resistance [K·m^2/W]
S = ratio of die timescale to IHS diffusion timescale, Eq. (49)
$\mathbf{T}$ = fin temperature matrix [K]
T_{air} = air temperature [K]
T_{die} = die temperature [K]
T_{ref} = reference temperature—often taken as zero [K]
T_{BF} = IHS die-side temperature [K]
t = time [s]
U, V = mathematical constants, Eq. (28)
W = complex temperature solution
X = real part of complex temperature solution [K]
x = distance from reference face of integrated heat [m] spreader

Greek Symbols

α, β, γ = phase shifts [rad]
α = shaped fin geometry factor
α_n = infinite series constant
λ = lumped frequency response of die, $1/(mc_pR_t)$ [s^{-1}]
τ = imaginary part of complex temperature; or period of square/triangular wave [s]
θ = temperature defect, $(T-T_{\text{ref}})$ [K]
ω = frequency of die power variation [rad/s]

References

[1] Pfahnl, A. C., Lienhard V, J. H., and Slocum, A. H., 1999, "Thermal Management and Control in Testing Packaged Integrated Circuit Devices," *Proc. 34th Intersociety Energy Conversion Conf.*, Vancouver BC, Paper No. 1999-01-2723.
[2] Tadayon, P., 2000, "Thermal Challenges During Microprocessor Testing," Intel Technology Journal, **Q3**.
[3] Kromann, G. B., 1996, "Thermal Management of a C4/Ceramic-Ball-Grid Array: The Motorola Power PC 603 and PowerPC 604 RISC Microprocessors," *Proceedings of the Twelfth IEEE SEMI-THERM Symposium*, pp. 36–42.
[4] Malinoski, M., Maveety, J., Knostman, S., and Jones, T., 1998, "Test Site Thermal Control System for At-Speed Manufacturing Testing," *Proc. IEEE Intl. Test Conf.*, Washington, DC, pp. 119–128.
[5] Pfahnl, A. C., Lienhard V, J. H., and Slocum, A. H., 1998, "Temperature Control of a Handler Test Interface," *Proc. IEEE Intl. Test Conf.*, Washington, DC, pp. 114–118.
[6] Viswanath, R., Wakharkar, V., Watwe, A., and Lebonheur, V., 2000, "Thermal Performance Challenges From Silicon to Systems," Intel Technology Journal, **Q3**.
[7] Sweetland, M., 2001, "*Design of Thermal Control Systems for Testing of Electronics*," Ph.D. thesis, Massachusetts Institute of Technology, Cambridge, MA.
[8] Tustantswkyj, J., and Babcock, J. B., 1998, "Temperature Control System for an Electronic Device Which Achieves a Quick Response by Interposing a Heater Between the Device and a Heat Sink," U.S. Patent #5,821,505.
[9] Tustaniwskyj, J. I., and Babcock, J. W., 1997, "Constant Temperature Control of a Device Under Test (DUT): Part 1, *Advances in Electronic Packaging*," **2**, pp. 2031–2036.
[10] Carslaw, H. S., and Jaeger, J. C., 1959, *Conduction of Heat in Solids*, 2nd edition, Oxford University Press, Oxford.
[11] Mills, A. F., 1995, *Heat and Mass Transfer*, Irwin, Chicago, IL.
[12] Robertson, J. S., Bolinger, K., Glasser, L. M., Sloane, N. J. A., and Gross, R., *CRC Standard Mathematical Tables and Formulas*, Daniel Zwillinger, ed. CRC Press, Boca Raton, Chpt. 1.
[13] Aziz, A., and Kraus, A. D., 1995, "Transient Heat Transfer in Extended Surfaces," Appl. Mech. Rev., **48**(7), pp. 317–350.

Journal of Heat Transfer

Technical Notes

This section contains shorter technical papers. These shorter papers will be subjected to the same review process as that for full papers.

Explicit Analytical Solutions of Linear and Nonlinear Interior Heat and Mass Transfer Equation Sets for Drying Process

Ruixian Cai
Academician
e-mail: crx@mail.etp.ac.cn

Na Zhang
Associate Professor
e-mail: crx@public.bta.net.cn

Inst. of Engg. Thermophysics, Academia Sinica,
P.O. Box 2706, Beijing 100080, China

Some algebraic explicit analytical solutions of the unsteady one-dimensional variable coefficient partial differential equation set describing drying process of an infinite plate are derived and given. Such explicit solutions have not yet been published before. Besides their irreplaceable theoretical value, analytical solutions can also serve as benchmark to check the results of recently rapidly developing numerical calculation and study various computational methods. In addition, some mathematical skills used in this paper are special and deserve further attention.
[DOI: 10.1115/1.1482401]

Keywords: Analytical, Drying, Heat Transfer, Mass Transfer, Unsteady

Introduction

Drying process is very common in industry and agriculture as well as in daily life, therefore, it is necessary and important to research this process. There have been many research works in the world on drying process both in experimentation and in theory as summarized by Mujumdar [1].

Generally, the basic theoretical research approach is: to express the physical law with mathematical model, then analyze, calculate and predict the process. Now, there have been rather mature physical—mathematical models and basic partial differential equation sets of drying process. But it is very difficult or even impossible to obtain the analytical solutions for these differential equation sets for arbitrary initial and boundary conditions, then, most solutions are numerical one for specific conditions. However, analytical solutions for basic equations (if only could be found) have significant meaning and irreplaceable function. First of all, they can absolutely precisely illustrate the physical situation of the equations, and deepen the theoretical study. For example, various analytical solutions played important roles in the early development of fluid dynamics (Lamb [2]) and heat conduction (Jakob [3]). They can also be used as benchmark solutions to verify the outcomes and codes of numerical calculation, and to check the accuracy, convergence and effectiveness of various numerical methods and their differencing schemes, grid generation ways as well. For example, several analytical solutions given by the first author [4] to simulate the three-dimensional incompressible potential flow in turbomachine cascades have been used successfully by some numerical calculation scientists to check their computational methods and computer codes (Cai et al. [4], Xu et al. [5], Gong and Cai [6], and Shen et al. [7]); and some other analytical solutions to simulate unsteady compressible flow were recently given by the first author [8]. In addition, some explicit analytical solutions were derived for the coupled partial differential equation set describing porous material drying and nonlinear heat conduction by the authors [9–10]. Therefore, some algebraic explicit analytical solutions of basic linear and nonlinear unsteady one-dimensional drying process equation set are derived and given in this paper to enrich the drying research.

Physical Model and Basic Equation Set

For the drying process of infinite plate with thickness equaling to d, the basic unsteady one-dimensional partial differential equation set can be expressed as:

$$\frac{\partial M}{\partial t}=\frac{\partial}{\partial x}\left(D\frac{\partial M}{\partial x}\right)$$
$$\rho C_P\frac{\partial \theta}{\partial t}=\frac{\partial}{\partial x}\left(K\frac{\partial \theta}{\partial x}\right)+\rho L\frac{\partial M}{\partial t} \tag{1}$$

Of course, there should be some other initial and boundary conditions to make the equation set posed. For example, the values of M and θ or their gradients for $t=0$, $x=0$, and $x=d$. However, as mentioned above, the aim of this paper is to find some explicit analytical solutions to enrich the theory and to serve as a benchmark solution to develop computational method, but not to obtain a proper solution for some specific case, therefore, the approach used here focuses on the derivation of possible solutions for the basic equation set itself first, and check what the initial and boundary conditions are afterwards; for example, substituting $t=0$ or $x=0$, $x=d$ into the derived explicit analytical solutions to obtain corresponding initial and boundary conditions.

Besides the ordinary method of separation of variables, an extraordinary method named the method of separation of variables with addition [10–11] was applied by the authors to solve equation set (1) analytically: it is assumed that the unknown solution is

Contributed by the Heat Transfer Division for publication in the JOURNAL OF HEAT TRANSFER. Manuscript received by the Heat Transfer Division June 1, 2001; revision received March 27, 2002. Associate Editor: M. L. Hunt.

a sum of two one-dimensional functions $T(t)+X(x)$ instead of a product of two one-dimensional functions $T(t)\cdot X(x)$ in ordinary method.

Linear Equation Set Solution With Constant Coefficients

When D, K, ρ, C_P, and L are constants, the basic equation set can be expressed as a linear one:

$$\frac{\partial M}{\partial t}=D\frac{\partial^2 M}{\partial x^2}$$
$$\frac{\partial \theta}{\partial t}=a\frac{\partial^2 \theta}{\partial x^2}+b\frac{\partial M}{\partial t} \tag{2}$$

where $a=K/(\rho C_P)$, $b=L/C_P$, a and b are positive numbers.

When the method of separation of variables with addition is applied to basic equation set (2), it is firstly assumed that $M=T(t)+X(x)$, then the first equation of equation set (2) becomes: $T'=DX''=C_1$, and the moisture content can be expressed as: $M_1=C_1t+C_1x^2/(2D)+C_2x+C_3$. Substituting M_1 into the second equation of equation set (2) and applying the method of separation of variables with addition again, the expression of temperature θ can be obtained similarly as $\theta=C_4t+(C_4-C_1b)x^2/(2a)+C_5x+C_6$. Therefore, an algebraically explicit analytical solution of equation set (2) is given as:

$$M_1=C_1t+\frac{C_1}{2D}x^2+C_2x+C_3$$
$$\theta_1=C_4t+(C_4-C_1b)x^2/(2a)+C_5x+C_6 \tag{3a}$$

where the subscript 1 of M and θ means the first solution, it is the same meaning for subscripts 2 and 3 in following solutions.

If the method of separation of variables with addition is only applied to the first equation of equation set (2), i.e., $M_2=M_1=C_1t+C_1x^2/(2D)+C_2x+C_3$, but the second equation is solved with the ordinary method of separation variables: $\theta=T(t)\cdot X(x)$, then it is obtained: $T'X=aTX''+C_1b$. However, for this expression it seems unable to separate variables. This difficult can be overcome for linear equations by neglecting the constant C_1b firstly and then adding some simple power functions to the solution to satisfy the existence of constant C_1b [11]. Rearranging $T'X=aTX''$, it is obtained: $T'/T=aX''/X=C_{7i}$. The solution of above mentioned relation is well-known in textbooks and expressed as (considering the superposition possibility for linear equations):

$$\theta_{20}=\sum_{i=1}^{n} e^{C_{7i}t}[C_{8i}\cosh(\sqrt{C_{7i}/a}\cdot x)+C_{9i}\sinh(\sqrt{C_{7i}/a}\cdot x)]$$
$$\text{when } C_{7i}>0 \tag{3b}$$

or

$$\theta_{20}=\sum_{i=1}^{n} e^{C_{7i}t}[C_{8i}\cos(\sqrt{-C_{7i}/a}\cdot x)+C_{9i}\sin(\sqrt{-C_{7i}/a}\cdot x)]$$
$$\text{when } C_{7i}<0 \tag{3c}$$

For satisfying the existence of constant C_1b, it can be done by adding C_1bt-C_{11} or $-[C_1bx^2/(2a)+C_{10}x+C_{11}]$ to θ_{20} or even their linear combination $(1-C_{12})C_1bt-C_{12}[C_1bx^2/(2a)+C_{10}x+C_{11}]$. Therefore, one of the final solution form of equation set (2) is as follows:

$$M_2=C_1t+\frac{C_1}{2D}x^2+C_2x+C_3$$
$$\theta_2=C_1b(1-C_{12})t-C_{12}[C_1bx^2/(2a)+C_{10}x+C_{11}]+\theta_{20} \tag{3d}$$

Actually, solution (3*a*) is a special case of solution (3*d*) with $C_{8i}=0=C_{9i}$ and $C_{12}=1-C_4/(C_1b)$.

If directly applying the ordinary method of separation of variables to the first equation of equation set (2), it is able to separate variables of the first equation: when $M=TX$, $T'/T=DX''/X=C_{13}$, its solution is well-known also and is expressed as follows:

$$M_3=\sum_{j=1}^{m} e^{C_{13j}t}[C_{14j}\cosh(\sqrt{C_{13j}/D}\cdot x)+C_{15j}\sinh(\sqrt{C_{13j}/D}\cdot x)] \text{ when } C_{13j}>0 \text{ or}$$
$$M_3=\sum_{j=1}^{m} e^{C_{13j}t}[C_{14j}\cos(\sqrt{-C_{13j}/D}\cdot x)+C_{15j}\sin(\sqrt{-C_{13j}/D}\cdot x)] \text{ when } C_{13j}<0 \tag{4a}$$

Then, substituting Eq. (4*a*) into the second equation of equation set (2) and applying the ordinary method of separation variables again: $\theta_3=T(t)\cdot X(x)$, the simplified result (only considering one term in the sum) is: $T'X=aTX''+bC_{13}e^{C_{13}t}[C_{14}\cosh(\sqrt{C_{13}/D}x)+C_{15}\sinh(\sqrt{C_{13}/D}x)]$. It seems unable to separate variables. However, it can be done with the assumption: $T=C_{16}e^{C_{13}t}$. An ordinary differential equation of X is then obtained as follows: $C_{13}X=aX''+bC_{13}e^{C_{13}t}[C_{14}\cosh(\sqrt{C_{13}/b}x)+C_{15}\sinh(\sqrt{C_{13}/b}x)]$. From this relation, it is guessed that the solution of X can be expressed as: $X=K_1\cosh(\sqrt{C_{13}/b}x)+K_2\sinh(\sqrt{C_{13}/b}x)]$, where K_1 and K_2 are undetermined constants. Determining K_1 and K_2 with the method of undetermined coefficients and comparing the θ expression with M_3, the expression of θ_3 can be obtained as following:

$$\theta_3=DbM_3/(D-a) \tag{4b}$$

So, considering the linear character of Eqs. (2), an algebraic explicit solution expressed by a summation of 2 parts can be given as following:

$$M=M_2+M_3$$
$$\theta=\theta_2+\theta_3 \tag{5}$$

The expression of M_2, M_3, and θ_2, θ_3 are given in Eqs. (3*b*), (3*c*), (3*d*), (4*a*), and (4*b*).

To obtain an explicit solution of partial differential equation is not so easy, however, to check its correction is an easy job since the only operation is substituting the solution into the basic equation set. For a dry process, C_1 and C_{13j} have to be negative. However, even in a dry process, ($C_1<0$ and $C_{13j}<0$), the temperature could be up or down depends on the sign of C_4 and C_{7i} as well as D-a. In physical meaning it is mainly dependent on the boundary condition. In addition, when $C_1=0$, $C_{14j}=0$, and $C_{15j}=0$, it is a steady moisture process.

Since the basic equation set with constant coefficients is linear, then the solution equation (3) includes summation formulas, they can form series such as Fourier series to represent various boundary and initial conditions.

By the way, if the solution includes M_3 and θ_3 only, the variations of humidity and temperature are completely similar and synchronic, it is an interesting solution.

Solution With Variable Density and Specific Heat

If the properties of the liquid to be dried can be simply represented with $\rho=l-k\theta$ and $C_P=m/(l-k\theta)$, and other coefficients D, K, and L are constants, then a specific explicit analytical solution for equation set (1) can be derived with above-mentioned method of separation of variables with addition as follows.

The moisture content expression is derived in the same way as the previous paragraph:

$$M = C_1 t + C_1 x^2/(2D) + C_2 x + C_3 \tag{6a}$$

Substituting Eq. (6*a*) into the second equation of equation set (1) and considering the expression of ρ and Cp, it is obtained: $m\partial\theta/\partial t = K\partial^2\theta/\partial x^2 + (l - k\theta)LC_1$. Applying the method of separation variables with addition: $\theta = T + X$, the previous equation becomes $mT' = KX'' + C_1 L(l - kT - kX)$ and $mT' + C_1 LkT = KX'' - C_1 LkX + C_1 Ll = C_4$. Then, the θ expression can be derived with common mathematical operation as follows:

$$\theta = C_5 \exp(-kC_1 Lt/m) + C_6 \cos(\sqrt{-kC_1 L/K}\cdot x) + C_7 \sin(\sqrt{-kC_1 L/K}\cdot x) + l/k \quad \text{when} \quad C_1 < 0$$

or

$$\theta = C_5 \exp(-kC_1 Lt/m) + C_6 \exp(\sqrt{kC_1 L/K}\cdot x) + C_7 \exp(-\sqrt{kC_1 L/K}\cdot x) + l/k \quad \text{when} \quad C_1 > 0 \tag{6b}$$

As an example, the initial and boundary conditions of Eq. (5) can be expressed as follows:

$$t = 0, \quad M = \frac{C_1}{2D} x^2 + C_2 x + C_3,$$

$$\theta = C_5 + C_6 \cos(\sqrt{-kC_1 L/K}\cdot x) + C_7 \sin(\sqrt{-kC_1 L/K}\cdot x) + l/k \quad (C_1 < 0)$$

or

$$\theta = C_5 + C_6 \exp(\sqrt{kC_1 L/K}\cdot x) + C_7 \exp(-\sqrt{kC_1 L/K}\cdot x) + l/k \quad (C_1 > 0)$$

$$x = 0, \quad M = C_1 t + C_3,$$

$$\theta = C_5 \exp(-kC_1 Lt/m) + C_6 + l/k \quad (C_1 < 0)$$

or

$$\theta = C_5 \exp(-kC_1 Lt/m) + C_6 + C_7 + l/k \quad (C_1 > 0)$$

$$x = 1, \quad M = C_1 t + C_1/(2D) + C_2 + C_3,$$

$$\theta = C_5 \exp(-kC_1 Lt/m) + C_6 \cos(\sqrt{-kC_1 L/K}) + C_7 \sin(\sqrt{-kC_1 L/K}) + l/k \quad (C_1 < 0)$$

or

$$\theta = C_5 \exp(-kC_1 Lt/m) + C_6 \exp(\sqrt{kC_1 L/K}) + C_7 \exp(-\sqrt{kC_1 L/K}) + l/k \quad (C_1 > 0)$$

It is the same for other solutions and will not superfluously dwell again.

The constant coefficient solution mentioned in previous paragraph can not be deduced directly with solution (6) since constant coefficients means $k = 0$, but expression (6) has no meaning when $k = 0$.

Similar to previous solution, for a dry process, C_1 has to be negative, and the temperature commonly goes up since k is positive for general case.

Nonlinear Solution With Variable Liquid Diffusivity

In the basic equation set (1), if only considering the liquid diffusivity variation with moisture $D = pe^{qM}$ and assuming all other coefficients being constant, then a nonlinear equation set is obtained as follows:

$$\frac{\partial M}{\partial t} = p \frac{\partial}{\partial x}\left(e^{qM}\frac{\partial M}{\partial x}\right)$$
$$\frac{\partial \theta}{\partial t} = a \frac{\partial^2 \theta}{\partial x^2} + b \frac{\partial M}{\partial t} \tag{7}$$

A specific explicit analytical solution of the non-linear equation set (7) can be derived with the method of separation of variables with addition as following.

Substituting $M = T + X$ into the first equation of equation set (7), it is obtained: $T' e^{-qT} = pe^{qX}(X'' + qX'^2) = C_1$. Solving these ordinary differential equations with general method and rearranging the solutions, the expression of M is derived as follows:

$$M = \frac{1}{q}\ln\left[\frac{(x - C_3)^2}{2p(C_2 - t)}\right] \tag{8a}$$

Substituting Eq. (8*a*) into the second equation of equation set (7) and applying the method of separation variables with addition again, it is easy to derive following expression:

$$\theta = C_1 t - b\ln(C_2 - t)/q + C_1 x^2/(2a) + C_4 x + C_5 \tag{8b}$$

The constant C_2 in solution (8) has to be larger than the time interval considered. This solution represents a process with increase of both moisture and temperature with time. Of course, after the temperature and moisture up to a certain value, other coefficients can not be treated as constant again, the basic equation set (7) and its specific solution will be no longer valid. However, the solution is very simple and includes not only polynomials but also transcendental functions, then it is very suitable to be a benchmark solution of the non-linear process.

Nonlinear Equation Solutions With Constant or Steady Moisture Content

Sometimes it is necessary to maintain the moisture content unchangeable with time. Some algebraically explicit analytical solutions can be derived with variable coefficients as follows (ρL is an arbitrary function in this paragraph):

Constant Moisture Content. In this case, the basic equation set degenerates into only one equation $\rho Cp\partial\theta/\partial t = \partial/\partial x(K\partial\theta/\partial x)$.

When $\rho C_P = m\exp(n\theta)$, $K = k\exp(l\theta)$ and D is an arbitrary function, a possible solution is derived with the method of separation variables with addition, since after separating variables the derivation procedure is a common and easy one, the final solution is directly given without any explanation:

$$M = M_0 = \text{Const.}$$
$$\theta = \ln\{2k(l + n)(C_1 t + C_2)/[(C_1 m(n - l)(x + C_3)^2]\}^{1/(n-l)} \tag{9}$$

When $\rho C_P = m\theta^n$, $K = k\theta^l$, and D is an arbitrary function, another possible solution is derived with the ordinary method of separation variables. The derivation is common and easy also and the final result is given directly too:

$$M = M_0 = \text{Const.}$$
$$\theta = \{2k(2 + l + n)(C_1 t + C_2)/[(C_1 m(n - l)(x + C_3)^2]\}^{1/(n-l)} \tag{10}$$

Steady Moisture Content. In this case, $M=M(x)$, the first equation of the basic equation set (1) becomes $0=d/dx(DdM/dx)$ and the second equation degenerates into $\rho Cp\partial\theta/\partial t=\partial/\partial x(K\partial\theta/\partial x)$ for solving θ.

When $\rho C_P=m\exp(n\theta)$, $K=k\exp(l\theta)$ and $D=p\exp(qM)$, a possible explicit analytical solution with $M(x)$ can be derived similarly as following:

From the degenerated equation $0=d/dx(DdM/dx)$, it is obtained:

$$M=\frac{1}{q}\ln[C_4(qx+C_5)] \tag{11a}$$

Applying the method of separation variables with addition to solve the degenerated equation for θ, the θ expression is derived as follows:

$$\theta=\ln\{2k(l+n)(C_1t+C_2)/[(C_1m(n-l)(x+C_3)^2]\}^{1/(n-l)} \tag{11b}$$

When $\rho C_P=m\theta^n$, $K=k\theta^l$, and $D=p\exp(qM)$, another possible explicit analytical solution with $M(x)$ can be derived similarly with ordinary method of separation variables as following:

$$M=\frac{1}{q}\ln[C_4(qx+C_5)]$$
$$\theta=\{2k(2+l+n)(C_1t+C_2)/[(C_1m(n-l)(x+C_3)^2]\}^{1/(n-l)} \tag{12}$$

Comparing Eqs. (9) and (11), as well as Eqs. (10) and (12), it is worth noticing the influence of the boundary conditions and the diffusivity function on the moisture variation.

The sign of the value inside the braces in each expression in this paragraph has to be positive, otherwise the solution does not exist. By the way, in common cases, the values of l, n, and q are low. The solutions in this paragraph can maintain constant or steady moisture content with different coefficient variation and temperature variation, it is worth studying further.

An Explicit Analytical Solution With $D(M,\theta)$ and $K(M,\theta)$

If D and K are linear functions of moisture content and temperature: $D=mM+n\theta+q$, $K=kM+l\theta+p$, but the temperature and pressure variation is small, it can be assumed that the ρC_P and ρL are constant, a rather simple explicit analytical solution of Eqs. (1) can be derived with above mentioned method of separation of variables with addition and a little bit inspiration (assuming $M=T_1+X_1$, $\theta=T_2+X_2$ and $X_1''=0$). With such simplification, the derivation procedure is an easy one and the final solution is given as follows:

$$M=C_1(C_1m+C_3n)t+C_1x+C_2$$
$$\theta=[C_3(C_1k+C_3l)+\rho LC_1(C_1m+C_3n)]t/(\rho C_P)+C_3x+C_4 \tag{13}$$

The variation of D and K in this solution depends both upon moisture content and temperature, then the basic equation is highly nonlinear, in addition, the solution is rather simple—linear relation, it is believed that this solution is very suitable to be a benchmark solution for the computational heat and mass transfer.

If $m=n=k=l=0$, then D and K are constant, this solution degenerates into a part of solution (3).

Conclusions

Analytical solutions have their own irreplaceable important meaning in theory. In addition, as the benchmark solution to check the accuracy, convergence and effectiveness of various numerical computational methods and their differencing schemes, grid generation ways and so on, the analytical solutions are very useful also for the newly developing computational heat and mass transfer. Therefore, some new algebraic explicit analytical solutions without special functions are derived in this paper for the linear and nonlinear unsteady one-dimensional partial differential equation set describing the drying process of infinite plate. The variation of different coefficients is considered also. The derivation method in this paper is perhaps a unique one and can be applied in other cases.

Acknowledgment

The authors are grateful to Prof. Liu, Dengying for his help and to the reviewers for their careful review and valuable proposal. The study was supported by National Natural Science Foundation of China (project No. 50246003) and NKBRSF Project of China (G2000026305).

Nomenclature

a = $K/\rho C_p$
b = L/C_P
C_i = various constants
C_p = specific heat
D = liquid diffusivity
d = thickness
i,j = positive integer
K = thermal conductivity
k,l,m,n,p,q = various constants
L = latent heat of liquid
M = moisture content
T = function of t
t = time coordinate
X = function of x
x = thickness direction geometric coordinate
ρ = density
θ = temperature

References

[1] Mujumdar, A. S., 1995, *Handbook of Industrial Drying*, Marcel Dekker Inc., New York.
[2] Lamb, H., 1932, *Hydrodynamics*, 6th ed., Cambridge University Press, London.
[3] Jakob, M., 1949, *Heat Transfer*, John Wiley & Sons, Inc. New York.
[4] Cai, R., Jiang, H., and Sun, C., 1984, "Some Analytical Solutions Applicable to Verify 3-D Numerical Methods in Turbomachines," *IMechE Conf. Publications C80/84*, pp. 255–263.
[5] Xu, J., Shi, J., and Ni, W., 1989, "Three Dimensional Incompressible Flow Solution of an Axial Compressor Using Pseudostream-Functions Formulation," ASME Paper 89-GT-319.
[6] Gong, Y., and Cai, R., 1989, "3D MSLM—A New Engineering Approach to the Inverse Problem of 3D Cascade," ASME Paper 89-GT-48.
[7] Shen, M., Liu, Q., and Zhang, Z., 1996, "Calculation of 3-D Transonic Flow in Turbomachinery with the Generalized von Mises Coordinates System," Sci. China, Ser. A: Math., Phys., Astron. Technol. Sci. **39**, pp. 1084–1095.
[8] Cai, R., 1998, "Some Explicit Analytical Solutions of Unsteady Compressible Flow," ASME J. Fluids Eng., **120**, pp. 760–764.
[9] Cai, R., and Zhang, N., 2000, "Explicit Analytical Solutions of the Coupled Differential Equations for Porous Material Drying," Prog. Nat. Sci., **10**, pp. 152–157.
[10] Cai, R., and Zhang, N., 2001, "Some Algebraically Explicit Analytical Solutions of Unsteady Nonlinear Heat Conduction," ASME J. Heat Transfer, **123**, pp. 1189–1191.
[11] Cai, R., and Zhang, N., 1998, "Unsteady 1-D Analytical Solutions for Bioheat Transfer Equations," Prog. Nat. Sci., **8**, pp. 733–739.

An Investigation of Simple Evaporation Models Used in Spray Simulations

G. F. Yao [1]
Research Engineer II

S. I. Abdel-Khalik
Professor

S. M. Ghiaasiaan
Professor

The George W. Woodruff School of Mechanical Engineering, Georgia Institute of Technology, Atlanta, GA 30332

In the present work, an unified derivation of simple evaporation models used in spray simulation is described and a new evaporation model is formulated. In the model, the Nusselt number, Sherwood number, and evaporation mass flux are derived using the traditional film theory. However, instead of determining the film thicknesses using the Nusselt and Sherwood numbers derived in the absence of high mass transfer rate, the film thicknesses are calculated from those derived from the fully numerical solutions which represent the realistic heat and mass transfer processes around a droplet. The model predictions are compared with the fully numerical solutions. [DOI: 10.1115/1.1517267]

Introduction

In simplified evaporation models, heat transfer inside a droplet is usually simulated using the infinite conductivity model by Law [1]; or the conduction limited model by Law and Sirignano [2], where liquid circulation inside the droplet can be accounted for by multiplying the thermal conductivity by an empirical factor [3,4].

Two methods are usually used to analyze the gas-phase transport. One is to solve the transport equations for a motionless droplet in an infinite stagnant medium and to employ an empirical multiplication correction to account for forced convection around the droplet [5]. This method is hereafter referred as the ''classic method.'' The other method is to employ the film theory [6,7] which involves analyzing a spherically symmetric layer of thickness δ_T for heat transfer and δ_M for mass transfer. The values of δ_T and δ_M are determined from empirical correlations and the effect of mass transfer on film thickness is neglected. With this latest suggestion, the two methods produce identical equations for the gas-side heat and mass transfer rates [5]. To account for the effect of high mass transfer on film thicknesses, Abramzon and Sirignano [8] determined the film thicknesses (δ_T^* and δ_M^*) by multiplying δ_T and δ_M by a factor obtained by boundary layer calculations.

A few fully numerical studies have also been performed to analyze evaporation of a single and moving droplet [9,10]. Although these detailed numerical models can not be directly incorporated into the computer codes for spray simulations, their results are very useful for validating the simple evaporation models and developing correlations.

The objective of the present work is to develop a simple novel evaporation model, based on the film theory, that includes effect of mass transfer on film thicknesses.

Model Derivations

Previous Models Based on the Classic Method. Simplified mass and energy conservation equations for a motionless and spherical droplet in an infinite and stagnant gas [5] with the following boundary conditions are considered.

$$r=r_d, T=T_s, Y_F=Y_{Fs} \tag{1}$$

$$r=\infty, T=T_\infty, Y_F=Y_{F\infty} \tag{2}$$

Solution of the conservation equations then yields:

$$\dot{m}''=\frac{\rho\mathcal{D}}{2r_d}\mathrm{Sh}B_M \tag{3}$$

$$\dot{m}''=\frac{K_g}{2C_{PF}r_d}\mathrm{Nu}B_T \tag{4}$$

$$\mathrm{Sh}=\mathrm{Sh}_0\frac{\ln(1+B_M)}{B_M} \tag{5}$$

$$\mathrm{Nu}=\mathrm{Nu}_0\frac{\ln(1+B_T)}{B_T} \tag{6}$$

where

$$B_M=\frac{Y_{Fs}-Y_{F\infty}}{1-Y_{Fs}} \tag{7}$$

$$B_T=\frac{C_{PF}(T_\infty-T_s)}{L+\dfrac{\dot{q}_l''}{\dot{m}''}} \tag{8}$$

$$\mathrm{Nu}_0=\mathrm{Sh}_0=2 \tag{9}$$

To account for the effect of convection, instead of Eq. (9), Nu_0 and Sh_0 are obtained from empirical correlations for heat and mass transfer around a solid sphere. This method, with $B_T=B_M$ assumed, constitutes the most frequently used model in spray simulations.

Instead of assuming $B_T=B_M$, from Eqs. (3) through (6), B_T can be represented in terms of B_M. Substitution into Eq. (6) then gives:

$$\mathrm{Nu}=\frac{(\mathrm{Nu}_0/\mathrm{Le})\ln(1+B_M)}{(1+B_M)^{1/\mathrm{Le}}-1} \tag{10}$$

Equations (3), (5), and (10) form the basic evaporation model used by Mao et al. [11], Aggarwal and Chitre [12], Park and Aggarwal [13], and Klingsporn and Renz [14]

Abramzon and Sirignano's Model

The film thicknesses in the absence of high mass transfer rate (Stefan flow) can be obtained by equating the rates of purely molecular transport through the film to the actual intensity of the convective heat or mass transfer between the surface and the external flow [7]. When modified to include the effect of high mass transfer rate, the external radii of the films are then obtained from [8]:

$$r_{f,T}=r_d\frac{\mathrm{Nu}^*}{\mathrm{Nu}^*-2};\quad r_{f,M}=r_d\frac{\mathrm{Sh}^*}{\mathrm{Sh}^*-2} \tag{11}$$

where Nu* and Sh* are called ''modified'' Nusselt and Sherwood numbers, respectively.

Using these assumed external radii, the gas-side mass and energy conservation equations are integrated, leading to Eqs. (3)

[1]Current address: Flow Science, Inc., 683 Harkle Rd., Suite A, Santa Fe, NM 87505; e-mail:gyao@flow3d.com

Contributed by the Heat Transfer Division for publication in the JOURNAL OF HEAT TRANSFER. Manuscript received by the Heat Transfer Division April 30, 2001; revision received July 8, 2002. Associate Editor: C. Thomas Avedisian.

through (8) with Nu_0 and Sh_0 replaced with Nu* and Sh*, respectively. The modified Nusselt and Sherwood numbers are obtained by assuming:

$$\frac{\delta_T^*}{\delta_T}=F(B_T) \quad \text{and} \quad \frac{\delta_M^*}{\delta_M}=F(B_M)=(1+B)^{0.7}\frac{\ln(1+B)}{B} \tag{12}$$

where it has been assumed that $B=B_T$ or B_M. Thus leading to

$$\text{Nu}^*=2+\frac{\text{Nu}_0-2}{F(B_T)} \tag{13}$$

$$\text{Sh}^*=2+\frac{\text{Sh}_0-2}{F(B_M)} \tag{14}$$

Derivation of the Present Model

Again, the simplified conservation equations are integrated using the following boundary conditions:

$$T=T_s, Y_F=Y_{Fs}, \text{ at } r=r_d \tag{15}$$

$$T=T_\infty, \text{ at } r=r_d+\delta_T^* \tag{16}$$

$$Y=Y_{F\infty}, \text{ at } r=r_d+\delta_M^* \tag{17}$$

The resulting temperature distribution across the film thickness is then derived, and is used to obtain:

$$h^*=\frac{\dot{m}''C_{PF}}{\exp\left(\dfrac{\Omega\delta_T^*}{\delta_T^*+r_d}\right)-1} \tag{18}$$

When $\dot{m}''\to 0$, h^*, and δ_T^* converge to h and δ_T respectively.

Energy balance at the droplet surface, and Eq. (18), give:

$$\dot{m}''=\frac{K_g}{C_{PF}r_d}\left(1+\frac{r_d}{\delta_T^*}\right)\ln(1+B_T) \tag{19}$$

$$\text{Nu}=2\left(1+\frac{r_d}{\delta_T^*}\right)\frac{\ln(1+B_T)}{B_T} \tag{20}$$

Integration of the mass species equation with the boundary conditions given in Eqs. (15) and (17), leading to the mass fraction distribution through the film thickness, and from there an expression for Sh is derived:

$$\text{Sh}=2\left(1+\frac{r_d}{\delta_M^*}\right)\frac{\ln(1+B_M)}{B_M} \tag{21}$$

From the mass balance at droplet surface, and using the expression for mass fraction distribution in the film, the following equation is derived.

$$\dot{m}''=(\rho\mathcal{D})\left(\frac{\delta_M^*+r_d}{r_d\delta_M^*}\right)\ln(1+B_M) \tag{22}$$

Equations (19–22) provide the gas-side transport equations of the presented model.

Remarks

1) Replacing δ_M^* in Eqs. (21) and (22) by δ_M expressed in terms of Sh_0, and δ_T^* in Eqs. (19) and (20) by δ_T expressed in terms of Nu_0, Eqs. (3) through (6) are obtained.

2) Substituting Eq. (12) for δ_T^* and δ_M^* into Eqs. (19–22), Abramzon and Sirignano's model are alternatively derived.

3) In the present model, instead of determining the film thicknesses based on emperical correlations and boundary layer calculations, film thicknesses are determined using the heat and mass transfer correlations derived from the fully numerical solutions.

The following solution procedure is repeated until convergence is achieved. Property values needed in the calculations are evaluated at a reference temperature equal to $(T_\infty+2T_s)/3$.

1) Guess a droplet surface temperature, T_s, and droplet radius, r_d. Then, the species mass fraction at droplet surface is determined by:

$$Y_{Fs}=\frac{W_F}{W_F+W_{\text{air}}\left[\dfrac{P}{P_{\text{sat}}(T_s)}-1\right]} \tag{23}$$

and, furthermore, B_M is calculated by Eq. (7).

2) Obtain δ_M^*, from Eq. (21), with its left side replaced by the appropriate Sherwood number correlation derived from the fully numerical solution, and obtain $\dot{m}''$ from Eq. (22); equivalently, $\dot{m}''$, can be calculated alternatively as suggested by Sirignano [15].

3) Cast Eqs. (19) and (20) into the following forms:

$$B_T=\exp\left(\frac{\Omega\delta_T^*}{r_d+\delta_T^*}\right)-1 \tag{24}$$

$$\text{Nu}=\frac{2\Omega}{B_T} \tag{25}$$

The left side of Eq. (25) is now replaced by the heat transfer correlation derived from the fully numerical solution, and B_T is solved for, followed by the calculation of $\dot{q}_L''$ using Eq. (8).

4) Calculate the time-rate-of-change of droplet radius using the same method as suggested by Klingsporn and Renz [14].

5) Solve for the temperature distribution inside the droplet using the diffusion-limited model as described by Yao et al. [16], where internal circulation is accounted for by multiplying the thermal conductivity by an emperical factor [3].

6) Update T_s using $\dot{q}_l''=K_d\partial T_d/\partial r|_{r=r_d}$

Remarks

1) To compare with the model used by Mao et al. [11], Aggarwal and Chitre [12], Park and Aggarwal [13], Steps 2 and 3 are replaced by the following two steps. First, $\dot{m}''$ is found from Eqs. (3) and (5). The heating rate, $\dot{q}_L''$, is then obtained from

$$\dot{q}_L''=\frac{\text{Nu}K_g}{2r_d}(T_\infty-T_s)-\dot{m}''L \tag{26}$$

with the Nusselt number determined by Eq. (10). The corresponding model is named ''Model 1'' for convenience.

2) Similarly, to compare with the model of Abramzon and Sirignano [4], Steps 2 and 3 are replaced by the following two steps. First, $\dot{m}''$ is found from Eqs. (3) and (5), where, Sh_0 is replaced with Sh* found from Eq. (14). The heat transfer number, B_T, is then found using Eqs. (4) and (6), along with Eqs. (12). The liquid heating rate is then found from Eq. (8). Again, for the convenience, this model will be referred to as ''Model 2.''

Results and Discussion

One-dimensional gas flow is assumed, and the following equation is used to update the relative velocity between droplet and surrounding gas.

$$\frac{d\overline{u}}{dt}=\frac{3}{8}\left(\frac{\rho_{g,\infty}}{\rho_d}\right)\frac{\overline{u}^2}{r_d}C_D \tag{27}$$

where the drag coefficient is calculated using the correlations derived from the fully numerical solutions to be given later. Convergence was assumed when the relative errors of all guessed and calculated values were within 10^{-4}.

Comparison With Other Models and Detailed Numerical Results

First, consider the numerical solutions of Haywood et al. [9]. The Nusselt and Sherwood numbers used in Eqs. (25) and (21),

and the drag coefficient in Eq. (27) are calculated using the correlations derived from their fully numerical solutions for a moving n-heptane droplet evaporating in air at 800 K and 1 atm.

Figures 1 and 2 show the results. The predicted droplet mass (and radius, not shown here for brevity) from the present model and Model 1 agree with the numerical data very well, while Model 2 slightly overestimates the droplet mass and radius. The predicted ratios of droplet heating rate to gas-side heat transfer rate from all three models are similar. Compared with the numerical data, all three models underestimate droplet heating rates, particularly in the middle of the droplet life time.

Now, consider the numerical solutions of Chiang et al. [10]. For these comparisons, the correlations developed by Chiang et al. [10] based on their fully numerical solutions of an n-octane droplet evaporating in a hot gas stream at temperature and pressure of 1250 K and 10 atm respectively, were used.

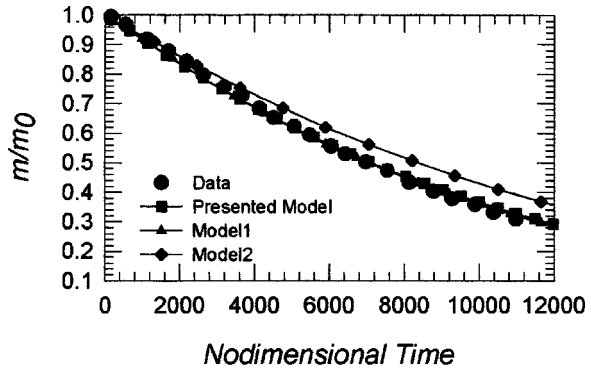

Fig. 1 Comparison of transient evolution of droplet mass with the data of Haywood et al. [9]

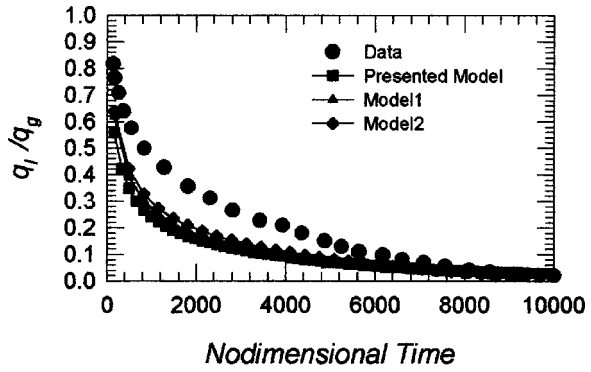

Fig. 2 Comparison of transient evolution of the rate of droplet heating with the data of Haywood et al. [9]

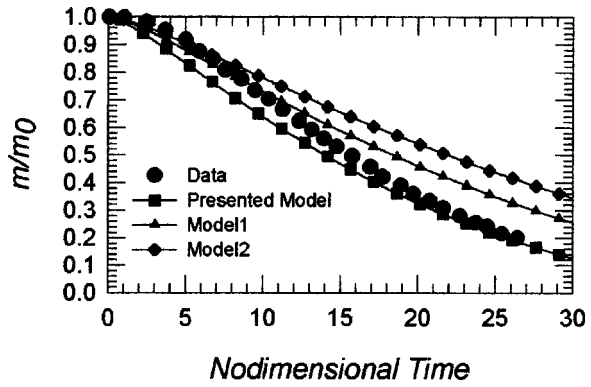

Fig. 3 Comparison of transient evolution of droplet mass with the data of Chiang et al. [10]

The results for m/m_0 are shown in Fig. 3. Again, the predictions of all three model for q_l''/q_g'' (not shown here for brevity) are similar. At the first half of droplet life time, the droplet heating rate is slightly underestimated while, at the second half, the heating rate is overestimated. However, the predictions of droplet mass by the model presented in this paper are more accurate than those from Models 1 and 2.

Conclusions

Derivations of simple droplet evaporation models frequently used in the spray simulations were briefly described. A new droplet evaporation model was developed where Nusselt number, Sherwood number, and evaporation mass flux were derived using the widely used film theory. The method is based on the calculation of the film thickness from the correlations for Nusselt and Sherwood numbers that have been derived from the relevant full numerical solutions. Comparison with the predictions of full numerical solutions shows that the presented model predicts the droplet radius and mass more accurately in comparison with two other widely used models.

Nomenclature

B_M = mass transfer number, Eq. (7)
B_T = heat transfer number, Eq. (8)
C_D = drag coefficient
C_p = specific heat, $(\mathrm{J\,kg^{-1}\,K^{-1}})$
$\mathcal{D}$ = species diffusion coefficient, $(\mathrm{m^2\,s^{-1}})$
h = heat transfer coefficient, $(\mathrm{J\,m^{-2}\,s^{-1}\,K^{-1}})$
K = thermal conductivity, $(\mathrm{W\,m^{-1}\,K^{-1}})$
$\mathcal{K}$ = mass transfer coefficient, $(\mathrm{kg\,m^{-2}\,s^{-1}})$
L = latent heat of vaporization, $(\mathrm{J\,kg^{-1}})$
L_e = Lewis number, $(Kg(\rho_g\mathcal{D})^{-1}\,C_{pg}^{-1})$
$\dot{m}''$ = mass flux at droplet surface, $(\mathrm{kg\,m^{-2}s^{-1}})$
Nu = Nusselt number, $(2r_dh/K_g)$
P = gas pressure, (Pa)
q'' = heat flux, $(\mathrm{J\,m^{-2}\,s^{-1}})$
r = droplet radius; radial coordinate, (m)
Sh = Sherwood number, $(2r_d\mathcal{K}/(\rho\mathcal{D}))$
t = time, (s)
T = temperature, (K)
$\overline{u}$ = relative velocity, $(\mathrm{m\,s^{-1}})$
W = molecular weight
Y = mass fraction

Greek Symbols

δ = film thickness, (m)
μ = molecular viscosity, $(\mathrm{kgm^{-1}\,s^{-1}})$
ρ = density, $(\mathrm{kgm^{-3}})$

Subscripts

d = droplet
F = fuel
g = gas
l = liquid
M = mass transfer
s = saturated; droplet surface
T = heat transfer
0 = initial condition; without high mass transfer rate
∞ = free stream condition

Superscripts

$\cdot$ = with high mass transfer rate

References

[1] Law, C. K., 1976, "Unsteady Droplet Vaporization with Droplet Heating," Combust. Flame, **26**, pp. 17–22.
[2] Law, C. K., and Sirignano, W. A., 1977, "Unsteady Droplet Combustion with Droplet Heating-II: Conduction Limit," Combust. Flame, **28**, pp. 175–186.
[3] Talley, D. G., and Yao, S. C., 1986, "A Semi-Empirical Approach to Thermal

and Composition Transients inside Vaporizing Fuel Droplets,'' *Twenty-First Symposium (International) on Combustion*, The Combustion Institute, Pittsburgh, PA, pp. 609–616.
[4] Abramzon, B., and Sirignano, W. A., 1989, ''Droplet Vaporatization Model for Spray Combustion Calculations,'' Int. J. Heat Mass Transf., **32**, pp. 1605–1618.
[5] Faeth, G. M., 1977, ''Current Status of Droplet and Liquid Combustion,'' Prog. Energy Combust. Sci., **3**, pp. 191–224.
[6] Bird, R. B., Stewart, W. E., and Lightfoot, E. M., 1960, *Transport Phenomena*, John Wiley, New York.
[7] Frank-Kamenetskii, D. A., 1969, *Diffusion and Heat Transfer in Chemical Kinetics*, second edition, Plenum Press, New York.
[8] Abramzon, B., and Sirignano, W. A., 1987, ''Approximate Theory of a Single Droplet Vaporization in a Convective Field: Effects of Variable Properties, Stefan Flow and Transient Liquid Heating,'' *Proc. 2nd ASME-JSME Thermal Engng. Joint Conf.*, Honolulu, Hawaii, **1**, pp. 11–18.
[9] Haywood, R. J., Nafziger, R., and Renksizbulut, M., 1989, ''A Detailed Examination of Gas and Liquid Phase Transient Processes in Convective Droplet Evaporation,'' ASME J. Heat Transfer, **111**, pp. 495–502.
[10] Chiang, C. H., Raju, M. S., and Sirignano, W. A., 1992, ''Numerical Analysis of Convecting, Vaporizing Fuel Droplet with Variable Properties,'' Int. J. Heat Mass Transf., **35**, pp. 1307–1324.
[11] Mao, C. P., Szekely, G. A., Jr., and Faeth, G. M., 1980, ''Evaluation of a Locally Homogeneous Flow Model of Spray Combustion,'' J. Energy, **4**, pp. 78–87.
[12] Aggarwal, S. K., and Chitre, S., 1991, ''Computations of Turbulent Evaporating Sprays,'' J. Propul. Power, **7**, pp. 213–220.
[13] Park, T. W., and Aggarwal, S. K., 1995, ''Gravity Effects on the Dynamics of Evaporating Droplets in a Heated Jet,'' J. of Propulsion and Power, **11**, pp. 519–528.
[14] Klingsporn, M., and Renz, U., 1994, ''Vaporization of a Binary Unsteady Spray at High Temperature and High Pressure,'' Int. J. Heat Mass Transf., **37**, (suppl.1), pp. 265–272.
[15] Sirignano, W. A., 1999, *Fluid Dynamics and Transport of Droplets and Sprays*, Cambridge University Press, Cambridge.
[16] Yao, G. F., Ghiaasiaan, S. M., Abdel-Khalik, S. I., Schoonover, K., ''Computational Modeling of Spray Cooling in Vapor Conditioning Equipment,'' *Proc. Int. Symp. on Computational Technologies for Fluid/Thermal/Chemical/ Systems with Industrial Applications*, Boston, MA. V. V. Kidriavtsev, C. R. Kleijn, and S. Kawano, eds., ASME PVP-Vol. 397-2, pp. 107–116.

A Mathematical Confirmation for Higher LMTD Value of Counter Flow Versus Parallel Flow Heat Exchangers

Farshad Kowsary
e-mail: fkowsari@chamran.ut.ac.ir

Mohammad Biglarbegian
e-mail: jbiglar@chamran.ut.ac.ir

Mechanical Engineering Department, Faculty of Engineering, University of Tehran, Tehran, Iran

A rigorous argument based on the characteristic of a monotonously increasing function is presented to establish the well-known fact of higher LMTD value of counter flow heat exchangers as compared to parallel flow ones. [DOI: 10.1115/1.1517270]

Keywords: Analytical, Heat Exchangers

Introduction

Most classical heat transfer textbooks state that under an identical situation a counter flow heat exchanger has a higher value of LMTD than a parallel flow one. Consequently, for exactly the same inlet and outlet hot and cold fluid temperatures, the counter flow heat exchanger requires a smaller heat transfer area. To demonstrate this fact, they sometimes resort to an intuitive thermodynamic argument that a counter flow heat exchanger is ''better'' because in counter flow configuration the average temperature difference between hot and cold fluids along the flow paths is lower than the parallel flow one; therefore, inducing a smaller irreversibility. This argument is usually further supported by use of a numerical example [1]. The purpose of this note is to provide a mathematical verification for this well-known fact.

Analysis

Consider parallel and counter flow heat exchangers with given inlet and outlet hot and cold fluid temperatures T_{hi}, T_{ho}, and T_{ci}, T_{co} as shown in Fig. 1. The problem, in essence, is to show that the required heat transfer area of the counter flow heat exchanger is smaller than the parallel flow one (i.e., $A_{CF<}A_{PF}$).

In parallel flow heat exchangers the inlet and outlet (hot and cold) temperatures are sorted out based on their levels according to

$$T_{ci<}T_{co<}T_{ho<}T_{hi}. \tag{1}$$

In counter flow heat exchangers, however, it is quite conceivable to achieve $T_{ho<}T_{co}$. Nonetheless, in order to have a fair and meaningful comparison between the two flow arrangements, we have no alternative other than allowing $T_{co<}T_{ho}$ in counter flow heat exchangers as well (although it is acknowledged that this forces the counter flow heat exchanger to operate on a fraction of its effectiveness). Therefore, the relative ordering of temperatures for our analysis would be as given by Eq. (1) for both counter flow and parallel flow heat exchangers.

From a text book heat transfer analysis we have

$$\frac{A_{CF}}{A_{PF}}=\frac{\Delta Tlm_{PF}}{\Delta Tlm_{CF}}\equiv X, \tag{2}$$

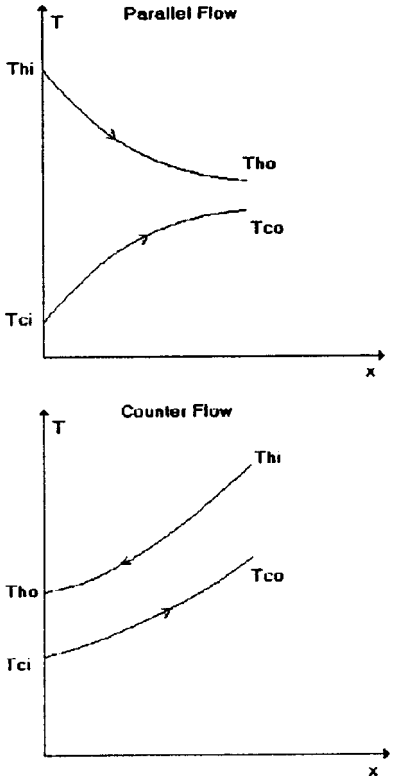

Fig. 1 Parallel and counter flow temperature profiles

Contributed by the Heat Transfer Division for publication in the JOURNAL OF HEAT TRANSFER. Manuscript received by the Heat Transfer Division January 17, 2002; revision received July 29, 2002. Associate Editor: M. K. Jensen.

where ΔTlm_{CF} and ΔTlm_{PF}, log-mean temperature differences for counter flow and parallel flow heat exchangers are given, respectively, by

$$\Delta Tlm_{CF}=\frac{(T_{hi}-T_{co})-(T_{ho}-T_{ci})}{\mathrm{Ln}\dfrac{(T_{hi}-T_{co})}{(T_{ho}-T_{ci})}} \quad \text{and}$$

$$\Delta Tlm_{PF}=\frac{(T_{ho}-T_{co})-(T_{hi}-T_{ci})}{\mathrm{Ln}\dfrac{(T_{ho}-T_{co})}{(T_{hi}-T_{ci})}};$$

and our task is to show that $X<1$.

After some algebraic manipulations, starting from Eq. (2), we would have

$$X=\frac{(T_{ho}-T_{co})-(T_{hi}-T_{ci})}{(T_{hi}-T_{co})-(T_{ho}-T_{ci})}\cdot\frac{\mathrm{Ln}(T_{hi}-T_{co})-\mathrm{Ln}(T_{ho}-T_{ci})}{\mathrm{Ln}(T_{ho}-T_{co})-\mathrm{Ln}(T_{hi}-T_{ci})}. \tag{3}$$

Let us at this instance, for convenience, define x, y, z, and t as

$$x\equiv T_{hi}-T_{ci}, \tag{4a}$$

$$y\equiv T_{ho}-T_{co}, \tag{4b}$$

$$z\equiv\max[(T_{hi}-T_{co}),(T_{ho}-T_{ci})], \quad \text{and} \tag{4c}$$

$$t\equiv\min[(T_{hi}-T_{co}),(T_{ho}-T_{ci})]. \tag{4d}$$

Assume for a moment that $T_{hi}-T_{co}>T_{ho}-T_{ci}$; that is, $z=T_{hi}-T_{co}$ and $t=T_{ho}-T_{ci}$. From the known ordering of temperatures (Eq. (1)) it is easy to show that

$$T_{hi}-T_{ci}>T_{hi}-T_{co}\Rightarrow x>z,$$

$$T_{hi}-T_{co}>T_{ho}-T_{co}\Rightarrow z>y, \quad \text{and}$$

$$T_{ho}-T_{ci}>T_{ho}-T_{co}\Rightarrow t>y.$$

Therefore, in condensed form this may shown as

$$0<y<t<z<x. \tag{5a}$$

Moreover, it holds that

$$x+y=(T_{hi}-T_{ci})+(T_{ho}-T_{co})=(T_{hi}-T_{co})+(T_{ho}-T_{ci})=z+t. \tag{5b}$$

Examination reveals that an identical conclusion as Eqs. (5*a*) and (5*b*) may be arrived at for the case of $T_{hi}-T_{co}<T_{ho}-T_{ci}$. Thus, using the definitions given by Eqs. (4(*a*–*d*)), the problem could mathematically be stated as *to show that for any four real numbers x, y, z, and t which satisfy the requirements given by*

$$\begin{cases} 0<y<t<z<x \\ x+y=z+t \end{cases}, \tag{6}$$

then it must hold that

$$X\equiv\frac{(x-y)\cdot(\mathrm{Ln}z-\mathrm{Ln}t)}{(z-t)\cdot(\mathrm{Ln}x-\mathrm{Ln}y)}<1. \tag{7}$$

Our approach may look vague at first, but it works at the end. First recall that the Taylor series expansion of the function e^w is given by

$$e^w=\sum_{k=0}^{\infty}\frac{w^k}{k!}$$

If, $w>0$, then it holds that $e^w>1+w+1/2w^2$. Now suppose that u,v, are real numbers with $0<v<u$. Then we would have

$$\begin{aligned} e^{(2uv/u^2-v^2)} &> 1+\frac{2uv}{u^2-v^2}+\frac{1}{2}\left(\frac{2uv}{u^2-v^2}\right)^2 \\ &= 1+\frac{2uv}{u^2-v^2}+\left(\frac{2v^2}{u^2-v^2}\right)\left(\frac{u^2}{u^2-v^2}\right) \\ &> 1+\frac{2uv}{u^2-v^2}+\frac{2v^2}{u^2-v^2} \\ &= 1+\frac{2v(u+v)}{u^2-v^2}=1+\frac{2v}{u-v}=\frac{u+v}{u-v} \end{aligned}$$

By taking natural logarithm of the two ends of this chain of inequalities, it becomes evident that

$$\frac{2uv}{u^2v^2}>\mathrm{Ln}\left(\frac{u+v}{u-v}\right). \tag{8}$$

Now consider the function $f(v)$ defined as

$$f(v)=\frac{\mathrm{Ln}(u+v)-\mathrm{Ln}(u-v)}{2v}, \tag{9}$$

whose derivative is given by

$$f'(v)=\frac{1}{2v^2}\left(\frac{2uv}{u^2-v^2}-\mathrm{Ln}\left(\frac{u+v}{u-v}\right)\right). \tag{10}$$

From Eq. (8) it holds unconditionally that $f'(v)>0$ and; therefore, $f(v)$ is a strictly increasing function for all v with $0<v<u$.

At this moment by choosing two real numbers v_1 and v_2 such that $0<v_1<v_2<u$, variables x, y, z, and t; introduced in Eqs. (4(a–d)) are defined by

$$x=u+v_2, \quad y=u-v_2, \quad z=u+v_1, \quad \text{and} \quad t=u-v_1. \tag{11}$$

Clearly, the two constraints given by Eq. (6) are adhered to. That is

$$\frac{x+y}{2}=\frac{z+t}{2}=u \quad \text{and} \quad 0<y<t<z<x.$$

Furthermore, it can be easily shown that

$$2v_1=z-t \quad \text{and} \quad 2v_2=x-y.$$

As $f(v)$ is a monotonously increasing function, there exists such a property which states that, for $v_1<v_2$, then $f(v_1)<f(v_2)$ [2]. Therefore, by using the definition of f given by Eq. (9), it must hold that

$$\frac{\mathrm{Ln}(u+v_2)-\mathrm{Ln}(u-v_2)}{2v_2}>\frac{\mathrm{Ln}(u+v_1)-\mathrm{Ln}(u-v_1)}{2v_1},$$

which, by using the definitions given in Eq. (11) above, can be written as

$$\frac{\mathrm{Ln}(x)-\mathrm{Ln}(y)}{x-y}>\frac{\mathrm{Ln}(z)-\mathrm{Ln}(t)}{z-t},$$

or

$$\frac{x-y}{z-t}\cdot\frac{\mathrm{Ln}(z)-\mathrm{Ln}(t)}{\mathrm{Ln}(x)-\mathrm{Ln}(y)}<1,$$

and, consequently, it is shown that

$$X<1$$

must hold unconditionally.

As a final remark it should be pointed out that the above reasoning breaks down when there exists phase change in one of the

flow paths. However, inspection of inlet and outlet temperatures for both cold and hot flow paths readily shows the trivial fact that in this case

$$X = 1,$$

which states that the log mean temperature difference is identical for both parallel and counter flow heat exchangers.

Acknowledgments

The authors wish to express their sincere gratitude to Mr. Daniel Jerome Katz of Caltech department of mathematics for the assistance he provided generously in completing the mathematical proof presented in this paper.

References

[1] Incropera. F. P., and Dewit, P. D., 1994, *Introduction to Heat Transfer*, 3rd ed., Wiley, New York.

[2] Folland, G. B., 1999, *Real Analysis: Modern Techniques and Their Applications (Pure and Applied Mathematics)*, second edition, Wiley Intersciences, New York.

Commentary on Correlations for Convective Vaporization in Tubes

Ralph L. Webb
e-mail: r5w@psu.edu
The Pennsylvania State University, Department of Mechanical Engineering, University Park, PA 16802

Keywords: Flow, Forced Convection, Boiling

Introduction

This technical note provides commentary on four recently published correlations for convective vaporization in tubes. It appears that they were formulated inconsistent with accepted practice. Hence, if applied per usual practice, errors will result in their use. The correlations addressed are those of Gungor and Winterton [1], Gungor and Winterton [2], Liu and Winterton [3], and Kattan et al. [4].

Webb and Gupte [5] described phenomenological models used for calculating heat transfer coefficients in convective vaporization. The principal models discussed are the superposition and the asymptotic models, which are of the form:

$$q^n = q_{nb}^n + q_{cv}^n \tag{1}$$

where q_{nb} represents the nucleate boiling contribution, and q_{cv} represents the forced convection contribution. The value of the exponent, n, is assigned on empirical grounds to the value that gives the best fit of the data set. Typically, it has been found that $2 < n < 3$ is best, as is shown by the Steiner and Taborek [6] correlation. Chen [7] introduced the first successful correlation of the form of Eq. (1), in which he used $n = 1$, which is the superposition model. Equation (2) may also be written in terms of the heat transfer coefficients by dividing by $\Delta T_{ws} (= T_w - T_{\text{sat}})$ to give:

$$h^n = h_{nb}^n + h_{cv}^n \tag{2}$$

The nucleate boiling component (h_{nb}) is a strong function of ΔT_{ws}, whereas the forced convection contribution (h_{cv}) should be independent of $\Delta T_{\Delta ws}$, as argued by Chen [7] and further validated in experiments by Kenning and Cooper [8], and by Wadekar [9]. Figure 1 shows the Wadekar ethanol data for boiling in a vertical tube. Figure 1 shows q versus ΔT_{ws} for curves at different vapor qualities. The data to the left of "Line A-A" show a linear dependence on heat flux (so h is independent of heat flux) and are convection dominated. The data to the right of Line A-A merge toward a common asymptote and are nucleate boiling dominated.

Chen [7] argued that the flow velocity suppresses nucleate boiling, and accounted for a "suppression factor" using $h_{nb} = S h_{nbp}$, where h_{npb} is for nucleate pool boiling. It is intended that the term h_{nbp} be predicted using the most appropriate correlation for nucleate pool boiling.

All correlations write $h_{cv} = F h_l$, where h_l is the single-phase heat transfer coefficient for the liquid phase flowing alone in the tube. Because h_{cv} and h_l are independent of heat flux, one clearly expects the F-factor to also be independent of heat flux.

Discussion of Four Published Correlations

The convective boiling correlations of interest here are composed of two sub-correlations—one for q_{nb} (or h_{nb}) and one for q_{cv} (or h_{cv}). The correlation developer uses a preferred correlation for nucleate pool boiling to calculate h_{nbp} and applies a suppression factor, if this is appropriate for the model. One may assume $S = 1$ for the asymptotic model ($n > 1$) and let the effect of boiling suppression be included in the exponent, n. The next step in the development of a convective boiling correlationion is to formulate a correlation for the F-factor. The commonly accepted approach is to manipulate the database by subtracting the heat flux dependent term (the nucleate boiling contribution) and obtain F-factors that are then correlated as a function of Prandtl number and the two-phase Reynolds number. Applying this approach to Eq. (1) (or Eq. (2)), one calculates the F-factor for each data point using:

$$F = \frac{[q^n - (S q_{nbp})^n]^{1/n}}{q_l} \tag{3a}$$

$$= \frac{[h^n - (S h_{nbp})^n]^{1/n}}{h_l} \tag{3b}$$

Having separated the heat flux dependent term (q_{nb}) from the total q, the next step in the development of a correlation is to correlate the F-factor as a function of flow variables. It is emphasized, that this F-factor should be independent of heat flux (or ΔT_{ws}). For example, the Chen [7] correlation gives $F = 1 + 1.8(X_{tt})^{-0.79}$. The nucleate pool boiling correlation may be written in either of the two forms given by Eqs. (4*a*) or (4*b*).

$$q_{nbp} = A \Delta T_{ws}^m \tag{4a}$$

$$h_{nbp} = A^{1/m} q^{(m-1)/m} \tag{4b}$$

If the nucleate pool boiling correlation is given in the form of Eq. (4*a*) it may be converted to the form of Eq. (4*b*).

All four of the developers of the correlations of present concern (Gungor and Winterton [1,2], Liu and Winterton [3], and Kattan et al. [4]) used the Cooper [10] correlation, which is was published in the form of Eq. (4*b*) above and is:

$$h_{nbp} = 55 q_{nbp}^{2/3} M^{-1/2} (p/p_c)^a [-0.434 \ln(p/p_c)]^{-0.55} \tag{5a}$$

where M is the molecular weight and $a = 0.12 - 0.4343 \ln R_p$ and R_p is a "roughness parameter." The four correlation developers of concern here used Eq. (5*a*) with $R_p = 1.0$ and substituted the total heat flux (q) in Eq. (5*a*) to evaluate h_{nbp}. Hence, they inappropriately calculated h_{npb} in Eq. (3*b*) by evaluating the heat flux in Eq. (5*a*) at the total system heat flux (q), rather than at the component q_{npb}. To use the Cooper correlation correctly, it should be converted to the form of Eq. (4*a*) above. Doing this results in:

Contributed by the Heat Transfer Division for publication in the JOURNAL OF HEAT TRANSFER. Manuscript received by the Heat Transfer Division November 20, 2001; revision received July 1, 2002. Associate Editor: D. B. R. Kenning.

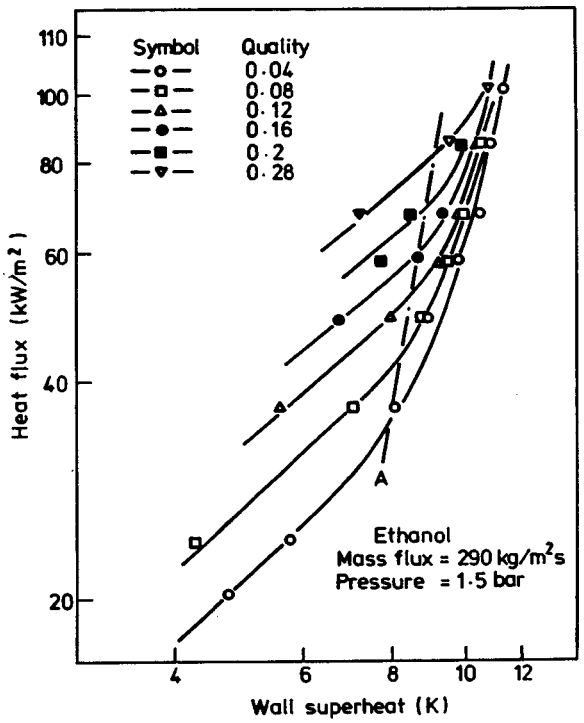

Fig. 1 Convective vaporization data for ethanol for different vapor qualities. Line A-A separates the heat flux independent convective vaporization regime from the heat flux dependent regime influenced by nucleate boiling, from Wadekar [9].

$$q_{nbp} = 1.674E + 5\Delta T_{ws}^{3}(M^{-1/2}(p/p_c)^{a}[-0.434\ln(p/p_c)]^{-0.55})^{3} \quad (5b)$$

Then, the four correlation developers calculated the F-factor by Eq. (3b), which uses heat transfer coefficients h, h_{nbp}, and h_l. Their use of Eq. (5a) resulted in subtracting a q_{npb} contribution that is too large, and the resulting F-factor is smaller than would result from the fundamentally correct procedure. This will result in an F-factor that may be heat flux dependent, as opposed to a term that depends only on two-phase Reynolds (and Prandtl) numbers.

Both of the Gungor and Winterton correlations are both based on use of the superposition model (Eq. (2) with $n=1$) and both use the F-factor of Gungor and Winterton [1], which is given by:

$$F = 1 + 24000\ \mathrm{Bo}^{1.16} + 1.37X_{tt}^{-0.86} \quad (6)$$

Equation (6) shows a strong dependency of heat flux, as indicated by the Boiling number (Bo). As previously noted, the F-factor should have no dependency on Bo. The Liu and Winterton [3] correlation is based on use of the asymptotic model (Eq. (2) with $n=3$). F-factor is given by:

$$F = \left[1 + x\mathrm{Pr}_l\left(\frac{\rho_l}{\rho_v} - 1\right)\right]^{0.35} \quad (7)$$

Surprisingly, Eq. (7) shows no dependency of heat flux. It is noted that the Gungor and Winterton [1,2] and the Liu and Winterton [3] correlations use much of the same data as Liu and Winterton, although the Liu and Winterton correlation has additional data sources. The Kattan et al. [4] correlation was based on a small refrigerant data base. It uses Eq. (2) with $n=3$ and $S=1.0$.

Although the correlations incorrectly evaluated the nucleate boiling component in their correlation development, it is expected that the correlations will reasonably predict the data. This is because the F-factor provides an empirical correlation of their database. But, errors will result, unless the user evaluates the h_{nbp} at the total system heat flux (q). The amount of error will depend on the fraction of the total heat flux due to nucleate boiling contribution, q_{nbp}/q. These correlations must be regarded as empirical, rather than based on the Eq. (2) (or Eq. (3)) phemonological model.

In contrast to the above four correlations, Steiner and Taborek [6] published a correlation for convective vaporization based on Eq. (2) with $n=3$ and $S=1.0$. This correlation used the Gorenflo [11] nucleate pool boiling correlation. The nucleate boiling correlation was developed consistent with Eq. (2); thus the q_{npb} was calculated at the system $(T_w - T_{\mathrm{sat}})$.

Recommendation

Users of these four correlations should be very careful to evaluate the nucleate boiling component in Eq. (2) consistent with the way the authors calculated the F-factors—thus at the total system heat flux.

Nomenclature

- Bo = boiling number $(=q/\lambda G)$
- F = two-phase convection multiplier factor, h_{cv}/h_l
- G = mass velocity
- h = heat transfer coefficient. h (total), h_l (liquid phase flowing alone), h_{lo} (total mass rate flowing as a liquid), h_{nbp} (nucleate pool boiling), $h_{nb}(=Sh_{nbp})$, h_{cv} (two-phase convection, without nucleate boiling)
- p = pressure, p_c (critical pressure)
- Pr_1 = liquid Prandtl number
- q = heat flux, q (total), q_{cv} (convective component), q_l (liquid phase flowing alone), q_{nb} (nucleate boiling component), q_{nbp} (nucleate pool boiling)
- S = suppression factor $(=h_{nb}/h_{nbp})$
- T = temperature, T_{sat} (saturation), T_w (wall), $\Delta T_{ws}(=T_w - T_{\mathrm{sat}})$
- x = vapor quality
- X_{tt} = Martinelli parameter $[=(\Delta p_{F,l}/\Delta p_{F,v})^{0.5}]$
- ρ = density, ρ_l (liquid), ρ_v (vapor)
- λ = latent heat

References

[1] Gungor, K. E., and Winterton, R. H. S., 1986, "A General Correlation for Flow Boiling in Tubes and Annuli," Int. J. Heat Mass Transf., **29**(3), pp. 351–358.

[2] Gungor, K. E., and Winterton, R. H. S., 1987, "Simplified General Correlation for Saturated Flow Boiling and Comparisons of Correlations with Data," Chem. Eng. Res. Des., **65**, pp. 148–156.

[3] Liu, Z., and Winterton, R. H. S., 1988, "Wet Wall Flow Boiling Correlation with Explicit Nucleate Boiling Term," *Multiphase Transport and Particulate Phenomena*, Edited by T. Nejat Veziroglu, Hemisphere Publishing Co., **1**, pp. 419–432.

[4] Kattan, N., Thome, J. B., and Favrat, D., 1998, "Flow Boiling in Horizontal Tubes: Part 3—Development of a New Heat Transfer Model Based on Flow Pattern," ASME J. Heat Transfer, **120**, pp. 156–165.

[5] Webb, R. L., and Gupte, N. S., 1992, "A Critical Review of Correlations for Convective Vaporization in Tubes and Tube Banks," Heat Transfer Eng., **13**, pp. 58–81.

[6] Steiner, D., and Taborek, J., 1992, "Flow Boiling Heat Transfer of Single Components in Vertical Tubes," Heat Transfer Eng., **13**, pp. 43–68.

[7] Chen, J. C., 1966, "A Correlation for Boiling Heat Transfer to Saturated Fluids in Convective Flow," Ind. Eng. Chem. Process Des. Dev., **5**(3), pp. 322–329.

[8] Kenning, D. B. R., and Cooper, M. G., 1989, "Saturated Flow Boiling of Water in Vertical Tubes," Int. J. Heat Mass Transf., **32**(3), pp. 445–458.

[9] Wadekar, V. V., 1990, "Flow Boiling—A Simple Correlation for Convective Heat Transfer Component," *Proceedings of Ninth International Heat Transfer Conference*, Jerusalem, Israel, **2**, pp. 87–91.

[10] Cooper, M. G. 1984, "Saturation Nucleate, Pool Boiling—A Simple Correlation," *International Chemical Engineering Symposium Series*, No. **86**, p. 785–792.

[11] Gorenflo, D., 1992, *VDI Warmeatlas*, (English ed.), Section Ha VDI Verlag, Düsseldorf.

Temperature Gradient in the Unfrozen Liquid Layer for Multiphase Energy Balance With Incoming Droplets

G. F. Naterer
Department of Mechanical and Industrial Engineering, University of Manitoba, 15 Gillson Street, Winnipeg, Manitoba, Canada, R3T 2N2

Phase change heat transfer with impinging supercooled droplets on an ice surface is examined. Partial solidification of incoming droplets leads to an unfrozen water layer above the ice. The significance of temperature variations within the water layer is considered. The multiphase energy balance is shown to approach the measured rate of ice growth when the surface heat input is lowered sufficiently. This asymptotic behavior is essential for establishing the proper role of heat conduction in the solid and liquid (unfrozen water) layers. Predicted results are successfully validated by comparisons with experimental data involving ice buildup on heated circular conductors.
[DOI: 10.1115/1.1532015]

Keywords: Droplet, Heat Transfer, Impingement, Multi-Phase

I Introduction

Heat transfer with impinging droplets on a solidified layer occurs in various technological applications [1,2], i.e., de-icing of power lines and aircraft surfaces, spray deposition in manufacturing processes and others. The phase change involves a nonlinear interfacial constraint at the solid/liquid interface [3]. The rate of growth of the solidified layer is affected by the surface heat input beneath the layer. For example, the proper amount of surface heating is required for effective thermal de-icing of overhead power transmission lines. In this example, *rime ice* (or dry ice) is collected when incoming supercooled droplets solidify immediately upon impact on the surface. An unfrozen water layer with surface runoff along the ice surface characterizes *glaze ice* (or wet ice) conditions. In this article, glaze ice with surface heating is examined, particularly the role of heat conduction in the unfrozen water layer.

During rime ice growth, the interfacial mass and energy balances are de-coupled, since all droplets solidify immediately upon impact on the surface (Naterer [4]). Nevertheless, their solutions must both independently yield the same (unique) ice growth rate. It has been shown that a mass balance alone (Goodwin's model; [5]) closely predicts the rate of ice growth over a wide range of conditions for unheated conductors (Lu, Popplewell et al. [6]), including glaze and rime ice. However, without an energy balance, it cannot be directly applied to other commonly encountered cases involving surface heating beneath the solidified layer [7].

It has been well documented that an energy balance is required in glaze ice conditions [8,9,10,11]. However, it is less understood how heat conduction occurs in the unfrozen water layer, particularly with surface heating beneath the solidified layer. Sufficiently meaningful measurements within the liquid layer are difficult to obtain, so it is often assumed that the film temperature is uniformly equal to the phase change temperature [12]. However, neglecting the spatial temperature gradient therein precludes the full role of heat conduction, thereby affecting the growth of the ice and water layers. In this article, heat conduction through the unfrozen water layer is considered. Its importance is demonstrated under asymptotic trends of ice growth with low surface heating.

Contributed by the Heat Transfer Division for publication in the JOURNAL OF HEAT TRANSFER. Manuscript received by the Heat Transfer Division February 4, 2002; revision received October 14, 2002. Associate Editor: J. N. Chung.

II Problem Formulation

The current problem involves three-phase conditions, i.e., multiphase flow with droplets and solid-liquid phase change [13]. Based on earlier studies (Messinger [8], Myers, Hammond [9]), the following terms contribute to the overall energy balance at the ice interface (see Fig. 1).

- $q_a = rhV^2/2c_p$; viscous heating (coefficients adopted as in Ref. [9])
- $q_{\text{conv}} = h_{aw}(T - T_a)$; convective heat loss (Nusselt correlation based on Ref. [14] for iced cables)
- $q_d = EVGc_w(T_w - T_a)$; cooling by incoming supercooled droplets
- $q_f = -k(\partial T/\partial y)$; rate of heat conduction through the ice (or water film)
- $q_k = (EVG)V^2/2$; kinetic energy of impinging droplets
- $q_l = \rho L(\partial B/\partial t)$; release of latent heat of fusion due to phase change

Individual variables are defined in the nomenclature and depicted in Fig. 1.

Initially, supercooled droplets arriving on the surface accumulate as dry (rime) ice, based on the following mass balance of incoming droplets (right side) and growing ice (left side),

$$\rho_i \frac{\partial B}{\partial t} = EVGN \tag{1}$$

The view factor (represented by $N = \int dx_p / \int dx$) is the projection of the curved surface in the direction of the droplet influx. The differential distances of dx_p and dx refer to the projected and actual distances along the curved surface, respectively. For example, the view factor is $N = 1/\pi$ for a circular conductor. Equation (1) can be solved directly, subject to an initial condition of $B = 0$ at $t = 0$, thereby yielding

$$B = \left(\frac{EVGN}{\rho_i} \right) t \tag{2}$$

This result represents a *dry growth limit* since it considers that all incoming droplets are solidified immediately upon impact on the surface, without any surface runoff. For circular conductors, this Goodwin's model [5] closely predicts both rime and glaze (wet) ice growth over a wide range of flow conditions involving unheated conductors [6]. Although it is based on a mass balance, the corresponding de-coupled energy balance must approach this same limit when the surface heating approaches zero (i.e., unheated conductor).

When sufficient energy is imparted into the ice surface (including the release of latent heat from the solidified droplets) to sustain an unfrozen water layer on the ice surface, then transition to glaze ice is encountered. Performing an energy balance across the unfrozen water layer and the ice yields

$$q_w + \rho_i L \frac{\partial B}{\partial t} + \frac{rhV^2}{2c_a} + \frac{1}{2} EV^3 G = h(T_w|_{y=B+b} - T_a) + EVGc_w(T_w - T_a) \tag{3}$$

where the specified wall heat flux is designated by q_w. The left side of Eq. (3) gives the energy inflows, such as the wall heat input and the release of latent heat of solidified droplets, whereas the right side gives the heat outflows. The third term represents viscous dissipation of kinetic energy of air (carrier phase) due to the boundary layer above the ice and liquid layers. It refers to the continuous phase, whereas the fourth term involves the discrete droplets. The fourth term refers to the kinetic energy of impinging

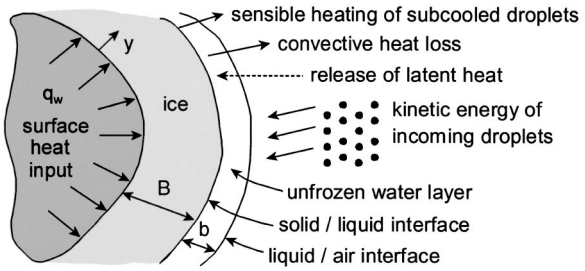

Fig. 1 Schematic of surface film and solidified layer with incoming droplets

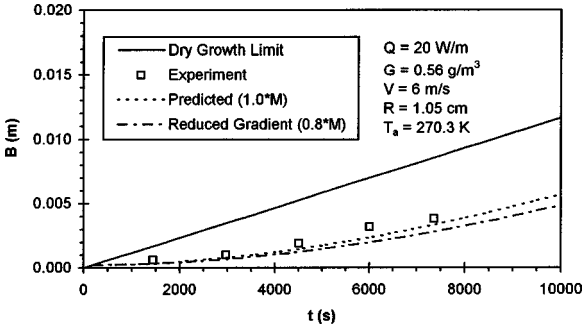

Fig. 2 Predicted and measured ice thickness

droplets (dispersed phase), which is transformed into internal energy as it impacts on the water/ice surface. This frictional dissipation occurs when the droplets deform under impact with friction in the water layer and along the ice/water interface.

The temperature gradient (denoted by M) in the unfrozen water can be determined by solving the following heat conduction equation in the water layer,

$$\frac{\partial^2 T_w}{\partial y^2}=0 \tag{4}$$

subject to $T(B)=T_f$ (phase change temperature) and an energy balance at the liquid/air interface ($y=B+b$), involving the heat flows outlined earlier. Solving Eq. (4) and differentiating the result to find the temperature gradient,

$$M=\frac{\partial T_w}{\partial y}=-\frac{C_2-C_1(T_f-T_a)}{1+C_1 b} \tag{5}$$

Substituting the water temperature into Eq. (3) and rearranging, it can be shown that

$$\frac{\partial B}{\partial t}=-\frac{q_w}{\rho_i L}-\frac{C_1 C_2 b}{1+C_1 b}+C_3-C_2 \tag{6}$$

where

$$C_1=\frac{h+EVGc_w}{k_w};\quad C_2=\frac{rhV^2}{2c_a\rho_i L}-\frac{k_w c_1(T_f-T_a)}{\rho_i T};$$

$$C_3=-\frac{EV^3G}{2\rho_i L} \tag{7}$$

Thus, the ice growth initially follows Eq. (1) during rime ice growth, and then Eq. (6) after the transition to glaze (wet) ice.

In Eq. (6), the thickness of the unfrozen water layer, $b(t)$, is required. A mass balance at $y=B$ (ice/water interface) requires that

$$\rho_i\frac{dB}{dt}+\rho_w\frac{db}{dt}=EVGN \tag{8}$$

where $B=B_w$ at $t=t_w$ at the onset of the glaze ice. The specific values of B_w of t_w can be determined in the following manner: (i) set $b\to 0$ in Eq. (6), (ii) equate this result with Eq. (1) since both results must match each other at the transition point, and (iii) solve the resulting values of ice thickness (B_w) and time (t_w). Then, solving Eq. (8),

$$b=\left(\frac{EVGN}{\rho_w}\right)t-\left(\frac{\rho_i}{\rho_w}\right)B+\frac{\rho_i}{\rho_w}B_w-\frac{EVGN}{\rho_w}t_w \tag{9}$$

In this article, the nonlinear, first-order ordinary differential equations in Eqs. (6) and (8) are solved numerically to yield solutions for $B(t)$ and $b(t)$ simultaneously. In the previous analysis, the droplet and air temperatures are assumed to be equal prior to droplet impact on the surface. Also, the temperature profile in the unfrozen water layer has been assumed to be predominantly linear in view of the sufficiently large time scale of ice growth (i.e., larger than the time taken for heat to be fully conducted through the layer). For a cylindrical layer, the temperature profile may be considered to be logarithmic, rather than linear. However, the effects of surface curvature are considered to be negligible for a thin water layer (see Appendix 1).

III Experimental Validation

The numerical predictions were validated through comparisons with experimental data [6,15]. This experimental data involved freezing rain experiments, whereby droplets were sprayed through air at sub-zero temperatures onto a heated circular conductor. A range of rime and glaze ice conditions was encountered. The experimental setup consisted of spray nozzles for spraying of droplets, fan, plenum and flow straighteners (downstream of the fan) and other instrumentation for flow measurements (described fully in Refs. [6], [15]). The mean diameter of droplets was about 1 [mm], which closely represents freezing rain and icing of overhead power transmission lines. Aircraft icing typically involves impinging droplets with 1–2 orders of magnitude smaller sizes.

A resistive type heater was used in the inner core of the circular conductor to simulate power line de-icing through Joule heating (internal electrical heat generation). During the experiments, the ice thickness, air temperature, air velocity, precipitation rate and heat input to the conductor were measured. Experimental uncertainties, such as the measurement of the precipitation rate (or liquid water content), led to an estimated accuracy of ± 10 percent in regards to the measured ice thickness. This thickness was reported in terms of an equivalent ice thickness, namely the uniformly radial ice thickness having the same equivalent ice mass as the actual observed ice accretion.

IV Results and Discussion

Predictions are compared with measurements of ice buildup on a circular conductor under the following conditions: $Q=20$ [W/m] (heat input per unit length of cable), $G=0.00056$ [kg/m^3], $T_a=270.3$ [K], $V=6$ [m/s], and $R=1.05$ [cm]. In Fig. 2, the dry growth limit is shown for reference purposes. Also, favorable comparisons between predicted and measured ice thickness can be observed. When the full temperature gradient ($1.0*M$) is included in the thermal analysis, better agreement is achieved than predictions utilizing a reduced temperature gradient ($0.8*M$).

The purpose of the comparison in Fig. 2 is to better understand the relative importance of heat conduction in the unfrozen water layer. A decreasing fraction of M represents a portion of heat conduction neglected through the unfrozen water layer. The temperature gradient (M) in this layer depends on the ice interface temperature (T_f), water layer thickness (b) and temperature at the water/air interface ($y=B+b$). There exists a lack of detailed experimental data and well understood modelling of the latter two variables. Errors in specifying or calculating those quantities di-

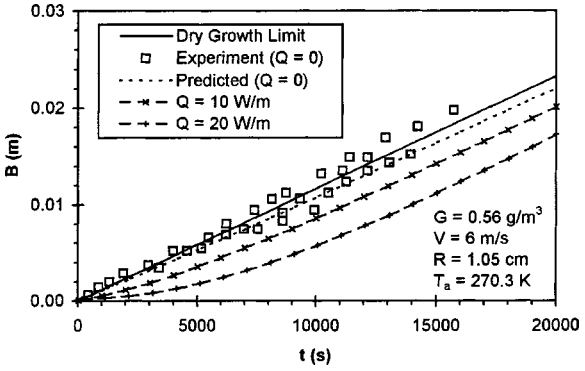

Fig. 3 Ice thickness for heated and unheated surfaces

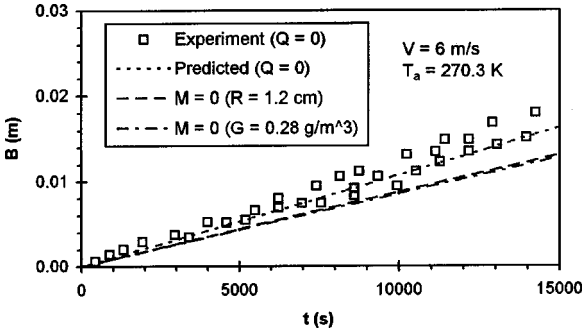

Fig. 4 Effects of temperature gradient on solidified layer growth

rectly affect the temperature gradient and heat conduction in the unfrozen layer. Thus, Fig. 2 shows how variations of the temperature gradient, possibly due to errors in the aforementioned variables, affect the predicted ice growth. The results show that a 20 percent variation of M can have an adverse impact on the predicted ice growth.

This temperature gradient affects the energy balance in Eq. (3) through the resulting temperature at the liquid/air interface. The value of $T_w|_{y=B+b}$ arises in the convective heat exchange and it is determined from the extent of heat conduction through the water layer in Eq. (4). The temperature difference between $T_w|_{y=B+b}$ and T_f (at the solid/liquid interface) is reduced when the temperature gradient in the unfrozen water layer decreases. Also, the current study includes surface heat input, which reduces the difference between T_f and $T_w|_{y=0}$ (at the conductor/ice interface). With this reduced heat conduction in the ice, the relative significance of heat conduction in the glaze film at the solid/liquid interface is likely higher than cases without surface heating.

During rime ice growth, the latent heat released by incoming droplets is insufficient to raise the ice temperature enough to sustain an unfrozen water layer on the ice surface. It is anticipated that the ice growth closely follows the dry growth curve during this period. Shortly after $t=0$ in Fig. 2, the predicted ice growth (dashed line) departs from linear growth over time (dry ice; solid line) to slower non-linear transient growth (glaze ice) due to surface runback of unfrozen water. This time of transition to glaze ice is represented by the intersection between the dashed line (glaze ice) and the solid line (rime ice) in Fig. 2 (at about $t=180$ [s]).

Higher surface heating rates reduce the rate of ice buildup in Fig. 3 (as expected). A gradual change in profile curvature occurs between early stages and late stages of glaze ice accumulation. The slope of each curve increases gradually over time in Fig. 3 until it reaches a nearly constant value (approximately equal to the dry growth slope). It appears that beyond a certain stage of time, an insulating effect of ice renders the ice growth rate (slope of curve) nearly independent of Q.

The predictive model should approach the proper asymptotic limit for low surface heating, particularly $Q\rightarrow 0$ (unheated cylinder). In Fig. 3, it can be observed that this trend is properly captured over a range of measured data for an unheated cylinder. As expected, the ice growth increases when the surface heating rate is lowered. The experimental data in Fig. 3 represents ice growth on unheated conductors over a range of conditions, i.e., $-25°\text{C} < T_a < -1°\text{C}$ (ambient air temperature), $0<V<10$ [m/s] (wind speed), $0.8<d<1.4$ [mm] (droplet diameter) and $0.65<R<2.2$ [cm] (cable radius). More than one data point may be shown at nearly the same time due to this range of conditions. The measured data points lie within a close proximity of Goodwin's model (dry growth limit [6]; solid line). The predictive model should approach this same range of measured data (enclosing the dry growth limit) when the surface heating rate approaches zero.

In Fig. 4, the measured ice growth on unheated conductors was compared to predictions with and without ($M=0$) assumed temperature gradients in the unfrozen water layer. The measured data represents the asymptotic limit required when the surface heating diminishes to zero. Using the current model with its predicted temperature gradient in the glaze film, close agreement is achieved between the measured and predicted results. However, under a range of conditions involving different cable sizes (R) and liquid water contents (G), the analysis tends to under-predict the underlying trend of ice growth when an isothermal film ($M=0$) is adopted. It appears that heat conduction through the unfrozen water layer contributes sufficiently to the energy balance at the solid/liquid interface to alter the rate of ice growth.

Other sensitivity studies have been performed to examine the effects of ambient air temperature and surface heating rates for combined rime and glaze ice growth. These studies indicated that the rate of ice growth increases when the ambient air temperature is lowered (as expected). Also, sensitivity studies involving thermophysical property variations were performed. For example, over the range of temperatures between $-1°\text{C}$ and $-25°\text{C}$, the maximum change of ice density with temperature is about 0.5 percent. When this density is lowered from 917 kg/m^3 at 0°C to 922 kg/m^3 at $-25°\text{C}$ (about 0.5% change), the change of predicted ice growth is less than about 0.7 percent. In the predicted results of Fig. 2, the temperature range is less than 25°C, so the error due to the constant density assumption becomes less than about ± 0.1 percent. These values represent small uncertainties, as compared with other types of larger uncertainties (such as convection coefficient uncertainties [13]).

V Conclusions

The significance of temperature variations within the unfrozen water layer is investigated in regards to ice accretion on a curved, heated conductor. A well established asymptotic limit has been reached in the energy balance for glaze ice growth. The magnitude of surface heating (Q) is varied over a range of conditions, particularly down to the limiting case of an unheated conductor ($Q\rightarrow 0$). In this limit, the predicted results stay within the range of experimental data encompassing Goodwin's model. It is shown that heat conduction in the unfrozen water layer contributes to this proper asymptotic behavior when approaching low surface heating.

Acknowledgments

The assistance, insight and/or support provided by Dr. N. Popplewell, Mr. M. Lu (University of Manitoba), Mr. G. Venn and Dr. G. Richardson (GKN Westland Helicopters Ltd), Mr. J. Chan (Manitoba Hydro), and Dr. T. Myers (Cranfield University), are appreciated. Also, financial support from the Natural Sciences and Engineering Research Council of Canada is gratefully acknowledged.

Nomenclature

b = unfrozen water thickness
B = ice thickness
c_a,
c_w = specific heats
E = collection efficiency ($E=1$)
G = liquid water content
h = convection coefficient
k = thermal conductivity
L = latent heat of fusion
r = local recovery factor
R = cable radius
t = time
V = air velocity (magnitude)

Greek

ρ = density

Subscripts

a = ambient (air)
f = freezing point
i = ice
s = surface
w = water, transition to glaze ice

Appendix 1

Reduced Form of Heat Equation in the Unfrozen Water Layer. The general form of Eq. (4), including transient, convective and conduction terms, is [13]

$$\rho_w c_w \frac{DT}{Dt} = k_w \left(\frac{\partial^2 T}{\partial y^2} + \frac{\partial^2 T}{\partial y^2} \right) + \mu_w \Phi \tag{10}$$

where DT/Dt and Φ refer to the total (substantial) derivative of temperature, and the viscous dissipation function, respectively. The total derivative includes transient and convective terms. By scaling and non-dimensionalizing Eq. (10), it can be shown that the transient term becomes negligible. From results in Fig. 2, a typical length scale (about 1 [mm] of ice) and time scale (buildup over about 3600 [s]) are predicted and measured. These scaling parameters lead to a much smaller temporal derivative, as compared with the y-derivative for conduction in Eq. (10). It can be shown that the entire nondimensionalized transient term becomes negligible (compared with y-conduction) when $b \ll 0.15$ [m]. This result is obtained when the leading nondimensional coefficient of the transient term is much less than unity, which is realized under conditions studied in this article.

For scaling of the convective terms, a representative thickness of the unfrozen layer is on order of 1 [mm]. A characteristic length scale is the half-circumference of the 1.05 [cm] radius cable of Fig. 2. In Fig. 2, a representative temperature difference is $T_f - T_a \approx 3°C$. Also, from the mass balance in Eq. (8), the second term on the right side represents the mass flow rate of unfrozen water (per unit area of cable surface). The characteristic scale of ice growth rate in the first term of Eq. (8) can be estimated based on the predicted slope shown in Fig. 2.

When these values and other parameters of Fig. 2 are substituted into Eq. (8), a typical mass flow rate of 0.036 [g/ms] (per unit width of cable) is obtained. Using these and their resulting velocity and time scales, the approximate order of terms in Eq. (10) becomes

$$1.38\times10^{4} \leftrightarrow 1.57\times10^{3} + 1.71\times10^{6} + 6.3\times10^{-2} \tag{11}$$

This result shows that the heat conduction across the film layer is much larger (at least two orders of magnitude) than the other terms. This means that heat conduction in the y-direction is much larger than transient, convective and dissipative terms of the energy equation. Thus, Eq. (4) and its resulting linear temperature profile are considered to be representative of heat transfer within the unfrozen water layer. The profile includes a time dependence through the variation of b with time in Eq. (5) and the effects from both ice/water and water/air interfaces.

Surface curvature can affect the ice growth since a varying area is available to heat transfer in the direction of the heat flow. In Eq. (3), the individual terms represent energy fluxes (per unit area). When applied to curved surfaces, these fluxes are multiplied by appropriate surface areas to yield the total energy flows at the inflow and outflow boundaries of the selected control volume. For example, in the case of the iced circular conductor, the wall heat flux in Eq. (3) is multiplied by the ratio of the inner to outer areas of the annular region comprising the ice layer. Also, when different boundary conditions are applied (i.e., specified temperature [9]), a thick layer (ice) curvature correction is included in the model. In that case, an explicit expression for the ice temperature profile is determined based on corrections of the thermal resistance for curved layers. This correction involves thermal resistances constructed for general curvilinear coordinates (i.e. linear or cylindrical) and assembled together by integrating across the layer. Unlike the ice layer, a thin layer assumption is adopted for the unfrozen water layer, thereby leading to the planar form of Eq. (4).

Appendix 2

Thermophysical Properties. For ice, $\rho_i = 917$ [kg/m^3], $c_i = 2{,}030$ [J/kgK], and $k_i = 1.8$ [W/mK]. For water, $\rho_w = 1{,}000$ [kg/m^3], $c_w = 4{,}220$ [J/kgK], $k_w = 0.57$ [W/mK], and $L = 3.3\times10^5$ [J/kg]. For air, $c_a = 1{,}014$ [J/kgK], $k_a = 0.024$ [W/mK], and $v_a = 1.3\times10^{-5}$ [m^2/s]. Other parameters and coefficients have been adopted from Refs. [9] and [14].

References

[1] Al-Khalil, K. M., Keith, Jr., T. G., and De Witt, K. J., 1994, "Development of an Improved Model for Runback Water on Aircraft Surfaces," AIAA Journal of Aircraft, **31**, pp. 271–278.
[2] Aziz, S. D., and Chandra, S., 2000, "Impact, Recoil and Splashing of Molten Metal Droplets," Int. J. Heat Mass Transf., **43**, pp. 2841–2857.
[3] Naterer, G. F., 2001, "Establishing Heat—Entropy Analogies for Interface Tracking in Phase Change Heat Transfer with Fluid Flow," Int. J. Heat Mass Transf., **44**(15), pp. 2903–2916.
[4] Naterer, G. F., 2002, "Multiphase Flow with Impinging Droplets and Airstream Interaction at a Moving Gas/Solid Interface," Int. J. Multiphase Flow, **28**(3), pp. 451–477.
[5] Goodwin, E. J., Mozer, J. D., Di Gioia, A. M., and Power, B. A., 1982, "Predicting Ice and Snow Loads for Transmission Lines," Proceedings, 1st IWAIS, pp. 267–273.
[6] Lu, M. L., Popplewell, N., Shah, A., Barrett, W., and Au, A., 1998, "Mass of Ice Accretion from Freezing Rain Simulations," Proceedings, 8th IWAIS, Reykjavik, Iceland.
[7] Naterer, G. F., Deng, H., and Popplewell, N., 1999, "Predicting and Reducing Glaze Ice Accretion on Electric Power Lines with Joule Heating: Theory and Experiments," CSME Transactions, **23**(1A), pp. 51–70.
[8] Messinger, B. L., 1953, "Equilibrium Temperature of an Unheated Icing Surface as a Function of Air Speed," J. Aeronautical Sciences, **20**, pp. 29–42.
[9] Myers, T. G., and Hammond, D. W., 1999, "Ice and Water Film Growth from Incoming Supercooled Droplets," Int. J. Heat Mass Transf., **42**, pp. 2233–2242.
[10] Al-Khalil, K. M., Keith, T. G., and De Witt, K. J., 1993, "New Concept in Runback Water Modeling for Anti-Iced Aircraft Surfaces," AIAA Journal of Aircraft, **30**(1), pp. 41–49.
[11] Hansman, R. J., and Turncock, S. R., 1989, "Investigation of Surface Water Behaviour During Glaze Ice Accretion," AIAA Journal of Aircraft, **26**(2), pp. 140–147.
[12] Poots, G., 1996, *Ice and Snow Accretion on Structures*, John Wiley and Sons Inc., New York.
[13] Naterer, G. F., 2002, *Heat Transfer in Single and Multiphase Systems*, CRC Press, Boca Raton, FL.
[14] Makkonen, L., 1984, "Modeling of Ice Accretion on Wires," J. Clim. Appl. Meteorol., **23**, pp. 929–939.
[15] Lu, M., Popplewell, N., Shah, A. H., Deng, H., and Naterer, G. F., 1999, "A Semi-Empirical Icing Model for an Energized Power Line," internal report, Department of Mechanical and Industrial Engineering, University of Manitoba, Winnipeg, Canada.

Influence of Heat Transfer at the Interface on the Thermocapillary Convection in the Adjacent Phase

Y. Jiang and J. M. Floryan
Department of Mechanical and Materials Engineering,
The University of Western Ontario, London,
Ontario, N5A 5B9, Canada

Thermocapillary convection in a cavity is considered. It is shown that when the cavity is heated through its sides, reduction of heat transfer across the interface leads to an increase of the interface deformation. When the same cavity is heated through the interface, similar reduction of heat transfer across the interface results in diminished convection and reduced interface deformation.
[DOI: 10.1115/1.1535448]

Keywords: Heat Transfer, Microgravity, Natural Convection, Surface Tension, Thermocapillary

Introduction

Thermocapillary flows are driven by the imbalance of tangential stress on the interface caused by temperature dependence of surface tension [1]. These flows are important in many technical processes involving non-isothermal fluid interfaces. Their effects could be dominant (e.g., zero-gravity containerless materials processing, thermal management of spacecrafts) or could represent a contributing factor (e.g., conventional crystal growth or welding). Control and optimization of these processes critically depend on the complete understanding of system dynamics driven by surface forces arising at non-isothermal interfaces. The focus of the present work is on studying thermocapillary flows in the absence of any body forces, and especially in the absence of gravity.

The character of the response of liquid exposed to thermocapillary effect depends on the type of heating. In the geometrically simplest case of liquid contained in a rectangular cavity open from above, the heating can be applied either through the bottom, or through the sidewalls, or from above. The dynamics of the system is remarkable different in each of these cases.

The simplest case of heating through the bottom involves liquid with initially flat interface resting on an isothermal, flat, solid plate. The resulting temperature field gives rise to the temperature gradient vector that is normal to the interface at the interface. The motion of the liquid is driven by the Marangoni instability, first studied by Pearson [2]. There are two mechanisms possible. The first one relies on convective effects and the second one relies of the interface deformation. Pearson [2] determined the relevant critical conditions for the former one while Czechowski and Floryan [3] for the latter. When the cavity is sufficiently long, the second mechanism dominates resulting in an unconditional instability that initiates process leading to rupture of the interface [3].

When the liquid is heated through the sidewalls, the resulting temperature gradient has a component in the direction parallel to the interface. Floryan and Chen [4] showed that a long continuous liquid layer exposed to such heating may exist only when the temperature field satisfies restrictive existence conditions. The simplest form of the heating corresponds to the conduction-dominated heat transfer in the gas phase resulting in the linear temperature distribution along the interface [5]. Hamed and Floryan [6] showed that large interfacial deformations may occur, leading to rupture of the interface through formation of dry spots at the sidewalls. They determined location of the limit points in the parameter space beyond which a steady, continuous interface cannot exist. Jiang et al. [7] showed that the range of parameters guaranteeing existence of steady interface is significantly reduced when the interface is allowed to slide along the side walls and, at the same time, the magnitude of the deformation is significantly increased.

Direct heating of the interface from above attracted less attention. The interface will undergo large deformation unless the temperature field satisfies restrictive existence conditions, as shown by Floryan and Chen [4]. An infinite interface subject to periodic heating may rupture, as shown by Tan et al. [8]. Higuera [9] considered concentrated heat flux applied to the interface but neglected effects of interface deformation. Hamed and Floryan [10] analyzed simulated point heating and demonstrated existence of large deformations and possible rupture of the interface. The interface rupture may occur through formation of dry spots at the cavity bottom. Jiang et al. [7] showed a significant increase of the interface deformation when the interface is allowed to slide along the sidewalls.

The present study is focused on the analysis of dynamics of liquid bounded by an interface characterized by various levels of heat transfer efficiency. The heat transfer is modelled using Newton's Law of Cooling and the efficiency of this process is expressed using Biot number Bi. This model represents an idealization [11], which is sufficient for the purposes of the intended analysis nevertheless. Since the strength of the thermocapillary effect depends on the effective temperature of the interface, variations of heat transfer efficiency may potentially have a dominant effect on the overall system response. We shall study this response for two types of heating. The first type involves cavity heated through the sidewalls where the heat transfer at the interface is expected to play a secondary role. The second one involves cavity heated from above using a point heating that mimics laser heating. The heat transfer at the interface is expected to play a significant role in this case.

The flow response to both types of heating is sought with the interface subject either to the fixed contact points constraint or to the fixed contact angles constraint. Determination of the pattern of interface deformation and the associated convection under conditions leading to large interfacial deformations is of particular interest. This includes search for the limit points that guarantee the existence of a single, continuous interface as well as determination of changes in the location of the limit points in the parameter space as a function of Biot number.

Problem Formulation

Consider liquid in a cavity of length L and height H, as shown in Fig. 1. The cavity, which is open from above, is formed by isothermal solid walls on the left and right sides, and by an insulated solid plate on the bottom. The liquid is incompressible, Newtonian, has density ρ, thermal conductivity k, specific heat per unit mass c, thermal diffusivity $\kappa = k/\rho c$, kinematic viscosity ν and dynamic viscosity μ. The free surface, described by $y = h(x)$, is bounded by a passive gas of negligible density and viscosity. This free surface is associated with surface tension σ, which is a function of the local temperature. A linear equation of state for surface tension is assumed, i.e., $\sigma(T) = \sigma^* - \gamma(T - T^*)$, where σ^* is the surface tension of the liquid at the reference temperature T^* and the constant γ is the negative of the derivative of the surface tension with respect to temperature. It is assumed, without loss of generality, that the pressure in the gas phase is negligible.

The problem is scaled using H as the length scale, u^* as the velocity scale, $\mu u^*/H$ as the pressure scale and σ^* as the surface tension scale. The dimensionless temperature T is defined as $T - T^* = (T_{max} - T_{min})T$, $T_g - T^* = (T_{max} - T_{min})T_g$. Here T_{max} and T_{min} denote a measure of the maximum and the minimum of the

Contributed by the Heat Transfer Division for publication in the JOURNAL OF HEAT TRANSFER. Manuscript received by the Heat Transfer Division December 10, 2001; revision received September 20, 2002. Associate Editor: G. P. Peterson.

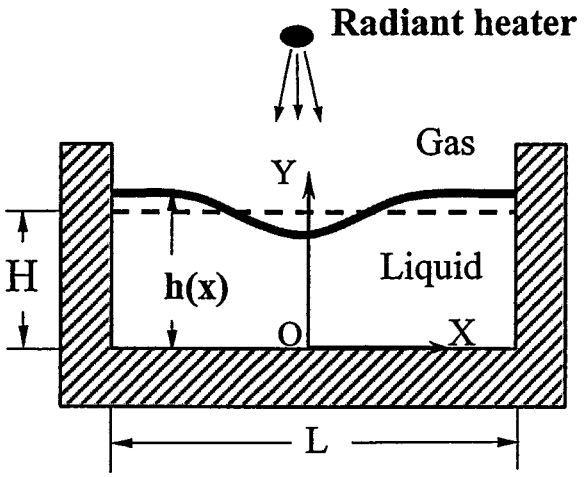

Fig. 1 Sketch of the model problem

interface temperature, respectively. The characteristic velocity u^* is derived from the so-called Marangoni effect, i.e., the jump in the shear along the interface balances the surface tension gradient. This leads to $u^*=\gamma(T_{\max}-T_{\min})/\mu$. In the absence of gravity, the steady two-dimensional motion of the liquid is governed by the continuity, Navier-Stokes and energy equations in the form

$$u_x+v_y=0, \tag{1a}$$

$$\mathrm{Re}(uu_x+vu_y)=-p_x+u_{xx}+u_{yy}, \tag{1b}$$

$$\mathrm{Re}(uv_x+vv_y)=-p_y+v_{xx}+v_{yy}, \tag{1c}$$

$$\mathrm{Ma}\ (uT_x+vT_y)=T_{xx}+T_{yy}. \tag{1d}$$

where p denotes pressure, (u,v) denotes velocity vector and all quantities are dimensionless. Reynolds number Re and Marangoni number Ma have the standard definitions, i.e., $\mathrm{Re}=u^*H/\nu$, $\mathrm{Ma}=u^*H/\kappa$. The boundary conditions have the form

$$x=-1/2L:\ u=v=0,\quad T=T_L;\quad x=+1/2L:\ u=v=0, \tag{2a}$$

$$T=T_R;\quad y=0:\quad u=v=T_y=0, \tag{2b}$$

$$y=h(x):\ uh_x-v=0, \tag{2c}$$

$$-p+\frac{2[v_y-h_xu_y+h_x(-v_x+h_xu_x)]}{(1+h_x^2)} \tag{2d}$$

$$=\frac{\mathrm{Ca}^{-1}(1-\mathrm{Ca}T)h_{xx}}{(1+h_x^2)^{3/2}}, \tag{2e}$$

$$2h_x(-u_x+v_y)+(1-h_x^2)(v_x+u_y)$$

$$=-(T_x+h_xT_y)(1+h_x^2)^{1/2}, \tag{2f}$$

$$(-h_xT_x+T_y)(1+h_x^2)^{-1/2}+\mathrm{Bi}[T-T_g(x)]=0 \tag{2g}$$

where $(2d)$ is the kinematic condition, $(2e)$ and $(2f)$ are the stress balances in the normal and tangential directions, respectively, and $(2g)$ describes a general heat transfer condition at the interface. In $(2e)$ Ca is the capillary number, given by $\mathrm{Ca}=\mu u^*/\sigma^*$. Equation $(2g)$ assumes that the Newton's Law of Cooling is valid. The Biot number Bi is defined as $\mathrm{Bi}=h_gH/k$ and measures the heat transport between the gas and the liquid phases. Here h_g is the dimensional heat transfer coefficient in the gas phase. The thermal boundary condition presumes that the temperature $T_g(x)$ in the gas phase is known and that the heat transport at the liquid-gas interface can be described by using coefficient h_g. The cavity sidewalls are assumed to be isothermal and the bottom is assumed to be insulated. Heating of the cavity through the sidewalls can be simulated through appropriate specification of the walls' temperature, and from above through specification of the gas temperature $T_g(x)$.

Two types of contact made by the interface at the sidewalls are considered, i.e., (i) the case of an interface with fixed contact points and (ii) the case of an interface sliding along the sidewalls with the a constant contact angle. Specifying mass conservation constraint closes the problem. These additional conditions have the form

$$x=\pm L/2:\ (i)\ \ h=1\ \ \text{or}\ \ (ii)\ \ h_x=0; \tag{3a}$$

$$\int_{-L/2}^{L/2}h(x)dx=V. \tag{3b}$$

Flow problem (1)–(3) has to be solved on an irregular solution domain whose shape is determined by the unknown location of the free surface $h(x)$. The relevant algorithm is described in [12] and is based on the second-order, finite-difference discretization. The maximum acceptable grid size has been determined using grid convergence studies discussed in [13]. Most of computations have been carried out with approximately 30 grid points per unit length in the x direction, and 61 and 121 grid points in the vertical η-direction for the cavity heated through the sidewalls and from above, respectively. Such grids guarantee accuracy no worse than 1 percent for the location of the interface.

Discussion of Results

The interface is assumed to be flat before application of any heating. The initial contact conditions between the interface and the sidewalls are preserved during the heating. The main objective of our work is the determination of the form of the interface deformation and the limits of existence of a continuous interface as a function of Biot number for different types of heating. In order to simplify discussion, we shall only consider conduction limit $\mathrm{Ma}\to 0$.

Cavity Heated Through the Sidewalls. The liquid is subject to a heating through the cavity sidewalls which are maintained at a constant temperature, i.e., $T_L=1/2L$ and $T_R=-1/2L$. Temperature distribution in the gas phase along the interface has a linear form, i.e., $T_g(x)=-x$. Analysis of Hamed and Floryan [6] for the case of fixed contact points and $\mathrm{Bi}\to\infty$ forms a good reference

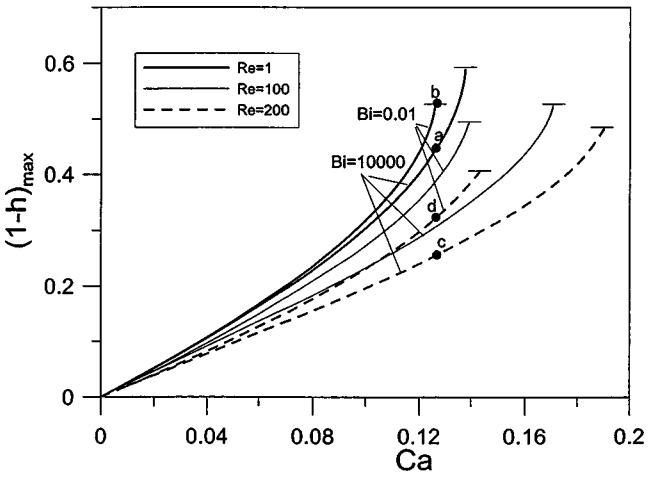

Fig. 2 The maximum interface deformation on the left side of a cavity subject to heating through the sidewalls as a function of the capillary number Ca for different values of the Biot number Bi and for Re=1,100,200. The flow and deformation patterns corresponding to points (*a–d*) are shown in Fig. 3. The cavity has length *L*=6 and the interface is subject to the fixed contact points constraint.

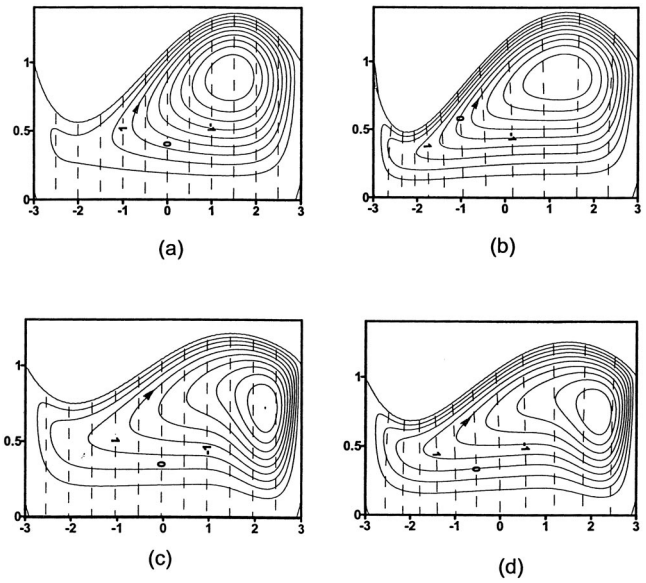

Fig. 3 The evolution of the flow, temperature and deformation patterns in a cavity subject to heating through the sidewalls as a function of the Biot number Bi for Re=1 and 200, $L=6$, and Ca=0.126. Figures (*a,b*)—Re=1, Bi=10^4, and Bi=10^{-2}, (*c,d*)—Re=200, Bi=10^4 and Bi=10^{-2}. (*a–d*) correspond to points (*a–d*) in Fig. 2. Contour lines of the stream function and temperature are shown every 10 percent of ψ_{max} and with $\Delta T=0.5$, respectively. In (*a–d*) $|\psi_{max}|$=0.07765, 0.04749, 0.05599, 0.04875, respectively. The interface is subject to the fixed contact points constraint.

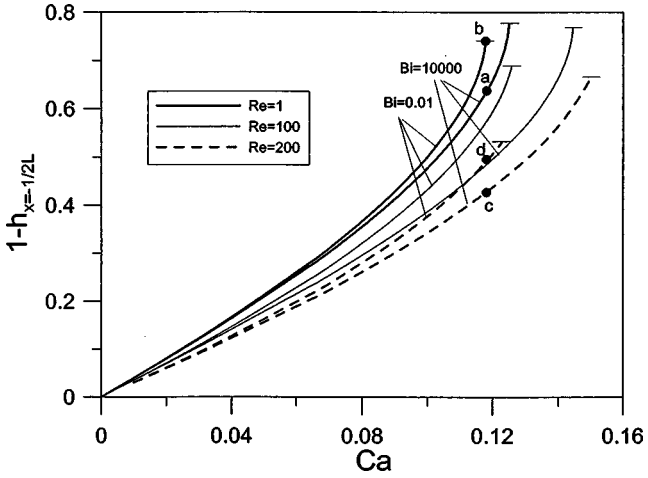

Fig. 4 The maximum interface deformation on the left side of a cavity subject to heating through the sidewalls as a function of the capillary number Ca for different values of the Biot number Bi and for Re=1,100,200. The flow and deformation patterns corresponding to points (*a–d*) are shown in Fig. 5. The cavity has length $L=4$ and the interface is subject to the fixed contact angles constraint.

point. Cavity of length $L=6$ is selected for the present discussion. Figure 2 illustrates evolution of the interface deformation as a function of Ca for two extreme values of the Biot number, i.e., Bi=10^4 and Bi=10^{-2}, and for three illustrative values of the Reynolds number, Re=1,100,200. The deformation curves were obtained by repeating calculations with Ca increasing in steps as small as ΔCa=0.0001 until a critical value Ca_{cr} was identified above which no steady solutions were found. It is clear that when Ca reaches a certain critical value Ca_{cr} a continuous, steady interface connecting contact points cannot exist. This value of $Ca=Ca_{cr}$ defines a limit point for the system. It was shown by Hamed and Floryan [6] that deformation increases continuously in time for $Ca>Ca_{cr}$ without reaching a saturation state. Results shown in Fig. 2 demonstrate that reduction of Bi increases the magnitude of the deformation and reduces Ca_{cr}. An increase of the Re from Re=1 to Re=200 makes this effect much more pronounced. The reasons for the increase of the deformation can be explained using flow and temperature fields displayed in Fig. 3. The heat flows from the left wall to the right wall. When the interface is flat, there is not heat transfer across the interface regardless of the value of Bi. When the interface deforms and Bi $\rightarrow\infty$, there is some heat transfer across the interface (see Figs. 3*a*,*c*) and its magnitude is a function of the interface deformation. The temperature gradient along the interface is not affected by the deformation as it is dictated by the assumed distribution of $T_g(x)$. When Bi decreases, the interface becomes progressively more insulated, the heat loss across the interface is reduced and, in the limit of Bi$\rightarrow$0, the complete heat flux that leaves the left wall must reach the right wall. Since the heat transport is due to conduction only, the thermal resistance is determined by the cross sectional area available for conduction. The bulging in of the interface on the left side of the cavity increases thermal resistance there and thus temperature gradient must increase in order to maintain the same heat flux (see Figs. 3*b*,*d*). The resulting increase of the temperature gradient along the interface at this location increases the strength of the thermocapillary effect and this, in turn, leads to a more vigorous pulling of the liquid towards the right side of the cavity (compare Figs. 3*a* and 3*b*, 3*c* and 3*d*). As a result, the interface on the cavity left side moves down even further. One should also note a reduction of the velocity of convection associated with the reduction of Bi, as illustrated by the reduced value of the maximum of stream function ψ_{max} (see Fig. 3). This is due to the fact that part of the available "thermocapil-

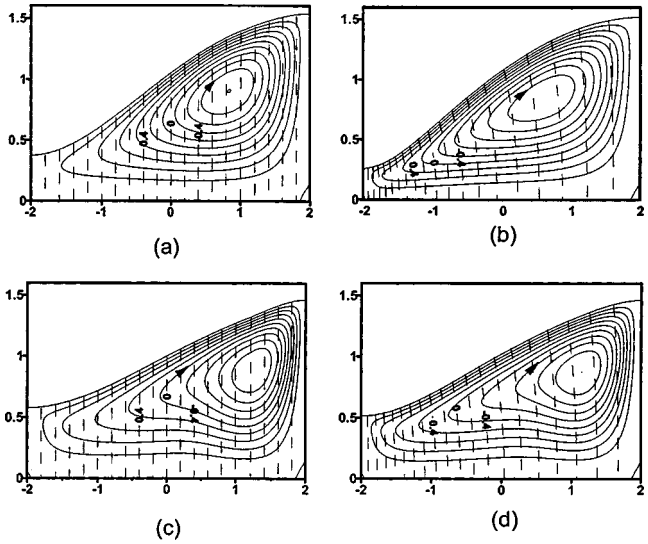

Fig. 5 The evolution of the flow, temperature and deformation patterns in a cavity subject to heating through the side walls as a function of the Biot number Bi for Re=1 and 200, $L=4$ and Ca=0.1178. Figures (*a,b*)—Re=1, Bi=10^4 and Bi=10^{-2}, (*c,d*)—Re=200, Bi=10^4 and Bi=10^{-2}. (*a–d*) correspond to points (*a–d*) in Fig. 4. Contour lines of the stream function and temperature are shown every 10 percent of ψ_{max} and with $\Delta T=0.2$, respectively. In (*a–d*) $|\psi_{max}|$=0.05775, 0.03375, 0.04540, 0.04061, respectively. The interface is subject to the fixed contact angles constraint.

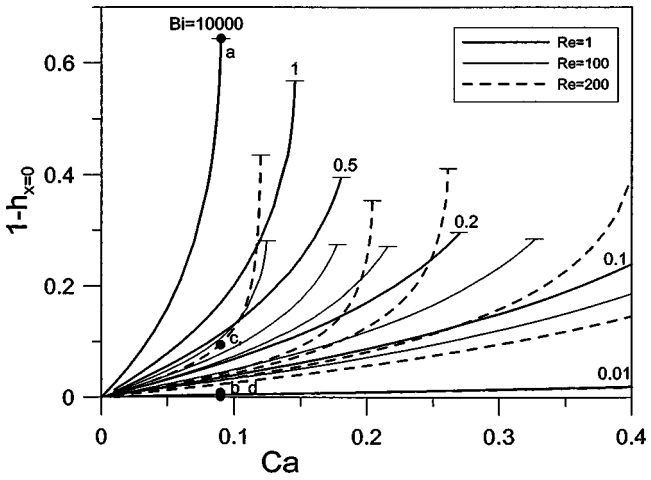

Fig. 6 The interface deformation in the middle of a cavity subject to point heating from above as a function of the capillary number Ca for different values of the Biot number Bi and for Re=1,100,200. The flow and deformation patterns corresponding to points (*a–d*) are shown in Fig. 7. The cavity has length *L*=6 and the interface is subject to the fixed contact points constraint.

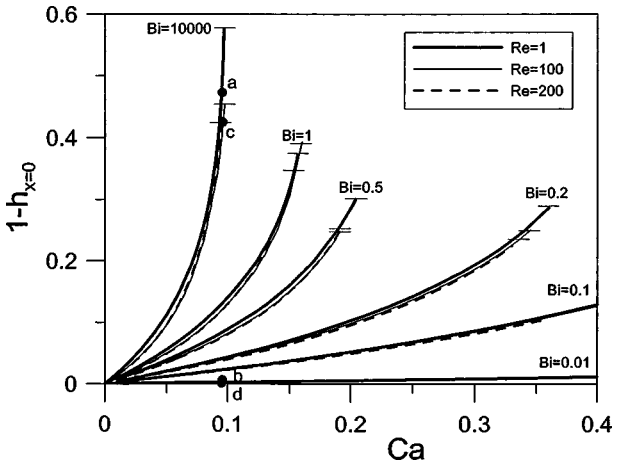

Fig. 8 The interface deformation in the middle of a cavity subject to point heating from above as a function of the capillary number Ca for different values of the Biot number Bi and for Re=1,100,200. The flow and deformation patterns corresponding to points (*a–d*) are shown in Fig. 9. The cavity has length *L*=4 and the interface is subject to the fixed contact angles constraint.

lary propulsion'' is used to increase convection in the flow narrowest area on the left side at the expense of convection on the right side (compare Figs. 3*a* and 3*b*, 3*c* and 3*d*).

Imposition of the fixed contact points conditions changes response of the system. Analysis of Jian et al. [7] in the case of Bi$\rightarrow\infty$ forms a good reference point. Cavity with length $L=4$ is selected for this discussion. Figure 4 illustrates evolution of the interface deformation as a function of Ca for Re=1,100,200. Comparison of Figs. 2 and 4 demonstrates higher ''deformability'' of the interface with fixed contact angles. The effect of Biot number is similar as in the case of interface with fixed contact points. The flow and temperature fields are illustrated in Fig. 5. Since the interface has larger deformation as compared to the case of fixed contact points, the temperature gradients must be higher on the left side, and the resulting increase in thermocapillary ''suction'' must also be higher (compare Figs. 3 and 5).

Cavity Heated From Above by a Point Source. Liquid subject to surface heating in the form that mimics laser heating is considered. The temperature distribution in the gas phase is assumed to have a Gaussian distribution in the form $T_g(x)$

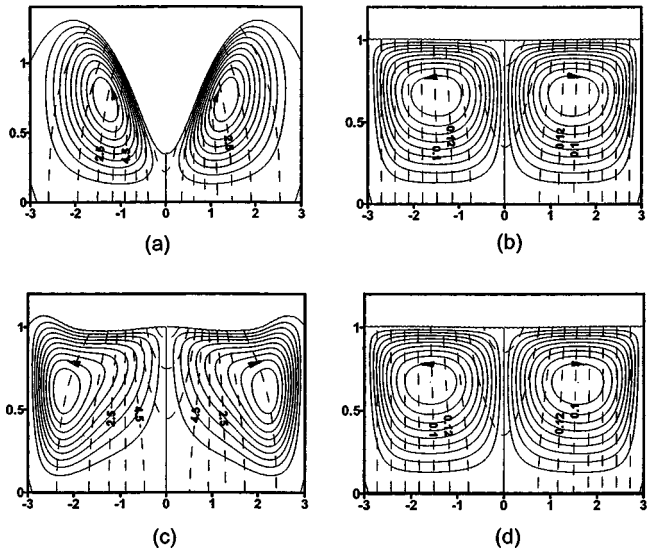

Fig. 7 The evolution of the flow, temperature and deformation patterns in a cavity subject to point heating from above as a function of the Biot number Bi for Re=1 and 200, *L*=6, and Ca=0.0899. Figures (*a,b*)—Re=1, Bi=10^4 and Bi=10^{-2}, (*c,d*)—Re=200, Bi=10^4, and Bi=10^{-2}. (*a–d*) correspond to points (*a–d*) in Fig. 6. Contour lines of the stream function are shown every 10 percent of ψ_{max}. In (*a–d*) $|\psi_{max}|$=0.1938, 0.00267, 0.0942, 0.00266, respectively. The isotherms are shown with ΔT=1, 0.02, 1, 0.02 in (*a–d*), respectively. The interface is subject to the fixed contact points constraint.

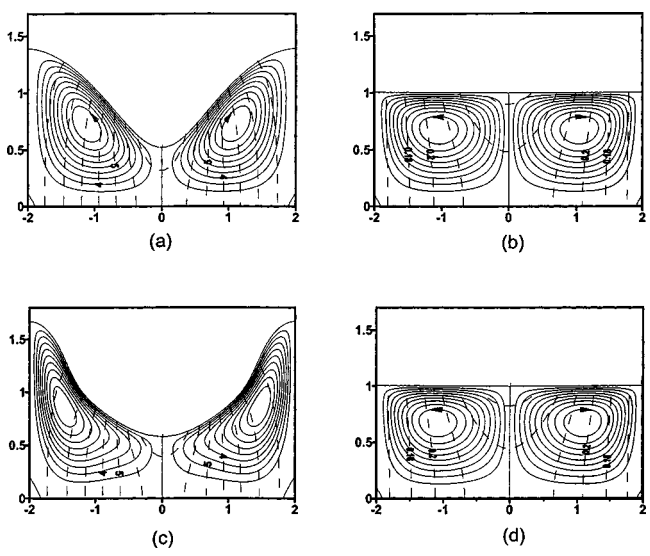

Fig. 9 The evolution of the flow, temperature and deformation patterns in a cavity subject to point heating from above as a function of the Biot number Bi for Re=1 and 200, *L*=4 and Ca=0.0952. Figures (*a,b*)—Re=1, Bi=10^4, and Bi=10^{-2}, (*c,d*)—Re=200, Bi=10^4 and Bi=10^{-2}. (*a–d*) correspond to points (*a–d*) in Fig. 8. Contour lines of the stream function are shown every 10 percent of ψ_{max}. In (*a–d*) $|\psi_{max}|$=0.1685, 0.00226, 0.07532, 0.002256, respectively. The isotherms are shown with ΔT=1, 0.02, 1, 0.02 in (*a–d*), respectively. The interface is subject to the fixed contact angles constraint.

$=8e^{-x^2}$. Analysis of Hamed and Floryan [10], carried out for fixed contact points conditions and Bi$\rightarrow\infty$, forms a reference point. Figure 6 illustrates evolution of the interface deformation as a function of Ca. It can be seen that reduction of Bi significantly reduces the magnitude of the deformation and increases the value of Ca_{cr}. An increase of the Reynolds number from Re=1 to Re =200 makes this effect much more pronounced if Bi is not too small. The effect of Re disappears for approximately Bi$\leqslant$0.01. The reasons for the reduction of the deformation due to reduction of Bi can be illustrated using the flow and temperature fields displayed in Fig. 7. The cavity is heated from above and the heating is concentrated in the center of the interface. The heat flows approximately from this point towards the sidewalls. When Bi $\rightarrow\infty$, the total heat flux entering the liquid is determined by the gas temperature $T_g(x)$ and the shape of the interface. A reduction of Bi insulates interface and permits only part of this heat to enter the liquid. As a result the temperature gradients in the liquid become much smaller (compare Figs. 7*a* and 7*b*, 7*c* and 7*d*), the thermocapillary effect becomes much weaker, the convection also becomes much weaker and the resulting interface deformation becomes much smaller. In the limit Bi$\rightarrow$0 the liquid becomes isothermal and the convection disappears all together. When Bi is very small, the effect of changing Re becomes insignificant, as illustrated in Figs. 7*b*,*d*. This is due to the fact that the magnitude of the convection is so small (as illustrated by the value of $\psi_{\max}$, see Fig. 7) that the nonlinear convective in terms in the field equations play a negligible role.

Interface with fixed contact angles has been investigated by Jian et al. [7] for Bi$\rightarrow\infty$. Figure 8 illustrates evolution of the interface deformation as a function of Ca. Comparison of Figs. 6 and 8 demonstrates higher ''deformability'' of the interface with fixed contact angles. The effect of Bi is similar as in the case of interface with fixed contact points. The effect of Re appears to be negligible in the range of parameters studied. The flow and temperature fields are illustrated in Fig. 9. The reduction of the temperature gradients in the liquid associated with the reduction of Bi can be easily seen. All these effects result from the increase of the insulation of the interface as quantified in terms of decreasing value of Bi.

Acknowledgment

The NSERC of Canada supported this work.

Nomenclature

Bi = Biot number (Bi=h_gH/k)
c = specific heat
Ca = Capillary number (Ca=$\gamma\Delta T/\sigma^*$)
H = cavity depth
h = location of the interface
h_g = heat transfer coefficient
k = thermal conductivity
L = cavity length
Ma = Marangoni number (Ma=u^*H/κ)
p = pressure
Re = Reynolds number (Re=u^*H/ν)
T = temperature
$T_L(T_R)$ = temperature of the left (right) wall
T_g = gas temperature
(u, v) = velocity vector.
u^* = velocity scale
V = volume of the liquid
x, y = Cartesian reference system
γ = surface tension gradient
κ = thermal diffusivity
μ = dynamic viscosity
ν = kinematic viscosity
ρ = density
$\sigma(\sigma^*)$ = surface tension (reference surface tension)
ψ = stream function

References

[1] Scriven, L. E., and Sterling, C. V., 1960, ''The Marangoni Effect,'' Nature (London), **187**, p. 186.
[2] Pearson, J. R. A., 1958, ''On Convection Cells Induced by Surface Tension,'' J. Fluid Mech., **4**, pp. 489–500.
[3] Czechowski, L., and Floryan, J. M., 2001, ''Marangoni Instability in a Finite Container—Transition Between Short and Long Wavelengths Modes,'' ASME J. Heat Transfer, , **123**, pp. 96–104.
[4] Floryan, J. M., and Chen, C., 1994, ''Thermocapillary Convection and Existence of Continuous Liquid Layers in the Absence of Gravity,'' J. Fluid Mech., **277**, pp. 303–329.
[5] Sen, A. K., and Davis, S. H., 1982, ''Steady Thermocapillary Flows in Two-Dimensional Slots,'' J. Fluid Mech., **121**, pp. 163–186.
[6] Hamed, M. S., and Floryan, J. M., 2000, ''Marangoni Convection. Part 1. A Cavity With Differentially Heated Sidewalls,'' J. Fluid Mech., **405**, pp. 79–110.
[7] Jiang, Y., Badr, H., and Floryan, J. M., 2001, ''Thermocapillary Convection with Moving Contact Points,'' Expert Systems in Fluid Dynamics Research Laboratory Report ESFD-3/2001, Department of Mechanical and Materials Engineering, The University of Western Ontario, London, Ontario, N6A 5B9, Canada.
[8] Tan, M. J., Bankoff, S. G., and Davis, S. H., 1990, ''Steady Thermocapillary Flows of Thin Liquid Layers. I. Theory,'' Phys. Fluids A, **2**, pp. 322–333.
[9] Higuera, F. J., 2000, ''Steady Thermocapillary-Buoyant Flow in an Unbounded Liquid Layer Heated Non-Uniformly From Above,'' Phys. Fluids, **12**, pp. 2186–2197.
[10] Hamed, M. S., and Floryan, J. M., 2000, ''Marangoni Convection. Part 2. A Cavity Subject to Point Heating,'' J. Fluid Mech., **405**, pp. 111–129.
[11] Perez-Garcia, C., Echebarria, B., and Bestehorn, M., 1998, ''Thermal Properties in Surface-Tension-Driven Convection,'' Phys. Rev. E, **57**, pp. 475–481.
[12] Chen, C., and Floryan, J. M., 1994, ''Numerical Simulation of Non-Isothermal Capillary Interfaces,'' J. Comput. Phys., **111**, pp. 183–193.
[13] Jiang, Y., and Floryan, J. M., 2002, ''Relation Between Heat Transfer at the Interface and Thermocapillary Convection,'' Expert Systems in Fluid Dynamics Research Laboratory Report ESFD-2/2002, Department of Mechanical and Materials Engineering, The University of Western Ontario, London, Ontario, N6A 5B9, Canada, 2002.

Investigation of a Two-Equation Turbulent Heat Transfer Model Applied to Ducts

Masoud Rokni and Bengt Sundén
Division of Heat Transfer, Lund Institute of Technology, 221 00 Lund, Sweden

This investigation concerns numerical calculation of fully developed turbulent forced convective heat transfer and fluid flow in ducts over a wide range of Reynolds numbers. The low Reynolds number version of a non-linear eddy viscosity model is combined with a two-equation heat flux model with the eddy diffusivity concept. The model can theoretically be used for a range of Prandtl numbers or a range of different fluids. The computed results compare satisfactory with the available experiment. Based on existing DNS data and calculations in this work the ratio between the time-scales (temperature to velocity) is found to be approximately 0.7. In light of this assumption an algebraic scalar flux model with variable diffusivity is presented. [DOI: 10.1115/1.1532017]

Keywords: Channel Flow, Convection, Heat Transfer, Modeling, Turbulence

Contributed by the Heat Transfer Division for publication in the JOURNAL OF HEAT TRANSFER. Manuscript received by the Heat Transfer Division December 27, 2001; revision received September 25, 2002. Associate Editor: K. S. Ball.

Introduction

The simple Eddy Diffusivity model (SED) is the classical Boussinesq assumption for modeling the heat transfer. Using the known eddy viscosity μ_τ, the unknown eddy diffusivity (conductivity) for heat can be expressed as $\alpha_\tau = \nu_\tau / \sigma_\tau$, where the turbulent Prandtl number σ_τ needs to be prescribed. The zero-equation model of SED assumes that the turbulent Prandtl number is constant in the whole region, e.g., 0.89 for air, irrespective of wall proximity effect. This is a crude approximation since the calculated temperature field strongly depends on the chosen value for the turbulent Prandtl number.

So and Sommer [1] discussed that the physical arguments for constant turbulent Prandtl number are applicable only for fluids whose molecular Prandtl numbers are approximately unity. Their discussions are supported by flow shear measurements (Krishnamoorthy and Antonia [2]) and direct simulation data (Kim and Moin [3]) which have shown that the analogy between heat and momentum transport through a constant turbulent Prandtl number is not a suitable assumption. In narrow ducts the wall effect on turbulent Prandtl number may be more important.

Besides, the zero equation of the SED model may not be adequate for non-adiabatic boundary conditions or fluids with very low (or very high) molecular Prandtl numbers. However, a two-equation model for the heat fluxes may diminish these deficiencies.

The results obtained from numerical simulations are compared with experiments in terms of friction factor and Nusselt number. The turbulent Prandtl number variation in the cross section is also studied and compared with experimental data.

Several fundamental investigations concerning turbulent flow in square and rectangular ducts exist, e.g., direct numerical simulations have been performed for a square duct by Huser and Biringen, [4] and Gavrilakis [5]. Large eddy simulations for square ducts are reported by Su and Friedrich [6] at a Reynolds number of 49000 and by Madabhushi and Vanka [7] at a Reynolds number of 5800. Hirota et al. [8] measured the turbulent Prandtl number variation in a square duct. However, none of these studies concern Prandtl number variation, diffusivity distribution and time-scales ratio.

In the literature no numerical investigations have been presented in terms of Prandtl number variation in the cross section of ducts, using Reynolds average Navier Stokes (RANS) models. In this work, the numerical calculation is focused on fully developed periodic flow and may be regarded as a further application and evaluation of the computational method developed by the authors in their previous work.

The calculated results are compared with some available experimental data in duct flows and it has been found that the computed results match the experimental data very well. The study contributes with some ideas concerning the ratio between the dynamic time-scale to scalar time-scale in duct flows. In addition, a new algebraic scalar flux model with variable diffusivity is presented.

Problem Statement

Straight ducts with square, rectangular and trapezoidal cross-sections are considered in this study. Only one quarter of the duct with square and rectangular cross section and half of the duct with trapezoidal cross-sections are considered by imposing symmetry conditions. Sketches of the ducts are shown in Fig. 1.

The calculation method has been focused on fully developed, three-dimensional turbulent duct flow. Mean velocity distributions, secondary motions, turbulent Prandtl number, friction factor and Nusselt number are determined numerically for fully developed conditions.

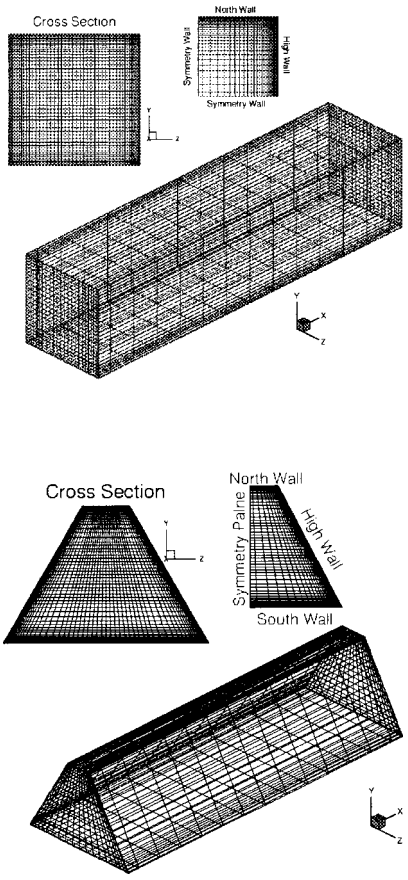

Fig. 1 Ducts under consideration

Governing Equations

The governing equations are the continuity, momentum and energy equations, see, e.g., Wilcox [11]. Fully developed periodic turbulent flow is considered in this investigation. The following assumptions are employed: steady state, no-slip at the walls and constant fluid properties. The turbulent stresses ($-\rho\overline{u_i u_j}$) and the turbulent heat fluxes ($\rho c_p \overline{u_j \theta}$) are modeled as described in the following sections.

Turbulence Model for Reynolds Stresses

The most widely used two-equation turbulence model, namely the k-ε model, is used here with the conventional *isotropic dissipation equation*. The model is combined with damping functions to increase the accuracy near the walls. The conventional low Reynolds-number form of the k-ε model (Wilcox [9]) for steady state is given by

$$\frac{\partial}{\partial x_j}(\rho U_j k) = \frac{\partial}{\partial x_j}\left[\left(\mu + \frac{\mu_\tau}{\sigma_k}\right)\frac{\partial k}{\partial x_j}\right] + P_k - \rho\varepsilon \tag{1}$$

$$\frac{\partial}{\partial x_j}(\rho U_j \varepsilon) = \frac{\partial}{\partial x_j}\left[\left(\mu + \frac{\mu_\tau}{\sigma_\varepsilon}\right)\frac{\partial \varepsilon}{\partial x_j}\right] + f_1 C_{\varepsilon 1}\frac{\varepsilon}{k}P_k - f_2 C_{\varepsilon 2}\rho\frac{\varepsilon^2}{k} \tag{2}$$

where $P_k = -\rho\overline{u_i u_j}\partial U_i / \partial x_j$ is the production term and f_1 and f_2 are damping functions. The turbulent eddy viscosity μ_τ is calculated as $\mu_\tau = \rho f_\mu C_\mu k^2/\varepsilon$, where f_μ is the damping function for the turbulent viscosity.

A nonlinear constitutive relation for the Reynolds stresses in incompressible flow was proposed by Speziale [10]. The nonlinear terms in this model are a form of quadratic terms, which

enable calculation of anisotropic normal stresses and consequently prediction of the secondary velocity field in ducts.

The constants and coefficients in (4) and (5) are set to

$$\sigma_k = 1.4, \quad \sigma_\varepsilon = 1.4, \quad C_{\varepsilon 1} = 1.5, \quad C_{\varepsilon 1} = 1.9 \text{ and } C_\mu = 0.09.$$

The Damping Functions f_1, f_2, and f_μ

The high Reynolds number form of the k-ε model suggests that f_μ should approximately be equal to unity in the fully turbulent region remote from solid walls. However, in a region very close to a wall where the viscous effects become very important, f_μ will differ considerably from unity. In this study, the Abe-Kondoh-Nagano [11] type of damping functions are used, hereafter named the AKN model. In this model the formulations of f_μ, f_1, and f_2 are given by

$$f_\mu = (1 - e^{-y^*/14})^2 \left(1 + \frac{5}{\mathrm{Re}_t^{0.75}} e^{-(\mathrm{Re}_1/200)^2}\right) \tag{3}$$

$$f_1 = 1, \quad f_2 = (1 - e^{-\gamma^*/3.1})^2 (1 - 0.3 e^{-(\mathrm{Re}_\tau/6.5)^2}) \tag{4}$$

$$\text{where} \quad y^* = u_\varepsilon \frac{\rho \eta}{\mu} = \left(\frac{\mu \varepsilon}{\rho}\right)^{0.25} \frac{\rho \eta}{\mu} \text{ and } \mathrm{Re}_\tau = \frac{\rho k^2}{\mu \varepsilon}.$$

In these equations η is the normal distance to a wall.

Turbulence Models for Heat Flux

The turbulent diffusivity may be expressed as $\alpha_\tau \propto$ (turbulent velocity) x (spatial extent of temperature fluctuations) so that α_τ may be written as $\alpha_\tau \propto k^{0.5} \times L_m$ where L_m is the characteristic length-scale and equal to $L_m = k^{0.5} \tau_m$. Therefore, the turbulent diffusivity can be written as

$$\alpha_\tau = C_\lambda f_\lambda k \tau_m \tag{5}$$

where C_λ is a constant, f_λ is a damping function, and τ_m is an appropriate turbulent time-scale equivalent to the relative "lifetime" of the energy-containing eddies or temperature fluctuations. τ_m can be assumed to be related to the dynamic time-scale $\tau_u = k/\varepsilon$ and the scalar time-scale $\tau_\theta = (\overline{\theta\theta}/2)/\varepsilon_\theta$. Zeman and Lumley [12] introduced the following composite time-scale in modeling buoyancy driven mixed layer

$$\tau_m \propto (1/\tau_u + C_m/\tau_\theta)^{-1} = \tau_u [R/(C_m + R)] \tag{6}$$

which is adopted since it reflects the harmonic average of the velocity- and temperature-field time scales. This τ_m suggests that the shorter time-scale among τ_u and τ_θ is more important for turbulent heat transfer. In Eq. (6), C_m is a constant and R is the ratio between the time-scale for the temperature fluctuation and the time-scale for the velocity fluctuation, $R = \tau_\theta / \tau_u$.

The two-equation model for the temperature field based on the temperature variance and its dissipation rate used here is similar to the model of Abe et al. [11] and modified by Rokni [13]. The equations for $\overline{\theta\theta}$ and ε_θ are

$$\frac{\partial}{\partial x_j}(U_j \overline{\theta\theta}) = \frac{\partial}{\partial x_j}\left[\left(\alpha + \frac{\alpha_\tau}{\sigma_h}\right)\frac{\partial \overline{\theta\theta}}{\partial x_j}\right] - 2P_{\theta\theta} - 2\varepsilon_\theta \tag{7}$$

$$\frac{\partial}{\partial x_j}(U_j \varepsilon_\theta) = \frac{\partial}{\partial x_j}\left[\left(\alpha + \frac{\alpha_\tau}{\sigma_\phi}\right)\frac{\partial \varepsilon_\theta}{\partial x_j}\right] + P_{\varepsilon_\theta} - f_{D1} C_{D1} \frac{\varepsilon_\theta^2}{t^2} - f_{D2} C_{D2} \frac{\varepsilon \varepsilon_\theta}{k} \tag{8}$$

where the production term for the temperature variance $P_{\theta\theta}$ is expressed by

$$P_{\theta\theta} = -\overline{u_j \theta} \partial \Theta / \partial x_j \tag{9}$$

and the production term for the dissipation of temperature variance P_{ε_t} is expressed as

$$P_{\varepsilon_\theta} = f_{p1} C_{p1} \frac{\partial_\theta}{\theta\theta} P_{\theta\theta} + f_{p2} C_{p2} \frac{\varepsilon_\theta}{k} P_k + f_{p3} C_{p3} \frac{\varepsilon}{k} P_{\theta\theta} \tag{10}$$

The difference between the presented model and the AKN model is that the AKN model involves only the thermal time-scale in the production term for the dissipation of temperature variance P_{ε_t} while in the presented model both the thermal time-scale and the velocity time-scale are involved.

The model constants C_{P1}, C_{P2}, C_{P3}, C_{D1}, and C_{D2} are set to 1.20, 0.52, 0.62, 2.0, and 0.8, respectively (Torii and Yang [14]). The constants σ_ϕ and σ_h are set to 1.6.

The turbulent eddy diffusivity α_τ is proposed to have the form of

$$\alpha_\tau = \underbrace{C_\lambda \left\{1 - e^{\left(\frac{-\gamma^*}{14}\right)}\right\}\left\{1 - e^{\frac{-\sqrt{\mathrm{Pr}}y^*}{14}}\right\} x \left\{\frac{k^2}{\varepsilon}\left(\frac{R}{C_m + R}\right)\right.}_{f_\lambda} + 3k^{0.5}\left(\frac{\mu^3}{\rho^3 \varepsilon}\right)^{0.25} \frac{R^{0.5}}{\mathrm{Pr}} f_d \Bigg\}$$

-025301

(11)

where $C_m = 0.14$, $C_\lambda = 0.1$, and $R = \tau_\theta / \tau_u$, where τ_θ and τ_u have been defined previously. The second part of the third bracket is included to account for different behavior of various fluids in the shear layers. The functions f_{P1}, f_{P2}, f_{P3}, f_{D1}, f_{D2}, and f_d are

$$f_{D1} = (1 - e^{-y^*})^2$$

$$f_{D2} = \left(\frac{1}{C_{D2}}\right)(C_{\varepsilon 2} f_{C2} - 1)(1 - e^{-\gamma^*/5.7})^2$$

$$f_{P1} = f_{D1}, \quad f_{P2} = f_{p3} = 1.0 \tag{12}$$

$$f_d = \exp\{-(\mathrm{Re}_t/200)^2\}$$

$$f_{C2} = 1 - 0.3 \exp\{-(\mathrm{Re}_t/6.5)^2\}$$

Now the turbulent heat fluxes can be described using the simple eddy diffusivity concept as

$$-\overline{u_j \theta} = \alpha_\tau \frac{\partial \Theta}{\partial x_j} \tag{13}$$

The thermal eddy diffusivity used here is not constant and changes but the turbulent heat fluxes are still based on an isotropic concept, i.e., the thermal diffusivity is independent of direction. To summarize this subsection, the modified AKN model can correctly reproduce the near-wall limiting behavior of scalar turbulence quantities for any wall thermal conditions (constant wall temperature, constant wall heat flux). Further discussions can be found in Abe et al. [11].

Periodic Conditions

The periodic condition may be explained by considering a series of cyclic domains, where the flow entering a domain is equal to the flow leaving the preceding domain. The fully developed region of a duct can be treated as periodic. By imposing realistic periodic conditions in the main flow direction, it is possible to calculate the fully developed region only. Thus, the computational time and cost decrease considerably since the number of grid points in the main flow direction can be reduced significantly. The idea of using periodic conditions for calculation of fully developed region was initiated by Patankar et al. [15] and since then it has been widely used by several research groups, such as Müller and Fiebig [16] (in DNS) and Held and Fuchs [17] (in LES), and many others.

The details of the implementation of periodic condition can be found in Rokni [13].

Boundary Conditions

Periodicity conditions are imposed at the inlet and outlet for all variables, see [13]. The boundary conditions $k=\overline{\theta\theta}=0$ at the walls and $\partial k/\partial\eta=\partial\varepsilon/\partial\eta=\partial\overline{\theta\theta}/\partial\eta=\partial\varepsilon_\theta/\partial\eta=0$ at the symmetry lines are adopted. The dissipation rate is set along the points adjacent to a wall as $\varepsilon=2\upsilon k/\eta_{\text{wall}}^2$ and $\varepsilon_\theta=2\upsilon\overline{\theta\theta}/\eta_{\text{wall}}^2$. η is the normal distance to a wall or a symmetry line. The effect of one wall, namely the nearest one, is adopted in this investigation, $\eta=\min(\eta_1,\eta_2)$.

Numerical Solution Procedure

The partial differential equations are transformed to algebraic equations by a general finite-volume technique. The momentum equations are solved for the velocity components on a non-staggered grid arrangement. The Rhie-Chow interpolation method (Rhie and Chow, [18]) is used to interpolate the velocity components to the control volume faces from the grid points. The SIMPLEC-algorithm is employed to handle the pressure velocity coupling. TDMA based algorithms are used for solving the equations. The convective terms are treated by the QUICK scheme while the diffusive terms are treated by the central-difference scheme. The hybrid scheme is used for solving the k and ε equations.

Grid Sensitivity and Validation Against Experimental Data

The Reynolds number is calculated based on the hydraulic parameter and the pressure drop, Fanning friction factor and Nusselt number are calculated thereafter. Details can be found in Rokni [13].

A non-uniform grid distribution is employed in the plane perpendicular to the main flow direction. Close to each wall, the number of grid points or control volumes is increased to enhance the resolution and accuracy. The computations were terminated when the sum of the absolute residuals normalized by the inflow was less than 10^{-6} for all variables. Different numbers of grid points were used in the cross sectional plane. In this study, it was shown that the overall friction factors and Nu-numbers, which are the most interesting parameters from an engineering point of view, do not change significantly if the number of grid points were increased beyond 31×31 in a square duct, see Table 1.

Because of the periodic nature of the fully developed flow, which repeats itself in every cross section, the number of grid points in the main flow direction is not important. Thus only 3 grid points were used in this direction. The results do not change if the number of grid points increased in this direction. Similar studies were also carried out for other Reynolds numbers as well as other duct configurations, but due to space limitation, the results are not included. Thus care has been paid in choosing the number of grid points.

While the secondary motion has been the subject of previous work by the authors, it can be used here to illustrate the range of applicability of the current methodology. As an example, Fig. 2 shows the calculated main flow velocity with experimental data at the center line in a rectangular duct with aspect ratio as 8 and Re=5800, see [19]. As can be seen the predicted streamwise velocity profile was in good agreement with the experimental data. The centerline velocity to friction velocity ratio (U_c/u_τ) was calculated to 18.22 which is very close to the value of 18.20, reported by Kim et al. [20] for a plane duct. The friction coefficient based on centerline velocity calculated by the non-linear model was 6.02×10^{-3}, which was in excellent agreement with the value 6.04×10^{-3} obtained by Kim et al. [20]. The predicted Reynolds stresses are also in satisfactory agreement with the experiment.

Table 1 Grid influence on hydraulic parameters for a square duct

Grid arrangement	Re	$f\times10e3$	Nu
$15\times15\times3$	6261	10.160	23.8
$21\times21\times3$	6639	9.036	22.6
$31\times31\times3$	6773	8.682	22.1
$31\times31\times4$	6773	8.682	22.1
$31\times31\times5$	6773	8.682	22.1
$41\times41\times3$	6791	8.638	22.1
$51\times51\times3$	6797	8.630	22.1

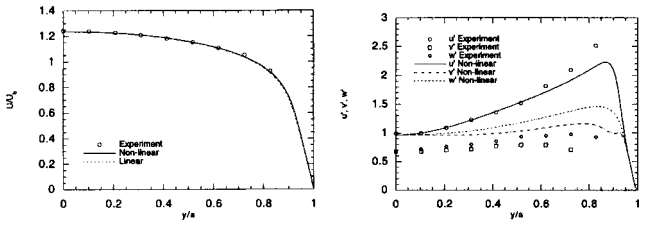

Fig. 2 Calculated main flow velocity and Reynolds stresses compared with experiment (Rokni et al. [19]) at centerline in a rectangular duct with aspect ratio 8. Re=5800.

The experiments carried out by Lowdermilk et al. [21] showed that the friction factor in straight ducts can be correlated by the Prandtl friction law, given as $(4f_{pr})^{-1/2}=2\log[\text{Re}(4f_{pr})^{1/2}]-0.8$ for Reynolds numbers greater than about 3000. Their experiment showed also that the Nusselt number can be correlated by the Dittus-Boelter equation, given by $\text{Nu}_{\text{DB}}=0.023\ \text{Re}^{0.8}\,\text{Pr}^{0.3}$, for Reynolds numbers greater than about 8000. These hydraulic parameters are calculated for a wide range of Reynolds number and compare excellently with the their experiment.

The damping approach used in this study demands small y^+-value near a solid wall. The authors' experience shows that the average y^+-value near a wall should be in the order of about unity yield the best results.

Results and Discussions

While the secondary motion has been the subject of previous work by the authors, it can be used here to illustrate the range of applicability of the current methodology. As alluded to previously, the present calculation procedure can be used for determination of turbulent Prandtl number variation in the cross section of the duct, using the two-equation formulation expressed in previous section.

The Ratio *R* Between Time-Scales

The ratio R was defined as the ratio between the time-scale for the temperature fluctuations (τ_θ) and the time-scale for the velocity fluctuations (τ_u). It has been discussed in many studies that

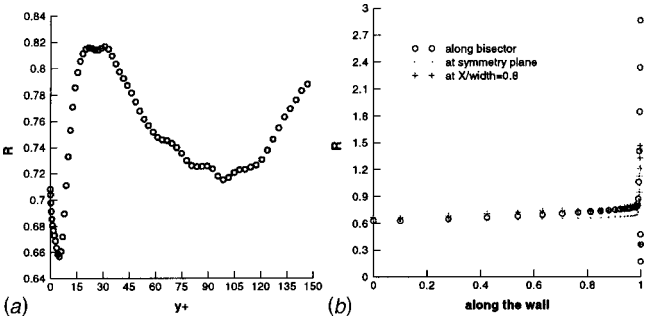

Fig. 3 Variation of time-scale-ratio, *R*, in DNS channel flow (*a*) and in a square duct (*b*)

the time-scale-ratio, R, is almost constant and values of 0.5 to 0.6 are assumed, see, e.g., [11,14]. Figure 3 shows the variation of this time-scale-ratio in the fully developed DNS channel flow at Re=4560 (Kasagi and Lida [22]) and as calculated here in a square duct at Re=64350. Due to similarity the results along the bisector, symmetry plane and X/width=0.8 are shown. In the DNS channel flow this variation is small (from about 0.66 to about 0.82) and thus assuming a constant for this ratio is logical. In the square duct flow R is almost constant, around 0.7, unless very close to the corner. Therefore, it is reasonable to assume that this ratio is constant and equal to 0.7. By this assumption the two differential equations for the temperature variance and its dissipation rate (Eqs. (7) and (8)) are no longer needed and the turbulent diffusivity will be simplified and it is determined by essentially flow quantities. The following simple algebraic equation holds (by inserting Eq. (11) into Eq. (13))

$$\alpha_\tau = C_\lambda \{1-e^{(-y^*/14)}\}\{1-e^{-\sqrt{\mathrm{Pr}}y^*/14}\} x \left\{ 0.83\frac{k^2}{\varepsilon} + 2.51k^{0.5}\left(\frac{\mu^3}{\rho^3\varepsilon}\right)^{0.25}\frac{1}{\mathrm{Pr}} f_d \right\}. \quad (14)$$

The authors re-calculated all the sample problems with this method and found no difference compared with a varying dimensionless R, in terms of temperature field and Nusselt number.

Turbulent Prandtl Number and Diffusivity

The turbulent Prandtl number can be calculated by

$$\sigma_\tau = \frac{\mu_\tau/\rho}{\alpha_\tau} \quad (15)$$

where μ_τ is the turbulent viscosity and α_τ is the turbulent diffusivity defined previously. As was discussed previously, the turbulent Prandtl-number σ_τ increases in the region close to a wall. The model presented here (Eq. 14) is used to calculate σ_τ in a square duct with two different Reynolds numbers, 6800 (representing a low-Re-number) and 64350 (representing a high-Re-number), for air with the molecular Prandtl number as 0.72, see Fig. 4.

These figures show that at high Reynolds number (64350) the turbulent Prandtl number is almost constant (about 1.1) in the whole region, while in a region very close to a wall it increases and reaches a value about 1.5, near the corner. However, changes in σ_τ are more obvious at low Reynolds number (6700) and the value 1.1 exists only in a very narrow region. Experimental results of Hirota et al. [8] in a square duct at Reynolds number 65000 and wall temperature 373 K, yielded a value of σ_τ of about 2.4 near the duct corner and about 1.16 in the major part of the region, higher than the values predicted here.

Figure 5 shows the comparison between the calculated turbulent Prandtl number variation from the present model and the experimental data at the plane X/width=0.8. The Abe et al. [11] (AKN model) and the Kays and Crawford [23] model are also included. As can be seen, the present model performs much better than the other two models (whether Eq. (14) is used or the two-equation model is used). The results show that assuming the constant Prandtl number as 0.89 for air is not generally true.

A good prediction of the flow field is the first step for satisfactory capturing the thermal field. The center-to-bulk velocity ratio (U_c/U_b) for a square duct with Re~4600 is calculated as 1.33 which is in excellent agreement with the value 1.33 obtained by Gavrilakis [5] for a square duct at the Reynolds number 4410 by using direct numerical simulations. The calculated Fanning friction factor and Nusselt number are 9.618×10^{-3} and 16.5, respectively. These results can be compared with Prandtl friction law and Dittus-Boelter correlation, which yield 9.534×10^{-3} and 18.0, respectively. The model slightly underpredicts the Dittus-Boelter correlation for Re-numbers less than about 8000, as was also confirmed in the experiments by Lowdermilk et al. [21].

The model described here enables the calculation of the diffusivity behavior using Eq. (14). The diffusivity contours in a square duct are presented in Fig. 6. These figures show that diffusivity in the cross section of the duct is not only constant but varies from the center to the wall, and also varies with Reynolds number. Hirota et al. [8] have also reported that the diffusivity in the cross section of a square duct is not constant.

The calculation procedure has also been applied to a square duct with an oil flow with Prandtl number 471. The oil (BP Olex WF 0801) flow characteristics at 20°C are $\mu=39.10\times10^{-3}$ Ns/m^2 and $\rho=1029$ kg/m^3. The results are shown in Fig. 7.

An interesting feature from Figs. 4 and 7 is that the turbulent Prandtl number variations in oil flow is almost the same as in the

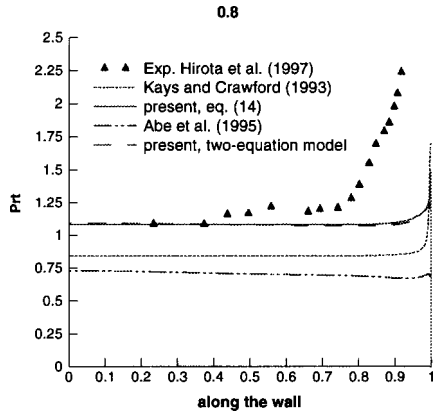

Fig. 5 The calculated turbulent Prandtl number in comparison with the experiments of Hirota et al. [8]

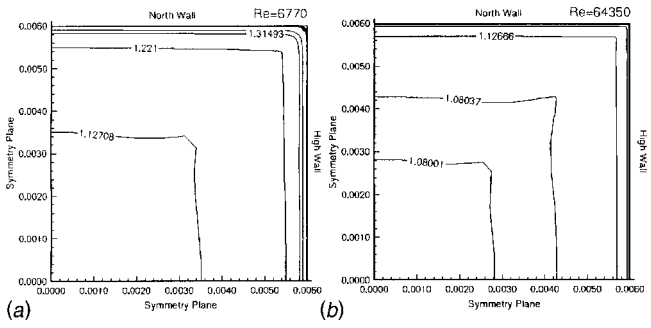

Fig. 4 Turbulent Prandtl number variation in the cross section of a square duct for two different Reynolds numbers (*a*) 6770, and (*b*) 64350. The molecular Prandtl number is 0.72.

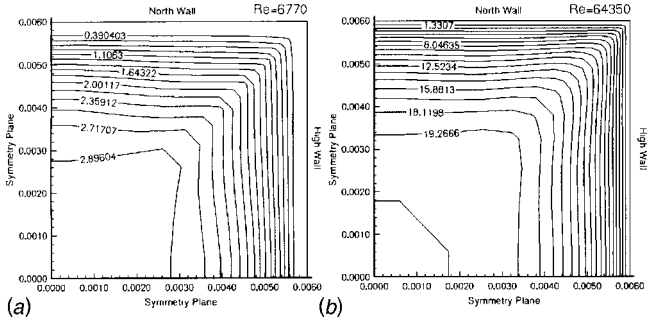

Fig. 6 Contours of turbulent diffusivity in a square duct at two different Reynolds numbers (*a*) 6770 and (*b*) 64350. The values are times 10^{-3}, e.g., 2.89604×10^{-3} m^2/s.

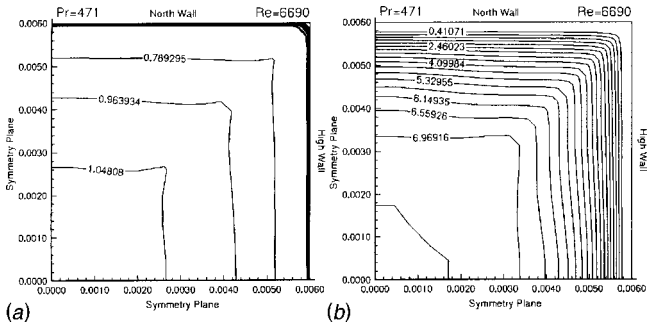

Fig. 7 Turbulent Prandtl number variation (*a*) and turbulent diffusivity variation (*b*) in a square duct with oil flow. The diffusivity values are times 10^{-3}, e.g., 6.96916×10^{-3} m^2/s. Pr=471 and Re=6990.

airflow. One may conclude that the turbulent Prandtl number depends slightly on the type of the fluid and changes slightly with Reynolds number. Such a conclusion can also be drawn from Eq. (14), by studying the terms including Pr.

The calculated friction factor and Nusselt number for this oil are 8.711×10^{-3} and 203.5, respectively. The friction factor agree very well with the Prandtl friction law which yields 8.612×10^{-3}. The calculated Nusselt number cannot be compared with the Dittus-Boelter equation, because it is valid for Prandtl numbers less than about 160. However, it agrees satisfactory with the Petukhov correlation (see, e.g., [24]) which is valid for Prandtl numbers less than about 2000 and yields the value 191.5.

Trapezoidal Ducts

The calculation procedure is also applied for a straight trapezoidal duct with isothermal wall boundary condition and with several height to base ratios and Re-numbers. However, due to space limitation only the height to base ratio of 4/3 is considered here. Close to each corner a counter-rotating vortex is generated, similar to the results obtained from Rokni and Gatski [25] and the experimental observation carried out by Nikuradse [26].

Figure 8(*a*) shows that the turbulent Prandtl number is almost constant in the whole cross section (~1.1) unless close to the walls. The predicted Fanning friction factor and Nusselt number is 7.487×10^{-3} and 47.7, respectively. These values can be compared with the Prandtl friction law and Dittus-Boelter correlations, which yield 6.846×10^{-3} and 48.3, respectively. The center-to-bulk velocity is calculated as 1.28.

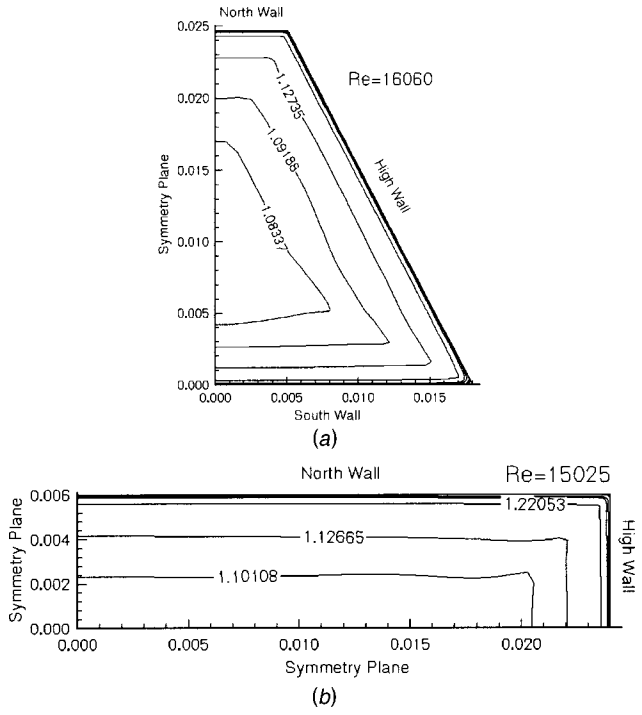

Fig. 8 Prandtl number variation in a trapezoidal straight duct (*a*) and in a rectangular straight duct (*b*). The molecular Prandtl number is 0.72.

Rectangular Ducts

The calculation procedure has also been extended to rectangular ducts with several aspect ratios and Re-numbers, however due to space limitation and similarity only one of them is discussed here. Similar counter-rotating vortices as in [1–25] are also predicted here.

As is the case for the square duct, the turbulent Prandtl number in the rectangular duct is almost constant in the whole cross section (~1.1) unless close to the walls. The discussion for square ducts can also be applied to the rectangular duct.

The predicted Fanning friction factor and Nusselt number is 7.226×10^{-3} and 42.1, respectively. These values can be compared with the Prandtl friction law and Dittus-Boelter correlations, which yield 6.950×10^{-3} and 44.3, respectively. The center to bulk velocity is calculated as 1.25.

Conclusions

A numerical method for turbulent heat transfer and fluid flow in ducts has been presented. Speziale's nonlinear eddy viscosity model together with a two-equation model for the heat transfer have been used successfully to predict the secondary velocity field, the streamwise velocity, friction factor and Nusselt number and other heat related parameters.

The predicted average friction factors and Nusselt numbers agree very well with the experiment of Lowdermilk et al. [21]. However, a general conclusion can not be drawn until the performance of the model has been shown in more complex channels, such as wavy ducts.

The predicted turbulent Prandtl number increases as a wall is approached. However, the results are somewhat under-predicted compared to experiments of Hirota et al. [8], especially close to the corner.

It has also been shown that the turbulent diffusivity is not constant and changes in the cross section of the ducts, as was found in the experiments of Hirota et al. [8].

To have a physically correct description of the secondary flow, local axial velocities and temperatures, advanced models are needed.

Using both the DNS data and the calculation by the presented two-equation model it is shown that the ratio R between the time-scales can be assumed to be constant in the whole region of ducts. This assumption has been extended to different fluids and in light of this a new model for prediction of the scalar fluxes is presented. Assuming that R is a universal constant then the two-equation model for the temperature variance and its dissipation rate do not need to be solved and the turbulent heat fluxes can be modeled by an algebraic equation with variable diffusivity as defined in Eq. (14). This method would be more cost effective.

Acknowledgment

This research has been financially supported partially by various projects from Swedish Energy Agency (STEM).

Nomenclature

C = constant
f = turbulent damping function

k = kinetic energy, m^2/s^2
Nu = Nusselt number
P = pressure, Pa
P_k, $P_{\theta\theta}$ P_{ε_θ} = production term
Pr = Prandtl number
Re = Reynolds number
U = velocity, m/s
u_ε = Kolmogorov velocity scale$=(\nu\varepsilon)^{0.25}$, m/s
$-\rho\overline{u_i u_j}$ = Reynolds stress, N/m^2
$\overline{u_i\theta}$ = velocity-temperature correlation, mK/s

Greek Symbols

α = diffusivity, m^2/s
ε = dissipation, m^2/s^3
η = normal distance to the nearest wall, m
μ = dynamic viscosity, kg/ms
θ = temperature, K
ρ = density, kg/m^3
τ = time-scale, s
σ = turbulent Prandtl number

Subscripts

τ = turbulent
b = bulk
c = center

References

[1] So, R. M. C., and Sommer, T. P., 1994, "A Near-Wall Eddy Conductivity Model for Fluids with Different Prandtl Numbers," ASME J. Heat Transfer, **116**, pp. 844–854.
[2] Krishnamoorthy, L. V., and Antonia, R. A., 1987, "Temperature Dissipation Measurements in a Turbulent Boundary Layer," J. Fluid Mech., **176**, pp. 265–281.
[3] Kim, J., and Moin, P., 1989, "Transport of Passive Scalars in a Turbulent Channel Flow," *Turbulent Shear Flows*, **6**, Springer, Berlin, pp. 85–96.
[4] Huser, A., and Biringen, S., 1993, "Direct Numerical Simulation of Turbulent Flow In a Square Duct," J. Fluid Mech., **257**, pp. 65–95.
[5] Gavrilakis, S., 1992, "Numerical Simulation of Low-Reynolds-number Turbulent Flow Through A Straight Square Duct," J. Fluid Mech., **244**, pp. 101–129.
[6] Su, M. D., and Friedrich, R., 1994, "Investigation of Fully Developed Turbulent Flow in a Straight Duct with Large Eddy Simulation," ASME J. Fluids Eng., **116**, pp. 677–684.
[7] Madabhushi, R. K., and Vanka, S. P., 1991, "Large Eddy Simulation of Turbulence-Driven Secondary Flow In a Square Duct," Phys. Fluids A, **3**, pp. 2734–2745.
[8] Hirota, M., Fujita, H., Yokosawa, H., Nakai, H., and Itoh, H., 1997, "Turbulent Heat Transfer in a Square Duct," Int. J. Heat Fluid Flow, **18**(1), pp. 170–180.
[9] Wilcox, D. C., 1993, *Turbulence Modeling for CFD*, DCW Industries, Inc., ISBN 0-9636051-0-0, USA.
[10] Speziale, C. G., 1987, "On Non-linear K-1 and K-ε Models of Turbulence," J. Fluid Mech., **178**, pp. 459–475.
[11] Abe, K., Kondoh, T., and Nagano, Y., 1995, "A New Turbulence Model for Predicting Fluid Flow and Heat Transfer in Separating and Reattaching Flows-II. Thermal Field Calculations," Int. J. Heat Mass Transf., **38**(8), pp. 1467–1481.
[12] Zeman, O., and Lumley, J. L., 1976, "Modeling Buoyancy Driven Mixed Layers," J. Atmos. Sci., **33**, pp. 1974–1988.
[13] Rokni, M., 1998, "Numerical Investigation of Turbulent Fluid Flow and Heat Transfer in Complex Ducts," *Doctoral thesis*, Dept. of Heat and Power Engng., Lund Inst. of Tech., Box 118, 22100 Lund, Sweden.
[14] Torii, S., and Yang, W. J., 1996, "New Near-Wall Two-Equation Model for Turbulent Heat Transport," Numer. Heat Transfer, Part A, **29**(4), pp. 417–440.
[15] Patankar, S. V., Liu, C. H., and Sparrow, E. M., 1977, "Fully Developed Flow and Heat Transfer in Ducts Having Streamwise-Periodic Variations of Cross-Sectional Area," ASME J. Heat Transfer, **99**, pp. 180–186.
[16] Müller, U., and Fiebig, M., 1997, "Instantaneous and Time Averaged 3D Flow and Temperature Structure in 2D Ribbed Channels," private communication, Ruhr-University, Bochum, Germany.
[17] Held, J., and Fuchs, L., 1998, "Large Eddy Simulation of Separated Transonic Flow Around a Wing Section," *AIAA 98-0405*, January 12–15, Reno, NV.
[18] Rhie, C. M., and Chow, W. L., 1983, "Numerical Study of the Turbulent Flow Past an Airfoil with Trailing Edge Separation," AIAA J., **21**(11), pp. 1525–1532.
[19] Rokni, M., Olsson, C. O., and Sundén, B., 1998, "Numerical and Experimental Investigation of Turbulent Flow in Rectangular Ducts," Int. J. Numer. Methods Fluids, **28**, pp. 225–242.
[20] Kim, J., Moin, P., and Moser, R., 1987, "Turbulence Statistics in Fully Developed Channel Flow at Low Reynolds Number," J. Fluid Mech., **177**, pp. 133–166.
[21] Lowdermilk, W. H., Wieland, W. F., and Livingood, J. N. B., 1954, "Measurements of Heat Transfer and Friction Coefficients for Flow of Air in Noncircular Ducts at High Surface Temperature," *NACA RM E53J07*.
[22] Kasagi, N., and Lida, O., 1999, "Progress in Direct Numerical Simulation of Turbulent Heat Transfer," *Proceedings of the 5th ASME/JSME Joint Thermal Engineering Conference*, In CD-ROM, March 15–19, San Diego, California.
[23] Kays, W. M., and Crawford, M. E., 1993, *Convective Heat and Mass Transfer*, Third Edition, McGraw-Hill, New York.
[24] Incropera, F. P., and DeWitt, D. P., 1996, *Fundamentals of Heat and Mass Transfer*, Fourth Edition, John Wiley & Sons, New York.
[25] Rokni, M., and Gatski, T. B., 2001, "Predicting Turbulent Convective Heat Transfer in Fully Developed Duct Flows," Int. J. Heat Fluid Flow, **22**, pp. 381–392.
[26] Nikuradse, J., 1930, "Untersuchungen uber Turbulente Strömungen in Nicht Kreisförmigen Rohren," Ing. Arch., **1**, pp. 306–332.

Application of a Higher Order GGDH Heat Flux Model to Three-Dimensional Turbulent U-Bend Duct Heat Transfer

K. Suga
e-mail: k-suga@mosk.tytlabs.co.jp
Senior Researcher

M. Nagaoka and N. Horinouchi

Toyota Central R & D Labs., Inc., Nagakute, Aichi, 480-1192, Japan

A higher order version of the generalized gradient diffusion hypothesis (HOGGDH) for turbulent heat flux is applied to predict heat transfer in a square-sectioned U-bend duct. The flow field turbulence models coupled with are a cubic nonlinear eddy viscosity model and a full second moment closure. Both of them are low Reynolds number turbulence models. The benefits of using the HOGGDH heat flux model are presented through the comparison with the standard GGDH. [DOI: 10.1115/1.1532018]

Keywords: Computational, Heat Transfer, Modeling, Three-Dimensional, Turbulence

1 Introduction

Understanding turbulent heat and fluid flow through curved ducts is one of the primary factors for designing cooling passages in heat exchangers and turbine blades. It is well known that owing to the curvature, pressure induced secondary motions produce significant consequences in the turbulent strain and heat transfer fields. In order to understand and predict such flow and thermal structures, many experimental and numerical studies have been made for curved ducting. Chang et al. [1] measured the detailed flow structure in a square-sectioned 180 deg U-bend duct whose curvature ratio was $Rc/D=3.35$ (Fig. 1). The corresponding thermal field was measured by Johnson and Launder [2]. These experiments revealed the appearance of a *camel back* shaped profile in the streamwise velocity at the curvature section. This characteristic flow behavior is associated with a modification of the secondary flow pattern [2].

Iacovides and Launder [3] summarized numerical studies on the

Contributed by the Heat Transfer Division for publication in the JOURNAL OF HEAT TRANSFER. Manuscript received by the Heat Transfer Division February 15, 2001; revision received September 18, 2002. Associate Editor: S. P. Vanka.

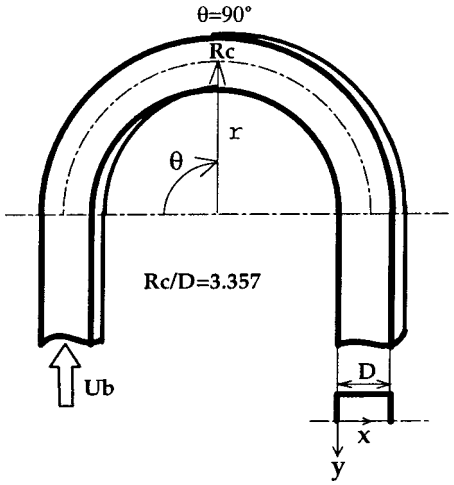

Fig. 1 Square-sectioned 180 deg U-bend duct flow

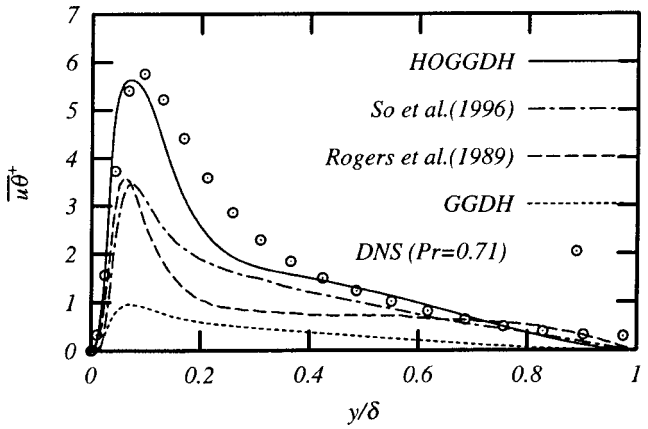

Fig. 2 Streamwise turbulent heat flux in a channel flow at Re_τ=180

blade cooling passages which had been made until early nineties. They concluded that the best way of predicting duct flows was applying a second moment closure (SMC). (They also expected that a newly emerging cubic nonlinear eddy viscosity model (NLEVM) would be validated against the curved duct heat transfer.) In fact, in their following-up paper [4] on the U-bend, they showed that full SMCs performed well to predict the characteristic *camel back* shaped velocity profiles.

In the last five years, as a newly emerged alternative approach, a cubic NLEVM has been subjected to a fair amount of testing in turbulent flow fields [5–7]. It also showed comparable performance to that of full SMCs for predicting the U-bend duct flow [8]. Successful results are thus reasonably expected in the U-bend duct heat transfer fields if it is coupled with a good turbulent heat flux model.

A turbulent heat flux model with a prescribed turbulent Prandtl number: Pr_t, has been widely used. However, Launder [9] noted that the generalized gradient diffusion hypothesis (GGDH) of Daly and Harlow [10] produced much more reliable results if near wall turbulence anisotropy was well captured. Even with the GGDH heat flux model, one cannot predict a reasonable level of the streamwise heat flux component though it is much better than that by the Pr_t model which is virtually always zero [9]. Although the streamwise heat flux component is unimportant in a fully developed wall flow, it does not necessarily mean that one can always ignore the component. Thus, several research groups (e.g., Rogers et al. [11] and So et al. [12]) tried to capture the streamwise component correctly in the context of the algebraic models. Suga and Abe [13] proposed a higher order version of the GGDH (HOGGDH) for turbulent heat flux. This model reproduces the level of the streamwise heat flux component more successfully than the other algebraic models. In fact, as shown in Fig. 2, the HOGGDH reproduces a more reasonable level of the streamwise heat flux $\overline{u\theta}$ in the turbulent channel flow than the other models.

Therefore, the present study focuses on the validation of the HOGGDH heat flux model in the square sectioned 180 deg U-bend duct flow [1,2]. Along with the heat flux models, the low Reynolds number three equation version of the cubic NLEVM (the $k-\varepsilon-A_2$ model [5]) and the low Reynolds number full SMC of Launder and Shima [14] (L-S SMC) are applied to predict the flow field turbulence.

2 Turbulent Heat Flux Models

The simplest way to deal with turbulent heat flux $\overline{u_i\theta}$ is the following form with a prescribed turbulent Prandtl number: Pr_t (which is normally assumed to be 0.9 for near wall flows) as

$$\overline{u_i\theta}=\frac{\nu_t}{\mathrm{Pr}_t}\frac{\partial\Theta}{\partial x_i} \tag{1}$$

where ν_t is the eddy viscosity and Θ is the mean temperature. But, this form has a significant drawback of its inability to produce streamwise heat flux if the streamwise temperature gradient is absent. As Launder [9] noted, the GGDH [10] is far more successful when the Reynolds stress: $\overline{u_iu_j}$, is reasonably captured all the way to the wall by a flow field turbulence model. The model form may be written as

$$\overline{u_i\theta}=-c_\theta\tau\overline{u_iu_j}\frac{\partial\Theta}{\partial x_j} \tag{2}$$

where c_θ is a model coefficient typically set as 0.3 and τ is a turbulent time scale k/ε. (In fact, the present study confirmed that c_θ=0.3 with the L-S SMC leads to reasonable thermal field predictions for turbulent channel flows.) However, after the calibration of the model performance in channel flows, Craft et al. [5] proposed a functional form of the coefficient c_θ just for their $k-\varepsilon-A_2$ model as $c_\theta=(0.3+0.2\sqrt{\hat{\varepsilon}/\varepsilon})/(1+0.5A_2^{0.5}+0.007A_2^3)$, where $A_2\equiv a_{ij}a_{ji}$, $a_{ij}\equiv\overline{u_iu_j}/k-2/3\delta_{ij}$ and $\hat{\varepsilon}=2\nu(\partial k^{1/2}/\partial x_j)^2$.

Table 1 Model coefficients and functions for the HOGGDH

c_θ	$c_{\sigma1}$	$c_{\sigma2}$	$c_{\alpha1}$
$\dfrac{0.4}{\{1-\exp(-R_t/100)\}^{1/4}}$	$0.2f_b+0.1f_{\mathrm{Pr}}$	$1-f_b-f_{\mathrm{Pr}}$	$(1-f_{\mathrm{Pr}})\left\{\dfrac{-0.5g_AS}{1+5S^2}-\dfrac{0.02\exp\{-(S/2.2)^2\}}{g_A+(S+0.2)^2}\right\}$
f_b	f_{Pr}	g_A	τ
$(1-f_{\mathrm{Pr}})^2\exp\{-(S/2.2)^2-(g_A/0.3)^2\}$	$\dfrac{1}{1+(\mathrm{Pr}/0.085)^{3/2}}$	$0.3[1-\exp\{-(R_t/70)^2\}]$	$\dfrac{k/\varepsilon}{1-\exp\{-(R_t/70)^{1/2}\}}$

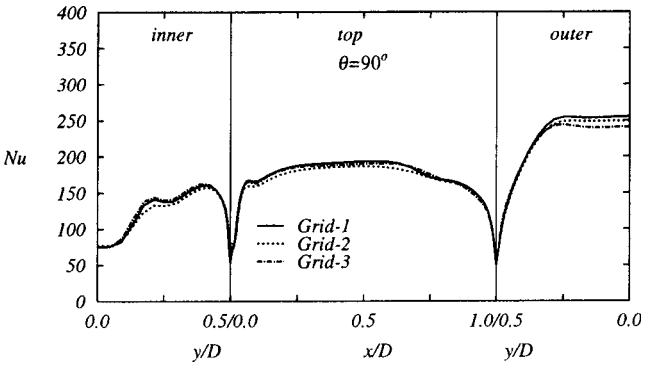

Fig. 3 Grid sensitivity of the Nusselt number distribution

This GGDH for turbulent heat flux still far underpredicts the streamwise heat flux component. Hence, Suga and Abe [13] extended the applicability of the GGDH introducing higher order (quadratic) terms and successfully reproduced each heat flux component in channel flows of a wide range of fluid Prandtl numbers. Their HOGGDH may be written as

$$\overline{u_i\theta} = -c_\theta k\tau(\sigma_{ij}+\alpha_{ij})\frac{\partial\Theta}{\partial x_j}. \tag{3}$$

The symmetric tensor σ_{ij} contains linear and quadratic terms as

$$\sigma_{ij} = c_{\sigma 1}\frac{\overline{u_iu_j}}{k} + c_{\sigma 2}\frac{\overline{u_iu_l}\,\overline{u_lu_j}}{k^2} \tag{4}$$

and the asymmetric part α_{ij} is modeled as

$$\alpha_{ij} = c_{\alpha 1}\tau\left(\Omega_{il}\frac{\overline{u_lu_j}}{k} + \Omega_{li}\frac{\overline{u_ju_l}}{k}\right) \tag{5}$$

where $\Omega_{ij}=\partial U_i/\partial x_j - \partial U_j/\partial x_i$, and U_i is the mean velocity. The set of the model coefficients and functions used is the wall flow version listed in Table 1. Note that in Table 1, $R_t=k^2/(\nu\varepsilon)$ is the turbulent Reynolds number and $S=\tau\sqrt{S_{ij}S_{ij}/2}$ is a strain parameter with $S_{ij}=\partial U_i/\partial x_j + \partial U_j/\partial x_i$. This HOGGDH was successful to predict each component of turbulent heat flux in channel flows with correctly captured near wall turbulence anisotropy [13]. Thus, for the flow field models, this study employs the cubic $k-\varepsilon-A_2$ three equation NLEVM [5] and the full low Reynolds number SMC of Launder and Shima [14] which were well calibrated to reproduce near wall Reynolds stress behavior. Note that it has been also confirmed that the HOGGDH with these flow field models performs well in turbulent channel flows in the preliminary discussion.

3 Results and Discussions

The considered bulk Reynolds number Re and the fluid Prandtl number Pr are respectively 56700 and 0.71. In this case, no separating flow was observed in the experiments [1,2]. The computational grid used extends up to the symmetry plane and consists of 121 (streamwise)$\times$81(x)$\times$41(y) (with 1$\times$D inlet and 3$\times$D outlet tangents) nodes (Grid - 1). The grid dependency of the solutions has been systematically checked. (Several other grids consisting of twice grid points such as Grid-2 (121$\times$121$\times$61) and Grid-3 (241$\times$81$\times$41) have produced less than 2 percent difference in the mean heat transfer coefficients though locally there can be found about 5 percent difference at some sections as shown in Fig. 3.) Since all the presently discussed turbulence models are low Reynolds number models, the first grid node points from the walls are located under 0.5 of the wall unit. Numerical computations have been performed by a general unstructured grid code [8] using the third order MUSCL-type scheme for the convection terms. A constant wall heat flux condition is set as the thermal

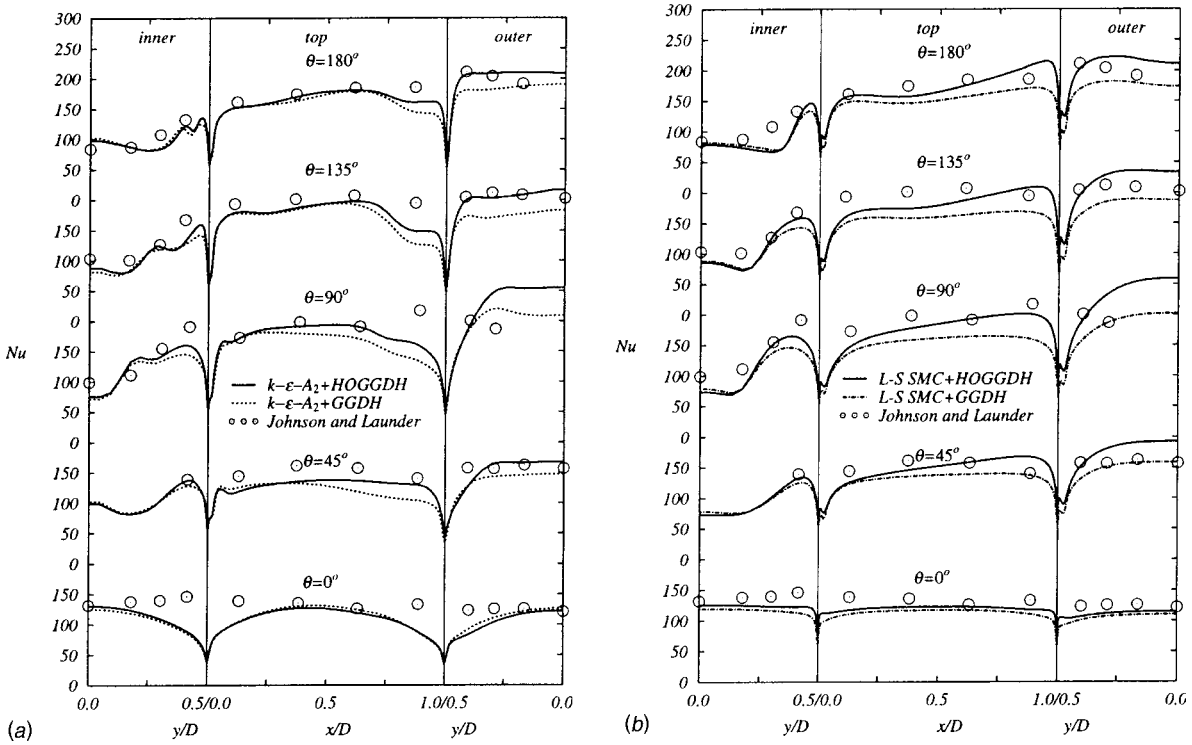

Fig. 4 Nusselt number distribution in the U-bend duct by the HOGGDH and the GGDH; (*a*) 3-eq. *cubic* NLEVM for the flow field; and (*b*) Launder-Shima SMC for the flow field

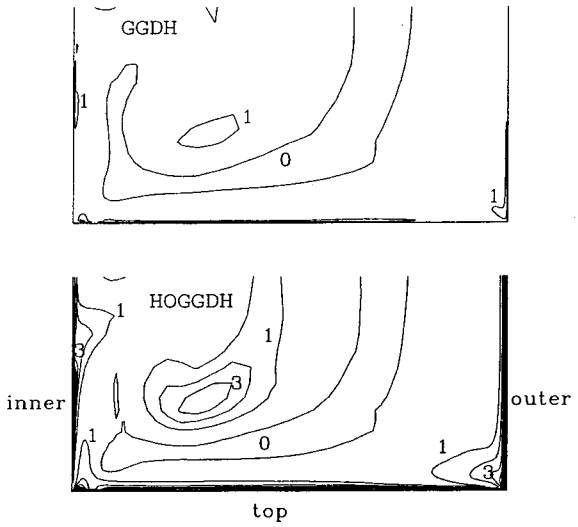

Fig. 5 Streamwise heat flux ($-\rho c_p \overline{u_\theta \theta}/q_w$) contours at the 90 deg section

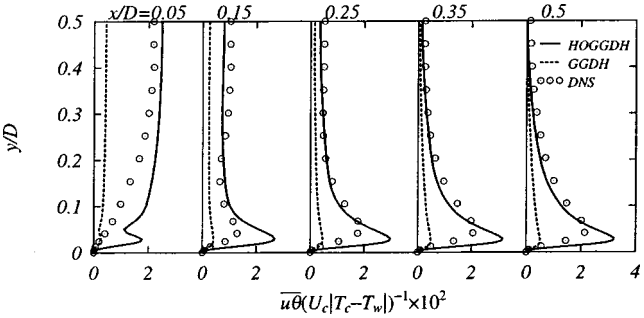

Fig. 6 Streamwise heat flux in a straight square-sectioned duct at Re=4500, Pr=0.71; DNS: Fukushima and Kasagi [15]

boundary condition. For providing the inlet conditions, separate computations of a fully developed straight duct flow have been performed.

Since the main performance of the flow field models for the present case is well documented in [4,8] (The L-S SMC is a low Reynolds number version of the basic model discussed in [4].), the present study focuses just on the thermal field. In Fig. 4, the performance of the HOGGDH heat flux model is compared with that of the standard GGDH. Figures 4(*a*) and 4(*b*) show the predicted local Nusselt number: Nu, distribution respectively with the $k-\varepsilon-A_2$ three equation NLEVM and the L-S SMC at the sections of $\theta=0$ deg, 45 deg, 90 deg, 135 deg, and 180 deg. As shown in Fig. 4(*a*), both the heat flux models predict almost the same Nu distribution at $\theta=0$ deg and the agreement between the predictions and experiments [2] becomes worse toward the corners ($x/D=0.0,1.0$). This is due to the insufficient magnitude of the predicted turbulence driven secondary flows by the NLEVM as in a square-sectioned straight duct flow [8]. However, the predicted profiles of Nu at $\theta=0$ deg with the L-S SMC are much closer to the experiments as shown in Fig. 4(*b*). In the downstream sections, Fig. 4(*a*) shows that although both the linear and the higher order GGDH perform similarly, the difference becomes larger along the outer wall and the outer region of the top wall. It is evident that the HOGGDH generally improves the predictions of the standard GGDH except for the region along the outer wall at $\theta=90$ deg. The same tendency is also found in Fig. 4(*b*) though the discrepancies between the heat flux models are slightly larger. The predicted profiles near the corner of $x/D=1.0$ in Fig. 4(*b*) show more reasonable agreement with the experiments than in Fig. 4(*a*). This also confirms that the full SMC is more reliable for predicting this type of flows.

Figure 5 compares the normalized streamwise heat flux contour maps which correspond to the $\theta=90$ deg section of Fig. 4(*a*). Obviously, the maps look very asymmetric and the HOGGDH predicts much larger values of the streamwise heat flux component, particularly near the walls. Unfortunately, there are no experimental or DNS data for the streamwise heat flux of this case. Hence, to assess them using results in a relevant flow case, Fig. 6 compares the predictions with the DNS data in a straight square-sectioned duct flow. Although the peak values are overpredicted, generally more reasonable agreement with the DNS data is obtained by the HOGGDH. This suggests that the predicted level of the heat flux in Fig. 5 by the HOGGDH is also generally closer to the reality and this results in the better prediction of the Nu distribution.

4 Conclusions

The present paper has presented the performance of the HOGGDH turbulent heat flux model in a turbulent square-sectioned U-bend duct flow. It is concluded that the HOGGDH heat flux model generally improves the prediction of the standard GGDH. This implies that it is important to take account of streamwise heat flux for predicting complex three dimensional heat flows since the HOGGDH has better performance for predicting the streamwise heat flux.

Acknowledgments

The authors thank Mr. N. Fukushima of University of Tokyo for his kindly providing the DNS data in a machine readable format.

References

[1] Chang, S. M., Humphrey, J. A. C., and Modavi, A., 1983, ''Turbulent Flow in a Strongly Curved U-bend and Downstream Tangent of Square Cross-Sections,'' Physico Chemical Hydrodynamics, **4-3**, pp. 243–269.
[2] Johnson, R. W., and Launder, B. E., 1985, ''Local Nusselt Number and Temperature Field in Turbulent Flow Through a Heated Square-Sectioned U-bend,'' Int. J. Heat Fluid Flow, **6**, pp. 171–180.
[3] Iacovides, H., and Launder, B. E., 1995, ''Computational Fluid Dynamics Applied to Internal Gas-Turbine Blade Cooling: a Review,'' Int. J. Heat Fluid Flow, **16**, pp. 454–470.
[4] Iacovides, H., Launder, B. E., and Li, H.-Y., 1996, ''Application of a Reflection-free DSM to Turbulent Flow and Heat Transfer in a Square-Sectioned U-Bend,'' Exp. Therm. Fluid Sci., **13**, pp. 419–429.
[5] Craft, T. J., Launder, B. E., and Suga, K., 1997, ''Prediction of Turbulent Transitional Phenomena With a Nonlinear Eddy-Viscosity Model,'' Int. J. Heat Fluid Flow, **18**, pp. 15–28.
[6] Chen, W. L., Lien, F. S., and Leschziner, M. A., 1998, ''Computational Prediction of Flow Around Highly Loaded Compressor-Cascade Blades with Non-Linear Eddy Viscosity Models,'' Int. J. Heat Fluid Flow, **19**, pp. 307–319.
[7] Barakos, G., and Drikakis, D., 2000, ''Investigation of Nonlinear Eddy-Viscosity Turbulence Models in Shock/Boundary-Layer Interaction,'' AIAA J., **38**, pp. 461–469.
[8] Suga, K., Nagaoka, M., Horinouchi, N., Abe, K., and Kondo, Y., 2001, ''Application of a Three Equation Cubic Eddy Viscosity Model to 3-D Turbulent Flows by the Unstructured Grid Methods,'' Int. J. Heat Fluid Flow, **22**, pp. 259–271.
[9] Launder, B. E., 1988, ''On the Computation of Convective Heat Transfer in Complex Turbulent Flows,'' ASME J. Heat Transfer, , **110**, pp. 1112–1128.
[10] Daly, B. J., and Harlow, F. H., 1970, ''Transport Equation in Turbulence,'' Phys. Fluids, **13**, pp. 2634–2649.
[11] Rogers, M. M., Mansour, N. N., and Reynolds, W. C., 1989, ''An Algebraic Model for the Turbulent Flux of a Passive Scalar,'' J. Fluid Mech., **203**, pp. 77–101.
[12] So, R. M. C., and Sommer, T. P., 1996, ''An Explicit Algebraic Heat-Flux Model for the Temperature Field,'' Int. J. Heat Mass Transf., **39**, pp. 455–465.
[13] Suga, K., and Abe, K., 2000, ''Nonlinear Eddy Viscosity Modeling for Turbulence and Heat Transfer Near Wall and Shear-Free Boundaries,'' Int. J. Heat Fluid Flow, **21**, pp. 37–48.
[14] Launder, B. E., and Shima, N., 1989, ''Second Moment Closure for the Near-wall Sublayer: Development and Application,'' AIAA J., **27**, pp. 1319–1325.
[15] Fukushima, N., and Kasagi, N., 2001, ''The Effect of Walls on Turbulent Flow and Temperature Fields,'' *Proc. Turbulent Heat Transfer 3*, Anchorage, AK, U.S.A., (CDROM).

Journal of Heat Transfer

Errata

Erratum: "Self-Preserving Properties of Unsteady Round Nonbuoyant Turbulent Starting Jets and Puffs in Still Fluids" [ASME J. Heat Transfer, 124, pp. 460–469 (2002)]

F. J. Diez, R. Sangras, O. C. Kwon, and G. M. Faeth

The formulas for the temporal variations of the maximum streamwise penetration distances of self-preserving unsteady round nonbuoyant turbulent starting jets and puffs in still fluids were stated incorrectly in the originally published paper. The correct versions can be found from conservation of the specific momentum flux, $\dot{Q}_o u_o$, for starting jets and from conservation of the specific momentum force, $Q_o u_o$, for puffs, as follows:

$$(x_p - x_o)/d = C_x((t - t_d)/t^*)^n, \tag{1}$$

where

$$t^* = d^2/(\dot{Q}_o u_o)^{1/2}, \quad n = 1/2, \quad \text{starting jet} \tag{2}$$

and

$$t^* = d^4/(\dot{Q}_o u_o), \quad n = 1/4, \quad \text{puff.} \tag{3}$$

Within the self-preserving region a specific source property, such as the source diameter, is no longer relevant and can be factored out of Eqs. (1)–(3) to yield the following compact equations for the maximum streamwise penetration distances within the self-preserving region:

$$(x_p - x_o)/((\dot{Q}_o u_o)^{1/2}(t - t_d))^{1/2} = C_x, \quad \text{starting jet} \tag{4}$$

and

$$(x_p - x_o)/((Q_o u_o)(t - t_d))^{1/4} = C_x, \quad \text{puff.} \tag{5}$$

The corresponding variations of the maximum radial penetration distances of self-preserving starting jets and puffs, however, are identical:

$$r_p/(x_p - x_o) = C_r. \tag{6}$$

Measurements of maximum streamwise and radial penetrationdistances of starting jets and puffs are plotted in Figs. 1 and 2 according to Eqs. (4)–(6). These results were obtained from new measurements over the test range considered in the original paper.

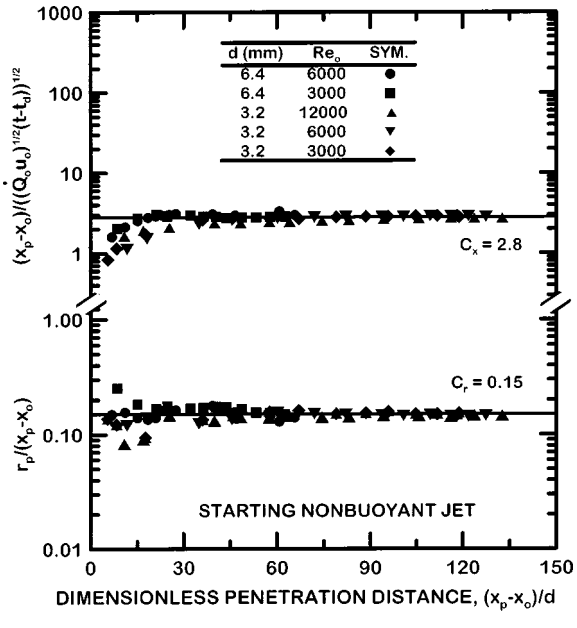

Fig. 1 Normalized streamwise and radial penetration distances as a function of normalized streamwise penetration distances for round nonbuoyant turbulent starting jets in still fluids

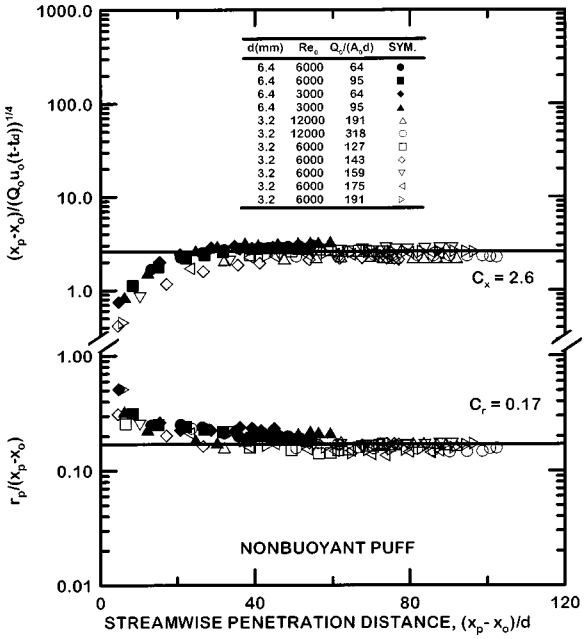

Fig. 2 Normalized streamwise and radial penetration distances as a function of normalized streamwise penetration distances for round nonbuoyant turbulent puffs in still fluids

The near-source properties of both flows vary as source properties are varied, however, self-preserving behavior satisfying Eqs. (4)–(6) is achieved for streamwise distances greater than 20–30 source diameters from the source. The various parameters of Eqs. (4)–(6), with uncertainties (95 percent confidence) shown in parentheses, are as follows:

$$C_x = 2.8(0.06), \quad C_r = 0.15(0.003), \quad x_o/d \approx 0, \quad \text{starting jet} \tag{7}$$

and

$$C_x = 2.6(0.06), \quad C_r = 0.17(0.005), \quad x_o/d = 8.5(2.0), \quad \text{puff} \tag{8}$$

where x_o/d for starting jets could not be distinguished from the exit of the source whereas x_o/d for puffs was independent of the amount of source fluid injected for the present test range, e.g., $Q_o/(A_o d) = 60-320$. This includes flows that were identified as interrupted jets, with $Q_o/(A_o d) = 159-191$, in the originally published paper.